Edited by R. d'Agostino, P. Favia,
C. Oehr, and M. R. Wertheimer

WILEY-VCH

Plasma Processes and Polymers

16th International Symposium on Plasma Chemistry
Taormina/Italy, June 22-27, 2003

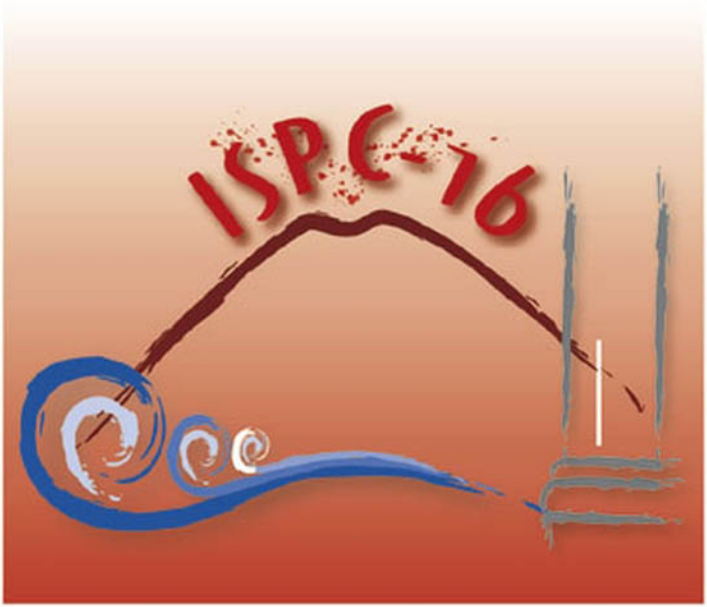

Plasma Processes and Polymers

Edited by
Riccardo d'Agostino, Pietro Favia, Christian Oehr, Michael R. Wertheimer

WILEY-VCH Verlag GmbH & Co. KGaA

Plasma Processes and Polymers

Edited by

Riccardo d'Agostino, Pietro Favia,

Christian Oehr, Michael R. Wertheimer

Plasma Processes and Polymers

Edited by
Riccardo d'Agostino, Pietro Favia, Christian Oehr, Michael R. Wertheimer

WILEY-VCH Verlag GmbH & Co. KGaA

Editors

Prof. Riccardo d'Agostino
Dipartimento di Chimica
Universita di Bari, Italy

Prof. Pietro Favia
Dipartimento di Chimica
Universita di Bari, Italy

Dr. Christian Oehr
Fraunhofer Institute for Interfacial
Engineering and Biotechnology IGB
Stuttgart, Germany

Prof. Michael R. Wertheimer
Department of Engineering Physics
Ecole Polytechnique, Montreal,
Canada

Library of Congress Card No.: applied for

British Library Cataloguing-in-Publication Data
A catalogue record for this book is available from the British Library.

Bibliographic information published by Die Deutsche Bibliothek
Die Deutsche Bibliothek lists this publication in the Deutsche Nationalbibliografie; detailed bibliographic data is available in the Internet at <http://dnb.ddb.de>.

Printed in the Federal Republic of Germany.
Printed on acid-free paper.

Composition Kühn & Weyh, Satz und Medien, Freiburg
Printing Strauss GmbH, Mörlenbach
Bookbinding Litges & Dopf Buchbinderei GmbH, Heppenheim

ISBN 3-527-40487-2

Contents

Preface

At the 16th International Symposium on Plasma Chemistry (ISPC-16) in Taormina, which took place in June 2003, we launched the idea to edit a new journal, named *Plasma Processes and Polymers*, and published by Wiley-VCH. The purpose was to collect under the same cover the great majority of articles dealing with plasma processing of polymers and related issues, which at that time were scattered throughout a vast number of journals. The new journal was intended to "correct this unfortunate situation" and to provide a home for the community working in low-temperature plasma surface modification of polymers and other materials, in applications ranging from packaging, biomedical products, displays, to components for aerospace and automotive industries, etc.

We met with such an enthusiastic response at that conference, considered the most representative forum for scientists working in the field of plasma technology, that we decided, right there and then, to solicit original papers from authors who presented suitable contributions. The present book can, therefore, be considered "Volume zero" of the journal bearing the same name, and it has the same editors and publisher. At the same time as this book will be published, the journal will be at its third issue; although still in its infancy, it is already clear that the original idea was very good, because the journal is now attracting the best articles in the world relating to this field.

Plasma Processes and Polymers, the book, is a comprehensive collection of 37 peer-reviewed articles which were presented as contributions at ISPC-16, in several different sessions dealing with low-temperature plasma processes. All of these articles have been carefully examined by the editors and by numerous referees, and the English has been revised according to the highest scientific standards.

The articles have been divided into four chapters, namely: *plasma deposition of thin films; plasma-induced grafting of functional groups; plasma in the life sciences; chemical synthesis, powders and non-equilibrium effects*. Altogether, these articles offer a good overview of recent advances in non-equilibrium low-and high-pressure glow discharges for materials processing, from fundamentals to industrial applications, from diagnostics to materials performance, and from biomedical to environmental applications. We are confident that *Plasma Processes and Polymers*, the book and the journal, will soon become the reference for materials scientists, chemists, physicists, engineers, biologists and physicians, and others who are either experts in the field

or just starting to work in it. In addition, it will constitute a very useful tool for foresightful managers who do not wish to "navigate by the stars", but want to orient themselves in a rigorous manner while "sailing on the ocean of plasma applications".

At the end of this enterprise, we like to warmly thank Ms Grazia Retto and Ms Roberta Giordano, from the staff at the University of Bari, who have dedicated for almost one year their professional care and great dedication to this project.

We hope that you will enjoy reading this book as much as we enjoyed editing it!

Riccardo d'Agostino
Pietro Favia
Christian Oehr
Michael R. Wertheimer

List of Contributors

d'Agostino, R.
Department of Chemistry, University of Bari, Bari, Italy

Aoucher, M.
Laboratoire de physique des matériaux, Equipe couches minces et semiconducteurs, Faculté de Physique, El Alia, Bab-ezzouar, Alger, Algérie

Argitis, P.
Institute of Microelectronics, NCSR "Demokritos", Athens, Greece

Aréfi-Khonsari, F.
LGPPTS, E.N.S.C.P., Paris, France

Balazs, D. J.
Laboratory for Functional Fibers and Textiles, Swiss Federal Laboratories for Materials Testing and Research (EMPA), St. Gallen, Switzerland

Balazs, D. J.
Materials Science Institute, Swiss Federal Institute of Technology (EPFL), Lausanne, Switzerland

Bayiati, P.
Institute of Microelectronics-NCSR "Demokritos", Athens, Greece

Bellas, V.
Institute of Microelectronics, NCSR "Demokritos", Athens, Greece

van Berkel, J. J. B. N.
Department of Biomedical Engineering, Eindhoven University of Technology, Eindhoven, The Netherlands

Bertrand, P.
PCPM, Université Catholique de Louvain, Louvain-la-Neuve, Belgique

Bobin, S.
Biomatech, Chasse sur Rhone, France

Brani, O.
Institute of Microelectronics, NCSR "Demokritos", Athens, Greece

Bratescu, M. A.
Division of Electronics and Information Engineering, Hokkaido University, Sapporo, Japan

Cardinaud, C.
Laboratoire des Plasmas et des Couches Minces, Institut des Materiaux, Nantes, France

Cartry, G.
Laboratoire des Plasmas et des Couches Minces, Institut des Materiaux, Nantes, France

Chen, Z.
College of Sciences, Donghua University, Shanghai, China

Constantoudis, V.
Institute of Microelectronics, NCSR "Demokritos", Athens, Greece

De Mitri, R.
European Commission, Joint Research Centre, Institute for Health and Consumer Protection, Ispra, Italy

Debarnot, D.
Laboratoire Polymères, Colloïdes, Interfaces, Université du Maine, Le Mans, France

Detomaso, L.
Department of Chemistry, Institute of Inorganic Methodologies and Plasmas (IMIP), University of Bari, Bari, Italy

Deyneka, A.
Institute of Physics, Academy of Sciences of the Czech Republic, Prague, Czech Republic

Đorđević, A. R.
Faculty of Electrical Engineering, University of Belgrade, Belgrade, Serbia and Montenegro

Durand, A. E.
Institut de Chimie de la Matière Condensée de Bordeaux (ICMCB-CNRS), Université Bordeaux, Pessac, France.

Durand, S.
Laboratoire Polymères, Colloïdes, Interfaces, Université du Maine, Le Mans, France

Eichhorn, K.-J.
Institute of Polymer Research Dresden, Dresden, Germany

Eloy, R.
Biomatech, Chasse sur Rhone, France

Eon, D.
Laboratoire des Plasmas et des Couches Minces, Institut des Materiaux, Nantes, France

Farrera, E.
Escuela de Química, Facultad de Ciencias, Universidad Central de Venezuela, Caracas, Venezuela

Favia, P.
Department of Chemistry, University of Bari, Bari, Italy

Finke, B.
Materials Science Institute, Swiss Federal Institute of Technology (EPFL), Lausanne, Switzerland

Fortov, V.
Institute of Problems of Chemical Physics, Chernogolovka, Russia

Fortov, V. E.
Institute for High Energy Densities, Russian Academy of Sciences, Moscow, Russia

Friedrich, J.
Federal Institute for Materials Research and Testing (BAM), Berlin, Germany

Gerlach, G.
Institute for Solid State Electronics, Dresden University of Technology, Dresden, Germany

Giba, Z.
Institute of Botany, Faculty of Biology, University of Belgrade, Belgrade, Serbia and Montenegro

Gisbert-Soler, S.
AIJU Toy Research Institute, Ibi (Alicante), Spain

Glidle, A.
Nanoelectronics Research Centre, Department of Electronics and Electrical Engineering, Glasgow University, Glasgow, United Kingdom

Gogolides, E.
Institute of Microelectronics, NCSR "Demokritos", Athens, Greece

Gristina, R.
Institute of Inorganic Methodologies and Plasmas, Bari, Italy

Grubišić, D.
Institute for Biological Research "Siniša Stanković", Belgrade, Serbia and Montenegro

Guenther, M.
Institute for Solid State Electronics, Dresden University of Technology, Dresden, Germany

Guo, Y.
College of Sciences, Donghua University, Shanghai, China

Hanic, F.
Institute of Measurement Science, Slovak Academy of Sciences, Bratislava, Slovakia

Harms, H.
Institute of Environmental Science and Technology, Swiss Federal Institute of Technology (EPFL), Lausanne, Switzerland

Hegemann, D.
Swiss Federal Laboratories for Material Testing and Research EMPA, St. Gallen, Switzerland

Henda, K.
Centre de Développement des Technologies Avancées, Division des milieux ionisés & Lasers, Baba Hassan, Alger, Algérie

Hirose, A.
Plasma Physics Laboratory, University of Saskatchewan, Saskatoon, Canada

Hodson, C.
Oxford Instruments Plasma Technology, Bristol, United Kingdom

Iacobelli, L.
Department of Chemistry, University of Bari, Bari, Italy

Iacoviello, G.
Department of Chemistry, University of Bari, Bari, Italy

Ivanov, A.
RCC "Kurchatov Institute", Moscow, Russia

Janca, J.
Department of Physical Electronics, Masaryk University, Brno, Czech Republic

Jastrabik, L.
Institute of Physics, Academy of Sciences of the Czech Republic, Prague, Czech Republic

Kado, S.
Department of Mechanical and Control Engineering, Tokyo Institute of Technology, Tokyo, Japan

Karpiński, L.
Institute of Plasma Physics and Laser Microfusion, Warszawa, Poland

Kawajirim, K.
Institute of Fluid Science, Tohoku University, Sendai, Japan

Khrapak, A. G.
Institute for High Energy Densities, Russian Academy of Sciences, Moscow, Russia

Kieft, E. R.
Department of Applied Physics, Eindhoven University of Technology, Eindhoven, The Netherlands

Kieft, I. E.
Department of Biomedical Engineering, Eindhoven University of Technology, Eindhoven, The Netherlands

Kijeński, J.
Industrial Chemistry Research Institute, Warsaw, Poland

Kimura, Y.
Department of Mechanical and Control Engineering, Tokyo Institute of Technology, Tokyo, Japan

Kinsey, C. R.
Oxford Instruments Plasma Technology, Bristol, United Kingdom

Kodama, S.
Department of Chemical Engineering, Tokyo Institute of Technology, Tokyo, Japan

Krawczyk, I.
Faculty of Process and Environmental Engineering, Technical University of Lodz, Lodz, Poland

Kudrle, V.
Department of Physical Electronics, Masaryk University, Brno, Czech Republic

Kuznetsov, A. V.
The Research Center for Biomaterials, Research Institute of Transplantology and Artificial Organs, Moscow, Russia

Kühn, G.
Federal Institute for Materials Research and Testing (BAM), Berlin, Germany

Labrugère, C.
Institut de Chimie de la Matière Condensée de Bordeaux (ICMCB-CNRS), Université Bordeaux, Pessac, France.

Lahmar, H.
Centre de Développement des Technologies Avancées Division des milieux ionisés & Lasers, Baba Hassan, Alger, Algérie

Laurens, P.
LALP-CNRS, Arcueil, France

Liang, J.
Department Of Materials Science and Technology, University of Cincinnati, Cincinnati, Ohio, USA

Lopez, L. C.
Department of Chemistry, Institute of Inorganic Methodologies and Plasmas (IMIP), University of Bari, Bari, Italy

Martín-Martínez, J. M.
Adhesion and Adhesives Laboratory, Department of Inorganic Chemistry, University of Alicante, Alicante, Spain

Martínez-García, A.
AIJU Toy Research Institute, Ibi (Alicante), Spain

Mathieu, H. J.
Materials Science Institute, Swiss Federal Institute of Technology (EPFL), Lausanne, Switzerland

Mejía, A.
Escuela de Química, Facultad de Ciencias, Universidad Central de Venezuela, Caracas, Venezuela

Milella, A.
Department of Chemistry, University of Bari, Bari, Italy

Misiakos, K.
Institute of Microelectronics-NCSR "Demokritos", Athens, Greece

Mitin, V.
Institute for Inorganic Materials, Moscow, Russia

Mix, R.
Federal Institute for Materials Research and Testing (BAM), Berlin, Germany

Molotkov, V. I.
Institute for High Energy Densities, Russian Academy of Sciences, Moscow, Russia

Morva, I.
Faculty of Mathematics, Physics and Informatics, Comenius University, Bratislava, Slovakia

Morvová, M.
Faculty of Mathematics, Physics and Informatics, Comenius University, Bratislava, Slovakia

Müller, M.
Fraunhofer Institute for Interfacial Engineering and Biotechnology IGB, Stuttgart, Germany

Nishiyama, H.
Institute of Fluid Science, Tohoku University, Sendai, Japan

Nozaki, T.
Department of Mechanical and Control Engineering, Tokyo Institute of Technology, Tokyo, Japan

Oehr, C.
Fraunhofer Institute for Interfacial Engineering and Biotechnology IGB, Stuttgart, Germany

Ohl, A.
Materials Science Institute, Swiss Federal Institute of Technology (EPFL), Lausanne, Switzerland

Okazaki, K.
Department of Mechanical and Control Engineering, Tokyo Institute of Technology, Tokyo, Japan

Van Ooij, W. J.
Department Of Materials Science and Technology, University of Cincinnati, Cincinnati, Ohio, USA

Opalińska, T.
Industrial Chemistry Research Institute, Warsaw, Poland

Opalska, A.
Industrial Chemistry Research Institute, Warsaw, Poland

Ortiz-Magán, A. B.
Adhesion and Adhesives Laboratory, Department of Inorganic Chemistry, University of Alicante, Alicante, Spain

Ouchabane, M.
Centre de Développement des Technologies Avancées, Division des milieux ionisés & Lasers, Alger, Algérie

Pal, A.
Institute of Nuclear Physics, Moskow State University, Gory, Moskow, Russia

Pascu, M.
Laboratoire Polymères, Colloïdes, Interfaces, Université du Maine, Le Mans, France

Pastor-Blas, M. M.
Adhesion and Adhesives Laboratory, Department of Inorganic Chemistry, University of Alicante, Alicante, Spain

Patiño, P.
Escuela de Química, Facultad de Ciencias, Universidad Central de Venezuela, Caracas, Venezuela

Petit, S.
LALP-CNRS, Arcueil, France

Petrov, O. F.
Institute for High Energy Densities, Russian Academy of Sciences, Moscow, Russia

Petrović, Z. L.
Institute of Physics, Zemun, Serbia and Montenegro

Poncin-Epaillard, F.
Laboratoire Polymères, Colloïdes, Interfaces, Université du Maine, Le Mans, France

Poustylnik, M. Y.
Institute for High Energy Densities, Russian Academy of Sciences, Moscow, Russia

Puač, N.
Institute of Physics, Zemun, Serbia and Montenegro

Ramachandran, K.
Institute of Fluid Science, Tohoku University, Sendai, Japan

Rossi, F.
European Commission, Joint Research Centre, Institute for Health and Consumer Protection, Ispra, Italy

Ryabinkin, A.
Institute of Nuclear Physics, Moskow State University, Gory, Moskow, Russia

Sahre, K.
Institute of Polymer Research Dresden, Dresden, Germany

Sakai, Y.
Division of Electronics and Information Engineering, Hokkaido University, Sapporo, Japan

Sakura, N.
Division of Electronics and Information Engineering, Hokkaido University, Sapporo, Japan

Sammynaiken, R.
Department of Chemistry, University of Saskatchewan, Saskatoon, Canada

Sardella, E.
Department of Chemistry, University of Bari, Bari, Italy

Schmidt-Szałowski, K.
Faculty of Chemistry, Warsaw University of Technology, Warsaw, Poland

Schröder, K.
Materials Science Institute, Swiss Federal Institute of Technology (EPFL), Lausanne, Switzerland

Schütz, U.
Swiss Federal Laboratories for Materials Testing and Research EMPA, St. Gallen, Switzerland

Sciarratta, V.
Fraunhofer Institute for Interfacial Engineering and Biotechnology, Stuttgart, Germany

Segura-Domingo, A.
AIJU Toy Research Institute, Ibi (Alicante), Spain

Sekiguchi, H.
Department of Chemical Engineering, Tokyo Institute of Technology, Tokyo, Japan

Sekkal, A.
Centre de Développement des Technologies Avancées, Division des milieux ionisés & Lasers, Alger, Algérie

Senesi, G. S.
Institute of Inorganic Methodologies and Plasmas, Bari, Italy

Serov, A.
Institute of Nuclear Physics, Moskow State University, Gory, Moskow, Russia

Sevastianov, V. I.
The Research Center for Biomaterials, Research Institute of Transplantology and Artificial Organs, Moscow, Russia

Shi, Ch.
College of Sciences, Donghua University, Shanghai, China

Shi, D.
Department Of Materials Science and Technology, University of Cincinnati, Cincinnati, Ohio, USA

Shulga, Y. M.
Institute of Problems of Chemical Physics, Moscow, Russia

Sim, C.
Nanoelectronics Research Centre, Department of Electronics and Electrical Engineering, Glasgow University, Glasgow, United Kingdom

Singh A.
Plasma Physics Laboratory, University of Saskatchewan, Saskatoon, Canada

Skryleva, E.
Institute of Problems of Chemical Physics, Chernogolovka, Russia

Starostin, A.
RCC "Kurchatov Institute", Moscow, Russia

Stoffels, E.
Department of Biomedical Engineering, Eindhoven University of Technology, Eindhoven, The Netherlands

Storr, M.
Gambro dialysators GmbH & Co. KG, Hechingen, Germany

Suchaneck, G.
Institute for Solid State Electronics, Dresden University of Technology, Dresden, Germany

Suda, Y.
Division of Electronics and Information Engineering, Hokkaido University, Sapporo, Japan

Sugawara, H.
Division of Electronics and Information Engineering, Hokkaido University, Sapporo, Japan

Sun, L.
College of Sciences, Donghua University, Shanghai, China

Sánchez-Reche, A.
AIJU Toy Research Institute, Ibi (Alicante), Spain

Talsky, A.
Department of Physical Electronics, Masaryk University, Brno, Czech Republic

Tegou, E.
Institute of Microelectronics, NCSR "Demokritos", Athens, Greece

Torchinsky, V. M.
Institute for High Energy Densities, Russian Academy of Sciences, Moscow, Russia

Tressaud, A.
Institut de Chimie de la Matière Condensée de Bordeaux (ICMCB-CNRS), Université Bordeaux, Pessac, France

Triandafillu, K.
Institute of Environmental Science and Technology, Swiss Federal Institute of Technology (EPFL), Lausanne, Switzerland

Tserepi, A.
Institute of Microelectronics, NCSR "Demokritos", Athens, Greece

Tyczkowski, J. I.
Faculty of Process and Environmental Engineering, Technical University of Lodz, Lodz, Poland

Ulejczyk, B.
Faculty of Chemistry, Warsaw University of Technology, Warsaw, Poland

Vasilets, V. N.
The Research Center for Biomaterials, Research Institute of Transplantology and Artificial Organs, Moscow, Russia

Vohrer, U.
Fraunhofer Institute for Interfacial Engineering and Biotechnology IGB, Stuttgart, Germany

Vourdas, N.
Institute of Microelectronics, NCSR "Demokritos", Athens, Greece

Wang, Y.
College of Sciences, Donghua University, Shanghai, China

Wilkinson, C. D. W.
Nanoelectronics Research Centre, Department of Electronics and Electrical Engineering, Glasgow University, Glasgow, United Kingdom

Wolf, B.
Dept. of Computer Science, Electr. and Mech. Engineering, University of Applied Sciences, Senftenberg, Germany

Woźniak, B.
Leather Research Institute, Lodz, Poland

Xie, H.
College of Sciences, Donghua University, Shanghai, China

Yamaoka, D.
Division of Electronics and Information Engineering, Hokkaido University, Sapporo, Japan

Yang, P. J. Q.
College of Sciences, Donghua University, Shanghai, China

Yang, Q.
Plasma Physics Laboratory, University of Saskatchewan, Saskatoon, Canada

Zhang, J.
College of Sciences, Donghua University, Shanghai, China

Zhou, H.
Nanoelectronics Research Centre Department of Electronics and Electrical Engineering, Glasgow University, Glasgow, United Kingdom

Zhou, R.
College of Sciences, Donghua University, Shanghai, China

Zhu, F.
College of Sciences, Donghua University, Shanghai, China

Zieliński, T.
Industrial Chemistry Research Institute, Warsaw, Poland

Živković, S.
Institute for Biological Research "Siniša Stanković", Belgrade, Serbia and Montenegro

Part I
Plasma Deposition of Thin Films

1
Polymer Surface Modification with Monofunctional Groups of Different Type and Density

J. Friedrich, G. Kühn, R. Mix

Abstract

The retention of chemical structure and functional groups during pulsed-plasma polymerisation was used for producing adhesion-promoting plasma polymer layers with high concentrations of exclusively one sort of functional groups such as OH, NH_2, or COOH. The maximum content of functional groups was 31 OH using allyl alcohol, 18 NH_2 using allylamine, or 24 COOH groups per 100 C atoms using acrylic acid. To vary the density of functional groups a chemical copolymerisation with ethylene as "chain-extending" comonomer or butadiene as "chemical crosslinker" was initiated in the pulsed plasma.

The composition of these copolymers was investigated by XPS and IR spectroscopy. The concentration of functionalities was measured by XPS after attaching fluorine-containing derivatives. These labelling reactions were audited with reference substances and different markers. A set of plasma parameters was found to be a compromise between a high number of functional groups and complete dissolubility in water, ethanol or THF as needed for further chemical processing. Here, these monotype functionalised polymers are used in metal-polymer composites as an adhesion-promoting interlayer to examine the influence of type and density of functional groups on the adhesion.

1.1
Introduction

The aim of this work was to produce plasmachemically monotype functionalized polymer surfaces as models for the investigation of the influence of each type of metal-functionality interactions to the adhesion (Fig. 1). Moreover, the density of monosort functionalization with different types of functional groups (OH, NH_2 and COOH) should be varied to study the influence of the concentration of metal-functional group anchoring points (Fig. 2). Three ways to produce monotype functionalized polymer surfaces were investigated, the O_2-plasma treatment with subsequent wet-chemical reduction (vitride-Na-complex, B_2H_6, $LiAlH_4$) of the majority of O functional groups to OH groups (process 1, Fig. 3), the pulsed-plasma polymeriza-

tion of functional groups carrying monomers under retention of their functionalities (process 2, Fig. 3) and, in the same way as the pulsed-plasma polymerization, the plasma-initiated (chemical) copolymerization for varying the concentration of monotype functional groups (process 3, Fig. 3). In this work processes 2 and 3 were investigated, whereas process 1 was studied previously [1].

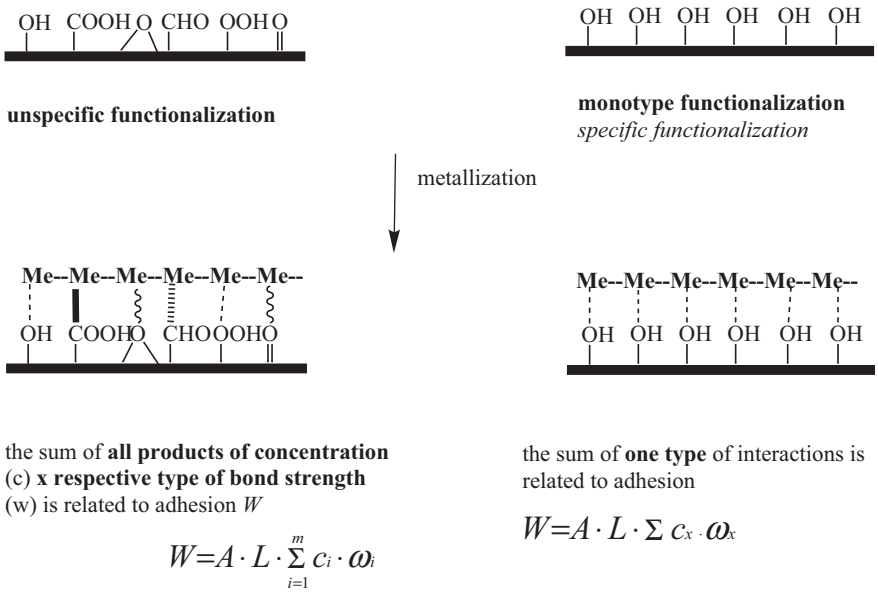

Figure 1 Scheme of unspecific and monotype surface functionalization of polymers. Attached a tentative model of summation of each type of metal-functionality interactions resulting in the global adhesion (W-adhesion, A-area, L-Loschmidt/Avogadro constant, c-concentration, ω-binding energy).

The general concept for the plasma polymerization was to approximate the structure of plasma polymers to that of classic polymers as much as possible. Therefore, low power input to the plasma, substrate and growing plasma polymer layer seems to be necessary because the average energy input per monomer molecule has to be <0.01 eV for a classic (pure chemical) radical polymerization. Thus, the constant energy flux in continuous wave (cw) plasma is too high. Pulsed plasma with long off-time offers an alternative and possibly a tool to initiate pure chemical chain propagations (Fig. 4).

Using chemically reactive monomers, which are qualified to undergo a classic radical chain propagation only one activation incident with ≈1.5 eV is required to start a chain polymerization with a resulting molar mass of about 100 000 and the respective polymerization degree of $X \approx 1000$. Therefore, 0.0015 eV per monomer are needed to initiate and propagate a chemical polymerization (Fig. 5). The advantage of a chemically produced polymer compared to a plasmachemically synthesized material is the defined structure, the exact stoichiometry, often the presence of a su-

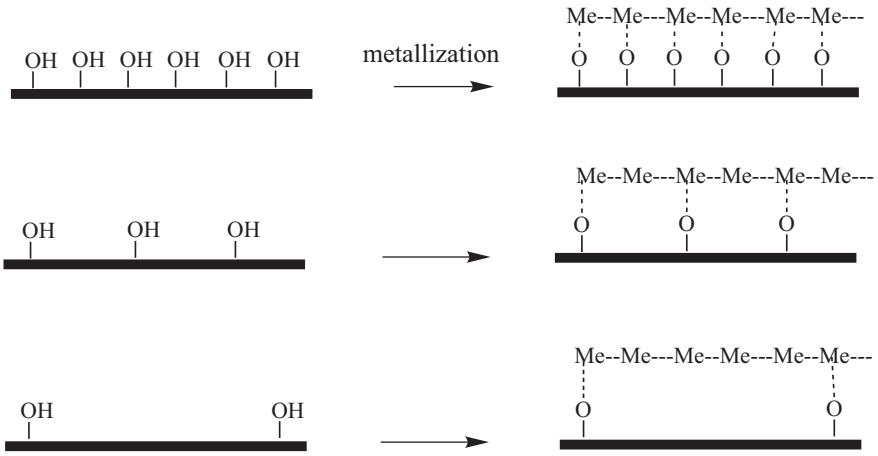

Figure 2 Schematic presentation of adhesion in dependence on concentration of metal-functional groups anchoring points.

permolecular structure (crystallinity), the defined properties and the significantly better ageing stability. Thus, we intend to exclusively initiate such a chemical polymerization through the plasma but the chain propagation should be performed on a pure chemical way. Monomers with active double bonds as vinyl or acrylic groups or moderately qualified allyl groups and dienes are a precondition of such a chemical chain propagation. Using nonclassic monomers and the cw mode only a nonchemical formation of low-quality polymer layers is possible. Examples for nonqualified monomers are alkanes (hexane), aromatic, cyclic, etc., monomers.

In practice, the low pressure and, therefore, the low sticking rate of monomers with a radical site of a growing macromolecular chain limit the chain propagation. Such termination reactions are radical recombination, chain transfer and disproportionation.. Therefore, the use of pulsed plasma is necessary to reinitiate the chain propagation. Short plasma pulses (0.01 to 1 ms) activate the monomer molecules and the surface of the growing polymer layer. During the plasma-off period reactive monomer molecules strike the radical sites at the polymer surface, graft and thus form the growing macromolecular chain. The chain propagation is a pure chemical process. Using typical pulse conditions as 0.1 ms plasma-on and 1 ms plasma-off the very reactive monomer styrene forms a polymer layer during every pulse that is thinner than <0.1-monolayer styrene. Comparing the deposition rates of cw r.f. plasma and pulsed r.f. plasma a difference of 1:2000 was found if the deposition rates were referenced to the same plasma-on durations. This difference in deposition rates demonstrates the dominant role of the chemical chain propagation using the pulsed plasma. Obviously the plasma polymerization in the cw plasma mode can be characterized as a process of only a slight preponderance of the deposition in comparison to the simultaneous plasma etching/sputtering of the growing polymer layer.

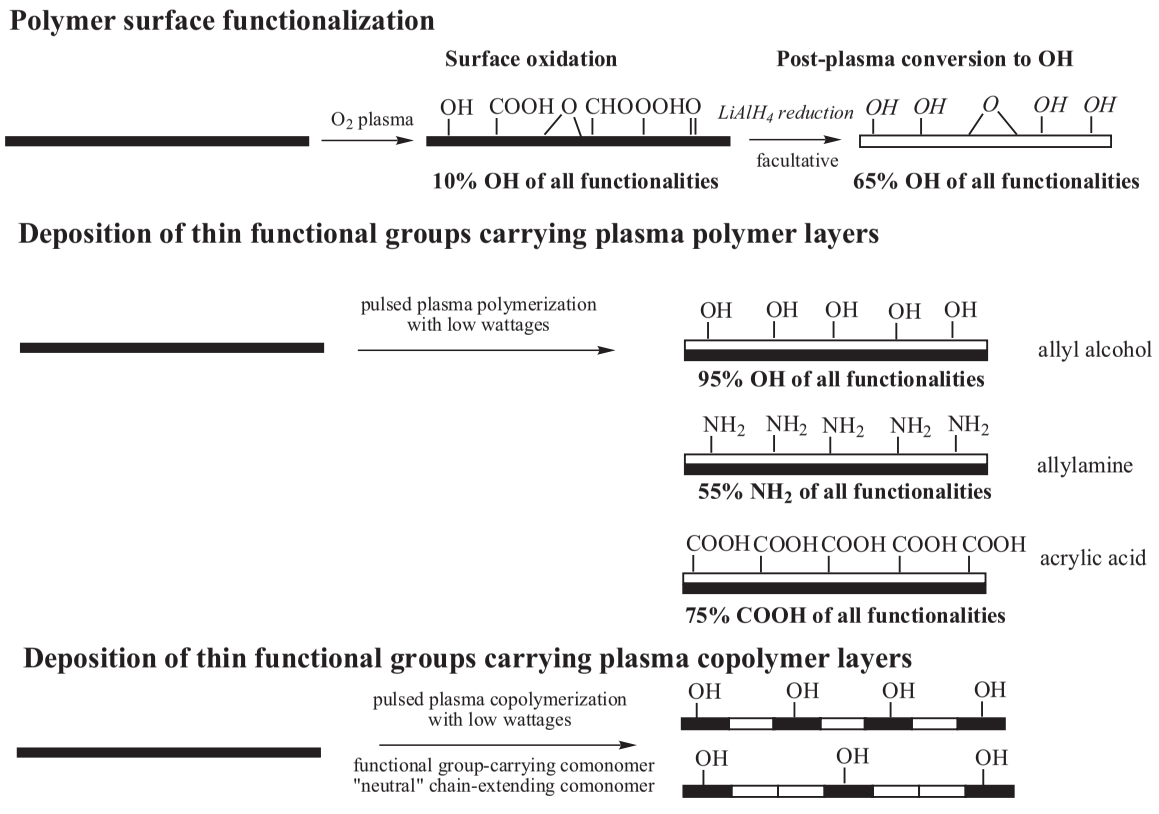

Figure 3 General ways to produce monotype functionalised polymer surface with different types and variable concentration of functional groups using the plasma and chemical techniques. Selectivity is given in per cent of all measured functional groups.

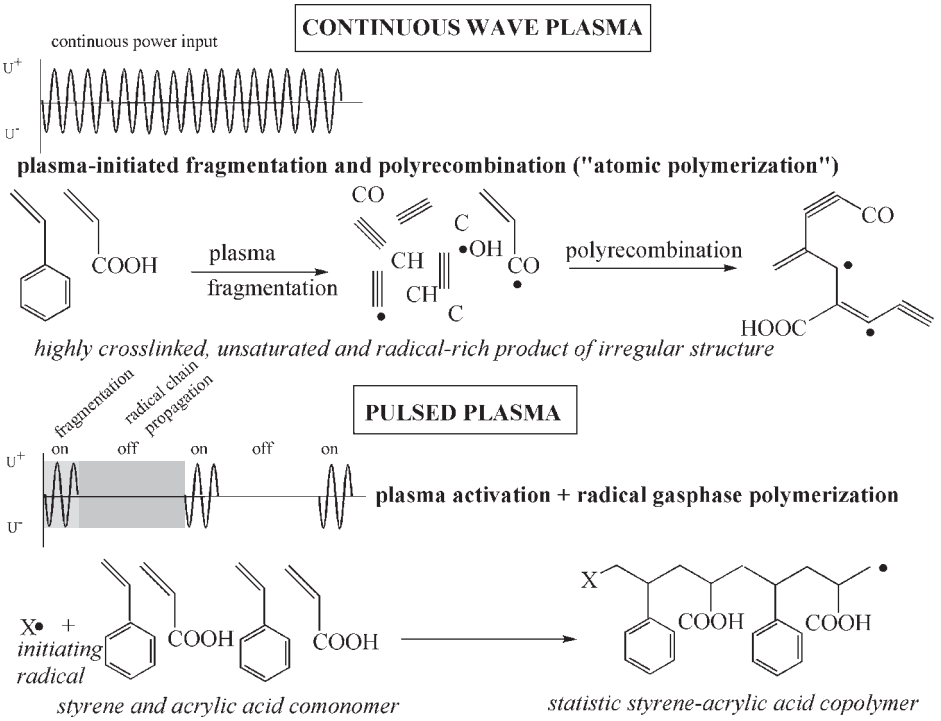

Figure 4 Principle of continuous-wave and pulsed plasmas and the expected structures of resulting plasma polymers.

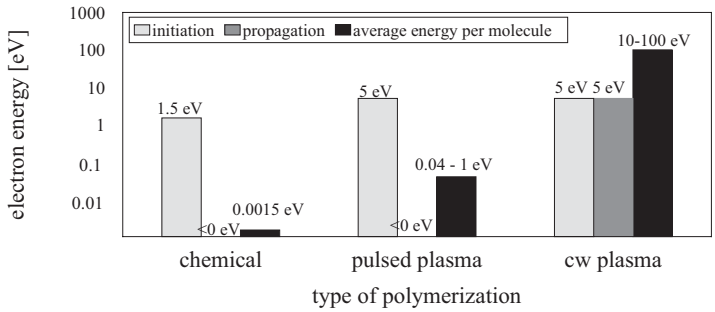

Figure 5 Comparison of energies needed for the initiation of a radical polymerization and the average kinetic energies available in different modes of low-pressure glow-discharge plasmas (pulsed plasma and cw = continuous-wave plasma; without consideration of plasma UV, self-bias, etc.).

The structure of polymer sequences formed in the plasma-off period should correspond to those of classic polymers. However, the more degrees of freedom for adsorbing molecules in the low-pressure gas phase compared to polymerizations in the liquid phase should hinder all types of supermolecular structure or tacticity. Only amorphous and atactic polymers are anticipated. Nevertheless, such structures are also chemically defined. However, these defined structures and compositions are strongly disturbed by every new plasma pulse due to the UV irradiation and particle bombardment. In addition, no hints for a significant contribution of ion–molecule reactions to the polymer formation were identified on analyzing the polymer structure. The monomers used are all qualified for a radical and not for ionic polymerizations in the gas phase.

In 1971, Westwood [2] found that the plasma polymers possess a chemically better defined structure and composition using low power input, however, unfortunately, thus-produced polymers are also characterized by inclusions of oligomers and monomers within the partially crosslinked polymer matrix. Tibbitt et al. [3] proposed an actual model of such a plasma polymer. Pulsed low-power plasma helps to avoid the excessive monomer fragmentation in the plasma phase and reduces the number of plasma-induced damages in the polymers. This opens the way for enhancing the pure chemical radical polymerization in the gas phase or adsorption layer. Pulsed-plasma polymerization was introduced first by Tiller in 1972 [4], later continued by Yasuda [5,6], Shen and Bell [7,8], and then further developed by Timmons [9,10] and our group [11–14].

The copolymerisation in pulsed plasmas was designed as a plasma-initiated (chemical) radical chain propagation reaction preferentially in the plasma-off period [13,14]. This kind of copolymerisation is strictly different from those introduced by Schüler or Yasuda [15,16]. They simply mixed two gases or monomers without any consideration of their chemical reactivities. Using the cw plasma, which fragments all monomer molecules and allows their random recombination as nondefined plasma polymers, the reactivity of comonomers does not play any role. However, the more the chemical reactions dominate the more important the chemical copolymerisation ability of comonomers becomes. In polymer chemistry this behavior is expressed in terms of copolymerisation parameters (coefficients) r_a and r_b for free-radical copolymerizations to linear, branched or crosslinked copolymers [17]. For $r_i = r_a$ and $r_i = r_b$ two of five cases are important: $r_i = 1$ both comonomers add to any active center with equal probability if [A] = [B] and $r_i = ($ only homopolymerization occurs, no copolymerization. Hence, the pairs of comonomers must be accurately compiled to avoid homopolymerization. An example for a genuine classic copolymerisation is that of styrene and methylmethacrylate with $r_s = 0.52$ and $r_m = 0.46$. Vinyl, acrylic, allyl and diene comonomers are generally suited for plasma copolymerization. In Fig. 6 examples of co- and homopolymerization and also chemical crosslinking in the pulsed plasma are shown.

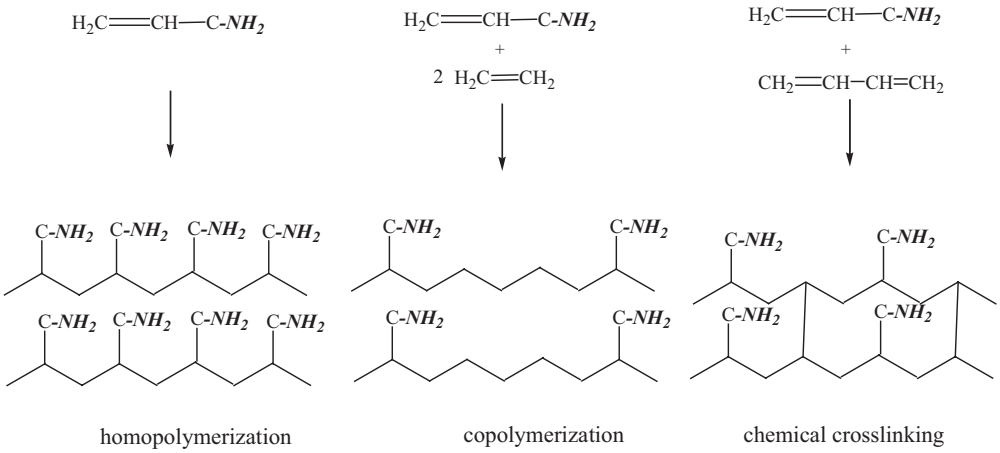

Figure 6 Schematics on the formation of functional group carrying homo and copolymers as well as chemically crosslinked copolymers.

1.2 Experimental

Plasma polymerisations were carried out in a vacuum system with a base pressure of 10^{-3} Pa or lower. The principal design of the plasma reactor was described earlier [12,13]. The r.f. power was varied from 50 to 300 W, the duty cycle from 0.05 to 1 and the pressure was 25 Pa. The samples are kept under floating potential. The XPS data acquisition was performed with a SAGE 150 Spectrometer (Specs, Berlin, Germany) using nonmonochromatized MgK_α or AlK_α radiation with 12.5 kV and 250 W settings at a pressure $\approx 10^{-7}$ Pa in the analysis chamber. This instrument is equipped with a plasma reactor separated by a gate valve from the UHV system, where surface treatments can be carried out at a pressure of 10^{1}–10^{-7} Pa. XPS spectra were acquired in the constant analyser energy (CAE) mode at 90° take-off angle. Peak analysis was performed using the peak fit routine from Specs. The FTIR spectra were recorded with a NEXUS instrument (Nicolet, USA) using the ATR technique (attenuated total reflectance) with a diamond cell ("Golden Gate", Specac, Kent, UK). Contact-angle measurements were performed in the sessile drop mode using water, formamide, ethylene glycol, benzyl alcohol and diiodomethane as test liquids. The equipment consists of a G2 goniometer and the appropriate software (Kruess, Hamburg, Germany). The derivatization of OH groups was performed using trifluoroacetic anhydride (TFAA) or m-trifluoromethylphenylisocyanate (TMPI), that of NH_2 by applying pentafluorobenzaldehyde (PFBA) or 4-trifluoromethylbenzaldehyde (TFMBA) and that of COOH by exposure to trifluoroethanol (TFE) [1,11]. The number of functional groups was calculated by considering the percentage of the introduced fluorine (F1s peak) and the theoretical stoichiometry of the derivatized polymer. It was supposed that the XPS analysed outermost layer (≈ 3 nm) was

homogeneously derivatized. The completeness of the derivatization and the absence of nonconsumed functional groups in the deposited polymer layer were checked using ATR-FTIR spectroscopy. Further methods were the C1s peak fitting (CF_3, COOR) or the measuring of the concentrations of introduced oxygen (OH, COOH – O1s peak) or introduced nitrogen (NH_2 – N1s peak). The metal evaporation onto plasma-polymer-modified PP foils was performed in situ by using a plasma reactor equipped with two sources for thermal evaporation (Ilmplasma 1200, Saskia, Ilmenau, Germany). This technique was applied for analytical purposes. For measuring the peel strength the samples are transferred to a metallizer equipped with the electron beam technique (Edwards, UK). The 90° peeling technique of metal-PP composites follows DuPont's preparation and peeling procedure. It was described in detail elsewhere [18–20].

1.3 Results

1.3.1 Kinetics of the Deposition of Copolymers

In Fig. 7 the deposition rates of different copolymerized mixtures of allyl alcohol and allylamine with ethylene, styrene and butadiene are plotted as a function of the composition of the comonomer mixture. The deposition rates of these mixtures are shown to be not quite a linear combination of those of the comonomers as expected for comonomers with different copolymerisation coefficients.

The curve regressions (nonlinearity) are characteristic of chemical copolymerizations. However, they are not yet completely understood. Moreover, the type of substrate and therefore the possibility of dissipation of charges have an influence on the deposition characteristics. Attempts were made to interpret the deposition characteristics in terms of classic copolymer kinetics. Here, the Fineman and Ross approaches were applied [21]. For example, it could be shown that the copolymer formation of the allyl alcohol-butadiene copolymerisation can be linearized by applying these methods. Two linear dependencies are found for different compositions of the comonomer mixture corresponding to preferred homopolymerization (of butadiene) and preferred copolymerisation. The structure of copolymers is alternating if $r_a = r_b = 0$, which was assumed for the investigated copolymer systems.

1.3.2 Variation of the Density of Functional Groups

Ethylene and styrene as linear "chain extenders" and 1,3-butadiene as "chemical crosslinker" were copolymerized with allyl alcohol, allylamine or acrylic acid as carrier for OH, NH_2 or COOH groups. Thereby the composition of comonomer mixtures was systematically varied. Then the resulting number of OH, NH_2 or COOH groups in the copolymers was measured by applying the derivatization methods in

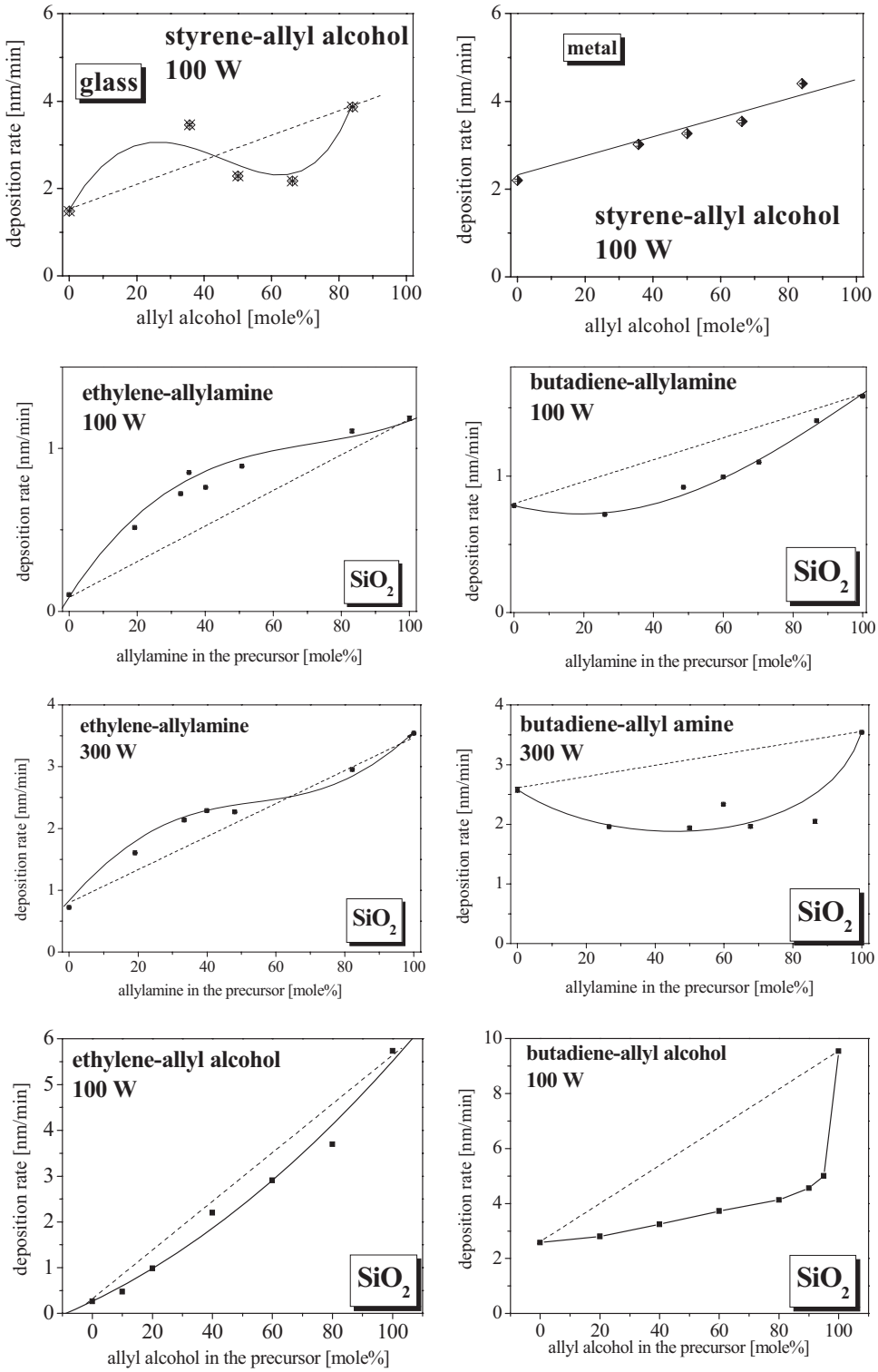

Figure 7 Different shapes of deposition rates vs. comonomer ratio on Si, glass or metal.

connection with the XPS and IR spectroscopy as described before. The structure of the copolymers is reflected in the respective C1s-XP spectra as shown for an ethylene-allyl alcohol copolymer (Fig. 8). The spectrum of the copolymer seems to be a linear superposition of the spectra of homopolymers.

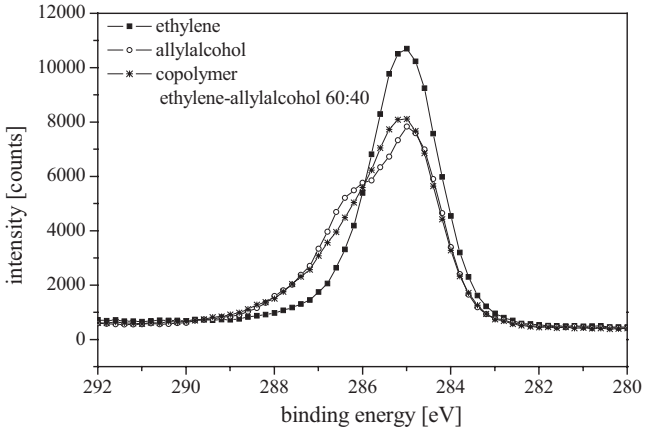

Figure 8 XPS-C1s peaks of an allyl alcohol and ethylene homopolymer and also of an allyl alcohol-ethylene copolymer.

To determine the extent of retained functional groups the copolymers were derivatized in the same manner as the homopolymers. Figure 9 shows a nearly linear correlation between the concentration of functional groups in the resulting copolymer and the composition of the comonomer mixture for the copolymerisation of acrylic acid-butadiene in the subsequent measurement of COOH groups as TFE derivatives. In Fig. 10 the number of OH groups of an ethylene-allyl alcohol copolymer, determined by derivatization with TFAA, is plotted. In the range of 60 to 100% allyl alcohol in the gas–vapor mixture of ethylene only homopolymerization of allyl alcohol can be observed. From 0 to 60% copolymerization occurs. This behavior can be observed for both the copolymerization at 100 W or 300 W. Using 300 W the maximum yield in OH groups is 23 per 100 C atoms whereas the maximum concentration is near 31 OH groups per 100 C atoms using 100 W. This can be interpreted as leaving the region of soft plasma power responsible for the preferred chemical chain propagation at polymer deposition and passing to the region of plasma parameters characteristic for the preferred fragmentation of monomers and the random recombination of fragments and atoms to irregular polymer structures. Therefore, the chemical structure of copolymers should change from a more chemically defined (100 W) to a more irregular one (300 W).

In contrast to the ethylene-allyl alcohol system the copolymerization of butadiene-allyl alcohol is dominant in the full range of allyl alcohol in the gas/vapor comonomer mixture as shown by the (nearly) linear increase in the number of OH groups with growing percentage of allyl alcohol (Fig. 10). Homopolymerization seems to be negligible. The maximum concentrations of OH groups were 29 OH groups per

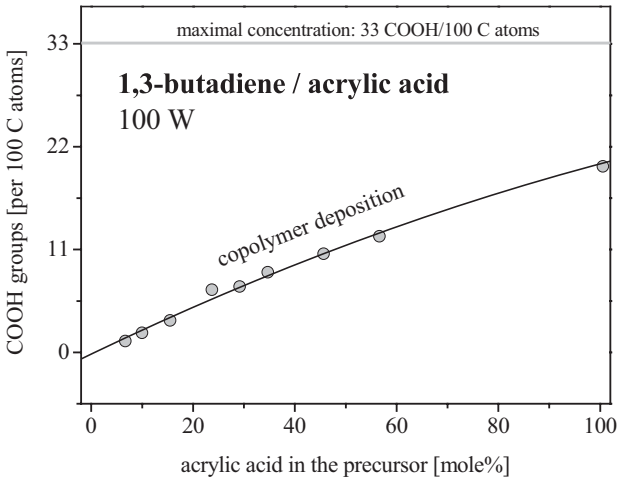

Figure 9 Yield in COOH groups at copolymerisation of acrylic acid with butadiene.

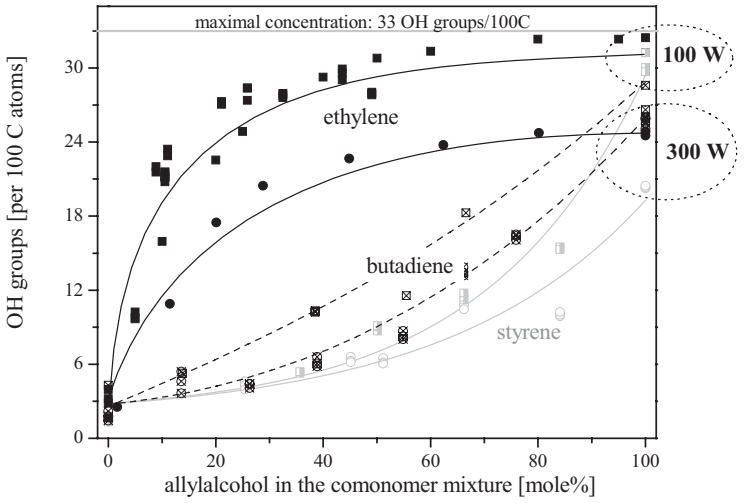

Figure 10 Yield in OH groups at copolymerisation of allyl alcohol with different comonomers.

100 C atoms using 100 W and 20 OH per 100 C atoms using 300 W. Copolymerization with styrene is dominated by its homopolymerization (0 to 50 mole% allyl alcohol, see Fig. 10).

IR spectroscopy of the ethylene-allyl alcohol copolymer confirmed roughly the results of XPS measurements using 100 W power input (Fig. 11). It should be mentioned that the recorded ATR signal collects the structural information of the complete layer (200 nm). With increasing allyl alcohol percentage the $[Blockade]_{OH}$ inten-

sity grows considerably in the range of 0 to 60 mole% allyl alcohol in the comonomer mixture. In the range of 60 to 100 mole% the absorbance of the [Blockade]OH signal remains constant. However, using 300 W power input, a linear dependence of the [Blockade]OH absorbance on the chemical composition of the gas/vapor mixture is observed (see Fig. 11). The absorbance of the $[Blockade]_{OH}$ signal (3350 cm^{-1}) was referenced to that of the neighbouring $[Blockade]_{as}CH_2$ vibrations at 2925 cm^{-1} used as internal standard.

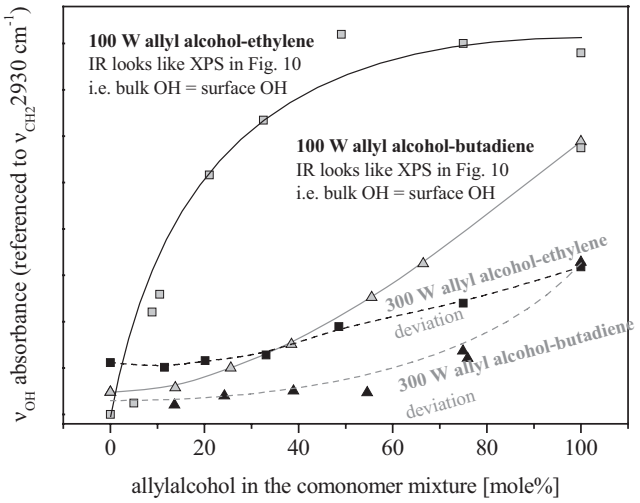

Figure 11 OH-stretching vibrations of copolymers of allyl alcohol and ethylene or butadiene.

1.3.3
Structure and Stability of Copolymers

Studies on structure and stability of pulsed plasma polymers were performed using styrene as the best-qualified (vinyl) monomer. It could be shown using FFF (field flow fractionation) that linear molecules with 20 000 Da molecular weight were synthesized. XPS and NEXAFS results corresponded completely to those of polystyrene standards [11–15]. However, deviations from classic composition and structure were found at the polymer backbone using FTIR spectroscopy. Here, branched structures were identified also using FFF (>10^8 Da). Functional groups carrying homopolymers from allyl and acrylic monomers were completely soluble, thus showing the absence of crosslinked structures. In particular, allyl alcohol was easily pulsed-plasma polymerised under retention of 95% of all OH groups introduced with the monomer allyl alcohol, e.g. 31 OH groups per 100 C atoms were detected after derivatization with trifluoroacetic anhydride. The OH layers were stable during long-time exposure (1 year) to air. COOH groups introduced by acrylic acid decomposed partially in the pulsed plasma giving a selectivity of about 75%. The resulting layers were stable during storage. Primary amino groups were difficult to retain dur-

ing the plasma-deposition process, since they further react at the nitrogen by forming secondary amines. Furthermore, they are also difficult to store since they are oxidized at the α-C atom in an auto-oxidation process resulting in an oxygen uptake up to 17 O per 100 C after 1 month exposure to air. The selectivity amounted to 55%. Copolymers show similar properties, however, they were fractionally insoluble or generally soluble. The retention of functional groups was the same as by homopolymerization. The number of functional groups could be continuously varied between 0 and the maximal number characteristic for the homopolymers.

1.3.4
Relation between Functional Groups of Copolymers and Surface Energy

The surface energy increased with higher percentage of allyl alcohol in the mixtures with ethylene or butadiene as comonomers. The pure ethylene homopolymer shows a surface energy of 36 mJ/m^2, which is slightly higher than that of conventional polyethylene (32 mJ/m^2 [22]). It is argued that some imperfections in the structure of the ethylene homopolymer (C=C double bonds, branched structures and other inhomogeneities) increase the dispersive component. However, the polar component is also near zero thus demonstrating the absence of polar groups (O functional groups). This absence of the polar component in the pure ethylene homopolymer reflects its qualification as a pure chain-extending component in the copolymer and the appropriateness of copolymers with ethylene sequences as model surfaces with variable concentrations of exclusively one type of functional group. Pulsed-plasma polymerized poly(allyl alcohol) homopolymer shows a surface energy of 50 mJ/m^2. The linear characteristic of the polar component of surface energy of allyl alcohol-butadiene copolymers between 6 and 31 OH groups per 100 C atoms reflects the copolymerisation region (see Fig. 12) whereas in the region 0 to 5 OH/100 C groups the polar component remained constant.

1.3.5
Relation between Functional Groups of Copolymers and Adhesion

Figure 1 presents the differences between unspecific and specific (monotype) functionalization of polymer surfaces for evaluating the contribution of each functional group to the adhesion (interaction) between polymers and metals.

Thus, homopolymers with OH, NH_2 and COOH groups are produced and the respective copolymers with ethylene or butadiene applied as adhesion-promoting interlayers in Al-PP composites. Such modified surfaces/interlayers are good models for studying the interaction between metal atoms and monotype functional groups in terms of metal–polymer peel strengths. Therefore, after evaporation of aluminum onto such model surfaces the peel strengths of the Al-plasma polymer-PP composites were measured and the loci of failure were determined. The interactions between the monotype functional groups and aluminum depend strongly on the type of functional groups (see Fig. 13): $COOH > OH \gg NH_2 > CH_2$ [22]. This

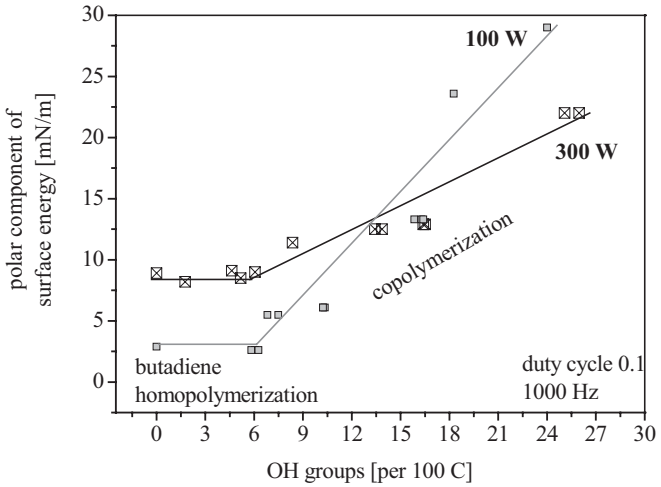

Figure 12 Correlation of polar contribution vs. concentration of OH groups (allyl alcohol-ethylene copolymer).

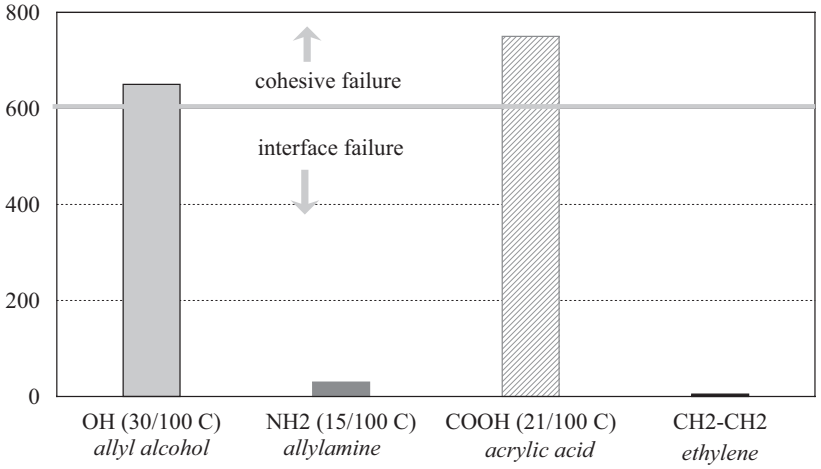

Figure 13 Comparison of Al-plasma homopolymer-PP peel strength in dependence on the type of monotype functional group.

adhesion-promoting behavior was also compared with the unspecific O_2 plasma polymer surface functionalization of PE, PP and PET, which then were evaporated with Al and form Al-polymer composites (Fig. 14). Here, maximum peel strength was measured on introduction of 20 O atoms per 100 C atoms (see Fig. 13). With PET the introduction of O functionalities in the O_2 plasma was accompanied by decarbonylation/decarboxylation of the ester groups, thus, the resulting elemental ratio remained nearly unchanged, however, the nature of O containing groups differs

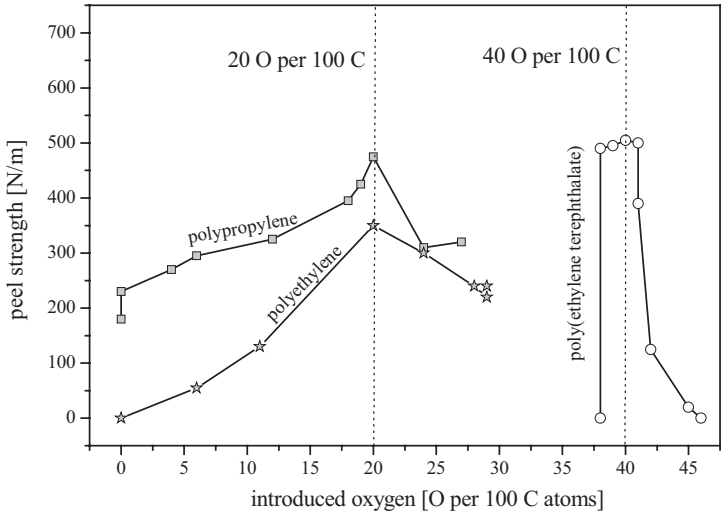

Figure 14 Peel strength of Al-O_2 plasma-modified PE, PP and PET composites.

from those of the original PET (Fig. 14). Using the post-plasma diborane reduction of O functional groups to produce a monotype OH group functionalised PP surface the measured Al peel strength was the same as with the unspecific O functionalization.

In the case of ethylene-allyl alcohol copolymers the maximum adhesion was measured at 27 OH per 100 C atoms. A linear dependence of peel strength on the density of OH functional groups was observed in the range of 0 to 27 OH/100C (Fig. 15). A maximum plateau of peel strength at 27 to 29 OH groups was interpreted as a suc-

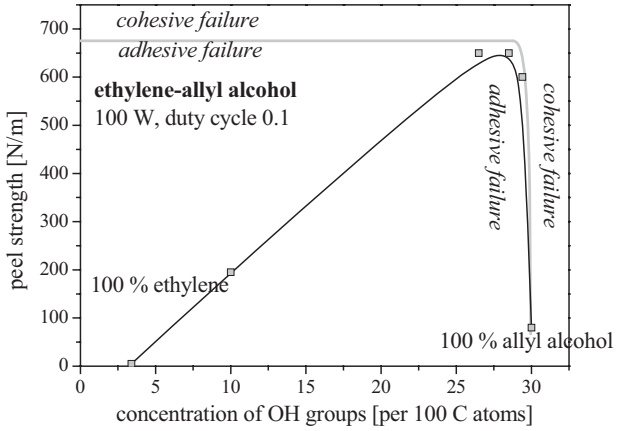

Figure 15 Peel strength of Al-copolymer composites with OH groups containing adhesion-promoting interlayers.

cessive weakening of the cohesive strength of copolymers with increasing content of allyl alcohol (> 90 mole%). Pure allyl alcohol was tacky, completely soluble and showed a low coherent strength resulting in low peel strength and a cohesive failure within the allyl alcohol homopolymer layer. As expected from the chemical point of view, NH_2 groups showed the lowest (Fig. 16) and COOH groups the highest peel strengths to Al (Fig. 17). In both cases over a wide range of concentration the Al peel strengths depend linearly on the concentration of functional groups. Only in the case of too strong interactions between Al and COOH groups was an interface failure observed within the polypropylene substrate (see Fig. 18). Using poly(allyl alcohol) the peel propagates through itself and using copolymers with allyl alcohol the peeling takes place at the plasma-polymer/PP interface (see Fig. 18).

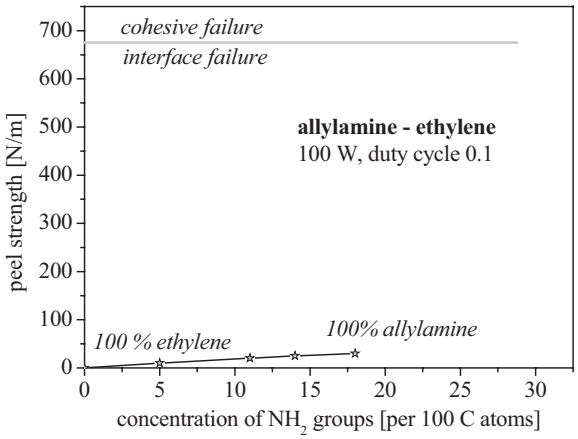

Figure 16 Peel strength of Al-copolymer composites with NH_2 groups containing adhesion-promoting interlayers.

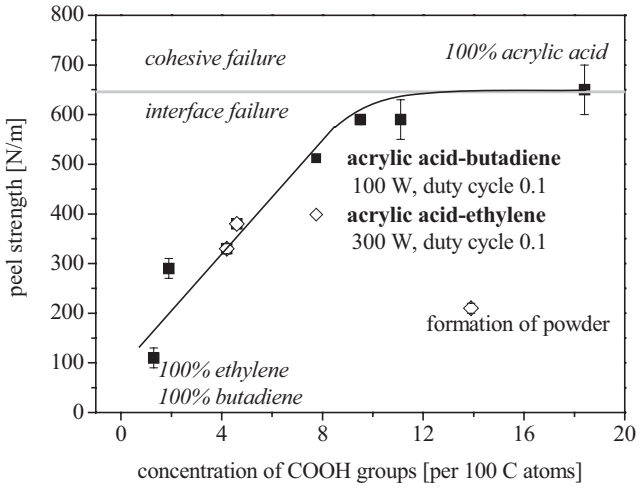

Figure 17 Peel strength of Al-copolymer composites with COOH groups containing adhesion-promoting interlayers.

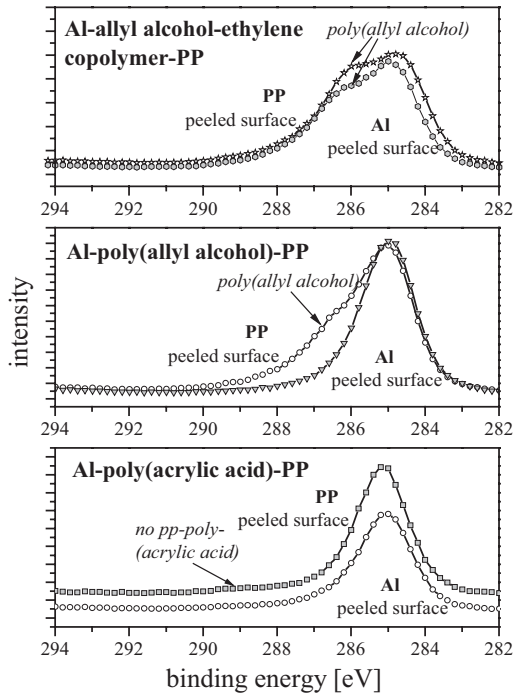

Figure 18 XPS-C1s signals of peeled Al-plasma polymer-PP composites with allyl alcohol-ethylene (60:40) comonomer, allyl alcohol homopolymer and acrylic acid homopolymer.

1.4 Discussion

The metal–polymer interactions and therefore, the peel strengths are based on the sum of discrete chemical bonds between aluminum and functional groups. CH_2–CH_2 groups do not show any interactions to aluminum and peel strength, the primary amino groups too, however, OH groups form Al-alcoholates and COOH groups form salts. The different slopes of the linear dependence with all three functionalities reflect the binding strength of these metal–polymer bonds. Thus, about 10 COOH and 27 OH sequences are needed to reach 650 N/m peel strength (maximum peel strength before appearance of cohesive failure) whereas NH_2 or CH_2–CH_2 sequences only allow weak interactions. These values correlate very well with the binding energies of Al bonds with OH and COOH groups of organic compounds in Al-alcoholates or Al-salts.

The linear increase of adhesive bond strength with growing number of functional groups at the polymer surface and the appearance of a plateau of peel strength at higher concentrations of functional groups, related to cohesive failure, correspond very well with observations on metal–polymer composites possessing functional

groups at the polymer surface [23]. Such models were chemically produced copolymers with COOH or other groups, which form aluminum- or iron-polymer composites. A correlation was found between adhesive bond strength (lap shear strength) of aluminum and the concentration of functional groups (COOH) at the polymer surface (poly (vinyl chloride)-maleic acid copolymers): $\sigma_f = \sigma_0 + k\, c^n$, whereby σ_f = measured adhesive bond strength, σ_0 = adhesive bond strength without functional groups, k,n= constants and c= concentration of functional groups [24]. Using the functional group-carrying adhesion-promoting plasma polymer layers n becomes 1 because the concentration is measured directly at the surface. The equation confirms the observed linear dependence of adhesive bond strength and concentration of functional groups at the interface. Thereby, the constant k reflects the binding energy between Al and the functional group.

1.5 Summary

Adhesion-promoting plasma polymer layers, equipped with maximal 31 OH or 18 NH_2 or 24 COOH groups per 100 C atoms, were produced by applying low wattages and using the pulsed-plasma technique. By carrying out a pulsed-plasma-initiated chemically dominated copolymerization, the density of monotype functional groups could be continuously varied between 0 and 31 OH, 0 to 15 NH_2 and 0 to 24 COOH groups. With aluminum the peel strength increased in the order: $CH_2 < NH_2 \ll OH < COOH$. Using carboxylic groups modified surfaces the adhesion at the Al/COOH interface was greater than the cohesive strength of the polypropylene substrate. The peel strength depended linearly on the density of functional groups.

Acknowledgements

This work was financed by VDI-TZ Düsseldorf under grant 13N7776.

References

[1] J. Friedrich, W. Unger, A. Lippitz, I. Koprinarov, A. Ghode, Sh. Geng and G. Kühn, Compos. Interf., **10**, Vol. 1, 139 (2003).
[2] J. M. Tibbitt, M. Shen and A. T. Bell, J. Macromol. Sci., Chem. **A10**, 1623 (1976)
[3] A. R. Westwood, Eur. Polym. J., **7**, 363 (1971)
[4] J. Meisel and H.-J. Tiller, Z. Chem., **7**, 275 (1972)
[5] H. Yasuda and T. Hsu, J. Appl. Polym. Sci., **20**, 1769 (1976)
[6] H. Yasuda and T. Hsu, J. Polym. Sci., Polym. Chem. Ed., **15**, 81 (1977)
[7] K. Nakajima, A. T. Bell, M. Shen and M. M. Millard, J. Appl. Polym. Sci., **23**, 2627 (1979)
[8] J. W. Vinzant, M. Shen and A. T. Bell, ACS Polym. Preprints, **19**, 453 (1978)

[9] C. R. Savage and R. B. Timmons, Polym. Mater. Sci. Eng., **64**, 95 (1991)
[10] C. R. Savage, R. B. Timmons and J. W. Lin, Chem. Mater., **3**, 575 (1991)
[11] G. Kühn, St. Weidner, R. Decker, A. Ghode and J. Friedrich, Surf. Coat. Technol., **116–119**, 748 (1999)
[12] J. Friedrich, I. Retzko, G. Kühn, W. Unger and A. Lippitz, in: *Metallized Plastics 7: Fundamentals and Applied Aspects*, K. L. Mittal (Ed.), pp. 117–142, VSP, Utrecht (2001)
[13] I. Retzko, J. F. Friedrich, A. Lippitz and W. E. S. Unger, J. Electron. Spectrosc. Relat. Phenom. **121**, 111 (2001)
[14] G. Kühn, I. Retzko, A. Lippitz, W. Unger and J. Friedrich, Surf. Coat. Technol. **142–144**, 494 (2001)
[15] H. Schüler and L. Reinebeck, Z. Naturforsch., **6a**, 271 (1951), **7a**, 285 (1952), **9a**, 350 (1954)
[16] H. Schüler and L. Reinebeck, Z. Naturforsch., **6a**, 271 (1951), **7a**, 285 (1952), **9a**, 350 (1954)
[17] H. G. Elias, An Introduction to Polymer Science, VCH, Weinheim, 1997
[18] J. Friedrich, P. Rohrer, W. Saur, Th. Gross, A. Lippitz and W. Unger, Surf. Coatings Technol., **59**, 371 (1993)
[19] J. F. Silvain, J. J. Ehrhardt and P. Lutgen, J. Adhes. Sci. Technol., **5**, 501 (1991).
[20] J. F. Silvain, J. J. Ehrhardt and P. Lutgen, Chemtracts-Macromolecular Chemistry, **3**, 195 (1992).
[21] H.-G. Elias, Makromoleküle, Vol. 1, Hüthig & Wepf, Basel, 1990.
[22] J. Friedrich, G. Kühn, R. Mix, A. Fritz and A. Schönhals, J. Adhesion Sci. Technol. **17**, 1591 (2003).
[23] S. Wu, Polymer Interface and Adhesion, Marcel Dekker, New York, 1982.
[24] A. D. McLaren and C. J. Seiler, J. Polym. Sci., **4**, 63 (1949).

2
RF-Plasma Deposition of SiO_x and a-C:H as Barrier Coatings on Polymers

D. Hegemann, U. Schütz, C. Oehr

Abstract

RF discharges of O_2/HMDSO and CH_4 were used to deposit SiO_x and a-C:H barrier coatings on PET foils using symmetrical and asymmetrical plasma reactors. Both processes were found to be radical-dominated since the reaction parameter power per gas flow W/F determines the film growth. By evaluation of the deposition rates, hints for the optimum deposition conditions were detected. Surface processes driven by ion bombardment result in rival ablation/deposition processes leading to a broadened interphase on PET. This inorganic/organic interphase was found to possess no barrier properties, whereas inorganic/inorganic interphases in two-layer systems of SiO_x/a-C:H contribute to the barrier properties. Moreover, it could be shown that in the two-layer system the layer having the lowest permeability controls the permeability of the overall system, both for OTR and WVTR.

2.1
Introduction

Siloxane- or hydrocarbon-based plasma films have been extensively studied, for example as protective or barrier coatings [1–4]. By using organic precursors like hexamethyldisiloxane (HMDSO) or methane (CH_4), the film properties can be varied from polymer-like to quartz- and diamond-like, respectively, at near room temperature. Thus, for example different wetting properties or gas-permeation rates can be achieved by depositing SiO_x and a-C:H films with different chemical composition or crosslinking degree [5,6]. However, optimized deposition conditions often depend strongly on the reactor geometry used. In particular for barrier coatings on polymers, surface roughness, adhesion, internal stresses, flexibility, and transparency – beside the permeation rates – must be considered. The concept of the barrier improvement factor (BIF) is useful to measure the effectiveness of a coating in reducing the permeability, where BIF is equal to the permeation rate of the uncoated polymer divided by the permeation rate of the coated polymer [1,7]. Barrier properties of flexible packagings are required, for example, in food packaging, for solar modules, LEDs, and OLEDs as replacements for metal and glass containers [8,9].

Therefore, this work investigates the plasma-deposition process of SiO_x and a-C:H films regarding deposition rate, plasma potentials, and film properties, using compact plasma reactors that can be scaled up [10]. Moreover, the "interphase" formation (broadening of the substrate/coating transition) of inorganic, hard coatings on soft polymers during the first stage of film growth is examined. The origin of this interphase was ascribed to an ablation/redeposition process involving volatile organic fragments from the polymer substrate [11,12]. Although the importance of this process for the adhesion of PECVD coatings is well known, the actual width of the interphase could be clarified only recently [12]. While the around 10-nm thick interphase enhances the adhesion of PECVD-derived coatings on polymers compared to PVD coatings, which exhibit almost no interphase formation, it might limit the critical film thickness needed for good barrier qualities due to its organic/inorganic hybrid character. Therefore, in this work OTR and WVTR values are compared for single layers and two-layer coatings of SiO_x and a-C:H on PET foils.

2.2 Experimental

Capacitively coupled RF discharges (13.56 MHz) were used in this study to deposit barrier coatings on polymers. For SiO_x films, a symmetrical reactor with plane parallel electrodes of size 29–39 cm^2 was developed, where the plasma is confined between the electrodes and fills the whole vacuum chamber. The upper electrode contains an integrated gas feeding and pumping system described in more detail in refs. [13,14]. For comparison, also a strongly asymmetrical reactor with an electrode size of 12–15 cm^2 was set up, where the active plasma zone is concentrated in front of the driven electrode. This reactor was also used for the deposition of a-C:H films beside a second – less asymmetrical – plasma reactor with plane parallel electrodes of size 24–39 cm^2. Note that the outer vessel in the asymmetrical set-up also contributes to the counterelectrode area. All three reactors possess a gas-feeding system to generate a uniform, vertical gas flow towards the driven electrode where a homogeneous deposition over the entire electrode area is obtained (Fig. 1). The lower (substrate) electrodes were always powered.

V/I probes (ENI Model 1065, Scientific Systems Smart PIM and Advanced Energy RFZ 60) and an oscilloscope were used to measure applied voltage, current, phase angle, and absorbed power.

The precursor hexamethyldisiloxane (HMDSO), $C_6H_{18}OSi_2$, used as obtained from FLUKA was thermostabilized and vaporized outside the apparatus. Oxygen as carrier gas is mixed with HMDSO and fed together into the plasma chamber. For the deposition of a-C:H coatings, methane, CH_4, was used as precursor alone. The parameter sets for the evaluation of the deposition rates given in Table 1 were chosen to achieve comparable power inputs per electrode area (0.05–0.5 W/cm^2). All films were deposited near to room temperature (max. 60 °C).

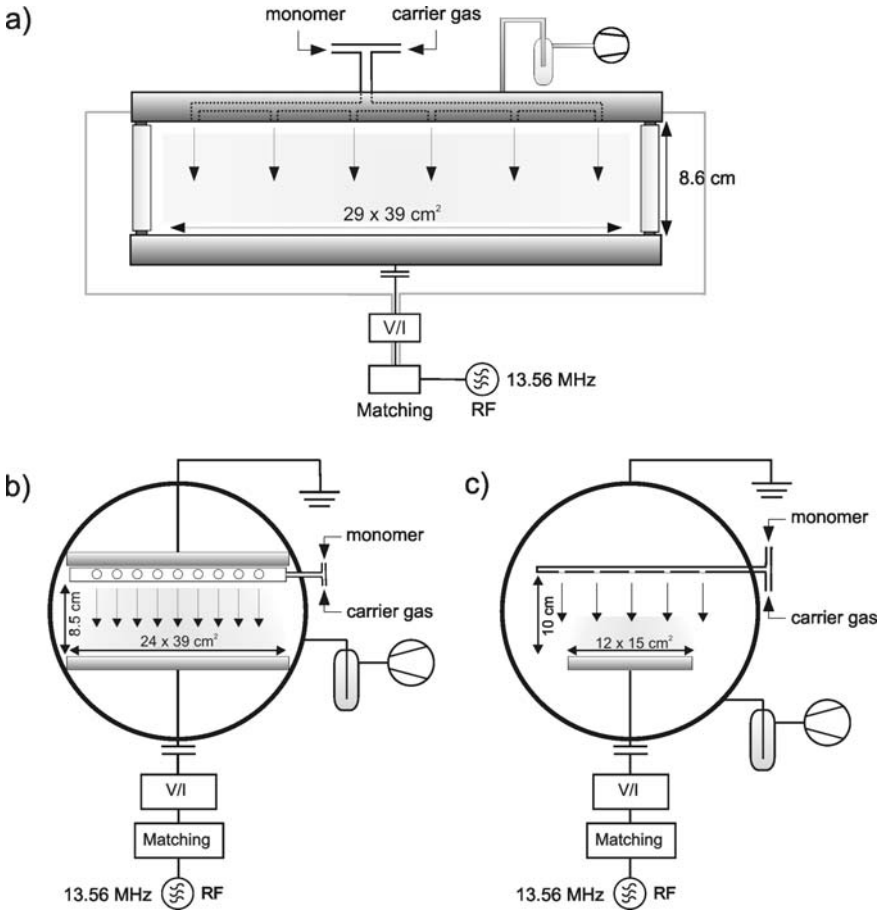

Figure 1 Schematic drawings of the used plasma reactors. (a) symmetrical reactor for SiO_x deposition, (b) asymmetrical reactor for a-C:H coatings, (c) strongly asymmetrical set-up used both for SiO_x and a-C:H.

Table 1 Parameter range used for the evaluation of the deposition rates (*W*: absorbed power, *p*: pressure, *F*: gas flow). The optimized parameters for the deposition of barrier coatings are given in brackets. The ratio of bias to excitation voltage is a measure for the asymmetry of the electrode configuration.

Process	Reactor	$-V_{bias}/V_0$	*W* [W]	*p* [Pa]	F_{HMDSO} [sccm]	F_{O2} [sccm]	F_{CH4} [sccm]
SiO_x	sym.	0	50–400 (300)	10–30 (15)	10–100 (15)	50–220 (220)	
	asym.	0.9	10–50 (40)	5–10 (10)	0.5–5 (0.5)	1–10 (5)	
a-C:H	less asym.	0.6	50–400 (240)	10–30 (15)			20–100 (50)
	asym.	0.9	10–50 (24)	5–10 (10)			2–5 (3)

To determine the deposition rate, glass slides and Si wafers (100) were coated. The mass deposition is obtained by weighing the substrates immediately before and after the coating procedure (Sartorius Balance H110 and Mettler AE 200; precision: 0.1 mg). It was proven that the deposition rate depends linearly on time. Additionally, thickness is measured on film edges via atomic force microscopy (PSI Autoprobe CP) and profilometry (KLA Tencor HRP 75). Both methods were calibrated using a standard sample with a known edge height. Film density is calculated from mass and volume of the coatings. As substrate material 23-µm thick PET foils (Hostaphan RD) were coated, which were placed on the driven electrode so that the smoother side with no antiblocking particles faced the plasma.

X-ray photoelectron spectroscopy (KRATOS Axis Ultra) with MgK_α excitation and a 110-µm spot and Auger electron spectroscopy (PHI 545C) were used to determine the chemical composition. The elemental composition of Si, O, and C were calibrated using a quartz standard with XPS. For the depth profiles the samples were sputtered with 5-keV Ar ions at an incident angle of 80°. As is well known, the sputtering rate depends on the type of material as well as on the actual sputtering depth. Due to shadowing and mixing effects, the actual rate decreases over the sputtering time. Therefore, crosslinked SiO_x and a-C:H as well as plasma-polymer films thereof were deposited on Si wafers with a known thickness between 10 and 50 nm to estimate the actual sputtering depth during the depth-profile analyses.

Oxygen (OTR) and water vapor transmission rates (WVTR) were measured by Mocon Oxtran and Permatran devices at 23 °C, 50% r.h. (DIN 53380-3) and 23 °C, 85% to 0% r.h. (DIN 53122-1), respectively.

By measuring the excitation voltage V_0, the negative bias potential V_{bias} and average thickness of the plasma sheath d_{sh} in front of the electrodes, the potential distribution can be calculated by using a simple model described in the literature [15,16]. The electric field is considered to be negligible within the bulk plasma and increases linearly across the oscillating plasma sheath in front of the driven electrode, where

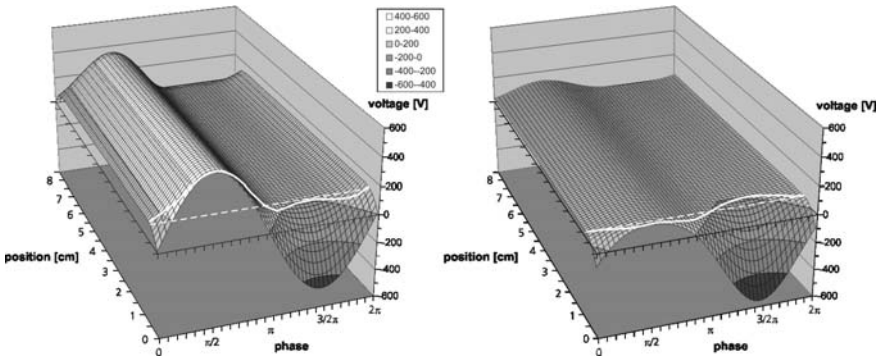

Figure 2 Potential distribution over one RF cycle for the symmetrical (left; O_2/HMDSO, 300 W, 15 Pa) and the asymmetrical plasma reactor (right; O_2/HMDSO, 40 W, 10 Pa). Both processes yield comparable potential drops (185 V left, 210 V right) across the plasma sheath (RF electrode in front). The white, bold line indicates the oscillation of the plasma sheath and the white, dashed line the width of the sheath.

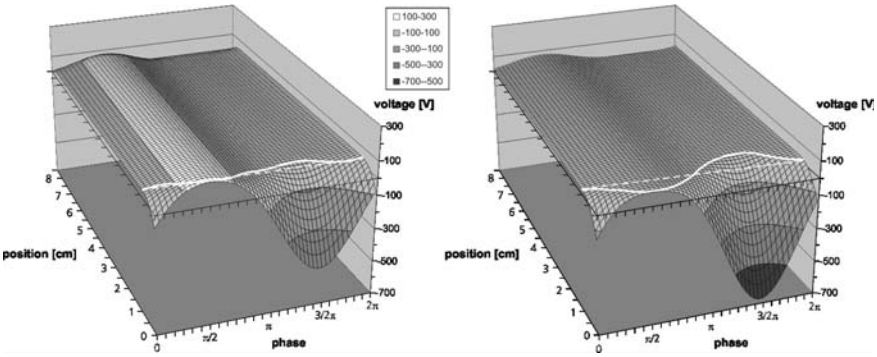

Figure 3 Potential distribution over one RF cycle for the less asymmetrical (left; CH_4, 240 W, 15 Pa) and the strongly asymmetrical plasma reactor (right; CH_4, 24 W, 10 Pa). In the left process a potential drop of about 180 V and in the right process of about 250 V is obtained. The white, bold line indicates the oscillation of the plasma sheath and the white, dashed line the width of the sheath.

the applied voltage is $V_{rf} = V_0 \sin(2\pi ft) + V_{bias}$. Typical potential distributions for the deposition of SiO_x and a-C:H barrier coatings are given in Figs. 2 and 3, respectively.

It can be seen that although there is no bias voltage in the symmetrical reactor, a sheath potential of about 185 V ($V_{sh} \approx 0.39\ V_0$) is applied on average in front of the powered electrode at typical parameters used to deposit SiO_x barrier coatings. On the other hand, the potential drop in the asymmetrical reactors is an addition of plasma potential and negative (average) bias potential ($V_{sh} \approx 0.39\ V_0 - 0.73\ V_{bias}$). For SiO_x, a slightly higher potential of about 210 V is obtained. For typical conditions to generate a-C:H barrier coatings, about 180 V is achieved in the less asymmetrical reactor and about 250 V in the strongly asymmetrical setup. These values are of importance, since we have shown that V_{sh} scales with the internal stresses of the plasma coatings [6].

2.3 Results and Discussion

According to the work of Yeh et al. [17] the mass deposition rate R_m for radical-dominated discharges depends on power input W, monomer gas flow F_m, and a geometrical, reactor dependent factor G, thus that

$$\frac{R_m}{F_m} = G \exp\left(-\frac{E_a}{W/F_m}\right). \quad (1)$$

It was found that W/F_m was the unique reaction parameter controlling the conversion of monomer in the gas phase to the plasma polymer in the solid phase primarily by activation of molecular bonds, where E_a is the apparent activation energy [18].

Only recently, our group showed that this concept also holds when oxygen is added to HMDSO as a reactive carrier gas [6,19]. It was found that power per unit

gas flow still determines the deposition rate, where the total gas flow F_{mc} is now an addition of monomer flow and carrier gas flow as

$$F_{mc} = F_m + aF_c. \tag{2}$$

The factor a was found to be 0.6, i.e. smaller than 1. This in turn means that keeping the total gas flow and the power input constant, the energy density W/F_{mc} increases with increasing O_2/HMDSO ratio. Thus, the addition of oxygen supports the film growth, since it contributes to the radical formation as well as to the production of volatile CO_2 and H_2O compounds beside C_nH_m in the gas phase that reduces the residual carbon content in the SiO_x coatings. Hence, it was found that an increasing energy density leads to an enhanced inorganic character, i.e. a reduced carbon content, which is also desirable for barrier coatings [6]. This concept holds both for symmetrical and asymmetrical reactor setups (Fig. 4).

CH_4 discharges in asymmetrical reactors can be described in the same manner (Fig. 5).

However, the apparent activation energy E_a, which divides the energy density into a more polymer-like and a more quartz-like, respectively diamond-like, regime, should be equal when using the same monomer. Noting that E_a is power per flow, either the actual power input or the actual gas flow is affected by the different reactor set-ups. The absorbed power was carefully measured resulting in 90–100% power input into the symmetrical plasma reactor and a 70–80% power conversion in the asymmetrical reactors. The data evaluation in Figs. 4 and 5 as well as in Table 1 already accounts for these power losses. On the other hand, the actual flow is inversely proportional to the residence time of the molecular species in the active

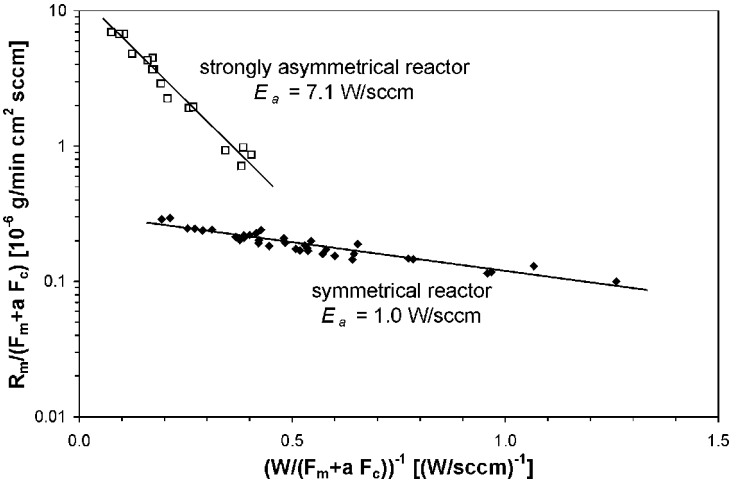

Figure 4 Mass deposition rate per gas flow for O_2/HMDSO discharges depending on the reaction parameter W/F. The bold lines represent the fits corresponding to Eqs. (1) and (2). In both cases the factor a was taken to be 0.6. The two different reactor set-ups exhibit different apparent activation energies E_{anti} (slope of the linear fit).

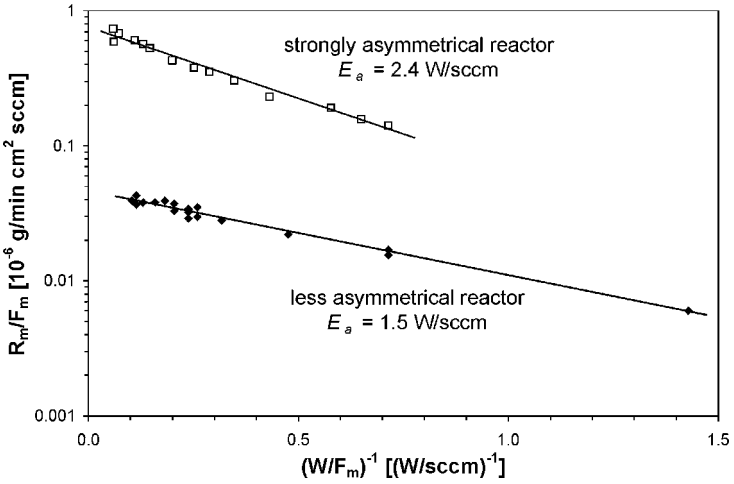

Figure 5 Mass deposition rate per gas flow for CH_4 discharges depending on the reaction parameter W/F. The bold lines represent the fits corresponding to Eq. (1). The two different reactor set-ups exhibit different apparent activation energies E_{anti} (slope of the linear fit).

plasma zone. Therefore, a shorter residence time adds up to an enhanced actual flow, which yields an increased nominal activation energy [20,21]. By comparing the symmetrical with the strongly asymmetrical reactor, it becomes evident that the RF discharge fills the whole plasma chamber between the symmetrical electrodes, whereas the discharge is concentrated in front of the RF electrode in the latter setup (Fig. 6).

Hence, we ascribe the about 7 times higher activation energy of O_2/HMDSO in the strongly asymmetrical reactor (E_{anti}= 7.1 W/sccm (58.7 MJ/kg) compared to 1.0 W/sccm (8.3 MJ/kg)) to a 7 times shorter residence time in the active plasma zone. The same argumentation holds for the comparison of the a-C:H deposition: the active plasma zone is wider in the less-asymmetrical reactor (E_{anti}= 2.4 W/sccm (200 MJ/kg)) compared to the strongly asymmetrical set-up (E_{anti}= 1.5 W/sccm (125 MJ/kg)). However, the differences are smaller.

As long as ion bombardment does not prevail, which may occur at higher energy inputs [10], the film growth is thus determined by gas-phase processes such as fragmentation and generation of radicals [22,23], as well as radical-promoted surface reactions [24]. For the growth of SiO_x coatings in RF plasmas, it could be shown that the contribution of ion bombardment to the deposition rate is negligible under typical experimental conditions [25]. Nevertheless, ions accelerated across the plasma sheath by the potential drop V_{sh} supports crosslinking of the growing films beside VUV [24]. But, V_{sh} also scales with the internal stresses in the SiO_x and most of all a-C:H films, whereby increased internal stresses result in a reduction of the barrier properties [6]. Hence, the two parameters, W/F and V_{sh}, which determine the plasma volume and surface processes, provide evidences for the optimum deposition conditions. For all reactor setups used, it was found that an energy density exceeding the

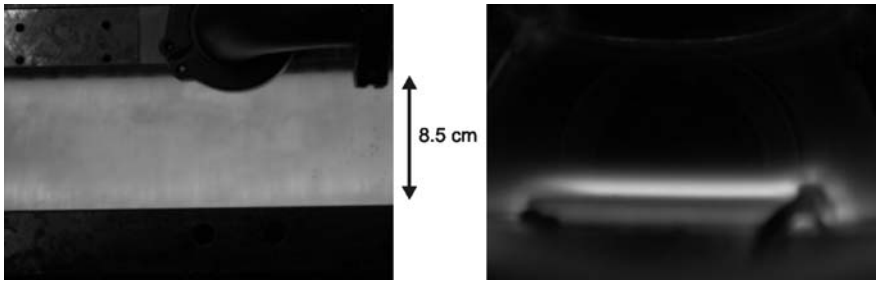

Figure 6 RF discharge between symmetrical electrodes (left) and in front of the asymmetrical electrode (right) for O_2/HMDSO plasmas. The bright plasma zone is remarkably smaller in the asymmetrical set-up. Both pictures are of the same scale.

activation energy E_{anti} by a factor of at least 1.5 for SiO_x and 2.5–3.5 for a-C:H, respectively, yields the optimum barrier properties (Table 2). Especially for plasma polymerized a-C:H coatings, a further enhanced energy density yields increasing permeabilities again [6] and a reduction in deposition rate due to a strongly raised ion bombardment accompanied by high internal stresses [26]. Compared to SiO_x films, a-C:H films are more flexible and smoother, but show higher oxygen permeation rates and internal stresses. Since thicker films do not improve the barrier properties noticeably, the permeability is determined by the coating defects (e.g. pinhole size and density) [1]. Hence, adhesion on polymers and transparency can be improved by applying the minimum film thickness required for barrier coatings. However, since the SiO_x coatings show a strongly reduced barrier improvement factor for water vapor compared to oxygen, an additional permeation mechanism for water vapor through the inorganic layer is revealed, which is ascribed to film microstructure, i.e. nanoscale morphology, and composition [8,27]. While in the plasma-polymerized SiO_x coatings some hydrophilic, polar Si–OH groups between SiO_x clusters are left [28], the a-C:H coatings exhibit hydrophobic, nonpolar C–H groups, which are assumed to influence the water vapor permeation in a different way. Hence, a slightly lower BIF value for water vapor is found compared to the BIF value for oxygen (Table 2).

Using the obtained deposition rates for SiO_x and a-C:H coatings, ultrathin layers of known film thickness can be deposited, where a density of 2.0 and 1.9 g/cm^3 was obtained for the optimized SiO_x and a-C:H films, respectively, regarding their barrier properties [6]. This can then be used to examine interphase formation of these coatings on polymers or in multilayer systems as well as to detect sputtering rates of quartz-like, diamond-like, and polymeric pp-HMDSO and CH layers in AES and XPS measurements. Therefore, different coatings of 10, 20, 30, 40, and 50 nm thickness on Si wafers were sputtered until the Si peak of the substrate increased. The obtained sputtering time is given in Fig. 7 for AES measurements. As can be seen, the sputtering rate is remarkably higher for polymeric films (~1.8 nm/s) compared to inorganic coatings (~1.2 nm/s) and decreases with increasing depth. Due to a larger spot area during XPS analysis, the sputtering rates are lower by a factor

Table 2 Oxygen (OTR) and water vapor (WVTR) transmission rates of SiO_x and a-C:H coatings on PET foil. BIF: barrier improvement factor (BIF_{100}: normalized to 100-µm foil thickness). The optimized parameters from Table 1 were used for all depositions.

Material combination	OTR [cm^3/m^2 d bar]	BIF/BIF_{100} (OTR)	WVTR [g/m^2 d]	BIF/BIF_{100} (WVTR)
23 µm PET	51 ± 2		11 ± 1	
PET/40 nm SiO_x	0.27 ± 0.02	188/43	1.1 ± 0.1	10/2.3
PET/125 nm SiO_x	0.19 ± 0.02	268/62	1.0 ± 0.1	11/2.5
PET/20 nm a-C:H	2.5 ± 0.2	20/4.7	0.35 ± 0.03	31/7.2
PET/65 nm a-C:H	2.4 ± 0.2	21/4.9	0.33 ± 0.03	33/7.7
PET/40 nm SiO_x/20 nm a-C:H	0.21 ± 0.02	243/56	0.29 ± 0.03	38/8.7
PET/40 nm SiO_x/10 nm a-C:H	0.24 ± 0.02	213/49	0.3 ± 0.03	37/8.4
PET/20 nm a-C:H/40 nm SiO_x	0.23 ± 0.02	222/51	0.28 ± 0.03	39/9.0

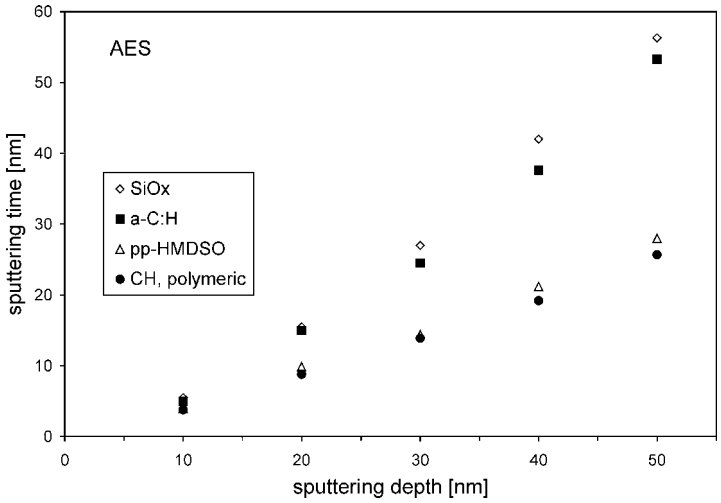

Figure 7 Determination of the sputtering rates of inorganic (SiO_x and a-C:H) and organic (pp-HMDSO an polymeric CH) coatings of known film thickness on Si wafers.

of 11, but show a comparable characteristic. Hence, an increased sputtering rate should be regarded during the depth profile of the interphase of an inorganic coating on a polymer [11]. Thus, the sputtering rate of the interphase that is an inorganic/organic gradient on the PET substrate was linearly interpolated.

To investigate the interphase formation, at first ~14-nm thick SiO_x coatings were deposited on smooth Si wafers (R_{rms} = 0.5 nm; R_{ave} = 0.3 nm) using the optimized plasma conditions for barrier coatings without a plasma pretreatment. Depth profile analyses by XPS and AES were performed by sputtering through the SiO_x layer. As can be seen in Fig. 8 for both methods an interphase width of about 5.5 nm was

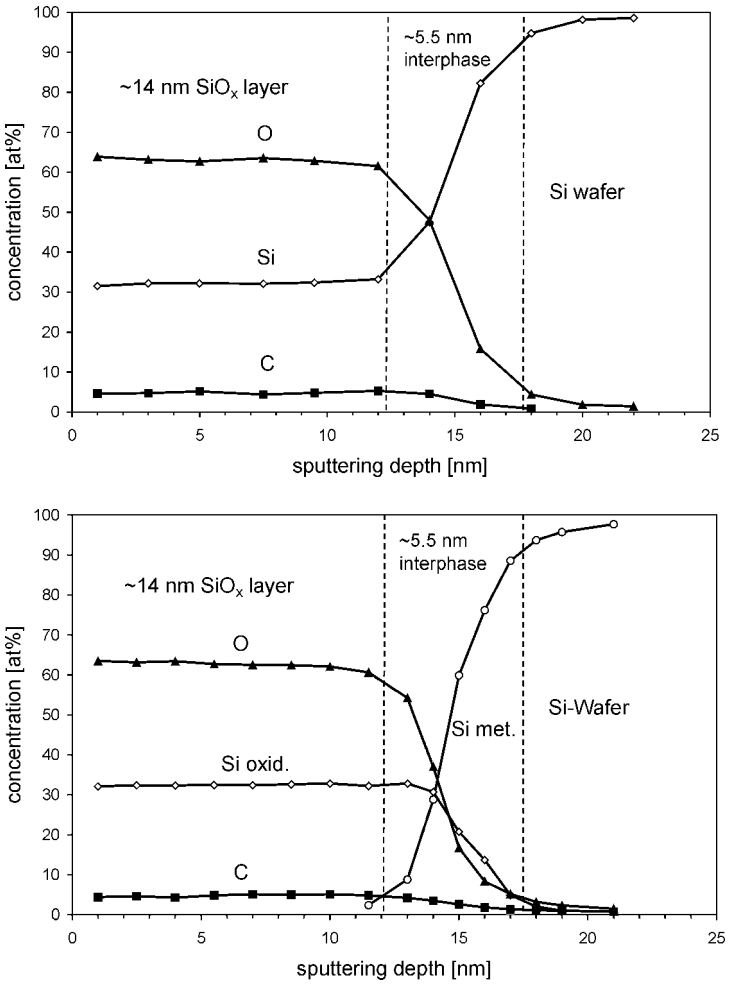

Figure 8 Depth profile analyses by means of AES (left) and XPS (right) of ultrathin SiO_x layers on Si wafers. With both methods the interphase width can be detected yielding comparable results. XPS can also differentiate the oxidic and metallic Si component.

detected. Due to the difficulty of getting the AES sensitivity factor of oxygen in oxide layers [29], the absolute chemical composition of the AES spectra was normalized with the XPS measurement, which was calibrated using a quartz standard. However, this has no influence on the sputtering depth. Assuming the real interphase width to be 1–2 nm due to Si–O bonds at the interface SiO_x/Si [30], a broadening of the interphase of about 4 nm occurs that can be assigned to the information depth of AES and XPS measurements [31] and surface roughening [32]. Mixing effects might not play an important role with these ultrathin coatings.

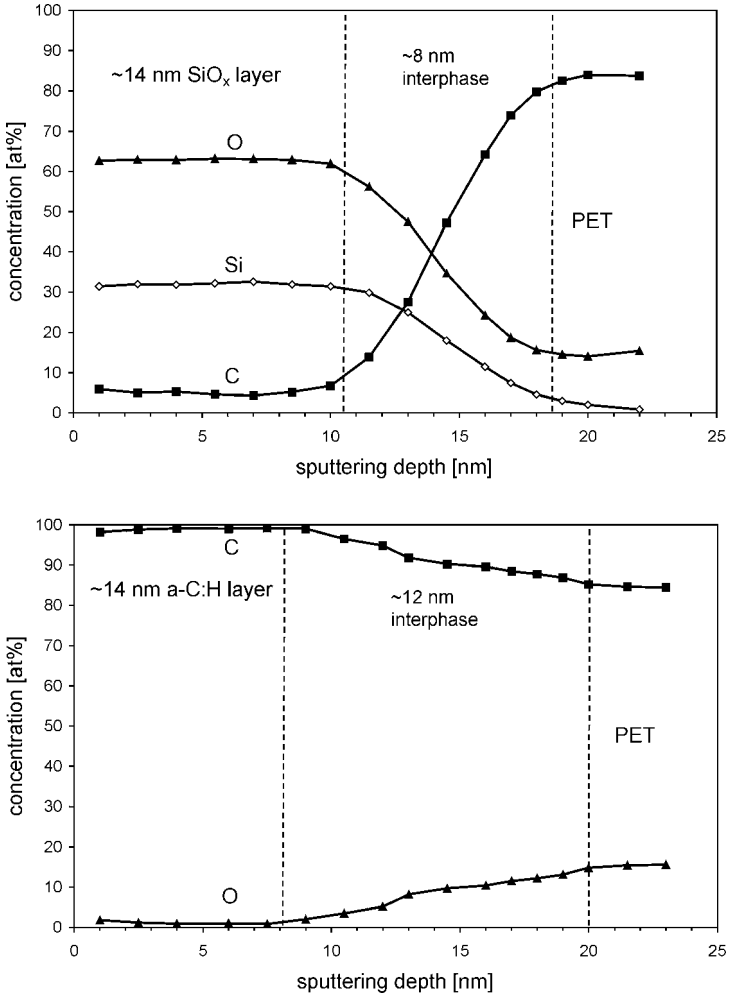

Figure 9 Depth profile analyses by means of XPS of ultrathin SiO_x (left) and a-C:H (right) layers on PET foils. The interphases are broadened due to rival ablation/deposition processes during the first stage of film growth.

With these findings, the interphase of a ~14-nm SiO_x layer on smooth PET foils (R_{rms} = 0.6 nm; R_{ave} = 0.45 nm) can be analyzed (Fig. 9). The apparent interphase width is around 8 nm, i.e. the real interphase might be ~4 nm derived in analogy with the SiO_x/Si interface. Hence, the deposition of SiO_x layers on PET leads to a broadened interphase formation due to ablation/deposition effects as long as the polymer surface is concerned through the plasma interaction [12,33]. To our understanding, the finding of thicker interphases might be attributed to an enhanced roughness of the polymer substrate [34], uncertainty in the actual sputtering rates within the interphase [11] or to a prolonged interaction between plasma and poly-

mer at low deposition rates [12,33]. This broadening of the interface yields a fairly good adhesion as long as the SiO_x layer does not become too thick. Then, the internal stresses of the films must be adopted to the polymer properties via a gradient layer [19].

Furthermore, it was found that a minimum thickness of about 15 nm is required to achieve barrier properties of the SiO_x coatings, i.e. to obtain dense, closed films [3]. Similar findings were obtained for a-C:H barrier coatings. Nevertheless, due to an increased ion bombardment during deposition (mainly H^+ ions), a further broad-

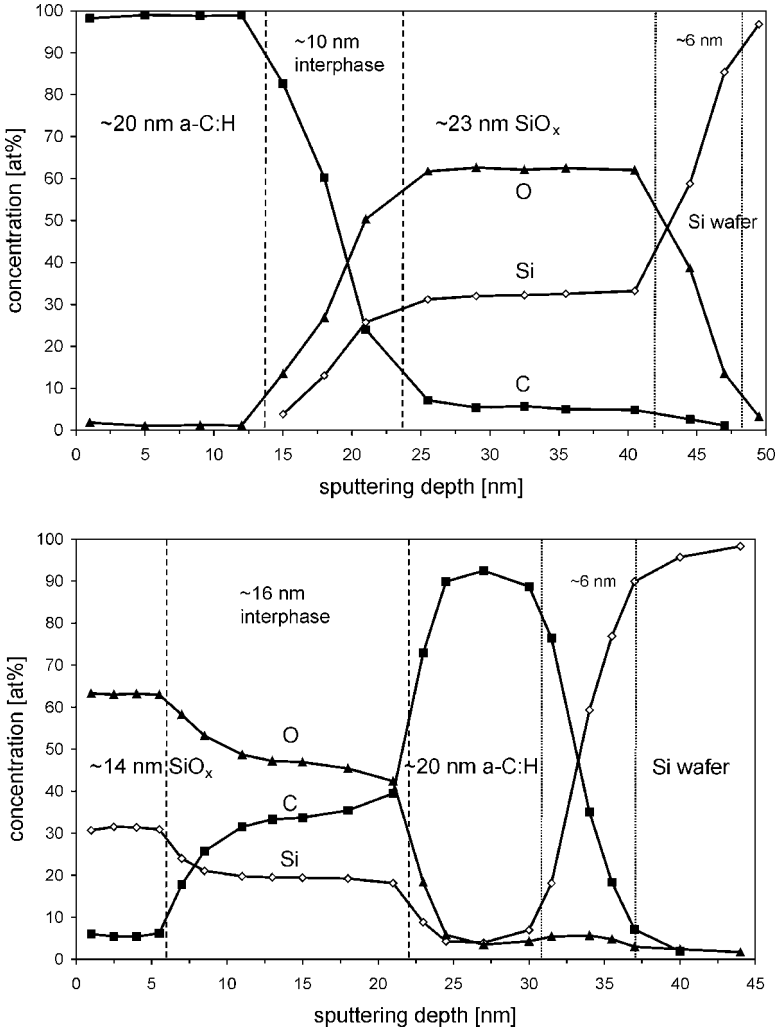

Figure 10 Depth profile analyses by means of AES of a-C:H on top of SiO_x (left) and SiO_x on top of a-C:H (right) layers on Si wafers. The interphases are broadened due to rival ablation/deposition processes during the first stage of the second film growth. Due to chemical etching, this is particularly pronounced when depositing SiO_x on a-C:H.

ening of the interphase (~8 nm) was detected and the minimum barrier layer thickness required is thus about 20 nm.

Next, two-layer systems of SiO_x and a-C:H were investigated. By depositing the a-C:H layer on top of the SiO_x layer, a corrected interphase width of about 6 nm was observed (Fig. 10). However, on inorganic SiO_x even 10 nm of a-C:H were found to be sufficient to achieve good barrier properties (Table 1). Therefore, it can be concluded that the inorganic interphase itself contributes to the enhancement of the barrier properties, whereas the organic/inorganic transition of the barrier layers on polymers does not.

When depositing the SiO_x layer on top of the a-C:H layer on the other hand, a noticeably broader interphase formation (~12 nm) can be observed (Fig. 10). Here, a strong interaction of the oxygen plasma with the a-C:H surface through chemical etching occurs, resulting in rival ablation/deposition processes. However, the adhesion of both two-layer systems was proven to be excellent. Moreover, since both combinations of SiO_x and a-C:H on PET exhibit comparable OTR and WVTR values (Table 1), the interphase SiO_x/a-C:H might also be regarded as possessing barrier qualities. However, considering the barrier improvement factors (BIF), these interphases add no additional or synergetical effects for improving the barrier properties, and WVTR (OTR) is hardly improved by SiO_x on top on a-C:H (a-C:H on SiO_x).

Agres et al. [35] deposited two-layer systems of rather organic pp-HMDSO and inorganic SiO_x films by varying the O_2/HMDSO ratio from 0% to 80%. They found comparable OTR values independent of the sequence of the layers. Thus, the composition and structure of the surface do not affect the barrier properties and sorption seems not to play a fundamental role in the permeability of plasma polymers. As with our two-layer system, these results can be qualitatively interpreted based on the principle of membrane-series superposition [36], in which the layer having the least permeability controls the permeability of the overall system.

2.4 Conclusions

By evaluating the mass deposition rates of O_2/HMDSO- and CH_4-derived RF plasma coatings, it appears that the deposition of SiO_x and a-C:H barrier layers is a radical-dominated process since the reaction parameter power per unit gas flow W/F determines the deposition rate, both for symmetrical and asymmetrical reactor setups. The resulting apparent activation energy E_{anti} gives hints to find the optimum deposition conditions. The actual value E_{anti} for a gaseous system also depends on the residence time in the active plasma zone and thus on the reactor geometry. Nevertheless, the interaction of fast ions and neutrals with the growing film is needed to attain dense, closed films with a low defect rate. On the polymer substrate rival ablation/deposition effects thus lead to a broadening of the interphase SiO_x/PET and a-C:H/PET with an interphase width of about 4 nm and 8 nm, respectively. The interphases were investigated by sputtering through ultrathin films of SiO_x and a-C:H during XPS and AES analyses considering the information depth as

well as shadowing and mixing effects. We suppose that these interphases do not contribute to the barrier properties, but enhance the adhesion of the layers. To obtain barrier properties on PET, a layer thickness of about 15 nm for SiO_x and 20 nm for a-C:H is required. On the other hand, when depositing a-C:H on top of a SiO_x layer, just 10 nm are sufficient to improve the barrier properties. Therefore, it can be concluded that the inorganic interphase itself contributes to the enhancement of the barrier properties, whereas the organic/inorganic transition of the barrier layers on polymers does not. While plasma polymerized SiO_x shows rather limited barrier properties for water vapor and a-C:H for oxygen, which is indicative of an additional permeation mechanism beside the defect-dominated permeation, the two-layer system reveals comparable permeabilities independent of the layer sequence. Thus the layer with the enhanced barrier properties for oxygen and water vapor, respectively, determines the overall properties. However, synergetical effects, like healing of defects, did not occur in the two-layer system of plasma-polymerized SiO_x and a-C:H coatings.

Acknowledgement

We thank Dr. H.-C. Langowski and A. Melzer, Fraunhofer IVV, Freising, Germany for gas permeation measurements within the Fraunhofer alliance POLO ("Polymere Oberflächen") as well as Dr. Z. Harmati for permeation measurements at EMPA, St. Gallen.

References

[1] H. Chatham, Surf. Coat. Technol. **78**, 1 (1996).
[2] C.-P. Klages, A. Dietz, T. Höing, R. Thyen, A. Weber, P. Willich, Surf. Coat. Technol. **80**, 121 (1996).
[3] A.S. da Silva Sobrinho, M. Latrèche, G. Czeremuszkin, J.E. Klemberg-Sapieha, M.R. Wertheimer, J. Vac. Sci. Technol. **A16**, 3190 (1998).
[4] E.M. Moser, R. Urech, E. Hack, H. Künzli, E. Müller, Thin Solid Films **317**, 388 (1998).
[5] D. Hegemann, H. Brunner, C. Oehr, Plasmas Polym. **6**, 221 (2001).
[6] D. Hegemann, H. Brunner, C. Oehr, Surf. Coat. Technol. **174-175**, 253 (2003).
[7] H.-C. Langowski, A. Melzer, D. Schubert, Proc. 45th SVC Conf., 475 (2002).
[8] H.-C. Langowski, Proc. 46th SVC Conf. (2003).
[9] J. Lange, Y. Wyser, Packag. Technol. Sci. **16**, 149 (2003).
[10] D. Hegemann, H. Brunner, C. Oehr, Proc. 16th Int. Symp. Plasma Chem., 22–27.6.2003, Taormina, Italy.
[11] A.S. da Silva Sobrinho, N. Schühler, J.E. Klemberg-Sapieha, M.R. Wertheimer, M. Andrews, S.C. Gujrathi, J. Vac. Sci. Technol. **A16**, 2021 (1998).
[12] G. Dennler, A. Houdayer, P. Raynaud, I. Séguy, Y. Ségui, M.R. Wertheimer, Nucl. Instrum. Methods Phys. Res. **B208**, 176 (2003).
[13] B. Elkin, J. Mayer, B. Schindler, U. Vohrer, Surf. Coat. Technol. **116–119**, 836 (1999).
[14] D. Hegemann, H. Brunner, C. Oehr, Surf. Coat. Technol. **142–144**, 849 (2001).
[15] M.A. Lieberman, A.J. Lichtenberg, Principles of Plasma Discharges and Materials Processing, John Wiley & Sons, Inc., New York, 1994.
[16] Y.P. Raizer, M.N. Shneider, N.A. Yatsenko, Radio-Frequency Capacitive Discharges, CRC Press, Boca Raton, 1995.

[17] Y.-S. Yeh, I.-N. Shyy, H. Yasuda, J. Appl. Polym. Sci.: Appl. Polym. Symp. **42**, 1 (1988).
[18] H. Yasuda, Plasma Polymerization, Academic Press, New York, 1985.
[19] D. Hegemann, H. Brunner, C. Oehr, Proc. 45th SVC Conf., 174 (2002).
[20] A. Rutscher, H.-E. Wagner, Plasma Sources Sci. Technol. **2**, 279 (1993).
[21] S. Candan, A.J. Beck, L. O'Toole, R.D. Short, J. Vac. Sci. Technol. **A16**, 1702 (1998).
[22] D. Korzec, D. Theirich, F. Werner, K. Traub, J. Engemann, Surf. Coat. Technol. **74–75**, 67 (1995).
[23] J. Schwarz, M. Schmidt, A. Ohl, Surf. Coat. Technol. **98**, 859 (1998).
[24] S.M. Han, E.S. Aydil, J. Vac. Sci. Technol. **A14**, 2062 (1996).
[25] M.T. Kim, Thin Solid Films **347**, 99 (1999).
[26] F. Fracassi, in: Plasma Processing of Polymers, eds. R. d'Agostino, P. Favia, F. Fracassi, Kluwer Academic Publ., Dordrecht, p. 47 (1997).
[27] A.G. Erlat, B.M. Henry, C.R.M. Grovenor, G.A.D. Briggs, Y. Tsukahara, Proc. 45th SVC Conf., 503 (2002).
[28] K. Teshima, Y. Inoue, H. Sugimura, O. Takai, Proc. 45th SVC Conf., 565 (2002).
[29] J.P. Deville, B. Lang, P. Raynaud, Appl. Surf. Sci. **137**, 136 (1999).
[30] K. Koh, H. Niimi, G. Lucovsky, Surf. Coat. Technol. **98**, 1524 (1998).
[31] M.R. Alexander, R.D. Short, F.R. Jones, M. Stollenwerk, J. Zabold, W. Michaeli, J. Mater. Sci. **31**, 1879 (1996).
[32] S. Hofmann, Surf. Interface Anal. **35**, 556 (2003).
[33] G. Dennler, A. Houdayer, P. Raynaud, I. Séguy, Y. Ségui, M.R. Wertheimer, Plasmas Polym. **8**, 43 (2003).
[34] D. Hegemann, U. Vohrer, C. Oehr, R. Riedel, Surf. Coat. Technol. **116–119**, 1033 (1999).
[35] L. Agres, Y. Ségui, R. Delsol, P. Raynaud, J. Appl. Polym. Sci. **61**, 2015 (1996).
[36] H. Takeuchi, K. Okazaki, J. Chem. Phys. **92**, 5643 (1992).

3
Upscaling of Plasma Processes for Carboxyl Functionalization

V. Sciarratta, D. Hegemann, M. Müller, U. Vohrer, C. Oehr

Abstract

RF-plasma polymerization of acrylic acid enables the formation of polyacrylic-like layers containing a substantial amount of carboxylic groups immobilized onto different polymeric as well as on metallic substrates. Stable layers with a high amount of accessible functionalities up to 1.7 mmol/cm^3 COOH groups per volume are deposited. The maximum in carboxyl group retention was found to depend on the equivalent power, but not on the type of plasma mode (pulsed or continuous). Therefore, an upscaling of the plasma process can be carried out using continuous-wave-driven glow discharges. For this purpose, a similarity parameter, power input times width of the active plasma zone per unit gas flow, was identified. This new concept also explains the influence of the electrode distance on the retention of carboxylic groups.

3.1
Introduction

For industrial applications it is an obvious requirement that plasma processes examined successfully on lab-scale reactors and with particular substrates can be transferred to larger systems and different materials. In this respect the retention of carboxylic groups in acrylic acid containing discharges is a relevant process [1]. We choose the acrylic acid process for its usefulness in two application areas. The first is the development of permanent hydrophilic surfaces, therefore hydrophilic functionalities only on the outer surface are needed, secondly for surfaces with defined reactivity. In this case the amount of accessible functionalities is of importance, the amount of chemical groups is here not restricted to the outer surface. In the later case groups accessible due to swelling of the thin layer are of importance. For application in the medical and pharmaceutical area the stability in aqueous media is a crucial point and thus it is examined routinely. Recently, we developed polyacrylic-like ultrathin (~10 nm) and thin (~100 nm) films containing high amounts of carboxylic functionalities on polypropylene (PP) by means of RF continuous plasma that are stable in different media (see Sect. 2.3.4) [2]. In the present work we investigated the possibility to obtain similar thin layers by means of a pulsed plasma and

examined the role of the equivalent power in those processes. The second purpose was to achieve comparable carboxyl functionalities on polycarbonate (PC), polyethylene (PE), and polystyrene (PS) as on PP, silicone as well as on Si-wafer, titanium, and nickel-free steel.

Finally, we assessed a semiempirical law for the transfer of the obtained results to reactors of different dimensions – in our case from a small cylindrical parallel plate reactor to a larger rectangular-shaped reactor with electrode areas of A3-size [3]. The criterion for successful transfer was the deposition of layers with comparable density and stability of these chemical functions in aqueous, alcoholic and surfactant-containing solutions.

Characterization of the films was performed using fluorescence spectroscopy in combination with derivatization techniques for the quantitative estimation of functional groups and FTIR (Fourier transformation infrared spectroscopy) for qualitative control of the presence of carboxylic groups. The thickness of the polymer films was determined by AFM (atomic force microscopy).

3.2 Experimental

3.2.1 Materials

Polypropylene films (PP) without additives, supplied by Alkor Folien GmbH, Germany with a thickness of 50 µm were used. Polystyrene and polycarbonate (144C, Makrolon 2405) slides were used without further purification. Low molecular weight polyethylene films, 25 µm thick, were cleaned with acetone before using. Acrylic acid (AAc) was obtained from Fluka with >99% purity and used as-received. Silicon wafers, needed for determination of the layer thickness via AFM, were preventively washed with ethanol and partially masked with a temperature-stable adhesive tape during the plasma deposition.

Thionin acetate (THA, Sigma), ethanol (EtOH, Chromatographie Handel Müller) and hydrochloric acid (HCl, Fluka), needed for the fluorescence labeling were also used without further purification.

3.2.2 Plasma-Deposition Apparatus

The plasma experiments were performed in pulsed mode and in continuous mode with different substrates in a cylindrical, symmetrical parallel plate (200 mm diameter) reactor (Fig. 1a). The discharge was confined between the electrodes and the interelectrode distance can be varied by moving the lower electrode.

The gas flow and monomer vapors were introduced through the “hot” shower electrode. The lower grounded electrode served as substrate holder. The experiments in the cylindrical reactor were carried out with continuous and pulse RF discharge

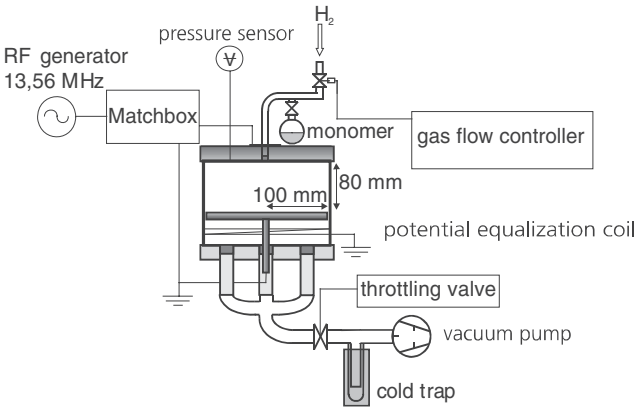

a)

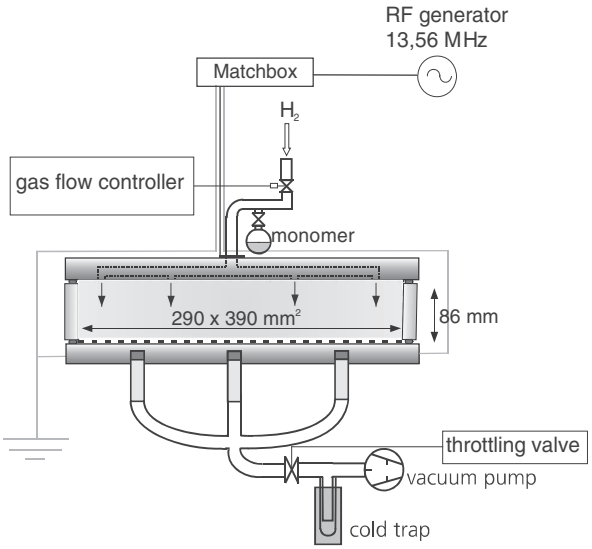

b)

Figure 1 Schematic view of the plasma reactors: (a) cylindrical reactor; (b) "A3" reactor.

(duty time 1 ms, plasma-off time 2 ms up to 9 ms) at different input powers. Plasma film deposition was carried out up to 30 min in continuous as well as in pulsed plasmas.

For the pulse plasma experiments, the average power $P_{\text{equivalent}}$ delivered to the system was calculated using the following expression:

$$P_{\text{equivalent}} = P_{\text{CW}} \frac{t_{\text{on}}}{t_{\text{on}} + t_{\text{off}}}, \qquad \text{where } \frac{t_{\text{on}}}{t_{\text{on}} + t_{\text{off}}} \text{ is defined as duty cycle.} \tag{1}$$

In a first step, the surfaces of the PP samples were cleaned/activated with an hydrogen plasma (H_2 flow 4 sccm, pressure 0.05 mbar, time 5 s) and afterwards, a mixture of hydrogen/acrylic acid (AAc flow approx. 1 sccm, total pressure 0.1 mbar) plasma was introduced. Plasma duration time and off-times t_{off} were varied.

In order to transfer the experimental conditions to a larger reactor a rectangular "A3" reactor with an electrode size of 290 × 390 mm^2 was used [3]. The activation/carrier gas as well as the monomer was introduced by means of a gas shower electrode with small tubes protruding through the hot electrode into the plasma chamber, thus providing a homogeneous flow and diffusion. As in the previous experiments, a symmetrical set-up was adapted where the plasma fills the whole vacuum chamber between the plane parallel electrodes (Fig. 1 (b)). The distance between gas inlet and deposition electrode was 60 mm, whereas the gap between the electrodes is comparable to the cylindrical reactor.

As with the foregoing experiments, the surfaces of polypropylene samples were cleaned/activated by means of hydrogen plasma (H_2 flow 10 sccm, pressure 0.05 mbar, time 5 s) and subsequently treated with a hydrogen/acrylic acid plasma (AAc flow ca. 2.5 sccm, total pressure 0.1 mbar). The activation/treatment discharge power was varied.

Both reactors enable power input with a minimum of losses, even in pulsed mode, to be controlled by *V*/*I* probe measurements (ENI Model 1065) since a direct, symmetrical RF connection to the outlying electrodes is possible and inductances are avoided.

3.2.3 Characterization Techniques

3.2.3.1 Fluorescence Spectroscopy

Fluorescence intensities were measured with a spectrometer (Spectrapro 275, Acton Research Corporation) after derivatization of the carboxylic groups with thionin acetate (THA) as described in [4,5]. The concentration of chemically bound fluorescence groups was determined in solution after calibration. The excitation wavelength of THA was 594 nm, the emission was measured at 618 nm.

3.2.3.2 Infrared Spectroscopy

HATR (horizontal attenuated total reflection) spectroscopy was performed with a Perkin Elmer FTIR Spectrometer (Spektrum 1000). A 45° ZnSe crystal was used; spectra were scanned 32 times between 4000 and 650 cm^{-1} with a resolution of 1 cm^{-1}. Prior to each set of analysis, the ZnSe crystal was cleaned with ethanol and dried with nitrogen. During the measurements the HATR mirrors compartment was purged with nitrogen to reduce water adsorption; the samples were pressed with a graduated pressure clamp to provide a reproducible contact to the ZnSe crystal.

3.2.3.3 Thickness Measurements by AFM

Thickness measurements are necessary to estimate the carboxylic groups concentration in plasma deposited layers. These were carried out by means of a Park Scientific Autoprobe CP microscope. The analyzed silicon wafers were partly covered with an

adhesive tape during the plasma deposition. To analyze the thickness of the plasma polymers, the adhesive tape was removed and the step height was measured.

3.2.3.4 Stability Tests

The treated samples were tested with different solvents, for example in bidistilled water, in ethanol or in 10% aqueous tween (an often used surfactant) solution by stirring for 30 min at room temperature. Moreover, a long-term stability was executed by immersion of a thionin acetate derivatized sample in ethanol for 10 days.

Under the conditions chosen here, sufficient crosslinking took place, thus we did not detect carboxylic residues in the washing water and in addition the weight of the samples before and after washing and drying was within the same the experimental deviation. Delamination sometimes occurs if the substrate-dependent pretreatment used was not sufficient, thus we used slightly different conditions for the pretreatment when we switched from polypropylene to silicon for substrate. Since no change in the carboxylic group concentration and in the layer morphology was detected applying these tests the main analytical examinations were performed after the routine washing was carried out.

3.3 Results and Discussion

The deposition of acrylic-like layers containing carboxylic groups by means of lab-scale plasma reactors is often difficult to reproduce on an industrial scale, since it depends on various plasma parameters. In this section it will be shown how input-power mode, substrate materials, and reactor geometry influence these processes and how it is possible to transfer process conditions to larger reactors.

3.3.2.1 Significance of Equivalent Input Power and Off-Times in Pulse Plasma

With the objective to investigate the effectiveness of a pulsed plasma compared with a continuous-wave-driven discharge, the influence of input power and pulse ratio on the amount of functional groups in the deposited film is examined. Therefore a first set of experiments in the cylindrical reactor was carried out. Plasma parameters were used as described in our recent paper [2]. The treatment time for all experiments was 30 min. Input power $P_{\text{equivalent}}$ was varied between 12 and 26 W and on/off pulse ratio between 1 ms/2 ms and 1 ms/9 ms. For a continuous-wave plasma an input power range of 16 to 34 W was applied.

In Fig. 2 the fluorescence measurements of the carboxylic group concentrations for different input powers and pulse ratios are reported. For lower continuous power inputs, some formation of powder in the chamber was observed. Also if any film deposition took place, a poor adhesion of the deposited layers is obtained. We suggest that this is probably due to inhomogeneities that are present in less-stable discharges generated at the limit of the ignition conditions. The ability to generate powder depends, furthermore, on the kind of monomer used, on reactor geometry, partial pressure of the monomer and of the interelectrode distance [6].

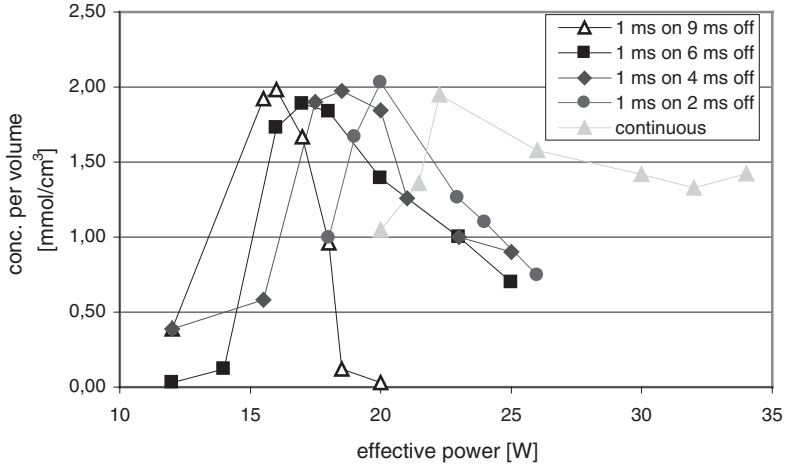

Figure 2 Dependence of COOH concentration on off-times and effective power.

Clearly, it appears that for a fixed pulse ratio varying the equivalent power, a maximum of carboxylic group retention in the films is achieved. These maxima depend on the dead times: the shorter the dead time, the higher the required energy. In the continuous mode the highest power input is necessary (off-time = 0).

Moreover, the maximum volume concentration of functionalities is, within the experimental uncertainty, independent of power on/off ratios and plasma mode. Therefore, the same quality of carboxylic-group-containing films can be obtained with continuous plasma compared with pulsed plasmas. However, with lower power modulation equivalent powers are sufficient.

To explain this striking result, we may consider two waveforms with dead times of 4 ms and 9 ms as depicted in Fig. 3.

In order to reproduce the same experiments with different pulse ratios in an ideal case (see solid line in Fig. 2) the equivalent power $P_{\text{equivalent}}$ has to remain constant, thus:

$$P_{\text{equivalent}\,1/9} = \frac{1}{10} P_{\text{Max}\,1/9} = P_{\text{equivalent}\,1/4} = \frac{1}{5} P_{\text{Max}\,1/4}$$
$$P_{\text{Max}\,1/9} = 2P_{\text{Max}\,1/4} \qquad (2\ \text{a/b})$$

Hence, it might be assumed that at 1 ms/9 ms a double input power is needed to obtain comparable conditions as at 1 ms/4 ms, as is often realized by comparing different pulse frequencies [7–9].

In the real case, however, the pulses have a form as depicted by the dashed lines in Fig. 2. When the generator is switching on, a spike occurs and this is clearly higher for higher maximal powers [10]. When the generator is switched off, the plasma discharge is sustained for a certain time [11]. Considering the areas below the dashed curves, it appears evident that with longer dead times a larger input energy

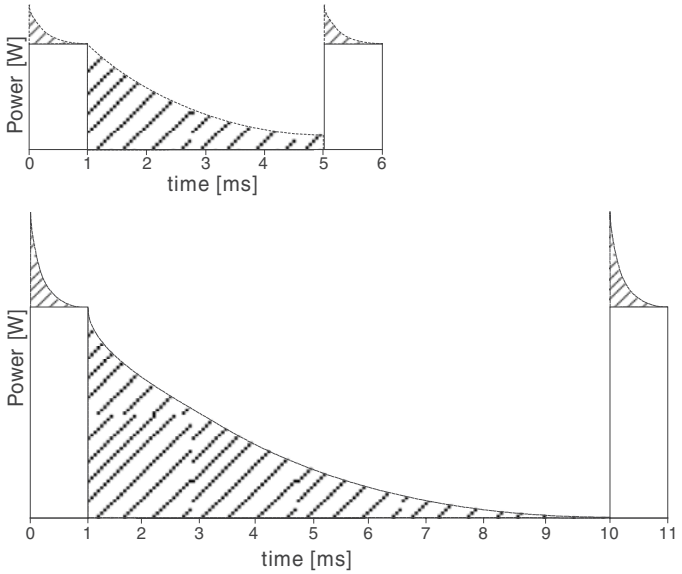

Figure 3 Comparison between ideal and experimental pulse sequence at 1 ms/4 ms and 1 ms/9 ms ratios.

is introduced. Consequently, to achieve equal results using longer off-times, a lower equivalent power $P_{\text{equivalent}}$ is required.

Generally, it could be supposed that in continuous mode a lower energy to activate/support plasma polymerization to avoid the fragmentation of carboxylic groups is necessary. But, during the on-period in pulsed mode, the electron density responsible for the existence of H^+ and for the building of free radicals is higher than in continuous mode [10]. Therefore a greater input power in continuous wave is required. These suppositions are confirmed by the results presented in Fig. 2.

3.3.2.2 Transfer to Different Substrates

Functionalization by means of carboxylic groups is not restricted to polypropylene, thus it can be extended to other substrates. In our experiments we also used polycarbonate, polyethylene, polystyrene, silicone as well as Si wafer, titanium, and nickel-free steel successfully.

For the achievement of these treatments, it is important to match the necessary activation energy in order to create free radicals for every substrate.

For all substrate materials investigated the power during the hydrogen cleaning/activation step was adjusted to achieve an optimum binding of the subsequent acrylic acid functionalization. For PP, PE, and PS 22 W was used, for PC 20 W, for silicone 28 W and for a Si wafer, titanium, and steel 22 W, again.

All treated samples were stirred in bidistilled water for 30 min and then dried. Infrared spectra, registered before and after washing, show no changes. In all spectra a new peak at 1715 cm^{-1} appears and it demonstrates that carboxylic groups on

the surfaces are present and chemically bound [2]. Furthermore, three peaks emerge: a broad band with center at about 3000 cm^{-1} is typical for –OH bridges stretching oscillations; another likewise broad band appears between 2700 and 2500 cm^{-1}, characteristic for carbon acid dimers, that is the result of combination oscillations of C–O stretchings and O–H deformations. Finally, a broad band between 1315 and 1280 cm^{-1}, but not always readily discernible, which is attributed to C–O stretching oscillations, is also expected.

All samples, apart from polystyrene, were also analyzed by means of fluorescence coupling [5,6] and the carboxylic groups were detected.

For a Si wafer, titanium, and steel we presume that an oxide layer already present on the surface of materials can contribute to the formation of O–H bridges.

3.3.2.3 Upscaling on Different Reactors

With the aim to transfer the experiments performed in the cylindrical reactor to the larger "A3" set-up or in general to another reactor with different geometry, it is important to consider the relevant plasma parameters as well as electrical connections, monomer inlet, and pumping system. In both reactors used, the generator was connected via a matching network and an V/I probe to the middle of the "hot" electrode in order to ensure a uniform power input and to maximize the absorbed power in the discharge. The lower electrode was centrally grounded maintaining the system as best as possible symmetrical. The monomer, in our case acrylic acid, was introduced into the cylindrical reactor, directly in the middle of the powered electrode, confining the polymerization process between the electrodes. Therefore, a vertical gas flow towards the samples (75 mm in diameter), which are placed in the middle of the lower electrode, is attained and the residence time of the plasma species can be given by

$$\tau = \frac{V}{F}\frac{pT_0}{p_0 T}, \tag{3}$$

where F is the flow rate of the molecular gas, p and T the pressure and temperature in the plasma chamber and p_0 and T_0 the standard (atmosphere) pressure and temperature, respectively. T remains near room temperature for the low powers used. Since the plasma fills the whole chamber between the electrodes, the plasma volume is $V = A_{dep}\ d_{act}$ with A_{dep} the electrode area (facing the plasma) and d_{act} the distance between the gas inlet and the deposition electrode, i.e. the distance the species travel through the active plasma zone. By this consideration the plasma sheaths of a few millimeters in width are neglected, which might be regarded as passive zones [12].

The distance between gas inlet and electrode influences the acrylic-like film growth that was proved by varying d_{act} and keeping other parameters like flow and pressure constant. The highest carboxylic group concentration was found at $d_{act} = 80$ mm for 1 ms/4 ms on/off times at 19 W. Since the residence time τ in the active plasma zone depends on the volume a smaller width of the plasma zone means a reduced residence time. A smaller plasma zone yields rather weak films with a reduced amount of carboxylic functionalities after stability testing. A wider plasma

zone, on the other hand, causes a stronger fragmentation. Thus, the variation of the electrode distance has the same effect as the variation of power. Accordingly, Kelly et al. [13] found that a longer residence time of acrylic acid molecules in the active plasma zone leads less retention of functionality.

Generally, power input per unit gas flow W/F is considered as a scaling parameter [6,14]. Moreover, we found that the addition of a reactive carrier gas can be treated as the addition of the monomer and carrier gas flows regarding a scaling factor [14]. Therefore, W/F is also applicable for gas mixtures. However, using Eq. (3), this reaction parameter is equivalent to $W\,\tau/V$ (at constant pressure) wherefore a variation in electrode distance should not influence the film properties. On the other hand, we recently show that $W\,d_{act}/F$ is an appropriate scaling parameter for radical-dominated plasma processes that is equivalent to $W\,\tau/A_{dep}$ [15,16]. This is consistent with the finding of a reduced functionalization on varying d_{act} or τ, respectively.

Moreover, this similarity parameter can be used to transfer the obtained results to a different reactor. The geometry of the "A3" reactor was chosen in a similar way (Fig. 1b): a shower system ensured that plasma particles encountered the rectangular samples lying on the grounded electrode by traveling a distance of $d_{act} = 60$ mm through the active plasma zone. In both reactors the plasma chamber was evacuated through three tubes connected to the pumping system also providing uniform monomer/activation gas flows in the plasma chamber.

In the smaller reactor a flow of 1 sccm AAc and 4 sccm H_2 at 22 W continuous power and a pressure of 0.1 mbar was used to optimize the carboxylic group retention. We focused our attention on the process in continuous mode, because it is easier to achieve an optimal matching that is relevant for the upscaling to production-type processes. Therefore, we attempt to reproduce the same results within the "A3" reactor.

Due to a relative low vapor pressure of acrylic acid at room temperature (3.8 hPa at 20 °C), the flow of AAc could only be set up to 2.5 sccm in order to maintain stable process conditions. The flow might be further increased by heating the monomer source. However, a higher monomer temperature may cause a polymerization of acrylic acid in the system before it reached the plasma chamber. Hence, in order to keep the pressure constant at 0.1 mbar, the vacuum system of the "A3" reactor was throttled. Accordingly, the hydrogen flow was set to 10 sccm to maintain a H_2/AAc ratio of four.

In Fig. 2 it was shown that an optimal polymerization process, in pulsed or in continuous mode, is only possible within a small input power range, where the carboxylic group concentration reaches a maximum.

Hence, in order to apply a corresponding input energy, an input power of 75 W at $d_{act} = 60$ mm was chosen to match the similarity parameter $W\,d_{act}/F$.

Note that the input power per area $W/A_{dep} = 22\,\text{W} / 314\,\text{cm}^2 = 0.07\,\text{W/cm}^2$ for the cylindrical reactor is equal to the power density in the "A3" reactor $W/A_{dep} = 75\,\text{W} / 1130\,\text{cm}^2 = 0.07\,\text{W/cm}^2$ and thus also the residence times in the corresponding active plasma zones were maintained.

Table 1 contains the results of plasma polymerization experiments as performed in the small and the "A3" reactor with three different deposition times at 22 W and 75 W, respectively.

Table 1: Fluorescence and thickness measurements results of samples treated in the cylindrical and "A3" reactor with different deposition times

	Plasma treatment time [min]	Film thickness after washing [nm]	–COOH group concentration [10^{-9} mol/cm^2] (fluorescence)	–COOH group concentration [10^{-4} mol/cm^3]
Untreated PP	–	–	0	0
AAc plasma coated PP in a	10	176 ± 7	26 ± 3	14± 2
cylindrical reactor	20	285 ± 9	37 ± 4	13 ± 2
	30	394 ± 8	53 ± 5	13 ± 2
AAc plasma coated PP in an	10	177 ± 19	30 ± 3	17 ± 2
A3 reactor	20	265 ± 25	46 ± 5	17 ± 2
	30	379 ± 7	60 ± 6	16 ± 2

It appears that in both reactors homogeneous, comparable layers can be produced: considering fluorescence measurements, the amount of carboxylic groups grows with the deposition time that means the density of the functionalities remains constant in the film volume.

3.4 Conclusions

We conclude that for the formation of acrylic-like layers with a very high concentration of carboxylic groups, according to our findings, a pulsed plasma is not necessarily required. For all investigated pulse frequencies as for continuous wave a comparable maximum of carboxyl groups in the as-deposited plasma coatings were achieved. However, the maximum shifts to lower equivalent powers when longer off-times are used. This finding is explained by an increased average power input due to beneficial effects during the plasma on and off periods in case of a high power absorption in the plasma.

The acrylic-like layers with high functionality were proven to be stable and can also be deposited on different substrates by adjusting a proper activation energy.

Moreover, the presented RF plasma polymerization with acrylic acid can successfully be performed within different reactor geometries when most parameters are kept constant and the distance between gas inlet and deposition electrode, i.e. the width of the active plasma zone d_{act}, is regarded as additional geometrical factor. Thus, a new similarity parameter $W\,d_{act}/F$, which is equivalent to $W\,\tau\,/A_{dep}$, is identified. In this sense W/F is a good scaling parameter as long as the widths of the active plasma zones are comparable and Wd_{act}/F is a good scaling parameter when the residence times (and pressures) are comparable. Both parameters are often used for the upscaling of plasma processes, whereas our concept enables a deeper understanding. The concept is proven for the upscaling on a rectangular parallel plate reactor of size 290 × 390 mm^2. Further work is in progress to clarify the validity of the concept for different reactor geometries and processes.

References

[1] M.R. Alexander, T.M. Duc, J. Mater. Chem. 8 (1994) 937–943.

[2] V. Sciarratta, U. Vohrer, D. Hegemann, M. Müller, C. Oehr, Surf. Coat. Technol. 174–175 (2003) 805–810.

[3] D. Hegemann, H. Brunner, C. Oehr, Surf. Coat. Technol. 142–144 (2001) 849–855.

[4] V.B. Ivanov, J. Behnisch, A. Holländer, F. Mehdorn and H. Zimmermann, Surf. Interf. Anal., 24 (1996) 257–262.

[5] J. Behnisch, F. Mehdorn, A. Holländer, H. Zimmermann Surf. Coat. Technol., 98 (1998) 875–878.

[6] H. Yasuda, Plasma Polymerization, Academic Press, Inc. (1985) 238–250 and 298–301.

[7] M.E. Ryan, A.M. Hynes, J.P.S. Badyal, Chem. Mater. 8 (1996) 37.

[8] J.-G. Calderon, R.-B. Timmons, Macromolecules 31 (1998) 3216.

[9] J. Zhang, W. van Ooij, P. France, S. Datta, A. Radomyselskiy, H. Xie, Thin Solid Films 390 (2001) 123–129.

[10] A. Brockhaus, St. Behle, A. Georg, A. Schwabedissen, Ch. Soll, J. Engemann, Contrib. Plasma Phys. 39 (1999) 399–409.

[11] L.J. Overzet, L.Y. Leong-Rousey, Plasma Sources Sci. Technol. 4 (1995) 432–443.

[12] A. Rutscher, H.-E. Wagner, Plasma Sources Sci. Technol. 2 (1993) 279–288.

[13] J.M. Kelly, R.D. Short, M.R. Alexander, Polym. 44 (2003) 3173–3176.

[14] D. Hegemann, H. Brunner, C. Oehr, Surf. Coat. Technol. 174–175 (2003) 253–260.

[15] D. Hegemann, U. Schütz, C. Oehr, in: Plasma Proc. Polym., eds. R. d'Agostino, M.R. Wertheimer, C. Oehr, P. Favia, Wiley-VCH, Weinheim, 2004, in press.

[16] D. Hegemann, C. Oehr, A. Fischer, J. Vac. Sci. Technol. A (2004), submitted.

4
Deposition of Fluorocarbon Films on Al and SiO_2 Surfaces in High-Density Fluorocarbon Plasmas: Selectivity and Surface Wettability

A. Tserepi, P. Bayiati, E. Gogolides, K. Misiakos, Ch. Cardinaud

Abstract

The present work focuses on the deposition of fluorocarbon (FC) films on aluminum and SiO_2 surfaces, and addresses the issue of selective deposition on Al versus SiO_2 in order to obtain surfaces of distinctly different wettability. If this is achieved, hydrophobic/hydrophilic patterning of substrates would be feasible by means of a self-aligned and relatively simple method. The selectivity of the deposition is optimized through proper selection of the deposition conditions, mainly gas-mixture composition and deposition time, and is demonstrated by means of contact-angle measurements on Al and SiO_2 surfaces. Chemical (XPS) analysis of the FC films deposited under various conditions is also performed and correlated with the wettability of the plasma-modified Al surfaces.

4.1
Introduction

Plasma-induced formation and deposition of polymer films on surfaces is an important issue in etching plasmas; for example, it allows selective etching of a SiO_2 layer over a Si or Si_3N_4 underlayer, while it provides side-wall passivation necessary for anisotropic high-aspect ratio Si etching. In fact, the majority of the current research effort relative to fluorocarbon etching plasmas invests in understanding plasma–surface interactions in order to improve etching performance mainly for selective SiO_2 over Si etching or for high aspect ratio Si etching [1–3]. In both of the aforementioned processes, deposition of FC layers of appropriate thickness and chemical composition is of vital importance to the etch selectivity. In particular, a general trend is observed, that the thickness of the FC film present on a surface is inversely proportional to the etch rate of the substrate material [2–5]. This has been demonstrated and used for explaining the SiO_2-to-Si and SiO_2-to-Si_3N_4 selective etching. However, analogous studies concerning selective deposition on other materials such as metals and consequent modification of their surface properties are rare in the literature.

The present work focuses on the selective deposition of fluorocarbon (FC) films on metal surfaces, specifically on aluminum, over SiO_2 surfaces, in order to obtain surfaces of distinctly different wettability, and thus achieve hydrophobic/hydrophilic patterning of substrates. Since polymer layers on surfaces are easily formed in fluorocarbon discharges with high concentrations of radical CF_x species, fluorocarbon gases such as CHF_3, C_4F_8 and mixtures of CHF_3/CH_4 were used in our experiments, in high-density plasmas known for their overwhelming polymerization ability. For the selection of conditions appropriate for selective deposition of FC films on Al-to-SiO_2, plasma parameters such as plasma power, bias voltage, electrode temperature, gas pressure and composition were varied, while etch and deposition rates were measured on SiO_2, resist and Al surfaces, in situ, by laser interferometry. We found that conditions that provide highly selective etching of SiO_2 over resist materials were also appropriate for selective deposition of FC films on Al surfaces. The modified wettability of SiO_2 and Al surfaces exposed to FC plasmas under various conditions was characterized by (static and dynamic) contact-angle measurements, which were used to demonstrate the selectivity of the deposition process. Finally, the plasma-deposited films on Al were chemically analyzed by means of X-ray photoelectron spectroscopy (XPS) and their composition was correlated to the processing gas and the wetting properties of the plasma-modified surfaces. In future work, the ability to electrostatically control the wettability of the plasma-deposited films on Al will be investigated as a means to switch the surface state from a hydrophobic to a hydrophilic one, and thus use this method for fluid transport in microfluidic devices (with Al electrodes patterned along a channel built on a SiO_2 substrate) [6].

4.2 Experimental

The high-density plasma reactor used in this work is an Alcatel (MET, Micromachining Etch Tool) inductively coupled plasma etcher, consisted of a load-lock and an ultra-high vacuum (10^{-6} mbar) main chamber. A one-loop ring-shaped antenna is supplied by a 0–2000 W rf (13.56 MHz) source, and it generates the plasma through a 150-mm diameter cylindrical alumina dome. The plasma diffuses from the generation area in the process chamber, where samples are introduced for processing, loaded on an anodized aluminum holder (100-mm diameter) mechanically clamped on a chuck. The chuck is located at a distance of 20 cm downstream from the ICP source and allows the sample to be biased and cooled during processing. The sample can be biased independently from the plasma source with a 300-W maximum rf (13.56 MHz) source. Biasing the processing electrode by means of a separate plasma source enables control of the ion energy independently from the production of the plasma. However, some effect of the bias power on the plasma generation cannot be completely excluded, in certain cases, as can be verified, for example, by ion-density measurements as a function of the applied bias power. A helium pressure of 12 mbar is applied on the backside of the sample holder to provide good thermal conduction between the sample and the chuck. The temperature of the chuck is con-

trolled by circulation of liquid nitrogen and simultaneous heat supply through six heaters, in order to achieve temperature regulation at a desired set point. Good thermal contact between the sample holder and the sample is achieved by means of a thermal paste. The electrode temperature is fixed at values between 0 and –50 °C in this study.

For this study, the fluorocarbon gases C_4F_8, CHF_3, and mixtures of CHF_3/CH_4 are used, while the substrates to be processed are SiO_2, Al, and AZ 5214 commercial photoresist. During plasma processing with the above gases, deposition occurs on the reactor walls. Therefore, before each experiment, the processing chamber is thoroughly cleaned using a O_2 or O_2/SF_6 plasma to remove fluorocarbon films from surfaces previously exposed to polymerizing plasmas. After the cleaning, the reactor is reconditioned under the process conditions for 2 min. Plasma parameters, such as the gas pressure and composition, the electrode temperature, the process time, the rf plasma power and bias voltage, are varied. In some experiments, a pretreatment of the sample surfaces prior to deposition is also carried out using Ar and O_2 and its affect on the wetting properties of the surfaces before and after deposition is investigated. The etching or deposition rates on SiO_2, Al, and resist surfaces are measured in real-time by means of in situ laser (650 nm) interferometry.

The wettability of the treated samples is characterized by contact-angle measurements using a GBX Digidrop system. The system allows automatic loading of single droplets on the surfaces under investigation and measurements of *static* contact angles are performed through observation of the droplet (and its reflection) almost at right angles to the sample surface. For static contact-angle measurements in this work, 4-μl droplets of deionized water are placed on the treated surface. The same system allows also measurement of the contact angle in the *dynamic* mode, where a droplet of increasing or decreasing volume is loaded on the surface, and the advancing and receding contact angles as well as the contact-angle hysteresis are measured. If, in addition, a voltage difference is applied between the droplet (through the droplet-depositing syringe) and the substrate, the modification of the contact angles in the presence of an electric field (electrowetting) can be observed.

Ex situ X-ray photoelectron spectroscopy (XPS) was used to monitor the chemical composition of the polymeric films deposited on Al as a function of the processing gas mixture and the deposition time. The samples were transferred to a Kratos Axis Ultra Spectrometer (AlK_α monochromatized X-ray source, pass energy 20 eV) in order to determine the chemical bonds and estimate the film thickness at different plasma deposition times.

4.3 Results and Discussion

4.3.1 Etching and Deposition in C_4F_8 Plasmas

4.3.1.1 Effect of Electrode Temperature

Numerous investigations of the SiO_2 etching mechanism in high-density etching tools have shown that the SiO_2 etching rate can be quite different depending on the bias voltage developed during the etching process [4, 5]. In particular, as the bias voltage increases, the fluorocarbon film deposition regime is followed by the fluorocarbon-suppression regime and finally by the oxide-sputtering regime, since deposition and etching have different dependencies on the energy of the ions bombarding the surface. In our work, we used the electrode temperature as the tuning parameter that could induce the transition from etching to deposition, as the temperature determines the rate of desorption of products from surfaces, and thus determines the balance between etching and deposition, when the other plasma parameters are kept constant. We conducted experiments in C_4F_8 plasmas, at substrate temperatures from 0 down to –50 °C. These experiments demonstrated that, on all of the tested surfaces, etching is followed by deposition that occurs at a rate inversely proportional to temperature. The interferometric signals shown in Fig. 1 correspond to a constantly changing top layer thickness on a resist film, as a function of the electrode temperature. In detail, the sinusoidal signals corresponding at $T = 15$ and –20 °C indicate etching of the resist film up to an endpoint, whereas the sinusoidal signal corresponding at $T = -50$ °C indicates a fluorocarbon film being continuously deposited on the resist surface. Etching and deposition rates determined from such interferograms are shown in Fig. 2 for a resist material as a function of electrode temperature, indicating the transition from etching to deposition as temperature decreases.

Similar experiments performed on a SiO_2 film indicated that etching of SiO_2 takes place even at lower temperatures (e.g. at –40 °C) compared to the etching of a resist layer. This is attributed to the fact that a SiO_2 surface consumes more CF_x radicals than a resist surface, thus there are fewer species available for deposition on a SiO_2 surface. Therefore, etching dominates deposition in the case of a SiO_2 surface at temperatures at which deposition takes place on a resist surface. For aluminum surfaces, deposition rates of FC films can be estimated from similar interferograms, and are shown on Table 1 together with deposition rates on a resist surface. Deposition rates are found to increase as temperature decreases, as shown previously in Fig. 1, and are higher on aluminum than on resist surfaces (see Table 1). The latter indicates that conditions that provide selective etching of SiO_2 to resist are also appropriate for FC deposition preferentially on aluminum compared to SiO_2. For example, exposure of surfaces to a C_4F_8 plasma at –40 °C leads to etching of a SiO_2 surface (E.R. = 230 nm/min), deposition on a resist surface (deposition rate = 50 nm/min), and even higher deposition on an Al surface (D.R. = 130 nm/min). Therefore, this temperature is appropriate for selective deposition on Al versus SiO_2 surfaces.

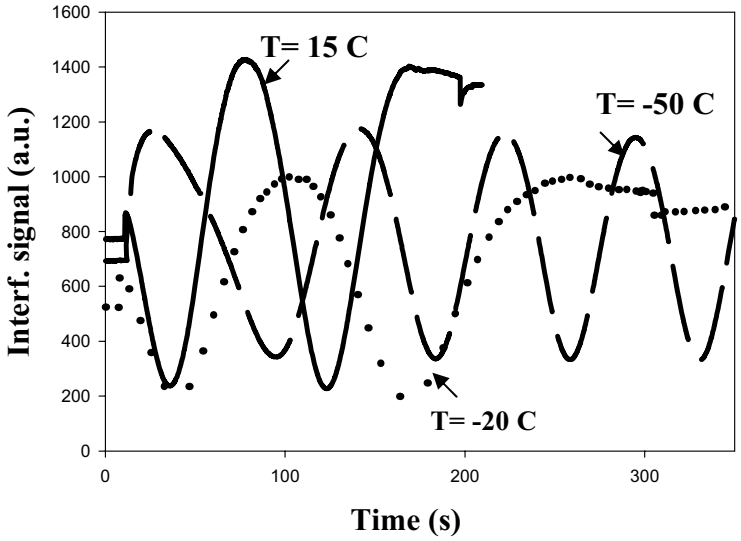

Figure 1 Interferometric signals from a resist surface (AZ5214) exposed to a C_4F_8 high-density plasma, at different electrode temperatures. Two of the signals ($T = 15\,°C$ and $-20\,°C$) indicate etching, while the signal at $T = -50\,°C$ indicates deposition of FC film.

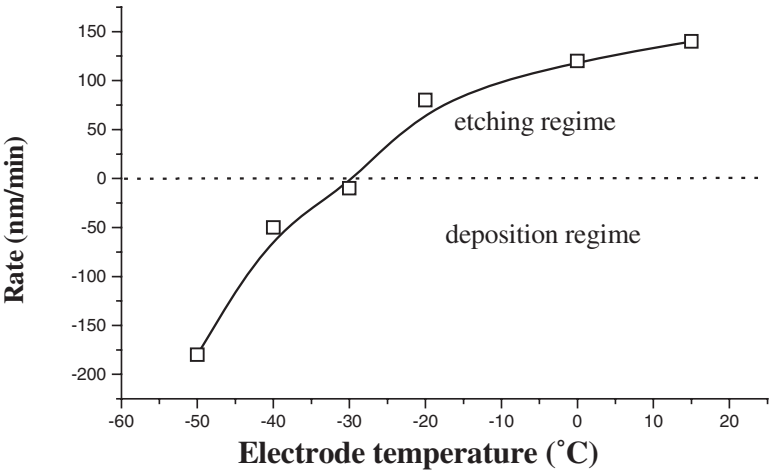

Figure 2 Etching and deposition rates of a resist (AZ5214) surface exposed to a C_4F_8 high-density plasma as a function of the electrode temperature.

Furthermore, we find that the selectivity for SiO_2/resist etching can be used as a guide to the selection of appropriate conditions for selective deposition on Al to SiO_2 surfaces. However, contact-angle measurements on Al and SiO_2 surfaces exposed to such conditions (–40 °C, 1500 W, 10 mTorr, –250 V_{bias}) for 1 min or more showed a small difference (smaller than 10°) in the water contact angles and thus in the hydrophobicity of the surfaces. Therefore, a wider space of plasma conditions was sought for better results.

Table 1. Deposition rates of FC films on Al and photoresist surfaces in C_4F_8 plasmas

Deposition rate (nm/min)		Temperature (°C)
Al metal	**AZ 5214 resist**	
90	10	–30
130	50	–40
200	180	–50

In the parameter space investigated (C_4F_8 pressure 1–5 mTorr, rf power 1000–1800 W, bias voltage –100 V to –150 V, and electrode temperature from –20 °C to 15 °C) for improved deposition selectivity, it was not possible to render Al surfaces exceeding SiO_2 in hydrophobicity by more than 10°. This result is surprising since, under the conditions used in these experiments, etching occurs on SiO_2 surfaces. However, studies in the literature [2, 3, 5] have shown that a (thin) fluorocarbon film is deposited even on etched SiO_2 surfaces, through which etching proceeds, in high-density plasmas (this is often called "the fluorocarbon-suppression regime"). If the deposited layer grows thicker than a certain value, the modified SiO_2 surface properties become indistinguishable from those of the modified Al surface. The measured difference in water contact angle between Al and SiO_2 surfaces modified in C_4F_8 plasmas is not considered large enough to allow exploitation for fluid control in microfluidic devices.

4.3.1.2 Effect of Surface Pretreatment in Nonpolymerizing Plasmas

In an effort to enhance the selectivity in the Al/SiO_2 deposition, a second set of experiments was designed to elucidate the role of the surface condition prior to the FC deposition. The Al and SiO_2 surfaces were pretreated in O_2 and Ar plasmas for a short time (15 s). The effect of pretreatment on the final contact angles is shown in Fig. 3. For pretreatment with a high bias voltage applied to the electrode, the Al surface remains always more hydrophilic than the SiO_2 surface for treatment times as long as 60 s, in contrast to the previously presented results in the absence of surface pretreatment. Only when the pretreatment is carried out at zero bias voltage does the Al surface become more hydrophobic (10° difference in contact angle) after a 60-s treatment in C_4F_8 plasmas (Fig. 3 (b)).

The observed behavior can be explained by the fact that application of a high bias voltage in the pretreatment contributes to the reduction of the oxidized layer on Al.

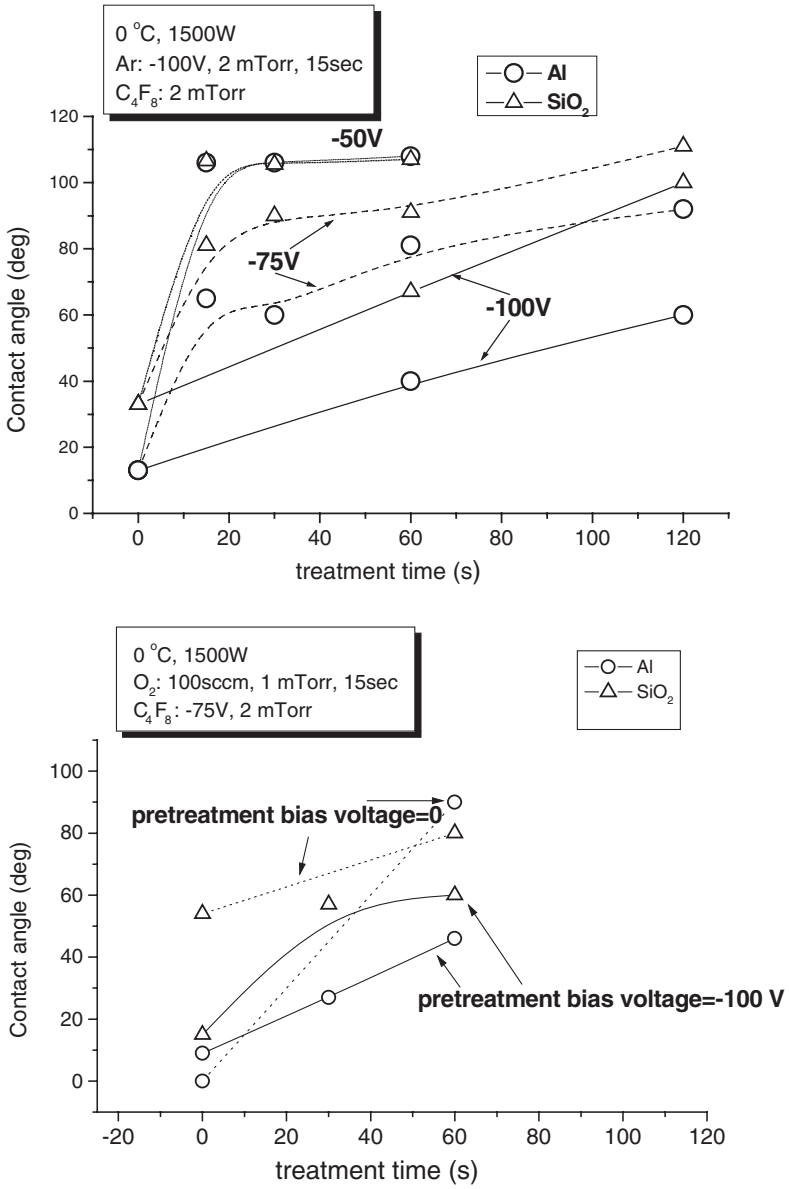

Figure 3 (a) Water contact angle as a function of treatment time in C_4F_8 after a pretreatment in Ar (15 s, bias voltage –100 V) for various values of the treatment bias voltage. (b) Water contact angle as a function of treatment time in C_4F_8 after a pretreatment in O_2 (15 s) for different values of the pretreatment bias voltage.

As a result, a clean Al surface characterized by a high sputtering yield is obtained, and, thus, during subsequent exposure in polymerizing plasmas, sputtering dominates deposition on the surface. Consequently, a surface less hydrophobic than that without the pretreatment is obtained. On the contrary, for the pretreatment without bias, the Al surface retains its surface oxide, a fact that allows after C_4F_8 treatment (60 s) a final surface more hydrophobic than a SiO_2 surface exposed to the same treatment. Certainly, the surface-wetting properties should be evaluated for different treatment times, in order to achieve enhanced selectivity.

4.3.2
Etching and Deposition Experiments in CHF_3/CH_4 Plasmas

In this series of experiments, we used mixtures of CHF_3/CH_4 in various proportions of the two gases to allow for a fine tuning of the gas composition and consequently for a better control of the deposited film thickness and the surface wetting properties. All measurements of etch rates and selectivity were carried out at a total pressure of 3 mTorr, plasma rf power 1500 W, bias voltage –150 V and at low temperatures (0 and –20 °C). As shown in Fig. 4, SiO_2-to-resist selectivity increases as the mixture becomes richer in CH_4, and it reaches a value of about 5 and 7 at 0 °C and –20 °C, respectively. When the content of CH_4 in the gas mixture is higher than 21%, selective deposition of a fluorocarbon film is observed on the resist (AZ5214), whereas the silicon oxide is still etched. We argue that around this CH_4 percentage FC films would be deposited preferentially on Al to SiO_2 surfaces.

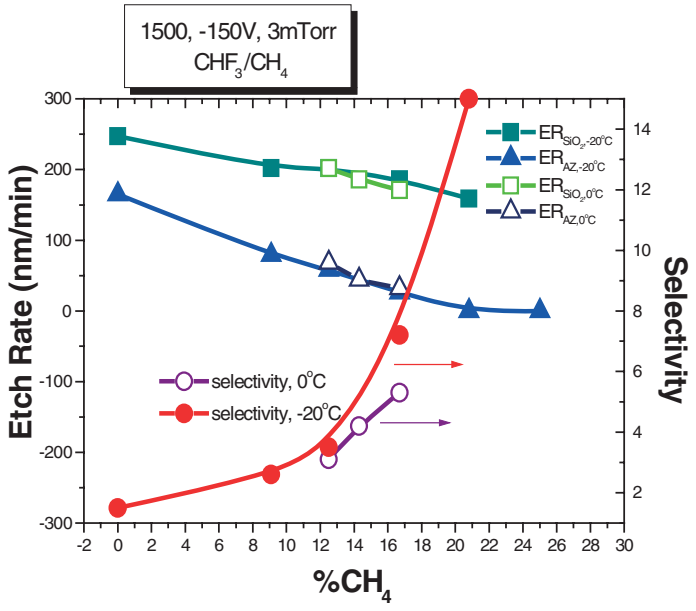

Figure 4 SiO_2 and resist etch rates and the selectivity as a function of the CH_4 percentage in a CHF_3/CH_4 high-density plasma.

Surfaces of silicon dioxide and aluminum were exposed to a plasma containing 79% CHF_3 and 21% CH_4, under the conditions that gave the best selectivity (pressure = 3 mTorr, $P = 1500$ W, $V_{bias} = -150$ V, $T = -20$ °C). The plasma exposure time was varied between a few seconds to a few minutes. Subsequently, we determined the water contact angle to verify the hydrophobic character of the treated surfaces. As shown in Fig. 5, both substrates exhibit surface modification and, specifically, a hydrophobic behavior even after a few seconds exposure to CHF_3/CH_4 plasmas. In fact, surfaces become hydrophobic within 15 s of plasma exposure. However, there is a difference in contact angle between the two surfaces, with a highest value of about 10(for 30–45 s of plasma exposure time. As shown in the figure, after 1 min of plasma exposure both surfaces exhibit the same contact angle. This was presumably due to the fact that deposition of even a thin FC film on the SiO_2 surface is sufficient to cause significant modification of the wetting properties of the SiO_2 surface. If the deposited layer grows thicker than a certain value, the modified SiO_2 surface properties become indistinguishable from those of the modified Al surface. Therefore, in order to achieve good selectivity for deposition between SiO_2 and Al surfaces, we should restrict the plasma exposure time for the surfaces to 30–45 s.

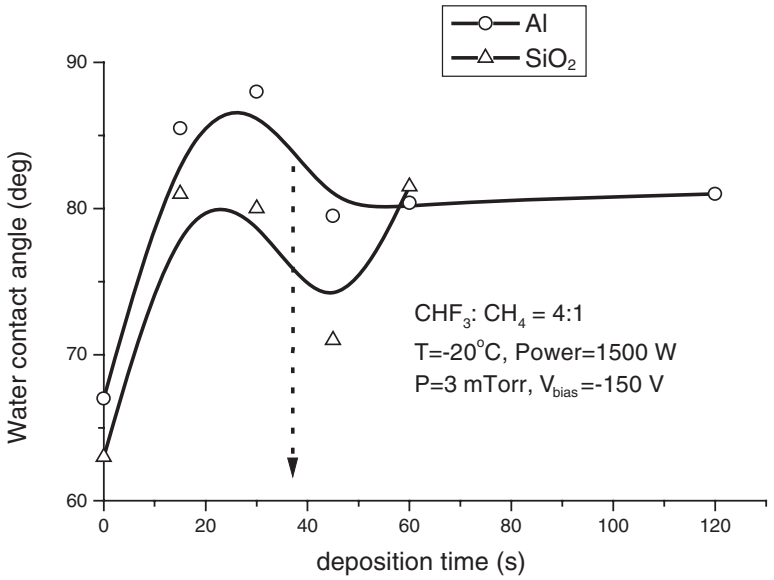

Figure 5 Evolution of the SiO_2 and Al water contact angle with treatment time in a CHF_3/CH_4 (4:1) plasma.

Figure 6 shows how the contact angle changes with the content of CH_4 in the gas mixture, for 45 s of deposition time (pressure = 3 mTorr, $P = 1500$ W, $V_{bias} = -150$ V, $T = 0$ °C). For a 27% CH_4 in the mixture, the difference in contact angles of Al and SiO_2 is as high as 30(. This difference seems satisfactory for allowing fluid movement control, exploitable in microfluidic devices driven by electrocapillarity, pro-

vided that the contact-angle hysteresis is smaller than the difference of the contact angles on Al and SiO_2 ($\Delta\theta \approx 30°$). In previous work [7], microfluidic actuation for droplet transporting has been demonstrated for a contact angle change 120°→80° ($\Delta\theta = 40°$). To further optimize the difference in contact angles of Al and SiO_2, we applied a post-treatment of the plasma-deposited surfaces in O_2 plasmas that can be used to completely remove the thin FC layer from the SiO_2 surface rendering it quite hydrophilic, while leaving the properties of the thick FC layer on the Al surface unchanged. Indeed, such post-treatment with zero bias voltage application resulted in an increased contact-angle difference $\Delta\theta \approx 55°$, a quite convenient difference to be exploited in microfluidic actuation based on the electrowetting effect. Investigation of successful post-treatments in other gases is currently in progress.

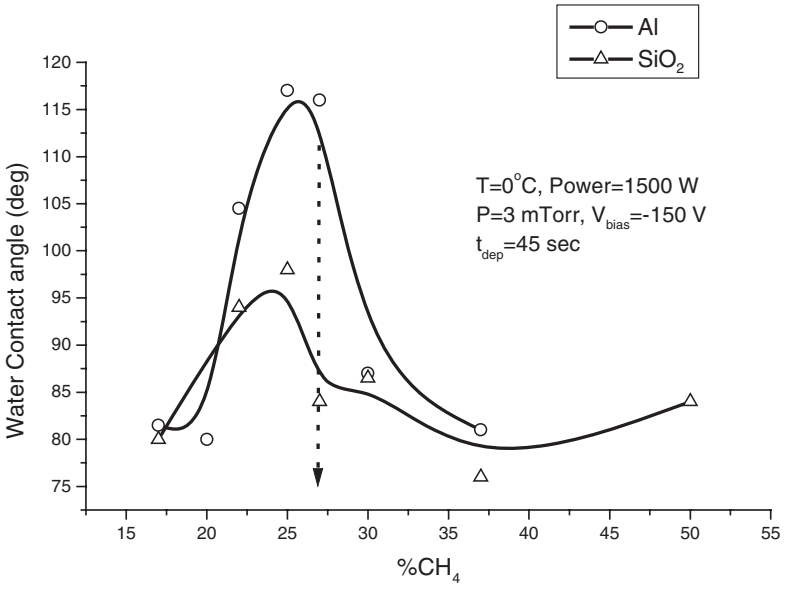

Figure 6 Dependence of the Al and SiO_2 water contact angle on the percentage of CH_4 in the CHF_3/CH_4 processing gas mixture.

4.3.3
FC Film Characterization: Chemical Composition

XPS analysis performed on the plasma-modified Al surfaces allowed determination of the chemical composition and estimation of the thickness of the plasma-deposited films. Al surfaces exposed to plasmas in CHF_3, CHF_3/CH_4, and C_4F_8 after pretreatment in O_2 (at 0 V bias voltage), were analyzed (deposition conditions and F/C ratios estimated from the area of the various components of the C1s spectra of FC layers are shown in Table 2 together with water contact angle, WCA, measure-

ments). In Fig. 7, the atomic composition (elemental quantification) of the plasma-deposited films is shown and its evolution with deposition time. In all gases, the film composition changes rapidly within the first minute of deposition, while it stabilizes at longer deposition times. The Al and oxygen content of the film, originating from the Al layer and its native oxide, decrease to zero, while the F and C content originating from the plasma deposited film increase to a plateau value. Figures 7 (a) and (c) show that after stabilization of their composition, the films deposited in CHF_3 and C_4F_8 are characterized by a higher content of F than C. However, the films deposited in CHF_3/CH_4 contain more C than F with the C content increasing with time. The first conclusion that can be drawn from Table 2 and Fig. 7 is that the processing gas affects the thickness and composition of the deposited films. Treatment with CHF_3 or CHF_3/CH_4 leads to deposition of a "pure" fluorocarbon layer of a thickness around 20 nm (after 1 min deposition), on top of a "mixed" interface layer consisting of Al-oxifluoride and CF_x species of total 7 nm in thickness. However, the composition of the films deposited in different gas mixtures is quite different: FC films deposited in CHF_3 contain more F than C (F/C = 1.2–1.3, with nonpolar CF_2 being the majority group), than the films deposited in CHF_3/CH_4 (F/C = 0.5, with polar C–C/C–H being the majority group). The observed difference in water contact angle (103° for the CHF_3-deposited films, and 88° for the CHF_3/CH_4-deposited films) can be attributed to the observed difference of the F content of the films, and the type of the majority groups (nonpolar and polar groups, for the CHF_3-deposited and CHF_3/CH_4-deposited films respectively). The pretreatment in O_2 before deposition in C_4F_8 results in deposition of a much thinner FC film (around 3.5 nm) with a small F content (F/C = 0.22). This small F/C ratio would hardly explain the relatively high values observed for the water contact angle (96°) on O_2-pretreated, C_4F_8-deposited films. However, since information about the distribution in-depth of the CF_x groups in the FC films is not available, such behavior may be attributed to the presence of more nonpolar groups on the outer surface (about 3–10 Å), a region known to mainly affect the contact angle values [8], of the FC films deposited in O_2/C_4F_8.

Table 2. Results of XPS analysis and water contact-angle measurements for FC films deposited on Al surfaces after 1-min exposure to fluorocarbon plasmas

Processing gas	Electrode *T* (°C)	Bias voltage (V)	Pressure (mTorr)	FC thickness (nm)	F/C	WCA (°)
CHF_3	–50	–150	10	19	1.2	103
CHF_3/CH_4	–20	–150	3	20	0.5	88
$O_2+C_4F_8$	0	–75	2	3.5	0.2	96
	Analysis of C1s spectrum					
	C–C/C–H	C–CF_x	CF	CF_2	CF_3	(O)C–F	(O)C–F_x
CHF_3	8.5%	24.8%	25%	27.6%	14.1%	–	–
CHF_3/CH_4	45.4%	16.1%	25.3%	10.9%	2.3%	–	–
$O_2+C_4F_8$	67.5%	15.8%	4.8%	3.6%	1.9%	3.7%	2.7%

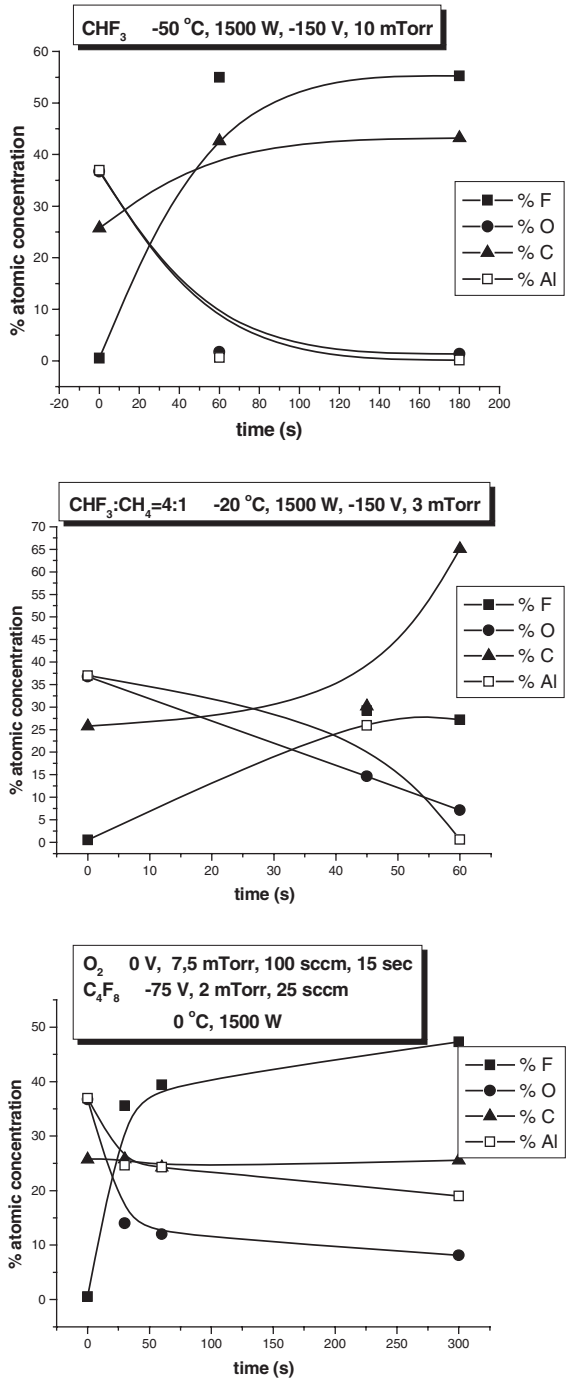

Figure 7 Atomic composition of plasma-deposited films in (a) CHF_3, (b) CHF_3/CH_4, and (c) C_4F_8 after pretreatment in O_2, and its evolution with deposition time. The plasma conditions at which the deposition was performed are shown on the plots.

4.4 Conclusions

Differential hydrophobicity of Al and SiO_2 surfaces was achieved through preferential deposition of FC film on these surfaces, by means of C_4F_8 and CHF_3/CH_4 high-density plasmas. Conditions ensuring high SiO_2/resist selectivity were found to be appropriate for selective deposition of FC films on Al versus SiO_2. However, a (thin) fluorocarbon film also seems to be deposited on SiO_2 surfaces even at conditions where SiO_2 is etched, thus, limiting selectivity. Therefore, the treatment time must be short enough (30–40 s) such that the SiO_2 surface stays less hydrophobic than the Al surface. The best results with respect to selectivity are obtained in CHF_3/CH_4, and can be further improved with a post-treatment of the surfaces in O_2 plasmas. The condition of the Al surface prior to deposition is found to be essential to the outcome of the treatment. Compositional analysis of the plasma-deposited films on Al surfaces through XPS measurements allowed determination of the F/C ratio of the FC layer and estimation of its thickness, which in turn were correlated with the modification of the surface-wetting properties.

Acknowledgements

This work was partially supported by a European Growth project "Microprotein" No G5RD-CT-2002-00744.

References

[1] G. Oehrlein, *Surf. Sci.* **386**, 222 (1997); and G. Oehrlein, et al., *J. Vac. Sci. Technol. A* **12**(2), 333 (1994).
[2] L. Rolland, M.C. Peignon, Ch. Cardinaud, G. Turban, *Microelectron. Eng.* **53**, 375 (2000).
[3] M. Matsui, T. Tatsoumi, M. Sekine, *J. Vac. Sci. Technol. A* **19**(4), 1282 (2001).
[4] M. Schaepkens, T.E. F.M. Standaert, N.R. Rueger, P.G.M. Sebel, G.S. Oehrlein, J.M. Cook, *J. Vac. Sci. Technol. A* **17**(1), 26 (1999).
[5] N.R. Rueger, J.J. Beulens, M. Schaepkens, M.F. Doemling, J.M. Mizra, T.E.F.M. Standaert, G.S. Oehrlein, *J. Vac. Sci. Technol.* A **15**(4), 1881 (1997).
[6] M. Pollack, R. Fair, A. Shenderov, *Appl. Phys. Lett.* **77**(11), 1725 (2000).
[7] H. Moon, S.K. Cho, R.L. Garrell, C.-J. Kim, *J. Appl. Phys.* **92**(7), 4080 (2002).
[8] E.E. Johnston, B.D. Ratner, *J. Electron Spectrosc. Relat. Phenom.* **81**, 303 (1996).

5
Hot-wire Plasma Deposition of Doped DLC Films on Fluorocarbon Polymers for Biomedical Applications

V.N. Vasilets, A. Hirose, Q. Yang, A. Singh, R. Sammynaiken, Yu.M. Shulga, A.V. Kuznetsov, V.I. Sevastianov

Abstract

Carbon layers doped with nitrogen and oxygen were deposited on polytetrafluoroethylene (PTFE) film by hot-wire plasma sputtering of a graphite target in the mixture of Ar with air. The surface atomic composition as well as chemical and electronic structure of carbon layers was studied by XPS, FTIR and Raman spectroscopy. It was shown that DLC layer with significant fraction of sp^3-bonded carbon and high surface adhesion is formed under hot-wire discharge conditions on the PTFE film. The blood compatibility of the DLC coating was tested by a comprehensive platelet-adhesion analysis. The results obtained demonstrate improved haemocompatibility of doped DLC coatings in comparison with untreated PTFE.

5.1
Introduction

Plasma-assisted deposition of amorphous isotropic carbon and diamond-like carbon (DLC) films on polymer substrates is one of the promising techniques for modification of the substrate surfaces. Due to a combination of superior mechanical and chemical properties including extreme hardness, low friction coefficients, high wear, and chemical resistance, deposition of carbon films has widespread applications in different areas and particularly in the biomedical field [1]. Although amorphous isotropic carbon as well as pyrolitic graphite have been applied for modification of implants for a long time [2], the potency of DLC films as a bio- and blood-compatible material has been proved only recently [3]. DLC-coated surfaces tested in vitro experiments and in vivo reactions in orthopedic applications have shown extended tolerance to the human body [4]. Modification of artificial heart valves and stents by DLC deposition was found to reduce the inflammatory reaction [5]. A higher ratio of adsorbed albumin/fibrinogen proteins was observed on a DLC surface compared to medical-grade silicon, indicating the ability of DLC coatings to prevent thrombus formation [6].

Due to its amorphous nature it is possible to functionalize the DLC films by addition a small amounts of different elements like N, O, F, Si and their combinations

without changing the hardness, low friction and other attractive mechanical properties of DLC matrix. A DLC layer may be a promising base coating to be doped with specific elements in order to control biological reactions, provide the surface with antibacterial effect or improve surface conductivity of the substrate.

The choice of fluorocarbon polymers in this work as a support for DLC coating is dictated by their wide applications in the field of cardiovascular surgery particularly for manufacturing of artificial vascular grafts [7]. Despite their chemical inertness and biocompatible nature fluorocarbon polymers are inherently thrombogenic. The haemocompatibility of polytetrafluoroethylene (PTFE) vascular grafts especially with small diameter (< 6 mm) is a problem that has to be resolved [8].

Our approach was to use hot-wire plasma sputtering of graphite in the mixture of Ar with air to deposit carbon layers containing nitrogen and oxygen groups onto PTFE. The hot-wire plasma causes heating and softening of the polymer surface layer thus stimulating the growth of carbon film with high adhesion to the polymer support. The heterogeneous hydrophilic/hydrophobic balance is very important for blood/surface interaction. This is why doping of a hydrophobic carbon layer with hydrophilic nitrogen- and oxygen-containing groups could improve hemocompatibility. The hypothesis of biomaterial blood compatibility based on the balance of polar and apolar groups on the surface was proposed by Hoffman and Ratner [9] and further developed by Sevastianov [10]. According to the "concept of complimentarity" the amphiphilic material suppresses the irreversible protein adsorption as well as platelet adhesion and activation thus improving the blood compatibility. Carbon- and nitrogen-containing groups could be also used for further immobilization of biomoleculars.

5.2
Experimental Details

5.2.1
Preparation of Samples

The substrate materials were polytetrafluoroethylene $-[CF_2\text{-}CF_2]_n$- (PTFE) films (GOST 5-1078-71) (thickness 60 μm) and Si (100) wafers were used as a witness samples. The size of PTFE and Si samples was 20× 10 mm. All samples were cleaned in an ultrasonic bath with methanol and distilled water prior to deposition.

5.2.2
Plasma Deposition Technique

The plasma parameters and scheme of the plasma source is shown in Fig. 1. The PTFE samples were exposed to deposition in dc glow discharge plasma by sputtering a graphite target in a flow of Ar with 5% air.

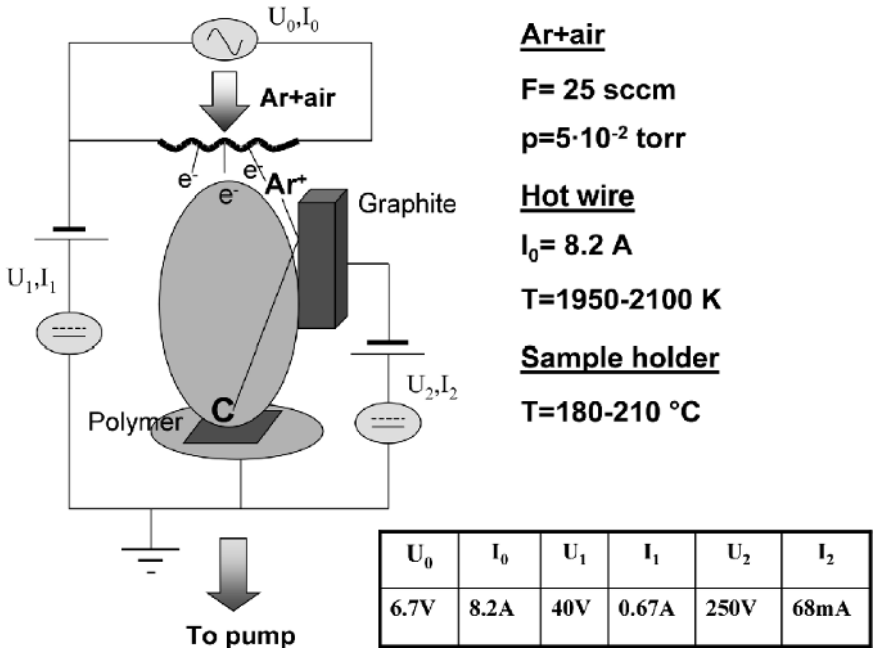

U_0	I_0	U_1	I_1	U_2	I_2
6.7V	8.2A	40V	0.67A	250V	68mA

Figure 1 Scheme of hot-wire plasma sputtering source.

The gas flow and pressure in the plasma chamber was maintained at 25 sccm and 5×10^{-2} torr respectively. The square graphite target (25×25 mm) was located 10 mm from a round sample holder (diameter 50 mm). The temperature of sample holder during deposition was measured by a chromel/alumel thermocouple and ranged between 180 and 210 (C depending on plasma conditions. The hot-wire temperature was controlled by Micro Optical Pyrometer (Pyrometer Instr. Co., USA) and varied in the range 1950–2100 K depending on the filament current. The time of deposition was varied from 15 min to 3 h. In each run deposition on polymer and Si wafer was done simultaneously.

5.2.3 Surface Characterization

The surface chemical composition before and after deposition on PTFE films was analyzed by XPS spectroscopy (Kratos Axis Ultra spectrometer, USA). The XPS spectra were obtained with 90-degree take-off angle by using monochromatised AlK_α source. The charge neutralizer was on for all the analysis.

The Raman spectra were measured using the 633-nm excitation wavelength of a helium-neon laser. The scattering light was collected in the backscattering made with a CCD camera, using a Renishaw Model 2000 Raman spectrometer. The incident laser power on the sample was in the range 0.3–1.2 mW.

IR spectra of a DLC layer deposited on Si substrate in the same run as the polymer film were recorded using a Perkin-Elmer 1720X (Perkin-Elmer, USA) FTIR spectrometer. The IR spectrum of the Si support was subtracted from the sample spectrum to obtain the transmittance spectrum of the DLC layer.

The surface morphology of the samples was examined by scanning electron microscopy (SEM) using secondary and backscattered electrons, 5 kV accelerating voltage, and magnification up to 5000 (JSM T330, JEOL, Japan).

The carbon layers deposited on the Si wafer were smooth enough and the crater depth after Ar^+ ion-beam etching could be measured accurately using a profilometer Alpha Step 500 (Fencor Inc. USA). From these data the thickness of carbon films and the rate of deposition under different deposition conditions were determined.

5.2.4
Platelet-Adhesion Technique

The study of platelet adhesion was performed with the informed consent of the donors. Five volunteers were included in the series of repeated experiments. Ten milliliters of blood was anticoagulated 1:9 with sodium citrate [11]. Platelet-rich plasma (PRP) was obtained by centrifugation of the whole blood at 100 g for 20 min at room temperature. The small PRP drops (50 μl) were placed onto sample surfaces and incubated in humid atmosphere for different periods (from 5 to 30 min). The samples incubated with PRP for 15 min were chosen for further analysis. The number of platelets adhered to the surface during this time interval was appropriate for quantification, and the platelets did not form large thrombus-like structures. The samples were rinsed in normal saline to remove unadsorbed plasma proteins and weakly adhered platelets and then fixed in 2.5% glutaraldehyde and dehydrated in a series of ascending ethanols by the standard technique [11].

5.3
Results and Discussion

5.3.1
Characterization of Deposited Film

Figure 2 shows XPS survey spectra of PTFE film before and after deposition of carbon layer. For untreated PTFE film the XPS spectrum consists of F1s peak (688.2 eV) and less intensive C1s peak (291.4 eV). In the XPS spectrum of the film obtained after 15 min deposition one can see intensive C1s peak (285.0 eV) as well as O1s (532.1 eV) and N1s (399.8 eV) peaks.

The important point is that no significant F1s peak was observed in the XPS spectrum of the carbon layer obtained after 15 min of carbon deposition. It means that pin-hole-free carbon coating with the thickness more then 30 Å (depth of free electron path for 800 eV [12]) is formed on the PTFE surface already after 15 min of

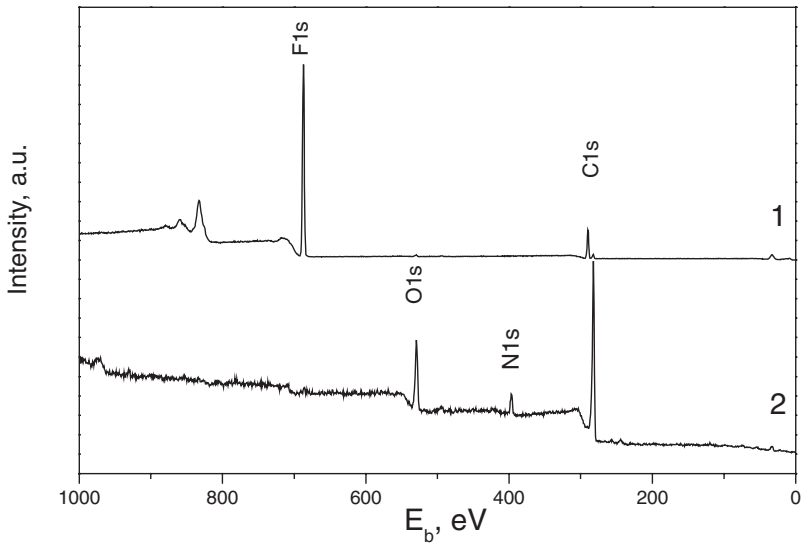

Figure 2 The XPS survey spectra of PTFE film before (1) and after carbon deposition (2).

graphite sputtering. The atomic surface concentrations calculated from measured integral intensities of XPS peaks for as deposited carbon film are: 72.2 at% C, 10.5 at% N and 14.0 at% O. The appearance of a relatively high concentration of oxygen on the surface of carbon layer may be explained by the surface contamination and/or bonding of oxygen in post reactions with carbon free radicals formed during plasma deposition. After a few minutes of Ar^+ ion sputtering oxygen content decreased by a factor of three while the nitrogen concentration only slightly changed. The chemical composition measured after ion etching was 86.8 at% C, 8.7 at% N, 4.5 at% O.

Plasmon loss structure accompanying the XPS C1s peak from the high binding energy side was studied for the carbon layers deposited on PTFE films and compared to that of the original graphite used as a target for plasma sputtering. Figure 3 compares C1s characteristic energy-loss spectra after background correction for graphite and carbon films deposited on PTFE film. The main plasmon ($\delta+\pi$) energy for our graphite (27.6 ± 0.3 eV) exceeds the 27 eV value obtained for HOPG (highly oriented pyrolitic graphite) by electron energy loss spectroscopy [13]. The difference may be explained by peculiarities of photoelectron spectroscopy measurements. The higher value of the main plasmon energy is due to the perturbation of electron density near the ionized atom formed as a result of photoionization process.

One of the important parameters to characterize the DLC structure of carbon films is the relative amount of carbon atoms in sp^2 and sp^3 hybridization. This information can be derived from the plasmon structure of C1s peak. The energy loss function was obtained by subtracting C1s peak fitted by C1s characteristic energy-loss spectra (after background correction) for graphite and carbon layers deposited on PTFE film.

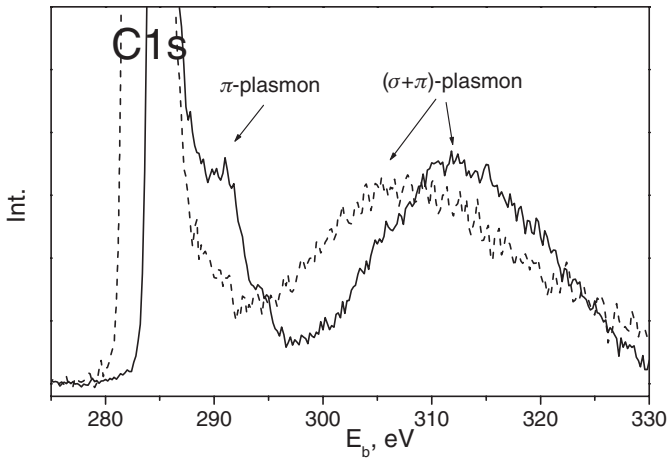

Figure 3 Electron energy-loss structure XPS spectra near C1s peaks (after background subtraction) for graphite (solid line) and carbon layer deposited on PTFE film (dashed line).

A Gaussian function from the spectra of graphite and carbon and zero energy alignment of C1s peak position was seen [14]. By using graphite as a reference spectrum containing 100% carbon atoms in sp^2 hybridization we can estimate the relative number of π-electrons in our carbon film comparing the plasmon loss spectra of our film with that of graphite. According to this estimation the subsurface layer of our film probed by XPS contains approximately 40 ±10% of carbon atoms in sp^3 hybridization.

The surface morphology of PTFE film and carbon layer formed on the support after 1 h of deposition is shown in Fig. 4. A complex fibril-type 1–2-micrometer regular structure could be observed on the surface of carbon layer.

The influence of topography and surface energy of carbon-coated polyethylene on platelet adhesion and protein adsorption was previously studied in detail [15]. It was

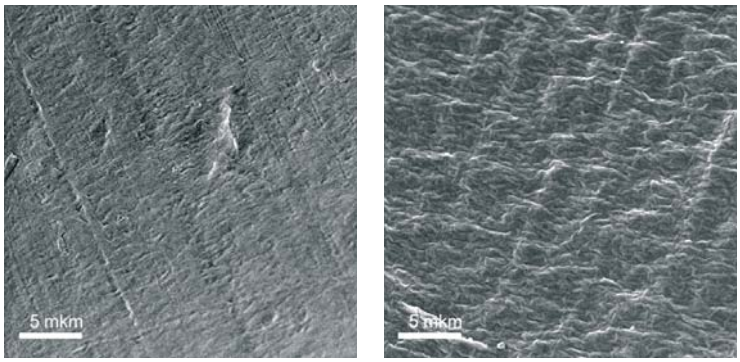

Figure 4 Scanning electron microscope images of PTFE film before (a) and after (b) 1 h of carbon deposition.

found that fibril-like surface morphology with several micrometers periodic carbon structures reduces protein adsorption and prevents adhered platelets from spreading and aggregating, thus suppressing the thrombus formation.

The adhesion of the carbon layer was checked by the adhesive tape test [16]. In this standard method an X-cut with the angle between the cuts equal to 30° was made in the coating. A cellophane adhesive tape was first carefully formed at the room temperature and then pulled off sharply after 2 min. No visible peeling was observed for carbon coatings deposited in our discharge conditions on PTFE. Usually hydrophobic PTFE film is a rather difficult object for carbon deposition with high adhesion. The enhanced adhesion of a carbon layer formed on PTFE in our experimental conditions may be explained by hot-wire heating and softening of the PTFE film during deposition.

The Raman spectra of PTFE films before and after deposition of carbon layer with different thickness are shown on Fig. 5. The characteristic bands of PTFE film: at 734 cm^{-1} assigned to stretching vibration of C–F, and two bands at 387 cm^{-1} and 293 cm^{-1} attributed to deformation vibration of C–C in polymer chains, are still detectable through the carbon layer with the thickness 225 nm deposited during 1 h but was not appeared in the spectra after deposition of carbon layer with the thickness 450 nm (2 h of deposition). This result is in agreement with the optical probing depth for Raman spectroscopy determined by the absorption coefficient α for carbon layer at our excitation wavelength 633 nm $d = 1/(2\alpha)$. Taking the optical constants for different carbons [17] we can estimate the Raman probing depth in our case as 100–200 nm that is much higher than the XPS analyzing depth (about 3 nm [12]).

The Raman spectrum of carbon coating consists of two broad bands at 1575 cm^{-1} and 1360 cm^{-1} usually detected in amorphous and diamond-like carbon films [18–20]. According to Wagner's model [21] developed for Raman scattering of carbon and polycrystalline diamond films, the peak at 1575 cm^{-1} has to be assigned to graphite-like sp^2-bonded carbon (G peak) while the scattering in low-frequency region around 1300 cm^{-1} has to be interpreted in terms of scattering by sp^3-bonded carbon plus a possible contribution of disordered sp^2-bonded carbon (D peak).

Figure 6 shows FTIR spectra for carbon layers of different thickness deposited on Si wafer. The broad main band in the region 1000–1700 cm^{-1} increases with increasing film thickness. The IR absorption in this range covers the frequency range of the stretching vibration of both CN and CC bonds that is often observed in carbon nitride films [22]. Usually C–C bonds in pure carbon films are not active in the IR absorption but only detected by Raman spectroscopy. Kaufman et al. [23] analyzed IR spectra of carbon films doped with different amount of nitrogen and found that Raman-active G (1575 cm^{-1}) and D (1360cm^{-1}) C–C bonds become IR-active due to the nitrogen replacement of carbon that breaks the symmetry in the six-fold carbon-ring structure. The nitrogen replacement gives rise to a net dipole moment and produces active IR absorption. The presence of C-N groups is indicated by the small IR absorption at 1230 cm^{-1}. Liu et al. [24] found that Raman and IR spectra of nitrogen containing carbon films deposited by dc magnetron sputtering are almost identical, and attributed the peaks at 1557 cm^{-1}, 1337 cm^{-1} and 1269 cm^{-1} to the G peak, the D peak and the single C–N bond, respectively.

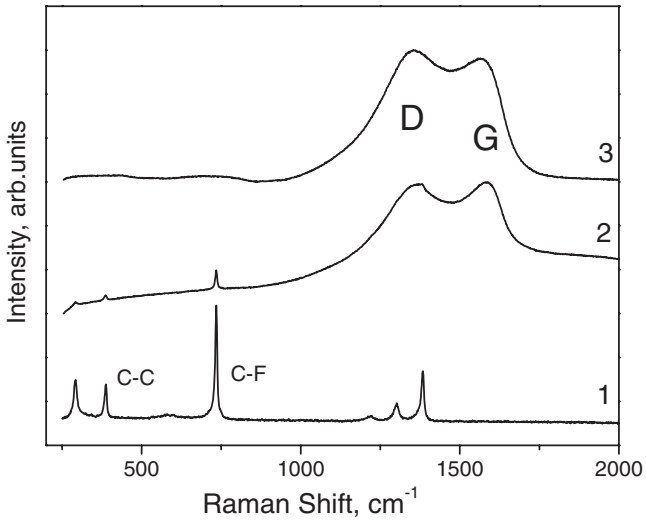

Figure 5 Raman spectra of PTFE film before (1) and after carbon deposition during 1 h (2) and 2 h (3).

In the IR spectra range 1700–3000 cm^{-1} an additional band at 2200 cm^{-1} can be observed and assigned to the stretching vibration of nitrile –C(N groups. A certain amount of oxygen was detected in the film by XPS spectroscopy.

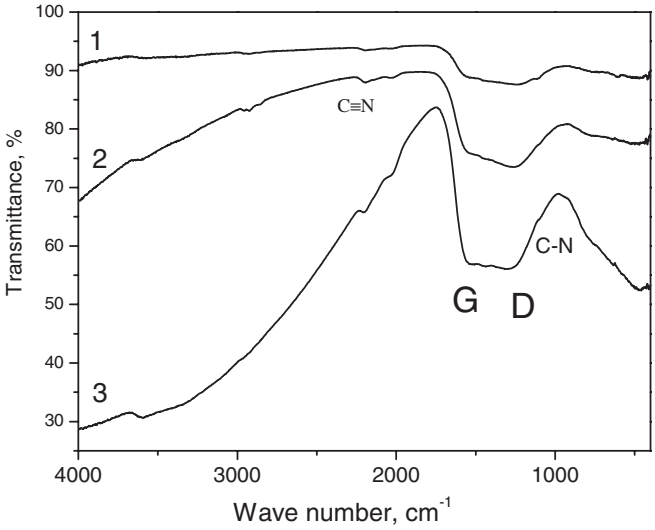

Figure 6 FTIR spectra of carbon layer deposited on Si wafer at (1) 0.5, (2) 1.0 and (3) 3.0 h.

But IR absorption bands in the range 1100–1300 cm^{-1} characteristic of C–O groups could not be observed due to the overlapping with the broad main carbon band at 1000–1700 cm^{-1}.

5.3.2
Platelet Adhesion

Platelet adhesion patterns were investigated by SEM. All samples were decorated with copper (thickness ~30 nm). For each sample 25 areas of 400 μm^2 were randomly chosen on the surface contacting with PRP. Then we qualified the total number of platelets N_{tot} and platelet numbers N_i in the following four morphological classes [25] (Fig. 7a).

1. Single – nonactivated cells
2. Slightly activated deformed cells and pseudopodical cells.
3. Spread – fully spread platelets.
4. Aggregates – two or more aggregated platelets.

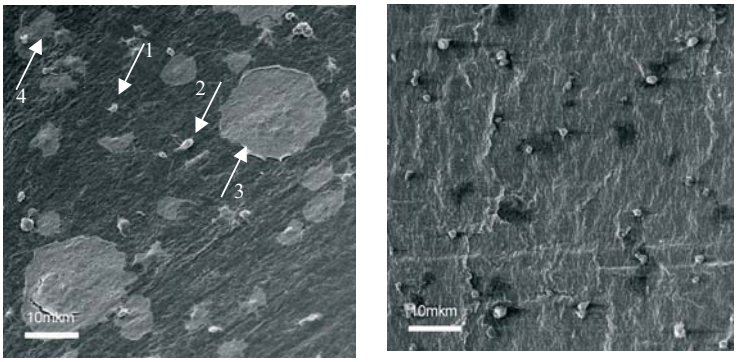

Figure 7 SEM qualification and morphology of platelet adhesion on PTFE support before (a) and after (b) 1 h of carbon deposition (×1500).

The key issue for blood-compatible materials is the ability of implant surface to prevent thrombus formation. It is generally known that the platelet adhesion process controls the formation of a thrombus.

The adhesion process is believed to run in several stages: platelet attachment to the surface, activation, pseudopodia formation, spreading, and aggregation (see Fig. 7a) [26]. The release of intracellular components from adhered or fully spread platelets (ADP, Ca^{2+}, serotonin, etc.) promotes further platelet adhesion, aggregation and finally thrombus formation [27]. The activation of platelets can be estimated by their morphology analysis. The stronger the impact of the material on platelets, the more adhered cells are activated, spread or aggregated. According to SEM images pre-

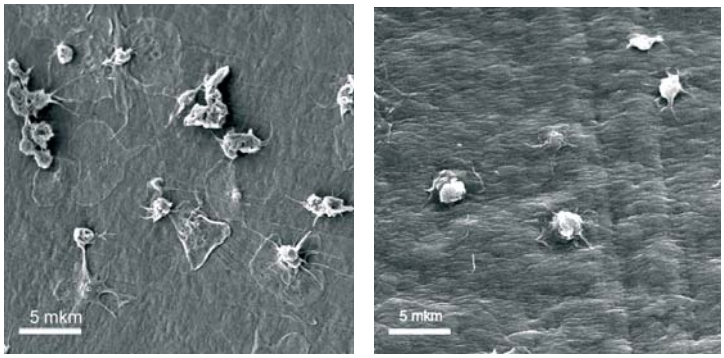

Figure 8 SEM images of platelet adhesion on PTFE film before (a) and after (b) 1 h of carbon deposition: (×3500).

sented -n Fig. 7, 8 doped DLC coating leads to the reduction of platelet adhesion and minimization of activation processes. In comparison with the surface of original PTFE that exhibits intensive platelet adhesion spreading and aggregation (Figs. 7 (a), 8 (a)), DLC coating shows substantially fewer single nonactivated or slightly activated adhered platelets (Fig. 7 (b), 8 (b)).

The usual approach for quantitative investigation of platelet adhesion consists in calculation of relative index of platelet adhesion for different morphological classes RIPA = N_i/N_{tot}, where N_i is the number of activated platelets qualified to one of the

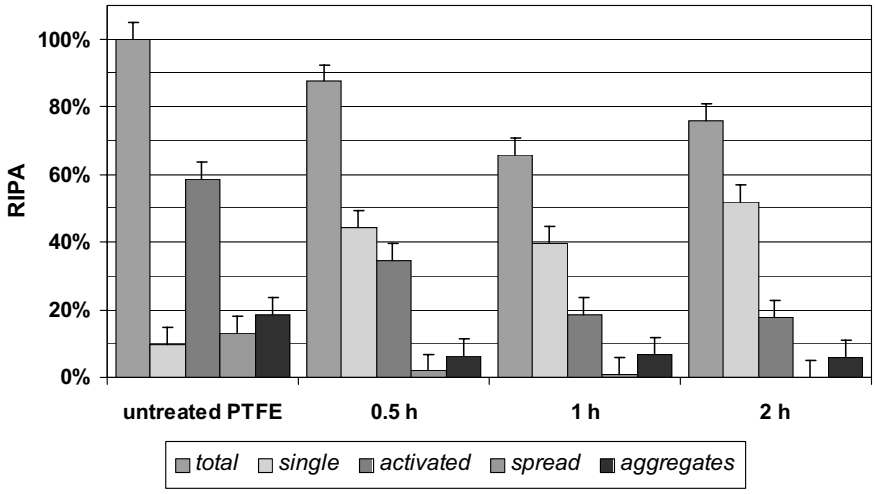

Figure 9 Diagram representing relative platelet quantities (RIPA) for different morphological classes observed by SEM for untreated and carbon coated PTFE (time of deposition 0.5, 1, 2 h; RIPA = 100% for the total number of adhered platelets on untreated PTFE, SD = 5%).

four morphological classes described above and N_{tot} – the total number of platelets adhered on the surface [28]. Presented in Fig. 9 are RIPA values for carbon coatings in comparison with that of untreated PTFE. From this point of view, all carbon coatings seem more preferable for contact with platelets than untreated PTFE. On all coatings the numbers of slightly activated cells, spread cells and cell aggregates were lower but number of single cells was higher than that of the surface of unprocessed PTFE. The total number of platelets was also lower on the carbon-coated surface for all three samples. For more quantitative investigation of platelets activation processes, further measurements like immune-fluorescence experiments [29] will be necessary. Assuming the existence of the adhesion stages, it can be suggested that platelet transition to later stages of activation was much slower on doped DLC coatings than on untreated PTFE.

In conclusion we could affirm that hot-wire plasma-deposited structural DLC layers containing oxygen and nitrogen groups promotes the minimization of platelet's reactions on foreign body thus extending the haemocompatibility of fluorocarbon polymers on the stage of adhesion and activation of platelets.

Acknowledgements

This research has been sponsored by the Canada Research Chair Program and by the Natural Science and Engineering Research Council of Canada.

References

[1] M.S. Sheu, D.M. Hudson, I.K. Loh, in Encyclopedic Handbook of Biomaterials and Bioengineering, Part A, vol.1, D.L. Wise, D.J. Trantolo, D.E. Altobelly, M.J. Yaszemski, J.D. Gresser, E.R. Shwartz (eds). Marcel Dekker, New York, 865, (1995).

[2] H.S. Shim, N.K. Agarwal, A.D. Haubold, J. Bioeng., **1**, 45 (1976)

[3] R. Hauert, Diam. Relat. Mater., **12**, 583 (2003)

[4] M. Allen, B. Myer, N. Rushton, J. Biomed. Mater. Res. **58/3**, 319 (2001)

[5] H.S. Tran, M.M. Puc, C.W. Hewitt, D.B. Soll, S.W. Marra, V.A. Simonetti, J.H. Cilley, A.J. DelRossi, J. Invest. Surgery, **12/3**, 133 (1999)

[6] I. Dion, X. Roques, C. Bacuey, E. Baudet, B. Basse Cathalinat, N. More, Bio-Med. Mater. Eng., **3/1**, 51 (1993).

[7] G.B. Koveker, L. M. Graham, W.E. Burkel, R. Sell, T.W. Wakefield, K. Dietrich, J.C. Stanley, Surgery **109**, 313 (1991).

[8] C.O. Esquivel, F. W. Blaisdell, J. Surg. Res. **41**, 1 (1986).

[9] B.D. Ratner, A.S. Hoffman, S.R. Hanson, L.A. Harker, J.D. Whiffen, J. Polym. Sci. Polym. Symp., **66**, 363 (1979).

[10] V.I. Sevastianov "Interrelation of protein adsorption and blood compatibility of biomaterials" in High-Performance Biomaterials, "A Comprehensive Guide to Medical and Pharmaceutical Applications". M. Szycher (ed.), Pennsylvania Technomic Publ. Co., Inc., Chapter 21, p. 245 (1991); V.I. Sevastianov, "Interrelation of protein adsorption and blood compatibility of biomaterials" in "High Performance Biomaterials" ed. M. Szycher, 313 (1991).

[11] L.V. McIntire (ed), Guidelines for Blood-Material Interactions. Report of the National Heart, Lung, and Blood Institute Working Group. U.S. Department of Health and Human Services. Public Health Service.

National Institutes of Health. (NIH Publication No.85-2185), 1985, Appendix 1.
[12] D. Briggs, M.P. Seah (eds.), Practical Surface Analysis by Auger and X-ray Photoelectron Spectroscopy, Wiley, Chichester (1983).
[13] H.C. Tsai, D.B. Bodi, J. Vac. Sci. Technol. **A 5**, 3287 (1987)
[14] F.R. McFeely, S.P. Kowalczyk, L. Ley, R.G. Cavell, R.A. Pollak, D.A. Shirley, Phys. Rev. **B 9**, 5268 (1974)
[15] I.A. Titushkin, S.L. Vasin, I.B. Rosanova, E.N. Pokidysheva, A.P. Alekhin, V.I. Sevastianov, ASAIO J, **47**, 11 (2001)
[16] I.S. Trakhtenberg, O.M. Bakunin, I.N. Korneyev., S.A. Plotnikov, A.P. Rubshtein, K.Uemura, Diam. Relat. Mater., **9**, 711 (2000)
[17] J. Wagner, P. Lautenschlager, J. Appl. Phys. **59**, 2044 (1986)
[18] E. Braca, J.M. Kenny, D. Korzec, J. Engemann, Thin Solid Films **394**, 30 (2001)
[19] A.C. Ferrari, J. Robertson, Phys. Rev. **B 64**, 75414 (2001)
[20] D. Liu, T. Ma, S. Yu, Y. Xu, X. Yang, J. Phys. D, Appl. Phys. **34**, 1651 (2001)
[21] J. Wagner, M. Ramsteiner, Ch. Wild, P. Koidl, Phys. Rev. **40**, 1817 (1989)
[22] A. Laskarakis, S. Logothetidis, M. Gioti, Phys. Rev. B, **64**, 125419 (2001)
[23] J.H. Kaufman, S. Metin, D.D. Saperstein, Phys. Rev. B, **39**, 13053 (1989)
[24] Y. Liu, C. Jiaa, H. Do, Surf. Coat. Technol., **115**, 95 (1999)
[25] S.L. Goodman, J. Biomed. Mater. Res. **45**, 240 (1999)
[26] S.L. Goodman, K.S. Tweden, M. Albrecht, J. Biomed. Mater. Res. **32**, 249 (1996)
[27] L.M. Waples, O.E. Olorundare, S.L. Goodman, Q.J. Lai, R.M. Albrecht, J. Biomed. Mater. Res. **32**, 65 (1996)
[28] V.I. Sevastianov, Z.M. Belomestnaya, N.K. Zimin, Artificial Organs **7**, 126 (1983).
[29] K.A. Ault, H.M. Rinder, J.G. Mitchel, C.S. Rinder, C.T. Lambrew, R.S. Hillman, Cytometry, **10(4)**, 448 (1989)

6
Properties of Silicon Nitride by Room-Temperature Inductively Coupled Plasma Deposition

H. Zhou, C. Sim, A. Glidle. C. Hodson, R. Kinsey, C. D. W. Wilkinson

Abstract

We have developed a low-temperature silicon nitride (SiN) deposition technique using inductively coupled plasma chemical vapor deposition (ICP-CVD) process with SiH_4/N_2 (i.e. NH_3 free). The process works well at room temperature. The effects of deposition parameters (temperature, pressure, power, SiH_4/N_2 ratio) on refractive index, deposition rate, uniformity, stress, composition, and dielectric strength are investigated over a wide range. From IR absorption measurements the composition of ICP-CVD SiN deposited at 20 °C is as good as or better than that in our plasma enhanced chemical vapor deposition (PECVD) SiN at 300 °C. Preliminary data on ion-induced damage shows that it is lower than our PECVD process. This room-temperature process looks very promising for SiN deposition on III-V semiconductors.

6.1
Introduction

Silicon nitride (SiN) has been widely used in silicon and III-V electronic and optoelectronic technologies. The main properties that make SiN an important dielectric are low current leakage, high breakdown voltage, and low interface-state density. These characteristics are dependent on the Si/N ratio and hydrogen content in deposited films [1, 2]. Conventional SiN deposition techniques are low-pressure chemical vapor deposition (LPCVD) and plasma-enhanced CVD (PECVD). LPCVD is a high temperature technique (>600 °C). This high temperature is not compatible with compound semiconductors or compatible with all device structures on a wafer. PECVD is able to deposit SiN at 300 °C. However, PECVD SiN has a lower dielectric strength than LPCVD Si_3N_4 and is not confined to the stoichiometric Si_3N_4 composition

There is considerable interest in low-temperature deposition of SiN films. The electron cyclotron resonance microwave (ECR-CVD) technique has been developed [3, 4]. SiN has been deposited using ECR-CVD at temperatures lower than 300 °C [5, 6]. In recent years, the inductively coupled plasma CVD (ICP-CVD) technique

has also been developed [7, 8]. ICP sources have been able to produce high-density and large-diameter plasmas in the low-pressure range. The main advantage of ECR-CVD and ICP-CVD techniques over conventional PECVD technique is their low-temperature deposition. This advantage will result in minimizing device degradation at high temperatures.

In this paper, we present the work on low-temperature deposition of high-quality SiN films using ICP-CVD technique with SiH_4/N_2 (NH_3 free) at deposition temperatures as low as 20 °C on Si substrates. The SiN films can possess very different characteristics, which depend greatly on the deposition conditions. Therefore, the effects of deposition parameters (temperature, pressure, power, SiH_4/N_2 ratio) on refractive index, deposition rate and uniformity, are investigated over a wide range. The film properties, such as stress, composition, dielectric strength, and ion-induced damage are briefly discussed.

6.2 Experimental Systems

The system used for deposition of SiN films was a Plasmalab System 100 ICP180 from Oxford Instruments Plasma Technology. A schematic diagram of the ICP-CVD system is shown in Fig. 1. The inductively coupled coil is connected to a 13.56-MHz, 2.5-kW RF generator via a matching unit. The RF current through the coil generates the RF magnetic flux along the axis of the cylinder. At the same time, this RF magnetic flux induces a RF electric field inside the cylinder. This induced electric field accelerates electrons. Finally, these accelerated electrons produce a high-density plasma in the ICP system. The ICP coil power controls the dissociation of the plasma and the density of the incident ions in the chamber. The lower electrode is separately powered by another 13.56-MHz, 300-W generator, which allows independent control of the bias voltage, i.e. the energy of the ions that impinge on the sample. In order to reduce the plasma-induced damage during deposition processes and the stress level in deposited films, the ICP-CVD system has been operated in a purely ICP mode by applying RF power (100 to 700 W) to only the ICP coil, but no RF power on the lower electrode.

Samples were loaded automatically from an evacuated load lock into the main chamber to maintain good stability of chamber vacuum and hence excellent repeatability of deposition results. The 4-inch Si wafers were mechanically clamped to a temperature-controlled electrode. Helium pressure was applied to the back of the wafers to provide good thermal contact between the chuck and wafer. The system has precise control of the substrate temperature from –150 °C to +200 °C by using an electrical heater and liquid nitrogen. This wide temperature range is important for the advanced plasma-deposition processes of different substrate materials.

Since the total hydrogen content in a SiN film and the type of hydrogen bonds has a strong effect on the film properties, N_2 replaces ammonia (NH_3) to reduce the hydrogen content in a ICP-CVD SiN film. High-purity N_2 was introduced into the ICP source chamber at the top of the cylinder, while pure silane (100% SiH_4) was

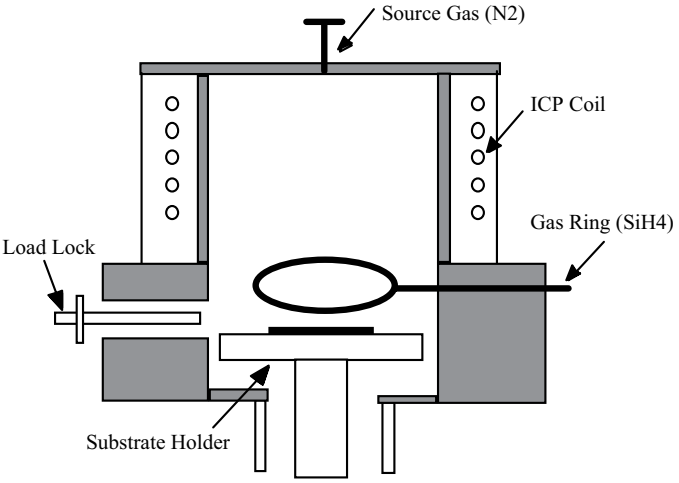

Figure 1 Schematic diagram of the ICP-CVD system.

introduced into the deposition chamber through a gas distribution ring as shown in Fig. 1. The gas flow rates were controlled by mass flow controllers (MFC) accurate to ~ 5% of the setting flow rate. An automatic pressure controller (APC) controlled the pressure (2 to 20 mTorr).

6.3 Results and Discussion

To investigate the properties of the low-temperature SiN deposited by the ICP-CVD technique, we studied the deposition rate and the refractive index as functions of chamber pressure, RF power, substrate temperature, and flow rate ratio of SiH_4/N_2, respectively. Refractive index and thickness of SiN films deposited on Si substrates were measured by a Gaerrner ellipsometer with a He-Ne laser operating at 632.8 nm. From the values of P1, A1 and P2, A2, refractive index and thickness were calculated. Film thickness was from 70 to 110 nm. Dektak Stylus Profiler was also used to directly confirm the thickness measurements. Fourier transform infrared (FTIR) spectra were obtained using a BOMEM MB120 FTIR system.

The deposition rate and the refractive index as functions of chamber pressure are shown in Fig. 2. It is very interesting to note that at pressures lower than 10 mTorr the deposition rate is constant, almost independent of the pressure. However, on increasing pressure to just above 10 mTorr, the deposition rate sharply increases to three times higher than that at 10 mTorr. When the pressure exceeds 15 mTorr, the deposition rate increases slowly again. The refractive index has the maximum 2.15 at the lowest pressure 4mTorr. At pressures lower than 10 mTorr, the refractive index decreases slightly, and then remains almost constant. However, as the pressure increases to just above 10 mTorr, the refractive index sharply decreases to less

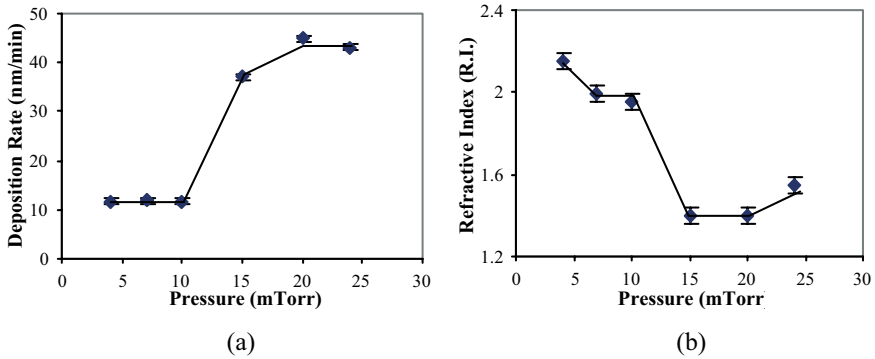

Figure 2 Pressure dependence of the deposition rate (a) and the refractive index (b) of SiN films.
(SiH_4/N_2 = 6:6 sccm, T = 20 oC, RF power = 100 W).

than 1.5. At pressures above 15 mTorr, the refractive index is almost independent of the pressure and then increases slowly again. The SiN films deposited at pressures higher than 15 mTorr show poor quality. The increased deposition rate at higher pressures may be a manifestation of lower film density and greater hydrogen incorporation. This pressure dependence of the deposition rate and refractive index of SiN films deposited by ICP-CVD is quite similar to that obtained by the ECR-CVD technique [9].

As shown in Fig. 3 (a) and (b), the deposition rate and the refractive index strongly depend on the RF power in the range of 100–500 W. It is understandable that the RF power provides energy to induce chemical reactions. This energy is important to the reactions especially when the substrate temperature is low. The increasing RF power speeds up the reactions (deposition rate). This suggests a reaction-controlled rather than a transfer-controlled type of mechanism at low temperature [10]. We can see that the deposition rate first linearly increases with the power till ~ 300 W, due to the enhanced dissociation of SiH_4/N_2 gases by the increased power. However, in the range of 300–500 W, the deposition rate has a slow increase and tends to saturate. At the same time, we see a symmetric effect on the refractive index, which first decreases with power till ~ 300 W, and then is almost constant in the range of 300–500 W. This may be explained by the fact that the N_2 has higher dissociation energy than the SiH_4, so that the fraction of the N_2 dissociated compared to the SiH_4 dissociation increases with increasing power [11]. Therefore the SiN films changes from Si-rich to N-rich, which results in the decrease of the refractive index with power. However, the observed trend in Fig. 3 (b) might also be explained by an increase of hydrogen content in the SiN film. This RF-power dependence of deposition rate and refractive index of SiN deposited by ICP-CVD is similar to that obtained by ECR-CVD [12].

To investigate the composition of the SiN films deposited at different RF power, the IR absorption spectra of the SiN films deposited at low and high power were obtained by the FTIR measurements in the mid-infrared region (400–4000 cm^{-1}).

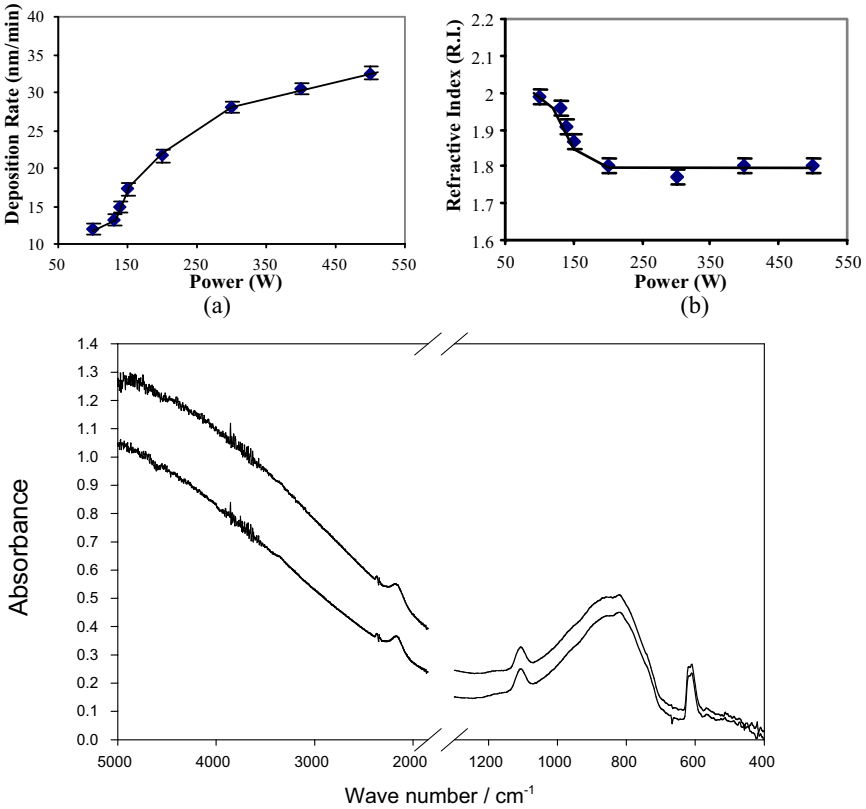

Figure 3 RF-power dependence of the deposition rate (a) and the refractive index (b) of SiN films.
(SiH_4/N_2 = 6:6 sccm, pressure = 7 mTorr, T = 20 °C). (c) IR absorption spectra for two samples deposited at 150 W (upper trace, offset upwards for clarity) and 100 W (lower trace), respectively. (SiH_4/N_2 = 6:6 sccm, pressure = 7 mTorr, T = 20 °C).

Figure 3 (c) shows the IR absorption spectra of the SiN films deposited at 100 W and 150 W, respectively. Since the Si substrate wafers used for SiN deposition were not double-side polished, SiN films were deposited only on the polished side. Therefore, the unpolished Si surface is oxidized in air, which will results in the absorption peak related to Si–O bonds at 1100 cm^{-1} in IR spectra. We observed the absorption peaks due to Si–Si, Si–N and Si–H bonds at ~610, ~850 and ~2160 cm^{-1}, respectively, for both films deposited at 100 W and 150 W. But none of the absorption peaks corresponding to N–H bonds were observed within the detectable limit of the spectrometer. We can see that in Fig. 3 (c), the two IR absorption spectra have approximately the same intensity in the Si–H peak. This equal intensity indicates that an equal number of Si–H bonds are present in these two films that have nearly the same thickness and similar hydrogen concentration. However, it is still probable that there is an amount of unbonded hydrogen in the films. The intensity of the Si–N peak of

the film deposited at 150 W is slightly greater than that of the film deposited at 100 W, which corresponds to different N contents in the two films.

The temperature dependence of the deposition rate and the refractive index of SiN was investigated for more N-rich films (i.e. Si_3N_4-like, n ~1.8). Figure 4 (a) shows clearly that in the temperature range of 30–200 °C, the deposition rate significantly decreases with increasing substrate temperature. This is expected because increasing temperature will reduce hydrogen content and increase the film density [12]. Higher density is a consequence of both lower hydrogen content and a lower deposition rate. However, as shown in Fig. 4 (b), the substrate temperature has a small influence on the refractive index, which only slightly increases from 1.77 to 1.83 in the temperature range of 30–200 °C.

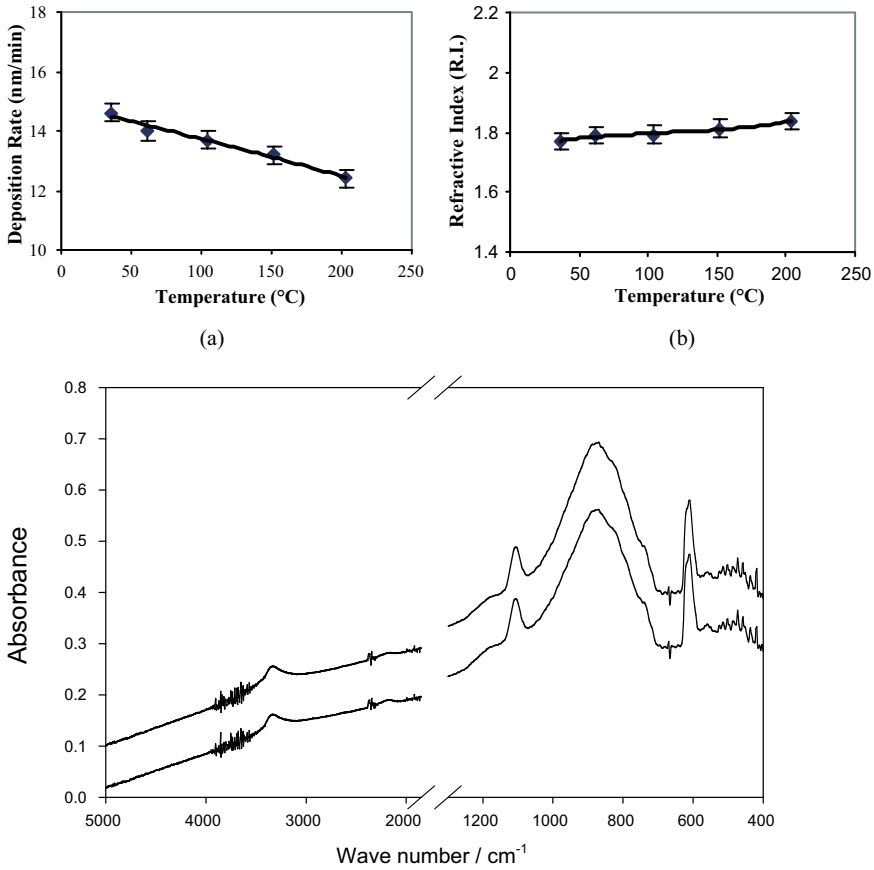

Figure 4 Temperature dependence of the deposition rate (a) and the refractive index (b) of SiN films. (SiH_4/N_2 = 5.8:6 sccm, pressure = 7 mTorr, RF power = 100 W). (c) IR absorption spectra for two samples deposited at 200 °C (upper trace, offset upwards for clarity) and room temperature (lower trace), respectively. (SiH_4/N_2 = 5.8:6 sccm, pressure = 7 mTorr, RF power = 100 W).

Figure 4 (c) shows the IR transmission spectra for N-rich films deposited at 200 °C and room temperature. In addition to the absorption peaks related to Si–Si, Si–N and Si–H bonds at ~610, ~880 and ~2160 cm^{-1}, respectively, the absorption peaks due to N–H bonds are also observed at ~1180 and ~3340 cm^{-1} for both SiN films deposited at 200 °C and room temperature. In the N-rich SiN films (i.e. n~1.8), the N–H peak at ~3340 cm^{-1} is the dominant peak associated with hydrogen. However, in the Si-rich SiN films (i.e. n~2), the dominant peak associated with hydrogen is the Si-H peak at ~2160 cm^{-1}, as shown in Fig. 3 (c). Therefore we can conclude that as SiN film composition changes from Si-rich to N-rich, the dominant bonds associated with hydrogen changes from Si–H to N–H according to the IR absorption spectra.

It is interesting to note that in Fig. 5, the deposition rate only has small variations when the SiH_4/N_2 flow rate ratio has changed from 0.5 to 1.33. It is thought that this situation in deposition rate is caused by the limited feed rate of N radicals [13]. However, at the same time, a small change of SiH_4 flow rate can increase the refractive index rapidly. This is quite reasonable because increasing SiH_4/N_2 ratio corresponds to increasing Si/N ratio, which results in a significant increase in refractive index [12]. This also indicates that more Si atoms are incorporated in SiN films with increasing SiH_4 flow rate.

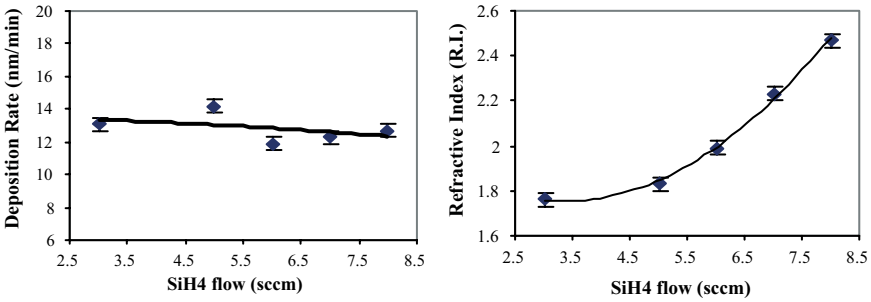

Figure 5 SiH_4 flow-rate dependence of the deposition rate (a) and the refractive index (b) of SiN films. (N_2 = 6 sccm, pressure = 7 mTorr, RF power = 100 W, T = 20 °C).

To further investigate the composition of ICP-CVD SiN deposited at 20 °C with a SiH_4-N_2 plasma and PECVD SiN deposited at 300 °C with a SiH_4-N_2-NH_3 Plasma, the IR spectra of both SiN films were determined by the FTIR measurements. Figure 6 shows the typical IR absorption spectra of ICP-CVD SiN deposited at 20 °C and PECVD SiN deposited at 300 °C. Absorption peaks due to Si–N and Si–H bonds were observed at ~840, ~870 and 2160 cm^{-1} for both SiN films. However the absorption peaks due to N–H bonds at ~1180 and ~3340 cm^{-1} were observed in the PECVD SiN, but not observed in the ICP-CVD SiN here. All of the ICP-CVD SiN films deposited at room temperature have H contents and SiN compositions as good as or better than the typical PECVD SiN deposited at 300 °C. We have used FTIR and XPS

to determine stoichiometry of the ICP-CVD SiN films, and more detailed FTIR and XPS analysis will be presented in other papers.

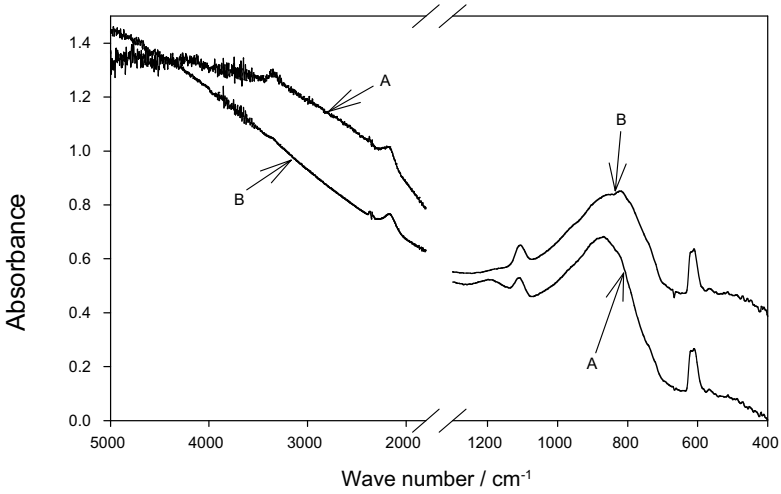

Figure 6 IR absorption spectra of PECVD and ICP-CVD SiN films deposited at 300 °C and 20 °C, respectively (trace A: PECVD, trace B: ICP-CVD, offset upwards for clarity)

Film stress was measured using a Dektak Stylus Profiler and calculated by stress measurement software from Veeco Metrology Group. The stress calculation was based on the formula:

$$\sigma = (E_s\, t_s^2) \,/\, 6\,(1-\nu_s)\, t_f\, R,$$

where σ is the stress in the film, t_s and t_f are the thickness of substrate and film, respectively, E_s is Young's modulus of the substrate, ν_s, is Poisson's ratio of the substrate, and R is its radius of curvature [14]. Using the above formula to calculate film stress, the key parameter is the radius of curvature of the substrate, before and after film deposition. The radius of curvature is calculated from scan height data. The film stress has been investigated as a function of deposition pressure, RF power and substrate temperature, respectively. It is very clear that the film stress is strongly dependent on the RF power and deposition pressure. For 500-nm thick SiN films deposited by ICP-CVD at room temperature, we have obtained both the lowest tensile stress 2.7×10^8 dyne/cm^2 and compressive stress 2.5×10^8 dyne/cm^2. We also noticed that if the lower electrode was applied with only 5W RF power, the stress of SiN films can be dramatically increased to 1.36×10^{10} dyne/cm^2 compressive. The detailed stress measurements of the ICP-CVD SiN films deposited on Si substrates will be presented in other papers.

The electronic properties of the SiN films have been investigated as a function of deposition pressure, RF power and substrate temperature, respectively. The electrical properties of the films (resistivity ρ, and breakdown field E_B) were obtained by

measuring the I–V characteristics of the metal-insulator-metal (MIM) capacitor structures. MIM devices were fabricated as follows: first, the Si wafers were coated with a layer of 20 nm of Ti and 150 nm of Au by e-beam evaporation. Then 100 nm of SiN was deposited on the top of Ti/Au layer. Finally, Ti/Au squares were evaporated through a photoresist mask by e-beam evaporation to define the top electrodes. In order to separate individual capacitors, SiN films lying outside the electrode areas were etched away by RIE etching. For room temperature deposition, the breakdown field E_B, ~3–4 × 10^6 V/cm has been obtained, which was defined at the field at which the MIM current is 1 μA/cm^2. When the SiN films lying outside electrode areas were not etched away, the actual breakdown field E_B of the SiN films might be higher than that we measured, because the breakdown may occur through the air beneath the two electrodes. The films having a higher value of E_B contain less hydrogen inside. The relation between E_B and the presence of hydrogen in the PECVD SiN films was already suggested [15]. The stress of the films, directly related with the presence/absence of hydrogen, may play some specific role in the understanding of breakdown properties of SiN films. Preliminary data on ion-induced damage of depositing SiN films on Si and III-V devices shows that it is lower than our PECVD process. The detailed results of electronic properties of the SiN films on Si/Ge and III-V devices have been presented in another paper [16].

6.4 Conclusions

We have developed a low-temperature SiN deposition technique using ICP-CVD with a SiH_4/N_2 process (NH_3 free) in the temperature range from 20 to 200 °C, and pressures lower than 10 mTorr. The ratio of SiH_4/N_2 was adjusted to give a refractive index in the range of 1.8–2.0. Both the lowest tensile stress 2.7 × 10^8 dyne/cm^2 and compressive stress 2.5 × 10^8 dyne/cm^2 have been obtained on room-temperature deposition without using RF power on the lower electrode. We discovered that the best film quality could be achieved at low ICP powers and low pressures. At room temperature, ICP power of 100–150 W and pressures of 4–7 mTorr, it is possible to obtain an acceptable deposition rate of 12–17 nm/min, with good film quality and reasonable uniformity typically between ±4% and ±7% across a 4-inch wafer. The dielectric strength is 3–4 × 106 V/cm. The composition of ICP-CVD SiN deposited at 20 °C is as good as or better than that of our PECVD SiN deposited at 300 °C. Preliminary data on ion-induced damage also shows that it is lower than the PECVD process. The new ICP-CVD technique works well at room temperature and looks very promising for SiN deposition on III-V semiconductors.

Acknowledgements

We would like to thank Mr. Dave Clifton, Colin Roberts and Ronnie Roger for their help in the Dry Etch Laboratory.

References

[1] S. V. Nguyen, J. Vac. Sci. Technol. **B4**, 1159 (1986).

[2] M. Maeda and Y. Arita, J. Appl. Phys. **53**, 6852 (1982).

[3] S. Matsuo and M. Kiuchi, Jpn. J. Appl. Phys. **22**, 210 (1983).

[4] T. Hamasaki, M. Ueda, A. Chayahara, M. Hirose, and Y. Osakkka, Appl. Phys. Lett. **44**, 1049 (1984).

[5] F. S. Pool, J. Appl. Phys. **81**, 2839 (1997).

[6] S. Y. Shapoval, V. T. Petrashov, O. A. Popov, M. D. Yoder, P. D. Maciel, and C. K. C. Lok, J. Vac. Sci. Technol. **A9**, 3071 (1991).

[7] D. V. Tsu and G. Lucovsky, J. Vac. Sci. Technol. **A4**, 480 (1986).

[8] H. Mito and A Sekiguchi, J. Vac. Sci. Technol. **A4**, 475 (1986).

[9] J. R. Flemish and R. L. Pfeffer, J. Appl. Phys. **74**, 3277 (1993).

[10] C. Juang, J. H. Chang, and R. Y. Hwang, J. Vac. Sci. Technol. **B10**, 1221 (1992).

[11] R. S. Rosler, W. C. Benzing, and James Baldo, Solid State Technol. **XX**, 45 (1976)

[12] S. Lee and A. Gopinath, J. Vac. Sci. Technol. **B8**, 402 (1990).

[13] H. Mito and A. Sekiguchi, J. Vac. Sci. Technol. **A4**, 475 (1986).

[14] C. Blaauw, J. Appl. Phys. **54**, 5064 (1983).

[15] S. Hasegawa, Y. Amano, T. Inokuma, and Y. Kurata, J. Appl. Phys. **75**, 1493 (1994).

[16] K. Elgaid, H. Zhou, C. D. W. Wilkinson, and I. G. Thayne, MNE 2003, Proc. Microelectron. Eng., (2003).

7
Structural Analysis of Diamond-like Carbon Films Deposited by RF (13.56 MHz) in a Methane Gas Plasma Atmosphere

M. Ouchabane, M. Aoucher, A. Sekkal, K. Henda and H. Lahmar

Abstract

A plasma-enhanced chemical vapor deposition (PECVD) technique is used to deposit hydrogenated carbon films on silicon wafers by methane gas plasma in both diode and triode reactors with a hollow RF electrode. It is well known that DLC films are elaborated under ion bombardment and their properties are determined by the amount of sp^3/sp^2 hybridization ratio. For structural analysis the films were characterized by X-ray Auger electron spectroscopy (XAES) in both $N(E)$ and $dN(E)/dE$ to assess the sp^3/sp^2 ratio of the DLC films. Also the electron energy loss (EELS) spectra are recorded to show features corresponding to plasmon and core loss energies. In comparison with an evaporated amorphous carbon films (a-C) and graphite structures, the specimens spectra show a mixed of sp^2 and sp^3 bonds in the DLC films in both XAES and EELS analysis.

7.1
Introduction

Hydrogenated amorphous carbon films a-C: H and diamond-like carbon films (DLC) have received much attention from many authors [1–3] because of their interesting properties such as extreme hardness [4], chemical inertness [5], high electrical resistivity [5], low IR absorption [6,7], their unique characteristic in wear durability [8] and biocompatibility [9,10]. They have been prepared by RF plasma decomposition of hydrocarbon (CH_4) gas [11,12] and dilution of hydrocarbon species such as CH_4 in H_2 and argon [13]. Traditional RF capacitive parallel electrodes are used to produce plasma by an RF 13.56-MHz generator. Because some of their mechanical, physical, optical and electrical properties appear to be determined by the relative amount of sp^3/sp^2 hybridization ratio and hydrogen content, this is why the assessment of this ratio is important in tailoring properties. This is done through the use of two different characterization techniques. In this investigation we present some results of structural characterization of the deposited hydrogenated carbon films by X-ray Auger electron spectroscopy (XAES) and electron energy loss spectroscopy (EELS).

7.2
Experimental Procedure

7.2.1
Deposition Apparatus

The films were deposited in an apparatus consisting of a stainless steel vacuum discharge chamber of 23 cm diameter and 25 cm in height with two electrodes (Fig. 1). Around its lateral wall, 12 lines of ferrite magnets with reversed polarity are arranged in order to produce a multicusp magnetic field of about 100 G. The discharge is created between the multihole electrode (upper electrode) and the electrode substrate holder (lower electrode). The transverse section in Fig. 1 shows the multihole RF electrode, which allows both an increase of the discharge efficiency, and a decrease in electrode sputtering that was published in a previous paper [14].

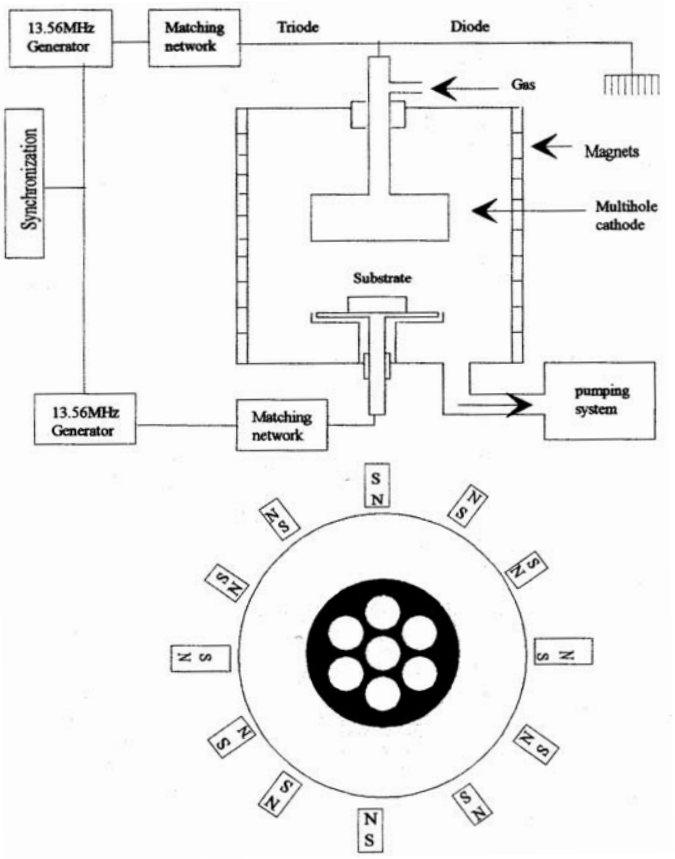

Figure 1 Experimental setup. General and transverse view.

This electrode is a metallic disc (stainless steel) of 12.6 cm diameter and 5 cm in height with 7 holes distributed throughout of 4 cm in diameter each. It is capacitively coupled to the RF power supply output via a matching network.

Before deposition, the plasma chamber is evacuated to a residual base pressure of 7.5×10^{-6} Torr and before introducing gas, the pressure was adjusted to 7.5×10^{-5} Torr. Methane gas (99.5%) was used as the feedstock into the plasma region through an orifice along the hollow electrode. For the triode configuration the plasma is primarily created by the hollow electrode and then the sample holder is RF (13.56 MHz) polarised with less power than the upper electrode to enhance ion bombardment. In this case, the two generators are driven by the same oscillator in order to avoid the signal beat at the bottom. However, for the diode mode the plasma is created by the lower electrode and the upper one is grounded. For all the experiments, in diode or triode system, the energy of the ion flux that bombards the growing film is adjusted by the input power at the substrate holder and the reflected power was adjusted at nearly zero. The self-bias potentials (V_{dcu} and V_{dcl}) developed, respectively at the upper and the lower electrodes, were measured with a voltmeter through a low-pass filter. Before deposition, the Si substrates were cleaned from contamination in an argon RF discharge at about –400 V self-bias potential.

7.2.2 Experimental Conditions

The carbon films were deposited by PECVD using methane gas plasma excited at 13.56 MHz. During all the experiments of deposition in triode or diode system, the substrate was always powered and consequently negatively polarized. To change the negative self-bias voltage we have to input more or less power to the substrate holder. The upper electrode is always polarized with 100 W incident power. To confirm that the deposited films are of DLC nature, we used two samples made with the diode system (DLC1 and DLC3) and two other samples made with the triode system (DLC2 and DLC4) with different experimental conditions, as they appear in Table 1. The dc voltages (V_{dcl}) mentioned in the table are functions of pressure and inputted power.

Table 1 Experimental conditions of deposited films

Sample	Mode	P_s (Torr)	V_{dcl} (V)
DLC1	Diode	0.1	200
DLC2	Triode	0.06	240
DLC3	Diode	0.04	210
DLC4	Triode	0.06	50

7.3 Results and Discussions

7.3.1 X-ray Auger Electron Spectroscopy (XAES)

The advantage of XAES technique is its nondestructiveness. In Fig. 2, the CKLL spectra, for all the samples in either integral $N(E)$ or derivative form dN/dE, are shown and compared to that of graphite structure. The kinetic energy of C KLL spectra in $N(E)$ ranges from 250 to 280 eV. It is reported [15] that the main feature for graphite occurs at 269 eV, and those for diamond occur at 262 eV, and it occurs at 260 eV for DLC films. We can see that the $N(E)$ spectra of DLC films are the same for all the samples; this indicates that their structures are nearly similar. The C KLL transition observed for graphite is especially broadened due to the high number of possible Auger transitions in graphite [16]. In the DLC samples, it is generally observed to be narrower, which may be indicative of mixed sp^3–sp^2 hybridization states of the C–C bonds. However, differences between the structures are pronounced when the data were smoothed out and differentiated for comparing the energy difference between the maximum and minimum values (D parameter), see Fig. 2 (b).

D is correlated from C–C bonding configuration, being found equal to 14.3 eV in diamond (100% sp^3) [17] and 20.4 eV for graphite (100% sp^2) (This was estimated from the measured spectrum and it is smaller than usual). The D values for the DLC films are given in Table 2 together with those of diamond and graphite references. This energy (D) indicates the state of hybridization of carbon in sp^2 or sp^3 [17–19]. From these values (14.9 to 16), we suppose that the DLC films consist of sp^3 (diamond) and sp^2 (graphite) hybridisations with different proportions neglecting sp^1 bonds and H content.

Table 2: Results of D values and sp^3/sp^2 ratio

Sample	D (Initial value)	D (After Ar^+ sputtering)	sp^2%	sp^3%	sp^3/sp^2
DLC1	14.9	19.2	11.3	88.7	7.8
DLC2	16.1	22.6	30.6	69.4	2.2
DLC3	15.6	21.3	22.6	77.4	3.4
DLC4	15.9	19.9	27.4	72.6	2.6
Graphite	20.4	Not measured			
Diamond	14.3	Not measured			

According to Lascovich et al. [17] the sp^2 percentage is evaluated by the relation:

$$sp^2\% = \left(\frac{D_{DLC} - D_{diamond}}{D_{graphite} - D_{diamond}}\right) \times 100, \quad (1)$$

where D_{DLC}, $D_{diamond}$ and $D_{graphite}$ are the D values of DLC films, diamond and graphite, respectively. From XAES studies, we find that the sp^2 percentages are 11.3 and 22.6 for the diode-mode configuration and 30.6 and 27.4 in the case of the triode-mode system. It is obvious that when the substrate holder is polarized enhancing ion bombardment the DLC films exhibit more diamond-like behavior with high sp^3 percentages of 88.7, 69.4, 77.4 and 72.6. In diode or triode configurations, and according to the results of Filik and coworkers [20], the negative self-bias voltage has an effect on the sp^3 fraction; it increases on increasing bias voltage until a certain value reached and then it decreases at extreme self-bias voltages. This behavior is in good agreement with our results and other works [17,18] when the deposit is bombarded with Ar^+ ions inducing disorder on the DLC films by the formation of sp^2 hybridizations, which indicates a tendency towards graphitic nature.

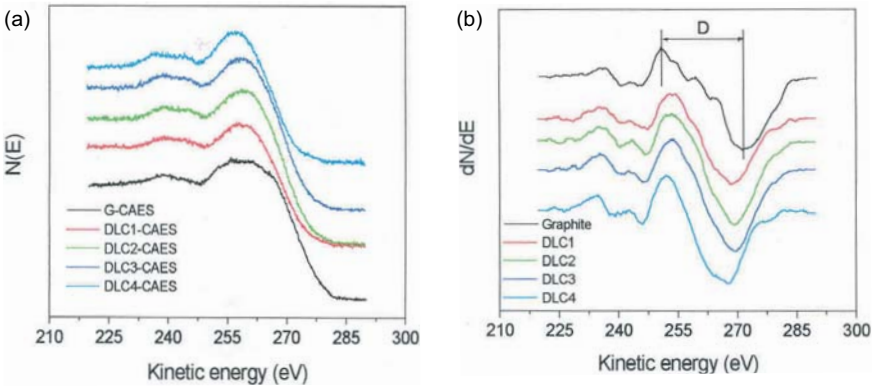

Figure 2 Typical (a) $N(E)$ and (b) dN/dE spectra of DLC films studied by XAES.

However, in the diode configuration, we can see that coatings are more diamond-like (7.8, 3.4) than those obtained in the triode system although the bias voltages are not very different (210, 200). This is certainly due to the assumption that all of the deposition processes, including ion bombardment, are at the vicinity of the substrate, which is not the case when samples are coated in the triode configuration. Also, when increasing pressure the deposit tends toward DLC behavior with sp^3/sp^2 ratio of 7.8 in DLC1 and 3.4 in DLC3. Lascovich et al. [17] have reported this effect of pressure.

7.3.2
Electron Energy Loss Spectroscopy (EELS)

EELS is a sensitive surface technique, which can provide reliable information about the bond structure in graphite, diamond and a variety of diamond-like carbon films [21]. The EELS data were performed in the low-loss or plasmon region and the core loss region characteristic of the atomic elements in the specimen. Figure 3 shows

low energy loss spectra from 0 to 50 eV. As reported by Wang and coworkers [22], the low-loss spectra for graphite displays two loss features that are attributed to π and $\sigma+\pi$ plasmon and two others attributed to plasma oscillations. The two formers appear at about 6 eV and 26.6 eV, respectively. In Fig. 3, in comparison with the graphite structure, all the samples present a slight response of plasmon energy near 5 eV, which is assigned to the π electron plasmon loss indicating a higher content of the sp^3 bonding in the films. For the $\sigma+\pi$ plasmon, samples 1, 2 and 3 exhibit plasmon energy near 23.3 eV and being different from sample 4, whose corresponding energy appears at 21.6 eV. It is reported [22] that $\sigma+\pi$ energy depends on the effective number of electrons contributing to the $\sigma+\pi$ electron plasmon oscillation per valence electron. These electrons come from carbon atoms with sp^3 and sp^2 hybridization and from H atoms. If the valence electrons act as free electrons, the effective number of electrons contributing to the $\sigma+\pi$ plasmon is equivalent to unity. Then the shift in the $\sigma+\pi$ plasmon peak at a reduced energy (sample 4) is due to the lower mass density of our samples with respect to graphite [23]. Also, this indicates that sample 4 has a lower density of free electrons compared to the others according to Riedo et al. [24]. These results allow us to have an idea of the electronic properties of our deposited thin films. Figure 4 depicts typical EELS spectra at the C K-edge for all the specimens after removal from the background. The spectra for an evaporated amorphous carbon films (a-C) and graphite specimen are also included for comparison. The main features are the two extremes values at about 285.5 eV and 295 eV corresponding to the 1s-π^* and 1s-σ^* transitions, respectively, observed in graphite. In comparison with graphite, all the samples and a-C spectra do not present the 1s-π^* peak so enhanced and the 1s-σ^* appears merged indicating higher sp^3 bonds. These signatures are typical of amorphous and nanocrystalline materials [25, 26]. The spectra for all the coatings look very similar, only sample 4 is slightly different, possibly due to a large amount of hydrogen contained in the films, which is a result of lower bias voltage of 50 eV. The spectrum for this sample resembles more that of an evaporated amorphous carbon film than the others.

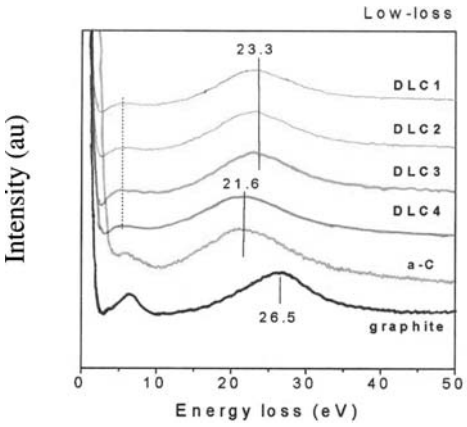

Figure 3 Low-loss EELS spectra of DLC films.

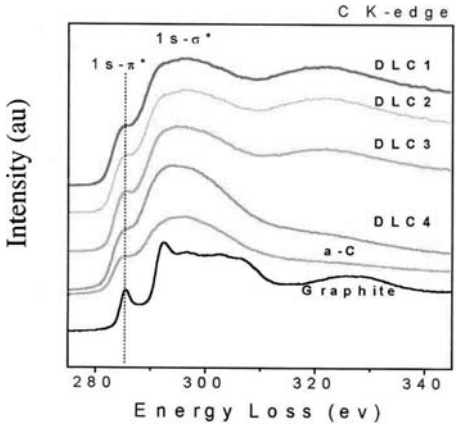

Figure 4 Core loss EELS spectra of DLC films.

7.4 Conclusion

Diamond-like carbon films have been deposited in diode and triode RF reactors under ion bombardment. We have studied the structural states of DLC films from XAES and EELS characterisations. In summary, we have shown that the films deposited, in both diode or triode reactor, contain high percentages of sp^3 bond fraction with small differences possibly due to deposition conditions and deposition mode. Moreover, the application of a negative self-bias voltage to the substrate has an important effect in modifying films structure and electronic properties.

Acknowledgements

The authors are grateful to J.C. Sánchez-López, Institue of Materials Science of Seville (Spain), for his helpful discussions and for EELS and XAES characterizations.

References

[1] S. Aisenberg and R. Chabot, J. Appl. Phys., **42**, 2953 (1971)

[2] A. Bubenzer, B. Dischler, G. Grandt and P. Koidl, J. Appl. Phys., **54(8)**, 4590 (1983)

[3] P. Couderc and Y. Catherine, Thin Solid Films **146**, 93 (1987).

[4] S. Bull, Diam. Relat. Mater., **4**, 827 (1995)

[5] K. Kobayashi, N. Mutsukura and Y. Machi, J. Appl. Phys., **59(3)**, 910 (1986)

[6] Y. Kokaku, M. Kohno, S. Fujimaki, and M. Kitoh, J. Vac. Sci. Technol **A9 (3)**, 1162 (1991).

[7] J. Esteve, M. C. Polo and G. Sánchez, Vacuum, **52**, 133 (1999)

[8] D. R. McKenzie, Rep. Prog. Phy., **59**, 1611 (1996)

[9] D. J. Li and H. Q. Gu, Bull. Mater. Sci., **25 (1)**, 7 (2002)

[10] J. Lettington, Philos. Trans. Roy. Soc. London., **A342**, 287 (1993)

[11] D. Bourgoin, S. Turgeon and G. G. Ross, Thin Solid Films., **357**, 246 (1999)

[12] M. Koós, I. Pócsik, J. Erostyák and A. Buzádi, J. Noncryst. Solids, **227-230**, 579 (1998)

[13] L. Valentini, J. M. Kenny, G. Mariotto, P. Tosi, G. Carlotti, G. Socino, L. Lozzi and S. Santucci, J. Vac. Sci. Technol., **A19 (4)**, 1611 (2001)

[14] S. Djahièche-Nencib, O. Kessi and R. Tadjine, J. Phys. D: Appl. Phys. **29**, 917 (1996)

[15] D. Sarangi, O. S. Panwar, S. Kumar and R. Bhattacharya. J. Vac. Sci. Technol. **A18 (5)**, 2307 (2000).

[16] D. Ramaker, J. Vac. Sci. Technol. **A7**, 1614 (1989).

[17] J. C. Lascovish, R. Giorgi, S. Scaglione, Appl. Surf. Sci. **47**, 17 (1991).

[18] Y. Mizokawa, T. Miyasato, S. Nakamura, K. M. Geib, and C. W. Wilm-sen, J. Vac. Sci. Technol. **A5**, 2809 (1987).

[19] Y. Mizokawa, T. Miyasato, S. Nakamura, K. M. Geib, and C. W. Wilm-sen, Surf. Sci. **182**,431 (1987)

[20] J. Filik, P. W. May, S.R. J. Pearce, R. K. Wild and K. R. Hallam, Diam. Relat. Mater., **12**, 974 (2003)

[21] S. Zhang, X. T. Zeng, H. Xie and P. Hing, Surf. Coat. Technol., **123**, 256 (2000)

[22] Yaxin Wang, Hsiung Chen, R. W. Hoffman and Jhon C. Angus, J. Mater. Res., **5 (11)**, 2378 (1990).

[23] Yaxin Wang, Hsiung Chen, R. W. Hoffman and Jhon C. Angus, J. Vac. Sci. Technol., **A8 (3)**, 2226 (1990)

[24] E. Riedo, E. Magnano, S. Rubini, M. Sancrotti, E. Barborini, P. Piseri and P. Milani, Solid State Commun. **116**, 287 (2000).

[25] J. C. Sánchez-López, C. Donnet, A. Erdemir, T. C. Rojas, Surf. Coat. Technol. **163-164**, 444 (2003).

[26] S. D. Berger, D. R. Mckenzie, P. J. Martin, Philos. Mater. 285 (1988)

8
Rate constant of HMDSO + O reaction in plasma afterglow

Vít Kudrle, Vojtěch Doležal, Antonín Tálský, Jan Janča

Summary
In this work the kinetics of the reaction between atomic oxygen and hexamethyldisiloxane (HMDSO) was studied by means of the flowing afterglow technique. The HMDSO vapor was injected into the oxygen afterglow and the loss of O atoms was measured by means of a electron paramagnetic resonance spectrometer. From the known reaction time and HMDSO flow the rate constant was then calculated. The resulting value is 2.4×10^{-14} cm^3 s^{-1}.

8.1
Introduction

Hexamethyldisiloxane (HMDSO, $(CH_3)_3SiOSi(CH_3)_3$) is often used for plasma enhanced chemical vapor deposition (PECVD) of the silicon-containing films [1]. It is quite popular due to the high deposition rates that can be achieved, its low toxicity and high vapor pressure. By varying the amount of oxygen in the discharge it is possible to prepare the films with properties ranging from the organic (polymer-like) to the inorganic (SiO_x-like) [2–5]. This is caused by the fact that monoatomic oxygen acts as a radical scavenger, decreasing the polymerisation rate of organic radicals, increasing conversion and fragmentation of monomers, and removing parts of the organic fraction of the film by means of gas–surface reactions [6]. The main reactions and precursors for the film growth were discussed in [5, 7–10]. However, better understanding of the processes involved in deposition reactors and especially quantitative data are still needed for industrial process optimisation and modelling.

In the present study we determined the rate constant of the HMDSO+O reaction using the flowing afterglow technique in continuation of our previous work [11]. Oxygen atoms produced in the discharge are recombining slowly and thus their density in the afterglow is relatively high. When the HMDSO vapor is injected into the afterglow, due to the HMDSO+O reaction the concentration of O decreases. From this decrease the rate constant was calculated. The absolute density of atomic oxygen was measured by means of the electron paramagnetic resonance (EPR) spectroscopy.

8.2 Experimental

A schematic drawing of the experimental apparatus is presented in Fig. 1. A radio-frequency electrodeless discharge was sustained in the quartz tube with inner diameter of 37 mm by an RF generator working at 13.56 MHz. Relatively low power (25 W) was fed into the plasma to maintain the discharge within the cavity; this prevents the possible presence (due to back diffusion) of HMDSO vapors in the active discharge. The main gas (99.995% oxygen) was fed from a standard gas bottle through a reduction valve and a mass flow controller. In the discharge the oxygen was partially atomised and passed through the right-angle bend into the afterglow tube and further to a measuring resonator (X-band) of the Zeiss ER9 EPR spectrometer. The density of O atoms at a distance of 35 cm from the discharge reached 10^{15} cm^{-3}.

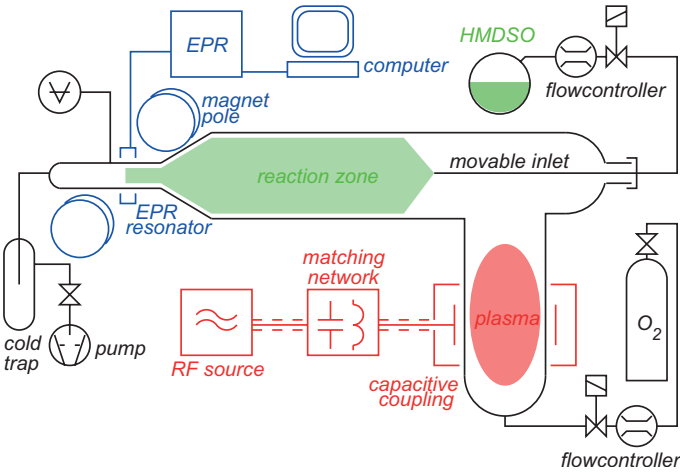

Figure 1 Experimental setup.

HMDSO vapor was developed by thermal evaporation (50 °C) of HMDSO liquid. The vapor flow rate (order of tenths of sccm) was controlled by a special flow controller and verified from a pressure rise in the closed apparatus. The whole monomer line was maintained in a temperature gradient to prevent a condensation of the vapor. Between the discharge and the measuring resonator the HMDSO vapor was injected into the flow of the partially atomised oxygen via a small-diameter tube. The distance between the injector and the EPR resonator (i.e. the reaction time) could be varied over a limited range from 5 to 30 cm. Because the distance from the discharge was as much as 10 times higher than the tube diameter, the back diffusion could be neglected. The total pressure in the EPR resonator during all measurements was maintained at 100 Pa (corresponding O_2 flow rate was 7 sccm and the velocity 0.1 ms^{-1}). This relatively low pressure was maintained because the HMDSO flow controller needs sufficient pressure drop between the inlet and outlet.

We employed an electron paramagnetic resonance spectrometer operating in the X-band (10 GHz) to measure the concentration of atomic oxygen. This measurement technique is based on resonance absorption of microwave energy by the transitions between Zeeman split levels. In the case of oxygen, the ground level $^3P_2$ splits into 5 levels in magnetic field, the slightly higher $^3P_1$ splits into 3 levels. The resulting EPR spectra have a typical structure of overlapping quartet and doublet. After a calibration of the EPR device by molecular oxygen [12], which is paramagnetic, the absolute concentration was obtained. The advantage of such calibration is a well-defined fill factor, which is not easy to achieve with traditional solid DPPH (α,α-diphenyl-β-picryl-hydrazyl) standard. In comparison with other techniques EPR has a big advantage in its non-invasivity and the ability to determine the absolute concentrations of a wide range of species [13].

8.3 Calculation of the rate constant

The overall reaction between O and HMDSO may be described [8, 9] as

$$Si_2O(CH_3)_6 + O \xrightarrow{k} (SiO_2, \text{radicals}, CO, CO_2, H_2O, O_2, \text{polymer}), \quad (1)$$

where k is the sought kinetic coefficient of the reaction O+HMDSO. For concentration of atomic oxygen [O] we can write

$$\frac{d[O]}{dt} = -k_{wall}[O] - k[HMDSO][O], \quad (2)$$

where k_{wall} is the wall recombination coefficient on the discharge tube walls and on the outer surface of the HMDSO injector. The second-order reactions of oxygen atoms (as O+O, O+O$^-$, ...) were not considered due to their insignificant role in our experiment.

This bimolecular reaction between different reagents is a second-order reaction. Solution of this differential equation depends upon the instantaneous concentrations of both species involved. Let us discuss the influence of the initial ratio [HMDSO]/[O] on the solution of (2). The extreme cases are

a. [HMDSO]/[O] $\ll$ 1
   In this case when [O] is greatly abundant we should not see any significant loss of O due to reaction with HMDSO.
b. [HMDSO]/[O] = 1
   When we have the same concentration of HMDSO and O, we should observe the hyperbolic dependence of [O] on the time of reaction. Actually, it is a hyperbola slightly modified by a wall-recombination term.
c. [HMDSO]/[O] $\gg$ 1
   When [HMDSO] greatly excess [O], it remains essentially constant during the reaction and the time dependence of [O] becomes exponential. In this case, the reaction exhibits pseudo-first order behavior.

Generally we strive to achieve the case (c), which makes the analysis of measured data rather simple. So let us assume in the following text the pseudo-first order reaction. The remaining task is to account for the losses due to surface recombination ($-k_{wall}$[O] term). It can be achieved by measuring [O] with and without HMDSO flow for each position of injector.

If there is no HMDSO flow, from (2) it follows that

$$\frac{d[O]_{off}}{dt} = -k_{wall} \cdot [O]_{off}. \tag{3}$$

The solution is

$$[O]_{off} = C_1 \cdot \exp(-k_{wall} t) \tag{4}$$

where C_1 is a constant depending on the experimental arrangement.

For the case with flowing HMDSO we have

$$\frac{d[O]_{on}}{dt} = -(k_{wall} + k \cdot [HMDSO]) \cdot [O]_{on}. \tag{5}$$

Under the assumption of pseudo-first order behavior we get

$$[O]_{on} = C_2 \cdot \exp\Big(-(k_{wall} + k \cdot [HMDSO]) \cdot t \Big), \tag{6}$$

where C_2 is constant given by experimental conditions.

By dividing (6) and (4) and taking the logarithm of both sides we have

$$\ln\left(\frac{[O]_{on}}{[O]_{off}}\right) = C_3 - k \cdot [HMDSO] \cdot t. \tag{7}$$

The time of residence t may be determined from the known pressure, flow rate and discharge tube diameter. [HMDSO] is measured by a flowmeter. Therefore, principally two types of experiment may becarried out:

- keeping [HMDSO] constant and moving the injector (varying t)
- residence time t fixed, varying HMDSO flow rate

In both cases the k is calculated from a slope of (7).

In our apparatus, uncertainty in t may arise because there is a change in diameter of the tube (as shown in Fig. 1). In such a region the flow is irregular and the simple relation between flow, diameter and velocity does not hold. This can be circumvented by "differential" measurement, where for two injector positions x the function $[O]=f_x([HMDSO])$ is measured. From these functions a new function $[O]=f_{\Delta x}([HMDSO])$ is constructed. In this form, only Δt plays a role and not the actual value of t. A disadvantage of such a calculation is the higher statistical error due to subtraction of close numbers. A similar arrangement can be used for differential measurement in [HMDSO], which can compensate additive errors in the HMDSO flow value.

8.4 Results and discussion

As explained in the previous section, we tried to achieve the pseudo-first order behavior, i.e. to get [HMDSO]≫[O]. Unfortunately, at such conditions the reaction was so fast that the concentration of oxygen atoms was below the detection limit of our apparatus. Therefore, we had to decrease the HMDSO flow until the oxygen concentration was measurable. In such a case, concentrations of O and HMDSO were around 10^{15} cm^{-3} and 10^{14} cm^{-3}, respectively. Formally, it is close to the case (a) ([HMDSO]≪[O]), i.e. we should observe very low, if any, loss of O due to reaction (1).

However, from Figures 2 and 3 it is evident that the observed dependencies are exponential. This corresponds to the pseudo-first order behavior of the case (c). This indicates that our measured k is not just the kinetic coefficient between O and HMDSO, but it also includes the set of reactions between O and the products of the first HMDSO+O reaction, i.e. the fragments of HMDSO molecule [8–10]. The first step of the HMDSO+O reaction generally involves CH_x, $Si_xO_yC_zH_t$ abstraction from a stable molecule. These are oxidised to CO, CO_2, COH_2,CO_2H_2, water, hydrocarbons, SiO_2 [5,8,9]. Because O is lost even by the reactions with the products of HMDSO+O, effectively the [O] is decreasing at a much higher rate than [HMDSO]

$$\frac{d[O]}{dt} = N \cdot \frac{d[HMDSO]}{dt}, \tag{8}$$

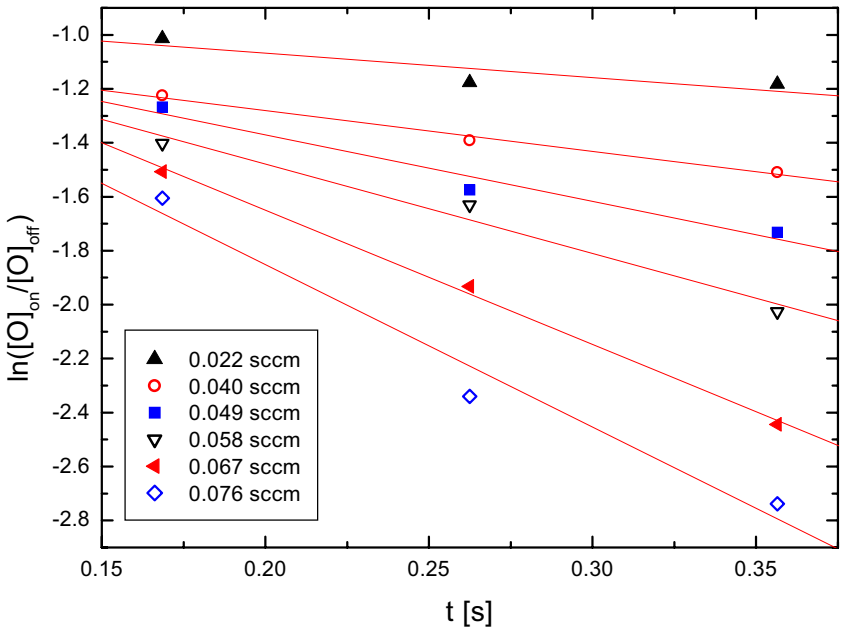

Figure 2 Dependence of O-atom loss (in logarithmic scale) on the reaction time for several HMDSO flows.

where factor $N(\gg 1)$ can be roughly estimated from stoichiometry (e.g. for full oxidation of HMDSO we need 24 atoms of oxygen). However, the actual value of N depends on the exact way the HMDSO is fragmented in the course of reaction and therefore its not known.

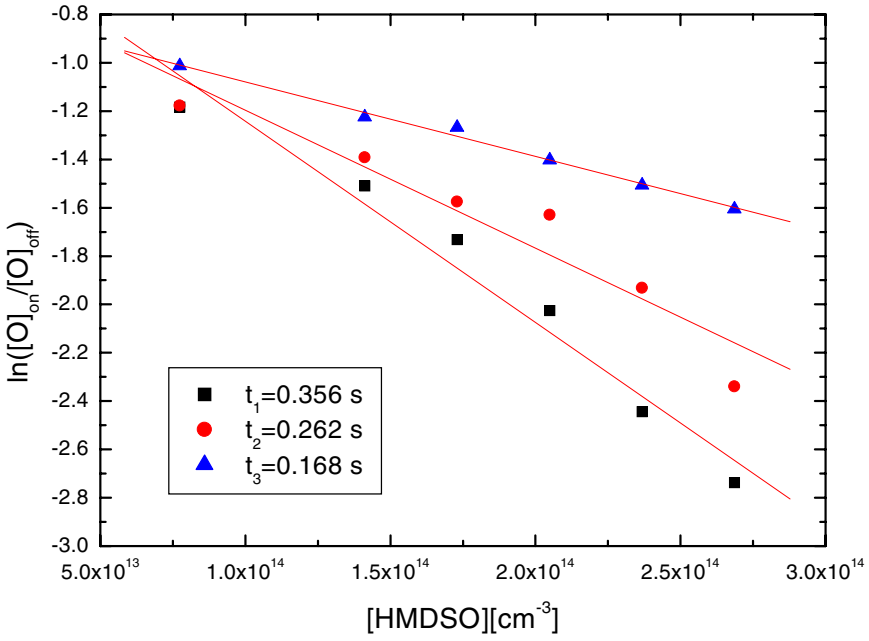

Figure 3 Dependence of O-atom loss (in logarithmic scale) on the HMDSO flow for several reaction times.

Because $N \gg 1$, the concentration of HMDSO and its oxidable fragments remains nearly constant in comparison with [O] and therefore the case (a) is transformed into the case (c). As a result we get pseudo-first order behavior (i.e. exponential decrease of [O] with [HMDSO]t) even in the case [HMDSO]<[O]. Our treatment based on pseudo-first order leading to (7) is valid, too.

However, we must realize that from the measured O atom loss we can get only the apparent value $k_{\mathrm{eff}} = N \cdot k$ and not the real rate constant k between O and HMDSO without its fragments. This means that the calculated rate constant k_{eff} is much higher than k (by factor N).

We have performed both principal types of measurement (see Fig. 2 and 3) together with both difference methods. The resulting apparent rate constants are quite close to each other, as is shown in Fig. 4.

Using all four methods (constant t, constant [HMDSO], difference Δt and difference Δ[HMDSO]) and the relation (7) we obtained

$k_{\mathrm{eff}} = (2.4 \pm 0.9) \times 10^{-14}\,\mathrm{cm}^3\,\mathrm{s}^{-1}$.

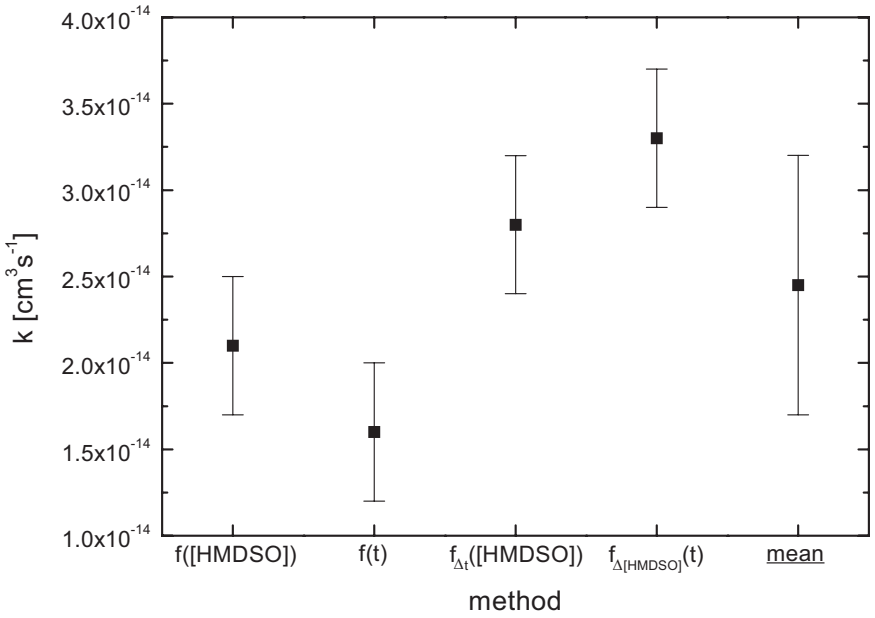

Figure 4 Comparison of the results of the four principal types of measurement, where the controlling quantities are [HMDSO], t, Δt and Δ[HMDSO]. Also the resulting average of these four values is presented.

8.5 Conclusion

The rate coefficient for the reaction of HMDSO with atomic oxygen was measured by means of the flowing afterglow technique. Electron paramagnetic resonance was used as the means for oxygen atom density measurement.

These experiments yield the total rate coefficient of the reaction O + HMDSO (and its fragments) to be $2.4 \times 10^{-14}\,\mathrm{cm}^3\,\mathrm{s}^{-1}$.

To the best of the authors' knowledge, this is the first report of the rate constant between O and HMDSO in the literature.

Acknowledgements

This work was financially supported by contracts MSM 143100003, ME 489 and COST 527.20.

References

[1] A. M. Wróbel and M. R. Wertheimer: *Plasma-polymerized Organosilicones and Organometallics*, in *Plasma Deposition, Treatment, and Etching of Polymers*, R. d'Agostino (ed.), Academic Press, (1990), 163–268

[2] S. Sahli, Y. Segui, S. Ramdani and Z. Takkouk: *Thin Solid Films* **250** (1994) 206

[3] L. Zajíčková, V. Buršíková and J. Janča: *Vacuum* **50 1–2 (1998) 19–21**

[4] L. Zajíčková, V. Buršíková, V. Peřina, A. Macková, D. Subedi, J. Janča and S. Smirnov: *Surf. Coat. Technol.* **142–144** (2001) 449-454

[5] M. Creatore, F. Palumbo and R. d'Agostino: *Plasmas Polym.*, **7** 3 (2002) 291–310

[6] F. Fracassi, R. d'Agostino, P. Favia: *J. Electrochem. Soc.* **139** (1992) 2636

[7] M. R. Alexander, F. R. Jones and R. D. Short: *Plasmas Polym.* **2** 4 (1997) 277–300

[8] R. Lamendola, R. d'Agostino and F. Fracassi: *Plasmas Polym.* **2** 3 (1997) 147–164

[9] D. Magni, Ch. Deschenaux, Ch. Hollenstein, A. Creatore and P. Fayet: *J. Phys. D: Appl. Phys.* **34** (2001) 87–94

[10] D. Theirich, Ch. Soll, F. Leu and J. Engemann: *Vacuum* **71** (2003) 349–359

[11] J. Janča, A. Tálský, V. Zvoníček: *Plasma Chem. Plasma Process.* **16** 2 (1996), 187–194

[12] S. Krongelb and H. W. P. Strandberg: *J. Chem. Phys.* **31** 5 (1959) 1196

[13] A. A. Westenberg: *Prog. React. Kinet.* **7** (1973) 23–82

Text for Table of Contents

In this work the kinetics of the reaction between atomic oxygen and hexamethyldisiloxane (HMDSO) was studied by means of the flowing afterglow technique. The HMDSO vapor was injected into the partially dissociated oxygen and the loss of O atoms was measured by EPR. From the known reaction time and HMDSO flow the rate constant was calculated.

9
Plasma-Enhanced Thin-Film Deposition On Polycarbonates

B. Ulejczyk, T. Opalinska, L. Karpinski, K. Schmidt-Szalowski

Abstract

Deposition of thin SiO_x films on polycarbonates in the pulsed dielectric barrier discharge has been investigated. Thin films were deposited from gas mixtures of helium, oxygen and tetraethoxysilane at atmospheric pressure. The deposition rate decreased and the thin-film roughness increased with increasing O_2 concentration. The chemical composition of the thin film changed with depth of the thin film. The thin film might comprise three layers of different chemical composition: mixture of the product of plasma polymerization and silica (1); silica (2) and a mixture of polycarbonates fragments and the deposition products (3).

9.1
Introduction

Polycarbonates (PC) are used in a wide range of products such as: basic medical devices (3%), electronic equipment (22%), cars (9%), and building and structural elements (32%), and consumer goods. PC are extensively used in optical data-storage applications, protection equipment and floodlights, transparent roofing in building and construction. The global market for PC at an average rate of approximately 10% with every new application, and attained 1 800 000 tons in the year 2000 [1]. PC is a high-quality, engineering plastic with a unique combination of properties including strength, lightness, durability, high transparency, and heat resistance. However, PC must be coated with a protective, thin film against scratching and action of solvents, oxygen, humidity or solar radiation.

The plasma-enhanced (assisted) chemical vapor deposition (PECVD/PACVD) technique improves the thin film surface properties. The process of depositing a protective film from the gas phase is initiated by electric discharge. The thin film is formed directly in the electric-discharge volume (PECVD) or out of it (PACVD). Reactive species like excited molecules, radicals and ions are formed by collisions of high-energy electrons with molecules of vapor precursors. These reactive species contribute to the thin-film formation on the surface. Various gases were used, as the

precursors, such as tetraethoxysilane, hexamethoxydisilazane or tetramethylosilane to deposit SiO_x film and methane or acetylene to deposit diamond-like film.

The thin film is usually deposited in glow discharges at low-pressure (1–1000 Pa) [2–4] or in filamentary barrier-discharges at atmospheric pressure [5,6]. The latter process is very attractive, but usually the obtained film is not uniform since the barrier discharges are nonhomogeneous. To improve the thin-film homogeneity, a new process has been developed. It consists in application of pulsed electric-discharges initiated from a dielectric barrier (PDBD) [7–9].

Two processes occur at the same time under plasma action under PDBD conditions: surface etching and thin-film deposition. This effect was published in our previous report [9]. It has been shown that:

1. The obtained thin film is more resistant to the discharges than virgin PC, since the etching rate of the virgin PC plates was about two times faster than that of the thin films;
2. To deposit the thin film on virgin PC takes more time than on PC that was previously etched.

These results prompted us to pursue this investigation, and two effects were examined:

1. An influence of the oxygen concentration on the deposition rate and on the thin-film roughness;
2. Chemical composition of lower layers of the thin film.

9.2 Experimental

The thin film was deposited in an apparatus composed of a plasma reactor, gas and electric supply systems. The plasma reactor is shown in Fig. 1. The gas and electric supply systems have been described in our previous reports [7,8].

The PC plates formed a double dielectric-barrier placed on both, high-voltage and ground electrodes, respectively. The relative electric permittivity of the PC plates amounted to 2.3 (as measured by a Precision LCR Meter, HP 4284A). Plasma was generated by discharges in the mixture of helium, oxygen and vapor of tetraethoxysilane (TEOS) between the PC plates. The thin film was deposited on both plates. In this experiment the PC was supplied by GE Plastics, under the trade name Lexan. The experimental parameters are shown in Table 1.

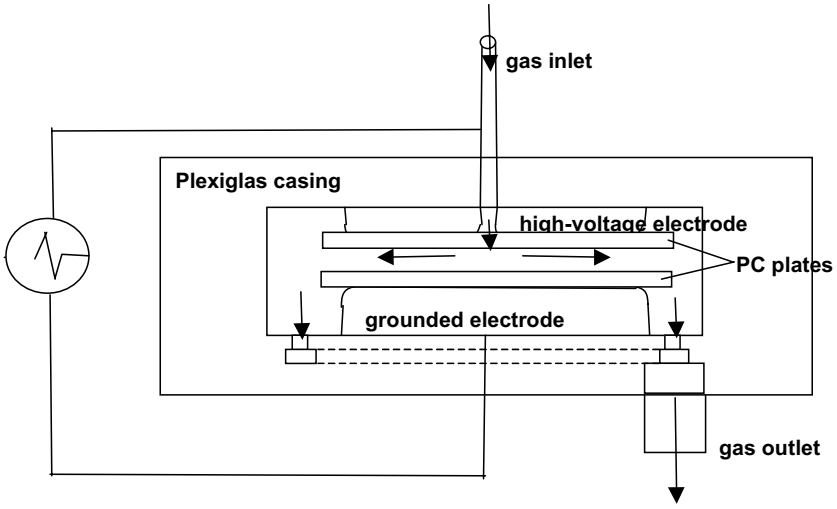

Figure 1 Schema of PDBD reactor.

Table 1 Experimental parameters

Total gas flow rate, l (s.t.p.)/h	100
Pressure, atm	1
He concentration, % by vol.	50–95
O_2 concentration, % by vol.	5–50
Concentration of TEOS vapor, ppm	230–250
Discharge gap, mm	0.2
Thickness of PC plates, mm	0.5
Frequency of pulse repetition, Hz	400

The mass of deposited film was weighted by a Sartorius BP 221S balance. The deposition rate was calculated from these measurements.

The dielectric-barrier discharge (PDBD) was supplied by voltage-pulses (50 ns) and current pulses (20 ns) of a very short time [7,8]. The current pulses are 40% of the duration of the voltage pulses because the current is stopped when the electric charge was accumulating in the discharge zone (ions in gas, electric charge on dielectric surfaces), but the potential is still on the electrodes. The voltage and current-pulse waveform as well as the pulse repetition frequency were recorded by a Tektronix TDS 3054 oscilloscope.

The thin-film surface topography was examined under controlled conditions (temperature 23 (C, humidity 50%) using an atomic force microscope. The silicon cantilever NSC12 type E used to measure the surface topography (length: 350 ± 5 µm, width 35 ± 3 µm, thickness 2 ± 0.3 µm, force constant 0.30 N/m, resonant frequency 21 kHz), was supplied by Mikromasch.

XPS (X-ray photoelectron spectroscopy) were measured using a VG Scientific ESCALAB-210 spectrometer. An AlKα radiation source was operated at a power of

300 W (15 kV, 20 mA). Vacuum in the analysis chamber was kept below 8×10^{-9} mbar during all measurements. Pass energy 20 eV and step 0.1 eV were used. The spectrometer binding-energy scale was calibrated by the Ag $3d_{5/2}$ peak at 368.27 eV, and by the Ag M_4NN peak at 895.75 eV. Data were analysed using the ECLIPSE VG program, including satellite subtraction, Shirley background subtraction fitting procedure and quantification. Sputtering was performed by use of an AG2 ion gun, working with Ar+ ions with an energy of 6 keV, and current of 5 μA.

9.3 Results

The deposition rates are shown in Fig. 2 for various oxygen concentrations in the plasma-generating gas. The deposition rate was determined from the slope of the linear regression lines. This describes the change of the thin-film mass, plotted against deposition time.

The topography of virgin PC and of the thin films is shown by selected AFM microimages (Fig. 3). Roughness parameters: R_a – average arithmetical deviation of profile of roughness, and R_q – average square deviation of profile of roughness, are shown in Table 2. The virgin PC roughness is lesser than that of the thin film. The R_a of virgin PC was 6.6 nm.

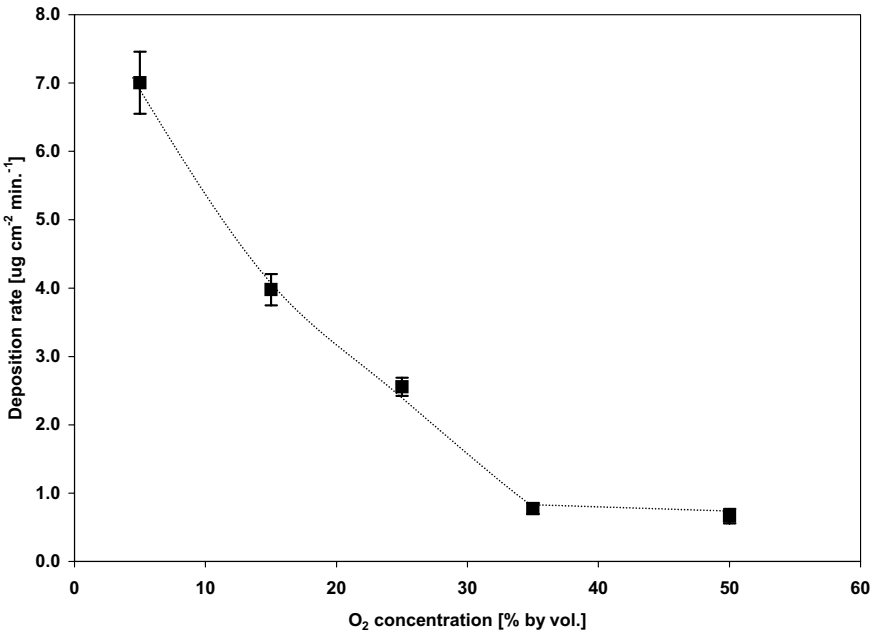

Figure 2 Effect of the O_2 concentration on the deposition rate.

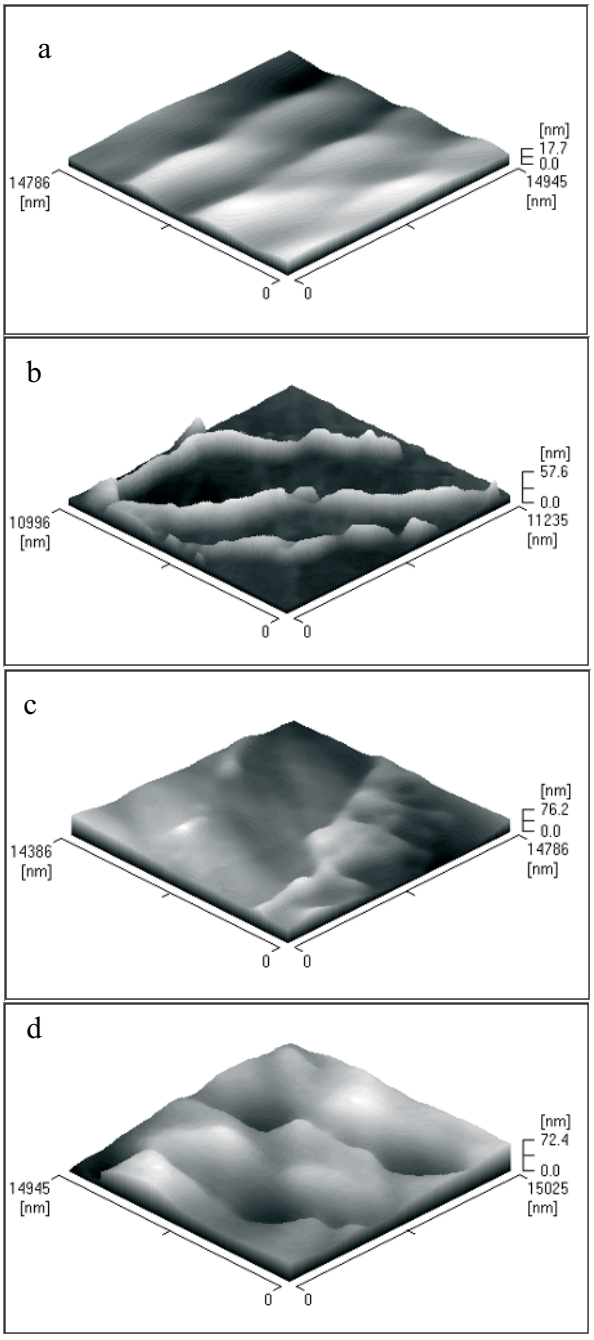

Figure 3 AFM micro-images of virgin PC (a) and thin films for various concentration of O_2 in plasma-generating gas: (b) 5 %, (c) 25 %, (d) 50 %.

Table 2 The roughness of virgin PC and the roughness of thin films for various O_2 concentration; R_a – average arithmetical deviation of profile of roughness and R_q – average square deviation of profile of roughness

O_2 concentration, % by vol.	R_a, nm	R_q, nm
Virgin PC	6.6	7.6
5	7.4	9.2
25	8.5	11.7
50	9.7	12.7

The elemental composition of thin film deposited from a He-O_2-TEOS gas mixture with 5% O_2, is shown in Table 3 and Fig. 4, as the XPS sputter profile. It was not possible to calculate the real analysis depth since the rate of thin-film etching by Ar^+ depends on the film composition. The C concentration was higher than 22% in the top of thin film and the concentration of C decreased to less than 5% after 5.8 min of the sputtering. At the same time, the concentrations of O and Si increased from 48 and 29% to almost 58 and 38%, respectively. Subsequently, the concentrations of C, O and Si were stable until 57 min of sputtering. The concentration of C increased after 57 min of the sputtering, and the concentrations of O and Si decreased as the sputtering time increased.

The content of various forms of Si, C and O, in thin film deposited from a He-O_2-TEOS gas mixture with 5% O_2, is shown in Tables 4–6. Example XPS spectra of C, Si i O are shown in Fig. 5. The C(1s) XPS spectra exhibited nine peaks at 292.5, 290.0, 289.6, 288.8, 287.6, 286.5, 285.0, 284.5 and 282.0 eV. Four peaks of C(1s) at 290.0, 286.6, 285.0 and 284.5 eV were found in XPS spectra of virgin PC too [10,11]. However, these peaks can be attributed to other chemical compounds formed under plasma conditions. For example, the peak at 285.0 eV was characteristic of olefins.

The peaks at 292.5, 289.6, 288.8 and 287.6 eV correspond to C bonded to O at different chemical groups and compounds. The peak at 282.0 eV corresponds to SiC.

Table 3 Change of the element composition versus the Ar^+ sputtering time (for 5% of O_2 concentration)

Element	Concentration, at%											
C	22.54	8.17	5.32	4.13	3.71	4.78	3.46	4.94	18.02	55.25	59.36	73.49
Si	28.98	35.29	36.73	37.62	38.39	37.97	39.08	38.70	33.34	17.76	16.21	10.25
O	47.69	56.23	57.64	57.97	57.59	56.88	57.14	55.96	48.23	26.73	24.16	15.97
N	0.79	0.31	0.31	0.28	0.31	0.37	0.33	0.40	0.40	0.27	0.27	0.29
Sputtering time, min.	0	1.5	3.3	5.8	16	26	36	57	80	99	110	130

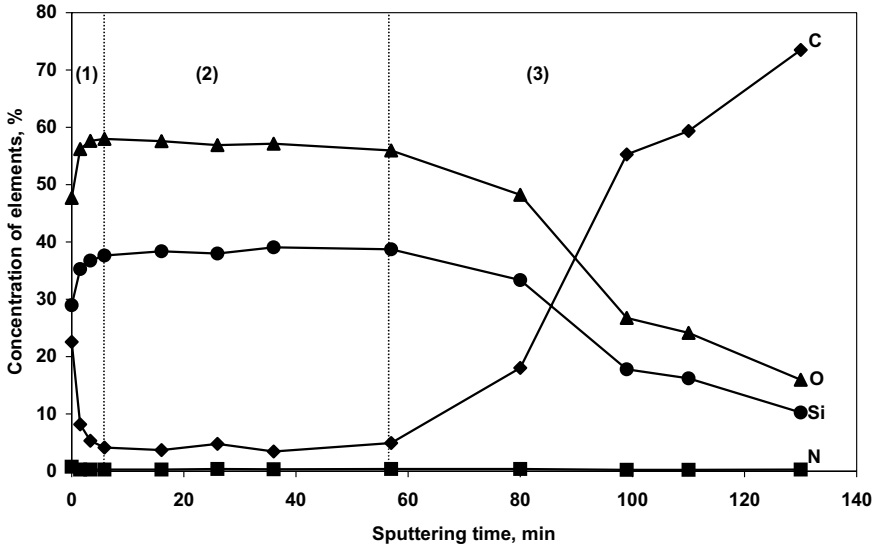

Figure 4 XPS depth profile of thin film deposited from a gas mixture with 5 % of O_2 (explanation in the text).

Table 4 Change of the concentration of various form of C versus the Ar^+ sputtering time (for 5% of O_2 concentration)

Peak assignment [10–18]	Binding energy, eV	Concentration, at%											
OC(O)O	292.5 and 290.0	47.69	0.29	–	–	0.2	0.22	0.44	0.21	0.58	0.93	2.15	2.11
C(O)OH	289.6	28.98	–	–	–	0.26	0.21	0.57	–	1.57	3.85	–	–
C(O)OC	288.8	0.79	0.69	0.33	0.24	0.33	0.67	0.95	0.49	0.88	–	2.24	2.56
C=O	287.6	–	–	–	–	–	–	–	–	–	2.38	2.46	2.56
aromatic C bonded to O	286.5	–	2.47	1.17	1.00	0.88	1.27	1.46	1.37	0.41	1.27	5.77	6.31
aliphatic C	285.0	–	18.85	5.86	3.49	2.02	0.84	0.71	0.6	0.82	2.55	11.60	12.73
aromatic C	284.5	–	–	–	–	–	0.38	0.46	0.47	1.11	6.80	31.00	33.95
SiC	282.0	–	0.25	0.54	0.41	0.41	0.14	0.14	0.15	–	–	–	–
Sputtering time, min.		0	1.5	3.3	5.8	16	26	36	57	80	99	110	130

Table 5 Change of the concentration of various form of Si versus the Ar^+ sputtering time (for 5% of O_2 concentration)

Peak assignment [16,19–21]	Binding energy, eV	Concentration, at%											
SiO_x	103.5	28.46	34.51	35.53	36.19	36.66	36.30	37.40	36.50	30.70	15.50	13.91	8.64
SiC	101.0	0.52	0.78	1.03	1.21	1.30	1.24	1.41	1.93	2.40	1.46	0.85	0.68
Si	99.0	–	–	0.17	0.22	0.43	0.43	0.27	0.25	0.22	0.84	1.44	0.93
Sputtering time, min.		0	1.5	3.3	5.8	16	26	36	57	80	99	110	130

Table 6 Change of the concentration of various form of O versus the Ar^+ sputtering time (for 5% of O_2 concentration)

Peak assignment [10,14,16,21–25]	Binding energy, eV	Concentration, at%											
H_2O	535.0	1.05	–	–	–	–	–	–	–	–	–	–	–
(aromatic C) –O–C, SiO_x, C(O)OH	533.0	45.02	53.22	54.94	55.16	54.77	54.12	54.10	52.70	45.70	22.70	19.98	13.10
C=O	530.0	1.62	1.86	1.70	1.73	1.70	1.65	1.83	1.97	1.58	1.37	1.24	0.74
O_2	527.0	–	1.15	1.00	1.08	1.12	1.12	1.22	1.27	0.93	2.67	2.95	2.15
Sputtering time, min.		0	1.5	3.3	5.8	16	26	36	57	80	99	110	130

The Si(2p) XPS spectra exhibited three peaks at 103.5, 101.0 and 99.0 eV. These peaks corresponded to: Si bonded to O (103.5 eV), Si bonded to C (101.0 eV) and Si bonded to Si (99.0 eV).

The O(1s) XPS spectra exhibited four peaks at 535.0, 533.0, 530.0 and 527.0 eV. These peaks corresponded to: H_2O (535.0 eV), O bonded to Si and/or C (533.0 eV), C=O (530.0 eV) and probably O in products of plasma polymerization of TEOS and/or plasma-modified PC (527.0 eV). The peaks of O(1s) at 533.0 and 530.0 were present in the XPS spectra of virgin PC [10,11], but the peak of O(1s) from PC at 533.0 eV overlapped the peak of O(1s) from SiO_x. Similarly, the peak of O(1s) from PC at 530.0 eV overlapped the peak of O(1s) from carbonyl and carboxylic groups in products of plasma polymerization of TEOS.

The elemental composition of thin film, which was deposited from He-O_2-TEOS gas mixture with 25% O_2, is shown in Fig. 6 as the XPS sputter profile. The C concentration C decreased from 15% in the top of thin film to less than 5% after 4 min of sputtering by Ar+. At the same time, the concentrations of O and Si increased from 54 and 31% to almost 59 and 36%, respectively. Subsequently, the concentrations of C, O and Si were stable until 14 min of sputtering. The concentration of C increased after 14 min of sputtering, and the concentrations of O and Si decreased as the sputtering time was increasing.

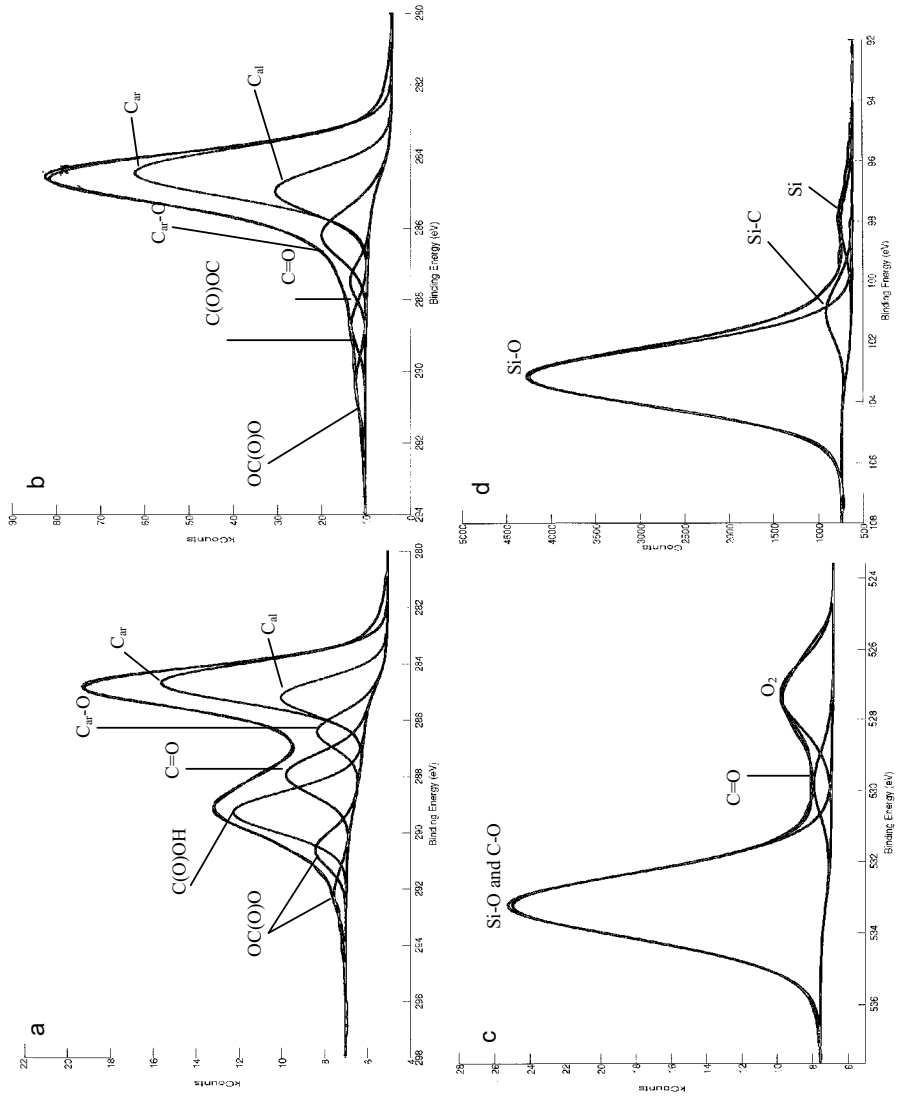

Figure 5 XPS spectra of thin film deposited from a gas mixture with 5 % of O_2: C(1s) after 80 min (a) and 130 min (b) of sputter, O(1s) after 130 min of sputter (c), Si(2p) after 130 min of sputter (d).

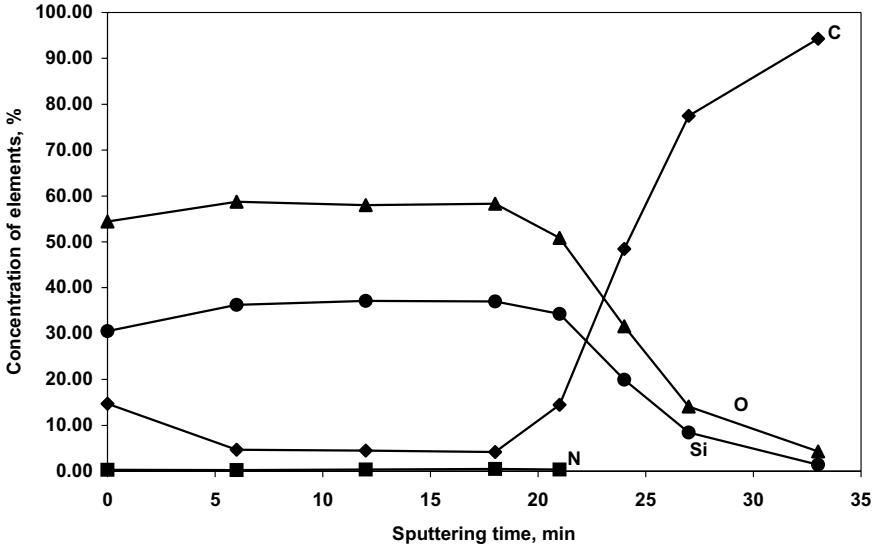

Figure 6 XPS depth profile of thin film deposited from a gas mixture with 25 % of O_2.

9.4 Discussion

O_2 and TEOS participated in the thin-film formation [26], however, a high concentration of oxygen has a negative influence on the deposition rate (Fig. 2). The deposition rate decreased with increase in the oxygen concentration in the plasma-generating gas. This behavior is similar to the results obtained with other forms of discharge [27–29] and may be explained by taking into account the increase of etching rate, with the increasing concentration of O_2 [9]. This explanation was confirmed by AFM observation of surface topography and XPS sputter profiles of thin films.

Thin films that were deposited from gas of small concentration of (5%) were characterized by the small roughness (R_a – 7.4 nm, R_q – 9.2 nm). The increase of O_2 concentration to 25% caused an increase of R_a to 8.5 nm and R_q to 11.7 nm. Thin film deposited from the gas mixture of the highest concentration of O_2 (50%), was characterized by the highest roughness (R_a – 9.7 nm, R_q – 12.7 nm) (Fig. 3, Table 2). The high roughness of the film may be caused by the high etching rate.

The XPS sputter profiles of thin films demonstrate that the C concentration at the top of the thin film decreased from 22 to 14% with increase of O_2 concentration from 5 to 25% (Figs. 4 and 6). This effect was caused by an increase of O_2 concentration. The organic components of the thin film were oxidized to CO_2 and CO faster when the O_2 concentration increased, and the film became less organic and the deposition rate decreased.

Based on the XPS sputter profiles (Figs. 4 and 6 and Table 3), the deposited films can be separated into three layers:

1. Layer (1) was composed of the mixture of the products of plasma polymerization and silica;
2. Layer (2) comprised mainly silica and some additives, like Si atoms, SiC and organic residues. The O/Si atomic ratio was about 1.5 (Tables 3–5);
3. Layer (3) of the thin film, called the interphase or interfacial region, was formed from PC fragments and the deposition products.

Such a structure of the film was a result of two processes:

1. Thin-film formation;
2. Etching of the surface.

The formation presence of the layers (1) and (2) followed the mechanism of thin-film formation from TEOS, proposed by Wróbel et al. [26]. TEOS in the reaction with oxygen radicals was decomposed into $(Et)_2Si{=}O$ (diethoxysilanone), which was the major film-forming precursor, according to this mechanism. Reactions between molecules of $(Et)_2Si{=}O$ gave rise to the formation of an organo-silicon layer on the basis material. This film was a product of the plasma polymerization process and it was modified during plasma treatment. The organic compounds of the organo-silicon layer were oxidized and eventually only inorganic compounds remained in the film. The results of these reactions are shown in Fig. 4 as (1) and (2).

The presence of the layer (3) in the thin film was unforeseen by the mechanism of thin-film formation from TEOS, because these mechanisms do not include the change of basis material during plasma treatment [26]. In the deposition of thin film on inorganic materials, like silicon wafers or metals, the change of basis material was negligible, but plastics were more sensitive than inorganic materials. During plasma treatment the surfaces of plastic were etched faster than the inorganic surfaces, and the structure of plastics was changed during plasma treatment [30]. Our previous study has shown that the etching rate of virgin PC is about two times faster than the etching rate of the thin film [9]. For this reason, the presence of layer (3) in our thin film might be explained by modification of PC structure, and by the PC etching during plasma treatment, as postulated by Bergeron et al. [31] and Denner et al. [32].

Layer (3)

The XPS studies have revealed an increase of C concentration with increasing sputtering time (Fig. 4, Table 3). The concentration of C from PC increased faster, while the C concentration from other chemical compounds decreased, including modified PC (Table 4, Figs. 5 (a) and (b)).

Peaks of Si(2p) were found in layer (3). The high concentration of Si bonded to O (at 103.5 eV) (Table 5) indicated that, the silica pervaded into PC during plasma treatment and mingled with PC fragments or the volatile fragments were liberated by the PC surface and mingled with SiO_x. The concentration of Si bonded to C (peak 101.0 eV) was in the range from 0.68 to 2.40% when the peak of C at 282.0 eV,

from SiC, was reduced in this region. This behavior was probably caused by Ar+ sputtering. The surface can be changed under the action of Ar+ and some chemical groups can decay or form. So, the data of XPS sputtering profile should be carefully analyzed [33].

Oxygen, besides PC and $SiO_{1.5}$, was present in the thin film in carbonyl and carboxylic groups. The peak of O(1s) at 527.0 eV (Table 6) was present in almost the whole volume of the thin film. This peak probably corresponded to O_2 molecules that were trapped in pores of the thin film.

Silicon, besides $SiO_{1.5}$ and SiC, was present as elementary Si (at 99.0 eV) in the whole volume of the thin film, but its concentration was low (Table 5).

The low concentration of nitrogen in the thin film (Fig. 4, Table 3) resulted from the presence of nitrogen in oxygen, which was used to make the plasma-generating gas mixture.

Layers (1) and (2)

Concentrations of C, Si and O amounted to 22.54, 28.98 and 47.69% in the top layer of the film (Table 3). This organo-silicon layer was the product of plasma polymerization of TEOS. In the lower layer, the concentration of C decreased to 4.13% with the sputtering time increasing to 5.8 min (Table 4). At the same time, the concentrations of O and Si increased to 57.97 and 37.62%, respectively (Tables 5 and 6). The main component of layer (1) was SiO_x and its share increased at the lower layers (Tables 5 and 6). The concentration of the other compounds decreased in the lower layers. It was assumed that there were no PC fragments in layer (1). With this assumption all peaks of C(1s) in the layer (1) were attributed to C in SiC and to products of plasma polymerization of TEOS (Table 4). Oxygen, besides SiO_x, was present in H_2O molecules at the top of thin film.

The concentrations of C, O and Si were stable in the layer (2), (Table 3). Layer (2) was consisted of SiO_x (Tables 5 and 6), which was the final product of thin-film deposition from TEOS. Beside SiO_x, some products of plasma polymerization of TEOS and SiC were present in layer (2) (Table 5).

9.5 Conclusions

Pulsed dielectric-barrier discharge (PDBD) is a useful technique to deposit thin SiO_x film on polycarbonate (PC) at atmospheric pressure. The obtained results show that:

1. The deposition rate decreases with an increase of the oxygen concentration in the plasma-generating gas.
2. The thin-film roughness was higher than the roughness of virgin PC, and increased with increasing oxygen concentration in the plasma-generating gas.

3. The film is divided into three layers (1), (2) and (3) (Fig. 4) of a variable chemical composition.
3.1. The top layer of the thin film (1) contains a mixture of the plasma-polymer and silica;
3.2. The second layer (2) contains silica and some additives, such as: Si atoms, SiC and organic residues;
3.3. The third, interphase layer (3) was formed from PC fragments and the deposition products.

References

[1] Special: Plastics Market; Plast Eur. **10**, 110 (2001).
[2] A.M. Wróbel, M.R. Wertheimer, Plasma Deposition, Treatment, and Etching of Polymers, ed. R. d'Agostino, Chap. 3, Academic Press Inc., San Diego, (1990).
[3] Y. Hatanaka, K. Sano, T. Aoki, A.M. Wróbel, Thin Solid Films, **368**, 287 (2000).
[4] J. Behnisch, J. Tyczkowski, M. Gazicki, I. Pela, A. Holländer, R. Ledzion, Surf. Coat. Technol., **98**, 872 (1998).
[5] K. Schmidt-Szałowski, Z. Rżanek-Boroch, J. Sentek, Z. Rymuza, Z. Kusznierewicz, M. Misiak, Plasmas Polym., **5**, 173 (2000).
[6] K. Schmidt-Szałowski, W. Fabianowski, Z. Rżanek-Boroch, J. Sentek, J. Chem. Vap. Deposition, **6**, 183 (1998).
[7] T. Opalińska, B. Ulejczyk, L. Karpiński, K. Schmidt-Szałowski, Pol. J. Chem. Technol., **4**, 30 (2002).
[8] T. Opalińska, B. Ulejczyk, L. Karpiński, K. Schmidt-Szałowski, Proceedings Int. Symp. High Pressure Low Temperature Plasma Chemistry (HAKONE VIII), Puhajarve, Estonia, 425 (2000).
[9] B. Ulejczyk, T. Opalińska, L. Karpiński, K. Schmidt-Szałowski, Acta Agrophysica, **80**, 275 (2002).
[10] J.M. Landon, Q. Meng, Surf. Sci. Spectra, **6**, 75 (1999).
[11] G. Beamson, D. Briggs, High Resolution XPS of Organic Polymers: the Scienta ESCA300 Database (1992).
[12] Y. Novis, M. Chtaib, R. Caudano, P. Lutgen, G. Feyder, Br. Polym., **21**, 171 (1989).
[13] B.M. DeKoven, P.L. Hagans, Appl. Surf. Sci., **27**, 199 (1986).
[14] D.T. Clark, H.R. Thomas, J. Polym. Sci. Polym. Chem. Ed., **14**, 1701 (1976).
[15] F. Yamamoto, S. Yamakama, J. Polym. Sci. Polym. Phys., **17**, 1581 (1979).
[16] C. Guimon, D. Gonbeau, G.P. Guillouzo, O. Dugne, A. Guette, R. Naslain, M. Lahaye, Surf. Interface Anal., **16**, 440 (1990).
[17] I. Tajima, M. Yamamoto, J. Polym. Sci. Part A, **25**, 1737 (1987).
[18] A.A. Galuska, J.C. Uht, N. Marquez, J. Vac. Sci. Technol. A, **6**, 110 (1988).
[19] A. Kumar, M.D. Rosenblum, D.L. Gilmore, B.J. Tufts, M.L. Rosenbluth, N.S. Lewis, Appl. Phys. Lett., **56**, 1919 (1990).
[20] A. Cros, R. Saoudi, C.A. Hewett, S.S. Lau, G. Hollinger, J. Appl. Phys., **67**, 1826 (1990).
[21] T.A. Clarke, E.N. Rizkalla, Chem. Phys. Lett., **37**, 523 (1976).
[22] A. Cimino, D. Gazzoli, M. Inversi, M. Valigi, Surf. Interface Anal., **10**, 194 (1987).
[23] P.D. Schulze, S.L. Shaffer, R.L. Hance, D.L. Utley, J. Vac. Sci. Technol. A, **1**, 97 (1983).
[24] M. Ayyoob, M.S. Hegde, J. Chem. Soc. Faraday Trans. I, **82**, 1651 (1986).
[25] K. Winer, C.A. Colmenares, R.L. Smith, F. Wooten, Surf. Sci., **183**, 67 (1987).
[26] A.M. Wróbel, A. Walkiewicz-Pietrzykowska, S. Wickramanayaka, Y. Hatanaka, J. Electrochem. Soc., **145**, 2866 (1998).
[27] A.M. Wróbel, M. Kryszewski, G. Czeremuszkin, Thin Solid Films, **289**, 112 (1996).
[28] M.R. Yang, K.-S. Chen, S.-T. Hsu, T.-Z. Wu, Surf. Coat. Technol., **123**, 204 (2000).
[29] M. Shirai, S. Umeda, M. Tsunooka, T. Matsuo, Eur. Polym. J., **9**, 1295 (1998).
[30] J. Czuprynska, Polimery, **47**, 8 (2002).
[31] A. Bergeron, J.E. Klemberg-Sapieha, L. Martinu, J. Vac. Sci. Technol. A, **16**, 3227 (1998).

[32] G. Dennler, A. Houdayer, P. Raynaud, I. Séguy, Y. Ségui, M.R. Wertheimer, Plasmas Polym., **8**, 43 (2003).

[33] A.S. da Silva Sobrinho, N. Schnuhler, J.E. Klemberg-Sapieha, M.R. Wertheimer, M. Andrews, S.C. Gujrathi, J. Vac. Sci. Technol. A, **16**, 2021 (1998).

10
Molecular Tailoring Coating on TiO_2 Nanoparticle Surface by Plasma Polymerization

Jing Zhang, Feng Zhu, Changnian Shi, Li Sun, Ying Wang, Zhan Cheng, Ping Ji, Qinyu Yang, Ying Guo, Rongming Zhou, Hankun Xie, W. J. van Ooij, Jie Lian, Donglu Shi

Abstract

In this paper, plasma polymerization was applied to deposit a thin film on a TiO_2 nanoparticle surface. The film morphology and chemical structure were tailored through appropriate polymerization conditions and characterized through high-resolution transmission electron microscopy (HRTEM), atom force microscopy (AFM), energy dispersion X-ray spectroscopy (EDS) and Fourier transform infrared spectroscopy (FTIR). The dispersion of TiO_2 nanoparticles in water and in ethyl glycol was analyzed through a laser scattering test and sedimentation velocity measurement. As displayed in HRTEM and AFM, TiO_2 nanoparticles were coated by an amorphous conformal plasma polymer film with adjustable thickness and surface roughness. The EDS results showed that the relative intensity of titanium and oxygen bands became indiscernible after AA plasma polymer coating. From FTIR results, it was demonstrated that this AA plasma polymer film on a TiO_2 nanoparticle surface contained some organic functional groups, such as COOH, CH_3CO, CH_2CO, CH_2OCO, etc., which were similar to those in the monomer structure and have good compatibility with water and ethyl glycol. It was concluded that plasma polymerization was an effective surface-coating method for nanoparticle tailoring not only in the physical morphology but also in the chemical structure. From particle-size-distribution experiments, it was summarized that the particle-size distribution of TiO_2 nanoparticles in water and in ethyl glycol shifted toward lower values and the dispersion was significantly improved after AA plasma polymer coating. It is estimated that the coating film provides a physical barrier between particles and compatible functional groups with the solution. The latter plays an important role in the dispersion improvement.

10.1
Introduction

Modification of a nanoparticle surface with a desired coating has been intensively studied with increasing interest. Applications include the super paramagnetic iron oxide nanocomposite for the magnetic resonance tracking of magnetically labeled

cells; polymer/nano-particle composites with particular mechanical, physical and chemical functions; structural ceramics with controlled microstructure, etc. In most cases, there is a requirement to change only the surface structure without changing its intrinsic properties [1–7].

The methods to form a controlled surface are usually classified into two categories: wet and dry chemical or physical processes. Some wet methods, such as sol-gel, intercalation polymerization and supermolecular self-assembly techniques, have been successfully applied in many solution cases [8–10]. Among the dry coating methods, plasma polymerization is an attractive coating technique because it has many advantages over other methods [2–5]. In plasma polymerization, the reactive species created by high-energy electrons and ions collide with the particle surface and form a depositing film through the energy loss or chemical bonding of the reactive species onto the surface. This coating process is suitable for a wide range of particles, irrespective of their chemical nature, shape, solubility or topography. It can form a thin coating film in a relatively simple one-step procedure.

van Ooij and Donglu Shi [2,11] used continuous RF plasma polymerization to obtain ultra-uniform films on Al_2O_3 and ZnO nanoparticles with size from 10 nm to 150 nm. Szabo and Vollath [3] synthesized Fe_3O_4 nanoparticles with a narrow size distribution and coated them with an ultra thin PMMA films through microwave discharge plasma. These studies show potential applications in low temperature consolidation of ceramics, in improving absorbency of heavy metal ions from polluted liquid and in superparamagnetic devices, etc.

Two tough technical challenges still exit in controlled coating of nanoparticles with plasma polymerization. One results from the very high surface energy of nanoparticles, which makes the nanoparticles agglomerate severely. Therefore it is very difficult to coat the individual nanoparticles while it is easier to coat particle aggregates. Another challenge comes from the inherent characteristics of plasma polymerization. Under the continuous bombardment of RF plasmas, the precursors are broken down seriously and the deposited film structure is usually crosslinked and a few functional groups can be retained in the film [12]. It is necessary to seek more flexile methods to control the coating structure with desired thickness, physical morphology and chemical structure.

Based on the previous study [2,11], some improvements were done in our fluidized-bed reactor. So that the nanoparticles have plasma sheaths around them and have the same sign of float voltage in the plasma atmosphere. Their surfaces are more easily renewed in the plasma by a continuous shearing disturbing for a conformal film coating. Besides this, a pulsed radio-frequency (RF) discharge was used to develop tailored chemical structure and physical morphology on TiO_2 nanoparticle surfaces. The physical morphology and chemical structure of this coating film on the TiO_2 nanoparticle surface were investigated through high-resolution transmission electron microscopy (HRTEM), atom force microscopy (AFM), energy dispersion X-ray spectroscopy (EDS) and Fourier transform infrared spectroscopy (FTIR). In order to detect the nanoscale thickness of the film (a few nm), a small electron probe (0.5 nm) and a very short collection time were applied in the EDS measurement. The dispersion behavior of coated and uncoated TiO_2 nanoparticles was also

investigated through the particle-size distribution obtained by laser-scattering test and sedimentation velocity measurement.

10.2 Experimental

The plasma coating experiments on nanoparticle surfaces were performed in a custom-built fluidized-bed plasma reactor. The schematic diagram of the fluidized-bed plasma reactor is shown in Fig. 1. RF power (13.56 MHz) is applied through an impedance-matching network to one of the concentric ring electrodes around the exterior of the Pyrex tube reactor. The other electrode is grounded. The RF power source is supplied by American Advanced Energy Inc. with an automatic matching network used to minimize the reflected power. The power could be supplied both in a continuous and in a pulsed mode with a variable duty cycle and pulse length. The pulse length can be as short as 1 μs.

The coating process can be summarized as follows: The anatase TiO_2 nanoparticles with a primary average size of 35 nm were put into the reactor. The reactor is then pumped down to a base pressure less than 3 Pa. The mixture of argon (12 sccm) and acrylic acid (AA, 3 sccm) or pyrrole (3 sccm) is fed into the reactor to fluidize the nanoparticles through a mass flow controller and a porous plate at a pressure of 160 Pa. The porous plate is composed of two layers of steel mesh and one

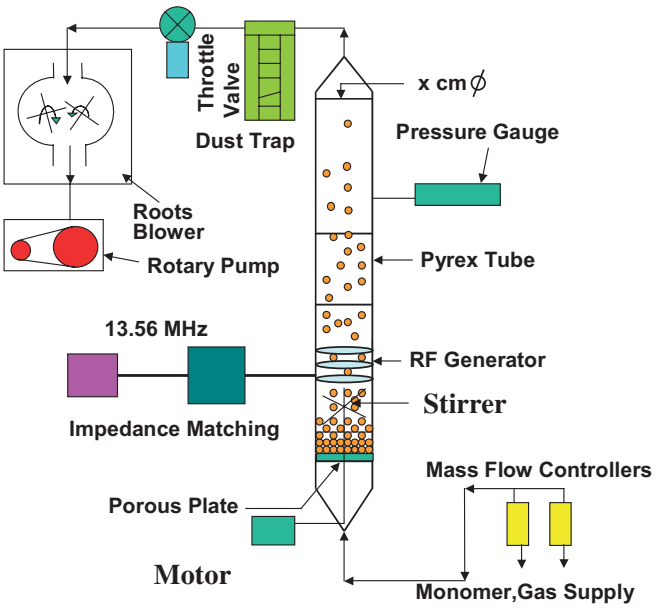

Figure 1 Schematic of the plasma fluidized-bed reactor for nanoparticle coating.

layer of ultrafine filter paper. The pressure drop is mainly caused by the filter paper and is approximately 1–2 Pa. Although the plate holes are big enough for the nanoparticles, the nanoparticles will not pass through the plate holes because of their agglomeration. Except when specifically mentioned, the coating is processed at a power of 55 w for 2 h in continuous-discharge mode; 2 W of power and 3% of duty cycle for 1 h in pulsed-discharge mode. The stirrer rotation rate is kept at 580 rpm/min in both cases.

Because of the improved fluidized-bed technique [13], the nanoparticles have plasma sheaths around them and have the same sign of float voltage in the plasma atmosphere. Their surfaces are kinetically renewed in the plasma by a continuous disturbing for an efficient conformal coating. After coated for a period of time, the nanoparticles are collected at the bottom of the reactor for further analysis.

The TiO_2 nanoparticles are dispersed onto a HRTEM copper grid with a carbon film for surface morphology analysis. The HRTEM experiment is performed on a JEX 4000EX TEM. Plasma polymer film is deposited on flat glass slides and observed with a QUOTATION-4 AFM made by the DI company. The chemical composition and molecular structure are investigated through EDS and FTIR. The EDS spectrum is obtained at the same time as the HRTEM photo is taken on the same JEX 4000EX TEM instrument. The FTIR spectra are recorded using the mixture flake of KBr powder and TiO_2 nanoparticles on a Nicolet NEXUS-670 FTIR spectrometer. The dispersion of TiO_2 nanoparticles in water and in ethyl glycol is analyzed separately through the particle-size distribution test using LS-100 manufactured by Coulter Company and sedimentation-velocity measurement using a Japan SA-CP3. The titanium dioxide concentration of the suspension solution is 0.05%. After ultrasonic treatment for 5 min, the measurement of the particle-size distribution is done immediately.

10.3 Results and Discussions

10.3.1 Surface Morphology

The HRTEM photographs of AA-plasma-polymer-coated and uncoated TiO_2 nanoparticles are shown in Fig. 2. In Fig. 2 (a), the crystal TiO_2 lattice is quite apparent but there is no observable coating film around it. After coating, an amorphous ultrathin film of AA plasma polymer is clearly seen over the TiO_2 nanoparticles (Fig. 2 (b)). The dense thin film is tightly bound to the nanoparticles and is about 3–5 nm thick. This indicates that a conformal AA plasma polymer coating on TiO_2 nanoparticles is indeed achieved using this fluidized-bed plasma technique.

In order to control and observe the physical morphology of the coating film, different conditions are applied to deposit plasma polymer films on glass slides. The AFM images of these films are taken and shown in Fig. 3. Their cross sections are displayed in Fig. 4. From Fig. 3 (a) and Fig. 4 (a) it is clearly seen that the coating

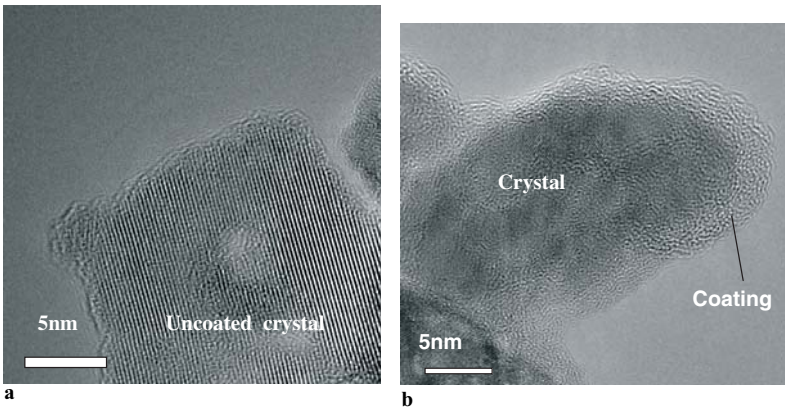

Figure 2 HRTEM micrographs of TiO_2 nanoparticles (a) uncoated (b) AA plasma polymer coated under continuous discharge.

film is packed with nano-clusters under pulsed discharge. These nanoscale clusters are uniformly distributed. The vertical variation of the nanoclusters is about 10 nm. But the clusters become larger under continuous discharge (vertical variation of the clusters is about 1.8 μm). It is known, in fact, that the film deposition rate in continuous-discharge mode is much higher than that in pulsed-discharge mode [12]. The newly formed cluster nuclei grow rapidly under continuous discharge. So the clusters are much larger than under pulsed discharge. Although the thickness of the film obtained with the same discharge conditions over the octahedron TiO_2 nanoparticles is much less than that on flat glass because of the high specific area of nanoparticles, the deposition situation is almost the same. Therefore it is reasonably

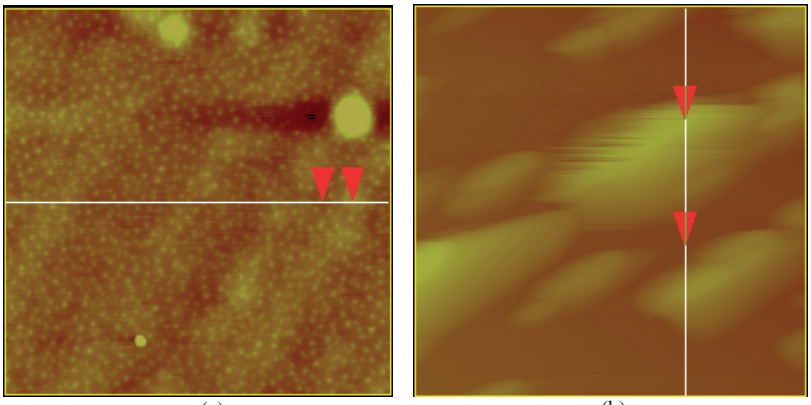

Figure 3 AFM images of AA plasma polymer films deposited on glass slides, (a) under pulsed discharge (2 W of power, 3% of duty cycle, 1 h) (b) under continuous discharge (30 W of power, 1 h).

believed that it is possible to control the roughness and thickness of the coating film on the TiO_2 nanoparticle surface by adjusting the discharge conditions. Plasma polymerization is indeed a flexible method to change the surface physical morphology of nanoparticles. This is one of its advantages over other coating methods.

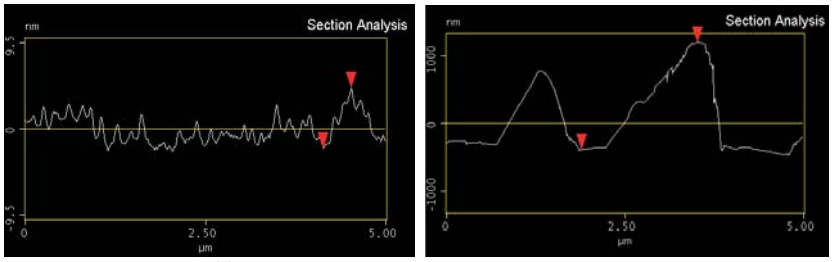

Figure 4 Cross sections of AA plasma polymer films deposited on glass slides, (a) under pulsed discharge (2 W of power, 3% of duty cycle, 1 h), (b) under continuous discharge (30 W of power, 1 h).

10.3.2
Surface Molecular Structure

To confirm the HRTEM observations shown in Fig. 2 and to investigate on the molecular structure of the coating film, EDS and FTIR spectra have been made and the results are shown in Fig. 5 and Fig. 6.

It can be noted from Fig. 5 (a) that the relative intensity of titanium and oxygen bands are very high for uncoated TiO_2 nanoparticles. The Ti and O signals in Fig. 5 (a) come from the TiO_2 nanoparticles, while the Cu and C signals come from the TEM support grid and carbon film, respectively. After AA plasma polymer coating, the relative intensity of titanium and oxygen bands become indiscernible. However, the relative intensity of C peak increases as shown in Fig. 5 (b). This increase mainly comes from the AA plasma polymer coating. Because carbon is more easily detected than oxygen in EDS, almost no O signal is detectable for AA-plasma-polymer-coated TiO_2. Therefore, it is deduced that the AA plasma polymer film covers the TiO_2 nanoparticles completely. These results correspond very well with those in HRTEM and show again that the plasma coating on TiO_2 nanoparticles is indeed dense and uniform.

FTIR spectra of coated and uncoated TiO_2 nanoparticles are shown in Figure 6. In uncoated TiO_2, Fig. 6 (b), both the broad band at about 3400 cm^{-1} and the medium intensity band at 1620 cm^{-1} belong to OH stretching vibrations caused by the absorbed water. In AA-plasma-polymer-coated TiO_2 in continuous-discharge mode (Fig. 6 (c)) and in pulsed-discharge mode (Fig. 6 (d)), these two bands still exit. One reason is that AA plasma polymer coating on TiO_2 surface contains OH groups.

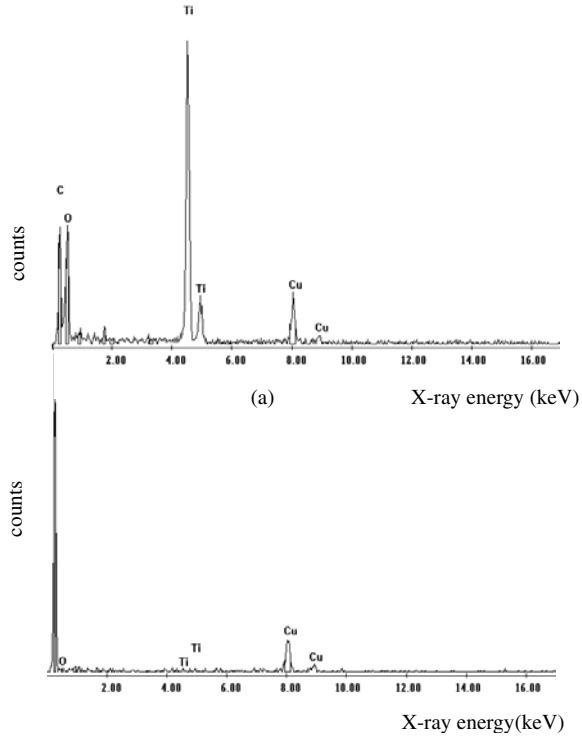

Figure 5 EDS spectra of TiO_2 nanoparticles (a) uncoated (b) AA plasma polymer coated in continuous-discharge mode.

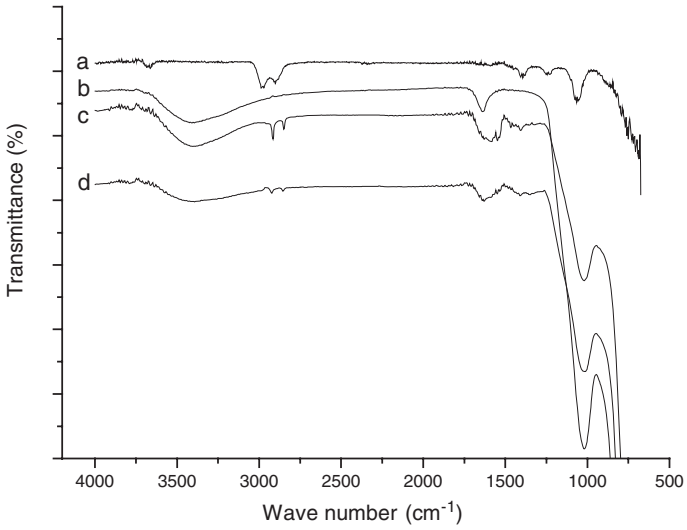

Figure 6 FTIR spectra of TiO_2 nanoparticles, (a) pyrrole plasma polymer coated under continuous discharge, (b) uncoated, (c) AA plasma polymer coated under continuous discharge, (d) AA plasma polymer coated under pulsed discharge.

Another reason is that AA-plasma-polymer-coated TiO_2 still absorbs water. The new peaks at 2930 cm^{-1} and 2880 cm^{-1} are assigned to C–H stretching of sp^3 CH_3 and sp^3 CH_2 groups, respectively. This indicates that the TiO_2 surface is coated by AA plasma polymer film effectively. The slightly broader bands at 1600 cm^{-1} in Fig. 6 (c) and in Fig. 6 (d) are assigned to the overlap of C=C and C=O stretching vibration. The medium intensity new band at 1346 cm^{-1} is due to O–H deforming vibrations that indicates the possible existence of CO–C=CH_2 ketones and CO–O–C=CH_2 esters. These findings further confirm the effects of AA plasma polymer film coating. It should be noted that the ratio of the band intensities at 1346 cm^{-1} and at 2930 cm^{-1} represents the relative content of OH group with respect to CH_3 or CH_2 or CH group. Since this ratio for AA-plasma-polymer-coated TiO_2 in pulsed-discharge mode is greater than in continuous-discharge mode, it can be reasonably deduced that in pulsed-discharge mode more OH than COOH groups are retained.

For pyrrole-plasma-polymer-coated TiO_2 in Fig. 6 (a), the new bands at about 2988 cm^{-1} and at 2900 cm^{-1} are assigned to the C–H stretching vibration absorption. The band at 3600 cm^{-1} occurs due to N–H stretching vibration. A very weak band at 1600 cm^{-1} and a medium intensity band at 1393 cm^{-1} are caused by the in-plane vibration of C=C and C=N groups. These FTIR results show the effective coating of pyrrole plasma polymer film on TiO_2 surface. Since no vibration bands are observed at 3400 cm^{-1} and at 1600 cm^{-1}, which are originally given by the water absorption in TiO_2, it is considered that the pyrrole plasma polymer film has much effectively and completely covered the TiO_2 surface [12].

From the above FTIR results, it is demonstrated that the surface coatings on TiO_2 nanoparticles are organic AA or pyrrole plasma polymer films. These organic films contain some functional groups such as COOH, CH_3CO, CH_2CO, CH_2OCO, CH=C–NH or CH_2–C=N, etc., which are similar to those in the monomer structure. In our previous studies, pulsed RF plasma polymerization has been applied in controlling the chemical structure of the plasma polymer film of vinyl acetic acid, etc. [13–17]. So it is possible to tailor the coating-film structure through selecting suitable monomers and changing the deposition conditions.

10.3.3
Dispersion Behavior of AA-Plasma-Polymer-Coated TiO_2 Nanoparticles

The dispersion behavior of nanoparticles in solution is associated closely to their surface structure and to the interface compatibility with the solution. When the dispersion is good, the particle-size distribution centers at the smaller size end. As dicussed above, the surface physical morphology and chemical structure of AA- or pyrrole-plasma-polymer-coated TiO_2 nanoparticles have been changed to some extent. This influences their dispersion behavior in water and in ethyl glycol. The particle-size distribution obtained by a laser-scattering test in water is shown in Fig. 7. The figure demonstrates that the whole distribution of particle size shifts toward lower values for AA-plasma-polymer-coating particles. Besides, the statistical mean particle size decreases from 3.82 μm to 2.89 µm after coating.

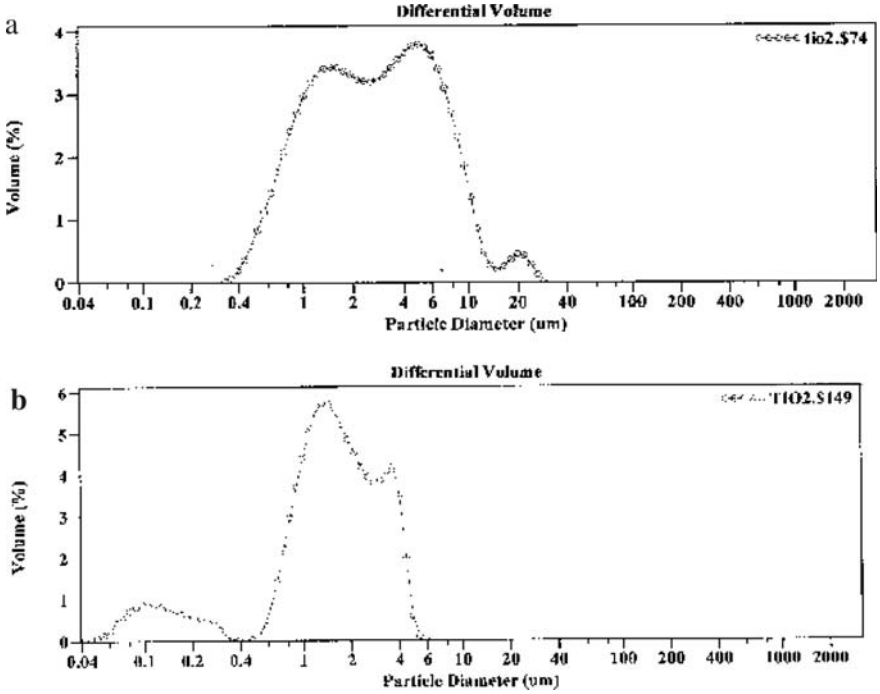

Figure 7 LS particle-size distribution of TiO_2 nanoparticles (a) uncoated (b) AA plasma polymer coated under continuous discharge.

The sedimentation velocity test in ethyl glycol solution shows similar trends (Fig. 8 and Table 1).

Table 1 Experiment results in sedimentation-velocity test

Sample	Median diameter (μm)	75 % diameter (μm)	Surface area (m^2/g)	Viscosity (MPa · S)
Control	4.72	1.10	2.92	17.4
Pyrrole-plasma-polymer-coated	10.16	1.28	2.39	17.4
AA-pulsed-plasma-polymer-coated	0.96	0.43	8.33	1.15
AA-continuous-plasma-polymer-coated	1.31	1.73	6.09	1.21

From Table 1, it is seen that the mean size of the particles in ethyl glycol suspension for AA-plasma-polymer-coated TiO_2 decreases under both pulsed and continuous discharges, but the data increase for pyrrole-plasma-polymer-coated TiO_2 under continuous discharge. This means that the AA plasma polymer coating is more favorable for the dispersion improvement of TiO_2 nanoparticles in ethyl glycol than pyrrole plasma polymer coating.

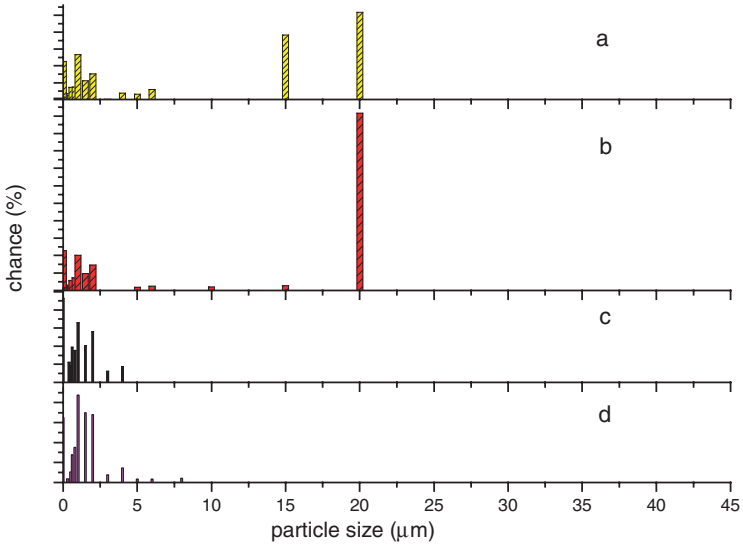

Figure 8 Particle-size distribution of TiO_2 nanoparticles in sedimentation-velocity experiment, (a) uncoated, (b) pyrrole plasma polymer coated under continuous discharge, (c) AA plasma polymer coated under pulsed discharge, (d) AA plasma polymer coated under continuous discharge.

In Fig. 8 (a), the particle-size distribution is shown to be in the range of 30 μm for the control of TiO_2 nanoparticles. However, (Fig. 8 (b)), the data move toward lower particle sizes for AA plasma polymer coating under both pulsed and continuous discharge. The particle-size distribution is still in the range of 30 μm for the pyrrole plasma polymer coating.

From these particle-size distribution experiments, it is summarized that the mean particle size of coagulated TiO_2 nanoparticles is effectively lowered and their dispersion in water and in ethyl glycol has been greatly improved after AA plasma polymer coating. As shown in HRTEM and AFM tests, a conformal AA plasma coating film covers the TiO_2 nanoparticles completely, which creates a sort of barrier between nanoparticles and reduces their agglomeration. This is one reason for the dispersion improvement. Another reason is that AA plasma coating film contains functional groups, such as COOH, CH_2CO, CH_2OCO, CH_3CO, etc. These functional groups make the nanoparticle surface more compatible with water and ethyl glycol, so TiO_2 nanoparticles with an AA plasma polymer coating disperse well in these two solutions. As indicated by FTIR, more functional groups such as COOH are retained in AA-plasma-polymer-coated TiO_2 nanoparticle surfaces under pulsed discharge, the dispersion behavior is better under pulsed discharge than under continuous discharge. Since a pyrrole plasma polymer film on TiO_2 nanoparticle surface does not have good compatibility with water and ethyl glycol, the dispersion behavior has not been improved obviously. Therefore, it is deduced that the latter reason plays a more important role in improving nanoparticle dispersion.

10.4 Conclusion

By using plasma polymerization an AA plasma polymer film is deposited on TiO_2 nanoparticles. The particle surface morphology and chemical structure are characterized. The dispersion behavior is evaluated through the particle-size distribution in water and in ethyl glycol solution. The conclusions are as follows:

1. Plasma polymerization is an effective coating method for TiO_2 nanoparticles. A conformal amorphous polymer film can cover the individual nanoparticles completely with an adjustable thickness and surface roughness. This method is appropriate to a wide range of nanoparticles because it is a dry process operated at room temperature.
2. Besides a flexible modification of the nanoparticle surface morphology, the chemical structure can also be tailored by selecting suitable monomers and discharge conditions. Under pulsed RF discharge, more COOH groups are retained than under continuous discharge.
3. The dispersion of TiO_2 nanoparticles in water and in ethyl glycol is much improved after AA plasma polymer coating, but remains almost the same after pyrrole plasma polymer coating. One reason is that the surrounding organic coating film creates a barrier between particles. Another reason is that the coating film contains functional groups that are compatible with the solution. The latter plays a more important role in improving the dispersion behavior. The particle-size distribution centers at lower values under pulsed RF discharges than under continuous discharge because more COOH functional groups are retained.

Acknowledgement

The authors would like to acknowledge the support from the "Dawn" Program of Shanghai Education Commission-01SG31, Foundation of Shanghai Science and Technology Commission-015207004.

References

[1] S. A. Majetich and Y. Jin, Magnetization Directions of Individual Nanoparticles, Science, 1999, 284:407–473

[2] D. Shi, S. X. Wang, W. J. Van Ooij, L. M. Wang, J. G. Zhao and Y. Zhou, Uniform Deposition of Ultra Thin Polymer Films on the Surfaces of Al_2O_3 Nanoparticles by a Plasma Treatment, Appl. Phys. Lett., 2001, 78(9):1243–1245

[3] D. V. Szabo, D. Vollath, Nanocomposites from Coated Nanoparticles, Adv. Mater., 1999, 11(15):1313–1316

[4] A. Kouprine, F. Gitzhofer, M. Boulos, A. Fridman, Graphite Coating of Nanoparticles in Capacitively Coupled RF Discharge, 15th International Symposium on Plasma Chemistry, Orleans, France, 2001, July, 335–340

[5] K. Rajan, O. Sajgalik, R. K. Singh, D. Kamar, and J. Fitz-Gerald, Synthesis and Microstructure of Conformal Coatings on Particulates, Mater. Res. Soc. Symp. Proc, 1998, 501:313–320

[6] D. Beydoun, R. Amal, G. Low, S. McEvoy, A Preliminary Investigation into the Synthesis of Titania Coated Magnetite as a Novel Photocatalyst, World Congress on Particle Technology 3, 1998, 385

[7] Lide Zhang, Jimei Mu, Nanomaterials and Nanostructure, Science Press, Beijing, 2001, 199 (in Chinese)

[8] Q. Wang, H. Xia, C. Zhang, Preparation of Polymer/Inorganic Nanoparticles Composite, through Ultrasonic Irradiation, J. Appl. Polym. Sci., 2001, 80(9):1478–1488

[9] W. Liang; G. Bognolo; Th. F. Tadros, Stability of Dispersion in the Presence of Graft Copolymer (II)Adsorption of Graft Copolymers on Titanious Dioxide and the Stability and Rheology of the Resulting Polymer, Langmuir (2000) 16(3):1306–1310

[10] I. Manas-Zloczower, M. Arellano, D. L. Feke, Assessment of the Dispersibility of Surfactant-Treated Titanium Dioxide Powders for Compounding with Polyethylene, Polym. Compos. (1995) 16(6): 489–494

[11] Peng He, Jie Lian, L. M. Wang, Wim J. van Ooij, and Donglu Shi, Deposition of Polymer Thin Films on ZnO Nanoparticles by a Plasma Treatment, Mater. Res. Soc. Symp. Proc. 2001, 635

[12] G. Socrates, Infrared Characteristic Group Frequencies, Second Edition, John Wiley & Sons, England, 1994

[13] H. Yasuda, Plasma Polymerization, Academic Press, New York, 1985

[14] CN03115252.X

[15] Jing Zhang, Meizhen Wu, Tian Shu Pu, Zheng Yang Zhang, Ruo Peng Jin, Zhi Sheng Tong, Investigation of the Plasma Polymer Deposited From Pyrrole, Thin Solid Films (1997) 307:14–20

[16] Jing Zhang, W.J. van Ooij, P. France, Saswati Datta, Arseniy Radmyselskiy, Hankun Xie, Investigation of Deposition Rate and Structure of Pulse DC Plasma Polymers, Thin Solid Films 2001, 390:123–129

[17] Jing Zhang, P. France, A. Radomyselskiy, S. Datta, Jiangang Zhao, W.J. van Ooij, J. Appl. Polym. Sci., 2003, 88(6): 1473–1481

Part II
Plasma-Grafting of Functional Groups

11
Introduction of Acidic Functional Groups onto the Surface of Activated Carbons by Atmospheric-Pressure Nonthermal Plasma

Satoshi Kodama and Hidetoshi Sekiguchi

Abstract

Granular activated carbon was modified by an oxygen nonthermal plasma with three types of reactors: dielectric barrier discharge (DBD) parallel-prate type reactor, atmospheric-pressure glow-discharge plasma-jet reactor and DBD coaxial-type reactor. The objective of this work is introducing acidic functional groups on the surface of the activated carbon (AC). The samples were characterized by selective neutralization method, scanning electron microscopy and energy dispersive X-ray spectroscopy. The results showed that the treatment could successfully introduce acidic functional groups on the surface of the AC and the modification was observed only in the neighborhood of surface of the AC.

11.1
Introduction

Activated carbon (AC) is widely used as an adsorbent because of its well-developed porous structure. AC is essentially a nonpolar material, therefore, it is used as an adsorbent for organics in water where the molecules of organics are captured with AC by van der Waals force. There are many reports about treating AC in various ways to modify the surface chemistry [1–3]. In our previous study, AC was treated by an oxygen nonthermal plasma induced by dielectric barrier discharge (DBD) [4]. The plasma was generated by applying alternating high voltage at a frequency of 50 Hz to parallel-plate electrodes. The sample was treated by an oxygen plasma by varying treatment time and the effects on adsorption ability for the copper ion in aqueous solutions were measured. The results showed that the saturated adsorption amount of copper ion was increased by the treatment. This was caused by the introduction of functional groups on AC. It was concluded that DBD treatment with the reactor was effective to introduce acidic functional groups on AC.

In this study, AC was treated in two types of DBD reactor and an atmospheric-pressure glow-discharge (APGD) reactor. The DBD method used in our previous study has the advantages that the treatment is easy to operate with small power consumption, however, it has a disadvantage that it takes much time for the treatment.

Recently, APGD has been applied for the surface treatment of materials [5]. The discharge generates a nonthermal plasma by applying high-frequency alternating current to the electrodes; one of which is at least covered with dielectric materials. This discharge is expected to generate higher energy density in the reactor and shorten the treatment time. The samples treated in the three types of reactors were analyzed by the selective neutralization method, scanning electron microscopy (SEM) and energy dispersive X-ray spectroscopy (EDS), and the affects of the treatment are discussed.

11.2 Experimental

11.2.1 Materials

Commercial granular activated carbon ("Ryujo-Shirasagi LH2c 20/48", Takeda Chemical Industries) was used in this study. The diameter range and specific surface area of the AC was 0.850–0.300 mm and 1596 m^2/g, respectively. Though the AC contains fewer impurities and less acidic functional groups compared with that used in our previous work [4], a little ash derived from raw material still existed. Therefore, the AC was rinsed with distilled water until the pH of it was near neutral and then dried at 40 °C in an oven for 5 days.

11.2.2 Plasma Treatment of the Samples

As mentioned above, three types of reactors had been used and are explained here.

11.2.2.1 DBD Parallel-plate-type Reactor

The schematic of the experimental apparatus for the DBD parallel-plate type reactor is shown in Fig. 1 (a), and the experimental conditions are shown in Table 1 (a). The reactor (a) was similar to that used in our previous work [4]. Two dielectrics made of glass were located between two disk-shaped copper electrodes. The gap between the electrodes was 8.5 mm and the thickness of the dielectrics was 1.5 mm. The AC weighed 0.4 g and was put on the lower dielectric so that the AC was treated directly by the plasma. The oxygen gas flow rate was set as 12 mL/min. The plasma was generated under atmospheric pressure at a discharge voltage of 10–23 kV and a frequency of 50 Hz.

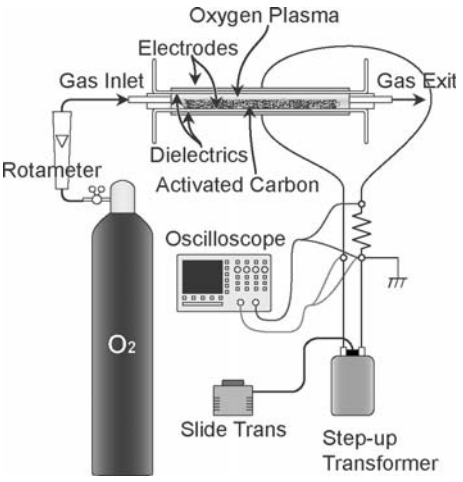

(a)

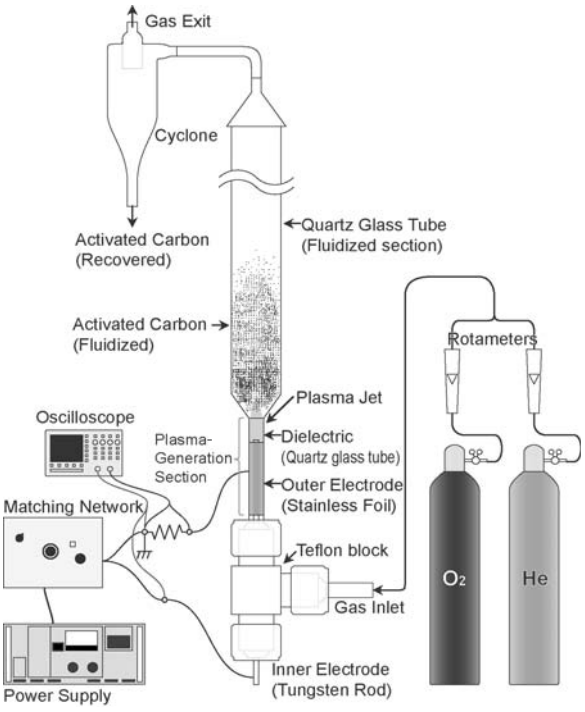

(b)

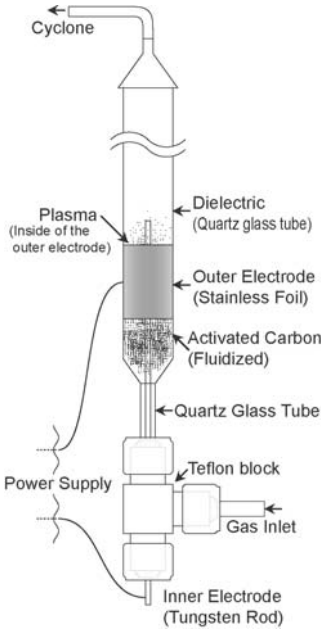

(c)

Figure 1 Experimental apparatus. (a) DBD parallel-plate-type reactor, (b) APGD plasma-jet reactor, (c) DBD coaxial-type reactor.

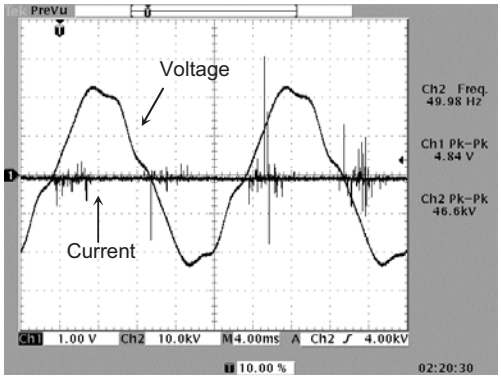

(a)

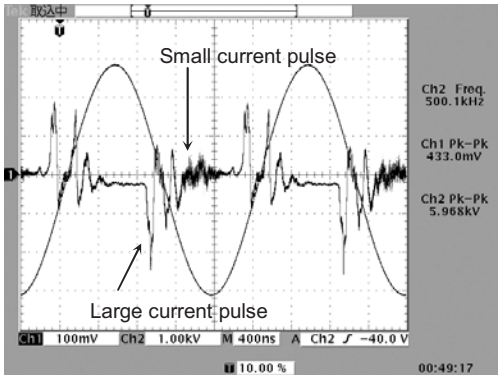

(b)

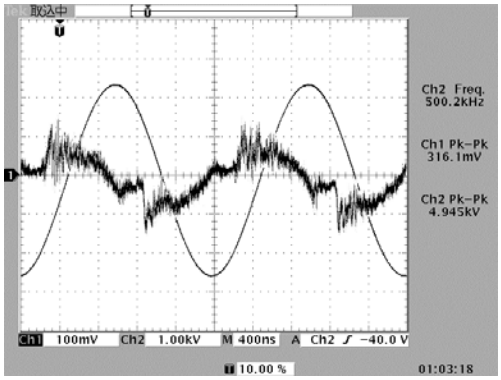

(c)

Figure 2 Waveforms of the voltages and currents applied to the reactor. (a) DBD parallel-plate-type reactor, (b) APGD plasma-jet reactor, (c) DBD coaxial-type reactor.

Table 1 Experimental conditions

Reactor		(a)	(b)	(c)
Sample		Ryujo-Shirasagi LH2c 20/48 (Takeda chemical industries, 0.85–0.30 mm in diameter)		
Type of discharge		DBD	APGD	DBD
Treatment time		60 min	60 min	30 min
Power consumption		2.5 W (at 23 kV)	60 W	120 W
Pressure in the reactor		1 atm	1 atm	1 atm
Frequency and voltage of the power supply		50 Hz, 10–23 kV	500 kHz, 3 kV	500 kHz, 2.5 kV
Distance between the electrodes		8.5 mm	1.5 mm	7.5 mm
Amount of sample		0.4 g	1 g	1 g
Gas flow rate	Oxygen	12 mL/min	1 L/min	1 L/min
	Helium	–	6 L/min	6 L/min
Yield		100–90%	75%	40%

Figure 2 (a) shows the waveform of the voltage and the current applied to the reactor. The waveform of the current was typically the shape of low-frequency DBD. The power consumption in the reactor was measured with a digital oscilloscope (Tektronix, TD-3012) and a high-voltage probe (Tektronix, P6015A) by integrating the Lissajous figure. After the treatment, the AC was recovered from the reactor and weighed to calculate yield. The yield was 100% (applied voltage of 23 kV) to 90% (applied voltage of 10 kV) though not all the sample could be recovered from the reactor.

11.2.2.2 **APGD Plasma-Jet Reactor**

Figure 1 (b) shows the coaxial-type APGD plasma-jet reactor. The reactor consisted of the plasma-generation section and the fluidized section. The plasma-generation section was made of dielectric (quartz glass tube, 6 mm outer diameter, 5 mm inner diameter and 40 mm length), inner electrode (tungsten rod, 3 mm diameter and 80 mm length) and outer electrode (stainless foil, 20 mm in length). The inner electrode was located coaxially at the center of the dielectric and they were mounted on a Teflon block. The outer electrode was wrapped around the dielectric. The experimental conditions are shown in Table 1 (b). The plasma jet was generated under atmospheric pressure by applying a high-frequency alternating voltage (500 kHz, 3 kV) to the electrodes using the high-frequency power supply (ASTECH, LG-10S). The plasma-generation section was connected at the bottom of the fluidized section. The fluidized section consisted of a quartz glass tube (21 mm outer diameter, 18 mm inner diameter, and 300 mm length). The AC sample weighed 1 g was fluidized in the fluidized section by the gas flow and treated by the plasma for 60 min. Helium 6 L/min and oxygen 1 L/min gases were mixed and introduced into the reactor. The flow rates were necessary for fluidization of the sample and generation of a stable plasma jet. The plasma jet reached to the fluidized section and the length of the jet was about 20 mm from the edge of the electrode to the bottom of the fluidized area. The cyclone was only used to recover the AC after the treatment by increasing flow

rate of helium. The yield of this experiment was approximately 75%. Figure 2 (b) shows the waveform of the voltage and the current applied to the reactor. Some current pulses exist after the large pulses. This discharge would be the mixture of the APGD and DBD [6, 7], however, the discharge seemed to be uniform. Therefore, it is termed APGD in this paper. The voltage applied to the reactor and the current were measured with a digital oscilloscope and a high-voltage probe.

11.2.2.3 **DBD Coaxial-type Reactor**

Figure 1 (c) shows the DBD coaxial-type reactor. The reactor was essentially the same as (b) except for the length of the inner electrode and the position of the outer electrode. The length of the inner electrode was 160 mm and the outer electrode was wrapped around the fluidized section. Thus, discharge occurred at the fluidized section and showed filament-like structure. The experimental conditions are given in Table 1 (c). The washed AC, weight 1 g, was fluidized in it. The entire sample was burnt by the treatment time of 1 h, therefore, the treatment time was set to 30 min. The yield was approximately 40%. Figure 2 (c) shows the waveform of the voltage and the current applied to the reactor. This is similar to the waveform of DBD [6].

11.2.3
Characterization

11.2.3.1 **Selective Neutralization Method**

The selective neutralization method (Boehm method) [2, 8, 9] was used to evaluate the carbon surface acidity. The solutions of NaOEt, NaOH, Na_2CO_3, and $NaHCO_3$, the concentration of each was 0.02N, were prepared using decarbonated water. The AC samples weighed 0.1 g and were mixed with the solutions in 100-mL Erlenmeyer flasks. After shaking the flasks at the temperature of 30 °C for 3 days, which was enough to reach equilibrium, the solutions were filtered with PTFE (polytetrafluoroethylene) membrane filters (ADVANTEC, 0.45 μm pore size) to separate the AC from the solution. The concentrations of the base in the filtrates were determined by back-titration with a titrator (Metrohm, 798 MPT Titrino) using 0.1N of HCl solution. The concentration of the acidic functional groups on the AC was determined from the amount of consumption of the bases.

11.2.3.2 **Adsorption of Metal Ions and SEM-EDS Analysis**

Adsorption of metal ions onto AC occurs by ion exchange of acidic functional groups on the surface with metal ions. When AC captured copper from aqueous solutions, the existence of Cu ions on the AC should indicate the existence of acidic functional groups. The adsorption was carried out as follows; 0.1 mg of the AC samples were mixed with 50 ml of 20 ppm Cu(II) solutions, made from copper standard solution and decarbonated water, in 100-mL Erlenmeyer flasks. After shaking the flasks at a temperature of 30 °C for 3 days, the AC was removed from the solution. SEM (JEOL JSM-5310LV) and EDS (JEOL JED-2140) were used for visualizing and semiquantitative analysis of the AC samples.

11.3 Results and Discussion

11.3.1 Surface Chemistry

Figure 3 shows the variation in the content of surface functional groups of the AC. The results show that for all the plasma-treated samples acidic functional groups were introduced on their surface. In Fig. 3 (1), the concentration of functional groups was the highest in the sample treated in reactor (a), while the lowest was in the sample treated in reactor (b). There seemed to be no relation between the concentrations and the power consumption because the power consumption of reactors (a), (b) and (c) were 2.5, 120 and 60 W, respectively. The concentrations of acidic functional groups were expected to have a relation between the strength of electric field of the reactor. However, the sample treated in reactor (c) contained higher concentrations of functional groups than the sample treated with (b), even though reactor (b) had a higher electric field strength than that of reactor (c). The discharge of the reactor (b) did not attack the AC directly because the fluidized area was separated from the electrode as mentioned above. Therefore, it is supposed that the direct discharge onto the surface enhances the generation of acidic functional groups. Figure 3 (2) shows the ratios in the content of the acidic functional groups of the AC. It is found that the ratio of the sample treated in reactor (a) is similar to that of treated in reactor (c) though the frequency of their power supply and power consumption during the treatment were different. The common condition of the treatment was that the samples were treated in the discharging zone. This also suggests that the introduction mechanisms of acidic functional groups onto the surface of the AC are different with and without the discharge onto the surface of AC.

The relation between applied voltage and concentration of acidic functional groups treated in reactor (a) is shown in Fig. 4 (1). The concentration of acidic functional groups decreased with lower applied voltage and was small for an applied voltage of 10 kV as well as the untreated sample. The concentration of the sample of 10 kV was so small that the ratios of the functional groups were difficult to distinguish from measurement errors. There should be a threshold for the introduction of functional groups by reactor (a) between the applied voltage of 10 kV and 15 kV. The effects of applied voltage in the ratio of surface functional groups of the AC treated in reactor (a) are shown in Fig. 4 (2). The ratio was similar in the samples with applied voltage higher than 15 kV.

The concentration of functional groups of the sample treated in reactor (a) with 23 kV was approximately two times higher than the previous results of other researchers [2, 3]. However, it should be noted that the results are affected by the difference of the brand or lot of AC and we can not simply compare the results because the structure, activation condition or impurity contained in the AC may have an affect on adsorption properties.

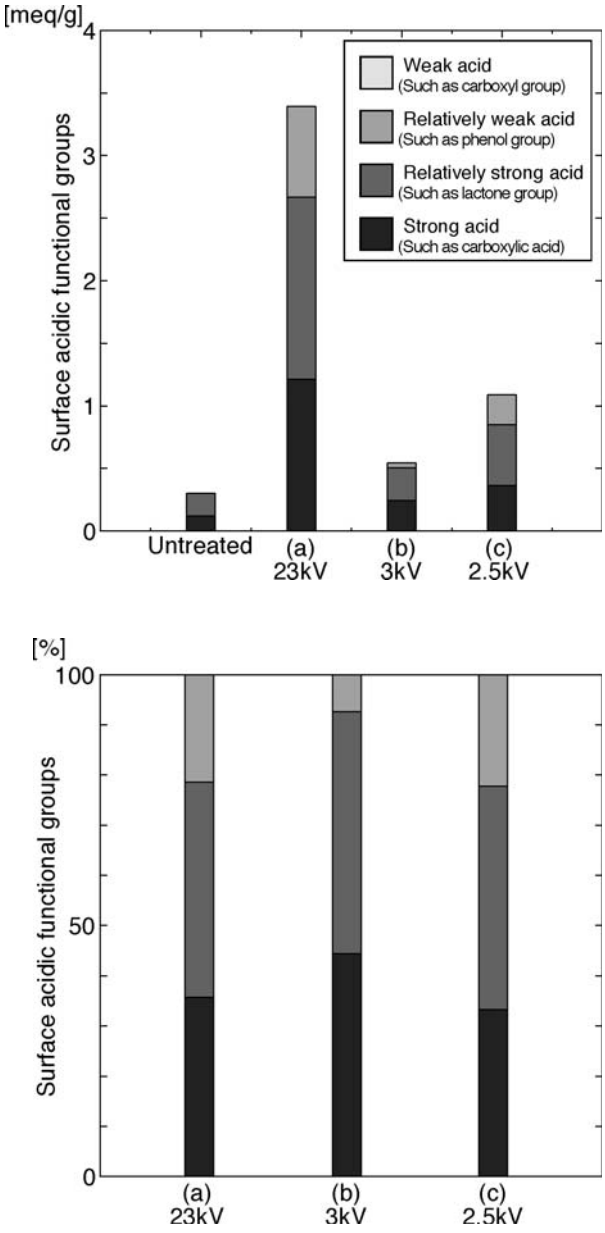

Figure 3 (1) The effects of reactor on the content of surface functional groups of the ACs, (a) DBD parallel-plate-type reactor, (b) APGD plasma-jet reactor, (c) DBD coaxial-type reactor. (2) The effects of reactor on the ratio of the surface functional groups of the ACs, (a) DBD parallel-plate-type reactor, (b) APGD plasma-jet reactor, (c) DBD coaxial-type reactor. Legends are the same as in Fig. 3 (1).

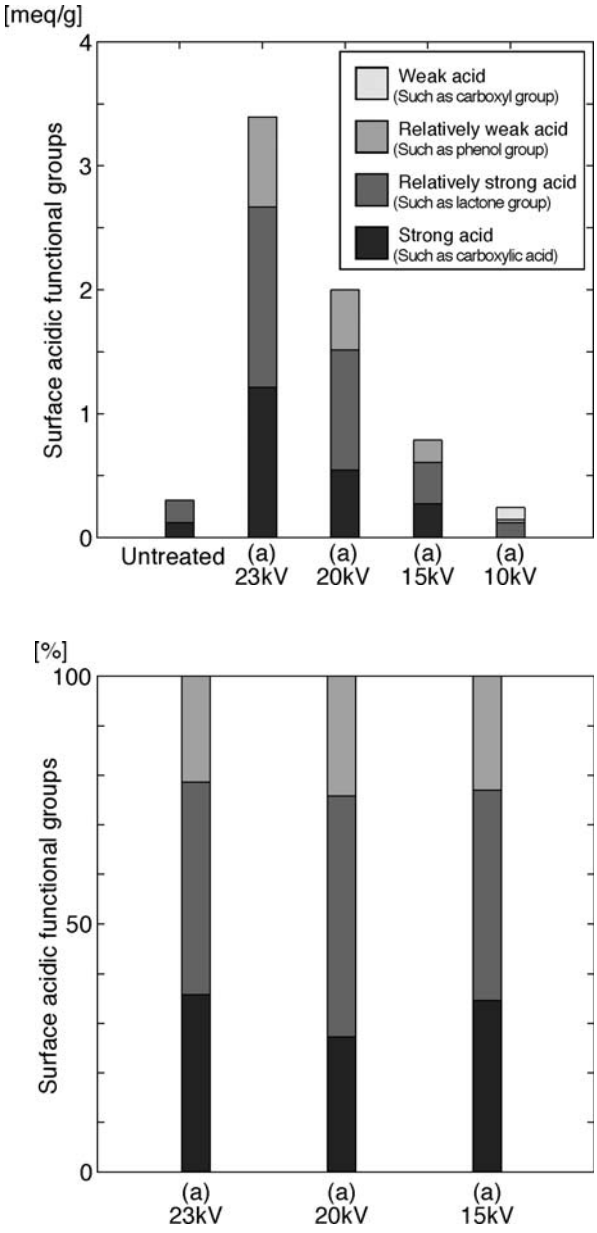

Figure 4 (1) The effects of applied voltage on the content of surface functional groups of the ACs treated in reactor (a); (2) The effects of applied voltage in the ratio of surface functional groups of the ACs treated in reactor (a) Legends are the same as in Fig. 4 (1).

11.3.2
Surface Morphology

Figure 5 shows the SEM images of the AC samples. The surface of the plasma-treated sample seems to be smoother. The particle size is smaller in (b) and (c) compared with (a) from visual observation, and the yield was lower in (b) and (c) compared with (a) from Table 1. This denotes the samples treated by the reactor (b) or (c) were attacked heavily and burned by the plasma. This would be because the discharge using high frequency increased the temperature of AC, while the discharge at low frequency has enough time to cool down after a streamer attacked the surface.

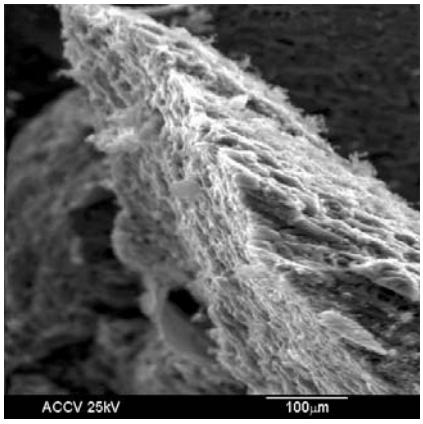

Untreated

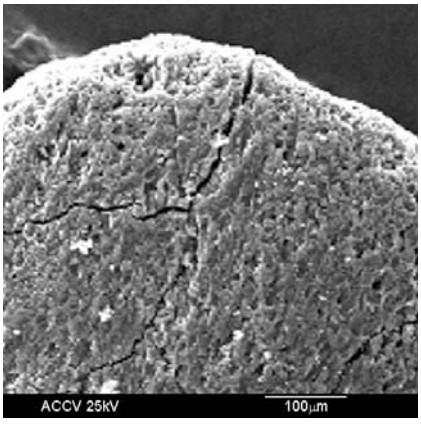

(a)

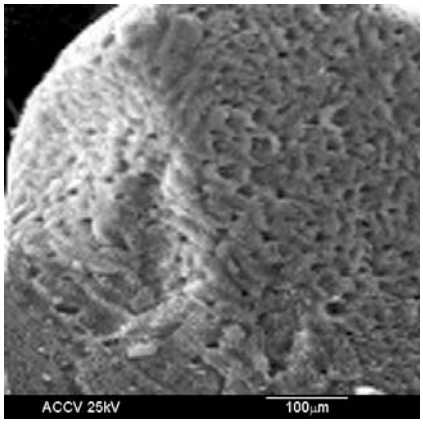

(b)

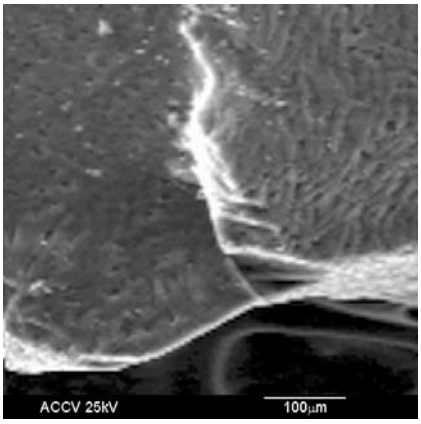

(c)

Figure 5 SEM images of ACs, (a) DBD parallel-plate-type reactor at 23 kV, (b) APGD plasma-jet reac/tor, (c) DBD coaxial-type reactor.

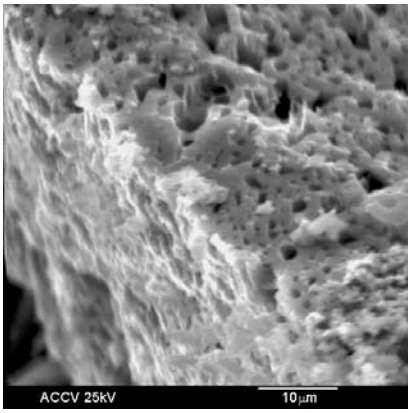

(1)

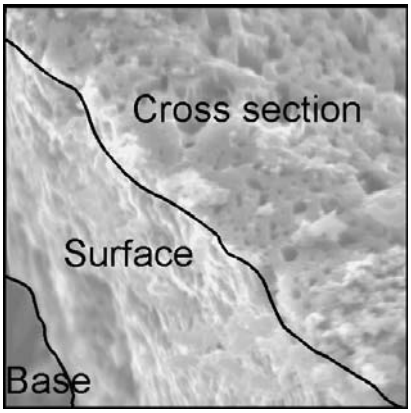

(2)

(3)

Figure 6 SEM and EDS images of the sample treated by (a) at 23 kV after Cu adsorption. (1): SEM image, (2) Boundary of the cross section, (3) EDS Cu mapping.

Figure 6 shows the SEM (Fig. 6 (1)) and EDS (Fig. 6 (3)) images of the sample (a) with an applied voltage of 23 kV. The sample was cut to observe the surface and the cross section. The boundary is shown in Fig. 6 (2). The presence of Cu was observed on the surface and its neighbor. The concentration became lower as the distance from the surface becomes larger and Cu exists approximately 10 μm from the surface. The reason for the penetration is suggested to be that the oxygen ions or radicals generated by the discharge diffuse into the pores of the AC and treat the inside of it. The EDS analysis of the samples treated (b) and (c) showed very low concentrations of Cu on the surface. Therefore, the distribution of Cu of the sample treated by (b) and (c) could not be analyzed.

11.4 Conclusion

The atmospheric nonequilibrium oxygen plasma treatment introduced the functional groups on the surface of granular activated carbon samples. The characterization by the selective neutralization method identified the introduction of acidic functional groups. The concentration was the largest in the sample treated by the DBD parallel-plate type reactor and smallest in the sample treated by the APGD plasma-jet reactor. In addition, the analogy was found between the samples treated in DBD parallel-plate-type and DBD coaxial-type reactors. This suggests that the introduction process of functional groups were affected by the kind of discharge. The yield showed that the burn-off ratio was higher in the sample treated with a high-frequency power supply. The EDS analysis also showed that the plasma treatment introduced acidic functional groups only in the neighborhood of the surface.

Acknowledgement

Financial supports by 'National Institute of Advanced Industrial Science and Technology (AIST)' and 'The 21st Century COE Program (Chemistry Field), Tokyo Institute of Technology' are gratefully acknowledged.

References

[1] J.L. Figueiredo, M.F.R. Pereira, M.M.A. Freitas, J.J.M. Órfão, Carbon, **32**, 1379, (1999)
[2] H. Valdés, M. Sánchez-Polo, J. Rivera-Utrilla, C.A. Zaror, Langmuir, **18**, **2111**, (2002)
[3] Joong S. Noh, J. A. Schwarz, Carbon, **28**, 675, (1990)
[4] S. Kodama, J. Kawasaki, H. Sekiguchi, H. Habaki, Thin Solid Films, **407**, 151, (2002)
[5] K. Tanaka, T. Inomata, M. Kogoma, Plasmas Polym. **4**, 269, (1999)
[6] T. Nozaki, Y. Miyazaki, Y. Unno, K. Okazaki, J. Phys. D: Appl. Phys., **34**, 3383, (2001)
[7] F Massines, G. Gouda, J. Phys. D: Appl. Phys., **31**, 3411, (1998)
[8] H. P. Boehm, Adv. Catal., **16**, 179, (1966)
[9] H. P. Boehm, Carbon, **32**, 759, (1994)

12
Treatment of Flexible Polyethylene with Low-pressure Plasma to Improve its Painting Properties

Asunción Martínez-García, Alejandra Segura-Domingo, Ana Sánchez-Reche, Santiago Gisbert-Soler

Abstract

Low-pressure plasma was selected as a surface treatment to improve the painting properties of elastomeric polyethylene (PE). Several experimental variables in the low-pressure synthetic air plasma treatment were considered: time of the treatment, plasma power and pressure inside the chamber. The durability of the treatment effects was also studied. Contact-angle measurements (water, 25 °C) showed an increase in the wettability of elastomeric PE after treatment with plasma, which corresponds to an increase in the O/C ratio on the treated surface. In fact, different oxygen-containing groups were created on the PE surface. The more intense and longer the plasma treatment, the greater the degree of surface oxidation, up to a certain value. The painting properties of the material were evaluated by joints produced with as-received and treated elastomeric PE and an acrylic paint and using T-peel tests. Peel strength values increased after low-pressure plasma treatment, especially after the first 3 s of treatment with a power of 200 W; and an adhesion failure between the paint and the adhesive tape was obtained. This failure was maintained during four hours after the treatment. For longer treatment times the paint does not adhere to the material, the peel-strength values decrease and the contact angles increase, indicating that the effects of the surface modifications are not maintained.

12.1
Introduction

Elastomeric polyolefins have excellent mechanical properties, low hardness and rigidity. For these reasons, elastomeric polyethylene materials are very suitable to the toy and childcare industry. However, polyethylene exhibits low surface energy and poor adhesion to paints and adhesives [1].

Low-pressure plasma treatment is a well-known method to modify the surface of polymers [2], presenting advantages in contrast to the other chemical treatments, as it does not involve hazardous atmospheres. It is a fast treatment, it is suitable for the treatment of complex geometric samples and it modifies the surface chemistry producing an increase in adhesion properties [3–6]. The addition of pigments to poly-

meric materials during processing is an effective way of coloring plastics, however, in the case of painting different parts of an article, some problems arise when polyolefinic materials are involved. The low surface energy of polyethylene materials makes adhesion of paints, adhesives, inks, etc., difficult. So, the application of a primer is necessary to improve the adhesion of the paint to PE. This primer contains solvents, which are not desirable in the toy industry. Therefore, in this study, we explored low-pressure plasma as an alternative to the solvent-based primers in the painting of elastomeric PE.

However, all the above literature deals with the improved adhesion of thin PE films. Thus, one of the objectives of this study was the improvement in the painting properties of a 4-mm thick elastomeric polyethylene using low-pressure plasma as a surface treatment.

On the other hand, considering that the efficiency of the treatment is a consequence of different experimental parameters [7–9], in this work, the treatment time, the plasma power and the pressure inside the chamber on the elastomeric PE treatment were studied. Also, the durability of the effect of the treatment of the polyethylene surface is another important parameter to be considered.

12.2 Experimental

12.2.1 Materials

An elastomeric polyethylene (PE) supplied by DOW PLASTICS was used in this study. The melt flow index is 5 g/10 min, its Shore A hardnesses is 75 and its density 0.870 g/cm^3 (data supplied by DOW PLASTICS). The PE polymer was received as pellets and molded using a DEMAG Ergotech 110-430h/310V injection machine to obtain test samples of 150 mm length, 60 mm width and 4 mm thickness. The injection molded pieces were cut into test samples of sizes 150×30×4 mm for painting tests.

An acrylic and flexible paint supplied by PINTURAS BLATEM (Torrent, Valencia) was used to perform the T-peel test. The paint was applied on the treated samples with a brush and dried for three hours in open air to facilitate the evaporation of the solvent. The thickness of the paint layer applied was about 80 µm. Then a polyisoprene-styrene adhesive tape of 30 mm width was applied on the painted samples to evaluate the paint–substrate adhesion. The adhesive tape was applied by pressing it on the substrate using a roller [10] to achieve a suitable joint.

12.2.2 Experimental Techniques

A Tantec Vacuted Plasma System model HV 2000 generator was used to modify the PE. The radiofrequency unit was set at 13 kHz. The PE samples were placed on an

aluminum plate inside the chamber. All the treatments were performed in synthetic air (21 vol% O_2, 79 vol% N_2) supplied by Abelló Linde, S.A. (Barcelona). Before being treated in the plasma, the samples were wiped with acetone and the solvent was evaporated for 30 min. All painting operations were performed within 1–2 min after the plasma treatment to minimise the possibility of surface molecular rearrangement and/or contamination from the atmosphere.

Contact angles on the treated elastomeric PE were measured at 25 °C using a Ramé-Hart 100-0 equipment by placing 4-μl drops of deionized and doubly distilled water on the surface. The samples were placed into a chamber saturated with water vapor at 25 °C, at least 15 min before the drop was placed on the elastomeric PE surface.

The failed surfaces obtained after peel tests were analysed using a Nicolet FTIR 550 spectrometer. To avoid deep penetration of the IR radiation into the sample, the attenuated total multiple reflection method was employed using a KRS-5 (thallium bromo-iodide) crystal. The incident angle of the IR beam was 45°. The resolution was 4 cm^{-1}.

XPS analysis was performed using a Vacuum Generator (VG) Scientific Microtech Multilab spectrometer, employing a MgK_α radiation ($h\nu$= 1253.6 eV). X-ray source operated at 15 keV and 300 W. The pressure inside the analysis chamber was held below 5×10^{-7} torr (6.6×10^{-5} Pa) during the course of the analysis. The dimension of the analysis areas on the samples was 1×3 mm. The spectrometer was calibrated for the $4f_{7/2}$ photopeak of gold at 83.8 eV and the $2p_{3/2}$ photopeak of copper at 932.4 eV. Binding energies of all photopeaks were referenced to the C1s band position for C–C and C–H species at 285.0 eV.

Scanning electron microscopy (SEM) micrographs of the as-received and plasma-treated PE were obtained in a JEOL SEM J840 instrument using an electron beam energy of 20 kV.

The paint–substrate adhesion was evaluated from T-peel tests on treated elastomeric PE/acrylic paint joints (72 h after bond formation) using an Instron 6025 instrument; a crosshead speed of 0.1 m/min was used. Five replicates for each experimental variable were obtained.

12.3 Results and Discussion

12.3.1 Effect of Treatment Time

The elastomeric PE was treated with synthetic-air plasma from 1 to 120 s, at a plasma power of 500 W and a pressure inside the chamber of 10 mbar. Advancing and receding contact angles were measured. The advancing contact-angle values were higher than the receding ones and always with the same differences between them (4–5 degrees) were obtained for the plasma-treated PE samples, so the advancing contact-angle values were used in this study to monitor the variations in wett-

ability in all treated PE as a function of the different parameters. The advancing contact-angle value (Fig. 1) of as-received PE is high (92°) and decreases considerably (to 55°) after 3 s of treatment due to the formation of polar groups on the PE surface after the treatment [11]. From 3 to 50 s of treatment the contact angles remain similar. Therefore, the treatment increases the wettability of elastomeric PE.

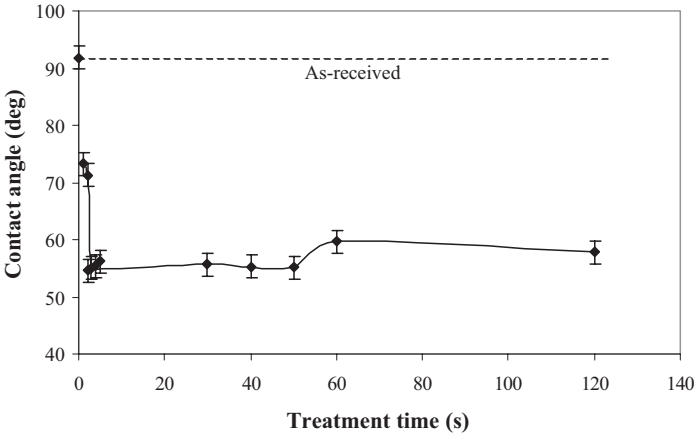

Figure 1 Advancing contact angles (water, 25° C) of low-pressure plasma-treated elastomeric PE as a function of the time of the treatment. Plasma power = 500 W; pressure inside the chamber = 10 mbar.

XPS analysis (Table 1) indicates that an oxidation of the surface was produced within a few seconds (1–3 s) of treatment, as a decrease in carbon and an increase in oxygen and in the O/C ratio is produced due to the introduction of oxygenated moieties on the PE surface [12]. Prolonged exposure (50 s) did not increase either the amount of oxygen-containing moieties on the PE surface or the O/C ratio. In previous studies [13,14] the plasma treatment using air produces an increase in the nitrogen content; as shown in Table 1, this content is higher with long treatment times.

Table 1 Elemental composition (at%) of as-received and some low-pressure plasma-treated elastomeric PE as a function of the treatment time. (500 W, 10 mbar)

Element	As-received (at%)	1 s (at%)	3 s (at%)	50 s (at%)
C	92.22	86.70	85.95	86.16
O	5.73	11.92	12.67	12.29
N	0.14	0.37	0.34	0.81
Si	1.73	1.02	1.04	0.73
O/C	0.062	0.137	0.147	0.143

According to the curve fitting of the C1s band (Fig. 2), the plasma treatment creates new –C=O and –COO moieties [13,15] (bands at 288.0 eV and 289.3 eV, respectively) and the bands of polyethylene are also modified: a decrease in the band at 285 eV is observed due probably to the cracking of C–C, C–H bonds. Curve fits of the C1s and O2p bands (Tables 2 and 3) show the marked increase in bands associated to C–O groups (286.9 eV), C–CO and C-N groups (285.7 eV) and carboxylic groups (533.6 eV) on the plasma-treated elastomeric PE. All these modifications did not change with the treatment time although they are more pronounced at a short treatment time. Therefore, the low-pressure plasma treatment introduces new oxygen-containing groups on the elastomeric PE surface, which are responsible for the decrease in contact-angle values (Fig. 1). On the other hand, some nitrogen moieties are also created on the plasma-treated PE surface as a consequence of extended oxidation in synthetic air, in agreement with previous results for other polymers [13,14].

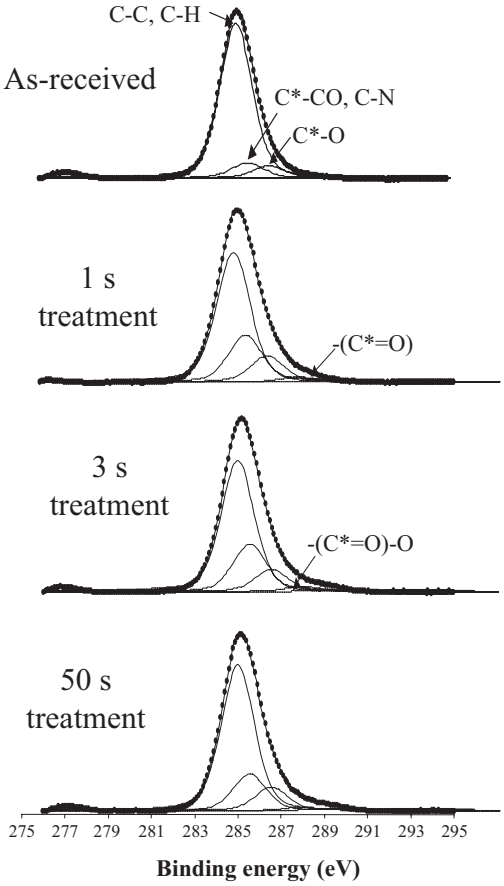

Figure 2 Carbon 1s XPS spectra of as-received and low-pressure plasma-treated elastomeric PE at different time of the treatment. Plasma power = 500 W; pressure inside the chamber = 10 mbar.

Table 2 Relative integrated intensities of XPS C1s component bands of as-received and low-pressure plasma-treated elastomeric PE. (500 W, 10 mbar)

Group	Binding energy (eV)	As-received (%)	1 s (%)	3 s (%)	50 s (%)
C–H, C–C	285	85.295	62.541	63.409	68.985
C*–CO, C–N	285.7	8.170	22.717	23.030	17.245
C*–O	286.9	6.535	12.423	10.584	11.074
– (C*=O),NH–CO	288	–	2.319	2.258	1.797
– (C*=O)-O	289.3	–	–	0.719	0.900

Table 3 Relative integrated intensities of XPS O2p component bands of as-received and low-pressure plasma-treated elastomeric PE. (500 W, 10 mbar)

Group	Binding energy (eV)	As-received (%)	1 s (%)	3 s (%)	50 s (%)
– (C=O*)–O	532.5	79.123	68.085	65.18	59.491
– (C=O) –O*	533.6	20.877	31.915	34.82	40.509

SEM micrographs (Fig. 3) show that surface ablation [15,16] is favored by increasing the time of the plasma treatment, which leads to the removal of the outermost polymer surface and obtaining rather smooth and clean surface.

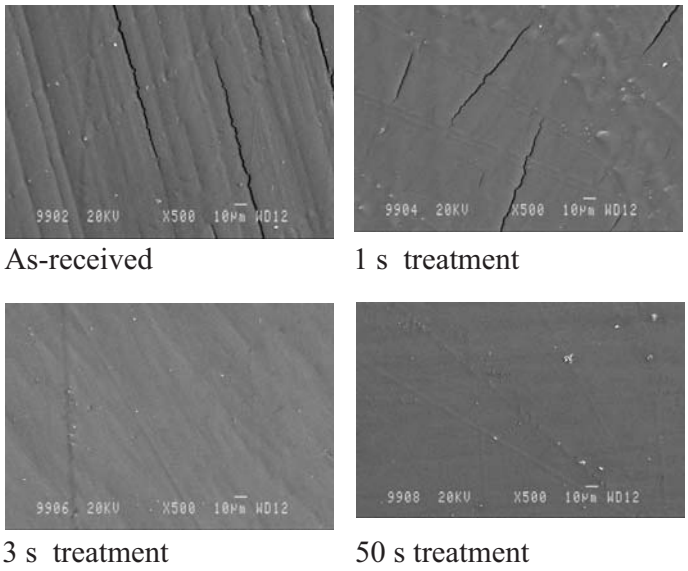

Figure 3 SEM micrographs of as-received and low-pressure plasma-treated elastomeric PE as a function of the time of the treatment. Plasma power = 500 W; pressure inside the chamber = 10 mbar.

T-peel-strength values of paint–substrate joints (Fig. 4) indicate that the as-received elastomeric PE has a low adhesion, according to their high contact angle (92°), and so, low surface energy. Plasma treatment for 3 s increases the peel-strength values from 130 N/m (as-received material) to 260 N/m. This value decreases until 30 s treatment and remains similar (about 200 N/m) for longer treatment times (Fig. 4). This decrease could be produced by a surface crosslinking, which can act as a weak boundary layer that makes difficult the adhesion of the paint. The ultraviolet radiation generated in the plasma could produce a crosslinked surface layer [17,18]. However, in all cases the T-peel values are higher that in the as-received material.

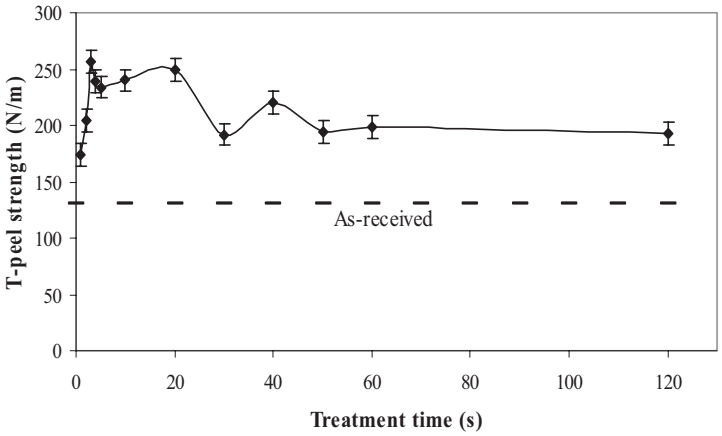

Figure 4 T-peel strength of as-received and low-pressure plasma-treated PE–acrylic paint joints as a function of the treatment time. Plasma power = 500 W; pressure inside the chamber = 10 mbar.

The loci of failure of the paint joints were assessed by characterisation of the failed surfaces obtained after peel tests using ATR-IR spectroscopy. In this study, the S surface corresponds to the failed surface that visually corresponds to the PE substrate and the P surface to that visually corresponding to the paint–adhesive tape part. The ATR-IR spectra of the paint, the adhesive tape and the as-received elastomeric PE are given in Fig. 5.

For the paint joint produced with the as-received PE (Fig. 6 (a)), an adhesional paint–substrate failure was obtained, because the ATR-IR spectrum of the P surface is the same as that of the paint, and the ATR-IR spectrum of the S surface corresponds to the ATR-IR spectrum of PE. This indicates that the paint is not adhered to the elastomeric PE.

The loci of failure of the plasma treated PE/paint joints are different (with treatment times ≥ 3 s). Whereas the ATR-IR spectrum of S surface (Fig. 6 (b)) mainly corresponds to that of paint, the ATR-IR spectrum of the P surface corresponds to the adhesive tape, indicating that an adhesional failure between the paint and the adhesive tape was obtained. Therefore, during peel test the paint remained on the elasto-

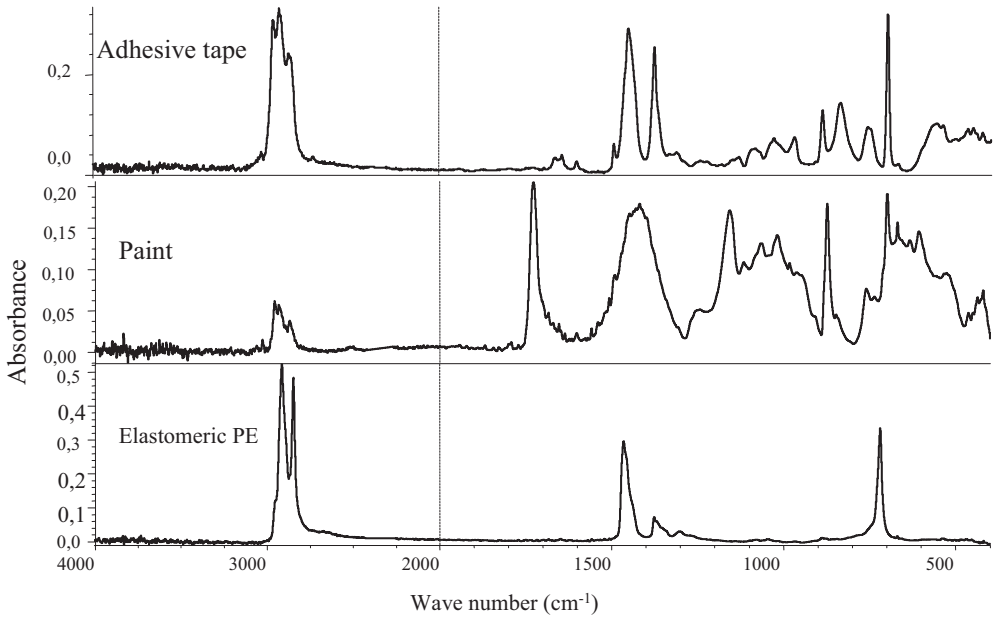

Figure 5 ATR-IR spectra of as-received elastomeric PE, adhesive tape and acrylic paint.

meric PE, achieving the objective of the present work. This failure is the same as the time of the treatment increases. Consequently, from the obtained results, we can conclude that 3 s of plasma treatment are enough to modify the surface of the elastomeric PE and improve its painting properties.

12.3.2 Effect of Plasma Power

Advancing contact angles of treated samples (Table 4) show an important decrease with the treatment at plasma power of 200 W or higher (59°) in comparison to the as-received PE (92°) and the values remain similar up to 700 W. The improved wettability of elastomeric PE treated with plasma can be ascribed to the introduction of both, oxygen- and nitrogen-containing groups to the PE surface, assessed by XPS analysis (Table 5). The increase in the plasma power from 200 to 700 W produces a slight increase in the O/C ratio (from 0.075 to 0.147) but somewhat higher increase in oxygenated functionalities. The increase in the plasma power further enhances the creation of oxidised species, mainly C=O (binding energy= 288.0 eV), C–O (286,9eV), C–CO and C–N (285,7 eV) and R–COO^- (289.2 eV). Higher T-peel-strength values (Table 4) of treated elastomeric PE/paint joints are obtained for plasma power from 200 to 700 W. A paint-adhesive tape adhesive failure is obtained in these cases. Therefore, the adhesion of the paint to the PE substrate is already effective with the treatment at plasma power of 200 W or higher.

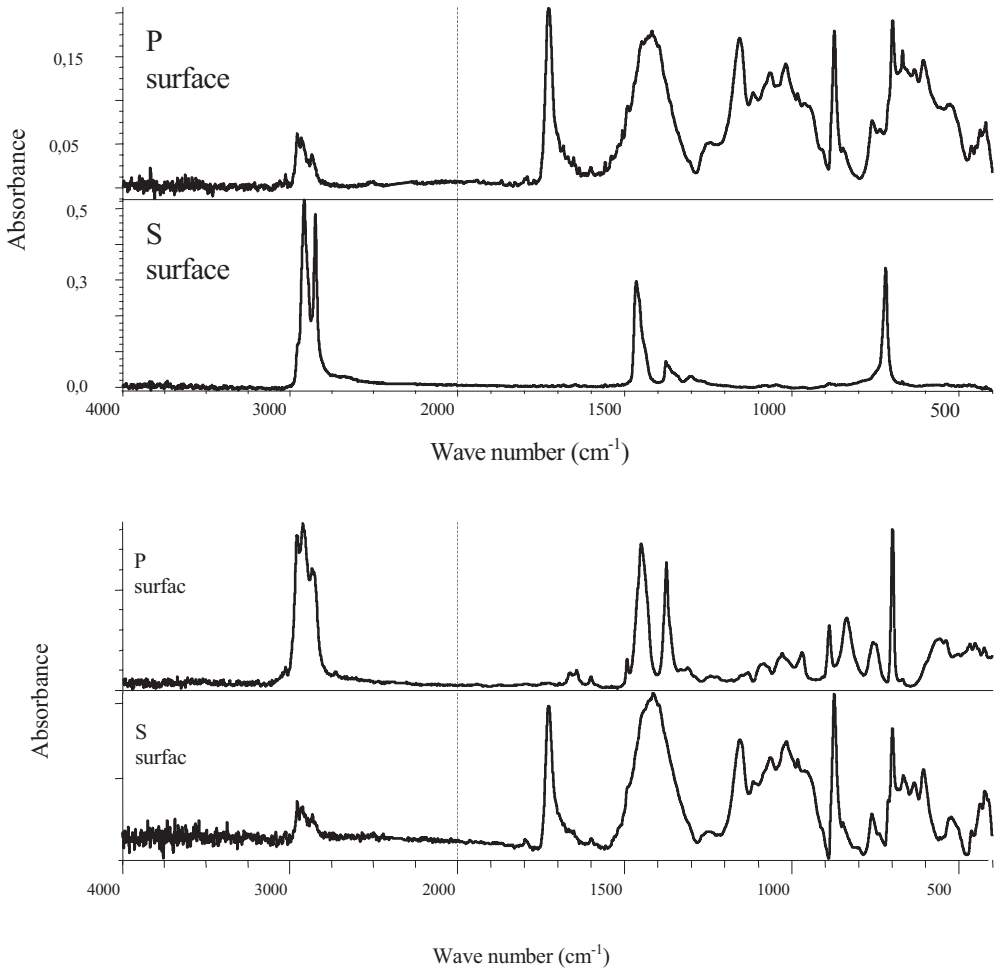

Figure 6 ATR-IR spectra of failed surfaces after peel tests on: (a) As-received elastomeric PE/acrylic paint joint; (b) low-pressure plasma-treated (3 s) elastomeric PE–acrylic paint joint; P surface = Failed surface that visually corresponds to the paint; S surface = Failed surface that visually corresponds to the elastomeric PE.

Table 4 Contact angles (water, 25° C) on as-received and low-pressure plasma-treated elastomeric PE; T-peel strength and locus of failure of low-pressure plasma-treated elastomeric PE/paint joints as a function of the plasma power. (3 s, 10 mbar)

Plasma power (W)	Contact angle (degrees)	T-peel strength (N/m)	Failure
As-received	92 ± 2	130 ± 10	Aa-p
100	90 ± 2	192 ± 11	Aa-p
200	59 ± 2	382 ± 8	Ap-s
300	64 ± 2	358 ± 12	Ap-s
500	55 ± 2	325 ± 10	Ap-s
700	59 ± 2	406 ± 9	Ap-s

Aa-p: Adhesive failure adhesive tape–paint, Ap-s: paint–elastomeric PE substrate

Table 5 Relative integrated intensities of XPS C1s component bands of as-received and plasma treated elastomeric PE as a function of plasma power. (3 s, 10 mbar).

Group	Binding energy (eV)	As-received (%)	100 W (%)	200 W (%)	500 W (%)
C–H, C–C	285	85.295	83.621	71.260	63.409
C*–CO, C–N	285.7	8.170	13.427	18.974	23.03
C*–O	286.9	6.535	2.952	9.701	10.584
– (C*=O), NH–CO	288	–	–	0.064	2.258
– (C*=O)–O	289.3	–	–	–	0.719

12.3.3

Effect of the Pressure inside the Chamber

Although a minimum value of the contact-angle value of the treated PE (Table 6) was obtained at a pressure of 7 mbar (55°), the chemical compositions after the treatment were similar with the treatment at different pressures (not shown here). Similarly, the T-peel-strength values of plasma-treated elastomeric PE (Table 6) were about 230–250 N/m for the different pressures of the gas, not showing marked differences. In all cases, the loci of failure of the adhesive joints produced with elastomeric PE treated with different pressure of the gas were the same (Table 6), i.e. a paint–adhesive tape adhesive failure was obtained. Therefore, the pressure into the chamber (from 7 to 10 mbar) did not greatly affect the adhesion of the paint to the elastomeric PE substrate.

Table 6 Contact angles of water at 25° C on as-received and low-pressure plasma-treated elastomeric PE; T-peel strength and locus of failure of low-pressure plasma-treated elastomeric PE/paint joints as a function of the pressure inside the chamber. (3 s, power of 200 W).

Pressure inside the chamber (mbar)	Contact angle (degrees)	T-peel strength (N/m)	Failure
As-received	92 ± 2	130 ± 10	Aa-p
7	55 ± 2	239 ± 10	Ap-s
10	66 ± 2	253 ± 15	Ap-s
12	69 ±2	220 ± 13	Ap-s

Aa-p: adhesive tape–paint, Ap-s: paint–elastomeric PE substrate

12.3.4 Durability of the Treatment Effect

From an industrial point of view the durability of the plasma treatment is an advance in the production because treated material can be stored until its use. The PE samples were treated at a plasma power of 200 W and 10 mbar of pressure during 3 s, and the paint was applied from 1 min to 10 weeks after the plasma treatment. The treated samples were stored in closed boxes at room conditions.

Figures 7 and 8 show the variation of the contact angle and the T-peel-strength values, respectively, of the plasma-treated elastomeric PE as a function of storage time. The decrease of contact angles value produced by the treatment remains similar from 30 min to 4 weeks (70–75°). From this time the obtained contact-angle values are the same as that of the as-received material, indicating that the surface

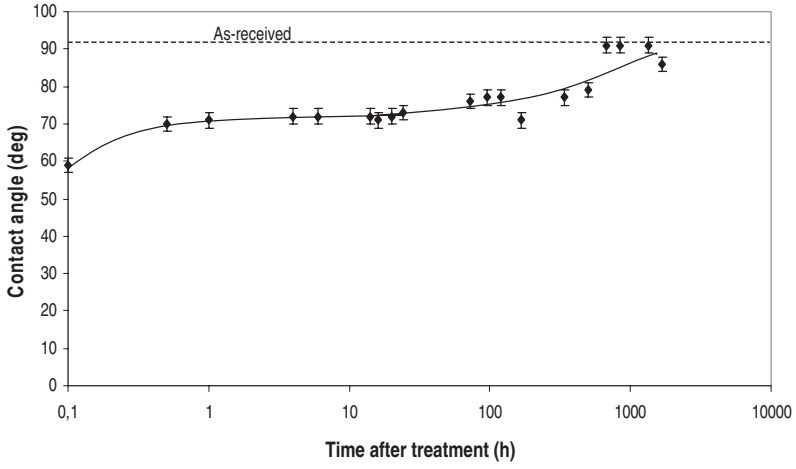

Figure 7 Contact angles (water, 25 °C) of low-pressure plasma-treated elastomeric PE at different time after treatment. The treatment time = 3 s; plasma power = 500 W; pressure inside the chamber = 10 mbar.

modifications were not maintained. The obtained T-peel-strength values (Fig. 8) oscillate between 230–300 N/m from 60 min to 8 weeks. From this time the T-peel values decrease up to the value of the as-received elastomeric PE. Although the effects of the treatment and the T-peel values are maintained for some weeks, from 4 h after the treatment the loci of failure of the plasma-treated PE/paint joints show that an adhesional failure between the paint and the elastomeric PE. Consequently, we can conclude that the modifications of the low-pressure plasma treatment of the elastomeric PE surface to improve its painting are effective from 1 min to 4 h after the treatment.

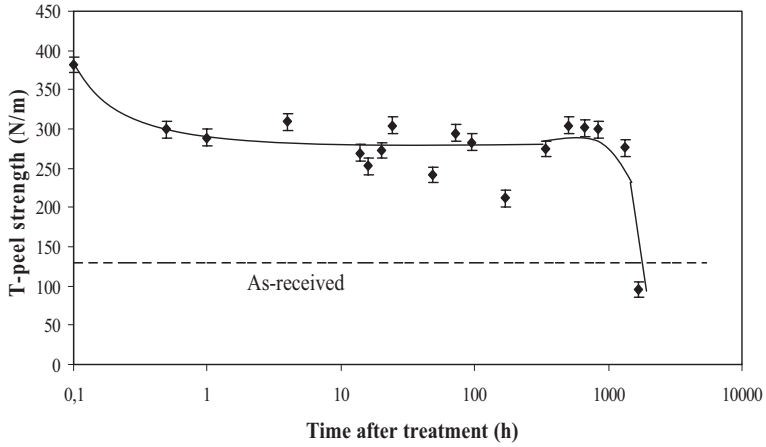

Figure 8 T-peel strength of as-received and low-pressure plasma-treated PE–acrylic paint joints at different time after treatment. The treatment time = 3 s; plasma power = 500 W; pressure inside the chamber = 10 mbar.

12.4 Conclusions

The treatment with low-pressure plasma using synthetic air increases the adhesion of an acrylic paint to elastomeric PE due to the physical (surface ablation) and chemical modifications (formation of C=O and $RCOO^-$ moieties). Three seconds of treatment is enough but plasma power values $\geq$ 200 W are needed to improve the painting of elastomeric PE. Treatment times higher than 30 s could produce overtreatment of the surface. All joints produced with these optimal conditions show an adhesion failure of the paint–adhesive tape, indicating that the paint remained on the elastomeric PE, which was the objective of the present work. The surface modifications and the improved painting are maintained with time until 4 h after the application of the plasma treatment.

Acknowledgements

The authors thank Prof. J.M. Martín Martínez from the Adhesion and Adhesives Laboratory of the University of Alicante for his help in XPS analysis. Financial support by MICYT (project CICYT MAT2000-1188) is also acknowledged.

References

[1] A. Zisman, *Ing. Eng Chem*, **50**(10), 19 (1963).
[2] M.J. Owen, P.J. Smith, *Polymer Surface Modification: Relevance to Adhesion*. Ed. K.L. Mittal, pp.3–15, Utrecht, The Netherlands (1996).
[3] M.D. Landete, J.A. Martínez, M.A. Rodríguez, J.A. de Saja, J.M. Martín Martínez, *J. Adhes. Sci. Technol.*, **16**, 1073–1101 (2002).
[4] S. Sapieha, J. Cerny, J.E. Klemberg-Sapieha, L. Martinu, *J. Adhes.*, **42**, 91–102 (1993).
[5] O.D. Greewood, R.D. Boyd, J. Hopkins, J.P.S. Badyal, *Polymer Surface Modification: Relevance to Adhesion*, 17–32, Ed. K.L. Mittal (1995).
[6] H.F. Webster, J.P. Whightman, *J. Adhes. Sci. Technol.*, **5**, no1, 93–106 (1991).
[7] T M. Charbonnier, M. Romand, M. Alami, Tran Minh Duc, *Polymer Surface Modification: Relevance to Adhesion*, Ed. K.L. Mittal, Vol.2 pp.3–27, Utrecht, The Netherlands (2000).
[8] Q. Quoc Toan Le, J.J. Pireaux, R. Caudano, *J. Adhes. Sci. Technol.*, **11**, 735, (1997).
[9] A. Nihlstrand, T. Hjertberg, H.P. Schreiber, J.E. Klemberg-Sapieha, *J. Adhes. Sci. Technol.*, **10**, 651, (1996).
[10] M.D. Landete, J.M. Martín-Martínez, A. Martínez-García, *II Jornadas Sobre Adhesivos*. University of Alicante, (2001).
[11] J.W. Chin, J.P. Wightman, *Surface Characterization of Plasma-modified*. ■, Ed. H.M. Clearfield, Blacksburg, Virginia, (1991).
[12] F. Arranz, *Revista de Plásticos Modernos*, **410**, 221 (1990).
[13] E.M. Liston, L. Martinu, M.R. Wertheimer, *J. Adhes. Sci. Technol.*, **7**, No.10, 1091–1127, (1993).
[14] R. Foerch, G. Kill, M.J. Walzak, *J. Adhes. Sci. Technol.*, **7**, No.10, 1077–1089, (1993).
[15] C.M. Cepeda-Jiménez, PhD, Alicante (2001).
[16] M. Morra, E. Ochiello, F. Garbassi, *J. Adhes. Sci. Technol.*, 7, 1051 (1993).
[17] A.K. Taraija, G.A. Orchard, I.M. Ward, *Plastics, Rubber Composites Processing Applications*, **19**, 273, (1993).
[18] A.V. Popoola, *J. Appl. Polym. Sci.*, **49**, 2115, (1993).

13
Surface Modification of PVDF by Microwave Plasma Treatment for Electroless Metallization

Mihaela Pascu, Dominique Debarnot, S. Durand, Fabienne Poncin-Epaillard

Abstract

Piezoelectric and nonpiezoelectric films of polyvinylidene fluoride (PVDF) have been treated in a microwave nitrogen and hydrogen plasma. Plasma parameters, e.g. ratio between N_2 and H_2, plasma power, gas flow rate, and the distance between the sample and the plasma have been varied in order to establish the treatment parameters that constitute a good compromise between an optimum functionalization and a minimum degradation. Under this treatment, the surface properties of PVDF have been modified in a controlled manner, allowing its metallization, necessary in a wide range of applications, without significantly changing its bulk properties.

13.1
Introduction

Surface modification, especially metallization, of fluoropolymers is of a particular interest, as these polymeric substrates are one of the most important families of engineering polymers, well known for their physical and chemical inertness [1]. Fluoropolymers are characterized by a small surface energy, which does not allow an adequate adhesion with a metal layer. This is why activation of polymer surfaces prior to metallization is absolutely necessary [2]. This activation process allows the polymer surface to become hydrophilic, in order to be well wet by an electrolessplating solution [3, 4]. Gas-plasma treatment under various glow-discharge conditions was extensively used for this type of surface modification of fluoropolymers [5]. To deposit copper, it was proved that the treatment by N_2, NH_3 or O_2 plasmas increased the reactivity of polymers [6–8]. Polar groups introduced by plasma treatment on the film surface favor the reaction of copper to form a copper–nitrogen–carbon complex in the interface region [9]. Different mixtures of N_2 and H_2, which are more environmentally friendly and easier to handle in industry than ammonia, were studied in order to improve the adhesion of copper onto fluoropolymers. Low-temperature plasmas of nitrogen/hydrogen mixtures contain NH_x gaseous precursors that can induce the formation of amino groups at the surface. For example, using a N_2/H_2 plasma for treating polypropylene (PP) surface, a signifi-

cant increase of the amino groups density was obtained (from 3.1 NH_2 sites/nm^2 for N_2 plasma treated PP, to 6.4 NH_2 sites/nm^2 for PP treated in an 1:2 mixture of N_2/H_2) [10]. Indeed, in the case of the adhesion improvement of copper on fluoropolymers, polytetrafluoroethylene (PTFE) and PVDF, for microelectronics and optical applications [11], the efficiency of N_2/H_2 plasmas was proved compared to that of NH_3. However, in the case of pure hydrogen, the adhesion of copper to hydrogen-plasma-treated fluoropolymers was very poor, indicating the important role of NH_x radicals [12].

An over-treatment of a polymer surface, leading to a high functional groups density and a weak boundary layer formation, is not always a good surface modification for electrical insulators. This is why the choice of the remote plasma as a pretreatment method for obtaining a Cu/fluoropolymer composite is often used [13].

In this study, piezoelectric and nonpiezoelectric polyvinylidene fluoride (PVDF) films have been treated in a nitrogen microwave plasma, under different treatment conditions, in order to modify its surface properties, without significantly changing the bulk ones. After applying the plasma treatment, PVDF surfaces have been covered with a copper layer, using an electrolessplating procedure, and the area of adhesion has been evaluated.

13.2 Materials and Methods

Nonpiezoelectric films of polyvinylidene fluoride (PVDF) (0.25 mm in thickness) have been purchased from Goodfellow, England. This is a white, semicrystalline, semiopaque and fluorinated polymer. Its density is 1.76 g/cm^3 and its upper working temperature ranges between 135 and 150 °C. Films of piezoelectric polyvinylidene fluoride (Goodfellow, England), with a thickness of 0.025 mm and a monoaxial orientation have also been studied.

PVDF films have been treated in a microwave nitrogen plasma (the gas flow: $D = 10$ sccm), for different conditions. Treatment power (P) was varied between 20 and 80 W, the distance between the sample and the surfatron (d) was between 2.5 and 30 cm, and the exposure time (t) between 30 and 300 s. PVDF surfaces have been also exposed to a mixture of N_2 and H_2 plasma, the ratio between these gases being: 75/25, 50/50, 25/75, and 0/100 vol%.

The precise plasma treatment of polymer films is given in our previous publication [10].

Modification of the surface and bulk properties of PVDF has been followed by contact-angle and weight-loss measurements, XPS, UV spectroscopy, and wide-angle X-ray diffraction. Subsequent surface metallization was realized by an electrolessplating procedure.

Contact angles between three pure liquids and the polymer surfaces have been determined by the sessile-drop method, at 20 °C, using a RAME-HART goniometer of 100-00 type, equipped with a 23× telescope. Young's complete equation has been used in order to determine the components of the free surface energy [14]. To deter-

mine the aging [15], contact angles and the components of the free surface energy have been evaluated for 1, 3, and 7 days, respectively, in standard conditions.

XPS spectra were obtained by using an LHS12 LEYBOLD spectrometer from Nantes University-CNRS, with a MgK_α X-ray source, with a take-off angle of 90°.

Surface amino groups titration has been followed by UV spectroscopy [10]. Immediately after the treatment, the PVDF-treated samples were dipped into a 10-ml solution of reagent (Ponceau 2R, acidified with 0.1 N HCl solution; concentration in water: 2×10^{-6} mol · l^{-1}). After degassing, the solution was heated at 70 °C, for 12 h, while stirring. Then, a back-titration of the solution was made on a UNICAM UV-Vis spectrometer. The results correspond to a number of sites per unit of geometric area.

Wide-angle X-ray diffraction: Crystallinity characteristics of the untreated and plasma-treated PVDF were determined by means of X-ray diffraction, carried out on a generator with rotating angle and CuK_α filtered radiation, $\lambda = 1.5418$ Å.

From the obtained X-ray patterns, crystallite size (L) was evaluated using Scherrer's equation [16]:

$$b = k \cdot \lambda / L \cdot \cos\theta \tag{1}$$

where: b is the full width at half maxima (FWHM, in radians); λ the wavelength of the X-ray beam (in Å); L the crystallite size (in Å); k a constant, which varies from 0.89 to 1.39, but for most cases it is close to 1 [17]. In their studies, Virk et al. [18] chose a value of 0.9 for this constant corresponding to PVDF.

The crystallinity degree has been evaluated using the intensity of the diffraction peak corresponding to a $2\theta = 20°$ [19].

The electrolessplating consisted in a metallization procedure by colloidal adsorption [20]. The following steps were applied before the metallization:

* *surface activation*, obtained by the immersion of the polymer surface in a mixed colloidal solution ($PdCl_2$ and $SnCl_2.2H_2O$ in a chlorhydric environment), at 2 different temperatures (20 °C, 40 °C).

* *acceleration*, by the immersion of the activated substrate in HCl 1M.

Palladium particles, which act as catalysts for the reduction reactions from Cu ions to Cu metal, are thus attached to the polymer surface [21]. The polymer surfaces containing a Pd nucleus have been immersed in the plating solution [8]: $CuSO_4.5H_2O$ (7 g/l), potassium sodium tartrate (25 g/l), NaOH (4 g/l), and formaldehyde (9.3 g/l).

Evaluation of the thermodynamic work of adhesion: Preliminary investigations on PVDF metallization have been achieved by the measure of thermodynamic work of adhesion (W_a), using the harmonic (Eq. (2)) and the geometric (Eq. (3)) mean equations [22]:

$$W_a = 4\left(\frac{\gamma_1^d \cdot \gamma_2^d}{\gamma_1^d \cdot \gamma_2^d} + \frac{\gamma_1^p \cdot \gamma_2^p}{\gamma_1^p \cdot \gamma_2^p}\right) \tag{2}$$

$$W_a = \left(\sqrt{\gamma_1^d \cdot \gamma_2^d + \gamma_1^p \cdot \gamma_2^p}\right) \tag{3}$$

where γ^d and γ^p represent the dispersive and the polar components, respectively, of the free surface energy. Indexes 1 and 2 stand for the values corresponding to the polymeric substrate and the metal layer, respectively.

For qualitative comparisons between the studied samples, a normalized scotch test was also performed, at room temperature, for untreated and plasma-exposed PVDF surfaces, in order to obtain some information on the adherence of the copper layer to the polymer surface.

Quasistatic piezoelectric analysis has been carried out by loading a mass of 150 g, periodically, to the sample, using a procedure described by Neugschwandtner et al. [23].

13.3 Results and Discussion

13.3.1 Contact-Angle and Weight-Loss Measurements

Whatever the applied treatment power and the exposure time, an important increase in the hydrophilicity of the PVDF surfaces was obtained. This behavior is evidenced by the significant decrease of the advancing and receding water contact angles in respect with the untreated sample (Fig. 1) as was also observed by other authors [24].

After plasma exposure, water contact-angle hysteresis increases when compared with the pristine PVDF (Fig. 2), indicating the obtainment of a significant roughness for the treated surface [25, 26], but also a possible chemical heterogeneity of the surface. An increase in the microroughness could be a sign for the obtainment of a better adherence of the surface with a metal layer [28]. Besides, the important hysteresis

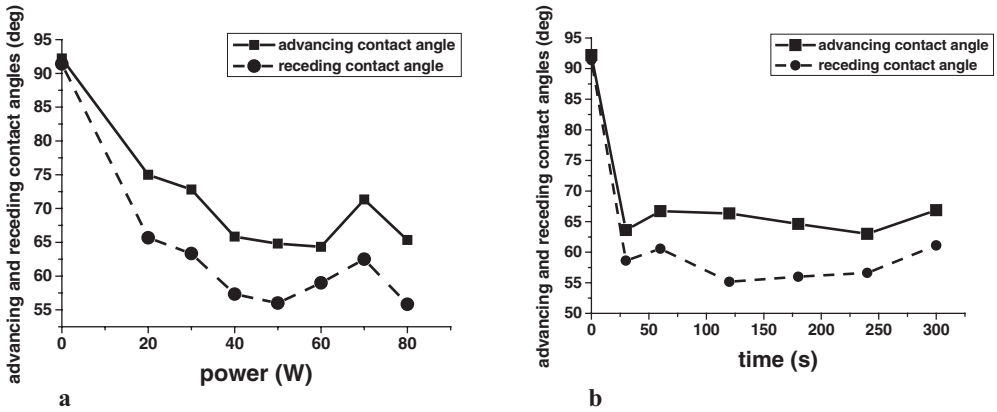

Figure 1 Water advancing and receding contact angles vs the discharge power and the treatment time for N_2 plasma treated PVDF; (a) $d = 15$ cm, $t = 120$ s; (b) $P = 50$ W, $d = 10$ cm.

of the water contact angle in the case of ammonia-plasma-treated PTFE is also explained by Badey et al. [27] by the fact that, in contact with water, nitrogen and oxygen containing groups reorient to minimize the interfacial energy, a very low receding water contact angle being measured.

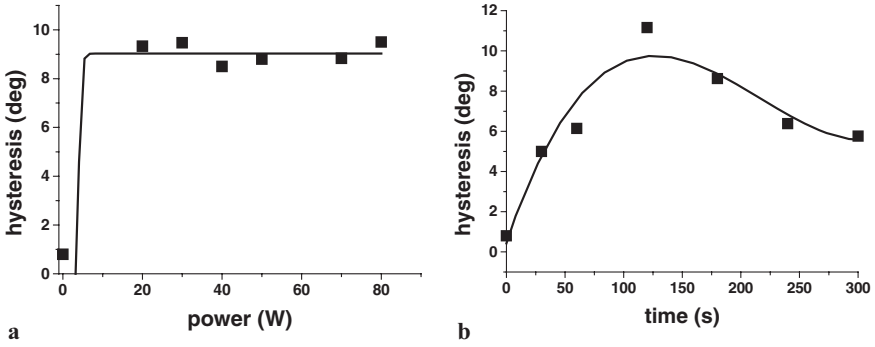

Figure 2 Water contact-angle hysteresis vs the discharge power and the treatment time for PVDF, N_2 plasma treated; (a) $d = 15$ cm, $t = 120$ s; (b) $P = 50$ W, $d = 10$ cm.

It is well known [25] that N_2 or NH_3 plasma treatments give rise to N-containing functionalities, such as: amine ($–NH_2$), imine (–CH=NH), nitrile ($–C\equiv N$) on polymer surfaces, as well as oxygen–containing groups, such as amides ($–CONH_2$), due to postdischarge atmospheric oxidation. This fact is also evidenced in our study, the increase of the acid-base component of the free surface energy with the discharge power and the treatment time being obvious (Figs. 3. (a) and (b)). This increase takes place up to 50 W, for higher treatment powers, the acid-base component remaining almost constant (Fig. 3 (a)).

As the polymer-surface functionalization under plasma exposure is a very rapid phenomenon that, generally, occurs during a period less than 1 min [29], the acid-base component of the free surface energy significantly increases during the first 30 s, after this period, its value remains almost constant for the entire period of plasma exposure (Fig. 3 (b)).

For a given power, treatment time and gaseous flow, the acid-base component decreases with the sample–surfatron distance (Fig. 3 (c)). This behavior evidences that, in the case of a polymer sample treated far enough from the direct plasma, the influence of the charged particles (electrons, ions) is cancelled [27], and radicals alone should be predominant as active species for the surface modification [30]. The density of the active species responsible for the polymer-surface degradation constantly decreases with increasing distance between the sample and the excitation source [31].

Taking into account also the weight losses results (Fig. 4), it could be concluded that the optimum treatment conditions that constitute a good compromise between an optimum functionalization and a minimum degradation for N_2-plasma-treated PVDF are: $P = 50$ W, $t = 60$ s, $d = 10$ cm.

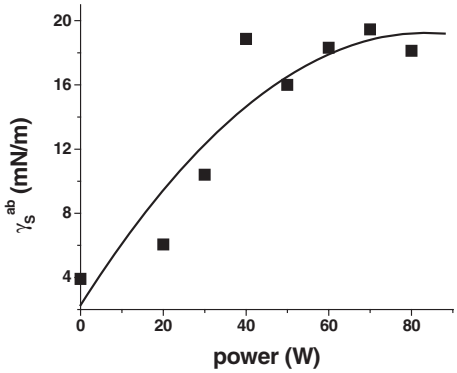

a

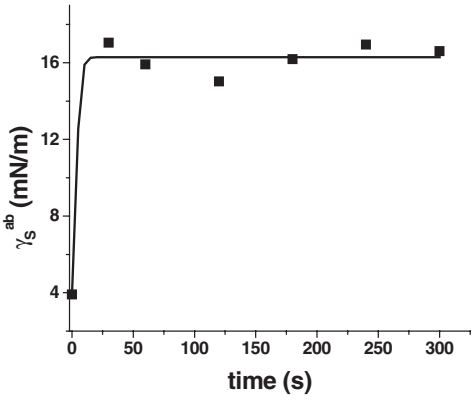

b

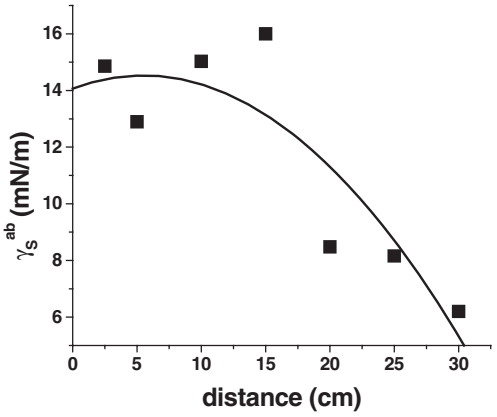

c

Figure 3 Acid-base component of the free surface energy for PVDF, N_2 plasma treated, vs: (a) the discharge power ($d = 15$ cm, $t = 120$ s); (b) the treatment time ($P = 50$ W, $d = 10$ cm); (c) the distance between the polymer sample and the surfatron ($P = 50$ W, $t = 120$ s).

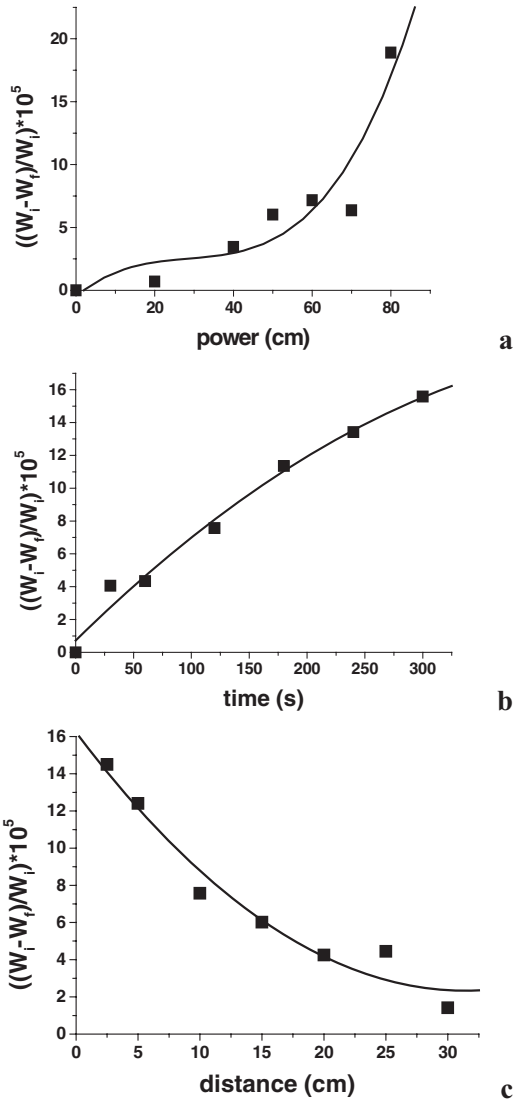

Figure 4 Weight losses for PVDF, N_2 plasma treated, vs: (a) the discharge power ($d = 15$ cm, $t = 120$ s); (b) the treatment time ($P = 50$ W, $d = 10$ cm); (c) the distance between the polymer sample and the surfatron ($P = 50$ W, $t = 120$ s). W_i, W_f – the weight of the polymer sample before and, respectively, after applying the plasma treatment.

On mixing N_2 with H_2, weight losses for treated PVDF generally increase with increasing content of H_2, up to 1:1 N_2/H_2 ratio, after this its value starts to decrease.

As expected, water contact angles decrease with increasing ratio of H_2 until 75% compared to N_2, whatever the applied power to the discharge (30, 50, 70 W), indicating a significant increase of the hydrophilic character of the PVDF surface (Fig. 5). From 75% to 100% H_2, water contact angle increases, possibly due to the fact that

this plasma is less efficient in modifying PVDF hydrophilicity, and that degradation is emphasized with such plasma parameters.

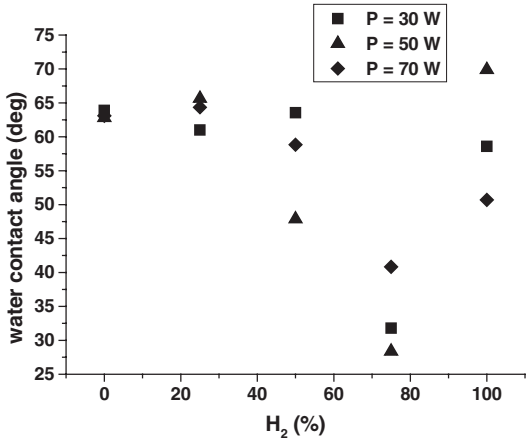

Figure 5 Variation of the water contact angle with H_2 content in N_2/H_2 plasma, for PVDF, plasma treated; the applied powers: 30, 50, 70 W ($t = 60$ s, $d = 10$ cm).

Water contact-angle hysteresis becomes higher, at higher H_2 percentage (Fig. 6). This behavior indicates the obtainment of a pronounced roughened character for PVDF surfaces as the H_2/N_2 ratio is increased.

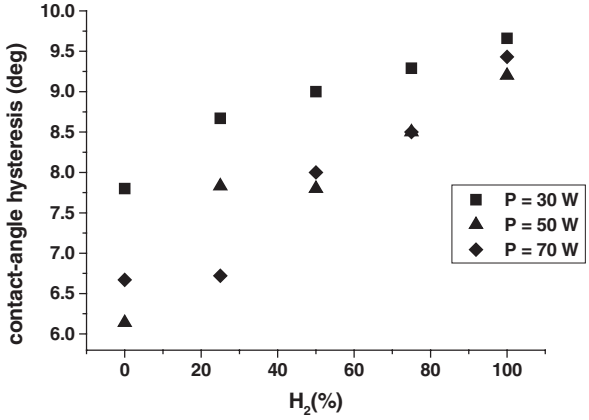

Figure 6 Variation of the water contact-angle hysteresis for treated PVDF surfaces vs H_2/N_2 ratio, for different applied powers ($t = 60$ s, $d = 10$ cm).

Components of the free surface energy are presented in Fig. 7. While the Lifshitz–van der Waals component presents similar values, whatever the treatment conditions, the other components of the free surface energy depend on the applied

treatment. Generally, the electron-acceptor parameter (γ_S^+) decreases with increasing H_2/N_2 ratio (Fig. 7 (a)), while – under the same conditions – the electron-donor parameter (γ_S^-) increases (Fig. 7 (b)). Variation of these two components (γ_S^+ and γ_S^-) determines the variation of the acid-base component (Fig. 7 (c)). For an applied power of 50 W, γ_S^S has a minimum value of 13.13 mN/m for a 1:1 N_2/H_2 ratio, possibly due to the important degradation of the polymer surface, obtained under these conditions; for higher ratios, its values increase with increasing H_2 content in the gaseous mixture. For $P = 30$ and 70 W, γ_S^S attains a maximum value for a 1:2 ratio between N_2 and H_2. The increase of the acid-base component of the free surface energy under N_2/H_2 plasma treatment when compared to the pristine sample

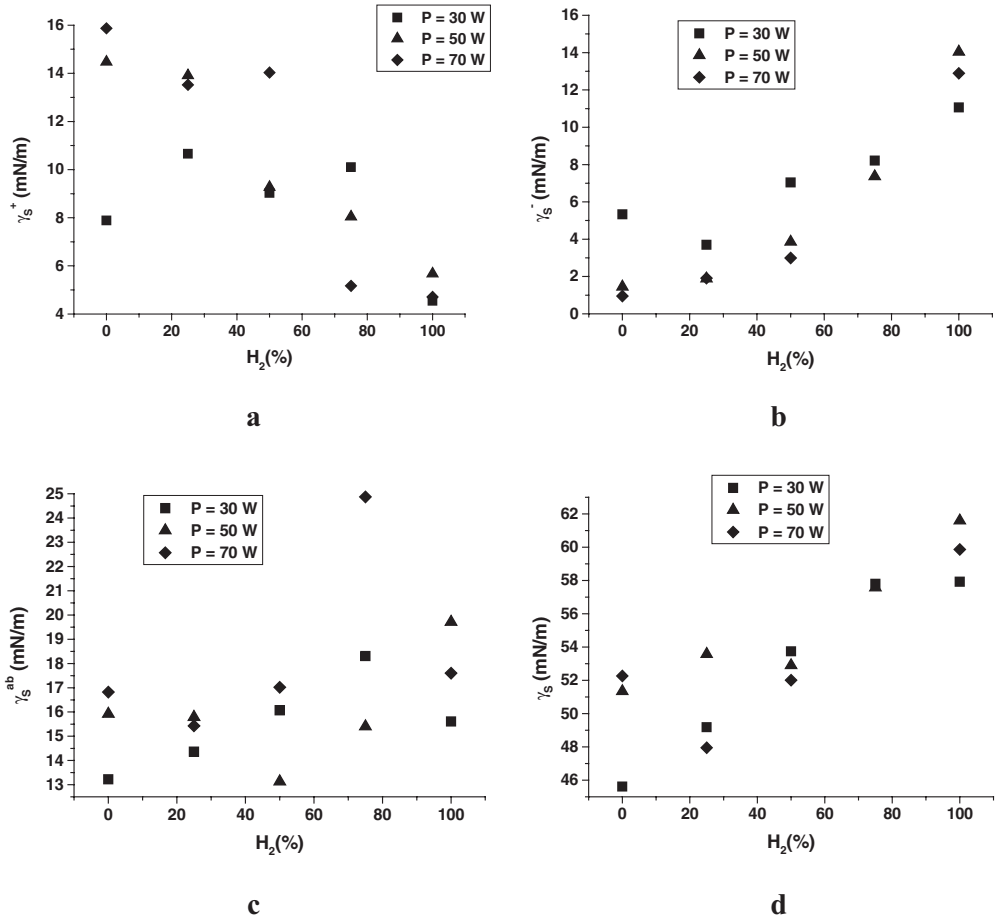

Figure 7 Variation of: electron acceptor (a) and donor (b) parameters, and acid-base component of the free surface energy (c), as well as of the total free surface energy (d) vs H_2 content in the N_2/H_2 plasma, for different applied powers ($t = 60$ s, $d = 10$ cm).

evidences the incorporation of polar functions (nitrogen-containing species). For $P = 50$ W, the total free energy remains almost constant up to 50% H_2, and increases at higher H_2 content in the gaseous mixture (Fig. 7 (d)). For an H_2 content up to 75%, the acid character of the polymer surface (higher values of the electron-acceptor parameter with respect with the electron donor parameter) is maintained also after plasma treatment (Figs. 7 (a) and (b)).

Concerning the piezoelectric PVDF, variations of its acid-base component of the free surface energy with increasing H_2/N_2 ratio ($P = 50$ W, $t = 60$ s, $d = 10$ cm) present the same behavior as that of the nonpiezeoelectric sample (Fig. 8). Maximum functionalization of the piezoelectric PVDF surface (highest value of the acid-base component of the free surface energy) takes place for a 25/75 N_2/H_2 ratio.

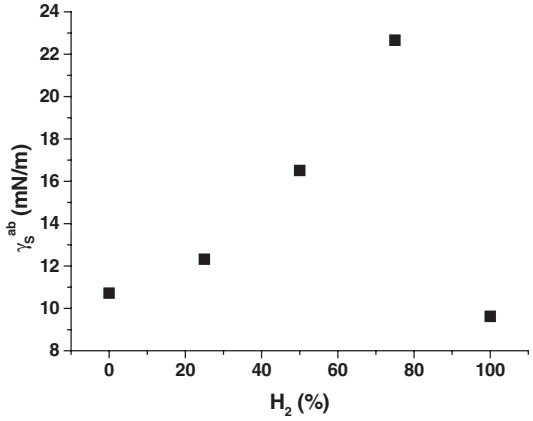

Figure 8 Variation of the acid-base component of the free surface energy with the H_2/N_2 ratio for the piezoelectric PVDF; treatment conditions: $P = 50$ W, $t = 60$ s, $d = 10$ cm.

13.3.2
Aging Studies

A way to find out what crosslinking is effectively present is to study the stability of the treated surfaces.

Excepting the case of a 25/75 N_2/H_2 ratio for the treatment gas, aging studies evidenced an important increase of the acid-base component of the free surface energy under plasma exposure, these values remaining almost constant for the entire observed period of aging (Fig. 9). This behavior evidences the time stability of the applied treatment, which can arise from an increase in the crystallinity degree, or from surface crosslinking. As is well known, PVDF presents a tendency towards crosslinking, when irradiated, due to its chemical composition, intermediary between that of polyethylene (PE) (which crosslinks) and that of PTFE (which degrades) under these conditions [32]. The obtained stability of PVDF surfaces treated under these conditions may be a very important behavior from the point of view of different possible applications.

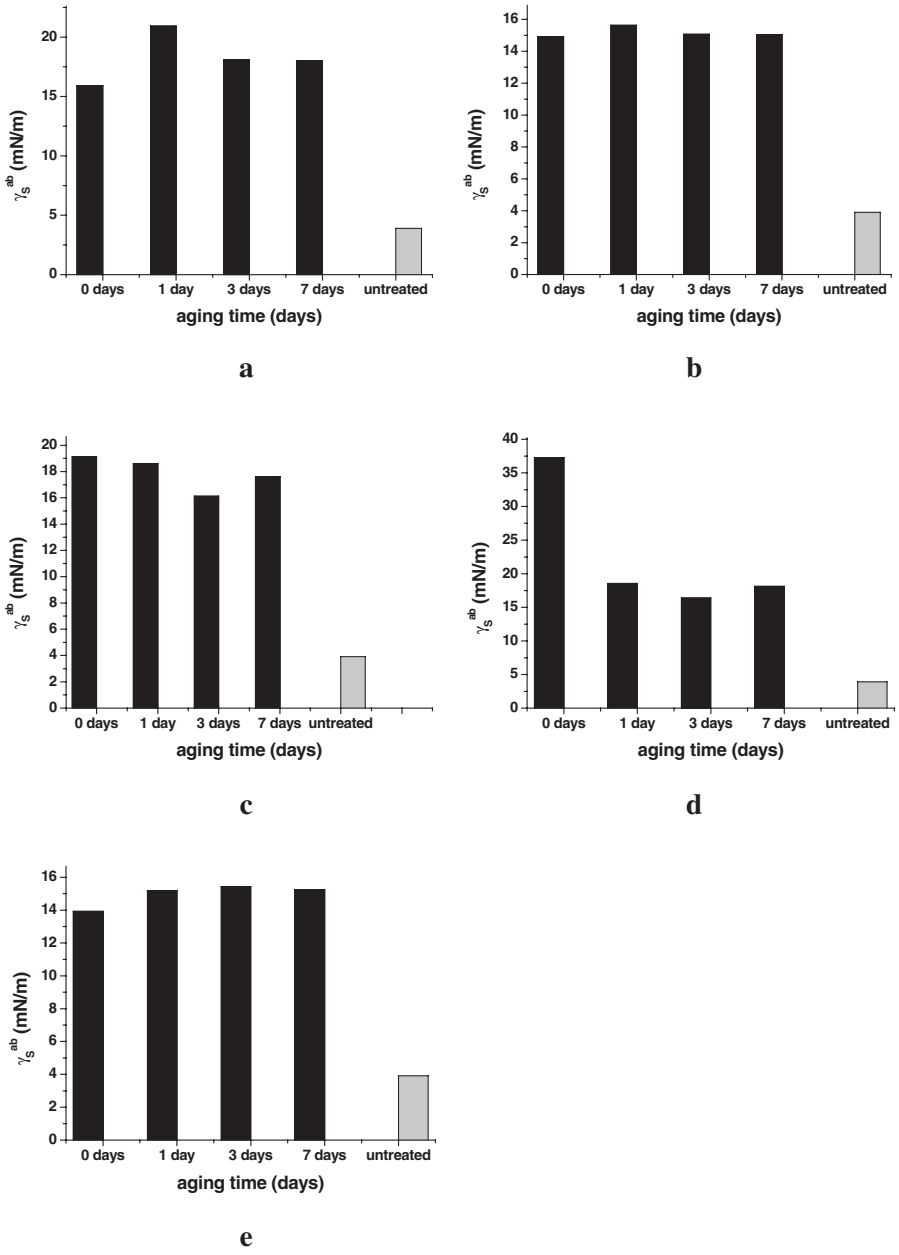

Figure 9 Acid-base component of the free surface energy vs the aging time, for different N_2/H_2 ratios: (a) 100/0; (b) 75/25; (c) 50/50; (d) 25/75; (e) 0/100.

For a 25/75 N_2/H_2 ratio, the acid-base component decreases with aging time, tending to the value corresponding to the untreated sample, but remaining, however, higher than this one (Fig. 9 (d)). The main mechanism proposed [27, 33] to explain the hydrophobic recovery of polymers is the reorientation of the polar surface groups away from the surface, as well as the sorption of hydrophobic moieties appearing in the laboratory air, and the migration of untreated polymer chains from the bulk to the surface, depending on the presence or not of crosslinks. The low value of the water contact angle, which does not increase to the value corresponding to the untreated surface means that most of the polar groups induced under plasma treatment stay at the extreme surface, most likely immobilized by adjacent crosslinking.

13.3.3 XPS results

As was expected [27], N-containing groups were detected on the polymer surface after the applied treatment (Table 1).

Table 1 Results of XPS analysis for untreated and plasma treated PVDF ($P = 50$ W, $t = 60$ s, $d = 10$ cm).

Sample	Spectrum	Position of the peaks (eV)	Attributed groups
untreated PVDF	C 1s	284.6	C–H, C–C
		285.9	C–O
		291.6	C–F
	F 1s	687.5	C–F
	O 1s	533.6	C–O
PVDF/N_2	C 1s	284.6	C–H, C–C
		286.6	C–O, C–N
		289.2	C–F
	F 1s	687	C–F
	O 1s	533.6	C–O
	N 1s	397.9	C–N

As was also pointed out by other authors [8, 24, 27, 36, 37], the atomic composition on PVDF surfaces generally evidences a surface defluorination under plasma exposure (Table 2). The loss of surface fluorine was attributed by Ryan and Badyal [38] to vacuum ultraviolet (VUV) photons, ion-beam bombardment, or electron-impact dissociation. In the meantime, an increase in oxygen atom concentration is obvious after the applied treatment (Tables 3 and 4), generally due to the postreactions of the plasma-treated surfaces [3, 27], because the samples were exposed to the atmosphere before XPS analysis. This result is in accordance with contact-angle measurements, the general decrease in contact angle being attributed to an increase in the surface nitrogen and oxygen concentrations [39]. Plasma treatment breaks the C–F bonds, leading to defluorination and to the formation of active species at the surface [8].

Table 2 Atomic composition on nonpiezoelectric and piezoelectric PVDF surfaces

Sample	C (%)	N (%)	O (%)	F (%)
untreated nonpiezoelectric PVDF	55.3	–	3.2	41.5
N_2 ; 50 W, 10 cm, 60 s	59.4	3.6	9	28
25 N_2/75 H_2 ; 50 W, 10 cm, 60 s	62.1	2.3	7.1	28.6
50 N_2/50 H_2 ; 50 W, 10 cm, 60 s	67.9	3.4	6.2	22.5
untreated piezoelectric PVDF	67.1	–	5.1	27.7
N_2; 50 W, 10 cm, 60 s	57	3.6	5.4	34
50 N_2/50 H_2 ; 50 W, 10 cm, 60 s	66.3	3.7	7.1	23

Table 3 Crystallinity degree evaluated from X-ray spectra for untreated and plasma-exposed PVDF, in different treatment conditions.

Treatment conditions	X_C
untreated nonpiezoPVDF	0.870
50 W, 30 s, 10 cm	0.870
50 W, 300 s, 10 cm	0.880
50 W, 120 s, 10 cm	0.876
70 W, 120 s, 15 cm	0.880
50 W, 120 s, 2.5 cm	0.876
untreated piezoelectric PVDF	0.81
piezo, N_2, 50 W, 60 s, 10 cm	0.80
piezo, 25 N_2/75 H_2, 50 W, 60 s, 10 cm	0.81

Table 4 Crystallite size for untreated and plasma-exposed PVDF

Sample	θ (deg)	b = FWHM (rad)	L (Å)
untreated PVDF	8.815	0.0075	187.52
	9.17	0.0056	252.29
	9.94	0.0075	187.52
N_2,	8.895	0.0075	187.52
50 W, 60 s, 10 cm	9.225	0.0056	252.29
	10.025	0.0075	187.52
25/75 N_2/H_2	8.83	0.0064	220.26
50 W, 60 s, 10 cm	9.16	0.0049	289.09
	9.96	0.0070	201.10
untreated piezoelectric PVDF	9.875	0.0113	125.01
	17.89	0.0130	111.90
piezo, N_2	9.93	0.0108	130.91
50 W, 60 s, 10 cm	17.945	0.0146	99.83
piezo, 25/75 N_2/H_2	10.04	0.0113	125.01
50 W, 60 s, 10 cm	18.055	0.0155	94.39

13.3.4
Titration of the Surface Amino Groups

Titration of the surface amino groups, followed by UV spectroscopy [10], was in good agreement with surface energetic results, the variation of the amino groups concentration with the treatment parameters following almost the same behavior as the polar component of the free surface energy (Figs. 10 (a)–(c)).

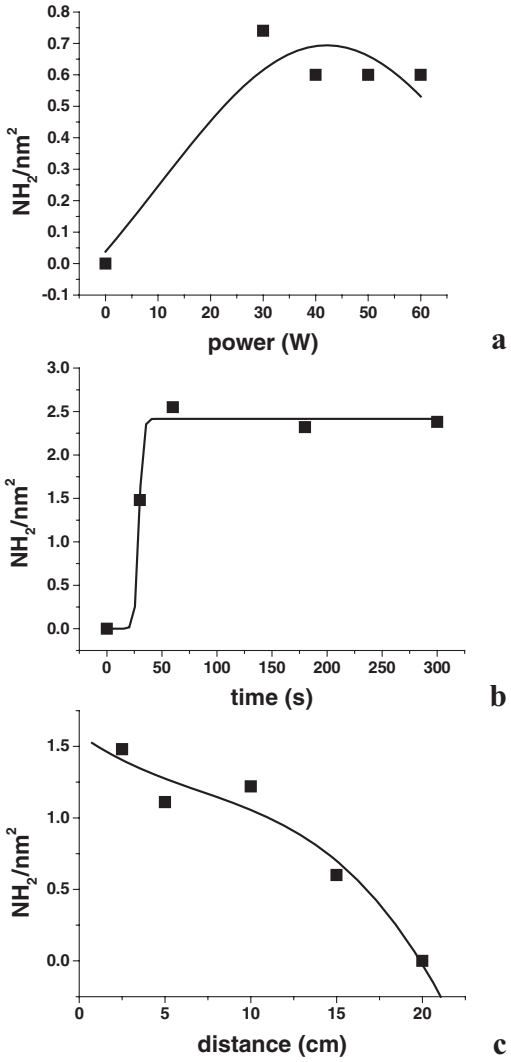

Figure 10 Concentration of the amino groups on PVDF surface, N_2 plasma treated, vs: (a) the discharge power ($d = 15$ cm, $t = 120$ s); (b) the treatment time ($P = 50$ W, $d = 10$ cm); (c) the distance between the polymer sample and the surfatron ($P = 50$ W, $t = 120$ s).

13.3.5
Wide-Angle X-ray Diffraction

The diffraction pattern of virgin nonpiezoelectric PVDF clearly indicates that this polymer is semicrystalline. The X-ray diffraction data of the virgin PVDF (Fig. 11 (a)) show three diffraction peaks, at 2θ= 17.6° (100), 18.4° (020), and the most intense

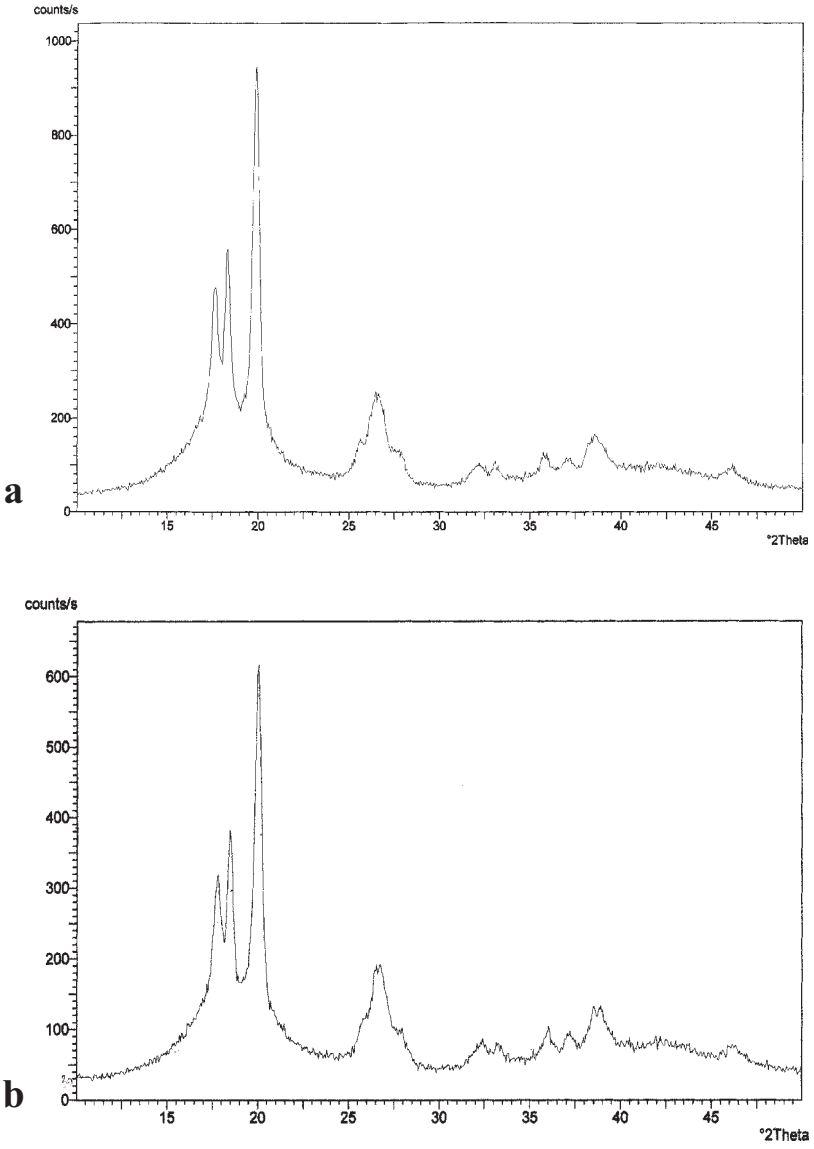

Figure 11 X-ray diffraction patterns for: (a) untreated PVDF, (b) N_2-plasma-treated PVDF (50 W, 60 s, 10 cm).

19.9° (110), with d= 5.03, 4.8, and 4.46 Å, respectively. No significant changes in the diffraction pattern for N_2 and N_2/H_2 plasma-treated PVDF have been observed, whatever the discharge power, the treatment time and the distance between the polymer sample and the core of the discharge (Fig. 11). In the meantime, the crystallinity degree and the crystallite size for PVDF do not change significantly under plasma treatment (Tables 3 and 4).

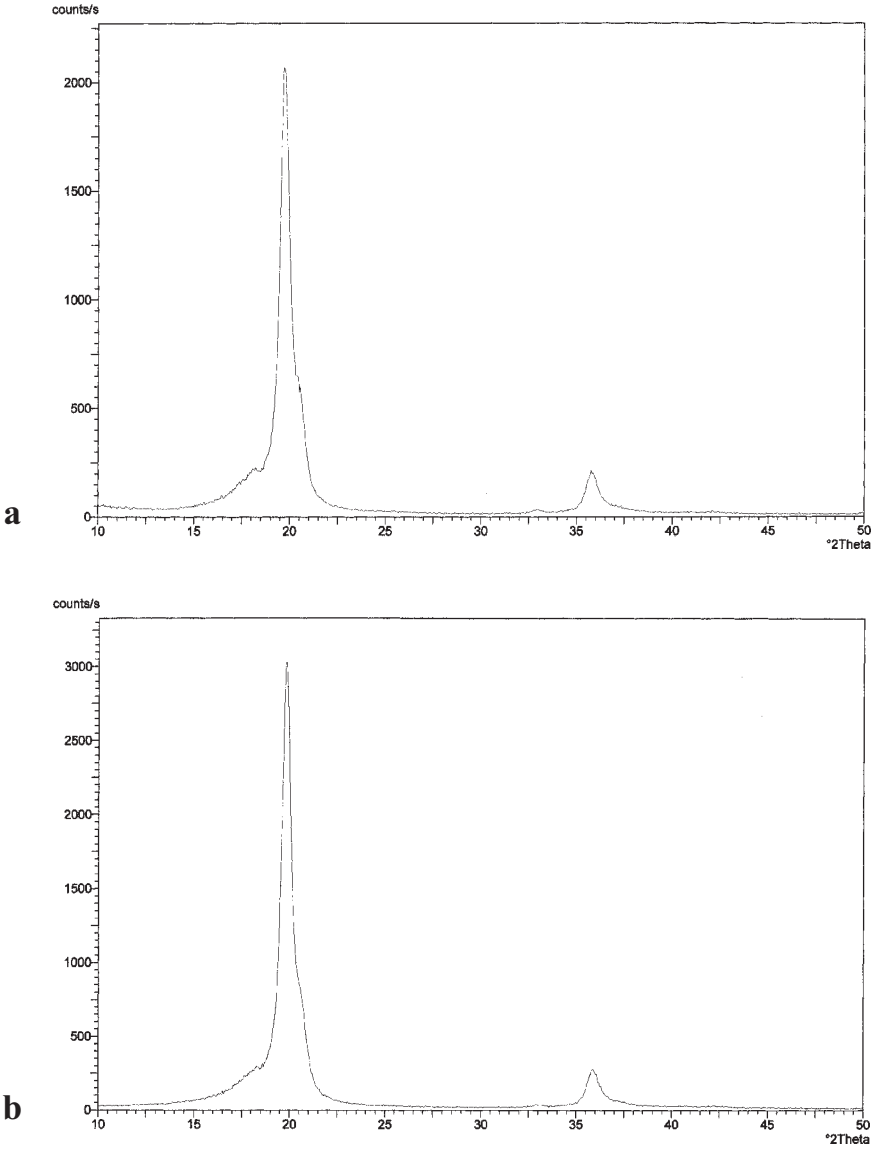

Figure 12 X-ray diffraction patterns for: (a) untreated piezoelectric PVDF, (b) N_2-plasma-treated piezoelectric PVDF (50 W, 60 s, 10 cm).

The diffraction pattern for the piezoelectric PVDF concerns only two diffraction peaks, namely at $2\theta = 19.9$ and 35.9°, corresponding to $d = 4.47$ and 2.5 Å, respectively. As for the nonpiezoelectric PVDF, no changes appear in the diffractograms and in the crystallinity degree of the plasma-treated samples with respect to the untreated one (Fig. 12 and Table 3). Crystallite sizes for piezoelectric PVDF are smaller than those of the nonpiezoelectric one (Table 4).

The fact that the bulk properties of PVDF seem not to change under plasma exposure could be a good sign for the maintenance of the piezoelectric character of polymer samples treated under these conditions, because it is well known that when crystallinity is destroyed by irradiation the ferroelectric and piezoelectric characters disappear [40].

13.3.6 Preliminary Results on PVDF Metallization

The characteristics of adhesion are simultaneously affected by two peculiar properties of the polymers, namely surface energy and macromolecular mobility. Good wettability of polymers is essential for a good absorption mechanism, leading to the formation of molecular interactions, acid-base interactions, and interfacial hydrogen bonds [41]. Due to the fact that plasma treatment improved the wetting of polymer surfaces, as well as the surface properties, a better adhesion between the metal layer and the plasma-treated polymer surfaces, compared to the untreated ones was expected to be obtained. While for the pristine PVDF surfaces, the copper adhesion was very poor (the metal layer being easily removed from the surface by a simple touch with the fingers), all the pretreated samples were covered with an homogeneous layer of copper, with an improved adhesion at the PVDF surface, compared to the pristine sample (Table 5).

The most important increase in the adherence between the copper layer and the PVDF surface seems to be obtained for the treatment in a 25/75 N_2/H_2 plasma, possibly due to the fact that there is a relationship between the functional-group density and the palladium-atom density, this one inducing the absorption of the metal atoms at the polymer surface [42]. The main reason for the adhesion improvement by plasma treatment could be the increase in the degree of chemical interaction between metallic atoms and the polymer backbone. Plasma treatment of PVDF samples led to roughened surfaces (evidenced by the increase in the hysteresis of the water contact angle), that means a larger area of contact for metallic atoms, which should favor their mechanical anchorage to the substrate [6].

Metallization realized after 1 month of aging led to the adherence results presented in Table 6. The fact that the adherence obtained for PVDF surface, treated in a 25/75 N_2/H_2 plasma, was no longer the best could be attributed to the significant decrease of its polar component of the free surface energy with aging time, while the modifications induced in the other treated samples were stable, according to the aging studies.

Table 5 Thermodynamic work of adhesion evaluated by harmonic and, respectively, geometric mean for untreated and plasma treated nonpiezoelectric and piezoelectric PVDF (P = 50 W, t = 60 s, d = 10 cm).

Sample/treatment conditions	W_a (mN/m), calculated using the harmonic mean		W_a (mN/m), calculated using the geometric mean	
	absolute values	relative values, reported to untreated PVDF	absolute values	relative values, reported to untreated PVDF
untreated PVDF	78.63		83.52	
N_2	105.30	1.34	106.81	1.28
75 N_2 / 25 H_2	101.87	1.29	103.08	1.23
50 N_2 / 50 H_2	111.93	1.42	112.17	1.34
25 N_2 / 75 H_2	106.36	1.35	113.14	1.35
H_2	90.36	1.15	92.11	1.10
untreated piezoelectric PVDF	92.97		95.28	
N_2	97.66	1.05	98.02	1.03
75 N_2 / 25 H_2	99.03	1.06	99.51	1.04
50 N_2 / 50 H_2	108.15	1.16	107.89	1.13
25 N_2 / 75 H_2	119.29	1.28	119.25	1.25
H_2	105.89	1.14	107.12	1.12

Table 6 Results obtained by the normalized scotch test for PVDF surfaces, untreated and plasma exposed (P = 50 W, t = 60 s, d = 10 cm) after 1 month of aging in laboratory conditions.

Sample	Adherence (%)	
	t = 20 °C	t = 40 °C
untreated PVDF	0	0
PVDF, N_2	72	93
PVDF, 75N_2/25H_2	37	77
PVDF, 50N_2/50H_2	53	75
PVDF, 25N_2/75H_2	67	67
PVDF, H_2	2	5

t – the temperature at which the mixed colloidal solution has been prepared.

13.3.7 Assays on Piezoelectric Coefficient Determination

The first assays on determination of the piezoelectric characteristics led to a value of the piezoelectric coefficient (d_{33}) for the untreated piezoelectric PVDF of 15 pC/N, while when treated in an N_2 plasma, its value increased to 25 pC/N. N_2/H_2 plasma

exposure under the mentioned treatment conditions led to a d_{33} value of almost 30 pC/N. It seems that plasma treatment not only maintains the piezoelectric properties of this polymer, but also induces their increase.

13.4 Conclusion

Surface properties of PVDF have been modified in a controlled manner, allowing its metallization, necessary in a wide range of applications. In the meantime, when choosing appropriate plasma-treatment parameters, the piezoelectric character of PVDF has been maintained, as expected, as no significant changes were observed in the bulk properties of this polymer.

Acknowledgements

Many thanks to the "Région des Pays de la Loire", which financed this work by offering a postdoctoral fellowship to M. Pascu, in the Laboratoire "Polymères, Colloïdes, Interfaces", Maine University, France.

References

[1] E.T. Kang, K.L. Tan, K. Kato, Y. Uyama, Y. Ikada. Macromolecules **29**, 6872 (1996).
[2] M. Tatoulian, F. Arefi-Khonsari, N. Shahidzadeh-Ahmadi, J. Amouroux. J. Adhes. Adhesives **15**, 177 (1995).
[3] N. Inagaki, S. Tasaka, T. Umehara. J. Appl. Polym. Sci. **71**, 2191 (1999).
[4] M.G. Fessehaie, S. McClain, C.L. Barton, G.S. Swei, S.L. Suib. Langmuir **9**, 3077 (1993).
[5] S. Wu, E.T. Kang, K.G. Neoh, H.S. Han, K.L. Tan. Macromolecules **32**, 186 (1999).
[6] M. Du, R.L. Opila, V.M. Donnelly, J. Sapjeta, T. Boone. J. Appl. Phys. **85**(3), 1496 (1999).
[7] G. H. Yang, E. T. Kang, K. G. Neoh, Y. Zhang, K. L. Tan. Langmuir **17**, 211 (2001).
[8] N. Inagaki, S. Tasaka, T. Baba. J. Adhes. Sci. Technol. **15**(7), 749 (2001).
[9] T.P. Nguyen, A. Lahmar, P. Jonnard. J. Adhes. **66**, 303 (1998).
[10] F. Poncin-Epaillard, N. Medard, J. C. Soutif. Macromol. Chem. Phys. **201**, 212 (2000).
[11] J.M. Park, L.J. Matienzo, D.F. Spencer, J. Adhes. Sci . Technol. **5**, 153 (1991).
[12] F. Arefi-Khonsari, J. Kurdi, M. Tatoulian, J. Amouroux. Surf. Coat. Technol. **142–144**, 437 (2001).
[13] M. Collaud, S. Nowak, P. Groning, H.P. Haerri, L. Schlapbach. Le Vide. Les Couches Minces 268, 39–45 (1993).
[14] C.J. van Oss in "Polymer Surfaces and Interfaces II", W.J. Feast, H.S. Munro, R.W. Richards, eds, John Wiley and Sons, New York, 1993, pp. 270–278
[15] C. Jama, O. Dessaux, P. Goudmand, B. Mutuel, L. Gengembre, B. Drevillon, S. Vallon, J. Grimblot. Surf. Sci. **352–354**, 490 (1996).
[16] H.S. Virk, P.S. Chandi, A.K. Srivastasa. Bull. Mater. Sci. **24**(5), 529 (2001).
[17] L.V. Azaroff, "Elements of X-ray Crystallography", USA, 1968, pp. 151.
[18] H.S. Virk, P.S. Ghandi, A.K. Srivastasa. Nucl. Instrum. Methods Phys. Res. **B183**, 329 (2001).
[19] "X-ray Diffraction Methods in Polymer Science", L.E. Alexander, ed., John Wiley and Sons, Inc., New York, 1969, ch. 3, pp. 173.

[20] D. Debarnot, PhD Thesis, Ecole Centrale de Lyon, France, 1997, July, 9.
[21] M.C. Burrell, B.R. Karas, D.F. Foust, W.V. Dumas, E.J. Lamby, W.T. Grubb, J.J. Chera in: "Metallized Plastics 1", K.L. Mittal and J.R. Susko, eds., Plenum Press, New York, 1988, pp. 233.
[22] A. Bismarck, M.E. Kumru, B. Song, J. Springer, E. Moos, J. Karger-Kocsis. Composites Part A: Appl. Sci. Manuf. **30**(12), 1351 (1999).
[23] G.S. Neugschwandtner, R. Schwodiauer, S. Bauer-Gogonea, S. Bauer, M. Paajanen, J. Lekkala. J. Appl. Phys. **89**(8), 4503 (2001).
[24] N. Inagaki, S. Tasaka, K. Narushima, K. Mochizuki. Macromolecules **32**, 8566 (1999).
[25] P. Favia, M. V. Stendardo, R. d'Agostino. Plasmas Polym. **1**, 91 (1996).
[26] J. Tsibouklis, P. Graham, P. J. Eaton, J. R. Smith, T. G. Nevell, J. D. Smart, R. J. Ewen. Macromolecules 33, 8460 (2000).
[27] J. P. Badey, E. Espuche, D. Sage, B. Chabert, Y. Jugnet, C. Batier, T.M. Duc. Polymer **37**, 1377 (1996).
[28] E. Sacher, L. Martinu, M. Meunier. J. Phys. Coll. **C6**, C6.239 (1997).
[29] D. A. Biro, G. Pleizier, Y. Deslandes. J. Appl. Polym. Sci. **47**, 883 (1993).
[30] N. Inagaki, "Remote plasma and pulsed plasma modification of polymeric materials for adhesion", 5th European Adhesion Conference, 2000, Sept. 18–21, Lyon, France, pp. 227–236.
[31] N. Inagaki. Macromol. Symp. **159**, 151 (2000).
[32] Christine Ducouret, PhD Thesis, l'Universite "Pierre et Marie Curie" (Paris VI), 1994, September, 20.
[33] I. Gancarz, G. Pozniak, M. Bruyjak. Eur. Polym. J. **36**, 1563 (2000).
[34] M.C. Zhang, E.T. Kang, K.G. Neoh, K.L. Tan. J. Adhes. Sci. Technol. **13**, 819 (1999).
[35] J.F. Moulder, W.F. Stickle, P.E. Sobol, K.D. Bomben, "Handbook of X-ray Photoelectron Spectroscopy", J. Chastain, R.C. King Jr., eds., Physical Electronics Inc., USA, 1995.
[36] E. T. Kang, Y. Zhang. Adv. Mater. **12**, 1481 (2000).
[37] G.J. Ross, J.F. Watts, M.P. Hill, P. Morrissey. Polymer **41**, 1685 (2000).
[38] M.E. Ryan, J.P.S. Badyal. Macromolecules **28**, 1377 (1995).
[39] J. Davies, C.S. Nunnerley, A.C. Brisley, R.F. Sunderland, J.C. Edwards, P. Kruger, R. Knes. Coll. Surf. A: Physicochem. Eng. Aspects **174**, 287 (2000).
[40] G. Szenes. Nucl. Instrum. Methods Phys. Res. **B155**, 301 (1999).
[41] S. Carlotti, A. Mas. J. Appl. Polym. Sci. **69**, 2321 (1998).
[42] M. Alami, M. Charbonnier, M. Romand. Le Vide. Les Couches Minces **266**, 392 (1993).

14
Different Performance of Ar, O_2 and CO_2 RF Plasmas in the Adhesion of Thermoplastic Rubber to Polyurethane Adhesive

Ana B. Ortiz-Magán, M. Mercedes Pastor-Blas, José Miguel Martín-Martínez

Abstract

In this study, an unvulcanized (thermoplastic) block styrene-butadiene-styrene rubber S0 was treated with argon, oxygen and carbon dioxide plasmas and the surface modifications produced were analyzed. The Ar, CO_2 and O_2 plasma treatments produced an increase in peel-strength values of S0 rubber/polyurethane adhesive joints due to improved wettability, chemical and morphological modifications. Ar plasma created polar moieties on the S0 rubber surface and a consequent increase of the polar component of the surface energy. On the other hand, CO_2 and O_2 plasma treatments produced ablation of the oxidized outermost S0 rubber surface. Short plasma treatment times are enough to produce adequate T-peel-strength values and a cohesive failure was obtained in the joint produced with S0 rubber treated with CO_2 plasma for 1 min. The increase in the length of treatment or the treatment with the other plasmas did not affect the peel-strength values but different loci of failure in the adhesive joints were obtained.

14.1
Introduction

Synthetic styrene-butadiene-styrene (SBS) rubbers are thermoplastic block copolymers containing hard and rigid blocks (styrene) and soft and flexible elastic (butadiene) domains. The main advantage of thermoplastic rubbers over the vulcanized elastomers is that upon heating above the melting temperature of the hard domains, they melt and therefore they may be processed by conventional techniques. For this reason in a variety of applications, the thermoplastic elastomers have replaced the conventional vulcanized elastomers [1]. Typical uses for the SBS rubbers include automotive components, shoe soles and heels, sporting goods, medical barrier films and protective coatings, where they find application as components in sealants, caulking and adhesives. However, due to the nonpolar nature of these rubbers, poor adhesion is produced and consequently a surface treatment is required to modify the rubber surface and produce suitable joints [2,3].

In the footwear industry, SBS rubber soles are joined to the upper leather by means of a polyurethane adhesive. The most widely used surface treatment for SBS

rubber soles is halogenation with organic chlorine donors (trichloroisocyanuric acid, bleach or chloramines). This surface treatment improves the wettability of these rubbers and enhances their adhesion properties [4], but this treatment needs organic solvents for application, the chlorinating solutions have a limited stability and evolution of chlorine is a potential threat. Thus, more environmentally friendly surface treatments need to be found as an alternative to halogenation for SBS rubbers.

Recent studies [5–7] have shown the effectiveness of RF plasma in the improvement of adhesion of synthetic vulcanized rubbers to polyurethane adhesive. The energetic environment of the plasma creates surface free radicals and produces cleaning, ablation, crosslinking and chemical modifications on the rubber surface. However, these effects are greatly dependent on the gas used to generate the plasma. In this study the treatment with argon, oxygen and carbon dioxide RF plasmas of a SBS rubber S0 was carried out. The energy of the radiation emitted from Ar and O_2 plasmas are in the UV region (Table 1), whereas CO_2 emits in the IR region [8]. The surface modifications produced by plasma treatments and the adhesion properties of the surface modified S0 rubber have been studied.

Table 1 Wavelength (nm) and energy (kcal/mol) of photons emitted by different plasmas (from NIST Atomic Spectra Database)

Gas	Ar	N_2	O_2	CO_2
λ (nm)	334–529	337	210–400	10 600
E (kcal/mol)	85–54	85	135–71	2.7

14.2 Experimental

14.2.1 Materials

A block copolymer synthetic thermoplastic styrene-butadiene-styrene rubber (S0), Fig. 1, was used in this study. The S0 rubber was provided by REPSOL QUÍMICA (Santander, Spain) and does not contain oils, plasticizers or fillers but only a small amount of antioxidant. The rubber samples were obtained by injecting the polymer into a heated mold at 150 °C, and test samples of 30 mm width, 150 mm length and 6 mm thickness were obtained. The styrene block content of the S0 rubber is 30%, its tensile strength is 17 MPa and the Shore A hardness is 72°.

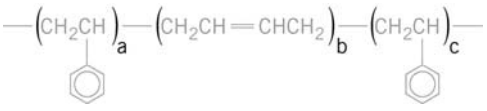

Figure 1 Structure of styrene-butadiene-styrene block copolymer (SBS rubber)

The S0 rubber was treated with low-pressure RF plasma in a barrel-type March Plasmod Instruments reactor at 13.56 MHz, using argon, carbon dioxide and oxygen atmospheres for 1 to 15 min. The samples were placed on a floating aluminum plate inside a Pyrex glass barrel-type plasma chamber (19 cm long and 14 cm diameter). The plasma reactor has upper and lower external electrodes and is sealed with a flat silicone gasket, which seats against a raised lip placed on the inner chamber. The gas delivery tube feeds through the back of the plasma reactor. The bottom of the plasma reactor is connected to the vacuum hose by a glass tube. The reaction chamber was evacuated to mild vacuum (<0.2 Torr) by a mechanical vacuum pump. Then, the gas used to generate the plasma was introduced over the specimen to be treated in the plasma reactor increasing the pressure to 1 Torr. A March GCM-200 Gas Control unit provided with a flow meter and a pressure gauge was used to control the gas flow into the plasma reactor. Argon, oxygen and carbon dioxide (99.999% minimum purity) used for the plasma treatment were supplied by Abelló Linde S.A. (Valencia, Spain). Care was taken to pump down and purge the plasma reactor for at least 10 min prior to activating the RF field. The discharge power was set at 50 W.

Adhesive joints between two identically plasma-treated S0 rubber samples using a polyurethane adhesive were produced within 1–2 min after plasma treatment, in order to minimize surface molecular rearrangements and/or contamination from the atmosphere. The polyurethane adhesive was prepared by dissolving 18 wt% polyester-urethane pellets (Desmocoll 540, provided by Bayer AG, Leverkusen, Germany) in 2-butanone in a laboratory mixer (850 rpm for 3 h). The resulting adhesive solution had a Brookfield viscosity of 4.0 ±0.1 Pa s (23 °C). To produce an adequate adhesion 5 wt% thionophosphoric acid-tris-(p-isocyanatephenil ester) (Desmodur RFE, provided by Bayer AG, Leverkusen, Germany) was added to the polyurethane adhesive solution just before adhesive joint formation.

14.2.2 Experimental Techniques

Contact-angle measurements. The plasma-treated S0 rubber pieces were placed into the thermostated chamber of a Ramé Hart 100 goniometer. The chamber was previously saturated with the vapor of the test liquid (doubly distilled deionized water or ethylene glycol) at 25 °C for at least 10 min before placing a 4-μl drop on the surface of the treated S0 rubber. The contact angles on the plasma-treated S0 rubber were measured immediately after treatment. Both the advancing and receding contact angles of at least 5 water drops placed on different regions of the treated S0 rubber were measured. The experimental error was ±2 degrees.

Fourier transform infrared spectroscopy (FTIR). This technique allows monitoring of the chemical modifications produced by plasma treatment in about 5 μm of the S0 rubber and therefore, information about surface rearrangements can be obtained. The ATR-IR spectra of plasma-treated S0 rubber were obtained using a Nicolet FTIR 205 spectrophotometer. A KRS-5 (thallium bromo-iodide) crystal was used; the incident angle was 45°. 200 scans were obtained and averaged at a resolution of 4 cm^{-1}.

X-ray photoelectron spectroscopy (XPS). X-ray photoelectron spectroscopy was used to determine the modifications produced on the outermost (50–100 Å) S0 rubber surface. The plasma-treated S0 rubber was analyzed using a V.G. Scientific Microtech Multilab spectrometer with a MgK_α achromatic X-ray source (1253.6 eV) operating at 15 keV and 300 W. The pressure inside the analysis chamber was held below 5×10^{-8} Torr (6.6×10^{-6} Pa) during the course of the analysis. Square sample pieces (5 mm × 5 mm) were used, although the dimensions of the analyzed areas on the samples were 5 mm × 2 mm. The measurements were taken using a take-off angle of 45°. Survey scans were taken in the range 0–1100 eV and high-resolution scans were obtained for all significant peaks in the survey spectra. Binding energies of all photopeaks were referenced to the C 1s photopeak position for C–C and C–H species at 285.0 eV. Multicomponent carbon 1s photopeaks were curve fitted using photopeaks of Gaussian peak shape with a full-width-at-half maximum (FWHM) of 1.8 ±0.1 eV.

Scanning electron microscopy. A *JEOL JSM-840* scanning electron microscope was used to obtain micrographs of the as-received and plasma-treated S0 rubber samples. The samples were secured on copper mounts using silver paint and coated with gold in a Polaron high-resolution sputter coater.

T-peel strength measurements. Adhesive bond strengths were obtained from T-peel tests of treated S0 rubber/polyurethane adhesive/treated S0 rubber joints. The S0 rubber pieces have dimensions of 150 mm × 30 mm × 5 mm. The T-peel tests were carried out in an Instron 4411 test instrument (peel rate = 0.1 m/min) and measured 45 min (immediate bond strength), 24 h and 72 h (final bond strength) after adhesive joints were produced. Four replicates were obtained and averaged with a standard deviation lower than 0.7 kN/m.

In order to precisely assess the loci of failure in the joints, the two failed surfaces obtained after the T-peel test of the adhesive joints were analyzed using ATR-IR spectroscopy.

14.3 Results and Discussion

As-received S0 rubber shows (Fig. 2) a high advancing contact-angle value (water, 25 °C), indicating a poor wettability due to its non polar nature. The ATR-IR spectrum of the as-received S0 rubber (Fig. 3 (a) and (b)) shows typical absorption of styrene (aromatic C-H stretching at 3010–3080 cm^{-1}, aromatic C–C stretching at 1600 cm^{-1}, and C–H out-of-plane deformation of phenyl group at 915, 760, 696 cm^{-1}) and butadiene (=CH stretching at ~3300 cm^{-1}, C–H stretching at 2920 and 2850 cm^{-1}, $–CH_2$ scissoring at 1448 cm^{-1}, $–CH_2$ twisting at 1380 cm^{-1}, and out-of-plane deformation of trans-1,4–C=C at 968 cm^{-1}). Plasma treatment of S0 rubber for 1 minute produced a noticeable decrease in advancing contact-angle values, i.e. increased wettability (Fig. 2), with the three plasmas (oxygen, argon and carbon dioxide), the lowest contact angle corresponds to the treatment with argon plasma. Besides, an extended plasma treatment (up to 15 min) further decreases the advancing contact-

angle value on the Ar-plasma-treated S0 rubber. On the other hand, the increase in the length of oxygen or carbon dioxide plasma treatment of S0 rubber does not produce a noticeable change in advancing contact-angle values.

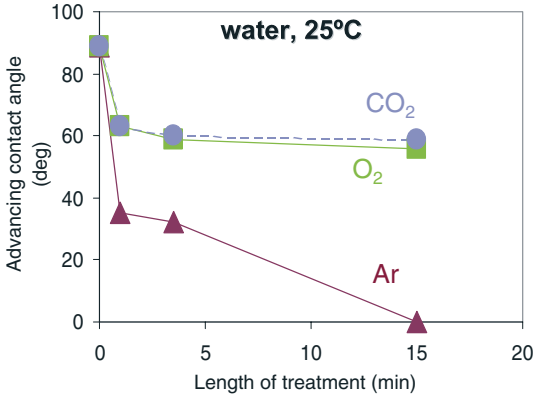

Figure 2 Advancing contact angle values (water, 25 °C) of as-received and plasma treated S0 rubber.

The surface energy was evaluated using the Owens and Wendt approximation [9] (Fig. 4). A noticeable increase of the polar component (γ^p) (Fig. 4 (b)) and a decrease of the dispersive component (γ^d) (Fig. 4 (c)) of the total surface energy (γ) (Fig. 4 (a)) are produced when the S0 rubber is treated with an Ar plasma. A lower increase in total surface energy is obtained for the oxygen and carbon dioxide plasma-treated S0 rubber, and there is an increase in both the dispersive and polar components of the surface energies.

The variations in surface energy of the plasma-treated S0 rubber can be explained on the basis of different chemical modifications. The ATR-IR spectra of plasma treated S0 rubber for 1 and 3.5 min (Fig. 3 (a) and (b)) show a decrease of hydrocarbon absorption (2920, 2850, 1448 cm^{-1}) when the S0 rubber is treated with an Ar plasma. This is in agreement with the decrease in the dispersive component of the surface energy (Fig. 4 (b)). However, the treatment of S0 rubber with O_2 or CO_2 plasmas for 1 and 3.5 min produces an increase of the hydrocarbon absorption (2920, 2850, 1448 cm^{-1}) which is in agreement with the increase in the dispersive component of the surface energy for relatively short treatment times (Fig. 4 (b)). Besides, the extended O_2 and CO_2 plasma treatment for 15 min (Fig. 3 (c)) removes hydrocarbon moieties from the S0 rubber surface, which is consistent with the decrease in the dispersive component of the surface energy observed for 15 min O_2 and CO_2 plasma-treated S0 rubber (Fig. 4 (b)).

The depth of analysis of ATR-IR spectroscopy under our experimental conditions is about 5 µm, while XPS restricts the depth of the analysis to the outermost 5 nm. According to XPS, the as-received S0 rubber is mainly composed (Table 2) of carbon and some oxygen and silicon (Si2p binding energy= 102.3 eV [10]). Because silicon moieties were not incorporated during S0 rubber manufacturing, it seems that it is

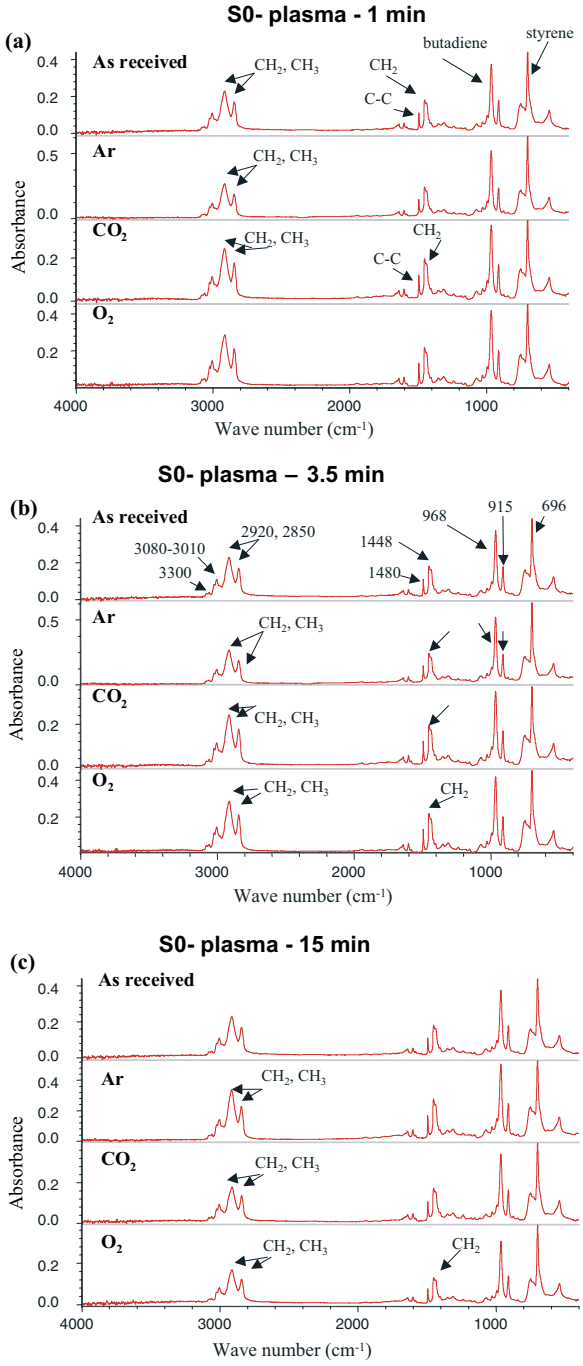

Figure 3 (a) ATR-IR spectra of as-received and plasma treated S0 rubber for 1 min. (b) ATR-IR spectra of as-received and plasma treated S0 rubber for 3.5 min. (c) ATR-IR spectra of as-received and plasma treated S0 rubber for 15 min.

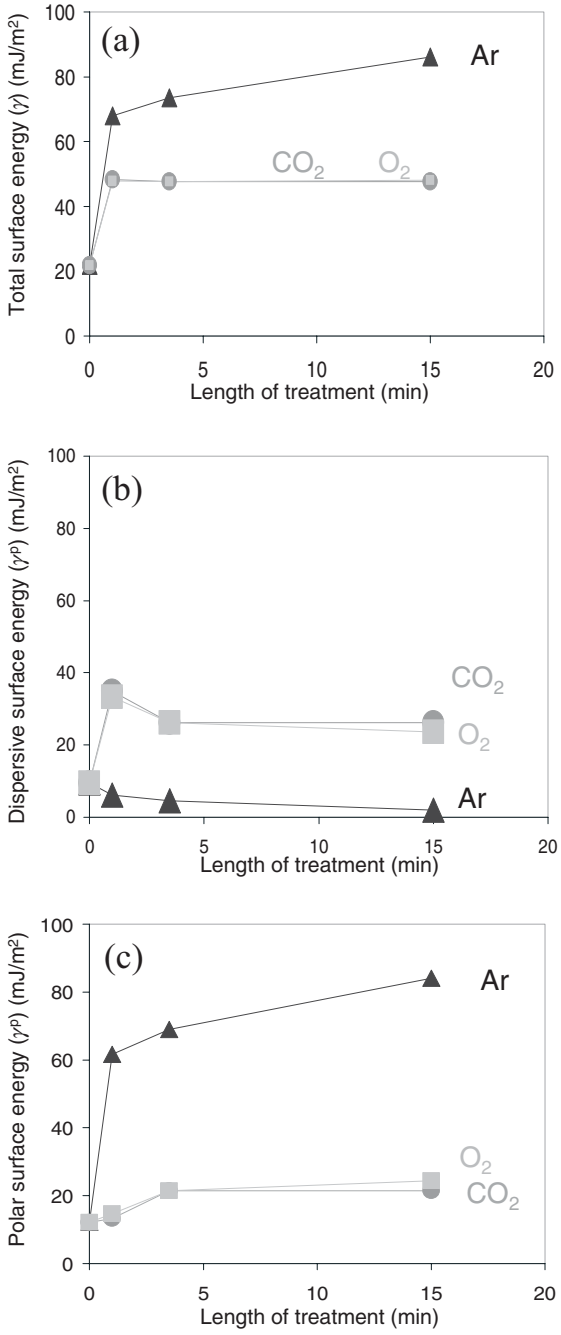

Figure 4 Surface energy of as-received and plasma treated S0 rubber: (a) total (γ); (b) dispersive (γ^d); (c) polar (γ^P).

contaminated by a homogeneously distributed silicon-containing material, likely an organic contaminant (e.g. polydimethylsiloxane [11]) or partially oxidized silicon – SiO_x [12]. Oxygen is mainly due to C–O species (Table 3) produced by oxidation of the S0 rubber surface under air exposition to ambient atmosphere. The plasma treatment for 3.5 min noticeably increases the oxygen concentration on the surface of the S0 rubber. This increase is more important when the S0 rubber is treated with an Ar plasma compared to CO_2 and O_2 plasmas (high O/C ratio is obtained), which is in agreement with the more pronounced increase in the polar component of the surface energy (γ^p) on the Ar-plasma-treated S0 rubber (Fig. 4 (c)). Curve fits of the C 1s and O 2p photopeaks (Tables 3 and 4 and Fig. 5) show the creation of C–O, C=O and R–O–C=O moieties on the plasma-treated S0 rubber, which contribute to increase the polar component of the surface energy (γ^p). Besides, C=O and Si–O moieties are removed from the S0 rubber surface (Table 4) when treated with plasma, this removal being more important with CO_2 and O_2 plasmas. These findings suggest that CO_2 and O_2 plasmas produce ablation of the S0 rubber surface and partially remove hydrocarbon and silicon moieties. On the other hand, Ar plasma does not produce such a degree of ablation, consequently, hydrocarbon and silicon moieties are not such effectively removed but a greater degree of oxidation is achieved.

Table 2 XPS atomic percentages (at%) on as-received and plasma-treated S0 rubber

Binding energy (eV)	Element	As-received S0	Plasma-treated S0 rubber (3.5 min)		
			Ar	CO_2	O_2
285.0	C 1s	94.2	71.6	73.6	75.4
532.0	O 1s	4.7	26.0	22.5	21.6
398.3	N 1s	–	1.2	1.4	1.0
99.6	Si 2p	1.1	1.2	2.5	2.0
532.0/285.0	O/C	0.05	0.36	0.31	0.29

Table 3 XPS atomic percentages (at%) obtained from C1s curve fitting of as-received and plasma-treated S0 rubber

Binding energy (eV)	Species	As-received S0	Plasma treated S0 rubber (3.5 min)		
			Ar	CO_2	O_2
285.0	C–C, C–H	96.3	65.0	74.9	78.9
286.5	C–O	3.7	27.6	20.3	16.5
288.0	C=O	–	4.5	2.9	2.7
289.2	RO–C=O	–	2.9	1.9	1.9

Table 4 XPS atomic percentages (at%) obtained from O 2p curve fitting of as-received and plasma-treated S0 rubber

Binding energy (eV)	Species	As-received S0	Plasma treated S0 rubber (3.5 min)		
			Ar	CO_2	O_2
532.2	C=O, Si–O	74.3	62.9	51.1	61.8
533.6	C–O	25.7	37.1	48.9	38.2

Ablation of the S0 rubber surface was monitored by SEM (Fig. 6). The topography of the S0 rubber is modified by the plasma treatment. The removal of surface layers (ablation) is mainly produced with CO_2 and O_2 plasmas. The increase in the length of CO_2 plasma treatment produces a smoothing of the rubber surface (Fig. 7) due to further ablation by an extended plasma treatment. This explains the decrease in the dispersive component of the surface energy (γ^d) when S0 rubber is treated with O_2 and CO_2 plasmas for 15 min (Fig. 4 (b)). The increase in the length of CO_2 and O_2 plasma treatments produces ablation of the oxidized rubber surface. On the other hand, Ar plasma is less aggressive with an S0 rubber surface and oxidized polar moieties remain on the treated surface producing an increase in the polar component of the surface energy (γ^p) (Fig. 4 (c)).

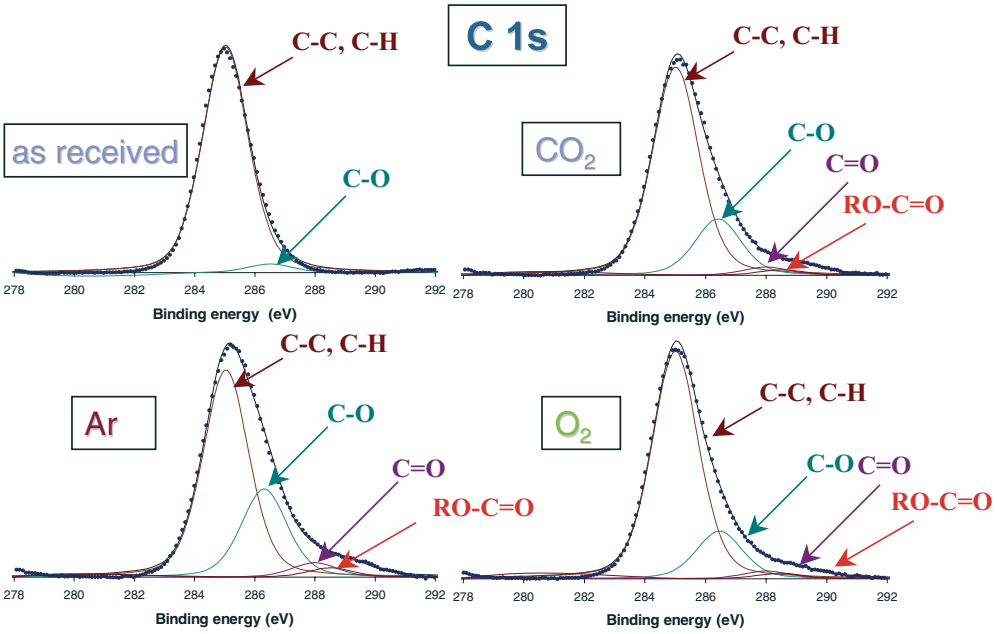

Figure 5 Curve fitting of C 1s (XPS) of as-received and plasma treated S0 rubber.

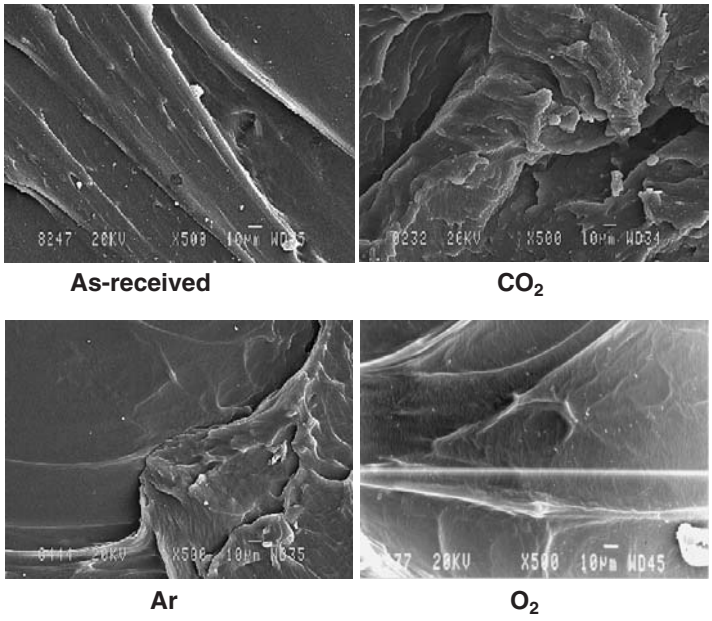

Figure 6 SEM micrographs of as-received and plasma treated S0 rubber for 3.5 min. x500.

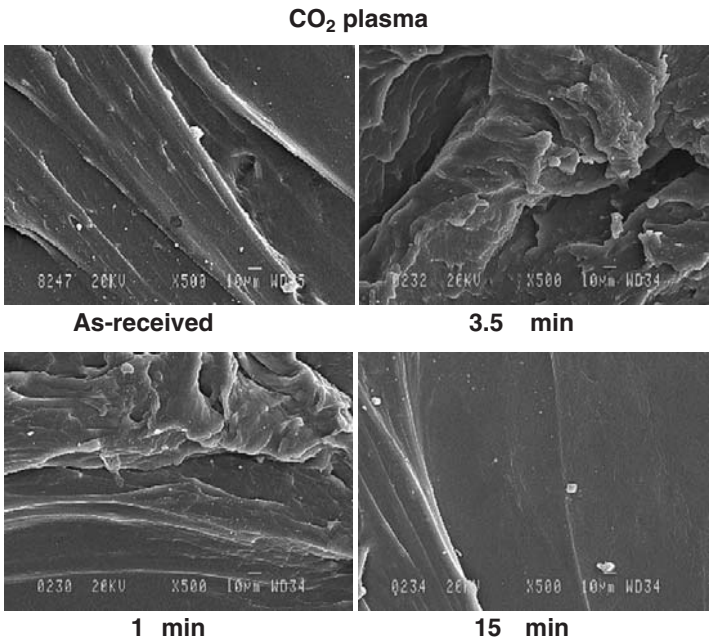

Figure 7 SEM micrographs of as-received and CO_2 plasma treated S0 rubber for different lengths of time. x500.

The different surface modifications produced by the different plasma treatments were expected to affect the adhesive bond strength of S0 rubber differently. Adhesive bond strength was evaluated from T-peel test of joints produced between two identically treated S0 rubber strip test pieces bonded by a polyurethane (PU) adhesive (Fig. 8). The nonpolar nature of the as-received S0 rubber is responsible for the low peel-strength value of the adhesive joints. The plasma treatment of the S0 rubber noticeably increases the adhesive bond strength in all joints produced with any plasma, irrespective of the length of treatment. Thus, the T-peel-strength values do not follow the different chemical and morphological surface modifications produced by the different plasmas. This suggests that additional factors might affect the adhesive bond strength of treated S0 rubber. For this reason, the loci of failure of the joints were analyzed by ATR-IR spectroscopy of the failed surfaces after the T-peel test was carried out.

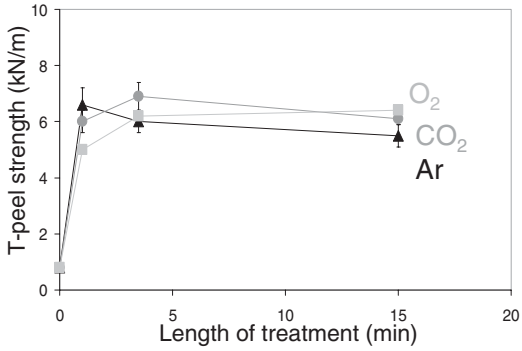

Figure 8 T-peel strength measurements (kN/m) of as-received and plasma treated S0 rubber/PU adhesive/S0 rubber joints.

ATR-IR spectra of the PU adhesive and the as-received S0 rubber are given in Fig. 9 (a). The ATR-IR spectrum for the raw PU adhesive shows typical absorption of N–H stretching (3300 cm^{-1}), C–H stretching (2942, 2863 cm^{-1}), C=O stretching (1730 cm^{-1}), N–H bending and N–C=O symmetric stretching (1530 cm^{-1}), C–O stretching (bands at 1200–1100 cm^{-1}), C–N stretching (1182 cm^{-1}) and N–H out-of-plane deformation (~700 cm^{-1}).

A comparison of the ATR-IR spectra of the raw materials (S0 rubber and PU adhesive) before joint formation (Fig. 9 (a)) to those of the failed surfaces (Fig. 9 (b)) allows assessment of the loci of failure of the different adhesive joints. The ATR-IR spectra of the failed surfaces of the joint produced with the as-received S0 rubber (Fig. 9 (b)) show absorption from the rubber on the surface that visually corresponds to the rubber after peel test (R-surface) and absorption from both the PU adhesive (3390, 2942, 2863, 1730, 1200–1100 cm^{-1}) and the S0 rubber (2920, 2850, 1480, 968, 915 cm^{-1}) on the failed surface that visually corresponds to the adhesive (A-surface). This suggests that a mixed failure (mainly adhesion) is produced.

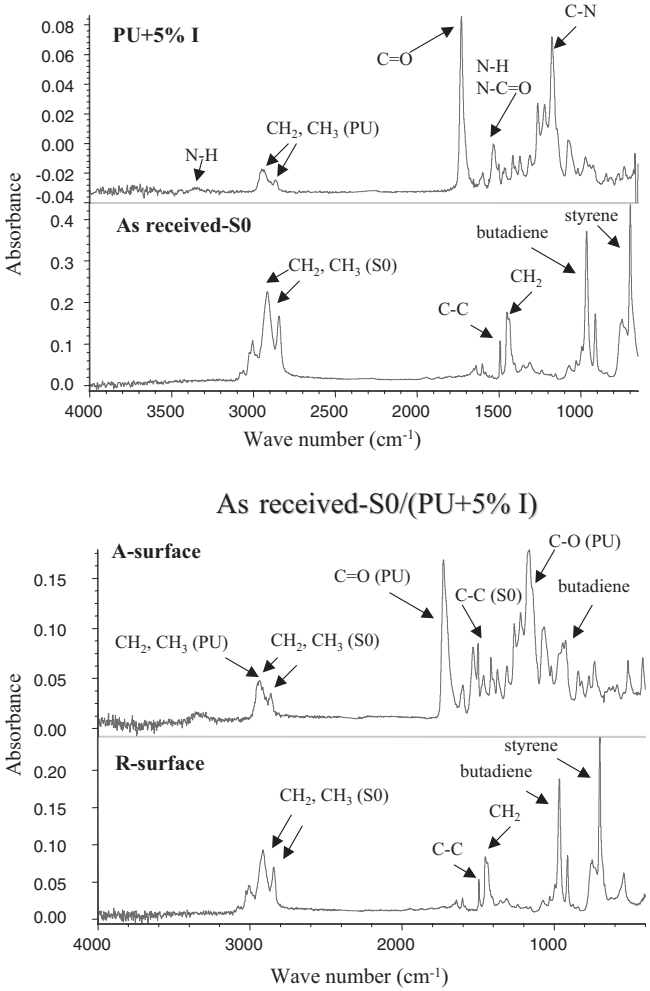

Figure 9 (a) ATR-IR spectra of the raw materials: (a) adhesive (PU + 5% isocyanate); (b) as-received S0 rubber. (b) ATR-IR spectra of the failed surfaces after T-peel test of as-received S0 rubber/ PU adhesive joints.

Oxygen and argon plasma treatment produce an increase in adhesive bond strength and only CO_2 plasma for 1 min produced a cohesive failure (Fig. 10 (a)). Thus, a short CO_2 plasma treatment is sufficient to produce an adequate adhesive bond strength of the S0 rubber. On the other hand, O_2 plasma (Fig. 10 (b)) treatment for 1 min produces a mixed failure (absorption from both PU and S0 rubber are observed on the A-surface and absorption from the rubber is shown on the R-surface. Ar plasma for 1 min (Fig. 10 (c)) also produced a mixed failure but more cohesive in a thin layer of S0 rubber (important hydrocarbon absorption from S0 rubber at 2920, 2851 cm^{-1} is observed on both failed surfaces).

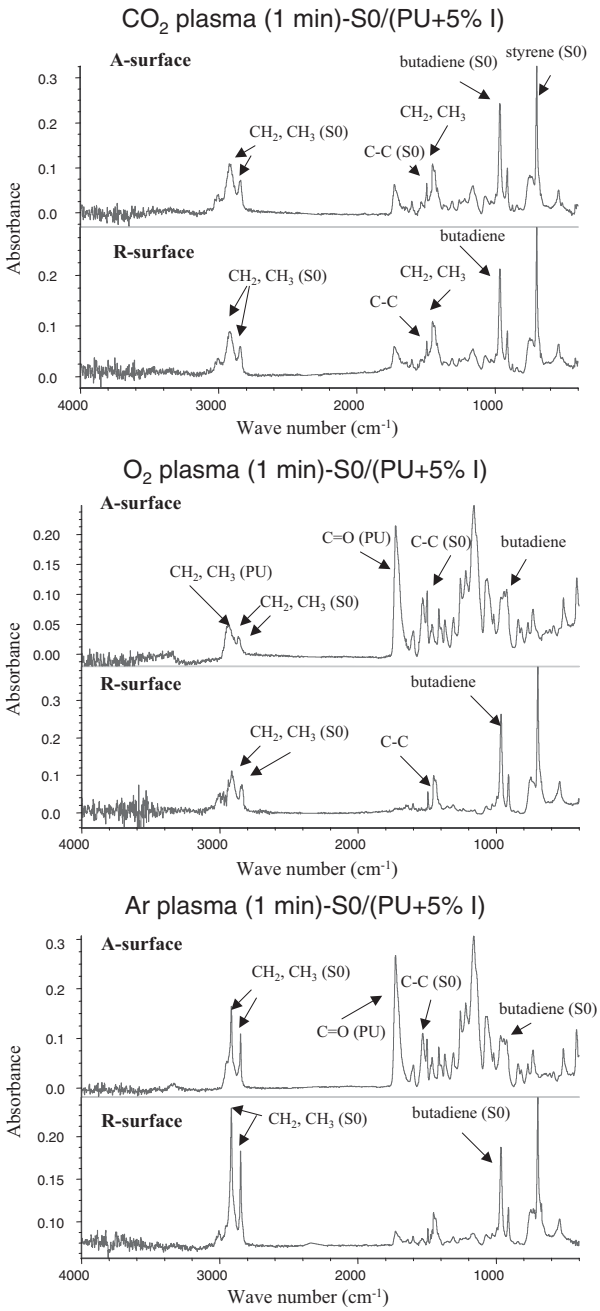

Figure 10 (a) ATR-IR spectra of the failed surfaces after T-peel test of CO_2 plasma treated S0 rubber (1 min)/PU adhesive joints. (b) ATR-IR spectra of the failed surfaces after T-peel test of O_2 plasma treated S0 rubber (1 min)/PU adhesive joints. (c) ATR-IR spectra of the failed surfaces after T-peel test of Ar plasma treated S0 rubber (1 min)/PU adhesive joints.

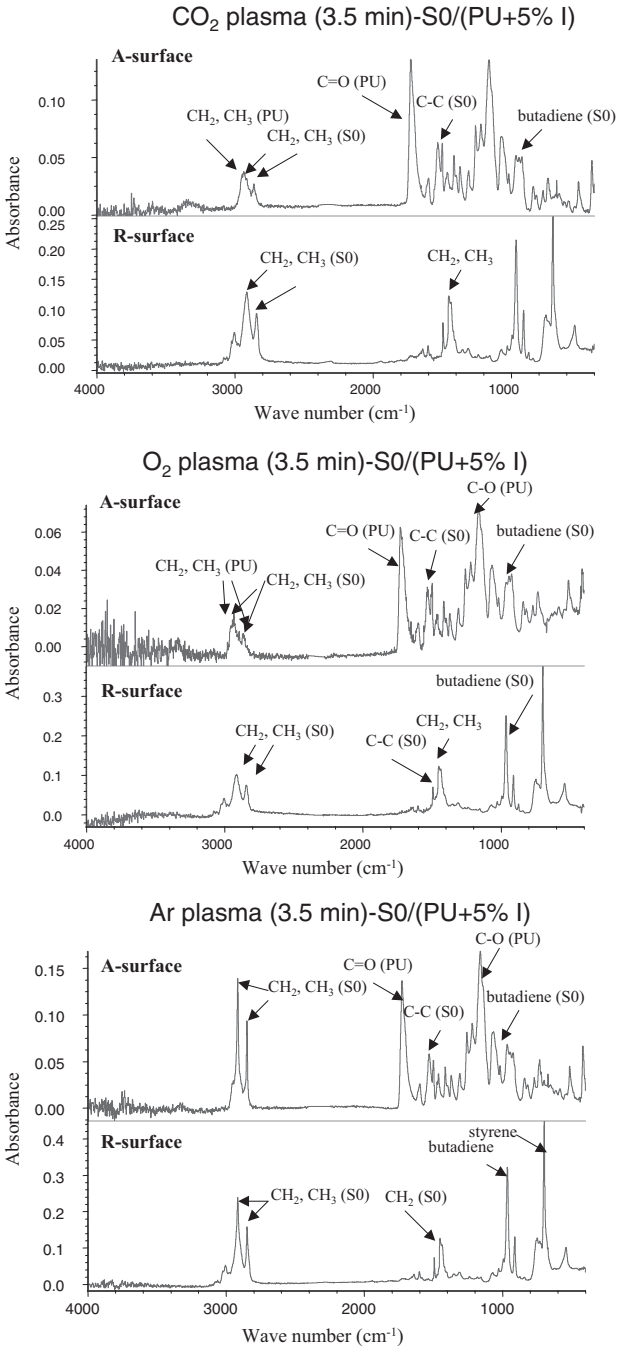

Figure 11 (a) ATR-IR spectra of the failed surfaces after T-peel test of CO_2 plasma treated S0 rubber (3.5 min)/ PU adhesive joints. (b) ATR-IR spectra of the failed surfaces after T-peel test of O_2 plasma treated S0 rubber (3.5 min)/PU adhesive joints. (c) ATR-IR spectra of the failed surfaces after T-peel test of Ar plasma treated S0 rubber (3.5 min)/PU adhesive joints.

The increase in the length of plasma treatment of S0 rubber did not affect the peel-strength values but modified the loci of failure of the joints. Thus, the treatment of the S0 rubber with CO_2 or O_2 plasmas for 3.5 min produced a mixed failure (mainly adhesion) (Figs. 11 (a) and (b)). This is consistent with the ablation of the oxidized outermost rubber surface produced by both the O_2 and the CO_2 plasmas. However, the Ar plasma treatment of S0 rubber for 3.5 min shows a failure mode somewhat different from those produced by O_2 and CO_2 plasmas. A mixed failure mainly cohesive in a thin rubber surface layer is observed in Fig. 11 (c) (rubber and PU absorptions are present on the A-surface while mainly rubber absorption is observed on the R-surface (Fig. 11 (c)). Therefore, the reduced mechanical properties of this thin crosslinked rubber layer, produced by an extended Ar plasma treatment, determines the failure of the joint.

14.4 Conclusions

The Ar, CO_2 and O_2 plasma treatments produced an increase in peel-strength values of the S0 rubber towards a PU adhesive due to improved wettability, chemical and morphological modifications. Ar plasma created polar moieties on the S0 rubber surface and a consequent increase of the polar component of the surface energy. On the other hand, CO_2 and O_2 plasma treatments produced ablation of the oxidized outermost S0 rubber surface.

Short plasma treatment times are enough to produce adequate T-peel-strength values and a cohesive failure was obtained in the joint produced with CO_2 plasma treatment for 1 min. The increase in the length of the CO_2 plasma treatment or the use of other plasmas (irrespective of the length of treatment) did not affect the peel-strength values but did affect the loci of failure of the joints. Thus, ablation was not produced with Ar plasma and the failure of the joints was located within a crosslinked oxidized rubber surface. CO_2 and O_2 plasma treatments removed the oxidized thin rubber layer and a mixed failure (mainly adhesion) was produced.

Acknowledgements

Financial support from CICYT (project MAT 2002-02463) and COST 527 Action of the European Commission are gratefully acknowledged.

References

[1] C.R. Wilder, "Thermoplastic Styrene Block Copolymers" in "Handbook of Elastomers. New Development and Technology". A.K. Bhowmick, H.L. Stephens (Eds), Wiley, NY, 1988.

[2] R.F. Wegman, Surface Preparation Techniques for Adhesive Bonding, Noyes Publications, pp. 141–143, Park, 1989.

[3] M.D. Ellul, D.R. Hazelton, *Rubb. Chem. Technol.* **67(4)**, 582–601 (1994).

[4] M.M. Pastor-Blas, M.S. Sánchez-Adsuar, J.M. Martín-Martínez, *J. Adhes.* **8(10)**, 1093–1114 (1994).

[5] M.M. Pastor-Blas, J.M. Martín-Martínez, J.G. Dillard, *Surf. Interf. Anal.* **26**, 385–399 (1998).

[6] M.M. Pastor-Blas, T.P. Ferrándiz-Gómez, J.M. Martín-Martínez, *Surf. Interf. Anal.* **30**, 7–11 (2000).

[7] A.B. Ortíz-Magán, M.M. Pastor-Blas, T.P. Ferrándiz-Gómez, C. Morant-Zacarés, J.M. Martín-Martínez, *Plasmas Polym.* **6(1,2)**, 81–105 (2001).

[8] On-line National Institute of Standards and Technology, NIST, Atomic Spectra Database: http://physics.nist.gov/cgi-bin/AtData/main_asd

[9] D.K. Owens, R.C. Wendt, *J. Appl. Polym. Sci.* **13**, 1741–1752 (1969).

[10] H.R. Thomas, Theoretical and Experimental Binding Energies for Organic Polymers. Xerox Webster Research Center (Ed.), Webster, NY, 1980.

[11] S.G. Abbot, D.M. Brewis, N.E. Manley, I. Mathieson, N.E. Oliver, *Int. J. Adhes. Adhesives* **23**, 225–230 (2003).

[12] R. Alfonsetti, L. Lozzi, M. Passacantando, P. Picozzi, S. Santuci, *Appl. Surf. Sci.* **70–71**, 222 (1993).

15
Low-temperature Plasma Treatment of Dry Empress-Tree Seeds

N. Puač, Z.Lj. Petrović, S. Živković, Z. Giba, D. Grubišić and A.R. Đorđević

Abstract

Seeds of *Paulownia tomentosa* were treated in low-pressure nonequilibrium RF discharges previously used for treatment of polymers and wool fibers (wool fabrics). The reactor was designed in such a way to minimize the energy of ions that hit the surface exposed to the plasma. Special probes were designed to monitor the voltage and current immediately before the discharge and the power was calculated from these measurements. Our goal was to determine the influence of glow-discharge parameters (power given by a RF power supply, pressure and treatment time) on germination of seeds and to find the optimum procedure for plasma treatment. Treatments were carried out in air and argon plasma. After determining the optimal plasma-treatment conditions, pH values of the treated samples under these conditions were measured. The results strongly indicate formation of reactive nitrogenous compound(s) at the surface that were already shown to improve germination.

15.1
Introduction

Interest in plasma treatment of biological systems has grown recently. Partly, the motivation is to develop new medical techniques as plasma offers some possibilities for inducing certain processes with minimum damage to the living tissue [1]. The other related issue is the treatment of organic materials, such as textile fibers, which has become a technology in production in the last five years [2, 3]. Usually, such treatment is limited to changing the hydrophobic nature of the surface layer of the material. Similar effects are also sought in treatments of polymers [4–6], so similar techniques have been applied. In the case of seed treatment, usually those seeds covered by a hydrophobic layer may be easily treated to facilitate absorption of water and thus trigger the germination. However, a large class of seeds do not depend on a hydrophobic layer to trigger germination. In this paper we describe a plasma-chemical reactor, which has a system designed to sample voltage and current transients and obtain the power. We show how this reactor was applied to improve germi-

nation of a specific seed that is well studied and documented in the literature. Empress-tree seeds (*Paulownia tomentosa)* are triggered by light after imbibition in water. Since this process will depend on interaction of radicals from the plasma with the surface of the seed, a quite different mechanism of interaction of plasma with living matter may be illustrated in this case.

Low-temperature plasma treatment of seeds with low efficiency of germination is a promising option due to high efficiency and low consumption of power. Also, this treatment is environmentally friendly. Increasing the percentage of seed germination is very important for fundamental studies and for practical use. In addition, such studies may provide further understanding of biochemical and biophysical processes involved in seed germination.

15.2
Experimental Setup

A capacitively coupled plasma (CCP) reactor used for treatment of Empress-tree seeds was designed to operate at a frequency of 13.56 MHz in a highly asymmetric mode. The idea was to reduce the energies of ions that fall on one electrode. Thus the damage due to ion bombardment is minimal and the gas temperature is close to room temperature. This system was previously used for treatment of polymers and wool fibers [7].

The apparatus consisted of a constant RF power supply, matching box, vacuum pump, chamber, gas supply with appropriate pressure gauges, current and voltage probes, digital oscilloscope and a computer (see Fig. 1). In order to keep the reflected power to a minimum, the impedance was adjusted by tuning the matching box. With reduction of the reflected power, the power transmitted to the system increased.

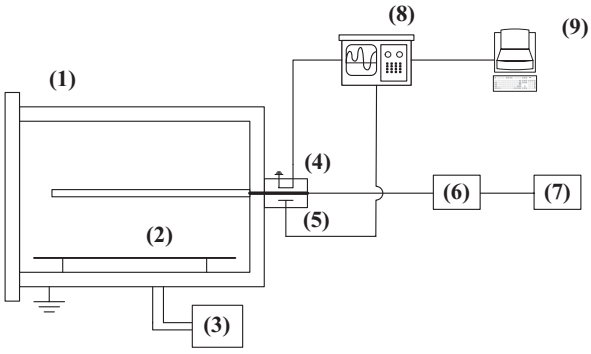

Figure 1 Experimental setup: (1) discharge chamber; (2) platform; (3) vacuum system; (4) current probe; (5) voltage probe; (6) matching box; (7) RF power supply; (8) digital oscilloscope; (9) PC.

The chamber used for seed treatments was a cylinder made of stainless steel of diameter of 37 cm and length of 50 cm. The central electrode, 14 mm in diameter, was the powered electrode, while the wall of the chamber was the grounded electrode. At the bottom of the chamber and clear of the sidewalls was a flat platform where uncovered Petri dishes with seeds were placed.

Glow-discharge treatment was carried out in capacitively coupled, radio-frequency air and argon plasma. Four Petri dishes with lots of 100 seeds were placed on the flat platform. Plasma treatments were carried out for different treatment times, pressures (100, 200 and 400 mTorr) and powers given by the RF power supply (50, 75, 100, 130 and 200 W). One control group was held under constant pressure of 200 mTorr without igniting the plasma. After glow-discharge treatments, the percentage of germination of treated seeds was determined.

The CCP reactor consisted of various electrical components (RF power supply, matching box, coaxial cables, etc.). Stability of the system was very important and had to be maintained throughout the whole treatment. Therefore, before processing each batch, the reflected power was checked and, if necessary, set to a minimum. Measurement of power input into the glow discharge was carried out by current and voltage probes.

15.2.1 Power Transmitted to the Plasma

One of the parameters for describing plasma conditions is the power dissipated in the plasma, which can be quite different from the value given by the meter at the RF power supply or measured at the matching box. To obtain the power dissipated in the plasma, it is necessary to know the instantaneous voltage and current at the powered electrode. Current and voltage probes were developed (see [8, 9] for preliminary reports) for obtaining the instantaneous voltage and current at the powered electrode. These probes are somewhat different from the derivative electrodes already proposed in the literature [10, 11].

Current and voltage waveforms were recorded for different powers given by RF power supply and then processed by using a numerical procedure. However, a displacement current occurs due to the capacitance between the feedthrough to the electrode and the ground shield. It is very important to eliminate this because this current can be quite large, even of the order of magnitude of the measured current. Usually, an LC shunt is used to remove the displacement current. However, this procedure is valid for the fundamental harmonic only and the correction for higher harmonics is performed numerically. Due to a large number of higher harmonics in our signals we avoided using the shunt and applied a numerical procedure for subtracting the displacement current for all harmonics. In order to achieve correct subtraction of the displacement current, we performed careful calibration of the system at different frequencies, which was the basis for correcting the voltage and current waveforms.

The voltage and current waveforms for different powers given by the RF power supply, after processing by numerical procedure, are shown in Fig. 2 and Fig. 3,

respectively. In Fig. 3, the current waveforms before subtracting the displacement current are also shown. In our case, the displacement current is about 30% of the measured current and this ratio stays constant with increasing of the power given by RF power supply (see Fig. 3).

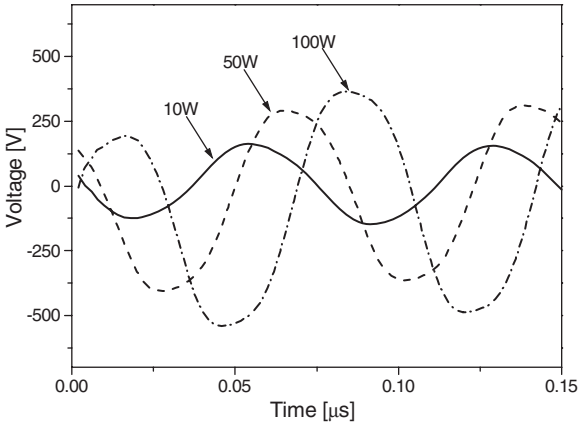

Figure 2 Voltage waveform obtained for three different powers of the RF power supply.

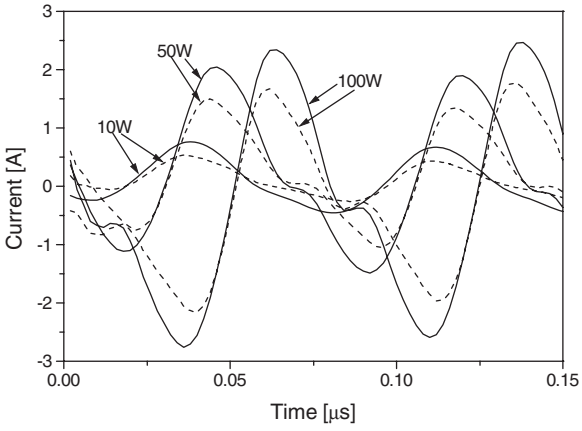

Figure 3 Current waveform obtained for three different powers of the RF power supply. Waveforms before (*i-solid line*) and after the subtraction of the displacement current (i_p*-dashed line) are shown.*

In Fig. 4, the volt–ampere (rms values) characteristic of the discharge is shown. We can see from the slope of this curve that our CCP discharge is operating in α mode where the resistivity of the discharge is relatively high, as opposed to the γ mode where the curve is almost constant.

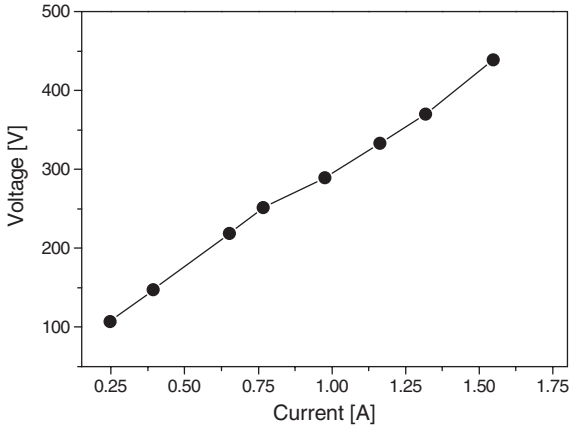

Figure 4 Volt–ampere characteristic of the RF discharge.

15.3 *Paulownia tomentosa* Steud

Seeds used in this experiment belong to the group of light-requiring seeds. Illumination of the samples with red light ($\lambda = 660$ nm) activates a photoreceptor called phytohrome that is responsible for the seed germination. On the other hand, light with wavelength of $\lambda = 730$ nm inhibits germination [12]. Three different batches of seeds were available, each with a different germination efficiency if untreated.

One of the main reasons for using Empress-tree seeds was its short process of germination, small dimensions (approximately 4×3 mm) and the fact that it is not liable to pathogen attack and infections. Also, the fact that characteristics of this seed are well known is very important. In particular, the effect of various factors, like temperature, light [13, 14] and electron acceptors [15] on *P. tomentosa* seed

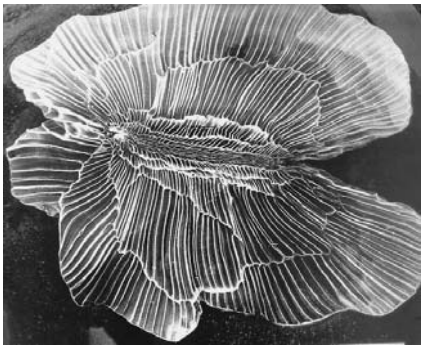

Figure 5 Electron scanning microscope photo of the *P. tomentosa* seed. Obtained with enlargement of 50×.

germination have been well documented. Additionally, the physiological effectiveness of NO-releasing compounds in seed germination was shown for the first time by using these seeds [16]. Figure 5 shows an electron scanning micrography of a *P. tomentosa* seed.

15.4 Results and Discussion

Seeds treated by plasma had a higher percentage of germination than untreated seeds in all cases except for very long exposition times. In Fig. 6, germination curves for plasma-treated and untreated seeds are shown. The untreated group of seeds was held under constant pressure of 200 mTorr for the same duration as the treated seeds. This group represented a control group in vacuum. The curve representing the vacuum control group shows that vacuum has almost no effect on seed germination.

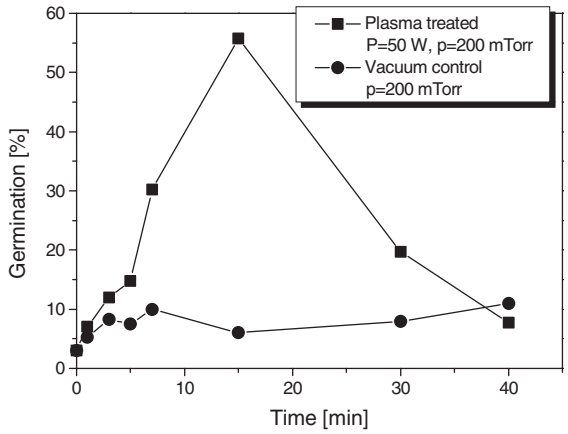

Figure 6 Efficiency of germination of plasma-treated seeds and vacuum control group

Figure 7 shows germination curves for constant powers of 100 W and 200 W and pressure of 200 mTorr. The percentage of germination for control groups for the samples used are 25% and 23% for powers of 100 W and 200 W, respectively. We can see that with the increasing power given by the RF power supply, the maximum of the germination curve shifts towards shorter times. The germination curve increases, until the maximum value is reached, and then, for longer treatment times and higher powers given by the RF power supply, the germination curve falls to zero. This implies that the overall effect of plasma is proportional to the integral effect of the flux of particles reaching its surface. Also, the ion bombardment damages the seed's surface and therefore after longer treatment times the seed cannot germinate.

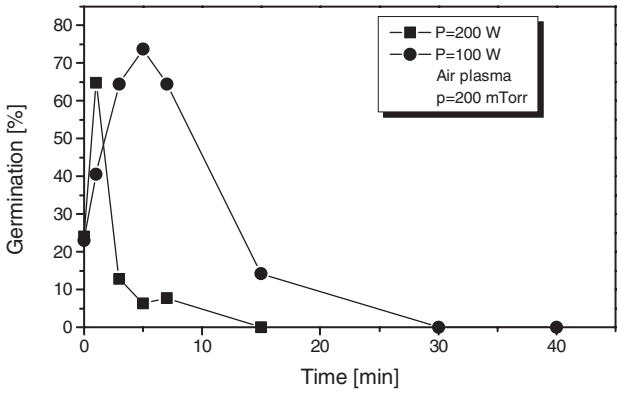

Figure 7 Efficiency of germination for two different powers obtained at the RF power supply and pressure of 200 mTorr. Feeding gas was air.

If we reduce the pressure (see Fig. 8), the germination curve widens and for the same power given by the RF power supply we have a larger range of times where the germination is increased. Control-group values for both pressures are 77.25% and the feeding gas was air. Inhibition in this case occurs only for the longest treatments times. For higher pressures, the germination curve is narrow, the maximum occurs for shorter treatment times and the inhibition is significant even for 5-min treatments (see Fig. 8). For higher pressures, one may expect higher fluxes arriving at the surface, especially fluxes of fast neutrals. However, the energies of particles would be smaller due to a larger number of collisions in the sheath. It appears, however, that in the range covered here the inhibitory effect is proportional to the pressure that may be associated mainly with the flux of particles and not with the combination of other plasma conditions (sheath potential, ion-collision frequency).

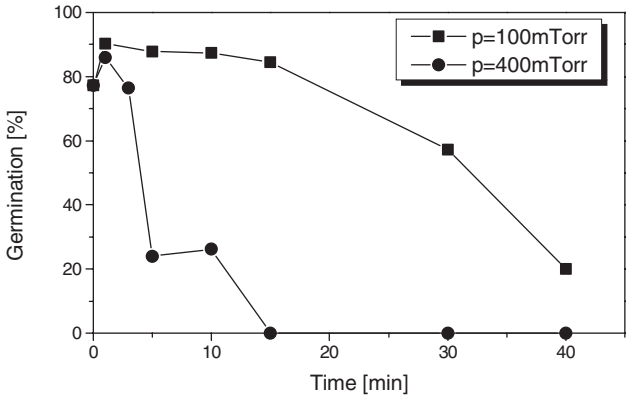

Figure 8 Efficiency of germination for two different pressures and power of 100 W at the RF power supply. Feeding gas was air.

In order to investigate the effect of UV irradiation on the germination of seeds, one set of samples (2 Petri dishes with lots of 100 seeds each) was covered by a glass cover (square shape, 10 cm wide, 30 cm long and 2.5 cm high) and was treated at the same time with another set of samples (2 Petri dishes with lots of 100 seeds each) which was uncovered. The flow of gas around the glass was not impeded very much and from the emission profile and design of the RF reactor we could make sure that the production of UV and other active particles in the very small volume of the Petri dish was negligible as compared to the bulk of the plasma volume. The curve representing the samples with the glass cover is wider. For longer treatment times the inhibition is smaller than for uncovered samples (see Fig. 9). The stimulation occurs in both cases and this fact indicates that, under present conditions, UV irradiation does not play a very important role in improving germination of the seeds in our experiment. For covered samples, the maximum of stimulation is somewhat smaller because the seeds are shielded by the glass and the total flux of particles reaching the surface was smaller than for uncovered samples. The maintenance of a relatively high improvement of germination percentage indicates the importance of active radicals from the plasma. This result is in accordance with a conclusion [17] based on experiments that UV radiation inhibits germination of a wide range of seeds over a wide range of wavelengths [18].

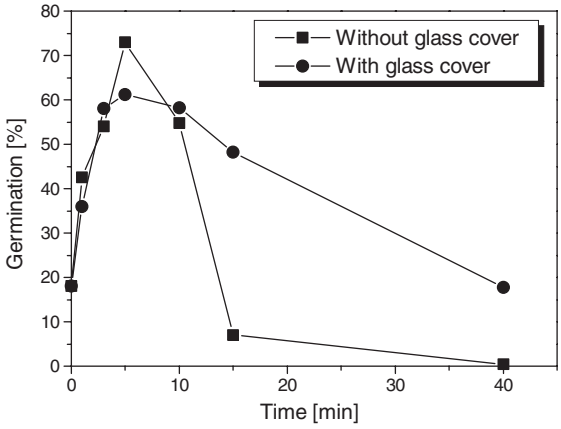

Figure 9 Efficiency of germination for a constant power of 100 W and a constant pressure of 200 mTorr. Feeding gas was air. Control group value: 18.25%

To test the importance of the active radicals, we also used argon as the feeding gas and the curves representing the data argon and air under the same conditions are shown in Fig. 10. Both curves are normalized to their control-group values. For argon, the percentage of germination for the control group was 59% and for the air it was 25%. The stimulation for argon is hardly noticeable; it is much smaller than that for the air. The small effect in argon may be due to the small amount of impurities or due to changes in the topography of the surface. The surface of seeds that

was subjected to the plasma treatment may either be modified so that it easily accepts radicals from the air, or may bond the radicals from plasma. It seems that the latter is the case, since the effect in argon is much smaller than that in the air, while one would expect argon ions to modify the surface quite efficiently.

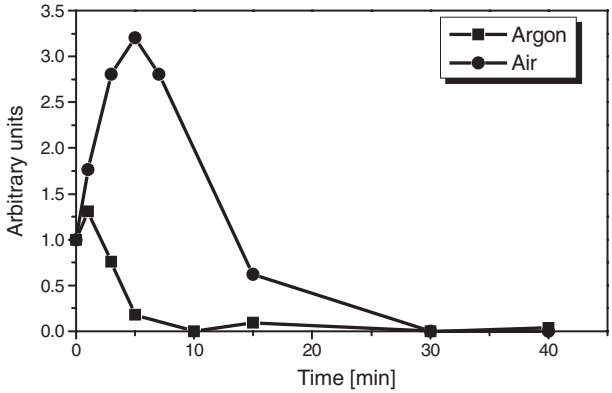

Figure 10 Normalized germination curves for air and argon at constant pressure of 200 mTorr and constant power of 100 W.

Thus, one may conclude that the plasma-produced radicals are the primary component that facilitates germination once the imbibition and light treatment are completed. Since the air is a mixture of gases and the predominant gaseous compound in this mixture is molecular nitrogen, the radicals that bond onto the activated surface are nitrogenous compounds. It was already shown that these compounds reduce the pH values of samples and play an important role in increasing the germination efficiency of the seeds [16, 19].

In Fig. 11, we show the pH values of samples treated by the air and argon plasmas for a power of 100 W and a pressure of 200 mTorr. The pH values that were

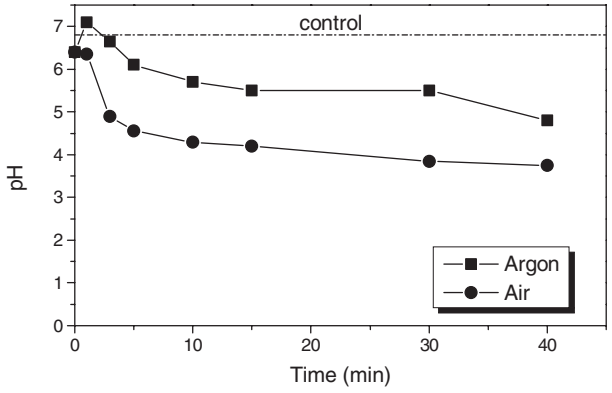

Figure 11 pH of water solution in which seeds were imbibed after air and argon plasma pretreatments.

measured one hour after the beginning of imbibition decreased rapidly with increasing treatment times. The pH of the samples treated by air plasma reduces from 6.8 (1-min treatment) to 3.8 (40 min). Based on this, one may expect that for longer treatment times the percentage of germination should be the largest. However, this is not the case due to the significant damage of seed and its germ by ion bombardment. The control value in Fig. 11 is the pH value of distilled water. In the case of treatment by the argon plasma, the decrement of pH is not so large and this concurs with the germination curve for argon plasma. It is especially small for the short times before the damage by ion bombardment starts the inhibition of germination.

Changes of pH pointed to the possibility that it was caused by the production of some water-soluble compound, probably acidic nitrogenous oxide. Nitrite anion was not detected in the incubation medium, by using the Greiss reaction. As plasma makes only a superficial modification, the total amount of chemisorbed radicals is very small and difficult to detect. However, there was a slight difference in the total amount of nitrogen between plasma-treated and untreated seeds obtained by elementary microanalysis (Fig. 12), which indirectly suggests generation and deposition of a bioactive nitrogenous compound.

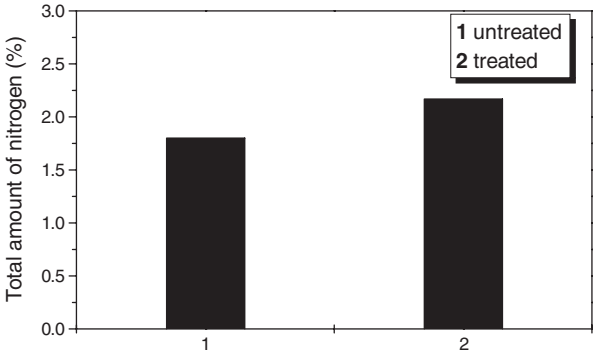

Figure 12 Total amount of nitrogen in *P. tomentosa* seeds. The results are obtained by using elementary microanalysis of whole seeds.

15.5 Conclusion

A plasma chemical reactor operating in asymmetric mode enabled treatment of dry seeds with stimulation of germination occurring for a broad range of operating conditions and treatment times. The power that was absorbed by the plasma was determined by using voltage and current probes located close to the powered electrode.

Dry seeds of *Paulownia tomentosa* were treated by the plasma and then imbibed and subjected to light that triggered the germination. In all cases, plasma treatment was able to improve germination though in the case of the argon plasma the

improvement was very small. However, for longer treatment times or higher particle fluxes, inhibition occurred. It appears that the plasma-produced radicals, most likely nitrogenous compounds, are the primary agent that facilitates the germination. This is supported by the fact that the effects of argon plasma are negligible in comparison with air-plasma treatment. At the same time the pH value of the imbibing solution of air-plasma-pretreated seeds gradually decreased, and depends on the duration of the pretreatment. Finally there is a small increase of the total amount of nitrogen at the surface of the air-plasma-treated seeds that is well within the uncertainty of the measuring technique.

In the present experiment we have an example of plasma-initiated chemical reactions at the surface of the seed that at a later stage stimulate the germination. Since the biochemical processes leading to germination of this seed are well known, it may be possible to identify the effect of plasma in this case. It also gives an indication of how biochemical processes may be induced or may occur in nature with the role of plasmas. Most other cases of seeds that were studied involved removal of the protection layer or one could argue that plasma removed the germination inhibitors from the seed coat. In the case studied here, the effect appears to be mainly biochemical.

Partially supported by MNZZS project No. 1478 and partially supported bei MNZZS project No. 1696.

References

[1] E. Stoffels, I.E. Kieft, J.L.V. Broers, F.C.S. Ramaekers, D.W. Slaaf, *Proc. ISPC 16 (International Symposium on Plasma Chemistry)*, Eds R. d'Agostino, P. Favia, F. Fracassi and F. Palumbo (2003) CD

[2] P. Jovančić, D. Jocić, M. Radetić, B. Tomčik, Z.Lj. Petrović, M.R. Julia and P. Erra, *European Microscopy and Analysis*, (2001) 5–7

[3] H. Thomas, M. Hedler, D. Labruier and H. Hocker, *Proc. 21st SPIG 2002 Soko Banja*, Eds. M.K. Radović and M.S. Jovanović (2002) 290

[4] C.M. Chan, T.M. Ko and H. Hiraoka, *Surf. Sci. Rep.*, **24**, (1996) 1–54

[5] B. Tomčik, D.R. Popović, I.V. Jovanović, and Z.Lj. Petrović, *J. Polym. Res.*, **8** (4) (2001) 259–266

[6] F. Denes, S. Manolache and R.A. Young, *J. Photopolym. Sci. Technol.*, **12** (1999), 27

[7] M. Radetić, D. Jocić, P. Jovančić, R. Trajković and Z.Lj. Petrović, *Textile Chem. Colorist Am. Dyestuff Rep.*, 32, (2000) 55–60

[8] N. Puač, A. Đorđević and Z.Lj. Petrović, *Proc. Appl. Phys. Serbia APS SANU*, Eds S. Koički, N. Konjević, Z.Lj. Petrović and Đ. Bek-Uzarov (2002) 249.

[9] N. Puač, A. Đorđević and Z.Lj. Petrović, *Proc. 21st SPIG 2002 Soko Banja*, Eds M.K. Radović and M.S. Jovanović (2002) 490–493.

[10] M.A. Sobolewski, *J. Res. Natl. Inst. Stand. Technol.* **100**, (1995) 341.

[11] P.J. Hargis et al., *Rev. Sci. Instrum.* **65** (1994) 140.

[12] D. Grubišić and Konjević, R. *Planta*, **181**, (1990) 239

[13] D. Grubišić, *Arch. Biol. Sci.*, **27**, (1975) 7

[14] D. Grubišić, R. Konjević, *Physiol. Plant.*, **86**, (1992) 479

[15] Z. Giba, Grubišić, D. and R. Konjević, *Physiol. Plant.*, **91**, (1994) 290

[16] Z. Giba, D. Grubišić, S. Todorović, L. Sajc, Ž. Stojaković, R. Konjević, *Plant Growth Reg.* **26**, 175 (1998)

[17] C. Wagne, *Physiologia Plantarum*, **19**, (1966) 128

[18] C.F. Musil, R.J. Newton, J.M. Farrant, *Plant Ecology*, **139** (1), (1998) 25

[19] Z. Giba, D. Grubišić, S. Todorović, R. Konjević, *Yugoslav. Physiol. Pharmacol. Acta*. **34**, No. 2, 447 (1998) (also available on web site http://www.ippa.bg.ac.yu)

16
Ion-induced Chemical and Structural Modification of Polymer Surfaces

G. Suchaneck, M. Guenther, G. Gerlach, K. Sahre, K.-J. Eichhorn, B. Wolf, A. Deyneka, L. Jastrabik

Abstract

Thin polymer films were irradiated with boron ions with energies from 50 to 180 keV and irradiation doses between 10^{13} and 10^{16} B^+/cm^2. For comparison, plasma modification was performed in NH_3 and N_2O low-pressure gas discharges. A complex investigation of chemical changes in the surface regions was carried out using attenuated total reflection (ATR)-FTIR spectroscopy, Raman spectroscopy and X-ray photoelectron spectroscopy (XPS). Optical properties were probed by spectroscopic ellipsometry. Hardness and elastic modulus profiles have been measured by a depth-sensing low-load indentation technique. Additionally, the surface and bulk conductivities of modified polymer films were determined.

It could be shown that the increase of ion fluence leads to a partial destruction of the imide, aromatic and sulfone groups. The effective modification depth estimated from the hardness, Young's modulus and refractive index depth profiles was 250–300 nm at an ion energy of 50 keV and 400–450 nm at an ion energy of 180 keV. In the case of low-pressure plasma treatment, the chemical modification of the polymer bulk extends only a few monolayers and is determined by the electronic-process-related linear energy transfer (LET). The destruction of chemical bonds under ion bombardment leads to the formation of new amorphous and graphite-like structures, which increase the modified surface film conductivity, the optical absorption index, the density, and the sensitivity of these polymer films to moisture uptake, and decrease the refractive index anisotropy and the Freundlich's coefficient of the moisture-uptake behavior.

16.1
Ion Modification of Polymers

Polymer thin films placed into a plasma or exposed to an ion beam are affected by a flux of charged particles. Thereby, ion bombardment of polymers significantly changes the chemical structure of the polymer surface including the degradation of chemical bonds, a crosslinking of polymer chains, and variations in the free volume and free-volume distribution of the polymer matrix. The specific property changes

depend on the parameters of the impinging ions, for instance the particular ion species, their energy, and total number of ions that impact the surface.

16.1.1 Modification of Polymer Properties

There are four possible mechanisms of energy transfer from an energetic incident ion to the atoms of the polymer film [1]: (i) electronic excitation, (ii) nuclear displacement, (iii) phonon decay, and (iv) plasmon decay. Electronic excitation includes the ejection of electrons and formation of excited states. This may cause a chemical bond to break, when the excited energy localizes in a particular chemical bond. Even this process is mainly responsible for the formation of radicals, the emission of volatile molecules and crosslinking, and largely responsible for changes in optical density, electrical conductivity and hardness [2–4]. Also, the elastic modulus of the polymer is directly proportional to the crosslink density, i.e., inversely proportional to the average molecular weight between crosslinks [5]. On the other hand, nuclear displacement is the major cause of chain scissions.

16.1.2 Energy Transfer from Ions to Polymer

The interaction of light ions like boron with a polymer is characterized by a high fraction of electronic excitation (ionization), a low fraction of nuclear displacement, and a long trajectory range. The energy deposition of one ion per unit path length is described by the linear energy transfer (LET) which in the case of boron ions in polyimide amounts to about 200 eV/nm [6]. This energy diminishes in a very short time (10^{-14} to 10^{-13} s) in a small volume surrounding the ion track.

Radio-frequency (r.f.) plasma-surface modification has been used successfully since the 1970s for polymer-surface modification [7]. Ion implantation and low-pressure plasma surface treatment provide similar ion fluxes to the polymer surface. However, due to large differences in ion energy, the energy flux seen by the polymer surface is very different. The ion energy determines the penetration depth, while in the case of ion implantation, the energy flux may be changed by selecting the irradiation dose. Low-pressure plasma treatment causes additional chemical attack on the polymer surface that depends on the nature of the involved species and that masks the ion-induced structure changes.

16.1.3 Ion-modified Polymers for Sensor Application

Ion implantation, i.e., the exposure to energetic ions penetrating the surface, improves the surface properties of polymers, such as electrical conductivity, hardness, chemical and wear resistance, and reduce friction [1,8–13]. The determination of the effective modification depth after ion implantation is essential for thin-film applications. For this purpose, the depth-sensing nanoindentation technique can be

used [14]. Sensor applications comprising surface ion-implanted polymer thin films are precise temperature sensors [15,16] and infrared bolometers [17]. Ion implantation has been applied also to modify polymer surfaces for improving their biocompatibility [18].

Usually, polymer surfaces suffer from uncontrolled absorption of moisture and other gas molecules. This can lead to significant changes in the electrical and mechanical properties of the material, which might have a negative effect on the long-term stability of the devices. On the other hand, bimorphic gas sensors make use of gas-absorption-induced swelling of polyimide and polyethersulfone thin films [19–22]. Gas uptake and selectivity to a partial gas are significantly increased by ion implantation [2,23,24] and plasma surface treatment [25], both forming microvoids with a narrow size distribution in the polymer matrix.

16.1.4 Objective of this Work

In this work, the influence of ion-induced surface changes on both polymer structure, mechanical and electrical properties, and moisture uptake of polymers and their dependence on ion energy and ion fluence are investigated. For a better understanding of the pure effect of ion bombardment, boron ions were implanted into similarly deposited polymer films due to their high ionization linear energy transfer (LET), low displacement LET, and a long trajectory range. The results are compared with those of plasma-surface modification.

First, a detailed study in the characterization of boron ion-induced molecular modifications of polymer films using methods of vibrational spectroscopy (FTIR- and Raman spectroscopy), XPS and spectroscopic ellipsometry is presented. The combination of these analytical methods gives a complete picture of the main processes driving polymer modification. Secondly, the hardness and the Young's modulus depth profiles within the polymer films are determined using low load indentations with partial unloading. In addition, surface acoustic wave (SAW) techniques have been used to determine the density and Young's modulus of the polymer film. Thirdly, the electrical properties dependence on dose and energy of implanted ions were determined. Fourthly, the swelling behavior in dependence on relative humidity was investigated using a bimorphic humidity sensor. The influence of ion-beam-induced modification on the moisture uptake was characterized by Freundlich's model of an exponential relationship between maximum moisture uptake and ambient relative humidity.

16.2 Experimental

16.2.1 Sample Preparation

A range of commercially available polymers was selected for the investigations (Table 1). The polyimides (PI2808: PMDA-ODA; PI2566: 6FDA-ODA; PI2611: BPDA-PPD) and polyethersulfone (PES UE2010) chosen for this study are the same as those widely used in the semiconductor industry.

Table 1 Polymers used for investigation

Name, formula	Structural formula	Polymer class	Manufacturer
PI2808 $[C_{22}H_{10}N_2O_5]_n$	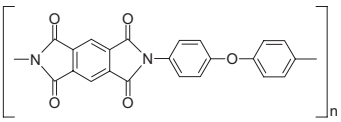	Polyimide	DuPont
PI2566 $[C_{31}H_{14}N_2O_5F_6]_n$	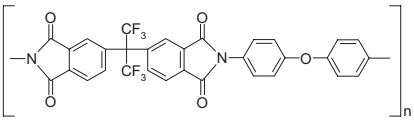	Polyimide	DuPont
PI2611 $[C_{22}H_{10}N_2O_4]_n$	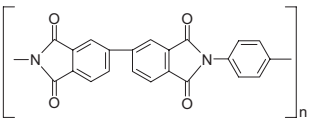	Polyimide	DuPont
UltrasonE2010 (abbr: UE2010) $[C_{12}H_8O_3S_1]_n$	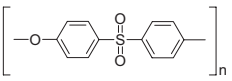	Polyethersulfone	BASF

The samples were deposited by spin coating of polyimide precursor solutions (polyamic acids / N-methyl-2-pyrrolidone) or polyethersulfone solution (20 wt% PES / N-methyl-2-pyrrolidone) onto 3-inch silicon wafers. Prior to coating, the thermal oxide layer on the silicon wafers was modified with a coupling agent. The polymer films were soft-baked at 90 °C for 20 min to remove the solvent and then cured in nitrogen at 400 °C for one hour. The chemical reaction completion was checked by FTIR spectroscopy. The final film thickness was typically between 1.0 and 3.5 µm.

The polymer films were modified by ion-beam implantation using boron ions with several energies (50, 130, and 180 keV) and irradiation doses (10^{13} to 10^{16} cm^{-2}). Ion implantation was performed at the Forschungszentrum Rossendorf, Germany. The boron ions are generated from BF_3 molecules, filtered and precisely

directed onto the target spot by magnetic deflection inside the implanter. The range of boron ions and the related doping profile were calculated by means of public-domain software SRIM-2000.39 [26].

Low-pressure NH_3 and N_2O plasma treatment of the deposited polymer films was performed in a Plasmalab 80^+ PECVD chamber (Oxford Plasma Technology) at a pressure of 65 Pa, a r.f. power of 20 W at 13.56 MHz, and flow rates of 200, 40 and 100 sccm, respectively. For dual-frequency treatment, two r.f. power supplies were used in a switched mode: A high-frequency unit (13.56 MHz) for a soft surface modification and a low-frequency unit (100 kHz) to enhance ion bombardment on the as-modified film surface. The low-frequency power was varied within 20 to 200 W, whereas the r.f. power was kept constant at 20 W. The duration of both the high-frequency and the low-frequency cycles were ten seconds. This allowed investigation of the influence of ion bombardment on plasma-surface modification.

The typical plasma treatment was performed for three minutes at a substrate temperature of 25 °C. Beyond that time, the thickness of the modified layer is still increasing, but the results are becoming more inconsistent.

16.2.2 Evaluation of Structural Changes

Changes in chemical composition by surface modification were investigated by X-ray photoelectron spectroscopy (XPS) using the MgK_α (1253.6 eV) radiation of a Physical Electronics PHI 5702 electron spectrometer. Measurements were performed within one week for samples stored in clean air. The spectra were recorded at a take-off angle of 45° with respect to the sample surface. The sampling depth of this technique amounts to about 3 nm. The surface composition was determined by calculating the peak areas of high-resolution XP spectra. The atomic element composition was estimated using tabulated sensitivity factors. All XPS peaks were referenced to the C1s hydrocarbon signal at a binding energy of 285 eV. The core-level peaks have been analyzed by means of a Gauss–Lorentz fitting computer program with background subtraction. Curve-fitting quality was evaluated by chi-convergence. The position of the fitted peaks were determined with an accuracy of about 0.1 eV.

The chemical structure of the modified polymer layers was additionally investigated by attenuated total reflection (ATR)-FTIR spectroscopy and by Raman spectroscopy. ATR measurements were carried out on a Bruker spectrometer IFS 66 with a "Golden Gate" unit (Ge crystal) for 200 scans with a resolution of 4 cm^{-1}. In this case, the penetration depth is much larger (166 to 1106 nm at 4000–600 cm^{-1}). The ATR deconvolution analysis was performed assuming Gaussian functions for the vibration modes. The assignment of the IR bands was taken from the literature [27]. Raman spectroscopy was performed using a sapphire probe in a HoloProbe 785 equipment (Kaiser Optical Systems, Inc.) at a laser wavelength of 785 nm for 20 scans with a resolution of 4 cm^{-1}.

To investigate larger penetration depths, refractive and absorption index spectra and the optical anisotropy of the films were calculated from the main ellipsometric

angles Δ and Ψ measured with a J. A. Woollam spectroscopic ellipsometer. Ten different angles of incidence allowed the calculation of refractive index depth profiles. The experimental data was analyzed with the software package WVASE32, which is based on least-squares regression analysis to minimize the differences between measured and calculated values.

Hardness and elastic modulus of polymer films were investigated by a Hysitron nanomechanical test equipment with Berkovich and cube-corner indenters. This instrument is attached to an AFM "Nanoscope" of Digital Instruments Corp. and measures force and displacement continuously. The load–displacement plot was used to determine the hardness and the Young's modulus according to the Oliver and Pharr method [28]. Depth profiles were determined using a sequence of loading–unloading cycles with incremental load increase from cycle to cycle.

In a complementary way, density and Young's modulus were determined by surface acoustic waves (SAW) technique as described in [29].

16.2.3
Evaluation of Moisture Uptake

The moisture uptake $c_S(\varphi)$ was determined as a value of the relative mass uptake within the polymer film of the polymer-coated silicon wafers. Using a completely enclosed precision balance, the measurement uncertainty amounted to about 20 µg under variable, tightly controlled ambient conditions with maximum deviations of $\Delta T = 0.5$ K and $\Delta\varphi = 2\%$ rh, respectively.

Moisture uptake depends on the mass of the polymer itself. So it is useful to relate the mass of the absorbed water to the mass of the dry polymer. Thus, a saturation concentration c_s can be defined as:

$$c_S(\varphi, T) = \frac{m_{\text{water}}(\varphi,T)}{m_{\text{dry polymer}}} = \frac{m_{\text{coated wafer}}(\varphi,T) - m_{\text{coated wafer}}(\varphi = 0\ \%\ rh)}{m_{\text{coated wafer}}(\varphi = 0\ \%\ rh) - m_{\text{uncoated wafer}}}. \quad (1)$$

The saturation concentration reaches its maximum $c_{s,max}$ at 100% rh. By using elaborate calibration procedures, repeated measurements, and polynomial data analysis (to minimize stochastic errors), we were able to determine the saturation concentration with a reduced uncertainty of about 15% for the absolute c_S value. This uncertainty is dominated by the relatively large systematic part in weighing the dry polymer. By calculating differences between successive measurements, uncertainties reduce to a few per cent. Besides, this derivation does not affect the general shape of the c_s vs. φ relationship.

16.2.4
Electrical Measurements

Volume and surface conductivity measurements were performed using electrode configurations consisting of the evaporated NiCr bottom electrode, a press measuring electrode and a guard electrode as described in IEC 93 [30].

16.3 Results and Discussion

16.3.1 Structural Changes

16.3.1.1 Polymer-surface composition

Table 2 summarizes the polymer-surface composition changes caused by ion implantation [3, 13] and low-pressure plasma treatment [25]. In the case of PES, the sulfone group in the near-surface area is reduced to a sulfide by ion bombardment [13]. For PI2566, C=O assigns the imide carbonyl group at 288.3 eV [3].

Table 2 Polymer-surface composition changes in dependence on surface treatment determined by XPS. ↑- increase, ↑↑ - strong increase, → independent of dose, ↗↘ increase followed by a decrease at higher doses, → ↗ increase only at higher doses

Elements, chemical bonds	PI2566[3]	PES[13]	PI2566 [25]	
	Ion implantation		Low-pressure plasma treatment	
	10^{14}–10^{16} B^+/cm^2		N_2O	NH_3
$C_{aromatic}$	↓↓	↓	↓	↓
C–C, C=C	↗↘	↑	↓	→
[O]	→ ↗	↓	↑	→
[N]	↓	–	↑	↑↑
S=O	–	↓	–	–
C–O	↑	–	↑	↑↑
C=O	↓	–	↓	↓↓
CF_3	↓	–	↓	↓
(O+N)/C	↓	–	↑↑	↑

Contrary to ion-beam modification, the (O+N)/C ratio at the surface increases after plasma treatment. Ellipsometry measurements give evidence that the increase of the (O+N)/C ratio is attributed to the formation of microvoids and the pick-up of nitrogen, oxygen, and moisture from the ambient atmosphere [31]. Obviously, oxygen and nitrogen are attached to radicals near the surface and in microvoids by plasma–polymer interactions. This leads to the obtained irreversible increase in oxygen and nitrogen content contrary to the discussed below reversible moisture uptake.

16.3.1.2 Polymer Bulk Composition

Furthermore, the ion-beam-induced modification of the chemical structure of inside the polyimide bulk was investigated by ATR. Practically no changes of the IR spectra were detected by ATR measurements of plasma-treated polymers because the modification is limited to a very narrow surface region [25]. For ion implantation, the spectra showed changes of the characteristic absorption bands of imide and aromatic groups at doses higher than 10^{15} B^+/cm^2. The intensities of the bands at 1776,

1720 (ν C=O), 1376 (ν C–N–C) and 1500 cm^{-1} (ν C=$C_{aromatic}$) were reduced because the imide and aromatic structures are partly destroyed. Simultaneously, a broad band in the region of 1550–1650 cm^{-1} is created by the formation of a graphite-like, carbon-rich amorphous structures at the surface. At doses higher than 10^{16} B^+/cm^2, new B–H, C≡C or C≡N bonds were formed as proved by the appearance of bands at 2331 cm^{-1} and 2208 cm^{-1} [1,32,33]. Additionally, the ATR spectra of PI2566 show the formation of CF=CF and CF=CF_2 bands at 1733, 1795–1780 cm^{-1} after ion implantation. Polyethersulfone films show also both a destruction of ν S–O bonds (1242, 1152 cm^{-1}) and a formation of a broad band of new carbonyl, olefinic and aromatic structures (1800–1550 cm^{-1}) at doses higher than 10^{15} B^+/cm^2. Table 3 summarizes the most important changes of the intensities of ATR absorption bands.

The formation of complex amorphous C–C structures was additionally proved by the appearance of an asymmetric broad band around 1500 cm^{-1} in the Raman spectra of PES films modified at 180 keV, 10^{16} B^+/cm^2 [13].

Table 3 Structural changes in polymers due to boron ion-beam modification determined by ATR measurements (doses 10^{15}–10^{16} B^+/cm^2)

Wave number cm^{-1}	Bond	PI2808	PI2566	PI2611	UE2010
1242, 1152	ν S–O				↘
1376	ν C–N–C	↘	↘	↘	
1487, 1579	ν C=$C_{aromatic}$	↘	↘	↘	↘
1550–1650	graphite	↑	↑	↑	↑
1650–1820, 1720, 1776	ν C=O	↘	↘	↘	↑
1733	ν CF=CF		↑		
1780–1795	ν CF=CF_2		↑		
2208	ν C≡C, C≡N	↑	↑	↑	
2331	ν B–H	↑	↑	↑	
2800–3000	ν C–H	↑	↑	↑	↑
3200–3700	ν O–H	↑	↑	↑	↑

↘ reduced ATR intensity; ↑ new bonds after ion implantation

16.3.1.3 Graphite-like Cluster Formation at the Polymer Surface

Ion implantation at high ion-energy fluxes destroys the anisotropic features of the refractive index at the surface of both polyimide [34–36] and polyethersulfone [13] films leading to its isotropization. This isotropization and the increasing values of their optical constants also give evidence of the above-mentioned formation of amorphous C–C structures due to the ion bombardment. The formation of graphite-like clusters enhances both optical absorption at the surface [3,25] and surface conductivity (see Sect. 3.3). In Fig. 1, the absorption index k at a wavelength of 670 nm is presented in dependence on the amorphous carbon fraction determined from the C 1s core-level XPS spectrum deconvoluted into Gaussian components. The relative quantity of each bonding component was estimated from the area it covers related to the total area of the C 1s spectrum. After ion bombardment, the low binding ener-

gy peak appears at 284.2 eV, in a position that is assigned to graphite-like, amorphous carbon (a-C) rings [10,37,38]. The intensity of this component increases with rising boron ion dose.

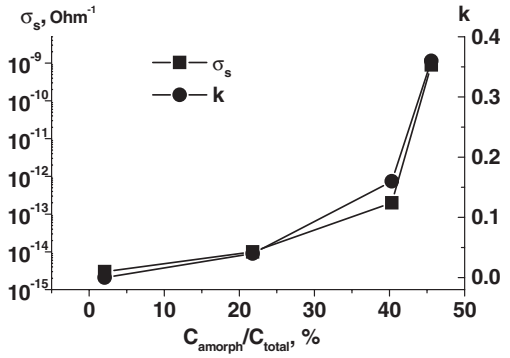

Figure 1 Surface conductivity σ_S and optical absorption index k in dependence on the amorphous carbon fraction.

A strong enhancement of k occurs when the fraction of amorphous-carbon clusters dispersed in a polyimide matrix reaches 40% at a dose of 10^{15} B^+/cm^2. This value corresponds to the percolation threshold for the appearance of three-dimensional hopping conductivity in the thin near-surface part of the polymer layer [1,39]. Therefore, a corresponding increase of surface conductivity is obtained too (Fig. 1). Beside the carbonization and partial graphitization, the radiation-induced crosslinking plays an important role in the enhancement of the electrical conductivity [1]. The crosslinking is responsible for the formation of three-dimensionally connected rigid networks and improves the carrier mobility, which is one of the most important parameters that governs the conductivity in implanted polymers.

An indication of the polyimide graphitization even by plasma surface treatment is given by the oscillator energy shift of the one-oscillator fit describing the spectral dependence of the refractive index. It shifts from 7.3 eV, which corresponds to the $^1A_{g1}$–$^1E_{u1}$ transition of benzene, to 1.75 eV, which is characteristic of π electrons bonded in more graphitic rings or delocalized over several rings [25]. At the same time, the surface layer forms that absorbs visible and UV light as mentioned above. It shows extinction coefficients as high as 0.25 to 0.40 after receiving 10^{16} ions/cm^2 [4]. Consequently, the polymer bulk is screened from the electron flux and the UV-radiation. Its chemical modification, i.e., crosslinking is then decisive determined by ion-energy dissipation via electronic linear energy transfer.

16.3.1.4 **Crosslinking inside the Polymer Matrix**

The degree of crosslinking of the polymer matrix can be estimated by the hardness, i.e. the resistance against mechanical penetration, and the Young's modulus, which is directly proportional to the crosslink density or inversely proportional to the average molecular weight between crosslinks [5]. Therefore, the mechanical properties

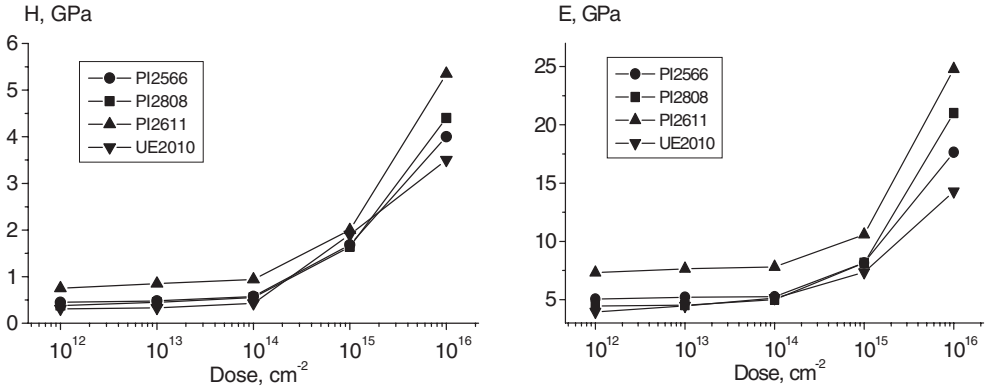

Figure 2 Hardness (a) and elastic modulus (b) of polyimide and polyethersulfone films after ion modification (ion energy 180 keV).

of both unmodified and implanted polymer surfaces were characterized by the low-load nanoindentation technique. The load–unload curves for the virgin PI and PES layers show the typical shape of most materials with elastic and plastic deformation. After irradiation the plastic deformation is reduced, whereas the elastic deformation is enhanced. Moreover, the radiation-induced crosslinking results in an enhancement of the hardness and the Young's modulus of the polymer layers up to an order of magnitude. Figure 2 shows this influence for polyimide and polyethersulfone layers. The hardness and Young's modulus values at 150 nm depth are used for comparison purposes, as was suggested in [11]. The hardness value is less influenced by subsurface deformation as well as by the substrate.

Hardness measurements in ion-implanted polymers are complicated since the hardness varies as a function of depth within the modified layer. This effect is induced by the distribution of ion-energy loss, which produces a depth-dependent variation in microstructure. The simplest way for mechanical-property profiling is to apply a varying load, resulting in different indentation depths (load-variation technique) [14]. However, when a film on a substrate is indented, both the film and the substrate deform elastically, even at small penetration depths of the indenter. Thus, the load-variation technique determines a composite (nonhomogeneous polymer film plus substrate) hardness, and the true hardness profile of the polymer film must be determined by complicated data processing. Therefore, an alternative technique was used where the layer was thinned stepwise by plasma etching in an oxygen atmosphere through a mask forming a staircase. The mechanical properties were determined for each stair using a small constant load. In this way, the influence of the coverage layer and the substrate on the measurement data is minimized.

The corresponding hardness depth profile was correlated with the ionization linear energy transfer (LET) mechanism (Fig. 3). The relationship between ionization LET and hardness was confirmed also by plotting LET values and nanohardness of polystyrene irradiated in [40] with up to 3.3×10^{13} He^+/cm^2 at 2 MeV ions versus irradiation depth. Thus, ionization is a significant factor for crosslinking that is respon-

sible for hardness increase [41]. Electronic excitations promote chemical reactions by creating various chemically active species and thus favor crosslinking. On the other hand, hardness is reduced with increased stopping since collision events are expected to cause more displacements and thus more molecular scissions.

In the next chapter, we give evidence that the modification depth in the case of low-pressure plasma processing is much less than the applied indentation depth of 30 nm. Therefore, secondary changes of the mechanical properties surface by oxygen low-pressure plasma exposure at the polymer do not affect the hardness measurements.

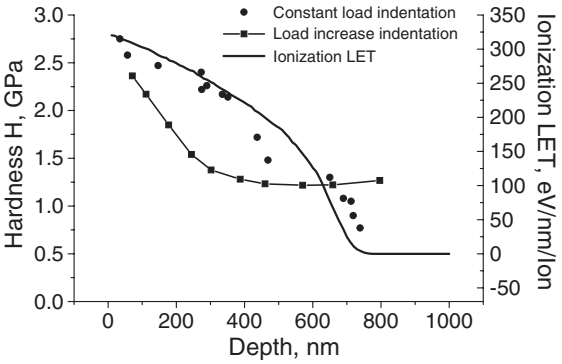

Figure 3 Hardness and ionization LET vs. depth of an ion-beam modified polyimide film.

16.3.1.5 **Thickness of the Ion-modified Surface Layer**

The thickness of the ion-modified surface layer is still an object of controversy [34,42]. Damage-depth profiling using a variable-energy positron beam results in a modification-depth of 700 to 800 nm (10^{15} B^+/cm^2 at 180 keV) that is in good agreement with SRIM (stopping and range of ions in matter) estimations [42]. The corresponding ellipsometric values are much lower. They amount to 200 to 400 nm (multilayer Cauchy model) [34] and 400 to 450 nm (refractive-index profiling) [4]. The latter data are in good agreement with hardness depth profiling [4].

The effective modification depth was also determined from hardness and Young's modulus using the load-variation technique where the load and the indentation, respectively, will become sequentially increased and decreased [14]. In this case, the modification depth could be obtained only for doses higher than 10^{15} ion/cm^2 at the point of inflection where the slope of the hardness or Young's-modulus profile changes its algebraic sign. The values obtained in this manner were in good agreement with ellipsometric measurements. In the case of low-pressure plasma treatment, ion energies of 100 to 500 eV result in maximal ion penetration depths of 1 to 3 nm that are too small to be measured optically. As a consequence, a refractive index was found that is independent of the film thickness and smaller than the values of untreated films. Thus, the ion impact on surface modification of low-pressure plasma treatment seems to be limited just to a few monolayers.

The disagreement between SRIM calculations and modification depths measured at high ion energy is likely caused by the assumption that the initial material properties do not change during ion bombardment. Since, hardness and Young's modulus change by half an order of magnitude, this assumption is no longer valid. Other parameters, such as stopping power, specific energy loss, etc., which strongly influence the trajectories of the ions inside the polymer, can be expected to be changed in a similar way. Consequently, the true penetration depth is less than the calculated one. The reason for the agreement between the modified layer thickness determined by damage-depth profiling using a variable-energy positron beam [42] and the calculated SRIM profile seems to be just fortuitous.

16.3.1.6 **Outgassing**

The modification of the polymer microstructure with energetic ions causes an emission of volatile molecules [1]. The polymer film thickness decreases due to the material loss as volatile decomposition products and due to polymer shrinkage at ion doses higher than 5×10^{14} B^+/cm^2 [4]. The loss of material is easy to detect since the intensities of the IR bands of the complete ATR spectra are reduced. The outgassing increases the density of the modified layer in comparison with the virgin polymer from an as-prepared value of 1.37 to 1.44 g/cm^3 up to 1.85 to 2.2 g/cm^3 (Fig. 4) [43]. The hardness, Young's modulus and density values at high irradiation doses reach those typical for a hydrogenated amorphous carbon [44,45].

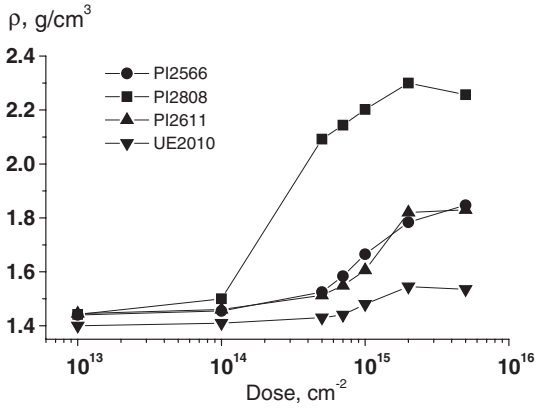

Figure 4 Impact of boron ion implantation on the density of polymer layers determined by a SAW technique [43].

16.3.2 **Moisture Uptake**

To characterize the morphology changes, the moisture uptake of surface-modified polymer films was compared to the virgin state. The investigation of the microphysical mechanisms of water uptake into thin unmodified polymer films showed that all

polymers interact with both ambient moist air and ambient gas molecules if the molecule size is smaller than the pore size of the polymer layer. Significant amounts of water are sorbed reversibly. This differs from the irreversible oxygen attachment to radicals obtained by XPS in the near-surface layer of low-pressure plasma treated samples. Moreover, the increase in sample mass by the auto-oxidation mechanism is expected to be small. The water uptake appears to take place through sorption in existing micropores; but no interactions with characteristic polar groups of the several polymers have been observed [46,47]. Experiments showed that each water molecule causes a volume expansion of about 0.01 to 0.02 nm^3, which is about half the effective volume of the water molecule. The maximum humidity-induced out-of-plane swelling of the ion-beam-modified polymer films is 2.5 to 5% at 95% rh [48]. Significant swelling is obtained only in a narrow implantation dose range of $0.3–2 \times 10^{15}$ B^+/cm^2 where the hydrophilicity increased by ion bombardment favors humidity adsorption. The swelling processes are very fast and completely reversible.

Figure 5 shows measured isotherms of the saturation concentration due to moisture uptake for the investigated polymers after ion implantation and plasma surface treatment. All curves are slightly nonlinear and can be described by Freundlich's formula [49]:

$$c_S(\varphi) = c_{S,max} \cdot \varphi^n, \tag{2}$$

where are $c_{S,max}$ is the maximum saturation concentration, φ is the relative humidity in the range between 0 and 1, and n is Freundlich's coefficient.

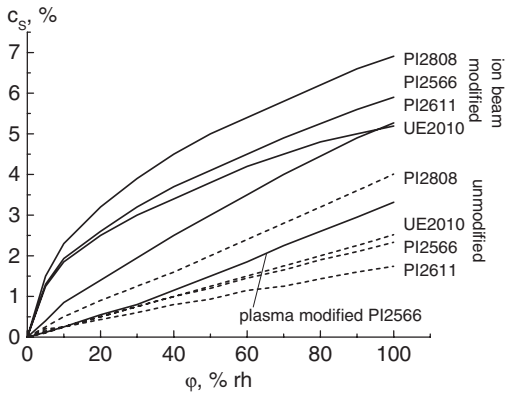

Figure 5 Isothermal saturation concentration c_s of unmodified (dashed lines) and modified (solid lines) polymer layers (ion implantation: 10^{15} B^+/cm^2, 180 keV; plasma treatment: NH_3, 1 min).

Because of the profile caused by surface modification inside the polymer layer, a mean saturation concentration $c_{S,mod}$ (φ) was defined, which characterizes the difference of c_S between modified and unmodified state only for the modified part of the polymer layer:

$$c_{S,mod}(\varphi) = \frac{1}{t_{mod}}\left[t_t \cdot c_{S,t}(\varphi) - (t_t - t_{mod})c_{S,0}(\varphi)\right], \quad (3)$$

where $c_{S,t}$ is the mean c_S value of the whole polymer layer (modified plus unmodified part), $c_{S,0}$ the c_S value of the unmodified or virgin polymer layer, respectively, t_t the total thickness of the whole polymer layer, and t_{mod} the thickness of only the modified part of the polymer layer.

Figure 6 (a) shows the increase of the saturation concentration in dependence on boron ion fluence. This rise appears at ion doses higher than 10^{13} B^+/cm^2 and goes up to a dose of 10^{15} B^+/cm^2. The achievable saturation decreases strongly at very high doses $>10^{15}$ B^+/cm^2. Here, the ion modification seems to form an amorphous passivating layer, which hinders or prevents the moisture diffusion into deeper layers of the polyimide film. This would also explain the smaller values of $c_{S,max,t}$ at the highest dose as well as the negative value of $c_{S,max,mod}$ compared to the unmodified polymer. In contrast to the ion dose, the energy of the implanted ions does not play such a role in moisture-uptake behavior. Figure 6 (b) shows the impact of the boron ion implantation on Freundlich's coefficient, which describes the linearity of the sorption process. It is seen that the $n_{c,t}$ value decreases slightly with increasing boron ion doses. By this, the growing saturation concentrations at higher ion levels, which means a higher sensitivity in the case of use in bimorphic humidity sensors, must be paid with a higher nonlinearity except for the polyethersulfone. For the UE2010 Freundlich's coefficient n reaches values of about 1.0 at boron ion doses of about 10^{14} B^+/cm^2 and smaller implantation energies.

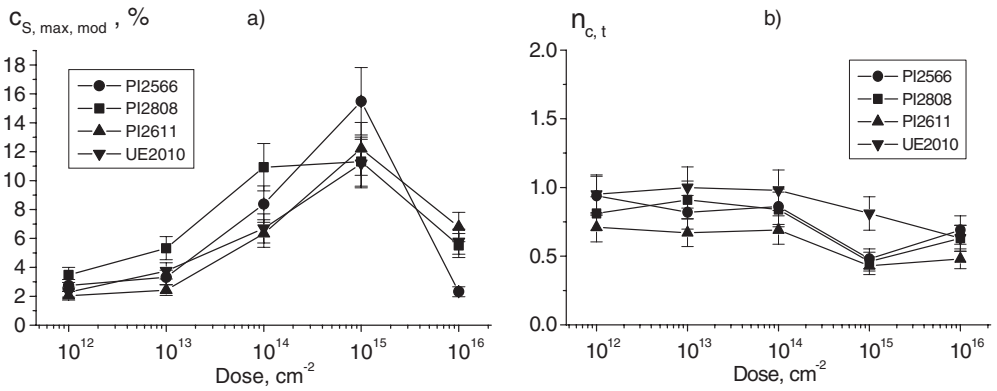

Figure 6 Impact of boron ion implantation (180 keV): (a) on the saturation concentration of the modified polymer area ($c_{S,max,mod}$; calculated from Eq. (3)); (b) on Freundlich's coefficient n.

16.3.3
Electrical Conductivity

With increasing boron ion fluence, the creation of amorphous and graphite-like structures is promoted, which increases the conductivity of the surface films by several orders (see Fig. 1). The surface conductivity rises from an as-prepared value of $10^{-15}\ \Omega^{-1}$ to a value of $10^{-8}\ \Omega^{-1}$ at a dose of $10^{16}\ B^+/cm^2$. Among several possible conduction effects in the ion-irradiated polymer films, two conduction mechanisms have most often been considered [1,50]: (i) One-dimensional variable-range hopping along the polymer chains. This can be excluded because of the extensive degradation of the polymer structure by ion implantation. (ii) Three-dimensional hopping or percolation between conducting islands that are separated by narrow insulating regions. As discussed in Sect. 16.3.1.3, a strong enhancement of the surface conductivity occurs when the fraction of amorphous carbon clusters dispersed in a polyimide matrix reaches the percolation threshold for the appearance of three-dimensional hopping conductivity in the polymer.

16.4
Conclusions

The results of the complex investigation of the microstructure and physical properties of polymer films modified by ion bombardment indicate that all surface changes strongly depend on the ion-flux parameters (energy and dose). The obtained surface restructuring by ion-beam implantation is to some extent similar to surface modifications by plasma exposure. By both techniques, carbonyl, sulfone, imide, and aromatic groups are partly destroyed and aromatic structures are degraded by hydrogen abstraction up to partial graphitization. The formation of graphite-like clusters enhances both surface conductivity and optical absorption at the surface. The optical anisotropy of the surface layer is lost and a visible and UV light absorbing surface layer is forming.

The radiation-induced structural changes result in an increase of the hardness and the Young's modulus of the polymer layers up to an order of magnitude. The effective modification depth determined from the hardness depth profiles is 250 nm at an ion energy of 50 keV and 420 nm at an ion energy of 180 keV. These values are in good agreement with refractive-index profiling by ellipsometry. This demonstrates that the SRIM calculation gives a correct estimation of the modification depth at 50 keV. Since the SRIM model assumes a constant density of the implanted material, higher ion enrgies lead to incorrect results, hence giving just an upper estimation. On the other hand, the penetration of ions during low-pressure plasma treatment is too small to generate a modification layer that could be seen by optical methods.

Contrary to ion-beam modification, the O+N/C ratio at the surface increases after plasma treatment and exposure to air due to the saturation of dangling bonds of radicals by nitrogen, oxygen, and moisture from the ambient atmosphere. This differs

from the reversible moisture uptake of ion-implanted polymer thin films that is caused by morphology changes. In the latter case, the moisture uptake was found to increase significantly upon ion dose, while Freundlich's coefficient n usually decreased. For very high implantation doses in the range of more than 10^{15} B^+/cm^2, the moisture uptake decreases strongly due the formation of the graphite-like surface layer, which hinders the moisture diffusion through the near-surface layer.

Acknowledgments

The authors gratefully acknowledge support of this work by the Deutsche Forschungsgemeinschaft (grants Ge 779/6-1,6-2, Ei 317/2-1,2-2), by Grants LN00A015 (Ministry of Education of the CR) and CZE00/002 (German Federal Ministry of Education and Research). The authors also acknowledge the support of sample preparation by AktivSensor GmbH and Forschungszentrum Rossendorf as well as the supply of polymers by DuPont and BASF. The authors thank Dr. Pigorsch of the Institute of Polymer Research Dresden e. V. for Raman measurements, Dr. Richter of Forschungszentrum Rossendorf e. V. for the ion implantation, Dr. M. Bertram (Dresden University of Technology Agency for Knowledge and Technology Transfer (GWT)) for XPS measurements and D. Schneider (Fraunhofer Institute for Material and Beam Technology, Dresden) for SAW measurements.

References

[1] E. H. Lee, in M. Ghosh, K. Mittal (eds) *Polyimides*, New York: Marcel Dekker, 1996, p. 471.
[2] M. Guenther, K. Sahre, G. Suchaneck, G. Gerlach, K.-J. Eichhorn, Surf. Coat. Technol. **142–144**, 482 (2001).
[3] M. Guenther, G. Gerlach, G. Suchaneck, D. Schneider, B. Wolf, A. Deineka, L. Jastrabik, Macromol. Symp. 212, 245 (2004).
[4] M. Guenther, G. Gerlach, G. Suchaneck, K. Sahre, K.-J. Eichhorn, B. Wolf, A. Deineka, L. Jastrabik, Surf. Coat. Technol. **158–159**, 108 (2002).
[5] A. Charlesby, Phys. Chem. **40**, 117 (1992).
[6] M.B. Lewis, E.H. Lee, Nucl. Instrum. Methods Phys. Res. **B69**, 341 (1992).
[7] N. Inagaki, S. Tasaka, K. Hibi, J. Polym. Sci. Polym. Chem. **30**, 1425 (1972).
[8] T. Venkatesan, S. R. Forrest, M. L. Kaplan, C. A. Murray, P.H. Schmidt, B. J. Wilkens, J. Appl. Phys. **54**, 3150 (1983).
[9] B. Wasserman, Phys. Rev. **B34**, 1926 (1986).
[10] G. Marletta, C. Oliveri, G. Ferla, S. Pignatoro, Surf. Interface Anal. **12**, 447 (1988).
[11] E. H. Lee, Y. Lee, W. C. Oliver, L. K. Mansur, J. Mater. Res. **8**, 377 (1993).
[12] G. Gerlach, M. Guenther, G. Suchaneck, K. Sahre, K.-J. Eichhorn, A. Deineka, L. Jastrabik, Mater. Res. Soc. Symp. Proc. **661**, KK2.8 (2001).
[13] K. Sahre, K.-J. Eichhorn, F. Simon, M. Guenther, G. Suchaneck, G. Gerlach, Mater. Res. Soc. Symp. Proc. **672**, O8.18 (2001).
[14] G. Suchaneck, B. Wolf, M. Guenther, G. Gerlach, Mater. Res. Soc. Symp. Proc. **725**, P4.12 (2002).
[15] R. E. Giedd, J. Shipman, M. Murphy, Proc. MRS **147**, 377 (1989)
[16] D. Xu, X. Xu, S. Zou, Rev. Sci. Instrum. **63**, 202 (1992).
[17] US Patent 5 753 523, Nov. 21, 1994.
[18] H. Tsuji, H. Satoh, S. Ikeda, Y. Gotoh, J. Ishikawa, Surf. Coat. Technol. **103**, 1124 (1998).

[19] German patent DE 43 12 788 C2 April 24, 1993.
[20] G. Gerlach, K. Sager, Sens. Actuators **A43**, 181 (1994).
[21] US patent 5 563 341, June 7, 1995.
[22] R. Buchhold, A. Nakladal, G. Gerlach, M. Herold, G. Gauglitz, K. Sahre, K.-J. Eichhorn, Thin Solid Films **350**, 178 (1999).
[23] R. Buchhold, A. Nakladal, G. Gerlach, K. Sahre, K.-J. Eichhorn, G. Dlubek, In: *Transducers '99*, Digest Techn. Papers, Vol. 1, IEEJ, Sendai, 1999, p.230
[24] German patents DE 198 42 414 C1, Sept. 17, 1998; DE 198 53 732 C1, Nov. 23, 1998.
[25] G. Suchaneck, M. Guenther, B. Adolphi, G. Gerlach, K. Sahre, K.-J. Eichhorn, A. Deineka, L. Jastrabik, ISPC-15, **VI**, 2485 (2001).
[26] J. F. Ziegler, J. P. Biersack, and U. Littmark, *The Stopping and Range of Ions in Solids*. New York: Pergamon Press, 1996; F. F. Ziegler, *The Stopping and Range of Ions in Solids*, vols 2–6, New York: Pergamon Press, 1977–1985; and J. P. Biersack, and L. Haggmark, *Nucl. Instrum. Methods*, **174**, 257 (1980). See also: http://www.research.ibm.com/ionbeams/SRIM/SRIMINTR.htm.
[27] B. Smith, *Infrared Spectral Interpretation: A Systematic Approach*, Boca Rota: CRC Press, 1999.
[28] W. C. Oliver, G. M. Pharr, J. Mater. Res. **7**, 1564 (1992).
[29] D. Schneider, Th. Witke, Th. Schwarz, B. Schoeneich, B. Schultrich, Surf. Coat. Technol. **126**, 136 (2000).
[30] Standard IEC 93: *Methods of test for insulating materials for electrical purposes*. Volume *Resistivity and surface resistivity of solid electrical insulating materials* (1980).
[31] G. Suchaneck, M. Guenther, J. Sorber, G. Gerlach, K.-F. Arndt, A. Deineka, L. Jastrabik, Surf. Coat. Technol. **174–175**, 816 (2003).
[32] E. H. Lee, M. B. Lewis, P. J. Blau, L. K. Mansur, J. Mater. Res. **6**, 610 (1991).
[33] D. Xu, X. L. Xu, G. D. Du, R. Wang, S. C. Zou, Nucl. Instrum. Methods **B80/81**, 1063 (1993).
[34] K. Sahre, K.-J. Eichhorn, F. Simon, D. Pleul, A. Janke, G. Gerlach, Surf. Coat. Technol. **139**, 257 (2001).
[35] K.-J. Eichhorn, K. Sahre, M. Guenther, G. Suchaneck and G. Gerlach, Thin Solid Films 2003 (in print).
[36] K. Hinrichs, E.D. Tsankov, E.H. Korte, A. Roeseler, K. Sahre, K.-J. Eichhorn, Appl. Spectrosc. **56**, 6, 737–743 (2002)
[37] D. Xu, X. Xu, S. Zou, Appl. Phys. Lett. **59** (24), 3110 (1991).
[38] H. Song, O. J. Ilegbusi, Thin Solid Films **388**, 114 (2001).
[39] J. Davenas, G. Boiteux, Adv. Mater. **2**, 521 (1990).
[40] G. Rao, L. Riester and E.H. Lee, in: *Beam-Solid Interactions for Materials Synthesis and Processing*, edited by D.C. Jacobson, D.E. Luzzi, T.F. Heinz and M. Iwaki (Mater. Res. Symp. Proc. **354**, Pittsburgh, PA, 1995) pp. 363–368.
[41] E.G. Lee, G.R. Rao, M.B. Lewis and L.K. Mansur, Nucl. Instrum. Methods **B74**, 326 (1993).
[42] G. Dlubek, F. Boerner, R. Buchhold, K. Sahre, R. Krause-Rehberg, K.-J. Eichhorn, J. Polym. Sci. **B38**, 3062 (2000).
[43] M. Guenther, G. Gerlach, G. Suchaneck, K. Sahre, K.-J. Eichhorn, V. Baturin, S. Duvanov, Nucl. Instrum. Methods Phys. Res. **B216**, 143 (2004).
[44] Y.Q. Wang, Nucl. Instrum. Methods **B161–163**, 1027 (2000).
[45] B. Schultrich, H.-J. Schiebe, G. Grandremy, D. Schneider, P. Siemroth, Thin Solid Films **253**, 125 (1994).
[46] R. Buchhold, *Bimorphe Gassensoren*, Dresden-Muenchen: Dresden Univ. Press, 1999.
[47] R. Buchhold, A. Nakladal, G. Gerlach, K. Sahre, M. Mueller, K.-J. Eichhorn, M. Herold, G. Gauglitz, J. Electrochem. Soc., **145**, 4012 (1998).
[48] K. Sahre, K.-J. Eichhorn, M. Guenther, G. Suchaneck, G. Gerlach, Anal. Bioanal. Chem **378**, 396 (2004).
[49] W. Kast, *Adsorption aus der Gasphase*, Weinheim: VCH, Weinheim, 1988.
[50] Y. Wang, S. S. Monite and L. B. Bridwel, J. Mater. Res., **8, 388 (1993).**

17
Plasma-Enhanced Fluorination of Nitrile Butadiene Elastomer: an XPS study

A. Tressaud, E. Durand, C. Labrugère

Abstract

This work is devoted to surface treatment of thin NBR nitrile gloves using plasma-enhanced fluorination in rf plasmas of fluorinated gases (CF_4, CHF_3). The mechanisms of fluorination of these co-elastomers are proposed on the basis of the assignment of the different components of the XPS spectra. When the treatments are carried out at room temperature a gradual fluorination occurs: monofluorinated C–F groups are the species most found at the surface and perfluoro groups CF_n are present in lower amounts. An addition reaction takes place at the (–CH=CH–) double bonds of the polybutadiene entities, leading to –(CHF–CHF–) units with large amounts of unfluorinated domains. When the reaction is thermally activated at 90 °C, an important increase of the fluorinated surface is noted from the elemental surface analysis, with a mean F/C ratio higher than 1.5. C1s spectra exhibit a maximum shifted of +6.8 eV with respect to the starting material, that can be assigned to CF_2 groups with first C neighbors bound to one F atom only, for instance CF_2–CHF groups. Additional contributions at higher BE correspond to CF_2 groups with CF_2 first neighbors, as in PTFE, and even to CF_3 groups. Similar trends are found in F1s XPS spectra. The relationships between fluorination experimental parameters and surface reactions are discussed and compared with direct fluorination results (10% F_2-gas diluted in N_2).

17.1
Introduction

The treatment of polymer surfaces with reactive gases has received much interest and several review papers on this subject have appeared [1–4]. Because of their exceptional reactivity, fluorine and fluorinated gases are of primary importance for the modification of the surface properties of these materials [2–8]. Several advantages can indeed be outlined, when compared to more conventional methods, in particular low-temperature reactions that can be achieved in many cases at ambient temperature, conditions that avoid the thermal degradation of the material. In addition, the chemical modifications are limited to surfaces only and bulk properties are

not perturbed. Depending on the type of the techniques employed, the improved properties may concern wettability, adhesion, chemical stability, permeation, electrical conductivity, biocompatibility, grafting, mechanical behavior, etc. As far as surface properties are concerned, X-ray photoelectron spectroscopy (XPS or ESCA) is particularly suitable to investigate changes in binding energies (BE) that occur within the outermost few nm of the material surface [9–11]. This technique has allowed assignment of the different components of fluoropolymers, determining the composition of fluorocopolymers [6] and proposing fluorination mechanisms [12].

Whereas most of these investigations have dealt with fluoro-(co-)polymers, surface fluorination of rubber materials has only been scarcely studied. It has been shown that the contact angle of ethylene-propylene rubbers (EPDM) and nitrile rubbers (NBR) was increased by cold-plasma treatments using fluorinated gases [13]. More recently, the use of XeF_2 has been proposed to lower the friction coefficient of NBR samples [14].

The main part of the article is devoted to surface treatment of thin nitrile gloves [made of carboxylated nitrile butadiene rubber latex (XNBR)] by plasma-enhanced fluorination (PEF) in radio-frequency (rf) cold plasmas using fluorinated gases (CF_4, CHF_3). The mechanisms of fluorination of these co-elastomers will be proposed on the basis of the assignment of the different components of the XPS spectra. The interest for fluorinating nitrile gloves is dual: the surface hydrophobicity should be increased and the filling of external pores of the material should tend to limit the permeation process.

17.2
Experimental Procedure

17.2.1
Elastomer Samples

The thin nitrile gloves submitted to fluorination have a thickness of 100 µm. They are made by dipping a porcelain former previously coated with calcium nitrate into a latex compound, leaching in warm water, drying and curing the form at elevated temperature, and then stripping the gloves. The compound comprises carboxylated nitrile butadiene rubber latex (XNBR) having about 40% dry rubber content and zinc oxide (at level in the range 1–2 parts par hundred parts dry rubber) . The compound also includes additives commonly used to make cured latex products such as potassium hydroxide as pH control agent, accelerators, sulfur and pigments. During the vulcanization, not only sulfur crosslinks are formed between the butadiene units, but also zinc and calcium salt (ionomer) bridges with the carboxylic side groups.

17.2.2
Fluorination Procedure: The Plasma-enhanced Fluorination (PEF)

The experiments in rf plasma conditions were carried out in a S.E. 80 Barrel Plasma Technology System working with a rf source at 13.56 MHz. CF_4 gas was chosen as

the fluorinated gas. The reactor consisted of two aluminum barrel electrodes that were coated with alumina. The inner electrode on which the sample was placed was connected to the rf source and the outer one was grounded. A primary vacuum was obtained by a 40 $m^3 h^{-1}$ Edwards E2M40-type pump equipped with a liquid-nitrogen condenser that trapped the residual gases. The chamber was thermostatically controlled and maintained either at room temperature or at about 90 °C during the process. Prior to each experiment, an O_2 treatment was carried out in order to complete the coating of the electrodes with an alumina layer that prevented further contamination of the sample by species degassed from the electrodes. In these PEF experiments several parameters could be tuned, in particular the inlet precursor composition, the inlet gas flow, the total pressure, and the rf power. Due to an important etching observed when O_2 was added, the fluorinated gas CF_4 was generally used alone. The other conditions were the following: inlet gas flow: $8 < Q$ (mL min^{-1}) <16; total pressure: $25 < p$ (mTorr) <200; rf power: $40 < P$ (W) < 110. Taking into account previous experiments of PEF on various types of carbon materials [16], optimized conditions could be established as follows: CF_4 gas flow rate $Q = 8$ ml min^{-1}; $p = 300$ mTorr; $P = 80$ W. After the fluorination treatment, the samples were generally handled and kept in a glove box under an Ar atmosphere.

17.2.3 XPS Characterization

XPS analysis were performed with a VG 220 i-XL ESCALAB. The radiation was an Mg nonmonochromatized source (1253.6 eV) at 200 W. A 250-μm diameter area was observed on each sample first prepared in a glove box, stored under neutral gas for transport, then quickly introduced in the fast entry air lock of the ESCA machine. Surveys and high-resolution spectra were recorded, then fitted with an Eclipse processing program provided by Vacuum Generators. Each C1s component was considered as having similar full width at half maximum (FWHM), i.e. 1.3 eV. This choice appears to be in good agreement with our experimental conditions. For instance, a C 1s spectrum taken with a pass energy of 20 eV yields for a monochromatized AlK_α source components with 1.0 eV FWHM – and even less – and with 1.2 to 1.5 eV for a nonmonochromatized MgK_α source. We have used a fitting procedure that had been applied with success to several types of carbon-based materials, in particular carbon blacks that contain numerous kinds of C–F bonds [12]. A good agreement between the experimental curve and the full calculated envelope was obtained, which could also explain subtle distinctions between the proportions of fluorinated components. Despite an important number of required components, this procedure allowed two major phenomena to be taken into account: a primary effect of electron withdrawing of F directly linked to C and a secondary one due to the inductive effect on C nondirectly bound to F and nearest neighbor of CF_n groups.

Besides the polybutadiene (PBD) and polyacrylonitrile (PAN) backbone of the material (C, O, N) the presence of other elements that are introduced during the different steps of the elaboration process of the glove can be noted in the XPS survey spectrum: Ca:calcium nitrate, used a coagulating agent. It is an ionomeric element

that is generally stabilized by the carboxylic groups of the rubber; Na: various sodium salts (sulfosuccinate, polyacrylate, etc.) used as wettable, dispersing and vulcanization accelerator agents; S: sulfur, used for vulcanization of vinyl bonds of butadiene and as vulcanization accelerator; Si: in antifoam products; K, Zn, Cl can also be found in samples. Using XPS, several analyses carried out on different zones of the treated samples allowed us to assume a homogeneous fluorination reaction on the overall exposed sample surface. Oxygen, which is present in large amount in pristine gloves, occurs as carboxyl, carbonyl, hydroxyl groups or as a contaminant. The results of these analyses for samples treated under different CF_4 plasma conditions are given in Table 1, together with that of untreated gloves. Because of the low contents of most of these inorganic components, we will only deal in the following with those elements that are able to provide an insight into the fluorination mechanisms, i.e. C and F.

Table 1 Elemental XPS analyses of the surface of XNBR gloves as-received and CF_4 rf-PEF treated (atomic per cent ± 10%).

Sample	C	F	O	Ca	N	S	Cl	Zn
As-received *	67.6	–	21.4	2.4	1.0	4.0	0.6	–
25 °C/120min	54.8	8.0	18.3	3.6	5.9	1.6	4.4	3.4
90 °C/30min	36.4	57.9	4.1	0.2	1.2	0.2	–	–

* Si: 2.9 at.%

17.3 Results and Comparison of the XPS Spectra

17.3.1 Plasma-enhanced Fluorination

17.3.1.1 Room-temperature Experiments

PEF treatments using CF_4 rf plasma without thermal activation (experiments at room temperature ranging from 1 min to 120 min) do not bring about important modifications of C 1s spectra, as shown in Fig. 1 (a) that corresponds to XNBR samples fluorinated in CF_4 plasma under the following conditions (Q= 8 mL min^{-1}, p= 300 mTorr, P= 80 W, t= 120 min, T= 25 °C). The main peak is located at 284.6 eV and corresponds to CH or CH_2 bonds that are present in both starting PBD and PAN and have not been modified by PEF. This peak serves as a reference for measuring the chemical shifts. On the high-energy side a shoulder is found between 287 and 289 eV. These contributions may be mostly due to carboxyl and carbonyl groups whose BE fall in the 287–288.5 eV range. Very small amounts of CF bonds may also be formed and more precisely attributable to CHF–CHF groups. About 8% of F are found at the surface (see Table 1).

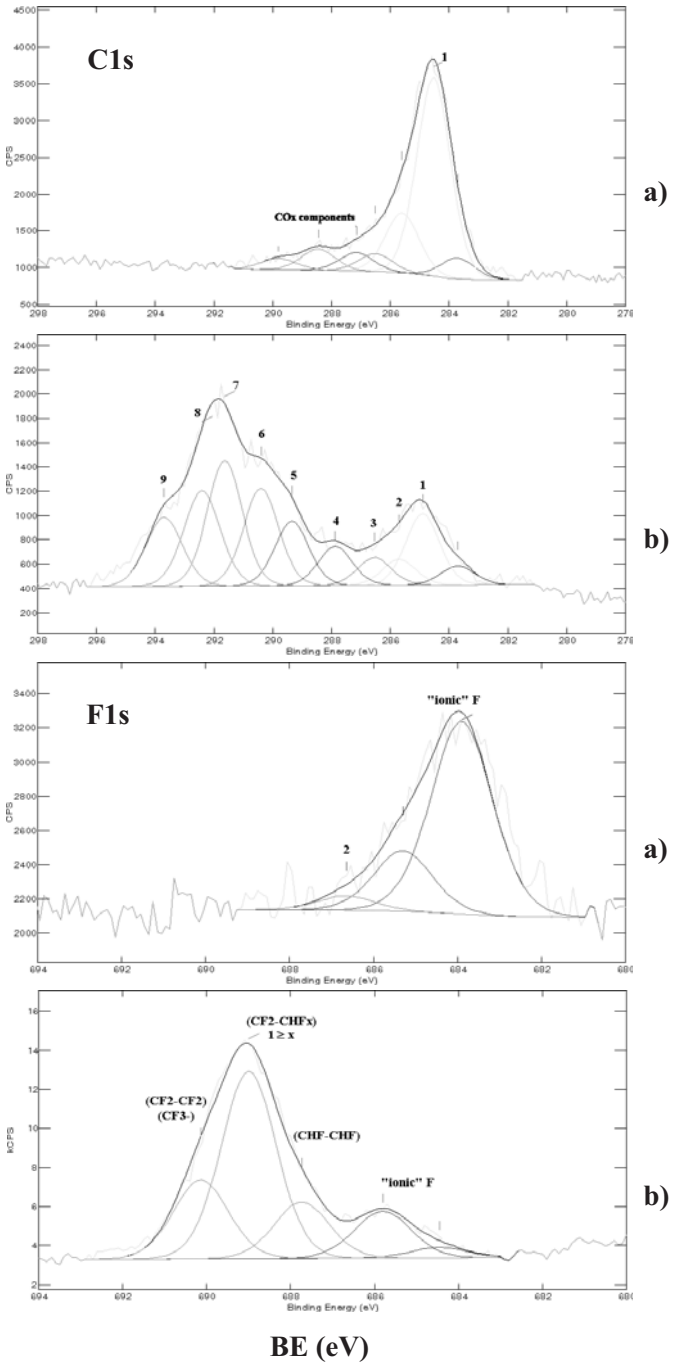

Figure 1 C1s and F1s XPS spectra of NBR sample PEF-treated 120 min at room temperature (a) and 30 min at 90 °C (b).

Among the three contributions of the F1s spectrum (Fig. 1a), the weakest one (**2**) at 687.3 eV (10%) corresponds indeed to the formation of C–F bonds, while the two major components can be attributed to those of "ionic" bonds in which fluorine is bound to inorganic elements that are present in the gloves: CaF_2 for the one at 684.3 eV, ZnF_2 or complex fluorides to the one at 685.3 eV (Reference values for the BEs of the different inorganic compounds involved in this study can be found in ref. [15]).

17.3.1.2 **Effect of Thermal Activation**

The effect of thermal activation is illustrated in Fig. 1 (b), which shows C 1s and F 1s spectra of the surface of XNBR gloves treated in a CF_4 rf plasma at 90 °C (experimental conditions: Q= 8 mL min^{-1}; p= 300 mTorr; P= 80 W; t= 30 min). An important increase of the surface fluorination is noted from the elemental analysis (Table 1), with a mean F/C ratio reaching 1.6. In this case, the C 1s spectrum exhibits a clear maximum (**7**) with a shift of + 6.8 eV besides the peak corresponding to the starting material. If we take the same procedure as previously used [12], this maximum can be assigned to CF_2 groups with first C neighbors bound to one F atom only, for instance CF_2–CHF groups. Another feature of the spectrum that is consistent with an increase of surface fluorination is the presence of two more contributions at higher BE (**8**, **9**). The one with a shift at +8.0 eV corresponds to CF_2 groups with CF_2 (or CF_3) first neighbors, or to CF_3 groups with nonfluorinated neighbors. The contribution with a shift of 9.1 eV can be assigned to terminal CF_3 groups with fluorinated neighbors.

The same trend is found in the F 1s spectrum, as shown in Fig. 1 (b). Although the amount of "inorganic" fluorides is more or less similar (12%), the maximum value of the envelope corresponding to the F–C components is shifted by about 5 eV towards higher BE. As previously stated, the value of the maximum at 688.7 eV should correspond to CF_2–CH_2, or CH<u>F</u>–CF_2 units. At lower BE, the CHF–CHF component at 687.3 eV is weaker (15%). In addition, a further component has been deduced from the fitting procedure at higher BE (689.8 eV), which can be assigned to perfluorinated CF_n groups, in particular PTFE-like CF_2–CF_2 units and terminal CF_3 groups.

17.3.2
Comparison with Direct F_2-gas Fluorination

In order to compare the reactivity of NBR samples in different fluorinating conditions, direct fluorination experiments have also been performed using 10%F_2 diluted in N_2 [16]. Even for room-temperature conditions, the F 1s peaks have considerably increased, with a mean F/C atomic ratio reaching 1.2 for samples treated for 30 min. Direct 10% F_2-gas fluorinations carried out for varied durations, e.g. 5, 30, 120 min, lead to C1s and F1s spectra with components occurring at the same BEs. In the C1s spectra (Figs. 2 (a)–(c)), the predominant C–F peak is the component (**4**) and the main effect of the fluorination duration is to weaken the intensity of the nonfluorinated C 1s peak (**1**) and to increase the contribution of CF_2 perfluoro groups (≥ **6**). The high-resolution C 1s spectra exhibit an envelope spread over 10 eV

with components located at BEs similar to those obtained for PEF experiments at 90 °C. Besides the unfluorinated elastomer component at 284.6 eV, new components have arisen at higher BE: the maximum of the envelope is now located at 288.1 eV (**4**), with a shift of 3.5 eV relative to the reference. This value is similar to those of CHF–CHF groups in poly(vinylene fluoride) [12]. A second maximum (**6**) is located

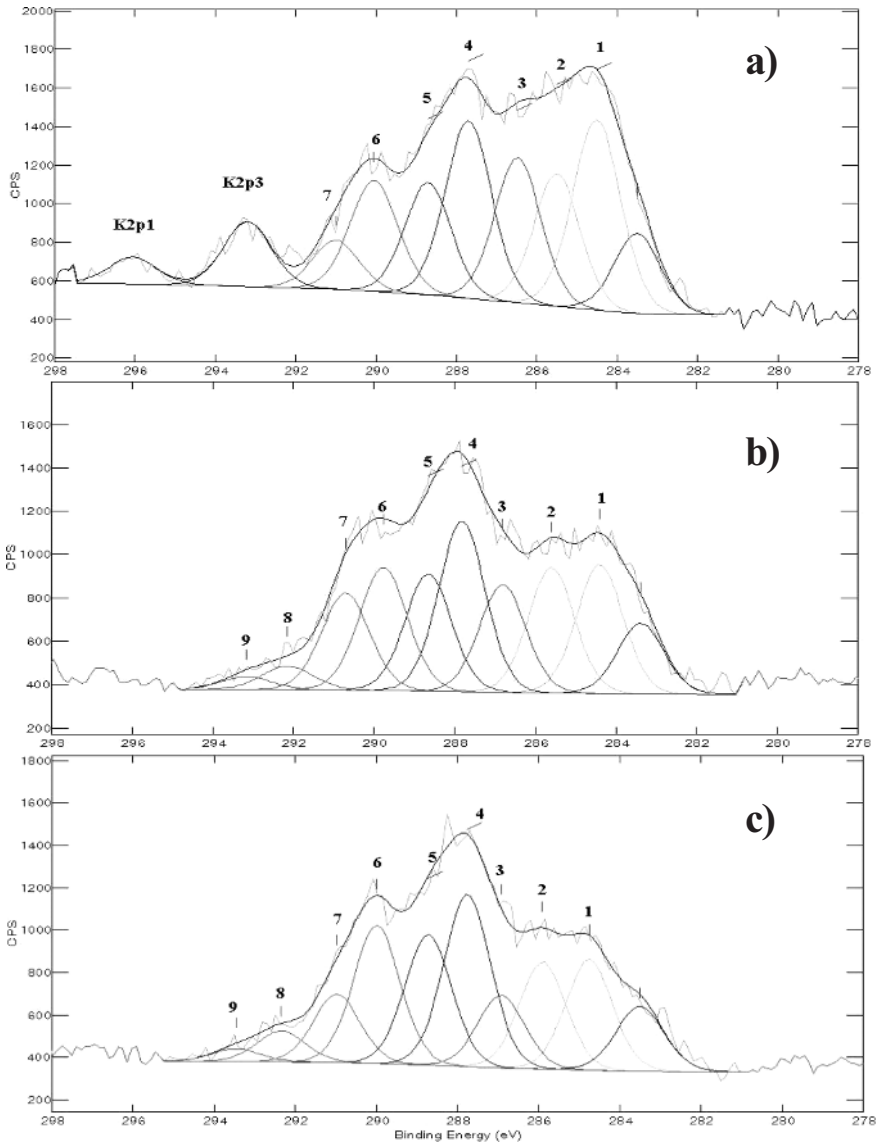

Figure 2 C1s XPS spectra of NBR sample fluorinated by F_2-gas at room temperature for different reaction times: 5 min (a), 30 min (b), 120 min (c).

with a chemical shift of +5.5 eV, which could be attributed to of –(CF_2–CH_2–) units coming from the substitution of F for H, or alternatively C–F bonds with highly fluorinated neighbors, such as CF_2 groups or terminal CF_3 groups. Further contributions can be assigned to CF_2–CHF and CF_2–CF_2 groups.

The F 1s peak, shown in Fig. 3 for a 30-min experiment, is displaced by about 4 eV toward higher BE, when compared with the room-temperature PEF. The FWHM is also much larger, reaching 3 eV, which points out the presence of several contributions. The "inorganic" part of the spectrum (CaF_2, ZnF_2) with components at BE ~ 685 eV is very weak and corresponds to less than 10%. The maximum of the peak, at 687.6 eV, can be ascribed to a F–C bond with first carbon neighbors presenting also C–F bonds, i.e. (CHF–CHF) groups (see Table 2), which is in good agreement with the C 1s spectrum (Fig. 2b). The contribution at lower BE, that is 686.5 eV, should correspond to F–C bonds with nonfluorinated C neighbors, i.e. (CHF–CH_2) groups. On the other hand, the contribution at higher BE, that is 688.8 eV, can be assigned to C–F bonds with CF_2 groups as first neighbors or alternatively to CF_2 groups with CH_2 (see Table 2) or CHF units as first neighbors. This component would therefore correspond to components C 1s (**5**) to (**7**).

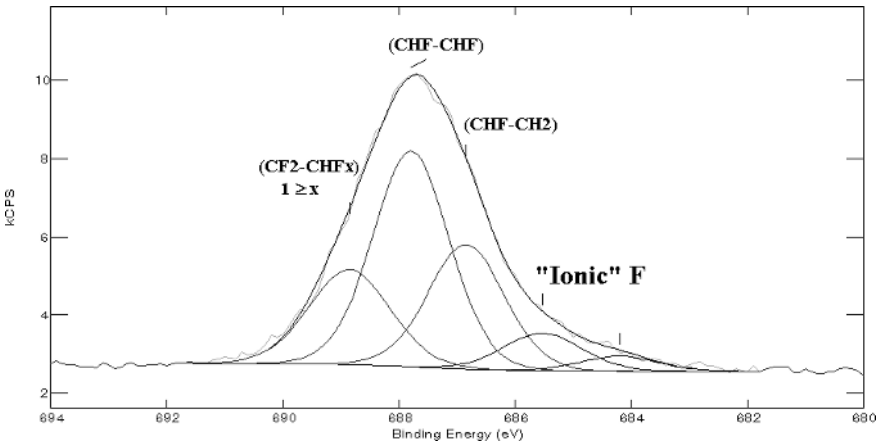

Figure 3 F1s XPS spectrum of NBR sample fluorinated by F_2-gas 30 min at room temperature.

For direct F_2-gas fluorinations carried out at 90 °C, the F1s and C1s spectra have similar features to those obtained for plasma fluorination at the same temperature. In the case of a 15-min treatment, the amount of fluorinated surface has increased relative to room-temperature F_2-gas fluorination, with an F/C atomic ratio of 1.86. The amount of pristine elastomer is subsequently lower. The strongest component (**7**) can be assigned to CF_2 groups that are surrounded by monofluorinated C with a BE shift of + 6.5 eV. Two components (**8**, **9**) at higher BE can be again attributed to perfluorinated CF_2–CF_2 units and terminal CF_3 groups.

Table 2 Assignment of the XPS C1s components of fluorinated NBR elastomer.

Peak number	Involved chemical bond	Binding energy (eV)
1	CH_n	284.5
2	$\underline{C}H_2$-CHF	285.2-285.6
3	$\underline{C}H_2$-CF_2	286.5
4	$\underline{C}$HF-CH_2	287.5-288.0
	CHF-CHF	
5	$\underline{C}$HF-CF_2	290.0
6	CF_x-$\underline{C}$F-$CF_{x'}$ (x,x′ = 2,3)	289.8-290.0
	$\underline{C}F_2$-CH_2	
7	$\underline{C}F_2$-CHF	290.7-291.3
8	CF_2-CF_2	292.3
9	$\underline{C}F_3$-CF_x	293.6

17.4 Concluding Remarks

These results clearly show that different mechanisms occur depending on the fluorination conditions. A coating of XNBR samples appears to be achieved when plasma-enhanced fluorination is carried out at 90 °C. The main component can be assigned to CF_2–CH_2, or CH$\underline{F}$–CF_2 units with the presence of components at higher BE corresponding to perfluorinated CF_n groups, in particular PTFE-like CF_2–CF_2 units. For CF_4 rf-plasma treatments at room temperature only a small amount of polymer is fluorinated, most fluorine species reacting with the inorganic cations present in the gloves, e.g. Ca^{2+}, Zn^{2+}. We should point out the better efficiency of F_2-gas treatments at room temperature. In this case, monofluorinated C atoms are the species most often found at the surface, with some CF_n perfluoro groups present in a lower amount. An addition reaction takes place at the –(CH=CH–) double bonds of the PBD, leading to –(CHF–CHF–) units. On the other hand, when the fluorination process is thermally activated at 90 °C, a more homogeneous fluorination of the surface occurs for both methods that finally lead to surface perfluorinated –(CF_2–) groups and terminal –CF_3 groups. It can be added that the importance of the thermal activation was already raised in the case of the fluorination by F_2-gas of PP and high-density polyethylene (HDPE). It was noted that CF_3 perfluorinated groups were not observed, the functionalization being limited to –CHF and –CF_2 groups [17,18]. Measurements of contact angles in progress have shown that the formation of a fluorinated layer onto the surface of XNBR samples increased the hydrophobic character and so the repulsion of water from the surface of the gloves.

Acknowledgments

Mapa-Hutchinson Company (M. Renaud, Centre Technique, Liancourt, France) is acknowledged for interest and support.

References

[1] "Physicochemical Aspects of Polymer Surfaces" Vol. 1, K.L. Mittal, Ed., Plenum Press, New York (1983), and articles herein.
[2] "Plasma Deposition, Treatment and Etching of Polymers", R. d'Agostino, Ed., Academic Press, Boston (1990), and articles herein.
[3] "Plasma surface modification of polymers for improved adhesion: a critical review" E.M. Liston, L. Martinu, M. R. Wertheimer, J. Adhes. Sci. Technol. **7**, (1993) 1091.
[4] Special issue of J. Fluorine Chem. **104**, (2000) pp.1 to 126 (Selected papers from Conference "Fluorine in Coating III", Orlando, Florida, January 1999).
[5] D.T. Clark, W.J. Feast, D. Kilcast, W.K.R. Musgrave, J. Polym. Sci. Polym. Chem. Ed. **11** (1973) 389.
[6] J.J. Pireaux, J.P. Delrue, A. Hecq, J.P. Dauchot, in "Physical Aspects of Polymer Surfaces", K.L. Mittal, Ed., Vol. 1, Plenum Press, New York (1983) p. 53.
[7] M. Anand, R.E. Cohen, R.F. Baddour, Polymer **22**, (1981) 361.
[8] C. Cardinaud, A. Tressaud, Chapter 14, "Advanced Inorganic Materials", T. Nakajima, A. Tressaud, B. Žemva, Eds, Elsevier (2000).
[9] D. Briggs, M.P. Seah "Practical Surface Analysis, Vol 1: Auger and XPS", D. Briggs, M.P. Seah Ed., John Wiley, New York (1990), and articles herein, (in particular Chap. 9 by D. Briggs p.437).
[10] G. Beamson, D. Briggs, "High Resolution XPS of Organic Polymers", John Wiley, New York (1992).
[11] D. Briggs, "Surface analysis by XPS and static SIMS", Cambridge University Press (1998).
[12] G. Nansé, E. Papirer, P. Fioux, F. Moguet, A. Tressaud, Carbon **35**, pp. 175–194, 371–388 and 515–528 (1997).
[13] G. Legeay, F. Epaillard, J.C. Brosse in "Second International Conference of Plasma Chemistry and Technology", H.V. Boenig, Ed., Technomic Publ. Co. (1985) p 29.
[14] G. Barsamian, V. Sokolov, H.B. Sun, Proceedings Int. Conf. "Fluorine in Coating II", Munich, Germany (1997).
[15] "Handbook of X-ray Photoelectron Spectroscopy" J. Chastain, R.C. King Ed., Physical Electronics, Inc., Eden Prairie, Minnesota (1995).
[16] E. Durand, C. Labrugère, A. Tressaud, M. Renaud, Plasmas Polym., **7**, 311 (2002)
[17] F.J. du Toit, R.D. Sanderson, W. J. Sanderson, J. Fluorine Chem. **74** (1995) 43.
[18] F.J. du Toit, R.D. Sanderson, J. Fluorine Chem. **98** (1999) 107.

18
Plasma-Surface Modification of Styrene-Butadiene Elastomers for Improved Adhesion

J. Tyczkowski, I. Krawczyk, B. Woźniak

Abstract

An attempt to replace a wet-chemical surface modification of styrene-butadiene elastomers (SBS), improving their adhesion to polyurethane adhesives, with a clean low-pressure plasma technique has been undertaken. The plasma has been generated by an RF discharge (13.56 MHz, plate electrode reactor) in various reactive mixtures (e.g. $CHCl_3$, CCl_4, CO_2, O_2) to create chlorine (C–Cl) and oxygen (>C=O, –OH, –COOH) functionalities on the elastomer surfaces. T-peel tests, contact-angle measurements, and FTIR spectroscopy have been utilized to investigate the surfaces. It has been found that an important role in the plasma-improved adhesion is played by the chemical interaction between the modified SBS surfaces and polyurethanes. The peel strength for plasma-treated samples in many cases is much higher than that for the wet-chemical modification. It clearly indicates that the plasma treatment is a very promising method of improving the adhesion properties of SBS elastomers.

18.1
Introduction

The gluing of elastomers, such as styrene-butadiene block copolymers (SBS), to other materials (e.g. artificial leather, textiles, ridge polymer elements) is an especially important problem in diverse branches of industry. It is obvious that the strength and quality of such adhesive-bonded joints depend to a great extent on the chemical structure and morphology of the elastomer surface and, therefore, can be controlled by various treatments, such as abrasion, mechanical roughening, washing, ultrasonic cleaning, and wet-chemical modification [1,2].

One of the common methods to improve the adhesion of SBS elastomers in joints prepared by polyurethane and epoxy adhesives is the chemical chlorination of the elastomer surfaces. It is performed by means of active halogen derivatives, mainly trichloroisocyanuric acid (TCI) or chloramine, feeding in an organic solvent. The most adequate solvents to prepare these solutions are alcohols, esters, ketones, and aromatic hydrocarbons [2–7]. In some cases aqueous solutions of sodium hypochlorite and hydrochloric acid are also used for the chlorination [8].

Although the kind of processes involved in the wet chlorination of SBS elastomers and the role that they play in the improvement of the adhesion between their surfaces and adhesives is not yet completely understood, the general trends in such a modification have already been determined. Four main effects are presented as a result of the chlorination process. The first is the formation of new functionalities that can improve chemical interaction of the elastomer surface. On the basis of investigations on model compounds [9], it has been established that C–Cl groups are created as a result of chlorine addition to the double carbon bonds of the butadiene segments [2,6,7]. It has also been found that reactions of cyclization as well as ring and chain substitution occur during the chlorination [8]. After the chlorination process, some amount of carboxylic groups is observed on the surface. This is connected with a chlorine surface-oxidation process [2].

The next effect of the SBS surface chlorination is an increase in the surface free energy and, in consequence, the increased thermodynamic adhesion [6]. It is obvious that the creation of such polar groups as C–Cl, C=O, and C–OH involves the higher value of the polar component of the surface free energy [10].

The creation of surface porosity that enhanced mechanical adhesion and the removal of the antiadherent compounds from the elastomer surface (e.g. the wax in the case of a typical synthetic rubber) make the other two effects attributed to the chlorination process [2,6].

Although the wet chlorination is a useful procedure to improve the adhesion of SBS elastomers, nevertheless some disadvantages of this method arise from the fact that both the vaporizing flammable solvent and educed gaseous chlorine are very toxic and hazardous substances for the environment. Furthermore, it has been shown that in the case of wet chlorination, at least a few hours are required to produce an adequate adhesive-bonded joint [5,7]. Thus, it is no wonder that we search for cleaner, more energy-saving and environmentally friendly ways as an alternative to the present wet-chemical method. It seems that plasma surface treatment is a very good candidate to come up to these expectations.

Over the last thirty years, it has been established that a plasma medium that is composed of electrons, ions, and radicals is able to interact with the surface of polymeric materials and to modify their surface properties. The main interactions are: etching and degradation of polymers; implantation of atoms present in the plasma on the polymer surface and creation there of new functional groups; formation of radical centers that afterwards can react, for example, with atmospheric oxygen forming new functionalities; and deposition of thin films of plasma polymers or glasses. The implantation process, as surface modification of polymer materials, is the most useful and commercially available [11,12].

As one can see, each of the four main effects occurring as a result of the wet chlorination can be achieved by plasma treatment. For example, chlorine functionalities, e.g. C–Cl groups, can be obtained on the polymer surface using plasma containing chlorine atoms. Such a modification has been already discussed in some papers [13–17]. It has been done with the purpose of increasing the hydrophilicity of the polymer surface. Although different plasmas have been used, such as CF_3Cl, CCl_4, $CHCl_3$, and different polymers have been treated (polypropylene, polybuta-

diene), in all these cases it has been found that chlorine atoms are bonded to the surface structure. The efficiency of the process, however, depends nontypically on the plasma power and the treatment time. Generally, the chlorination is favorable under a low discharge power and not too long plasma exposure.

As far as oxygen functionalities (e.g. –OH, >C=O, –COOH) are concerned, an abundance of works in this field has been done, see for example [11,12] and references therein. Most often O_2, CO_2, CO, NO, NO_2 plasmas are used as a source of oxygen atoms. The type of plasma and treatment conditions decide on the type and density of created oxygen functional groups.

Taking into account the wide prospects of the plasma surface treatment, an attempt has been recently made to use this technique in the place of the wet-chemical chlorination method [18–28]. In particular much attention has been paid to this problem by Martin-Martinez and his coworkers, who tested low-pressure N_2 and O_2 plasma for surface modifications of synthetic vulcanized styrene-butadiene rubbers. They have found that the treatment with these plasmas partially removes hydrocarbon moieties from the rubber surface and generates oxygen moieties. An increase in surface roughness was also observed. Generally, the plasma treatments improved the adhesion of the rubber to a polyurethane adhesive. In the case of oxygen plasma, only 1 min sufficed to noticeably increase the adhesion whereas an extended treatment (15 min) was needed when nitrogen plasma was applied. Unfortunately, strong aging processes that deteriorate the adhesion were observed. Probably, this effect was connected with a migration of waxes and zinc stearate (ingredients of synthetic vulcanized rubbers) to the surface [19–21].

Very recently, preliminary investigations on plasma chlorination of SBS rubbers have been performed using low-pressure plasma generated in various reactive mixtures containing chlorine moieties. It has been shown that in some cases a drastic increase in the adhesion of the rubber surface to adhesives is observed [23,24]. Some attempts to create oxygen functionalities on the SBS surfaces by low-pressure CO_2 and O_2 plasmas have been also undertaken. The results are very promising as well [27,28].

Besides the low-pressure plasmas, attempts to use atmospheric-pressure plasmas to surface modifications of vulcanized rubbers have also been undertaken. Both a corona discharge [22] and an oxygen cold-plasma torch [18] have already been tested. Likewise there is growing interest in other alternative techniques to the conventional chemical processes, analogous to the plasma-surface modification, for example ultraviolet radiation treatments [22,29,30].

To better understand the processes proceeding during plasma modification of the rubber surfaces, we have undertaken systematic investigations on model styrene-butadiene block copolymers (unvulcanized and without any ingredients). In this paper, results concerning the plasma creation of chlorine and oxygen functionalities on the elastomer surface are presented. Properties of the surfaces have been investigated by peel-strength tests, contact-angle measurements and infrared spectroscopy. The relations between these properties and plasma conditions such as type of plasma, power of discharge and treatment duration are analyzed.

18.2 Experimental

18.2.1 Materials

The thermoplastic elastomer-type radial styrene-butadiene block copolymers (Finaprene 435 (F435) and Finaprene 507 (F507)), provided by Atofina S.A. (Belgium), were used in this work. A general chemical formula of a typical SBS copolymer chain is drawn in Fig. 1. The copolymers were unvulcanized and did not contain any ingredients such as oils, plasticizers and fillers. A butadiene-to-styrene ratio was 69 to 31 wt% and 27 to 73 wt% for F435 and F507, respectively. The samples were obtained by an injection of the copolymers into a heated mold at 420 K, where plates of 120 mm width, 150 mm length and 6 mm thickness were formed. For additional tests, strips of 15 mm width and 75 mm length, cut from the plates, were used. All these samples were cleaned in an ultrasonic washer (with pure p.a. methanol) for 15 min.

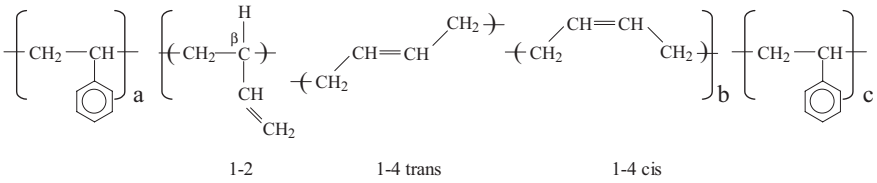

Figure 1 Chemical formula of a typical SBS copolymer chain. Different polybutadiene chain units are shown.

18.2.2 Plasma Treatment

The plasma treatment was carried out in a parallel-plate reactor with a radio-frequency (13.56 MHz) glow discharge. As precursors, trichloromethane ($CHCl_3$, pure p.a., POCh S.A.), tetrachloromethane (CCl_4, pure p.a., POCh S.A.), carbon dioxide (CO_2, 99.9%, Linde Gas Poland), and oxygen (O_2, 99.5%, Aga Gas GmbH) were used. The $CHCl_3$ precursor was supplied to the reactor as a pure agent or in a mixture with oxygen. The other precursors were introduced only as pure agents (without a carrier gas). A typical flow rate was ~3.5 sccm for pure $CHCl_3$ and CCl_4 vapors and 7.5 sccm for CO_2 and O_2 gases, whereas for the mixture of $CHCl_3$ and O_2, the flow rate was 9 and 5 sccm for these agents, respectively. An initial pressure in the reactor chamber of approximately 13 Pa was maintained in the whole study. The power of the glow discharge was changed from 10 to 80 W and the plasma treatment of the samples lasted from 5 s to 20 min.

18.2.3 Wet-chemical Treatment

To compare the plasma and wet-chemical treatments, samples of the elastomers with chemically chlorinated surfaces were prepared. The chlorination was performed by immersion of the samples for 30 s in the chlorination solution (2 wt% of trichloroisocyanuric acid (TCI) in propanone). The chlorination time was 1 h and then the samples were immersed in an aqueous solution of ethanol (25 wt%) for 30 s to stop the chlorination process. Finally, the samples were dried at room temperature in the open air for a few hours.

18.2.4 Surface-characterization Techniques

The sample surfaces were characterized using contact-angle measurements and Fourier transform infrared (FTIR) spectroscopy. A NRL model 100 Contact Angle Goniometer (Rame-Hart) equipped with a thermostated chamber, digital camera and programmable system to calculate the surface free energy was utilized for the contact-angle records. Bidistilled deionized water, pure p.a. glycerol and pure p.a. α-bromonaphthalene were placed in the form of a 5.0-μl drop on the surfaces at 298 K. FTIR spectra were recorded using a Bio-Rad model 175C spectrometer equipped with an IRS microscopic accessory (Split-Pea, Harrick Scientific), working in a total reflection mode. Signal accumulation from 20 scans was taken with the resolution of 2 cm^{-1} and was analyzed according to a numerical peak-fitting algorithm (PeakFit software by Jandel). The depth of the surface layer being penetrated by the IR beam depended on the wave number and changed in the case of SBS elastomers from approximately 0.3 to 2.3 μm for 500 and 3700 cm^{-1}, respectively [31,32].

To determine the adhesion strength of the elastomer surfaces, T-peel tests were carried out. Adhesive-bonded joints were made using the elastomer samples with the surface mechanically roughed before the modifying treatments and strips of a standard leather (box cow, chrome tanned, nonpigmented). A polyurethane adhesive (18 wt% polyurethane pellets in propanone/methylbenzene (3:1) + 1.3 wt% diizocyanomethane) was spread on each adherend and dried for 15 min. The dry adhesive film on the elastomer was reactivated at 353 K and the surfaces were placed in contact immediately under a pressure of 0.4 MPa for 10 s. Then, the adhesive joints were conditioned for 48 h at room conditions. The T-peel-strength measurements were performed using an Instron 5566 test instrument (peeling rate = 1.67×10^{-3} m/s). The average value of the peel strength for a given sample was determined from 10 measuring points.

18.3 Results and Discussion

18.3.1 Preliminary Peel Test

The most important feature of the elastomer surfaces, from the point of view of their applications, is the peel strength of adhesive-bonded joints formed between the elastomer and another materials. The main attention in this paper is paid therefore to the T-peel test investigations. In Fig. 2 examples of results for the F435 elastomer are presented to compare the modification of its surface by various plasmas. The $CHCl_3$, CCl_4, CO_2, and O_2 plasmas with discharge powers of 10, 20, 50, and 80 W were tested. In all these cases the plasma treatment was performed for 5 min. For comparison, T-peel test results for nontreated and wet chemically chlorinated samples are also shown.

The following general conclusion emerges from the results presented above: all the plasma treatments, irrespective of the discharge power used, give a considerable improvement in the adhesion properties of the elastomer. The greatest increase in the peel strength, about 4 times compared with the nontreated samples, is observed for CCl_4 plasma used as a modifier. In the case of CO_2 and O_2 plasmas, the peel strength is about twice as high as that before the treatments, and at the same time, about 30% higher than its value for the wet-chemical chlorination. It should be emphasized, however, that the plasma parameters have not been optimized (e.g. the treatment duration was 5 min in all cases) and we can expect still better results after process optimization.

Just the preliminary results of the peel test suffice to show that the plasma-surface modification by implanting both chlorine and oxygen functionalities can be a very promising method to improve the adhesion properties of SBS elastomers. Therefore, more thorough investigations have been undertaken to describe these processes in detail.

18.3.2 Plasma Chlorination

The plasma chlorination process has been studied for F435 and F507 elastomers treated by RF plasma with $CHCl_3$ as a chlorine source ($CHCl_3$ has been chosen because the production of CCl_4, according to international regulations, is now very restricted). This precursor was fed into the reactor either without any other components or in a mixture with O_2. The oxygen supply was aimed at the prevention against a presumable thin-film deposition and also at the additional modification of the surface by the formation of hydroxyl, carbonyl, and carboxyl groups. The plasma treatment was performed at two extreme values of the applied power, namely 10 W and 80 W, and lasted 5 min in every case.

Figures 3 (a) and 4 (a) present results of the peel test for the samples under discussion. The peel-strength values for nontreated and wet chemically modified (by

TCI) samples are also shown. As one can see, the plasma treatment can evidently improve the peel strength in comparison with the nontreated surface in the case of the F435 elastomer. When the pure $CHCl_3$ vapor is used, the peel strength is also higher (approx. 56%) than that for the samples treated by TCI. The use of oxygen in the reactive mixture deteriorates the adhesion properties of the treated surfaces, although the low power supplied to the plasma reactor gives the peel strength of a similar value to that measured for the TCI-treated samples. It is striking that for the low discharge power, better peel strength of adhesive-bonded joints is obtained. Such behavior is observed both for the plasma treatment by pure $CHCl_3$ and also when the $CHCl_3/O_2$ mixture is used. On the other hand, in the case of the F507 elastomer, the plasma treatment used gives the peel strength of the same or only a little higher value in comparison with the nontreated samples, but evidently lower than that obtained after the wet-chemical process.

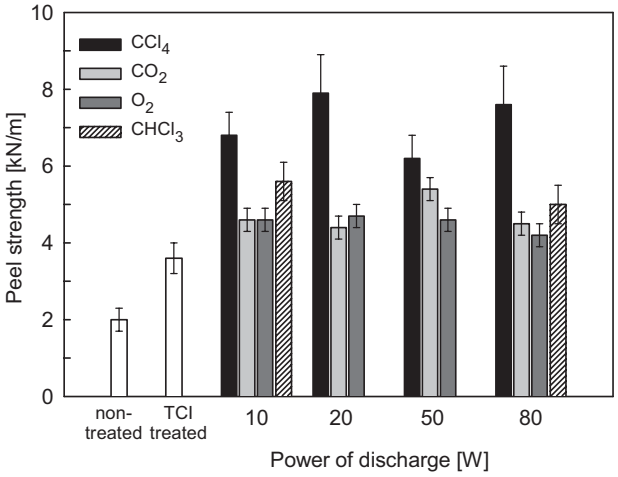

Figure 2 T-peel-strength measurements for F435 elastomer before and after wet-chemical and plasma treatments. Various plasmas at various glow-discharge powers were use. Time of all the plasma treatments – 5 min.

Comparing the results for F435 and F507, one should take into account the differences in the chemical constitution of these copolymers. The former copolymer contains 69 wt% of butadiene in the structure whereas only 27 wt% of this monomer is incorporated into the latter material. If we assume that the adhesion improvement produced by the plasma chlorination consists in the attachment of chlorine atoms to the elastomer surface, we can predict that the efficiency of the adhesive bonding should depend on the density and molecular position of these atoms on the surface. In this case, two mechanisms of the interaction between the elastomer surface and polyurethane adhesives can be considered: the formation of hydrogen bonds between urethane groups and Cl atoms [33], and the creation, by some of the Cl atoms, active sites that react with the adhesive. For instance, by analogy with polychloro-

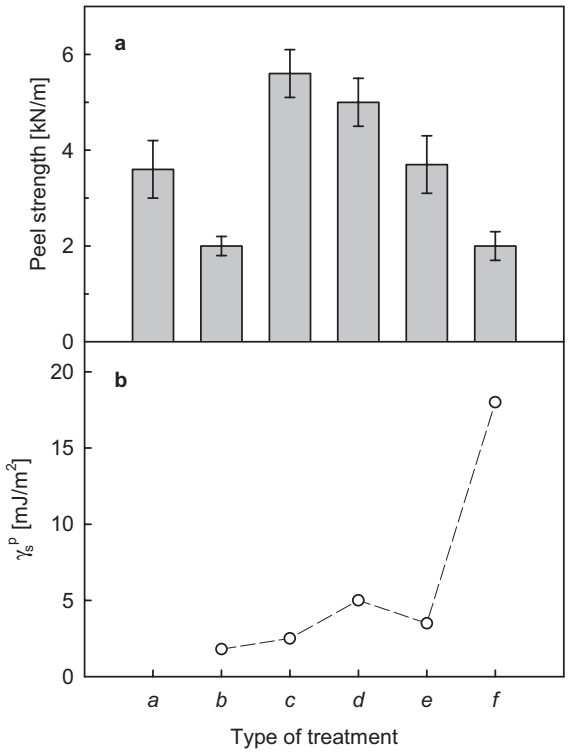

Figure 3 Measurements of the T-peel strength (a) and the polar component of the surface free energy γ_s^p (b) for F435 elastomer after various types of surface treatment: *a* – TCI treatment; *b* – nontreated; *c* – plasma $CHCl_3$, 10 W; *d* – plasma $CHCl_3$, 80 W; *e* – plasma $CHCl_3/O_2$, 10 W; *f* – plasma $CHCl_3/O_2$, 80 W.

prene, it can be expected that ß carbon atoms in 1,2 addition configuration of the monomer units in the polybutadiene blocks (Fig. 1), substituted with chlorine atoms are especially active crosslinking sites [34]. The presence of the 1,2-configuration in the elastomers under discussion is confirmed by FTIR spectra (Fig. 5). The bands at 910 and 995 cm^{-1} are attributed to this configuration whereas the band at 965 cm^{-1} is connected with the 1,4-trans configuration. Extremely low density of the 1,4-cis configuration also exists in our copolymers (band at 725 cm^{-1}) [35,36]. As one can see, there is evidently a higher concentration of 1,2-polybutadiene in F435 compared to F507, which could explain the greater peel strength of adhesive joints in the former case.

For better characterization of the surface properties of the elastomers under discussion, measurements of the contact angles were carried out. The calculated surface free energy γ_s and its components (the dispersive γ_s^d and polar γ_s^p components) for both types of elastomers after various treatments are shown in Table 1. The values of the polar component are also presented in Figs. 3 and 4 to discuss a

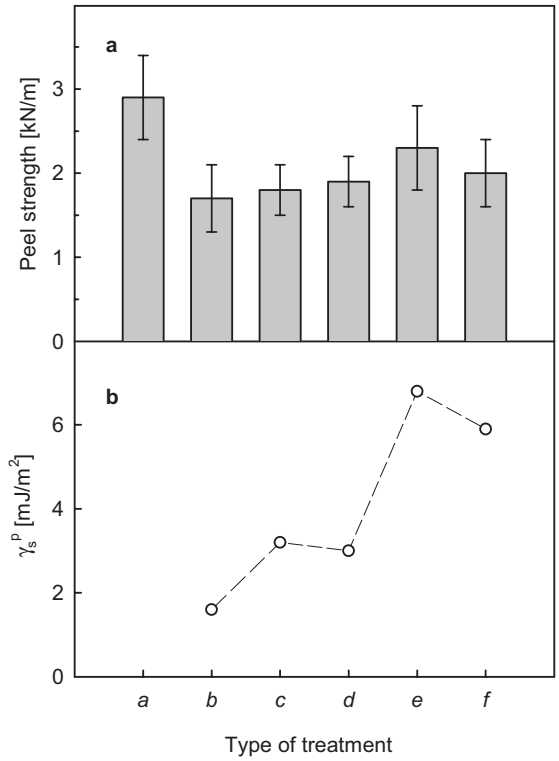

Figure 4 Measurements of the T-peel strength (a) and the polar component of the surface free energy γ_s^p (b) for F507 elastomer after various types of surface treatment: *a* – TCI treatment; *b* – nontreated; *c* – plasma $CHCl_3$, 10 W; *d* – plasma $CHCl_3$, 80 W; *e* – plasma $CHCl_3/O_2$, 10 W; *f* – plasma $CHCl_3/O_2$, 80 W.

role of the chemical and thermodynamic adhesion in the adhesive-bonding process. In the case of F435 a lack of any correlation between the polar component of the free surface energy and the peel strength is observed. For example, γ_s^p for the sample subjected to the $CHCl_3$ plasma action with the power of 10 W is similar to that for the nontreated sample, although the peel strength is 2.8 times higher in the former case. Meanwhile, the highest values of γ_s^p is recorded for the $CHCl_3/O_2$ plasma treatment with the power of 80 W, but the peel strength of such samples is practically the same as that for the nontreated samples. These observations confirm that the dominant mechanism of the adhesion improvement caused by the plasma chlorination consists in the chemical interaction between C–Cl groups on the elastomer surface and the polyurethane adhesive, and the thermodynamic adhesion (connected with the surface free energy) is unimportant in this case.

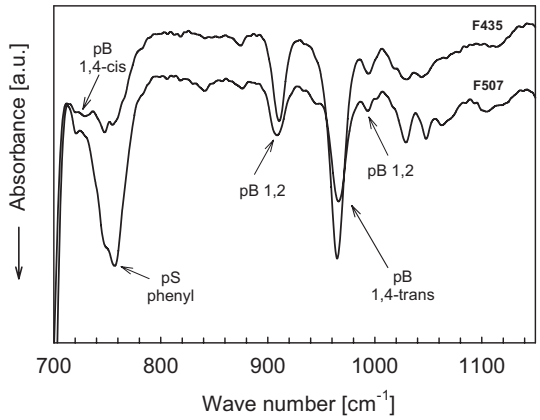

Figure 5 FTIR spectra of nontreated F435 and F507 samples. Characteristic bands for polystyrene (pS) and polybutadiene (pB) units are designated.

Table 1 Surface energies of the styrene-butadiene elastomers after various plasma treatments; (γ_s – total free energy, γ_s^d – dispersive component, γ_s^p – polar component)

Type of treatment	Elastomer F435			Elastomer F507		
	γ_s	γ_s^d	γ_s^p	γ_s	γ_s^d	γ_s^p
nontreated	32.5	30.7	1.8	33.3	31.7	1.6
plasma $CHCl_3$, 10 W	31.5	29.0	2.5	35.3	32.1	3.2
plasma $CHCl_3$, 80 W	33.2	28.2	5.0	40.6	37.6	3.0
plasma $CHCl_3/O_2$, 10 W	35.8	32.3	3.5	42.0	35.2	6.8
plasma $CHCl_3/O_2$, 80 W	41.7	23.7	18.0	42.4	36.5	5.9

On the other hand, for the F507 elastomer, we can see distinct correlation between γ_s^p and the peel strength. Generally, the higher γ_s^p corresponds to the higher peel strengths (Fig. 4). This observation together with the weak improvement of the adhesion (in relation to F435) indicate that the changes in the adhesion strength could be rather attributed in this case to the modification of the surface energy (thermodynamic adhesion) than to the chemical bonding (chemical adhesion).

To obtain more information on changes in the elastomer surface caused by the plasma chlorination, investigations by means of the FTIR technique were performed. First, the FTIR analysis was used to support the assumption that chlorine atoms are chemically bonded to the surface. Characteristic IR absorption bands corresponding to C–Cl modes in low-weight model compounds as well as for wet-chemical chlorinated and plasma-chlorinated polymer surfaces are collected in Table 2. Taking into account the chemical structure of the investigated copolymers, we should expect the bands in two regions: between 520 and 850 cm^{-1} for C–Cl bonds in aliphatic structure and between 1030 and 1100 cm^{-1} in aromatic structure. Thor-

ough analysis of the FTIR spectra for the copolymers before and after the plasma chlorination has shown that only new bands appearing in the first region can be attributed to C–Cl modes. This means that Cl atoms are mainly attached to the aliphatic structure of the copolymers whereas benzene rings are not chlorinated.

Table 2 IR absorption bands assigned to C–Cl groups in different low-weight and polymeric substances

Substances	C–Cl bands [cm^{-1}]	References
Model chlorine compounds:		
CH_3Cl	732.1	[39]
$CHCl_3$	680, 774	[39]
generally:		
C–Cl aliphatic (stretching)	560–830	[37]
CH_2–Cl, CH–Cl (wagging)	1240–1300	[37]
CH_2–Cl (deformation-scissors)	ca. 1440	[37]
chloro benzenes (Ar–Cl)	1034–1096	[38]
After wet-chemical chlorination:		
vulcanized SBS rubber:		
0.5 wt% TCI	539, 775, 1420	[7]
3 wt% TCI	730, 764, 835, 1420	[2]
unvulcanized SBS rubber:		
0.5 wt% TCI	528, 1058	[6]
7 wt% TCI	528, 1159–1166, 1401–1419	[6]
After plasma chlorination:		
polypropylene (in CCl_4 plasma)	605, 653	[16]
polybutadiene (in $CHCl_3$ plasma)	613, 670	[17]

In the case of the F435 elastomer, five new bands can be distinguished in the first region after the plasma chlorination, namely at 515, 520, 560, 612, and 622 cm^{-1}. Although the bands are relatively weak, their repeatability is very good. As the most characteristic band for C–Cl bonds in plasma-chlorinated aliphatic polymers (see: Table 2), the line at 612 cm^{-1} has been taken for further discussion. Figure 6 presents five spectra recorded in the region of 612 cm^{-1} for nontreated and various plasma-treated F435 samples. As one can see, the spectra of samples subjected to the pure $CHCl_3$ plasma action at 10 and 80 W (spectra b and c) clearly reveal the presence of the C–Cl band. If the samples are treated by the $CHCl_3/O_2$ plasma at 10 W, the weak band at 612 cm^{-1} is also observed (spectrum d). This indicates that some limited amount of C–Cl groups exist also in this case. The 612 cm^{-1} band, however, is practically absent in the spectrum of the sample treated by the $CHCl_3/O_2$ plasma at 80 W (spectrum e), like for the nontreated surface (spectrum a). It is readily noticeable that the higher intensity of the 612 cm^{-1} band (and in consequence, the higher density of aliphatic C–Cl groups) is related to the higher peel strength, irrespective of the surface polarity (Fig. 3).

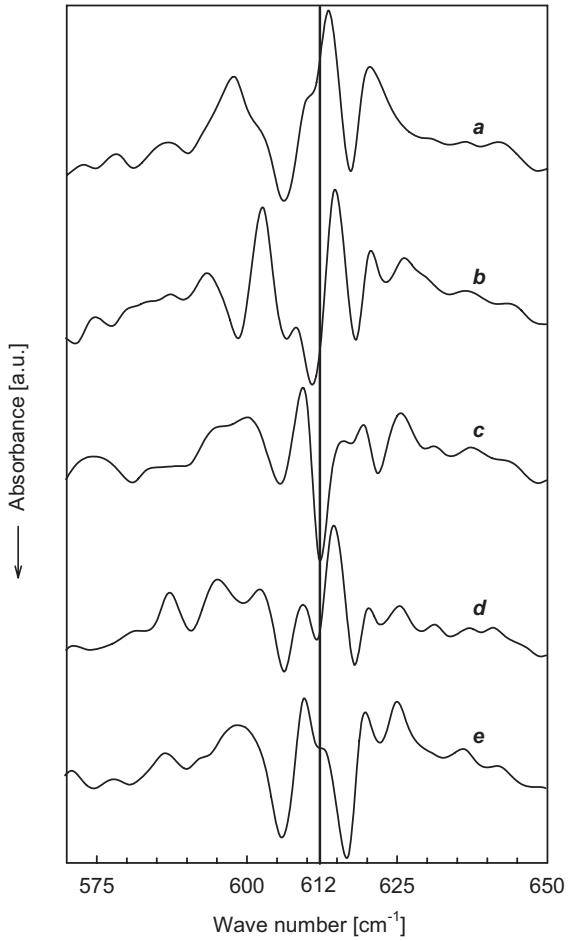

Figure 6 FTIR spectra of F435 samples in the region of C–Cl bands: *a* – nontreated; *b* – plasma $CHCl_3$, 10 W; *c* – plasma $CHCl_3$, 80 W; *d* – plasma $CHCl_3/O_2$, 10 W; *e* – plasma $CHCl_3/O_2$, 80 W.

The correlation between the C–Cl density and the peel strength is supported by the results obtained for the F507 elastomer. In this case, IR spectra show practically a lack of any changes in the region of 612 cm^{-1} after the plasma treatment. At the same time we do not see practically any improvement in the peel strength (Fig. 4).

The IR absorption investigations evidently indicate that the adhesive-bonding process activated by the plasma chlorination is based on the chemical adhesion that depends on the surface density of C–Cl groups. However, the following problem still exists – which kind of chemical reaction between the C–Cl groups and the polyurethane adhesive depends on the adhesive bonding.

Apart from the formation of C–Cl groups, the analysis of the whole measured range of the FTIR spectra (400–4000 cm^{-1}) has shown the other interesting change in the chemical structure of the copolymer surface, namely the destruction of the polystyrene and polybutadiene blocks. This is illustrated in Figs. 7 (a) and (b) for the F507 elastomer, for which this transformation is more evident in comparison with F435. The presented spectra reveal the diminishing intensity of polystyrene bands at 1492 and 1600 cm^{-1} (typical bands of benzene ring [37]) as well as a typical polybutadiene band at 965 cm^{-1} (see: Fig. 5). At the same time we observe the growth of broad bands culminating at 1650, 995 and 925 cm^{-1}, which are assigned to C=C stretching vibrations (1650 cm^{-1}) and =C–H wagging vibrations in aliphatic structures (995 and 925 cm^{-1}) [37]. Particularly drastic changes in the surface structure are visible when the $CHCl_3/O_2$ plasma of higher power (80 W) is used. In this case all polystyrene and polybutadiene blocks are destroyed (spectrum d). A similar but weaker effect is also observed for the F435 elastomer. As one can see, this process, most probably connected with plasma ablation [40], is very harmful to the adhesion properties (Figs. 3 and 4). Thus, such drastic plasma conditions should be avoided if we want to improve the strength of the adhesive-bonded joints.

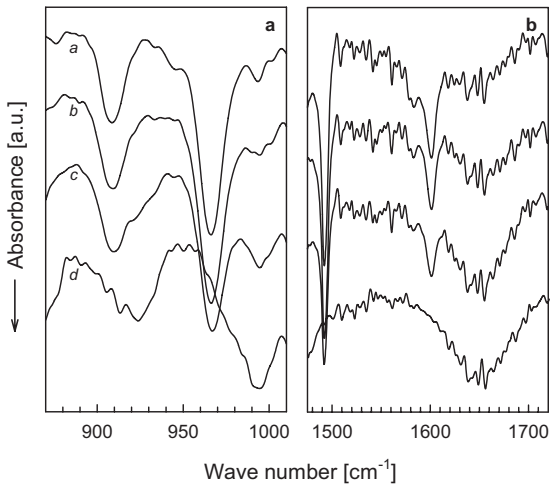

Figure 7 FTIR spectra of F507 samples, which suggest a plasma-ablation process: *a* – nontreated; *b* – plasma $CHCl_3$, 10 W; *c* – plasma $CHCl_3$, 80 W; *d* – plasma $CHCl_3/O_2$, 80 W.

Summarizing, it should be noted that the plasma chlorination seems to be a promising method to improve the adhesion properties of styrene-butadiene block copolymers.

It has been found that in this case the attachment of chlorine atoms to the elastomer surface plays a crucial role in the improvement of the adhesion properties. Although the mechanism of the interaction between the elastomer surface and polyurethane adhesives is not yet clear, there is no doubt that with increasing density of

C–Cl groups, the peel strength is also growing. The results presented in Fig. 2 show, however, that not only chlorinating plasmas but also CO_2 and O_2 plasmas give the desired effect. Taking into account the fact that these plasmas are much more environmentally friendly than those with chlorine precursors, recently we have focused our attention on such a treatment of the elastomer surfaces.

18.3.3
CO_2 and O_2 Plasma Treatment

The investigations on the elastomer surfaces modified by CO_2 and O_2 plasmas, performed in the framework of this paper, have been mainly focused on the optimization of plasma process parameters in the direction of a maximal improvement in the adhesive bonding of these surfaces. Two parameters of the plasma process have been discussed: the glow-discharge power and the duration of the plasma treatment. T-peel-strength test values obtained for F435 samples plasma modified at different times between 5 s and 20 min, and different powers (from 10 to 80 W), are given in Figs. 8 and 9 for CO_2 and O_2 plasmas, respectively.

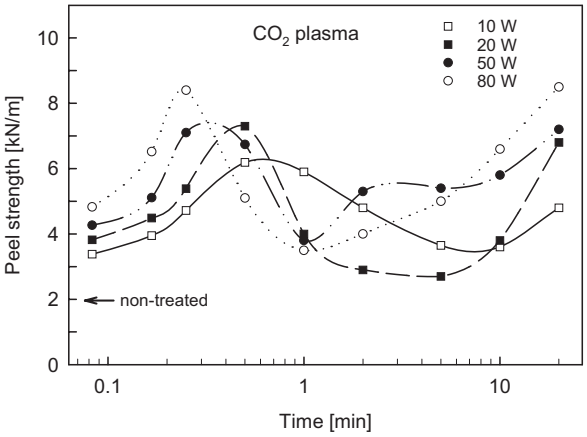

Figure 8 T-peel-strength measurements for F435 elastomer treated by CO_2 plasma as a function of the treatment time and the discharge power.

Let us start an analysis of the results from the CO_2 plasma treatment. As one can see in Fig. 8, three regions in relation to the treatment time can be distinguished irrespective of the applied power: (1) the region of evident increases in the peel-strength values at the beginning of the process, then (2) the reduction of these values, and finally (3) their increase after longer treatment times (at least a few minutes). The position of the peel-strength maximum that emerges at the beginning of the treatment process depends on the power. If the power is higher, the maximum occurs at shorter times. However, this dependence is relatively weak and in the whole region of the applied power the maximum lies between 15 and 40 s.

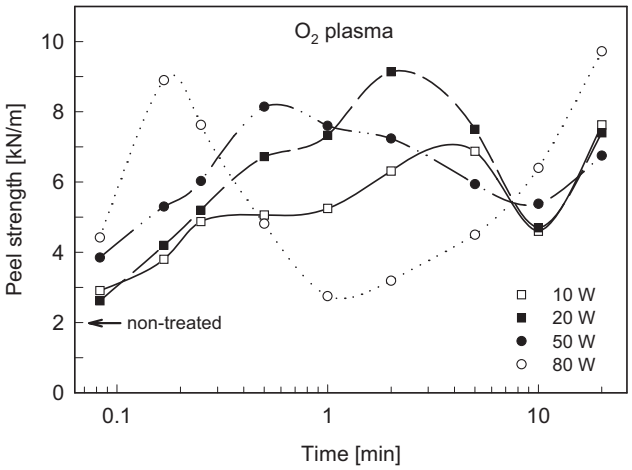

Figure 9 T-peel-strength measurements for F435 elastomer treated by O_2 plasma as a function of the treatment time and the discharge power.

For the O_2 plasma treatment (Fig. 9), we observe dependences of the peel strength versus treatment time similar in character to those for the CO_2 plasma treatment. In this case, however, the position of the peel-strength maximum depends much more on the discharge power (it is about 10 s for 80 W whereas for 10 W the maximum occurs not before the time of 4 min).

The FTIR measurements performed on the elastomer surfaces modified by CO_2 and O_2 plasmas turned out to be very useful for interpretation of the results presented above. It has been found that both CO_2 and O_2 plasma treatments produce carbonyl (>C=O) and hydroxyl (–OH) groups on the elastomer surface. Examples of IR spectra (for F435 samples) recorded in the regions characteristic for the stretching vibrations of these groups are presented in Figs. 10 (a)–(d). An evident increase in the intensity of bands at about 1691 and 1711 cm^{-1} (assigned to –C=O stretching vibrations) (Fig. 10 (c)) and about 3644, 3665 and 3683 cm^{-1} (O–H stretching vibrations) (Fig. 10 (d)) is visible. The formation of hydroxyl groups are confirmed by growing intensity of C–O stretching bands at about 1058, 1066, 1086 and 1110 cm^{-1} (Fig. 10 (a)). The presence of >C=O and –OH groups suggests that also carboxyl groups (–COOH) may exist on the surface. A new band growing at 1548 cm^{-1} (Fig. 10 (b)) can be just assigned to $–COO^-$ stretching vibrations. The formation of such groups on polymer surfaces treated by CO_2 plasma has been already shown [41]. It should also be added that any destruction of the polystyrene and polybutadiene blocks, which is observed in the case of the plasma chlorination, does not occur when CO_2 and O_2 plasmas are used.

The presence of carbonyl, hydroxyl and carboxyl groups on the elastomer surface can be closely connected with the adhesive bonding process, in which we can suspect chemical interaction between the surface and polyurethane adhesives. It is well

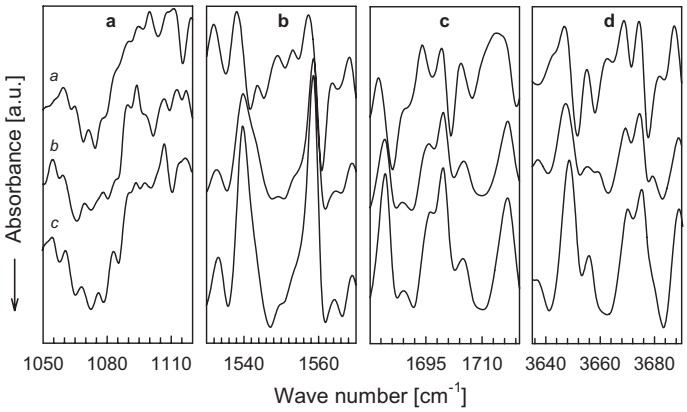

Figure 10 FTIR spectra of F435 elastomer treated by CO_2 and O_2 plasmas, shown in the regions (a–c) characteristic of >C=O, –OH, and –COOH vibration bands: *a* – nontreated sample; *b* – O_2 plasma, 20 W, 2 min; *c* – CO_2 plasma, 20 W, 0.5 min.

known that isocyanate groups (inherent in polyurethane adhesives) readily react with –OH, –COOH and >C=O [33]. If such reactions really take place on the surface, the strength of the adhesive-bonded joint should be dependent on the surface density of these active groups. Thus we could expect that the dependences from Figs. 8 and 9 would be a reflection of relations between the density of the active groups and the plasma-treatment time. Figure 11 presents, as an example, such relations for >C=O and –OH groups created by the O_2 plasma treatment at 20 W. The relations are expressed by normalized areas of appropriate IR bands (1691 and 1711 cm^{-1} for >C=O groups and 3665 and 3644 cm^{-1} for –OH groups). As one can see, a rise, reaching a maximum, and a decrease in the density of the active groups are in good agreement with the peel-strength dependence for the sample under discussion (Fig. 9, curve for 20 W). Hence we can suggest that the evident increase in the peel-strength values at the beginning of the plasma treatment and then the reduction of these values are connected with the chemical bonding between the elastomer surface and the adhesive. The maximum in the dependence of the density of the active groups on the plasma-treatment time is probably a result of competition between two processes: the creation of >C=O, –OH and –COOH groups on the elastomer surface, and their simultaneous destruction.

Investigations of the contact angle supply further information on the elastomer surface modified by CO_2 and O_2 plasmas and give arguments to support the idea discussed above. Figures 12 and 13 present the results of contact-angle measurements performed for F435 samples treated by the CO_2 and O_2 plasmas, respectively. The treatments were carried out for different times between 15 s and 20 min, and different powers from 10 to 80 W. In all the cases we observe a decrease in the contact angle with the treatment time down to practically constant values. It is interesting that these values are attained at the same time in which the maximum in the peel-strength dependences occurs (Figs. 8 and 9). Although it shows that the surface

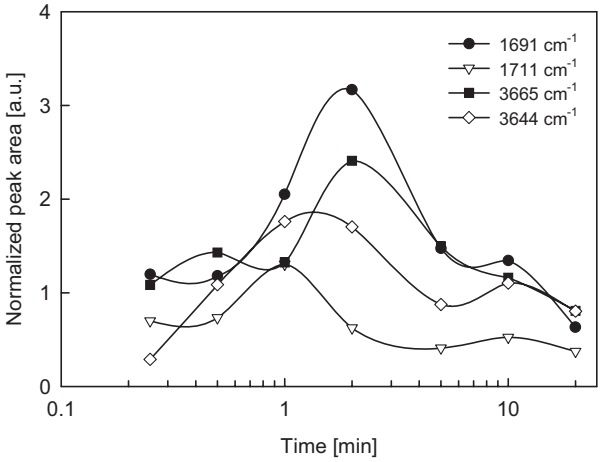

Figure 11 Dependence of the normalized area of bands characteristic for >C=O groups (1691 and 1711 cm^{-1}) and –OH groups (3644 and 3665 cm^{-1}) on the time of plasma treatment (O_2 plasma, 20 W; F435 elastomer).

modification determining the surface energy proceeds simultaneously with an increase in the peel strength (and consequently with the density of >C=O and –OH groups (Fig. 11)) at the beginning of the treatment process, the further reduction in the peel strength (as well as in the active group densities) do not reveal any relation with the contact angle. This can confirm that the strength of adhesive bonding between the SBS elastomer and polyurethane adhesives originates in fact from the chemical bonds and the thermodynamic adhesion is unimportant in this case.

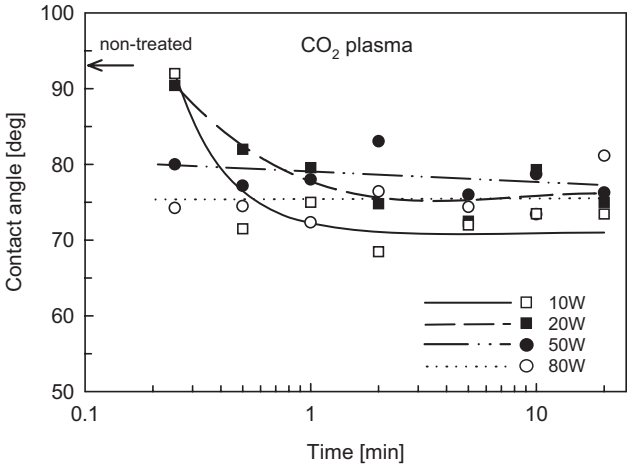

Figure 12 Measurements of the water contact angle for F435 elastomer treated by CO_2 plasma as a function of the treatment time and the discharge power.

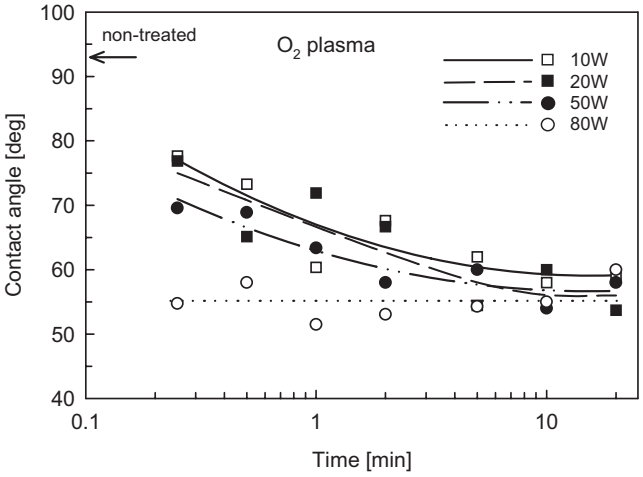

Figure 13 Measurements of the water contact angle for F435 elastomer treated by O_2 plasma as a function of the treatment time and the discharge power.

Similarly, for longer times of plasma action (at least a few minutes), we see an increase in the peel strength for both CO_2 and O_2 plasma treatments (Figs. 8 and 9), but the contact-angle values remain constant (Figs. 12 and 13). Also, any increase in the density of >C=O and –OH groups is not observed (Fig. 11). This may suggest that a surface microroughening, and hence the mechanical adhesion, begins to play a role in the adhesion properties of the SBS elastomers plasma modified for longer times. This problem needs, however, further investigations.

Summarizing, it should be emphasized that the CO_2 and O_2 plasma treatments have turned out to be an effective technique for the improvement of the adhesive bonding of the SBS elastomers. It has been found that the plasma-treatment time is a particularly important parameter of the surface-modification process. Generally, times from a few to over a dozen seconds are enough to obtain relatively high values of the peel strength. For longer times we observe a decrease in these values, and then, for times of the order of 10 min, again an increase. From the point of view of the adhesive force, three competing processes are proposed to explain these results: (1) the creation of >C=O and –OH groups on the elastomer surface, which can be engaged in chemical interaction between the surface and polyurethane adhesives, (2) the plasma destruction of these groups, and (3) some process that occur after longer treatment times, for example, surface microroughening.

18.4 Conclusion

The main conclusions concerning plasma modification of the SBS elastomer surface by chlorinating plasmas as well as CO_2 and O_2 plasmas are given in the last para-

graphs of the appropriate sections (Sects. 3.2 and 3.3). However, it should be stressed once more that the plasma treatment is a very useful method to improve the adhesion properties of SBS elastomers. Both plasma modification by chlorine functionalities (C–Cl) and oxygen functionalities (>C=O and –OH) effectively increase the strength of the adhesive-bonded joint between the elastomer surface and polyurethane adhesives. The utilization of CO_2 and O_2 plasmas arouses particular interest from the industrial point of view. These plasmas are a particularly time-saving (a treatment of 10–20 s is enough), clean and environmentally friendly technology of modifying the SBS elastomer surfaces. It seems that further thorough investigations on mechanisms of the plasma treatment may enable us to optimize this process still further.

Acknowledgements

This work is supported partially by the Polish Committee for Scientific Studies under project code 7 T09B 097 21 and the COST Action 527. The authors are grateful to Prof. W. Rzymski and Ms. A. Smejda-Krzewicka from the Chemistry Faculty of TU Lodz for the FTIR measurements as well as Prof. S. Slomkowski and Dr. S. Sosnowski from CMMS PAS for their help in the contact-angle measurements.

References

[1] J.C. Salamone (Ed.), *Polymeric Materials Encyclopedia, Vol. 10*, CRC, Boca Raton (1996).

[2] J.M. Martin-Martinez, J.C. Fernández-Garcia, F. Huerta, and A.C. Orgilés-Barceló, *Rubber Chem. Technol.* **64**, 510 (1991).

[3] D. Oldfield and T.E.F. Symes, *J. Adhes.* **16**, 77 (1983).

[4] J.M. Martin-Martinez, J.C. Fernández-Garcia, and A.C. Orgilés-Barceló, *J. Adhes. Sci. Technol.* **6**, 1091 (1992).

[5] M.M. Pastor-Blas, M.S. Sánchez-Adsuar, and J.M. Martin-Martinez, *J. Adhes. Sci. Technol.* **8**, 1093 (1994).

[6] M.M. Pastor-Blas, R. Torregrosa-Marciá, J.M. Martin-Martinez, and J.G. Dillard, *Int. J. Adhes. Adhesives* **17**, 133 (1997).

[7] M.D. Romero-Sánchez, M.M. Pastor-Blas, T.d.P. Ferrándiz-Gómez, and J.M. Martin-Martinez, *Int. J. Adhes. Adhesives* **21**, 101 (2001).

[8] D. Hace, V. Kovačević, D. Manojlović, and I. Šmit, *Angew. Makromol. Chem.* **176/177**, 161 (1990).

[9] R. Vukov, *Rubber Chem. Technol.* **57**, 275 (1984).

[10] D.K. Owens and R.C. Wendt, *J. Appl. Polym. Sci.* **13**, 1741 (1969).

[11] M. Strobel, C.S. Lyons, and K.L. Mittal (Eds), *Plasma Surface Modification of Polymers: Relevance to Adhesion*, VSP BV, Utrecht (1994).

[12] N. Inagaki, *Plasma Surface Modification and Plasma Polymerization*, Technomic Publ., Lancaster (1996).

[13] M. Strobel, S. Corn, C.S. Lyons, and G.A. Korba, *J. Poly. Sci.: Polym. Chem.* **23**, 1125 (1985).

[14] M. Strobel, K.P. Vara, S. Corn, C.S. Lyons, and M.C. Morgen, *J. Appl. Polym. Sci.: Appl. Polym. Symp.* **46**, 61 (1990).

[15] S. Corn, K.P. Vorna, M. Strobel, and C.S. Lyons, *J. Adhes. Sci. Technol.* **5**, 239 (1991).

[16] N. Inagaki, S. Tasaka, and M. Imai, *J. Appl. Polym. Sci.* **48**, 1963 (1993).

[17] S.H. Chen, W.H. Chuang, A.A. Wang, R.C. Ruaan, and J.Y. Lai, *J. Membr. Sci.* **124**, 273 (1997).

[18] B. Lee, Y. Kusano, N. Kato, K. Naito, T. Horiuchi, and H. Koinuma, *Jpn. J. Appl. Phys.* **36**, 2888 (1997).

[19] M.M. Pastor-Blas, J.M. Martin-Martinez, and J.G. Dillard, *Surf. Interface Anal.* **26**, 385 (1998).
[20] M.M. Pastor-Blas, T.P. Ferrándiz-Gómez, and J.M. Martin-Martinez, *Surf. Interface Anal.* **30**, 7 (2000).
[21] A.B. Ortiz-Magán, M.M. Pastor-Blas, T.P. Ferrándiz-Gómez, C. Morant-Zacarés, and J.M. Martin-Martinez, *Plasmas Polym.* **6**, 81 (2001).
[22] M.D. Romero-Sánchez, M.M. Pastor-Blas, J.M. Martin-Martinez, P.A. Zhdan, and J.F. Watts, *J. Mater. Sci.* **36**, 5789 (2001).
[23] J. Tyczkowski, I. Krawczyk, and B. Woźniak, *Acta Agrophys.* **80**, 231 (2002).
[24] J. Tyczkowski, I. Krawczyk, and B. Woźniak, *Surf. Coat. Technol.* **174/175**, 848 (2003).
[25] H. Koinuma, Y. Kusano, M. Yoshikawa, N. Kato, and K. Naito, *Eur. Patent* EP 0 788 870 B1 (1997).
[26] K.G. Reimer and J.R. Dykhouse, *World Patent* WO 00/01528 (2000).
[27] A.B. Ortiz-Magán, M.M. Pastor-Blas, and J.M. Martín-Martínez, *CD-Proc. 16th Int. Symp. on Plasma Chemistry*, Taormina (2003).
[28] J. Tyczkowski, I. Krawczyk, and B. Woźniak, *CD-Proc. 16th Int. Symp. on Plasma Chemistry*, Taormina (2003).
[29] M. Staeger, E. Finot, C.H. Brachais, S. Auguste, and H. Durand, *Appl. Surf. Sci.* **185**, 231 (2002).
[30] M.D. Romero-Sánchez, M.M. Pastor-Blas, J.M. Martin-Martinez, and M.J. Walzak, *J. Adhes. Sci. Technol.* **17**, 25 (2003).
[31] N.J. Harrick, *Internal Reflectance Spectroscopy*, Wiley-Interscience, New York (1967).
[32] D. Bielinski, P. Glab, L. Slusarski, G. Boiteux, and J.P. Chapel, *J. Appl. Polym. Sci.* **86**, 3368 (2002).
[33] Z. Wirpsza, *Polyurethanes – Chemistry, Technology and Applications*, Ellis Horwood, New York (1993).
[34] R.P. Kane, in: *The Vanderbilt Rubber Handbook*, R.F. Ohm (Ed.), R.T. Vanderbilt Company, Norwalk (1990).
[35] J. Haslam, H.A. Willis, and D.C.M. Squirrell, *Identification and Analysis of Plastics*, Butterworth & Co Publ., London (1972).
[36] D.O. Hummel, *Atlas of Polymer and Plastics Analysis*, Carl Hanser Verlag, Munich (1984).
[37] N.B. Colthup, L.H. Daly, and S.E. Wiberley, *Introduction to Infrared and Raman Spectroscopy*, Academic Press, New York (1964).
[38] R.M. Silverstein and G.C. Bassler, *Spectrometric Identification of Organic Compounds*, John Wiley & Sons, New York (1967).
[39] T. Shimanouchi, in: *NIST Chemistry WebBook, NIST Standard Reference Database Number 69 (http://webbook.nist.gov)*, P.J. Linstrom and W.G. Mallard (Eds), National Institute of Standards and Technology, Gaithersburg (2003).
[40] H. Yasuda, *Plasma Polymerization*, Academic Press, Orlando (1985).
[41] I. Gancarz, G. Pozniak, and M. Bryjak, *Eur. Polym. J.* **35**, 1419 (1999).

19
PET Surface after Plasma or Laser Treatment: Study of the Chemical Modifications and Adhesive Properties

P. Laurens, S. Petit, P. Bertrand, F. Aréfi-Khonsari

Abstract

The chemical modifications induced on PET by an excimer laser radiation or a low-pressure plasma were studied by XPS and Tof SIMS analyses. Both treatments induced surface oxidation but differences related to the type of oxidized groups and the level of degradation of the treated surface were evidenced. Both treatments can significantly enhance the adhesion but the surface change responsible for the improvement was different for each pretreatment.

19.1
Introduction

Al/PET adhesion has been extensively studied and it is widely known that a strong adhesion is obtained at the interface due to the formation of Al–O–C bonds from C=O and ether groups of poly(ethylene terephthalate) (PET) [1]. Failure of the Al/PET interface in a region near the initial PET surface, where the chemical composition differed from that of the PET bulk composition, was reported in crystalline PET [2]. Despite the natural affinity of PET to create bonds with Al atoms, the Al/PET interface strength can be further enhanced using surface pretreatments of PET [2–8].

Low-pressure glow discharge plasmas are increasingly used for the surface modifications of polymers without affecting the bulk properties of the material [9–13]. Plasma treatments in reactive gases (O_2, N_2, NH_3, etc.) have as a main effect the surface functionalization. Oxygen plasmas are largely used for this purpose. Oxygenated functions such as ethers, hydroxyls, carboxyls, carbonyls being grafted onto the surface, reactive surfaces are thus obtained. However the level of oxygenated functions should be limited in order to prevent the surface degradation by the formation of a weak boundary layer on the polymer surface [7]. The plasma parameters must thus be controlled with care and moderate plasma power densities, short treatment times and low percentages of O_2 in the plasma gas are usually used to favor polymer surface adhesion properties and stability. In particular, treatments in He-5% O_2 gas mixtures are interesting because they produce a surface oxidation, simultaneously with a crosslinking reaction [7].

Laser surface treatment can also enhance adhesion strength at the metal/polymer interface. This has been observed for both metal electroless deposition [14,15] and metal evaporation [15]. Improvements of adhesion at Co alloy/PET [16] or Al/PI (polyimide) [6] interfaces were reported for treatments performed below the polymer ablation threshold, whereas under similar conditions Al/PBT, poly(butylene terephthalate) adhesion was degraded [17].

Many investigations have been reported on the excimer laser irradiation of PET but most of the studies concerned the ablation regime [18–21]. Modifications induced on PET and other polymer surfaces by UV lasers below the ablation threshold have also been studied and the major changes such as surface amorphization [22–24], roughness evolution [25,26], chemical modifications [27–31] and increased wettability [28,32] are the well-known consequences of the low-fluence laser irradiation. The evolution of the polymer modifications under UV photon flux was reported to occur through absorption and scission of O=C–O groups leading to CO and CO_2 elimination; this led to a decrease of the oxygen content on the surface as observed in [32] when increasing the laser fluence. Surface deoxidation under UV photons is in competition with the surface oxidation when the treatment is carried out in air. It had been shown that oxidation only took place in the first layers of the polymer surface using X-ray photoelectron spectroscopy (XPS) with variable take-off angles [32]. Other works showing different results and a decrease of the O/C ratio at the outermost surface under UV photons were also reported [25,28].

The effects of the exposure of a PET film to laser irradiation in air or to a low-pressure glow discharge in a mixture of He-5% O_2 were investigated. Changes in the surface composition (using XPS) and adhesion properties were analyzed and compared. We previously showed the efficiency of both treatments to enhance adherence to aluminum [33]. However, the role of the surface oxidation on the strength improvement of the Al/PET interface remained uncertain, in particular, in the case of the laser treatment. In this study, we combine XPS and Tof SIMS analyses to investigate the chemical changes in the composition of the extreme surface. Tof SIMS appears to be an ideal complementary technique to XPS owing to its molecular information, high sensitivity and its selectivity to the uppermost surface layer. After thermal metallization, peel-test measurements were performed to evaluate the Al/PET adhesion.

19.2 Experimental Details

100-μm thick PET films (Melinex 400 from ICI, purchased from Goodfellow) were used after an ultrasonic cleaning in ethanol. According to the manufacturer's specifications, the PET films were biaxially oriented (the crystallinity of the film obtained by DSC analysis was 30%). The laser treatment was carried out using a pulsed excimer laser emitting a radiation at 248 nm with a pulse duration of 30 ns (krypton-fluorine gas). A beam-homogenizing system was used in order to perform a uniform treatment (uniform laser fluence distribution in the 15×15 mm interaction

zone). In order to treat large polymer surfaces (100 × 100 mm), an X-Y motorized table was used to scan the polymer under the laser beam (Fig. 1). Taking into account the irradiation zone dimensions (15 × 15 mm) and frequency of the laser pulse (10 Hz), the scanning speed was set to obtain the required number of laser pulses per surface unit (from 1 to 2000) on the whole polymer surface. Treatments were carried out in ambient air. The fluence (or energy density) of the incident beam during each laser pulse was 5 mJ/cm^2 or 20 mJ/cm^2. At 5 mJ/cm^2, the laser peak power density (during the 30-ns long laser pulse) and the average power density were respectively 1.67×10^5 W/cm^2 and 0.05 W/cm^2 (and respectively 6.66×10^5 W/cm^2 and 0.20 W/cm^2 when the fluence was 20 mJ/cm^2). The fluence was always below the PET ablation threshold fluence (27 mJ/cm^2) and either below (5 mJ/cm^2) or above (20 mJ/cm^2) the PET amorphization threshold fluence (located around 10 mJ/cm^2 depending on the authors). The evolution of the surface properties with the number of added pulses per surface unit was investigated for treatment carried out at 5 mJ/cm^2 or 20 mJ/cm^2.

Plasma treatments were realized in a bell jar glass reactor with a nonsymmetrical configuration of electrodes [7,9]. The low RF power (70 kHz) was capacitively

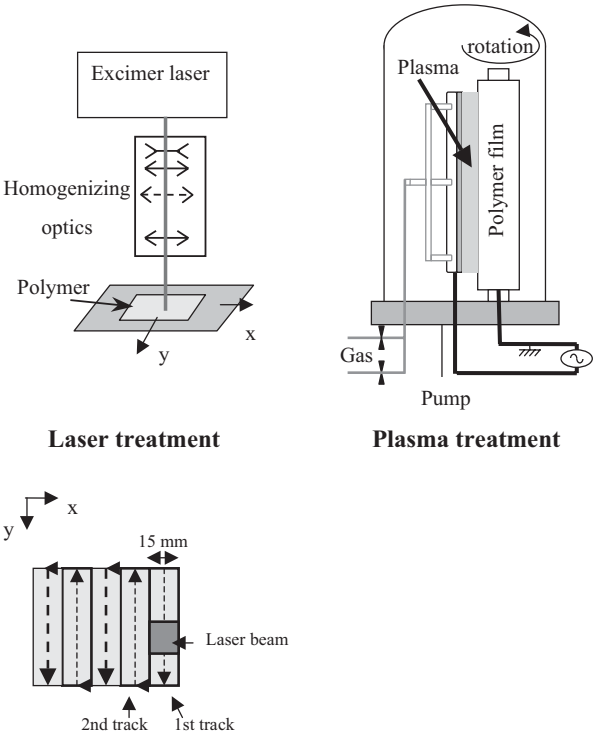

Figure 1 Laser and plasma experimental setup.

coupled to a blade-type electrode (Fig. 1). The polymer films were rolled on the grounded cylinder. The plasma power was between 2 and 3 W (the plasma power density was ranging between 0.2 and 0.3 W/cm^3 (or approximately between 0.10 W/cm^2 and 0.20 W/cm^2 on the polymer surface)) and the gas pressure was 100 Pa. Treatments were carried out in a He–O_2 (95–5%) optimized gas mixture. The treatment time ranged between 1 and 20 s.

After a short exposition to air of the polymer film, an Al film was deposited by thermal evaporation in a vacuum chamber ($P = 10^{-3}$ Pa). The average metal thickness was measured using a quartz crystal balance (Al thickness: 150 nm).

XPS spectra were obtained using an unmonochromatized aluminum X-ray source (Escalab). The binding energy scale was calibrated by setting the C_{1s} hydrocarbon photoelectron peak at 284.7 eV. Gaussian peaks were used for XPS signal fitting and decomposition. Uncertainty in setting the peak binding energies was estimated to be ± 0.2 eV. The relative atomic concentrations were calculated using peak areas. The surface modifications of the treated PET were studied by analyzing the C_{1s} photoelectron peak envelope and the O_{1s}/C_{1s} ratio.

Tof SIMS measurements were performed a few days after the treatments using a Trift 1 spectrometer from PHI-Evans. The primary ion source was a pulsed Ga ion source operating at 15 keV. Charge compensation was performed with a pulsed electron gun. Each peak intensity was normalized to the total secondary intensity in the spectrum, minus the $H^+/^-$ intensity. Owing to the high complexity of the spectra (both in positive and negative modes), the analysis of the Tof SIMS spectra was realized using statistical tools adapted to such multivariable data. A principal component method was used [34,35]. This technique permitted selection of the major changes in the spectra taking into account all the peaks intensities for all the registered spectra, both in the positive and negative modes.

Contact-angle measurements were performed using the sessile-drop technique to determine the reversible work of adhesion of the surface with the liquid (methylene iodide and double-distilled water). The contact angles were measured using a Digidrop contact-angle measuring system equipped with a camera and an image-processing system (from GBX). At least six measurements were carried out on each sample. The acid base contribution ($W_{ab/liq}$) to the total reversible work of adhesion of the polymer in the presence of a liquid ($W_{tot/liq}$) was determined from [36, 37]:

$$W_{tot/liq} = W_{d/liq} + W_{ab/liq} = \gamma_{liq}\,(1 + \cos\theta_{liq})$$

where $W_{tot/liq}$, $W_{d/liq}$ and $W_{ab/liq}$ are, respectively, the total reversible work of adhesion of the polymer in the presence of a liquid, the dispersive contribution of the reversible work of adhesion and acid base contribution to the reversible work of adhesion. γ_{liq} is the surface tension of the liquid.

Using methylene iodide as a non polar liquid and water as a polar liquid, the acid base contribution to the reversible work of adhesion of the polymer in presence of water, W_{ab}, can be obtained from:

$$W_{ab} = W_{ab/aq} = W_{tot/aq} - W_{d/aq} = \gamma_{aq}\,(1 + \cos\theta_{aq}) - 2\,(\gamma_{iodide}\,.\,\gamma_{d\ PET})^{1/2}$$

and

$$W_{tot/iodide} = \gamma_{iodide}\,(1 + \cos\theta_{iodide}) = 2\,(\gamma_{iodide}\,.\,\gamma_{d\ PET})^{1/2}$$

where γ_{aq}, γ_{iodide} are the surface tensions of water and methylene iodide, respectively. $\gamma_{d\ PET}$ is the critical surface tension of PET. θ_{iodide}, θ_{aq}, are the contact angles of PET in the presence of methylene iodide and water, respectively. $W_{tot/iodide}$ is the total reversible work of adhesion of the polymer in the presence of methylene iodide.

The strength of the Al/PET interface was investigated using a 180° peel-test technique for which the metallized polymer film was first fixed using an EAA (ethylene-acrylic acid) adhesive in a tensile machine. This test developed by Dupont de Nemours for Al/PET is described in detail elsewhere [3]. After metallization, the PET side is first fixed to the metal support with an adhesive tape and an EAA (ethylene-acrylic acid) adhesive film was laminated onto the Al side by maintaining the specimen for a few seconds at 105 °C under a constant force. The test was then performed by peeling off the EAA polymer strip in a tensile machine with a 180° peel angle and a peel speed of 50 mm/min (Fig. 2). The peeling occurred at the Al/PET interface and the peel force was recorded (N).

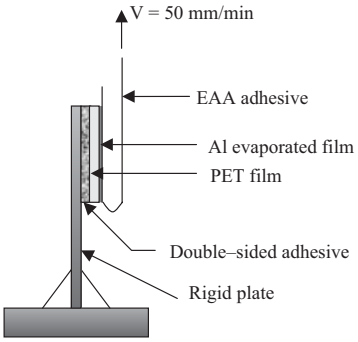

Figure 2 Schematic view of the 180° peel test.

19.3 Results

19.3.1 Untreated PET

19.3.1.1 Chemical Composition

XPS spectrum (C_{1s} (Fig. 3) and O_{1s}) of the untreated PET (after ultrasonic cleaning) was close to that of pure PET ($-(CO_2\Phi CO_2C_2H_4)_n$): $O_{1s}/C_{1s} = 0.38$ (instead of 0.4), C–O (286.3 eV)/C = 0.16 (instead of 0.2) and O=C–O (289.5 eV)/C = 0.14 (instead of 0.2). The weak lack of oxygen could indicate a slight hydrocarbon contamination of the surface.

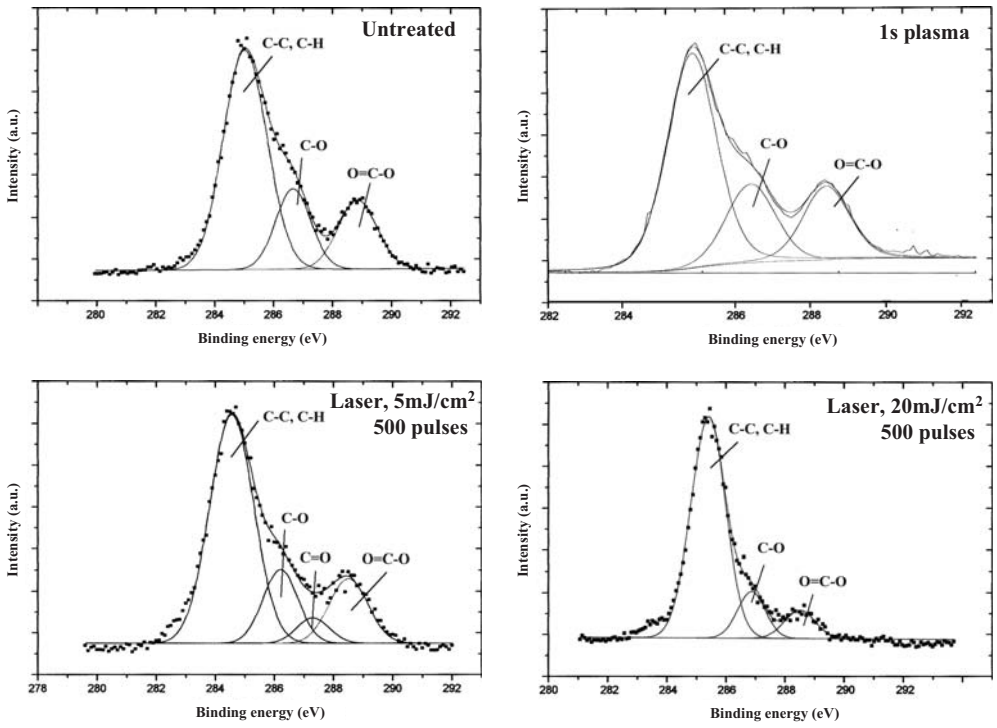

Figure 3 XPS analyses: C_{1s} photoelectron spectra of nontreated, plasma- and laser-treated PET.

The Tof SIMS spectrum of PET was in good agreement with already published data [38]. The main peaks were:

$-CHO^+$ (m/z= 29), $C_2H_3O^+$ (m/z= 43), $°\Phi^+(C_2H_3^+$, m/z= 76), Φ^+ ($C_6H_5^+$, m/z= 77), $°\Phi-CO^+$ (m/z= 104), $\Phi-CO^+$ (m/z= 105), $°\Phi-COO-CH_2CH_2^+$ (m/z= 148), $HOOC-\Phi-CO^+$ and $\Phi-COOCH_2CH_2^+$ (m/z= 149), $[M+H]^+$ (m/z= 193), $[2M+H]^+$ (m/z= 385), $[3M+H]^+$ (m/z= 577) in the positive spectrum,
$-CH^-$ (m/z= 13), OH^- (m/z= 17), $COOH^-$ (m/z= 45), $C_2H_3O_2^-$ (m/z= 59), $°\Phi-COO^-$ (m/z= 120), $\Phi-COO^-$ (m/z= 121), $HOOC-\Phi-COO^-$ (m/z= 165), $(2M-C_2H_3)^-$ (m/z= 357) in the negative spectrum,

with M, the PET repeat unit (m/z= 192).

19.3.1.2 Surface Properties

The contact angle on an untreated PET surface was 77° (±3°) with water and 26°(±3) with methylene iodide. W_{ab} and γ_d were, respectively, 26.0 mJ/m^2 and 45.8 mJ/m^2.

The peel force was negligible (F= 0.2 N/cm) and visual or SEM observations of the peeled surfaces showed that the failure took place at (or close to) the Al/PET

interface. In the absence of chemical analysis of the peeled sides, the interfacial or cohesive (within the PET near the Al/PET interface) nature of the failure could not be precisely determined. It is generally assumed that, due to the strong affinity between Al and PET, the failure occurred in the skin layer (which represents a weak boundary layer on the PET film surface due to the manufacturing process of biaxially stretched films [2]).

19.3.2 Plasma-treated PET

19.3.2.1 Chemical Composition

XPS: Besides C and O, traces of nitrogen were always evidenced by XPS after plasma treatments. Plasma always gave rise to an increase of the O_{1s}/C_{1s} ratio. The O_{1s}/C_{1s} ratio was 0.44 after 0.1 s and 0.46 after 1 s. After decomposition of the C_{1s} photoelectron peak, the surface oxidation was responsible for the increase of both O–C=O/C and C–O/C ratios owing to the formation of new chemical bondings (carboxylic acid, alcohol, etc.) but no other peak could be identified (Fig. 3).

Tof SIMS: Statistical analysis of both positive and negative spectra of untreated and plasma-treated PET indicated that surface oxidation was the main consequence of the plasma treatment. It was shown by the increase of the OH^-/CH^- ratio and relative intensities of $COOH^-$, $C_2H_3O_2^-$ and HOOC–Φ–COO^- ion for all treated PET films [34]. The evolution of the OH^-/CH^- ratio with the plasma treatment time (Fig. 4) shows that surface oxidation took place and can be detected for treatment times as short as 0.1 s. The OH^-/CH^- ratio increased for treatment times up to 1 s where it stabilized. No other significant change in the spectra was evidenced. In particular, no evolution of the relative intensity of ions being the fingerprint of PET molecule was noticed (Table 1).

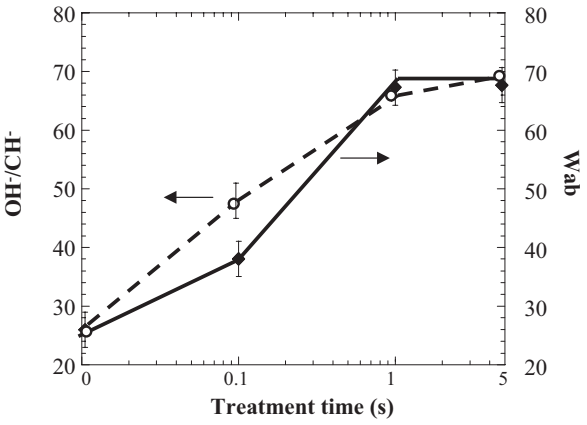

Figure 4 Evolutions of the OH^-/CH^- ratio (Tof SIMS) and acid base reversible work of adhesion of PET (W_{ab}) with the plasma-treatment time.

Table 1 Tof SIMS analyses: Evolution of the relative intensity of some ions (from the positive spectra) being a fingerprint of the PET molecule with the plasma treatment time.

Treatment time (s)	0	0.1	1	5
m/z= 76	1	0.8(+0.03)	0.8	0.8
m/z= 104	1	0.8	1	1
m/z= 193	1	0.8	1.05	1

19.3.2.2 **Surface Properties**

Surface oxidation after plasma treatment was responsible for the improvement of the surface energy due to the increasing content of oxidized polar groups as can be observed from the increasing reversible adhesion work after treatment. Increasing the plasma treatment time improved the acid base contribution to the work of adhesion, W_{ab}, that was stable after a 1-s treatment (Fig. 4).

In the investigated range of treatment time (0.1 to 5 s), Al–PET adhesion was always enhanced after a plasma treatment (Fig. 5).

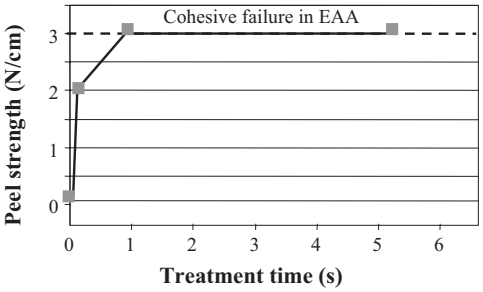

Figure 5 Al–PET adhesion after the plasma pretreatment: Al–PET peel strength vs the treatment time.

19.3.3 **Laser-treated PET**

19.3.3.1 **Chemical Composition**

XPS and Tof SIMS techniques were used to study the chemical composition of the treated PET.

XPS: After laser treatments, only carbon and oxygen were detectable and no other element was ever identified. The evolution of the O_{1s}/C_{1s} ratio of treated PET versus the number of pulses was sensitive to the laser fluence (Fig. 6). At a low fluence (5 mJ/cm^2), a global surface oxidation took place when the number of pulses exceeded 200. On the other hand, at a high fluence (20 mJ/cm^2), oxygen depletion was observed when cumulating more than 200 pulses per surface unit. This fluence-dependent behavior was a consequence of a competition between decarboxylation under UV photons (favored at high fluence) and oxidation (main reaction at

low fluence) of the UV activated surface in the presence of a reactive atmosphere [39]. The specific decarboxylation of PET under UV laser may be responsible for the rather moderate level of oxygen incorporation. After decomposition of the C_{1s} spectra, besides the presence of the two oxygen components corresponding to C–O and O=C–O groups, a third peak was identified in oxidation conditions (5 mJ/cm^2) probably corresponding to C=O groups (287.3 eV) (Fig. 3). Therefore the formation of the C=O groups on PET (not observed after plasma treatment) is specific to the reaction of the UV-activated surface with oxygen.

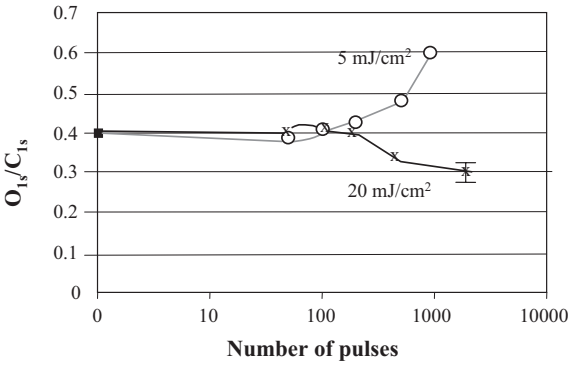

Figure 6 XPS analyses of the PET surface after laser irradiation: Evolution of the O_{1s}/C_{1s} ratio with the number of pulses for treatments at different laser fluences.

Tof SIMS: As already observed for plasma-treated surfaces, an increase of the OH^-/CH^- ratio, as well as the relative intensities of $COOH^-$, $C_2H_3O_2^-$ and HOOC–Φ–COO^- ions, was the main indication of the extreme surface oxidation after laser treatment.

The evolutions of the OH^-/CH^- ratio after laser treatment at 5 mJ/cm^2 and 20 mJ/cm^2 are shown in Fig. 7. At 5 mJ/cm^2, below 100 laser pulses, the OH^-/CH^- ratio was not modified but it increased for a higher number of laser pulses. Extreme surface oxidation only took place when a significant number of laser pulses were added. At 20 mJ/cm^2, no significant evolution of the OH^-/CH^- ratio was ever noticed.

Besides surface oxidation, new features could be detected on the positive and negative spectra of PET after laser treatment. As a matter of fact, a significant decrease of the relative intensity of some ions being the fingerprint of the PET molecule was observed as shown in Table 2. Those ions are: $^\circ\Phi^+$ (m/z= 76), $^\circ\Phi$–CO^+ (m/z= 104), $[M+H]^+$ (m/z= 193). Finally, a strong decrease of radical/non radical intensity ratio was also observed for: $^\circ\Phi^+$ (m/z= 76)/ Φ^+ (m/z= 77), $^\circ\Phi$–CO^+ (m/z= 104)/Φ–CO^+ (m/z= 105) and $^\circ\Phi$–COO^- (m/z= 120)/Φ–COO^- (m/z= 121). This indicates an increase of labile H atoms allowing the radical ions to be stabilized by recombination during the SIMS emission process.

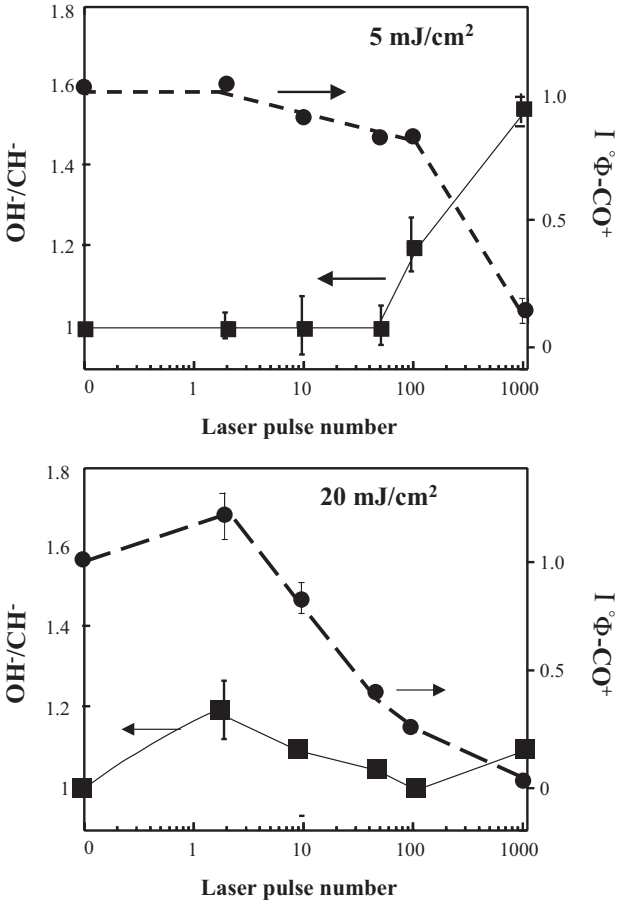

Figure 7 Tof SIMS analyses of PET after laser treatment at 5 mJ/cm^2 and 20 mJ/cm^2. Evolution of the OH^-/CH^- and $°\Phi–CO^+$ relative intensity with the number of laser pulse.

Table 2 Evolution of the relative intensity of some ions (from the Tof SIMS positive spectra) being a fingerprint of the PET molecule with the number of laser pulses at 5 mJ/cm^2 and 20 mJ/cm^2.

Number of pulses	0	2	10	50	100	1000
5 mJ/cm^2						
m/z= 76	1	1	1	0.9	0.8	0.23
m/z= 104	1	1	0.9	0.9	0.9	0.2
m/z= 193	1	1	0.98	0.95	0.9	0.2
20 mJ/cm^2						
m/z= 76	1	1.1	0.8	0.4	0.3	0.1
m/z= 104	1	1.2	0.8	0.4	0.3	0.1
m/z= 193	1	0.8	0.8	1.1	1	0.2

PET chain scissions and general degradation (due to oxidation and/or UV photolysis) are probably responsible for such evolutions in the Tof SIMS spectra [40]. In the following, the surface degradation will be illustrated by showing the decrease of the relative intensity of the $^{\circ}\Phi$–CO^+ ion (m/z= 104).

The evolutions of the relative intensity of $^{\circ}\Phi$–CO^+ after laser treatment at 5 mJ/cm^2 and 20 mJ/cm^2 are shown in Fig. 7. At 5 mJ/cm^2, no significant evolution of the relative intensity of $^{\circ}\Phi$–CO^+ surface is noticed below 100 laser pulses but it decreased when increasing the number of laser pulses. At 20 mJ/cm^2, a rapid decrease of the relative intensity of $^{\circ}\Phi$–CO^+ surface occurred after a few laser pulses (>10).

Oxidation and degradation were the consequences of the PET laser irradiation. However, the process parameters, the fluence and the number of laser pulses, had a major role on the level of such modifications. At 5 mJ/cm^2, both surface oxidation and degradation occurred simultaneously after an incubating period of approximately 100 pulses. When the polymer faced a higher UV dose (20 mJ/cm^2), the incubating period is dramatically reduced (10 pulses) and the photolytic degradation is the main consequence of irradiation.

19.3.3.2 **Surface Properties**

The lower the laser fluence, the higher was the increase of the acid base contribution to the work of adhesion, W_{ab}, (Fig. 8). Treatments at low fluence favoring surface oxidation were responsible for the increase of the acid base component of the surface energy.

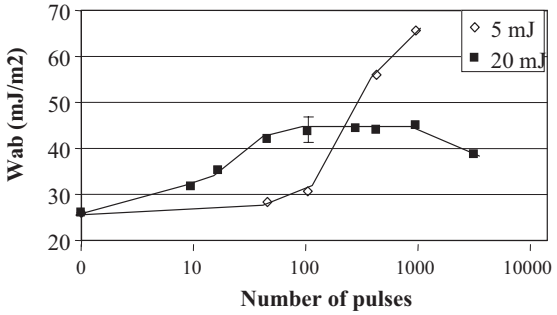

Figure 8 Acid base reversible work of adhesion, W_{ab}, vs number of pulses after laser treatment at 5 mJ/cm^2 and 20 mJ/cm^2.

The Al/PET interface strength was dependent on the laser treatment conditions (Fig. 9). The results obviously emphasized the influence of the laser fluence when the treatment was performed with a moderate number of pulses (< 100 pulses): as a matter of fact, the peeling force was maximum after a short treatment (1 to 10 pulses) at 20 mJ/cm^2 and the failure occurred within the EAA adhesive, even after a single laser pulse. On the contrary, after a low fluence treatment (5 mJ/cm^2), a limited improvement of the Al–PET strength was obtained. SEM examination showed

that the failure took place at the metal–polymer interphase (complementary XPS surface chemical analysis would be required to precisely determine the locus of the failure). Degradation of the Al/PET interface strength always occurred when the treatment time was increased (number of pulses > 100) independent of the laser fluence.

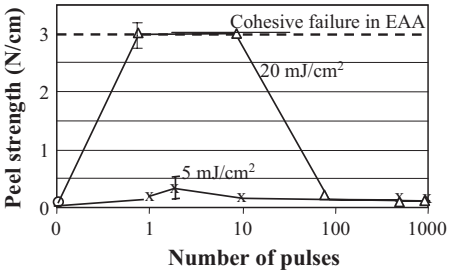

Figure 9 Al–PET adhesion depending on the laser-pretreatment conditions of PET: Al–PET peel strength for different laser conditions in air.

19.4 Discussion

The efficiency of the plasma and laser treatments to improve the strength of the Al/PET interface was undoubtedly demonstrated (in the latter, the laser process parameters must be carefully adjusted in order to observe the enhancement of the adhesion strength). Now the evolutions of the surface composition at different sampling depths (5 nm for XPS and 0.1 nm for ToF SIMS), the surface properties and Al–PET strength with the plasma or laser parameters will be discussed.

19.4.1 Surface Oxidation

Both XPS and Tof SIMS techniques indicated that the surface oxidation, responsible for the increase of the surface energy due to the formation of polar oxidized groups, took place as soon as the plasma treatment started (treatment time: 0.1 s).

In the case of laser treatments, XPS analyses have already shown that the composition of the surface depended on the laser fluence [30,36]. This is a consequence of the competition between surface decarboxylation under UV radiation and surface oxidation of the PET owing to the surrounding oxygen (air).

At a low fluence (5 mJ/cm^2), the decarboxylation rate is low and oxidation is the main reaction. This led to an increase of the O/C ratio. By using XPS, evidence for surface oxidation was only obtained when at least 100 pulses were used to irradiate the surface.

For shorter treatment times, XPS and Tof SIMS spectra were identical to untreated PET. This indicated that no chemical modification took place in the laser-affected depth of the polymer or on its extreme surface. Thus it can be concluded that modifications of PET required a certain dose of UV photons. The functionalization of the polymer is preceded by an activation phase. Such an activation phase is also observed at higher fluence. However, due to the higher UV dose in the laser pulse, the phase is reduced to the first tens of pulses. The phenomena taking place during this activation phase are not precisely understood; no UV stabilizers (such as Hindered Amine Light Stabilizer: Chimassorb, Tinuvin) were detected by ToF-SIMS.

As soon as the activation phase was over, surface oxidation occurred and was detected both by XPS and Tof SIMS and this led to the enhancement of the surface hydrophilicity due to the grafting of oxidized polar groups. For low-fluence treatments, surface composition and surface wetting properties are always correlated.

In contrast, after high-fluence treatments, diverging informations regarding the change in the surface composition could be obtained by XPS and SIMS. After the activation phase (number of pulse > 50), XPS gave evidence for surface decarboxylation (decreasing O/C and O–C=O/C ratios) at least in the first 5 nm from the surface while no change in the oxygen to carbon content of the topmost layer of the surface (OH^-/CH^-) was detected by Tof SIMS. Thus, it can be postulated that the surface decarboxylation under high UV radiation occurs in the UV irradiated layer (thickness: of the order of 100 nm) while surface reoxidation takes place. This surface oxidation at the topmost layer, that can take place during the laser pulse or as a post treatment owing to the presence of UV-excited PET radicals and surrounding oxygen, is responsible for the enhancement of the polar component of the surface energy. As the enhancement of the surface water wettability is observed just after the treatment is performed, we can postulate that the surface oxidation takes place rapidly during or just after the treatment.

Tof SIMS analysis of laser polymer treated below the ablation threshold has never been published before and our results can only be compared to what has been done by using XPS with a variable take-off angle (for a take-off angle as low as 15°, the analyzed depth is 1.3 nm, in the order of that analyzed by Tof SIMS (1 nm)). Kokai and Saito [29] reported that decreasing the take-off angle on laser-treated PET resulted in an increase of the O/C carbon ratio restoring thus to the PET surface an oxygen content close to that of the untreated PET (similar to us). On the contrary, Watanabe et al. [25] detected oxygen depletion when selectively analyzing the topmost surface.

19.4.2 Surface Degradation

Besides the monitoring of the chemical modifications produced by the treatments, one important piece of information obtained from Tof SIMS spectra, was the possibility to evidence surface degradation. Surface degradation and the formation of nodules under oxidizing conditions were often reported as a result of the formation

of low molecular weight oxidized fragments (LMWOF) obtained by other oxidative surface treatments of PET such as low-discharge plasmas or UV-ozone (UVO) treatments [3,6,9].

For the He-O_2 plasma used in this study, whatever were the treatment conditions, no significant evidence of degradation was detected by Tof SIMS. The optimized gas mixture and plasma conditions allowed us to avoid surface degradation under oxidation and thus prevented the formation of a weak oxidized surface layer (the He-O_2 plasma favored surface crosslinking [7]). In addition, for plasma-treated surfaces, the removal of a degraded layer (if any) by ions and excited plasma species bombardment as well as by UV could be possible. Surface etching was detected by mass spectrometry and weight-loss measurements for oxygen rich He+O_2 mixtures [7].

On the other hand, for laser treatment, polymer-chain degradation was always the consequence of long laser treatment. As a matter of fact, Tof SIMS analyses showed that the peaks corresponding to the PET signature suddenly decreased when a certain number of laser pulses is reached. The higher the fluence, the sooner the degradation occurred. This indicated that after the absorption of a certain dose of UV photons, severe photolytic and/or pyrolitic decomposition of PET occurred both in oxidation (low fluence) and decarboxylation (high fluence) conditions. The onset of the PET degradation (detected by Tof SIMS) is correlated with the detection of surface decarboxylation by XPS (decrease of O–C=O/C ratio). Evidence for surface degradation was also given by studying the treated surface before and after a further surface rinsing. In degradation conditions, AFM and contact-angle measurements have shown that rinsing strongly affects the surface due to the removal of a mobile loosely bonded material [33].

Comparison between plasma- and laser-treated surfaces shows that plasma treatment allowed the formation of an oxidized surface layer without degradation probably owing to surface crosslinking. Laser treatment strongly deteriorates the PET macromolecules and can lead to severe degradation with or without global oxygen enrichment. The negative degradative effect of laser treatment compared to plasma treatment when increasing the acid base properties, W_{ab}, is illustrated in Fig. 10. As

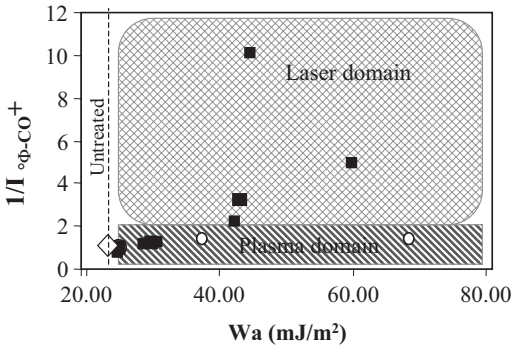

Figure 10 Level of PET degradation (1/I °Φ–CO^+ from Tof SIMS), versus the PET acid base reversible work of adhesion after laser or plasma treatments.

a matter of fact, in the former case (laser domain), increasing the acid base properties of the surface is always associated with an increase of the degradation level (the degradation level being expressed as the inverse of the relative intensity of the $^{\circ}\Phi$–CO^{+} ion (m/z= 104) characteristic of PET). In contrast, the increase of the acid base properties after plasma treatment is obtained without any surface degradation (plasma domain).

19.4.3 Al–PET Adhesion

For plasma treatments, an increase of the Al–PET adhesion was always obtained and the maximum adhesion level was reached after a 1-s treatment. No sign of adhesion degradation was ever noticed for treatment as long as 5 s in the limit of the adhesive test used. The improvement of the adhesion depended on the enhancement of the surface acid base contribution to the work of adhesion resulting from surface oxidation (Fig. 11). Besides this, the optimized plasma conditions prevented the formation of a weakly bonded oxidized surface layer.

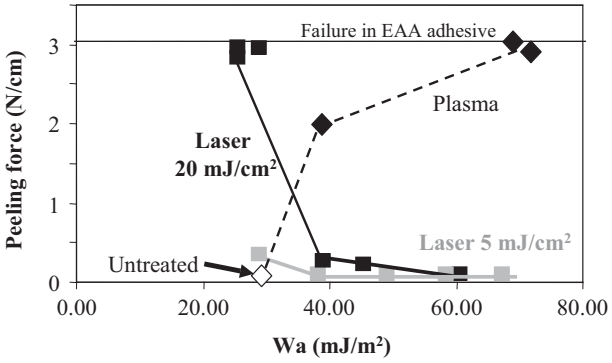

Figure 11 Al–PET peel strength versus the PET surface reversible work of adhesion after laser or plasma treatments.

In the case of laser treatment, it was found that the fluence and the number of pulses had a major influence on Al–PET adhesion. A high level of the adhesion is only reached when using a moderate number of pulses at a high fluence; a single laser pulse treatment at 20 mJ/cm^2 was enough to obtain the maximum Al–PET adhesion.

For a high number of pulses (> 100 pulses), the surface degradation that accompanied surface oxidation (low fluence) or decarboxylation (high fluence) was responsible for poor Al–PET adhesion, whatever the fluence conditions were. The increase of the PET wettability was not a factor that improved the adhesion (Fig. 11). The lack of adhesive properties after long laser treatment was attributed to the surface degradation and to the formation of low molecular fragments due to extended photolysis and/or photo-oxidation under UV radiation.

For high fluences (≥ 10 mJ/cm^2), the maximum Al–PET adherence was always reached after a few pulses (between 1 and 10 pulses). The nature of the physical and/or chemical effects responsible for this enhancement remained difficult to identify because for such short treatments, PET surface modifications were hardly detected. The absence of the change of the surface wettability and in the Tof SIMS spectra compared to the untreated surface indicated that such oxidation is not responsible for the adhesion enhancement. Consequently, the excellent efficiency of a high-fluence treatment with a very low number of pulses should possibly depend on the morphological modifications of PET under an intense flux of photons. Among possible changes, the removal (or modifications) of the initial skin layer (due to thermal and/or photolytic effects), changes of the surface crystallinity, increased surface mobility after chain scission could significantly participate in the adhesion improvement. The removal of the slight initial hydrocarbon surface contamination can also be supposed. At low fluences, the degree of surface morphological transformation would not be sufficient due to the small temperature increase and/or limited photolytic transformation. Adequate surface transformation would be fully achieved at higher fluences. Since surface amorphization after surface melting has been found to take place around 10 mJ/cm^2 [22–24], it is postulated that such surface morphological transformation after surface melting obtained above that threshold was responsible for the high adherence. Thus, maximum adhesion could be obtained after a treatment carried out at a fluence above the amorphization threshold. The value of the latter depends on the PET optical absorbing properties and thus composition (additives, impurities, etc., played an important role in the polymer-film UV absorption). It has not been strictly determined in this study, but from the present assumption, it is thought to take place between 5 mJ/cm^2 and 10 mJ/cm^2 at 248 nm. This is consistent with the amorphization threshold (5 mJ/cm^2) determined in ref. [23].

19.5 Conclusion

Chemical modifications induced on PET after an 248-nm excimer laser irradiation or a low-pressure plasma treatment performed below the polymer ablation threshold were characterized. Besides, the efficiency of the treatments on the Al–PET adhesion of thermally evaporated aluminum was investigated. The results clearly indicated that very significant improvement of the adhesion were obtained after very short treatment times both with laser and plasma. However, the present observations support the idea that the mechanisms responsible for the adhesion gain were different for the two types of pretreatments. In the case of plasma treatment, surface oxidation and increased wettability associated with surface crosslinking were probably responsible for the reinforcement of the Al–PET strength. In the case of laser treatment, surface oxidation had a deleterious effect on the adhesion because of an accelerated degradation of the surface by UV photons irradiation. The improvement of the Al–PET adhesion after laser treatment was particularly evident at high fluences

after a single or a few laser pulses. This is thought to result from the transformation (or removal) of the initial skin layer after surface amorphization and/or ablation. A single laser pulse above the amorphization threshold fluence allowed these effects to take place. Besides, in such conditions excessive surface photolysis was avoided.

Acknowledgments

The authors would like to thank M. M. Tatoulian from the Laboratoire de Génie des Procédés et des Traitements de Surface for help and discussions. Mariette Nivard and Miss Anna Vedineeva (CLFA) are also thanked.

References

[1] M. Bou, J. M. Martin, Th Le Mogne and L. Vovelle, *Appl. Surf. Sci.*, 47, 149 (1991).
[2] Y. Novis, M. Chtaïb, J. Vohs, J.J. Pireaux, R. Caudano, P. Lutgen and G. Feyder, in: Metallized Plastics 1: Fundamental and Applied Aspects, p.193, K.L. Mittal and Susko (Eds) Plenum Press, New York (1989).
[3] Q. T. Le, PhD Thesis, "Modifications of PET surface by plasma treatment – The Al-plasma modified interface study", University of Namur (Belgium) Presse Universitaire de Namur (1996).
[4] Q. T. Le, J. J. Pireaux, R. Caudano, R. Leclere, R. Lazzaroni, *J. Adhes. Sci. Technol.*, 12(9), 999 (1998).
[5] Y. de Puydt, P. Bertrand, Y. Novis, R. Caudano, G. Feyder and P. Lutgen, *Br. Polym. J.*, 21, 141 (1989).
[6] D.A. Wesner, R. Weichenhain and W. Pfleging, *Fresenius J. Anal. Chem.*, 358, 248 (1997).
[7] F. Arefi-Khonsari, G. Placinta, J. Amouroux and G. Popa, *Eur. Phys. J.* ,4, 193 (1998).
[8] M. Creatore, P. Favia, G. Tenuto, A. Valentini, R. D'Agostino, *Plasmas Polym.*, 5, 201 (2000).
[9] F. Arefi-Khonsari, J. Kurdi, M. Tatoulian, J. Amouroux, *Surf. Coat. Technol.*, 142–444, 437 (2001).
[10] M. Tatoulian, F. Arefi-Khonsari, I. Mabille-Rouger, M. Gheorghiu, D. Bouchier and J. Amouroux, *J. Adhes. Sci. Technol.*, 9, 923 (1995).
[11] A. Klomp, J. Terlingen, G. Tokens, A. Strikker, *J. Appl. Polym. Sci.*, 75(4) 480(2000).
[12] U. Schulz, P. Munzert, N. Kaiser, *Surf. Coat. Technol.*, 142–144, 507 (2001).
[13] D. J. Balzs, K. Triandofillo, Y. Chevrolot, B.O. Aronsson, *Surf. Interface Anal.*, 35(3), 301 (2003).
[14] H. Niino and A. Yabe, *Proc. Laser Advanced Material Processing (LAMP'92)* held in Nagoaka, Japan, Vol. 2, 1093, A. Matsunawa and S. Katayama (Eds) (1992).
[15] D.A. Wesner, H. Horn and E.W. Kreutz, *J. Adhes. Sci. Technol.*,11, 1229 (1997).
[16] E. Arenlotz, J. Heitz, M. Wagner and D. Bauerle, *Appl. Surf. Sci.*, 69, 16 (1993).
[17] E. Kreutz, H. Frerichs and D.A. Wesner, *Nucl. Instrum. Methods Phys. Res. B*, 105, 245 (1995).
[18] Y. Novis, J. J. Pireaux, A. Brezini, E. Petit, R. Caudano, P. Lutgen, G. Feyder and S. Lazare, *J. Appl. Phys.*, 64, 365 (1988).
[19] S. Lazare and V. Granier, *J. Appl. Phys.*, 63, 2110 (1988).
[20] W. Wang, A. Taniguchi, M. Fukuhara and T. Okada, *J. Appl. Polym. Sci.*, 74, 306 (1999).
[21] V. N. Tokarev, J. Lopez and S. Lazare, *Appl. Surface Sci.*, 168, 75 (2000).
[22] S. Lazare and P. Benet, *J. Appl. Phys.*, 74, 4953 (1993).
[23] D. S. Dunn, A. J. Ouderkirk, *Macromolecules* 23(3)770 (1990).
[24] P. D. Richards, E. Weitz, A. J. Ouderkirk, D. S. Dunn, *Macromolecules* 23(3)770 (1990).
[25] H. Watanabe, T. Takana and M. Tsuge, *Polym. Int.*, 31, 4953 (1993).
[26] S. Lazare, P. Benet and M. Bolle, *Proc. SPIE*, 1810, 546 (1992).

[27] M. Chtaib, E. Robertfroid and Y. Novis, *J. Vac. Sci. Technol.*, A7, 3233 (1989).
[28] H. Hiroaka and S. Lazare, *Appl. Surf. Sci.*, 46, 264 (1990).
[29] F. Kokai and H. Saito, *Macromolecules*, 23, 674 (1990).
[30] P. Laurens, B. Sadras, F. Decobert, F. Aref-Khonsari and J. Amouroux, *J. Adhes. Sci. Technol.*, 13, 983 (1999).
[31] Y. Novis, R. De Meulemeester, M. Chtaïb, J. J. Pireaux and R. Caudano, *Br. Polym. J.*, 21, 147 (1989).
[32] F. Kokai, *Jpn. J. Appl. Phys.*, 29, 158 (1990).
[33] P. Laurens, S. Petit, F. Arefi-Khonsari, *Plasmas Polym.*, 8, 4, 281 (2003).
[34] S. Petit, PhD Thesis, "Traitement de surface du PET par laser excimère et plasma – The Al-plasma modified interface study", University of Paris VI (Paris – France) (May 2003).
[35] X. Vanden Eynde, P. Bertrand, *Surf. Interface Anal.* **25** (1997) 878.
[36] F. W. Fowkes, *J. Adhes. Sci. Technol.*, 1, 1 (1987) 7.
[37] T. Young, *Philos. Trans. Roy. Soc.*, 95 (1805) 65.
[38] *The Static SIMS Library*, J.C. Vickerman, D. Briggs, A. Henderson, Eds.: Surface Spectra, Manchester UK, 1997.
[39] S. Petit, P. Laurens, M.G. Bathes-Labrousse, J. Amouroux, F. Aréfi-Khonsari, *J. Adhes. Sci. Technol.*, 17, 353 (2003).
[40] *Interaction of Charged Particles with Solids and Surfaces*, D. Leonard; Y de Puydt, P. Bertrand, Ed.: A. Gras-Marti, Plenum Press, New York USA, 1991.

20
Plasma Pretreatments and Treatments on Polytetrafluoroethylene for Reducing the Hydrophobic Recovery

P. Favia, A. Milella, L. Iacobelli, R. d'Agostino

Abstract

Different plasma treatments (NH_3, O_2) were carried out on polytetrafluoroethylene (PTFE) for grafting polar groups and obtaining a stable, permanent hydrophilic surface. Plasma pretreatments (H_2 and Ar) were also utilized to limit the aging, including the hydrophobic recovery, of the treated surface with time. Dynamic water contact-angle (WCA) measurements and X-ray photoelectron spectroscopy (XPS) analyses were performed to study in depth the chemical compositional changes as a function of ageing time. This paper illustrates mainly the remarkable effect of combining H_2 plasma pretreatments with low-power NH_3 plasma treatments for obtaining stable PTFE surfaces grafted with polar groups that exhibit permanent wettability. The results were expressed in terms of the fractions of mobile and immobile polar grafted groups.

20.1
Introduction

PTFE is widely used nowadays in many technological fields, including textiles and biomedical applications [1,2]. However, one disadvantage is its poor adhesion to other materials, molecules or biological systems; solving this problem would clearly extend its use to many other technological fields. A possibility to overcome this drawback is to change the chemical composition of PTFE surface by grafting polar groups by means of a proper plasma process, a well-known strategy for tuning surface properties of polymers.

Grafting chemical groups and/or inducing crosslinking by means of plasma treatments can deeply change the chemical characteristics and surface energy of polymers. Polar groups (e.g. $–NH_2$, –OH, etc.) can be conveniently grafted, for example, to increase wettability and the compatibility with proteins and cells of biomedical polymers, or to improve the adhesion of evaporated/sputtered Al layers at the surface of polyester films, in packaging applications [3]. An important issue in this context, often crucial for industrial applications, is the ageing of plasma-treated surfaces. In fact, when polar groups are covalently bound to the surface chains of a

hydrophobic polymer (down t_o ~20 Å from the interface), a dynamic polymer/air interface is created which experiences, to a different extent, the *hydrophobic recovery* of the original, untreated moieties of the polymer from the bulk to its surface. In the case of treated polymers stored in air, in fact, rotational and translational motions, when permitted, allow the original hydrophobic moieties of the polymer to emerge at the interface thus minimizing the interfacial energy, while polar groups are moved immediately below. Due to this phenomenon, which is probably the most subtle among all processes (i.e., oxidation, contamination, etc.) that usually lead to ageing, treated polymer surfaces tend to lose, within days or hours, the properties conferred by the treatment.

In this paper we report results obtained by treating PTFE surfaces with NH_3 and O_2 RF (13.56 MHz) plasmas under several sets of experimental conditions. Furthermore, we have evaluated the capability of Ar and H_2 plasma pretreatments in reducing the hydrophobic recovery of the plasma-treated PTFE surface. Contact-angle measurement can provide a quantitative description of polymer-surface dynamics since they probe the surface layers to a depth comparable with the range of the interfacial forces involved in surface restructuring processes. Moreover, such measurements can provide the fractions of nonpolar and polar chemical groups stabilized at a polymer surface.

Starting from the Cassie equation [4], Chatelier et al. [5–7] derived a time-dependent model to describe surface-restructuring processes of polymer surfaces in terms of fraction of mobile (i.e., able to rotate below the interface, $f_{p,m}$,) and immobile ($f_{p.im}$) polar groups, and of apolar surface groups (f_{np}); the method is based on dynamic WCA measurements as a function of the ageing time. The proposed ageing model is very simple, in that it assumes a first-order loss of polar groups from the surface of hydrophobic polymers; more complicated kinetics cannot, obviously, be excluded, as well as higher-order contributions to the trends of the WCA data, to fully understand all possible surface rearrangement and reactive processes (recovery, diffusion of oxygen in depth, oxidation of groups, reactions of chain radicals, etc.) involved in the ageing of a plasma-treated hydrophobic polymer surface.

Assuming an exponential decay for the fraction of mobile polar groups, the Cassie equation can be rewritten as in Eq. (1), where τ is the characteristic time constant for the aging process and θ_E^{np} is the equilibrium WCA of the untreated polymer.

$$\theta_E(t) = \arccos[f_{p.im} + f_{p.m}e^{-t/\tau} + (1 - f_{p.im} - f_{p.m}e^{-t/\tau})\cos\theta_E^{np}]. \quad (1)$$

Time-dependent values of the equilibrium contact angle, θ_E(t), can be calculated as the average from the cosine values of the experimental advancing (θ_A) and receding (θ_R) WCA angles, according to Eq. (2). Since Eq. (1) contains three unknown restructuring parameters, $f_{p.im}$, $f_{p.m}$, and τ, no analytical solution is possible, only a numerical one based on the Marquardt–Levenberg algorithm.

$$\cos\theta_E(t) = \frac{\cos\theta_A(t) + \cos\theta_R(t)}{2}. \quad (2)$$

The proposed model has nicely fitted our experimental WCA data, and could be quite easily utilized to rank the efficiency of different treatments in obtaining stable wettable polymer surfaces. One of the drawbacks of the model is that it does not help in identifying the chemical nature of the groups involved in the reorientation process.

20.2 Experimental

PTFE surface pretreatments and treatments were carried out in a parallel plate tubular pyrex RF (13.56 MHz) plasma reactor (Φ = 10 cm, L = 80 cm). The upper electrode is connected to the RF generator (ENI ACG-10) through a matching network; the lower one, 5 cm far apart, is grounded, and is used as sample holder. The reactor is continuously pumped by a rotary pump that allows a minimum pressure of 10^{-3} Torr. Gas flow rates were controlled with mass flowmeters (MKS); pressure is monitored with a baratron (MKS). All the discharges were sustained for 1 min with a flow rate of 10 sccm and pressure of 200 mtorr. In the case of O_2 and NH_3 plasma treatments, an input RF power value of 100 W was used; 20 W NH_3 treatments were also carried out. During Ar and H_2 pretreatments the input power was fixed at 40 W.

Samples of size 5×2 cm^2 were cut from PTFE sheets; before plasma modifications, the samples were cleaned in ethanol for 5 min. The disappearance of the hydrocarbon contaminants (C1s spectra, 285.0 eV peak) was checked by XPS analysis. After the treatments, samples were aged in lab air at room temperature, and stored in tissue-culture polystyrene boxes to reduce contaminations during the ageing. A fresh sample was used for each WCA measurement and each XPS analysis.

Advancing and receding WCA measurements were carried out as a function of the ageing time at room temperature, according to the sessile-drop method, using a Ramé-Hart A-100 manual goniometer. Contact angles were measured on both sides of five drops of double-distilled water for each treated PTFE sample, to calculate the average WCA value, with an uncertainty of ±3°. The changes of chemical composition during storage time were studied by XPS using a PHI ESCA 5300 spectrometer with a nonmonochromatic AlK_α radiation (1486.6 eV; 300 W). During polymer surface analysis the pressure in the analysis chamber typically was 1×10^{-8} torr. Atoms present were identified by survey (0–1000 eV) XPS spectra run at a pass energy of 89.45 eV in the fixed-analyser transmission mode. High-resolution spectra of C1s, N1s, O1s, and F1s signals were recorded with a pass energy of 35.75 eV. The C1s peak component relative to CF_2 groups (BE = 292.5 eV), was used as an internal standard for charging correction. XPS analyses were carried out at 45° and 20° take-off angles (TOA) to reveal any elemental distribution changes in depth.

20.3 Results and Discussion

As a first step, NH_3 plasma treatments, alone and coupled with H_2 pretreatments were investigated. The restructuring parameters are reported in Table 1, while WCA trends and curve fits are shown in Fig. 1; in this particular case, the effect of the H_2 plasma pretreatment has been found to be negligible. NH_3 plasma treatment results in a PTFE surface with improved hydrophilic character.

Table 1 Process conditions and surface restructuring parameters for plasma-modified PTFE

Plasma treatment	$f_{p.m}$ (%)	$f_{p.im}$ (%)	f_{np} (%)	τ (days)	$\theta_E(\infty)$ (deg)
NH_3 (100 W)	30 ± 1	67 ± 1	3 ± 2	3.8 ± 0.1	54 ± 3
1. H_2 (40 W)	30 ± 1	64 ± 1	6 ± 2	3.6 ± 0.5	56 ± 3
2. NH_3 (100 W)					

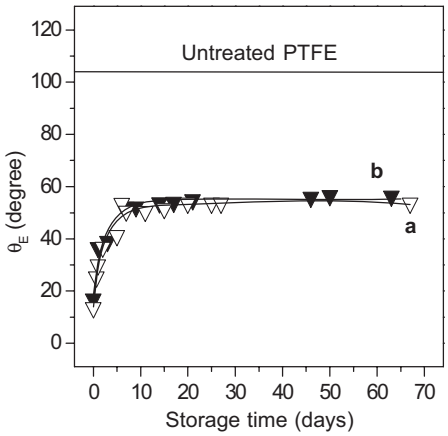

Figure 1 Equilibrium contact angles and best-fitting curves as a function of storage time for (a) ammonia plasma (100 W) treated and (b) two-step treated PTFE. Gas flow rate and pressure were fixed at 10 sccm and 200 mtorr, respectively.

Equilibrium WCA, in fact, reach constant values of 54° for $\theta_{E(\infty)}$, as shown in Table 1 within about ten days from the modification, thus lowering the original value for untreated PTFE by more than 50%. The fraction of immobile groups is 67% of the total fraction of polar grafted groups. It is also important to note that immediately after the modification, PTFE is left very hydrophilic, as revealed by a WCA of 14°, and by a nonpolar grafted groups fraction of only 3%. This is probably due to the presence of H atoms in NH_3 plasma; they can, in fact, scavenge F atoms from PTFE, thus activating its surface toward the grafting of N-containing polar species, according to reaction 1. In this reaction, R represents a N-containing group, such as $-NH_2$ or =NH, or a polymer chain radical; in this case it leads to crosslinking.

Since WCA trends and restructuring parameters are almost the same for the two-step process, it can be concluded that in the experimental conditions investigated H_2 pretreatment has no effect on limiting the hydrophobic recovery. In this case, H_2-plasma-pretreated PTFE was tested with WCA and XPS; advancing and receding WCA were found to be 74° and 52°, respectively. In any case these results show that a NH_3 treatment is already somewhat successful in reducing the WCA value of PTFE. From XPS analysis it appears that H_2 plasma pretreatment drastically defluorinates the PTFE surface. The C1s peak (Fig. 2) of H_2-plasma pretreated PTFE displays a strong decrease of the CF_2 peak component at 292.5 eV, evidently due to a marked loss of fluorine abstracted from PTFE by H atoms formed in the plasma to form volatile HF. At the same time the CF and C-CF peak components increase their importance, and a contribution due to CF_3 groups appears at higher binding energy, as a result of chain rearrangement and reaction of F atoms.

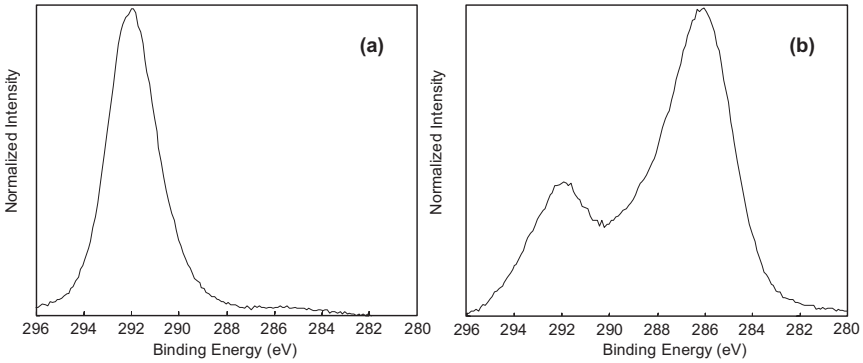

Figure 2 C1s signal for (a) untreated PTFE and (b) H_2 plasma (40 W, 200 mtorr, 10 sccm, 1 min) pretreated PTFE, at 45° take-off angle.

A very detailed WCA and XPS investigation concerning the ageing of PTFE and fluorinated ethylene-prophylene (FEP) after NH_3 plasma treatments has been published by Gengenbach et al. [8], but no use of any pretreatment is mentioned there to slow down the hydrophobic recovery. In this reference the contribution of F^- species in the F1s XPS spectrum is reported, after the NH_3 plasma treatments, which has been associated with the presence of surface $-NH_3^+$ groups after the treatment. Fluoride ions have been found to disappear from the surface within two weeks of ageing. A Similar behavior has been observed also by us (data not shown) during this investigation.

In spite of the fact that the H_2 pretreatment modifies PTFE extensively, and leads to a large extent of crosslinking, the two trends in Fig. 1 are practically identical, thus reflecting, for this case, no benefits given by the H_2 pretreatments. Further experiments have shown that NH_3 treatments performed at a low power on H_2-pretreated PTFE lead to much lower WCA stable values, as will be shown. Very likely, drastic NH_3 treatments (100 W, in our reactor) destroy the thin hydrogenated/cross-

linked interface generated on PTFE by the H_2 pretreatment. The following two-step process has been investigated, then, with a low power (20 W) NH_3 discharge:

1st step: H_2 plasma pretreatment at 40 W, 1 min;
2nd step: NH_3 plasma treatment at 20 W, 1 min.

Restructuring parameters for this second treatment, listed in Table 2, have been obtained by fitting the WCA data. WCA trends are reported in Fig. 3. These data show, with good evidence, how the H_2 pretreatment of PTFE is beneficial, in effect, but only when coupled to a low-power NH_3 treatment.

Table 2 Process conditions and surface restructuring parameters for plasma-modified PTFE

Plasma treatment	$f_{p.m}$ (%)	$f_{p.im}$ (%)	f_{np} (%)	τ (days)	$\theta_E(\infty)$ (deg)
NH_3 (20 W)	13 ± 1	31 ± 1	56 ± 2	0.37 ± 0.06	81 ± 3
1. H_2 (40 W)	12 ± 1	82 ± 1	6 ± 2	2.6 ± 0.5	40 ± 3
2. NH_3 (20 W)					

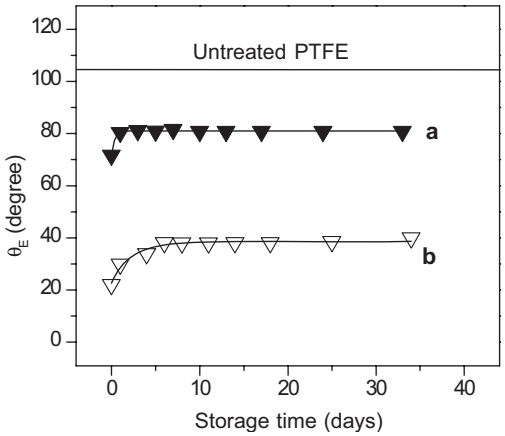

Figure 3 Equilibrium contact angles and best fitting curves as a function of storage time for (a) NH_3-plasma-treated PTFE (20 W) and (b) for the two step process. Gas flow rate and pressure were fixed to 10 sccm and 200 mtorr, respectively.

The following comments can be made:

1. H_2 pretreatments are really effective (compare traces a and b in Fig. 3) in preparing a PTFE surface more suitable to retain NH_3 plasma-grafted polar groups;
2. Lower, stable WCA values are obtained (compare traces b in Figs. 1 and 3) when low-power NH_3 treatments are performed after the pretreatment;
3. The fractions f_{np} and $f_{p.m}$ are strongly reduced (compare Table 1 with Table 2);
4. The fraction of immobile polar groups, $f_{p.im}$, is strongly increased (compare Table 1 with Table 2);

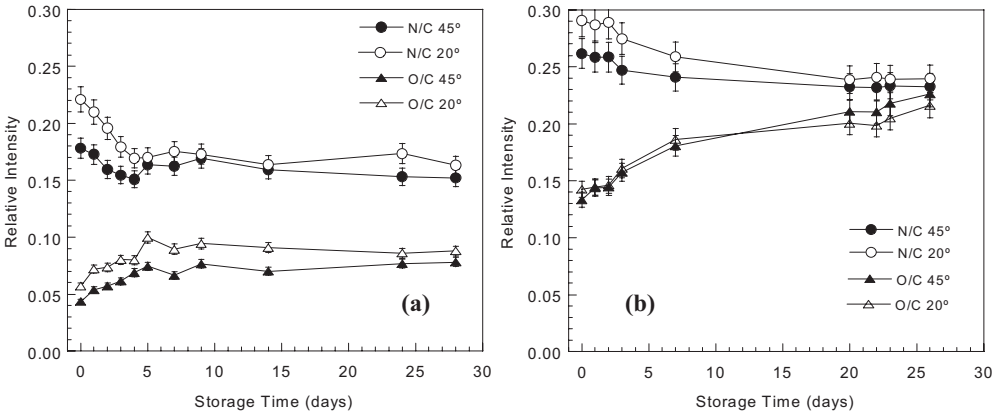

Figure 4 XPS atomic ratios as a function of ageing time in air at take-off angles of 20° and 45° for (a) NH_3-plasma-treated (20 W) PTFE and (b) two-step (NH_3, 20 W) treated PTFE.

The inhibition of the surface restructuring process is evidenced also by the sevenfold increase of τ after the plasma H_2 pretreatment (see Table 2) which means, according to Eq. (1), a lower rate of recovery. The pretreatment is particularly successful probably due to the combined effect of H atoms (scavenging surface F atoms from PTFE) with UV radiation produced in H_2 plasmas [9,10]; both processes lead to a crosslinked PTFE surface, where the hydrophobic recovery of the untreated chains underneath is inhibited.

The XPS evolution of O and N atom surface densities is reported for the two TOA probed, as a function of the ageing time, in Fig. 4 (a), for NH_3 (20 W) plasma-treated PTFE.

Both nitrogen and oxygen are present in the outer PTFE layer; the N density decreases with storage time due to chain/group restructuring motions at the polymer/air interface, and its density is higher in the topmost layer of the surface, as attested by data at the lowest TOA. At the same time a continuous increase in oxygen concentration is observed as a function of the ageing, due to post-treatment oxidation of PTFE surface. This other process, part of the overall ageing, can be ascribed both to reactions involving unsaturated radicals (dangling bonds) and to oxidation (oxygen insertion of some grafted groups, e.g. amines to amides). In particular, the oxygen incorporation is faster during the very first days, as evident from the steep increase of the O/C ratio. Then a plateau is reached, as happens also for WCA trends.

XPS density trends for H_2 plasma pretreated NH_3 plasma (20 W) treated PTFE are shown in Fig. 4 (b). By comparing the data with those in Fig. 4 (a) one can clearly note how the hydrophobic recovery is now much slower. N/C trends, in fact, decrease less steeply in the pretreated PTFE, suggesting that the surface is more polar and richer in grafted N groups, very likely due to the more pronounced crosslinking of the H_2 pretreated PTFE surface, that reduces the recovery. The increase of

the O/C ratio shows that, also in this case, the oxidation of the surface is happening. XPS data are in good agreement with the restructuring data in Table 2.

Pretreatments have been performed also using argon as gas feed, in similar experimental conditions; in these cases WCA results obtained were found to be comparable, although slightly worse, respect to the case of H_2 pretreatments. Better results, in term of lowered WCA and recovery could likely be obtained after the optimization of both pretreatments. XPS investigations revealed a remarkable surface defluorination of PTFE soon after the Ar pretreatment, most likely not due to chemical abstraction, rather to the sputtering of the substrate. Ar pretreatments result also in a crosslinked PTFE surface; the extent of defluorination, though, is lower with respect to H_2 pretreatments.

PTFE plasma-treatment experiments with O_2 have been performed in conditions comparable with the experiments previously shown. Figure 5 (a) shows equilibrium contact-angle data as a function of storage time for oxygen-plasma treated PTFE, using 100 W as input power.

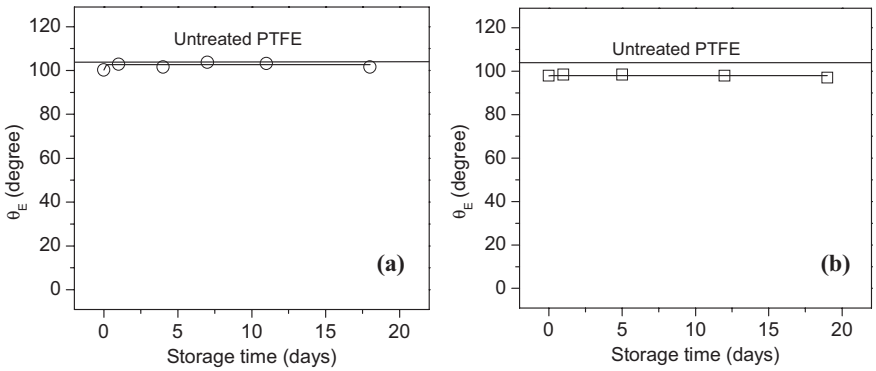

Figure 5 Equilibrium contact angles and best-fitting curves as a function of storage time for (a) O_2 plasma (100 W) treated PTFE and (b) two-step process (O_2, 100 W) treated PTFE. Gas flow rate, pressure and treatment time were fixed at 10 sccm, 200 mtorr and 1 min, respectively.

It is evident that the treatment was not effective at all in modifying the hydrophobic nature of PTFE, at least under the experimental conditions tested, since WCA after the modification remained practically the same as the untreated polymer. This result could be expected, due to the inertness of PTFE.

As found by other authors [11,12], in fact, the negligible degree of this modification probably reflects the preference of the radicals formed by the plasma on PTFE to react with their neighbors rather than with oxygen-containing species, in the plasma or in the atmosphere, after exposure to air. NH_3 treatments, instead, under the same discharge conditions, lead to a better hydrophilic surface character (see traces a in Figs. 1 and 3) at the PTFE surface. Very likely, this could be ascribed to the defluorination reaction of PTFE with H atoms generated by NH_3 molecules frag-

mented in the plasma that activate the surface for the grafting of N groups. H_2 plasma pretreatment (40 W) has been attempted, followed by O_2 plasma treatments (100 W). The resulting WCA ageing trends are reported in Fig. 5 (b) and show only a very little, negligible WCA decrease with respect to PTFE untreated and O_2 plasma-treated in our conditions. Very likely, the defluorinated hydrogenated outmost PTFE layer produced with the H_2 pretreatment has been etched away during the plasma treatment in O_2, thus revealing the untreated PTFE underneath with its wettability almost unchanged. Most likely, less drastic conditions of the O_2 treatment (lower RF power input, lower discharge time, modulated plasma, etc.) may result in lower WCA values, provided the pretreatment is performed before.

20.4 Conclusions

A mathematical model describing the phenomenon of the hydrophobic recovery of PTFE chains after plasma treatments has been utilized for evaluating, quantitatively, the capability of NH_3-plasma treatments at different RF power input, coupled with H_2-plasma pretreatments, in obtaining stable wettable PTFE surfaces with limited ageing and long shelf life. Extremely promising results were obtained by combining H_2-plasma pretreatments with NH_3-plasma treatments at low RF power input. O_2-plasma treatments resulted, in the drastic experimental conditions tested, in no improvements of the PTFE wettability after H_2 pretreatments.

Acknowledgments

Ms. Antonella Del Vecchio is gratefully acknowledged for coworking during the experiments in the framework of her undergraduate Thesis in Chemistry.

References

[1] E. M. Liston, L. Martinu, M.R. Wertheimer, in *Plasma Surface Modification of Polymers*, M. Strobel, C. Lyons, K. L. Mittal, ed., VSP (1994).

[2] F. Arefi-Khonsari, M. Tatoulian, J. Kurdi, J. Amouroux, *Vuoto*, **29**, 3–4 (2000).

[3] M. Creatore, P. Favia, G. Tenuto, A. Valentini, R. d'Agostino, *Plasmas Polym.*, **5**, 3/4 (2000).

[4] A.B.D. Cassie, *Discuss. Faraday Soc.*, **3**, 11 (1948).

[5] R.C. Chatelier, X. Xie, T.R. Gengenbach, H.J. Griesser, *Langmuir* **11**, 2576 (1995).

[6] R.C. Chatelier, X. Xie, T.R. Gengenbach, H.J. Griesser , *Langmuir* **11**, 2585 (1995).

[7] E.P. Everaert, R.C. Chatelier, H. C. Van der Mei, H.J. Busscher, *Plasmas Polym.* **2**, 41 (1997).

[8] T.R. Gengenbach, X. Xie, R.C. Chatelier, H.J. Griesser, *J. Adhes. Sci. Technol.*, **8**, 305, (1994).

[9] A. Hollander, R. Wilken, J. Behnisch, *Surf. Coat. Technol.*, **116-119**, 788 (1999).

[10] A. Hollander, J.E. Klemberg-Sapieha, M.R. Wertheimer, *J. Polym. Sci. A: Polym. Chem.*, **33**, 2013 (1995).

[11] C. Baquey, F. Palumbo, M.C. Porte-Durrieu, G. Legeay, A. Tressaud, R. d'Agostino, *Nucl. Instrum. Methods Phys. Res. B*, **151**, 255 (1999).

[12] D. Youxian, H.J. Griesser, A.W.H. Mau, R. Schmidt, J. Liesegang, *Polymer*, **32**, 1126 (1991).

21
Oxygen-plasma Modification of Polyhedral Oligomeric Silsesquioxane (POSS) containing Copolymers for Micro- and Nanofabrication

N. Vourdas, V. Bellas, E. Tegou, O. Brani, V. Constantoudis, P. Argitis, A. Tserepi and E. Gogolides, D. Eon, G. Cartry, C. Cardinaud

Abstract

Polyhedral oligomeric silsesquioxanes (POSS) represent a new class of well-defined nanomaterials that consist of a silicon-based inorganic cage (Si_8O_{12}) surrounded by eight organic corner groups. In this work, plasma-etching studies of POSS-containing polymers in oxygen plasmas are reported for micro- and nanofabrication. In our applications, POSS-copolymers are used as photoresists. As for most silicon-containing photoresists, the etch resistance of the POSS polymers is primarily related to their silicon content. The POSS content required for sufficient etch resistance is 30 wt% (i.e. the silicon content is 9 wt%). Surface roughness is monitored after various etch times with the aid of atomic force microscopy and scanning electron microscopy. Surface roughness can be controlled by the silicon content, the type of organic group of the POSS moiety, the type of reactor (ICP or RIE), and the temperature of the wafer. Both smooth and very rough (randomly oriented) periodic surfaces can be obtained by changing the material, the reactor, and the temperature.

21.1
Introduction and Experimental Conditions

Polyhedral oligomeric silsesquioxanes (POSS) represent a new class of well-defined materials that consist of a silicon-based inorganic cage (Si_8O_{12}) surrounded by eight organic corner groups (Fig. 1). Typically, a variety of inert substituents can be attached at the seven corner positions around the cage, while the remaining position is occupied by a reactive polymerizable group, permitting synthesis of various acrylate or other copolymers (Fig. 1) [1–3].

The POSS polymers can have numerous other applications in nanotechnology as evidenced in the international conference devoted to these materials [4]. Studies have already been reported with the use of POSS in catalyst technology as carrier matrix for the active elements, in the field of micromembrane separations, in rechargeable batteries, for mechanical enhancement of various polymers used in microengineering, etc.

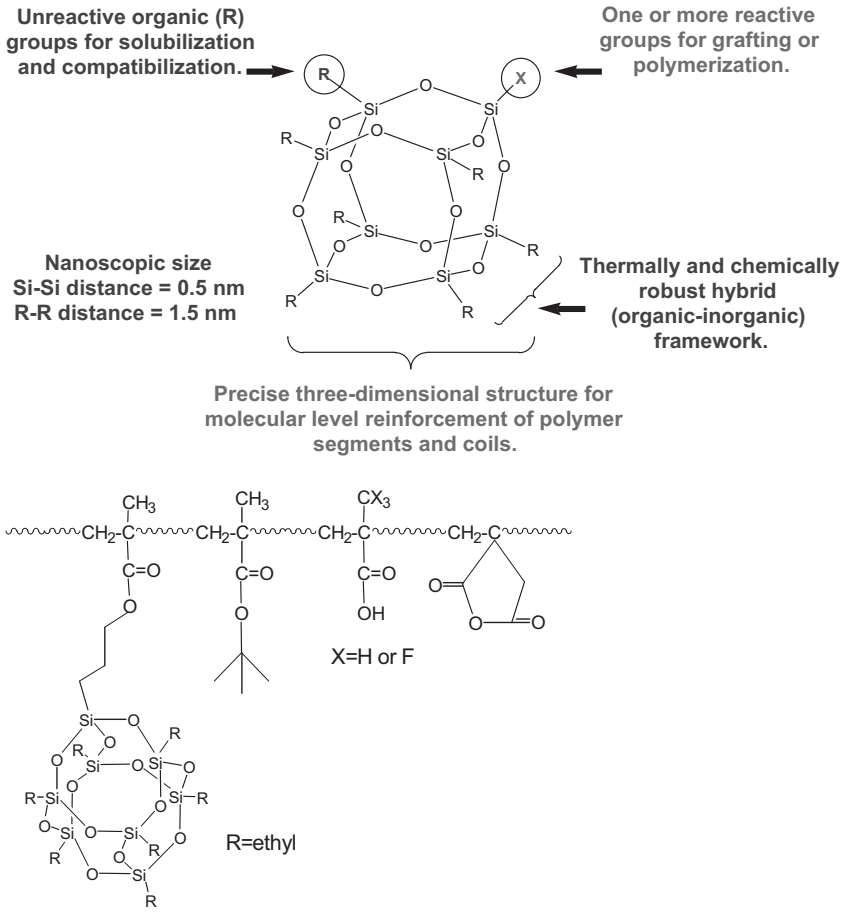

Figure 1 Schematic of the 3-D structure of a POSS monomer (left), and of a typical POSS copolymer (right). The X unit is a methacrylic unit, permitting copolymerization with other monomers.

In particular, POSS-based polymers may find important applications for microfabrication, using bilayer lithography. Bilayer lithography is chosen by many research groups in microelectronics [5]. In such a lithographic scheme, a pattern is imaged on a thin (~100 nm) silicon-containing photosensitive film (top layer) lying over a thick carbon-based polymer (underlayer) and is subsequently transferred to the bottom layer through oxygen-plasma etching. During oxygen-plasma etching the silicon-containing polymer is converted to nonvolatile silicon oxide protecting the underlayer, which is etched away in the areas not covered by the silicon-containing polymer (see schematic of the bilayer process in Ref. [6]). Ultra-high resolution can be achieved using bilayer schemes with, e.g., hydrogen silsesquioxane polymers (HSQ) [7], which are, however, negative-tone materials. Pattern transfer schemes

using silicon-containing polymers can also find applications in microfluidics and lab on chip device fabrication [8]. Contrary to HSQ the POSS copolymers are positive-tone resists, something that is desirable because of the ease of the positive-tone compared to the negative-tone lithography process. An additional advantage of these new resists is the use of aqueous solutions for their wet development instead of organic solutions. Thus, they can readily be applied for biological and biochemical purposes that require not only aqueous but also dilute developer solutions.

A final application of POSS copolymers is in next-generation lithography (NGL). Next-generation microelectronic circuits require minimum characteristic dimensions below 90 nm, a task achievable through the employment of 157-nm lithography and, in the future, through EUV (13.4 nm) lithography. However, the high absorbance values of carbon-based polymers at both wavelengths force the use of thin films, which must, however, be etch resistant, to withstand the subsequent plasma-etching step.

A variety of POSS-containing copolymers have been synthesized in this manner in the Institute of Microelectronics in Athens. The use of these hybrid materials as potential photoresists for bilayer lithography has recently been explored and their resolution capabilities have been demonstrated by our group [1,9,10]. To avoid repetition of these high-resolution, nanolithographic results, we refer the reader to the relevant publications.

The purpose of this work is to briefly present POSS polymers and their properties and to emphasize the plasma-etching studies in O_2 plasmas. The main issues we will address are the etching rate and the surface roughness induced by the plasma treatment, parameters affecting the quality of the structures fabricated using such polymers. The organic corner group R is mostly the ethyl group, although the cyclopentyl group was also compared. Comparison with polydimethyl siloxane (PDMS) and polymethylsilsesquioxane (PMSQ), a ladder rather than a cage silsesquioxane, is done. Table 1 shows the various polymers used in this study.

Plasma etching is done in an inductively coupled plasma reactor (Alcatel MET system) both at the "Institute of Microelectronics – NCSR Demokritos" (Athens) and at "Institut des Materiaux de Nantes" (Nantes). Oxygen plasma at 600–800 W source power and 0 or 100 V bias at a pressure of 10–15 mTorr and a flow rate of 100 sccm, are typically the conditions used in both laboratories. Comparison with RIE etching is also done in Athens. The etching rate is monitored with laser interferometry in Athens and in situ spectroscopic ellipsometry (Woollam M88 system) in Nantes and (Woollam M2000F system) in Athens. Surface roughness is measured with a Topometrix TMX 200 AFM in the contact mode in Athens. FTIR measurements are done in Athens, and in situ XPS in Nantes.

Table 1 Polymers and copolymers used for this study. Sxx refer to an in-house synthesized series of POSS-containing copolymers with various silicon contents, while PMSQ (polymethyl silsesquioxane) and PDMS (poly dimethyl siloxane) are commercial silicon-containing polymers. PTBMA: poly (tert-butyl methacrylate), MA: methacrylic acid, IA: itaconic anhydride, TFMA: trifluoromethacrylic acid

Name of polymer		S41	S48	S53	S47	S69	S71	S61	S83	S79	S43	S52	PMSQ	PDMS
Copolymer	TBMA		40	40	60	40	40	50	40	40	80			
composition	MA			20		20	10	20			20			
%w/w	IA					10	20			10				
	TFMA								30	20				
Ethyl POSS %w/w		100	60	40	40	30	30	30	30	30	20	100 cp-POSS	0	0
Si %w/w		30	18	12	12	9	9	9	9	9	6	21.8	41.8	37.8
T_g (°C)		251	–	153	145	142	–	147	132	–	114	350	–	–
Water contact angle (°)		101	101	–	100	96	91	90	94	91	92	116	–	–

21.2 Results and Discussion

21.2.1 Etching of POSS Copolymers in Oxygen Plasmas (see also Table 1)

The etching of POSS copolymers containing various contents of POSS monomer, and hence various silicon contents was studied with in situ spectroscopic ellipsometry and laser interferometry. A series of POSS copolymers containing 100% to 20% w/w ethyl-POSS was etched and compared with polymethylsilsesquioxane (PMSQ a ladder polymer), and crosslinked polydimethylsiloxane (PDMS). Figure 2 shows that all polymers exhibit a very fast initial thickness loss (large etching rate), followed by a much smaller etching rate. Although for PMSQ and 100% POSS the etching rate seems to stabilize to near zero values (constant slope in the figure), for smaller POSS contents the etching rate is higher and constantly decreases, i.e. it does not stabilize. S43 copolymer (20% e-POSS or 6% w/w Si) is not resistant to the oxygen plasma. All copolymers with 30% e-POSS (9% w/w Si) show adequate etching resistance and similar thickness loss. Laser-interferometry data confirm the ellipsometric results and reveal that for sufficient film resistance more than 20% ethyl-POSS content is required.

The thickness loss is a strong function of the POSS content and decreases as the POSS content increases as presented in Fig. 3. Figure 3 shows that thickness loss in the first 10 s is inversely proportional to the wt% content of Si. This fast thickness loss is attributed to etching of the organic groups from the surface of the film, while the subsequent etching-rate reduction is attributed to oxide formation. A similar mechanism has been proposed by our team for PDMS [6], however more studies are necessary to determine the surface oxide layer thickness for POSS materials.

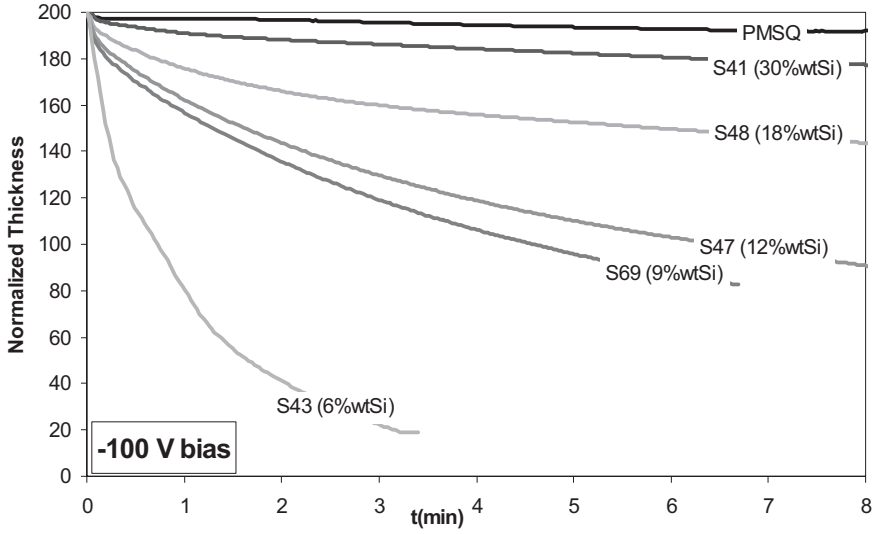

Figure 2 Normalized thickness loss from ellipsometry for the various POSS copolymers and PMSQ. Initial thickness has been normalized to 200.

FTIR spectroscopy has also been used for understanding the mechanism of etching. Figure 4 shows the FTIR spectra of one POSS copolymer containing 30% POSS (S69) before etching and after 150 s of etching with 100 V bias. The following peaks exist in spectrum A and become significantly weaker after etching (spectrum B): 2970 cm^{-1}: C–H stretch, 1454, 1371 cm^{-1}: C–H bend, 1734 cm^{-1}: C=O stretch, 1156 cm^{-1}: C–O stretch. On the other hand peaks that are predominant in spectrum B are the peaks corresponding to the Si–O part of the polymer: 1112 cm^{-1}: Si–O–Si

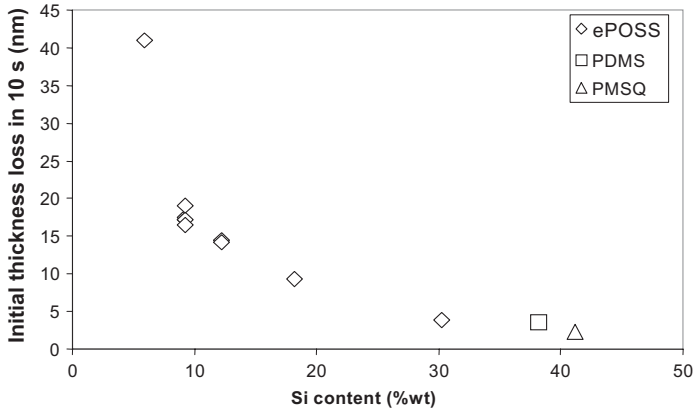

Figure 3 Thickness loss versus silicon content, after 10 s of etching in ICP oxygen plasma with 100 V bias.

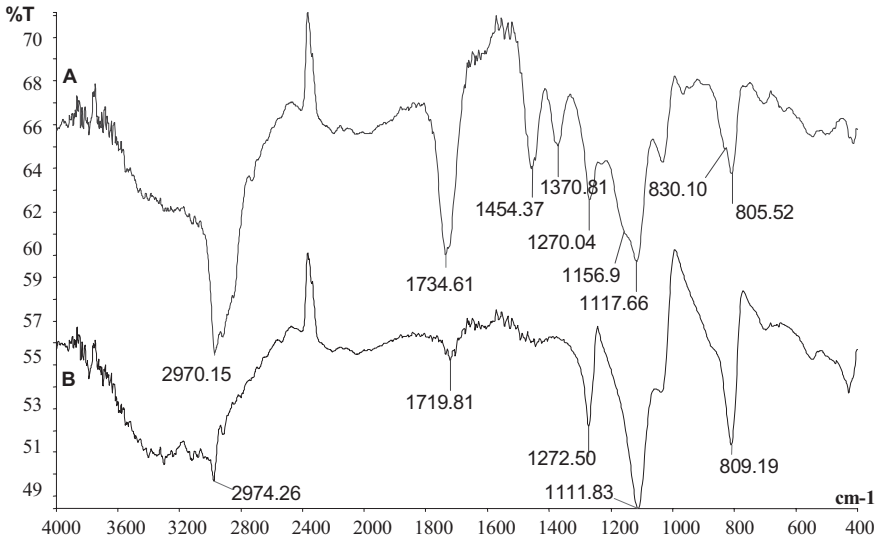

Figure 4 FTIR spectra of POSS copolymer before and after 150 s etching in oxygen plasma: A: S69 a copolymer consisting of ethyl POSS, TBMA, MA, IA before plasma etching (film thickness: 147 nm on 350 nm hard-baked novolac; the novolac spectrum has been subtracted) B: S69 copolymer after 150 s oxygen-plasma etching (film thickness: 70 nm).

stretch. These data point to a strong oxidation of the POSS layer and formation of an oxide-like surface. One should note that the C–H peaks do not disappear, since the oxide layer is just on the surface of the POSS material rather than on the whole thickness [6].

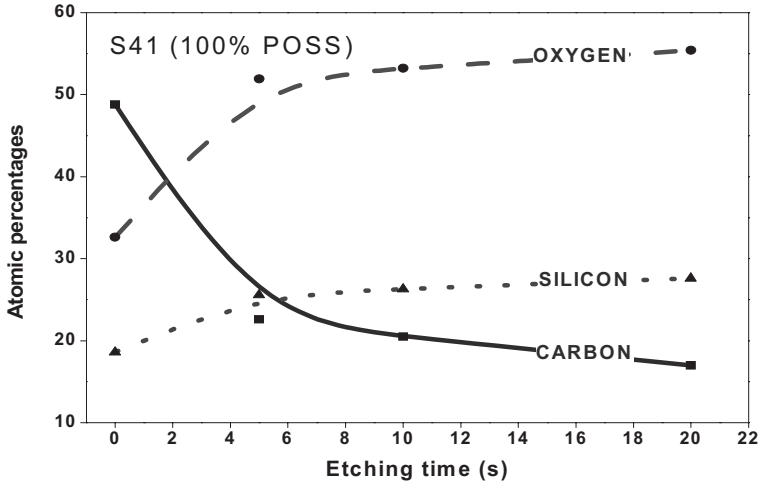

Figure 5 Carbon, silicon and oxygen atomic percentage evolution on the surface of S41 (100% e-POSS polymer) during O_2 plasma etching (XPS analysis)

The formation of a surface SiO_x-like layer, during O_2 plasma treatment has been also confirmed by means of XPS. As seen in Fig. 5, the carbon percentage falls below half of its initial value in the first 10 s, due to the oxidation of the surface and the formation of the SiO_x layer (increase of the oxygen and silicon percentage).

12.2 Surface Roughness of POSS Polymers after Plasma Treatment

High surface roughness may be undesirable or beneficial depending on the application. In nano-lithography, top and sidewall surface roughness are highly undesirable as they affect the quality of the fabricated electronic nanodevice. However, surface roughness may be beneficial, for example, when a high effective surface area is required (e.g. for adhesion promotion [11]). Surface roughness is an issue of great concern for application of the POSS materials to micro- or nanofabrication. In general, silicon polymers when treated in plasmas can give very rough surfaces, especially when the silicon content is low and etch resistance is not appropriate. In addition, surface roughness can be greatly enhanced by a high wafer temperature during etching, giving rise to periodic structures with controllable periodicity and height [12–14]. We will show below that POSS copolymers can give controlled small or high surface roughness depending on processing conditions. We will also briefly present a scaling analysis of the surface roughness from AFM images to determine not only the vertical extent of roughness, but also its horizontal spatial extent, characterized by the correlation length and the periodicity.

Figure 6 shows the surface roughness (rms value) for a series of e-POSS copolymers and one cyclopentyl-POSS (cp-POSS) polymer treated for 2 min in the oxygen plasma at 100 V bias. The electrode and wafer temperatures were 15°C. He-backside

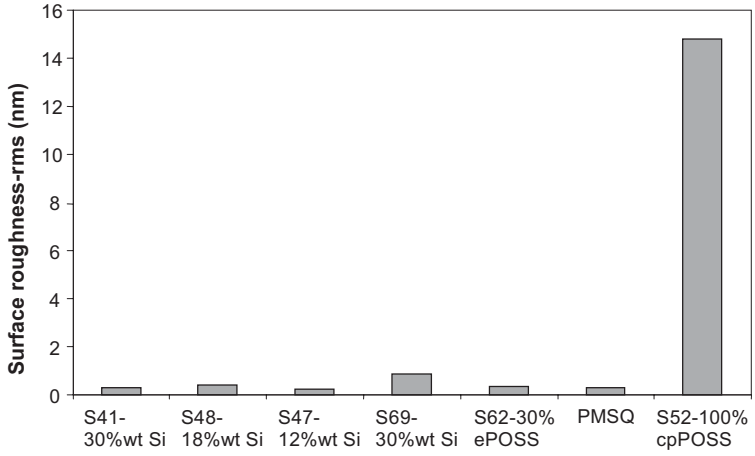

Figure 6 Surface roughness of various POSS copolymers (see Table 1) after 2-min oxygen plasma treatment, comparison with PMSQ.

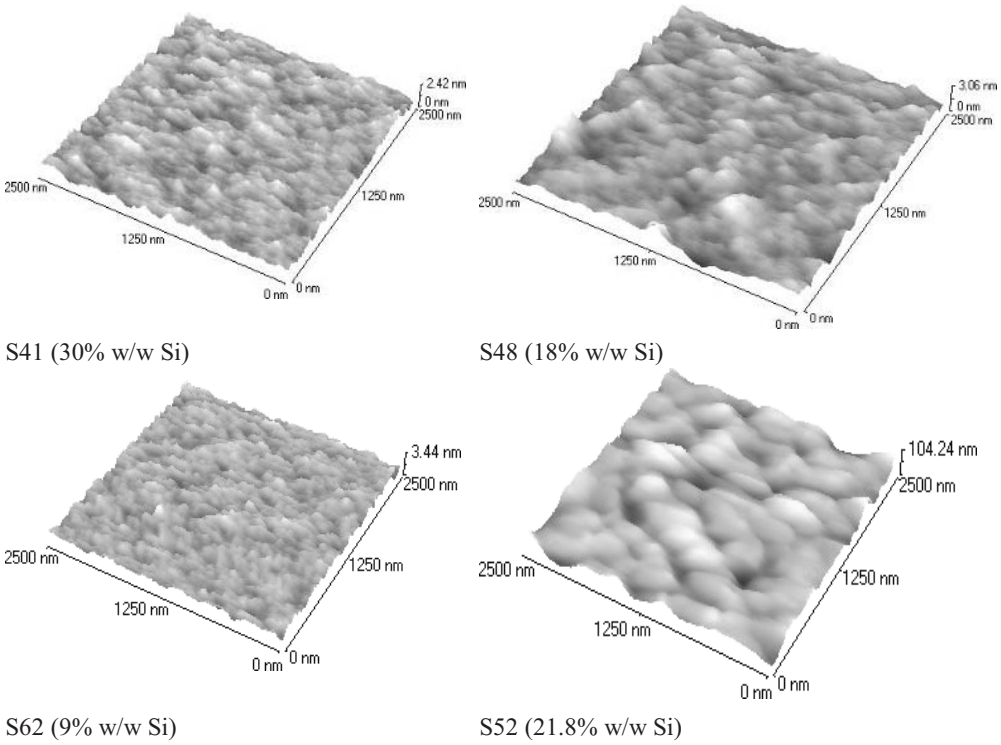

Figure 7 AFM images of various POSS copolymer (see Table 1) surfaces after 2-min oxygen plasma treatment.

cooling of the wafer maintains a constant wafer temperature. The e-POSS copolymers shown contain at least 30% POSS, i.e. they can withstand the oxygen plasma by forming a protective oxide film. While all e-POSS polymers exhibit very smooth surfaces, the cp-POSS polymer surface is very rough, as shown also in Fig. 7. This interesting observation reveals that bulky POSS organic corner groups can greatly hinder the surface-oxide formation in the plasma and result in very rough surfaces. Cp surfaces were rough enough before plasma etching and they were made rougher after plasma.

Next we show in Fig. 7 the effect of etching time at constant etching conditions for S69, a polymer containing 30% e-POSS and S41, a polymer containing 100% e-POSS. Polymers were post-apply baked at 160 °C, i.e. above the glass transition temperature of S69, or at 120 °C. Notice that both polymers are smooth at short plasma-etching times, while roughness increases for long etching times for the 30% POSS polymer, due to erosion of the film. Notice also that the 100% POSS film shows no roughness even at long etching times. This is due to the higher silicon content of the polymer (see also Fig. 2 and Fig. 3). The difference between the post-apply bake temperatures for S69 may reflect differences in the packing of the film and the reduction of the free volume, as in one case it is baked above, while in the other below the T_g (143 °C).

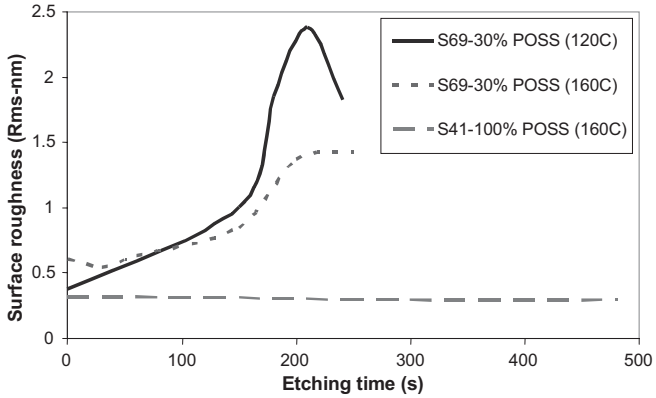

Figure 8 Surface roughness versus etching time in ICP reactor, oxygen plasma, 100 V bias, wafer temperature 15 °C.

While e-POSS surfaces look smooth after ICP etching, they look very rough after RIE etching, although etched at the same pressure and electrode bias potential. The wafers in the RIE reactor are not cooled efficiently, thus the temperature during etching rises to approximately 120 °C. The mechanism of roughness evolution due to this thermal effect is not yet completely understood. It can be attributed to buckle formation, due to differential thermal expansion and contraction of this bilayer system (different thermal expansion coefficients of polymers and the ceramic-like SiO_2 layer), during thermal cycles along the process (plasma etching – heating, subsequent – cooling). On the other hand, the different densities of the polymer and the formed SiO_2 layer can also enhance surface-roughness evolution as a result of the developed stress. This phenomenon is currently under study by our group. This temperature-reactor effect is shown in Fig. 9 and Fig. 10.

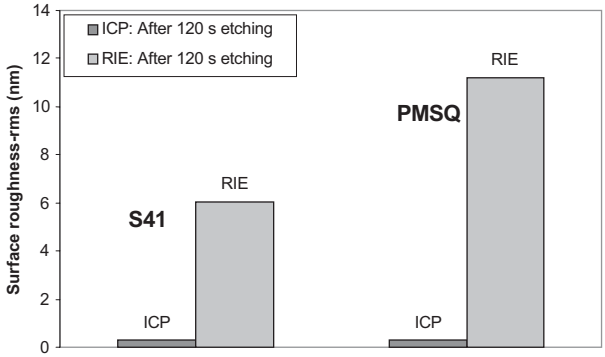

Figure 9 Surface roughness for RIE and ICP etching after 2-min etching in oxygen plasma at 100 V bias. In the RIE reactor the wafer temperature can reach 120 °C within 2 min of etching. In the ICP reactor the wafer is cooled with He backside cooling and maintains a constant temperature 15 °C.

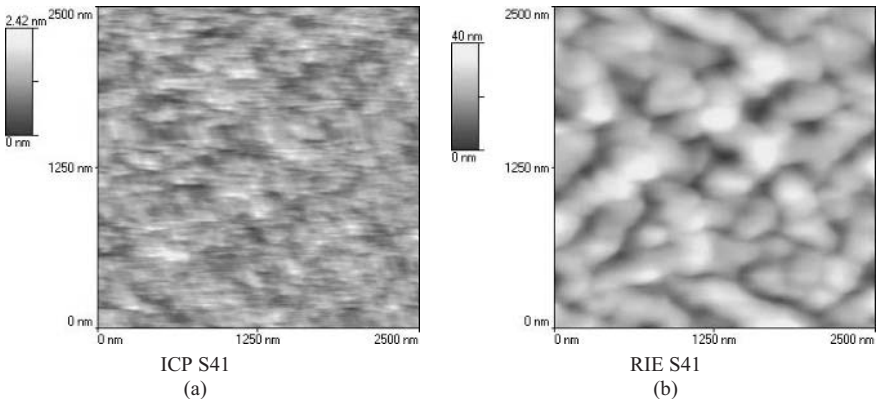

Figure 10 AFM images showing the surface of S41 after treatment in a RIE and an ICP reactor. After 2-min treatment, the rms roughness is 0.31 nm and 6.05 nm in ICP and RIE reactors, respectively.

Statistical analysis of the images shown in Fig. 10, based on the height-height correlation function, $G(r)$, [13], reveals the characteristics of a S41 surface, after treatment in an ICP and in a RIE plasma reactor, i.e. with and without cooling during the treatment (as described above) and is shown in Fig. 11. Both surfaces show a self-affine (fractal) behavior at small scales, i.e. G is a power law function of r, $G(r) \approx r^{\alpha}$, with exponent α the so-called roughness exponent related to the fractal dimension D, as $D = 3-\alpha$. The higher the roughness exponent (i.e. the smaller the fractal dimension) is, the smaller is the contribution of the high-frequency roughness components. G saturates at r values longer than the correlation length ξ. Also, the rms value of roughness depends on the length (surface) L, sampled by the AFM as a power law (rms $\approx L^{\alpha}$), up to a length equal to a few times the correlation length. Above this length, the surface roughness does not change. In addition, if the surface contains a periodic component this is demonstrated by oscillations in $G(r)$ and a large value of $\alpha \approx 1$. The wavelength λ is located at the first minimum of G.

The surface shown in Fig. 10 (b) shows a periodicity with a wavelength $\lambda = 550$ nm (mound-like structure), while the surface in Fig. 10 (a) is self-affine. From the analysis of $G(r)$, the rms value, the roughness exponent α, the correlation length ξ, and the periodicity λ are determined, as shown in the figure. Based on the AFM images and on the height-height correlation function, it can be concluded that treatment in ICP results in small roughness compared to the roughness obtained after RIE treatment. Moreover, the roughness exponent α, for an ICP-treated S41 surface is smaller than that of a RIE-treated surface (0.44 vs 0.92), indicating high-frequency spatial components domination for ICP-treated surfaces in contrast to low-frequency spatial components domination for the RIE-treated surfaces. The latter are responsible for their mound-like structure and periodicity (Fig. 11 (b)). We note also that we can control the surface roughness by changing the thickness of the POSS film and the temperature/duration of the plasma treatment. This interesting high

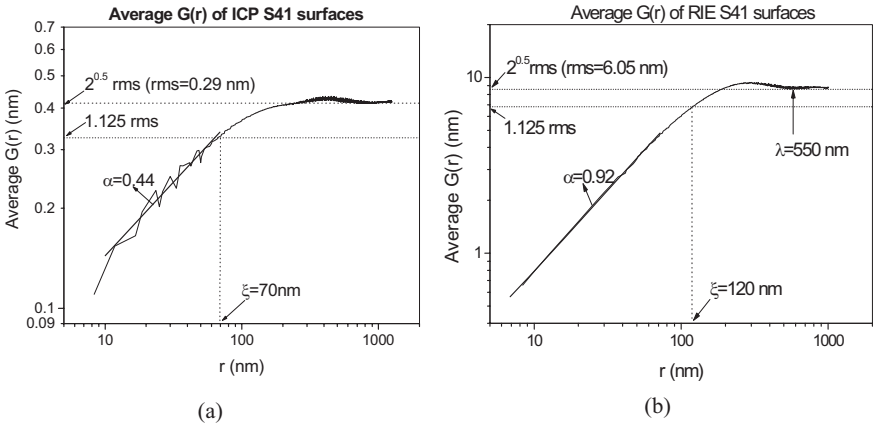

Figure 11 Height–height correlation function, $G(r)$, for the images shown in Fig. 10. From the analysis of $G(r)$, the rms value, the roughness exponent a, the correlation length ξ and the periodicity λ are determined. Note the formation of periodicity i.e. of mound-like structures on the surface of the RIE-treated POSS copolymer.

and periodic roughness may have applications in nonlithographic areas. A similar behavior has been observed for PDMS [12,14].

21.3 Conclusions

The behavior of POSS polymers under treatment in oxygen plasmas was studied. Etching rates and surface roughness depend on the amount of POSS and the organic corner group of the POSS monomer. Ethyl POSS copolymers can resist oxygen-plasma etching by forming surface oxide, and produce smooth surfaces in ICP reactors when the POSS content is higher than 20%. Wafer heating in RIE reactors and/or the presence of cyclopentyl corner groups on POSS monomers result in rough surfaces. The treatment in RIE reactors resulted in the formation of mounded surfaces with controlled high roughness and periodicity compared to the smooth surfaces formed in ICP reactors, a fact revealed by scaling analysis of the AFM images. Thus, POSS treatment can result both in smooth surfaces useful for lithography and in rough periodic surfaces useful in other applications.

Acknowledgments

The European Union IST project "157 CRISPIES" supported this work.

References

[1] V. Bellas, E. Tegou, I. Raptis, E. Gogolides, P. Argitis, H. Iatrou, N. Hadjichristidis, E. Sarantopoulou, A.C. Cefalas, J. Vac. Sci. Technol. **B 20**, (2002), pp. 2902–2908.

[2] KE. Gonsalves, J. Wang, and H. Wu, J. Vac. Sci. Technol. **B 18**, (2000), pp. 325–327.

[3] H. Wu, Y. Hu, K.E. Gonsalves, and M.J. Yacaman, J. Vac. Sci. Technol. **B 19**, (2001), pp. 851–855.

[4] Proceedings of the POSS Nanotechnology Conference, CA, USA (2002).

[5] S. Miyoshi, T. Furukawa, H. Watanabe, S. Irie and T. Itani, Proc. SPIE **4690**, 221 (2002).

[6] A. Tserepi, G. Cordoyiannis, G.P. Patsis, V. Constantoudis, E. Gogolides, E.S. Valamontes, D. Eon, M.C. Peignon, G. Cartry, Ch. Cardinaud, G. Turban, J. Vac. Sci. Technol. B **21(1)**, (2003), pp. 174–182.

[7] F.C.M.J.M. van Delft, J.P. Weterings, A.K. van Langen-Suurling, H. Romijn, J. Vac. Sci. Technol. B **18(6)**, (2000), pp. 3419–3423.

[8] H. Becker, L.E. Locascio, Talanta, **56**, (2002), 267–87.

[9] E. Tegou, V. Bellas, E. Gogolides, P. Argitis, E. Sarantopoulou, A.C. Cefalas, K. Dean, Proc. SPIE **5039**, (2003), pp. 453–461.

[10] E. Tegou, V. Bellas, E. Gogolides, and E. Argitis, submitted to Chem. Mater., December 2003.

[11] D.E. Packham, Int. J. Adhes. Adhesives, **23**, (2003), pp.437–448.

[12] A. Tserepi, E. Gogolides, V. Constantoudis, G. Cordoyiannis and I. Raptis and E.S. Valamontes, J. Adhes. Sci. Technol. **17(8)**, (2003), pp. 1039–1160.

[13] B.Y. Zhao, G.-C. Wang and T.-M. Lu, "Characterization of Amorphous and Crystalline Rough Surface: Principles and Applications", Experimental Methods in the Physical Sciences, 37, Academic Press, 2001.

[14] D.B.H. Chua, H.T. Ng, S.F.Y. Li, Appl. Phys. Lett. 76(6), 721 (2000).

Part III
Plasma and Life Science

22
Radicals of Plasma Needle Detected with Fluorescent Probe

Ingrid E. Kieft, Joep J.B.N. van Berkel, Erik R. Kieft, Eva Stoffels

Abstract

Nonthermal atmospheric plasmas can be used for fine treatment of heat-sensitive materials, including living cells and tissues. The newly developed "plasma needle" is capable of inducing sophisticated cell responses, which may become valuable in refined surgery. In our hypothesis, these effects are caused by interactions of plasma-produced radicals with the cell membrane and/or other cell components. Cells consist for the main part of water and are (especially in vitro) immersed in liquid. In this paper we study the diffusion of radicals from the plasma into liquids.

Raman scattering experiments were performed to determine the gas composition in the plasma. A fluorescent probe (5-(and-6)-chloromethyl-2′,7′- dichlorodihydrofluorescein diacetate, acetyl ester by Molecular Probes® inc.) was used to detect reactive oxygen species in the liquid phase. This probe reacts with reactive oxygen radicals and the oxidation product displays fluorescence when irradiated with a laser. After plasma exposure, liquid samples were analyzed using a microplate fluorescence reader. In order to gain insight into the behavior of radicals under various plasma conditions, several parameters like plasma-to-liquid distance and plasma composition (O_2 content in the plasma) were varied. The absolute density in the liquid was estimated by calibration against NO radicals, produced by the NO releaser NOR-1. Furthermore, an estimation was made for the radical density in the gas phase. The usage of fluorescent probes allows a quantitative study of plasma radicals in liquids. The method is powerful and easy to use, and the obtained data are important to understand plasma effects on living cells.

22.1
Introduction

Plasmas are widely used for industrial surface modification. In particular, atmospheric plasmas are becoming increasingly popular, because of their flexibility, convenience and low costs. Recently, nonthermal atmospheric plasmas have been developed for treatment (cleaning, sterilization) of heat-sensitive materials [1,2]. In principle, such plasmas can be applied in vivo for disinfection or local removal of diseased tissues.

Chemically reactive species, and especially short-lived radicals are of major importance in any surface treatment. For example, the efficiency of bacterial decontamination is conditioned by reactive oxygen species (ROS), produced in the plasma [3]. According to Laroussi [2], free radicals are the most important sterilizing agent in atmospheric-pressure plasmas. Apart from bacteria, the responses of living cells and tissues are also dependent on the plasma chemistry. For specific cell treatment, a nonthermal microplasma ("plasma needle") has been developed [4]. In vitro experiments have already shown that the plasma needle can trigger complex cell reactions [5,6]. Depending on plasma conditions, the treated cells can detach from each other and from the surface, or undergo apoptosis (programmed cell death). The mechanisms behind these responses are not yet completely understood, but we suspect that active radicals are responsible for the majority of the observed effects.

As in any medical therapy, plasma-produced species can play a double role. Moderate amounts of reactive oxygen species have a beneficial working, but an overdose leads to cell injury. Oxygen species react with and damage cell building blocks like lipids, proteins and DNA strands [7–9]. Montie et al. [10] suggest that membrane lipids may be most vulnerable to reactive oxygen species attack, because of their location near the cell surface, and their sensitivity to oxidation. Severe oxidative stress causes cell injury and accidental cell death (necrosis), while mild oxidative stress leads to apoptosis [11]. A small imbalance in oxidant/antioxidant regulation can result in adaptation of the cells to the new environment. Adaptation of cells is realized through changes in the gene expression, so that the cells are capable of surviving in a hostile environment.

Regarding the importance of reactive oxygen species for cell condition, it is essential to study the diffusion of radicals from the plasma into the liquid phase. In this paper we determined the densities of active species in a buffered solution that was exposed to the plasma. For these experiments we used the plasma needle: an RF discharge generated at the end of a metal pin. The main species in the plasma is helium. However, since it operates in open air at ambient pressure, some air admixture is always present. Thus, oxygen- and nitrogen-based active species like atomic oxygen, the metastable singlet state of molecular oxygen ($O_2(a)$), ozone, NO and NO_X are formed in the plasma. Due to air moisture, OH and HO_2 can be produced.

There are many methods to determine radical densities in the gas phase, e.g. laser-induced fluorescence (LIF) [12], broad-band UV absorption spectroscopy [13] and the cavity ring-down technique [14,15]. For radical detection in liquids laser-induced fluorescence in combination with fluorescent probes can be used: an easy and convenient method that is very popular in cell biology [16–19]. In this work we introduce LIF with a fluorescent probe as a new, powerful plasma diagnostics. This method is recommended for determining fluxes of radicals from atmospheric plasmas, concentrations of active species in plasma-treated fluids and gels, for dynamic studies of the plasma/liquid interface, and for many other applications.

22.2 Experimental

22.2.1 Plasma Needle

The plasma was generated at the end of a sharp metal pin electrode (needle), to which 13.56 MHz radio-frequency (RF) voltage was applied (Fig. 1). The needle had a diameter of 0.3 mm and was about 10 cm long. It was inserted in a Perspex tube with inner diameter 0.8 cm. A helium flow of 2 l min^{-1}, regulated by a mass flow controller of Brooks series 5850E, was directed through the tube.

For the plasma generation a Hewlett Packard 33120A waveform generator and an Amplifier Research 75AP250RF RF amplifier were used. The power was monitored using a dual directional coupler and an Amplifier Research PM 2002 power meter. The power dissipated in the plasma was below 100 mW. The effective voltage at the needle was about 200 V. The typical size of the plasma glow was below 1 mm. However, when the plasma was in contact with (water) surface, the glow expanded slightly so that the typical size of the treated spot was 1 mm^2.

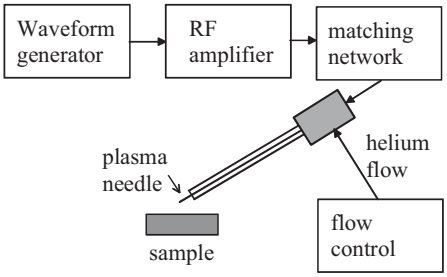

Figure 1 A scheme of the setup. Radio-frequency voltage generated by a function generator is amplified, impedance-matched and applied to the hand-operated plasma needle (a metal pin). Helium is supplied to the needle by a Perspex tube.

The position of the needle in the Perspex tube could be varied by moving the tube along the axis of the needle (Fig. 2). Normally, the tip of the needle and the end of the tube were at the same position, but the needle could also protrude from the tube up to 1 cm. In the latter case, more air was admixed in the plasma.

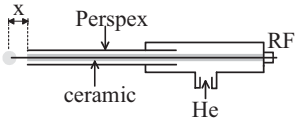

Figure 2 A drawing of the plasma needle. The position of the needle to the end of the Perspex tube can be varied as is indicated in the figure by *x*.

22.2.2
Raman Scattering

Raman scattering experiments were performed to determine the gas composition. Raman scattering is an inelastic photon scattering on molecules. Typically, laser photons in the visible region are used for irradiation. Their interaction with the molecule induces a vibrational/rotational transition, so the scattered photons display a small wavelength shift corresponding to the energy of the transition. A Raman spectrum consists of lines that are fingerprints of various molecules (e.g. O_2, N_2 and H_2O in air) and it can be used to quantitatively determine the composition of gas mixtures. Here we determined the air content in our plasma by recording Raman spectra in a helium/air flow, and comparing them to pure-air spectra. First, the spectra were integrated over wavelength, then the helium/air flow values were divided by the pure air value. Measurements with and without plasma were performed to check the plasma influence on the gas composition.

We used the setup developed by Van de Sande [20]. The system was equipped with an Nd:YAG type laser (frequency doubled, $\lambda = 532$ nm, pulse length 7 ns, pulse repetition rate 10 Hz), focused with a 30-cm lens. Spectra were taken with an intensified charge coupled device (CCD) camera. Spectra were collected for 300 s per measurement. The plasma needle was fixed vertically above a grounded metal plate (at the distance of 2 mm). In the horizontal plane, the laser focal point was coincident with the needle tip, and the vertical direction it was positioned at the distance of 1 mm below the tip. One-dimensional scans in the horizontal direction were taken.

22.2.3
Fluorescent Probe

To detect reactive oxygen species that were formed in the plasma we used a molecular probe, called 5-(and-6)-chloromethyl-2′,7′- dichlorodihydrofluorescein diacetate, acetyl ester (CM-H_2DCFDA). From the literature it is known that it can be used as an indicator of reactive oxygen species formation and oxidative stress [16]. Upon reaction with oxygen-containing reactive species, the probe is oxidized in such a way that a large multiple-conjugated double bond with a high degree of stability is formed (Fig. 3). This double bond is also responsible for the fluorescent properties.

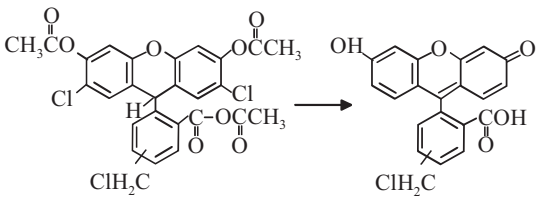

Figure 3 Chemical structure of CM–H_2DCFDA before (left) and after (right) reaction with reactive species. The acetate groups are removed by incubation in an alkaline solution.

The probe was delivered by Molecular Probes®. It was guaranteed to react with at least the following reactive oxygen species: H_2O_2, $OH^{\bullet}$, $HOO^{\bullet}$, and $ONOO^{-}$. The package contained a 50×10^{-6} g probe (8.653×10^{-8} mol). The content was dissolved in 100 µl of dimethylsulfoxide (DMSO, >99%, Merck). Then, 1 ml of 0.01 M solution of NaOH (99.99%, Aldrich Chem. Co.) was added to activate the probe. The solution was incubated for 30 min at room temperature and afterwards diluted to 10.81 ml with phosphate-buffered saline (PBS, Sigma-Aldrich Co.), resulting in a probe concentration of 8 µM. The PBS solution (pH 7.4 at room temperature) was a 0.01 M phosphate buffer with 0.0027 M potassium chloride, and 0.137 M sodium chloride. The probe is sensitive to light, so the solution was covered with aluminum foil and placed in a refrigerator. For the experiments a concentration of 1 µM was used.

The samples were prepared in 96-well plates with a flat bottom from Nucleon Surface. After plasma exposure, they were examined with a Microplate Fluorescence Reader FL600 of Bio-Tek. The oxidized CM-H_2DCFDA probe was irradiated by a quartz halogen lamp (P/N 6000556S) light source in combination with a 485/20X excitation filter (wavelength about 485 nm). Fluorescent emission was collected at about 530 nm using a 530/25M filter.

22.2.4 Calibration with NO Radicals

To obtain quantitative data, the probe was calibrated using NO radicals, produced by NOR-1, an NO releaser. From the work of Ueki et al. [21] it is known that NOR-1 can be used as a standard for absolute measurements of low NO densities. They showed that NOR-1 releases a 1.4 excess of NO after 15 min of incubation, so [NO] = 1.4 [NOR-1]. The CM-H_2DCFDA probe may react directly with NO, or with its autoxidation derivatives like N_2O_3 or NO_2^- [17,22].

The efficiency of the CM-H_2DCFDA probe to react with NO released by NOR-1 was tested by performing two experiments. In both experiments small amounts (10 to 100 µl) of the NO releaser NOR-1 in DMSO were dissolved in an Eppendorf tube containing 1 ml PBS with the CM-H_2DCFDA probe in varying concentrations. The tubes were incubated for 15 min at room temperature. Then 100 µl of the solutions were put in a 96-wells plate and data were collected with the microplate fluorescence reader.

In the first experiment (Fig. 4) an excess of NO was administered to different concentrations of the probe. This yielded a linear curve ($R^2 = 0.9999$) for the maximum intensity emitted by the probe, of which all molecules were activated. In the second experiment different concentrations of NO were added to the probe (concentration of 1 µM). The calibration curve (fluorescent intensity vs. NO concentration) showed that for NO concentrations below 10 µM the relation was linear (Fig. 5). At higher concentrations the probe was slightly saturated, which caused the curve to flatten. We can now compare the two figures by looking, for example, at the intensity of the 1 µM probe (Fig. 5) activated by addition of 5 µM NO; this gave 31 000 counts. The same intensity (31 000 counts) was reached by illumination of 0.25 µM fully activated probe. This means that about 5% of the NO molecules reacted with the probe.

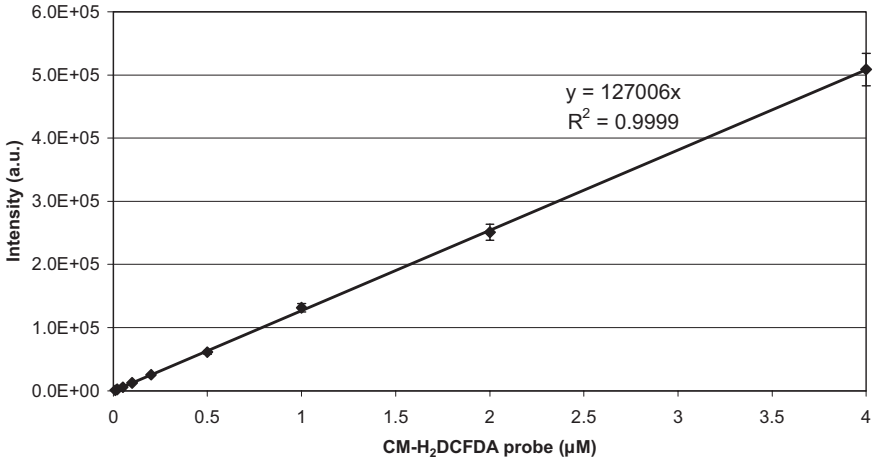

Figure 4 Intensity of CM–H_2DCFDA probe after reaction with an overload of NO (1 mM). The probe is maximally activated.

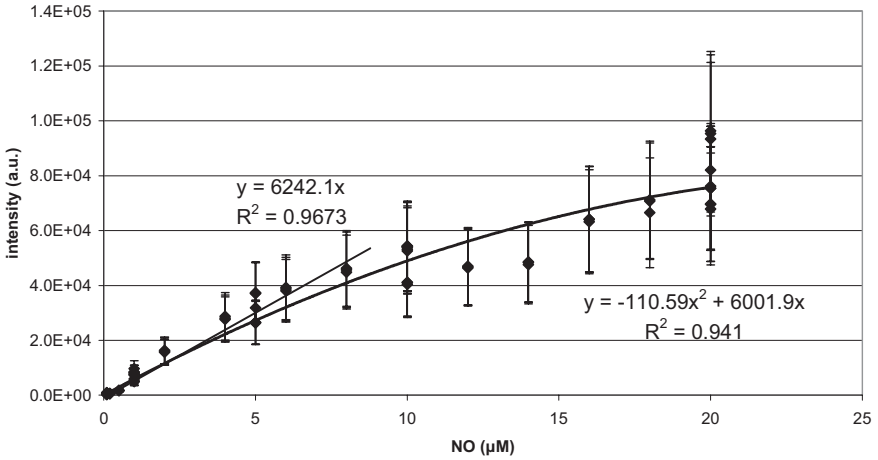

Figure 5 Intensity of CM-H_2DCFDA probe (concentration 1 µM) after reaction with NO from the NO-releaser. Figure shows two trend lines, the line fitted for concentration below 10 µM, and the polynomial curve fitted for all data points.

The radicals from the plasma were taken to have the same reactivity in this setup towards the probe as NO radicals. Reaction rates of this specific probe with plasma radicals (reactive oxygen species) are not given in the literature. Rate constants for reactions of inorganic radicals with organic compounds in aqueous solutions range roughly from 10^6 to 10^{10} l mol^{-1} s^{-1} [23–25]. The reactions rates of OH and O are mostly one or two orders higher than the reaction rates of NO. The calibration with NO then serves as an upper limit for the radical concentration. The lower limit is set by Fig. 4: In an ideal one-to-one reaction of radicals with probe molecules there needs to be at least the number of

radicals equal to the number of probe molecules to reach a certain fluorescence intensity. This minimum number of radicals can be derived from Fig. 4 and is a factor 20 lower than the number derived from calibration to NO.

In our setup the probe is the only reactive organic molecule in the liquid (not including reactions at the wall). It will efficiently capture any radical, independent of the actual reaction rate. The calibration against NO is thus valid in aqueous solutions with only inorganic species. In a real biological sample the situation may be somewhat different: the reactivity of the hydroxyl radical or atomic oxygen towards most organic compounds is higher than that of NO [23], while this of ozone is lower. This means that, e.g., cell damage inflicted by oxygen radicals is higher than the one caused by nitric oxide at the same concentration level. Thus, we must keep in mind that the concentration of ROS deduced from NO calibration is merely an indication of the "oxidizing activity" of the plasma.

22.2.5
Plasma Treatment

400 µl of fresh probe solution was treated with the plasma. Unless otherwise mentioned, the samples were treated for 2 min, with a distance of the tip of the needle to the liquid surface of about 1 mm and the tip of needle at the same position as the end of the Perspex tube. After plasma treatment an antioxidant was added to the solution to prevent further oxidation of the probe by air. Vitamin C or L-Ascorbic acid is known to be a very efficient, water soluble antioxidant [26]. In the experiments 10 µl of 10 mM solution L-Ascorbic acid was used. The antioxidant was tested by incubation of the untreated probe solution of 1 µM in open air at room temperature. When ascorbic acid with a concentration of 100 µM was used, a small increase in fluorescence intensity of about 10% was observed after 40 min. When the concentration was increased to 1 mM, no increase of intensity could be detected within half an hour. The samples protected in this way could be kept in the refrigerator even up to 24 h, but we analyzed them immediately after plasma treatment. The samples were divided into 100 µl portions, and transferred to the plate reader for data collection. 100 µl of untreated probe solution was used for background subtraction.

22.3
Results and Discussion

22.3.1
Raman Scattering

Raman scattering measurements were performed to determine the admixture of molecular species in the helium gas flow. In the series presented below the Perspex tube surrounding the needle was pushed back (the distance x in Fig. 2 was varied), exposing the tip of the needle and thus allowing more air admixture. From the Raman spectra (Fig. 6) it was established that the percentage of air in helium in the

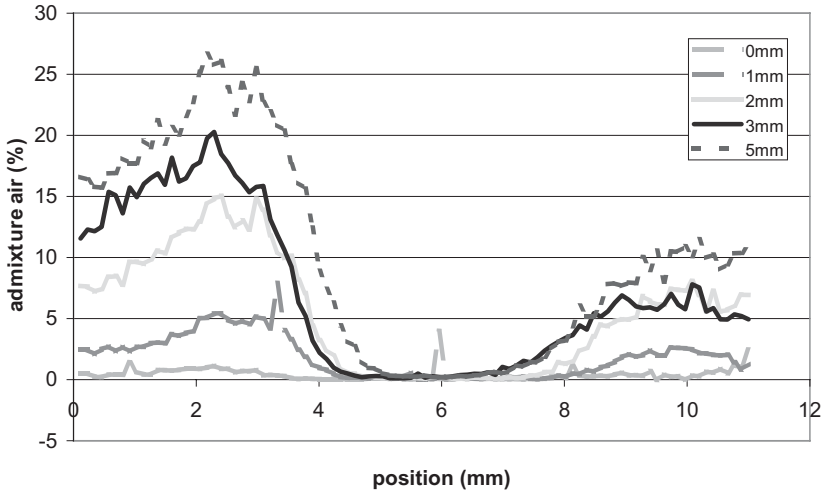

Figure 6 Raman spectrum of the helium flow from the Perspex tube without plasma. The horizontal position at 6 mm coincides with the tip of the needle; the laser is shot 1 mm below. Different curves correspond to the length of the exposed part of the plasma pin from the Perspex tube (*x* in Fig. 2). The sensitivity of the detection system decreases at peripheral positions due to alignment.

middle of the plasma (in the closest vicinity of the needle tip) was below 0.5%. It was actually below the detection limit of the method, so it was difficult to observe any changes when the needle became more or less exposed. However, it can be seen that at the sides of the needle the air admixture increased up to 25% in the case of a 5-mm distance between the tip of the electrode and the tube. The gradients of air concentration towards the middle also became higher, and therefore the influx of air into the active plasma zone was increased. Raman spectra that were recorded for the same helium flow but in the presence of the plasma did not significantly differ from spectra taken without plasma.

Raman scattering measurements were performed in a configuration with a grounded metal plate opposite to the plasma needle. During plasma treatment of cells or tissues this plate was replaced by a biological sample. This could in principle have an influence on plasma chemistry and/or gas composition, due to, for example, different conductivity of the sample and the metal plate. However, such small differences cannot be visualized using the Raman scattering technique. The Raman data can be used to estimate air concentration/influx, but not to study the molecular composition of the plasma.

22.3.2
The Fluorescent Probe Measurements

CM-H_2DCFDA was tested by applying the plasma to the probe solution, while the sample was scanned with a confocal laser scanning microscope (Fig. 7). In this way a time series was recorded, which allowed visualization of probe activation (fluores-

cence) within seconds after the onset of the plasma. Although the CM-H_2DCFDA probe is sensitive to light, the laser power was too low and the irradiation time was too short to affect the fluorescence significantly.

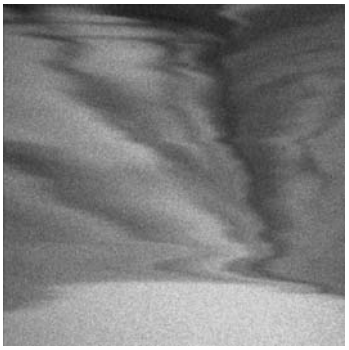

Figure 7 Fluorescence emitted by CM-H_2DCFDA probe during plasma treatment. Plasma was applied at the left-hand side of the picture (size 0.92 × 0.92 mm). Bright color indicates higher fluorescence intensity.

The real-time measurements revealed flow patterns in the solution, induced by the flow of helium from the plasma. These space- and time-varying fluorescent intensity patterns can be used to determine the dynamical behavior of radicals in the liquid. However, in this work we analyzed only the space-averaged intensities collected from a certain volume of liquid, treated by the plasma.

The radical concentration as a function of plasma treatment duration is depicted in Fig. 8. As expected, a linear dependence up to 8 min was found. At longer treatment times the method was less reliable, because the probe might become saturated. From these data the number of radicals in the plasma was estimated. The radicals diffusing into 400 µl of liquid produced an oxidized probe solution after one minute of treatment that was comparable to 0.65 ± 0.2 µM NO. The number of radicals reaching the liquid was then 2.6×10^{12} s^{-1}. For the calculation of the radical density in the plasma using Eqs (1) and (2) [27], we take the thermal velocity ν_{th}= 300 m s^{-1}, the surface through which radicals are transferred A= 1 mm^2 (the size of the plasma spot), gradient length λ= 0.1 mm (estimated plasma sheath thickness at the water surface) and mean free path $l_{fr} = 10^{-5}$ m.

$$\Phi_{rad} = n_{rad}.D.A.\lambda^{-1} \quad (1)$$

$$D = 1/3.\nu_{th}.l_{fr}. \quad (2)$$

This estimation yields $n_{rad} = 10^{19}$ m^{-3}, which is a reasonable value, noting that the admixture of air into the plasma was low (see the Raman scattering data).

In order to study the propagation of radicals in the gas phase (before they reach the fluid sample), we varied the distance between the tip of the needle and the

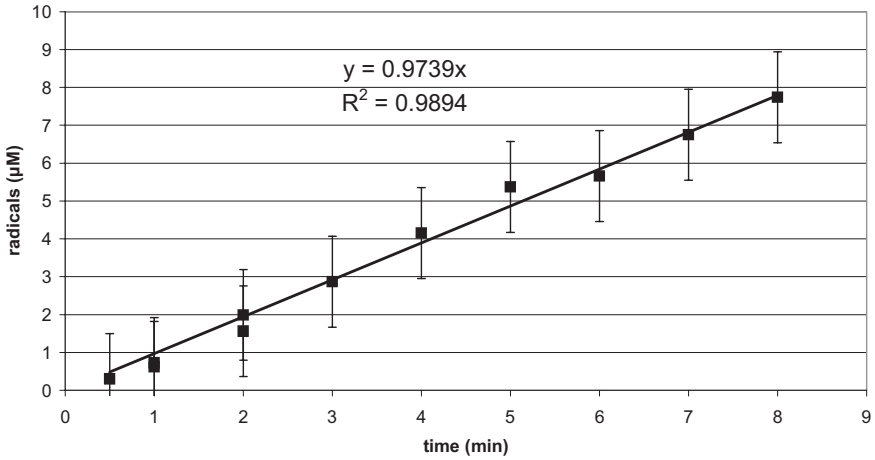

Figure 8 Radical density in liquid, resulting from plasma treatment as a function of treatment time. The *x*-position was 0 mm, the needle-to-surface distance was 1 mm. The radical density was measured using the fluorescence from the CM-H_2DCFDA probe, and calibrated using a known NO concentration.

surface of the liquid. A power fit of the data (the R^2 of the fit is 0.92) shows that the density decreased with distance approximately as the 1.2 power of $1/d$, where d is the distance (Fig. 9). This is weaker than the $1/d^2$, expected for homogeneous spatial expansion from the point-like source (glow). This means that at short distances the liquid preferentially absorbs the plasma species. Visually, we observed that at distances of about 1 mm the plasma was attracted to grounded objects, the glow

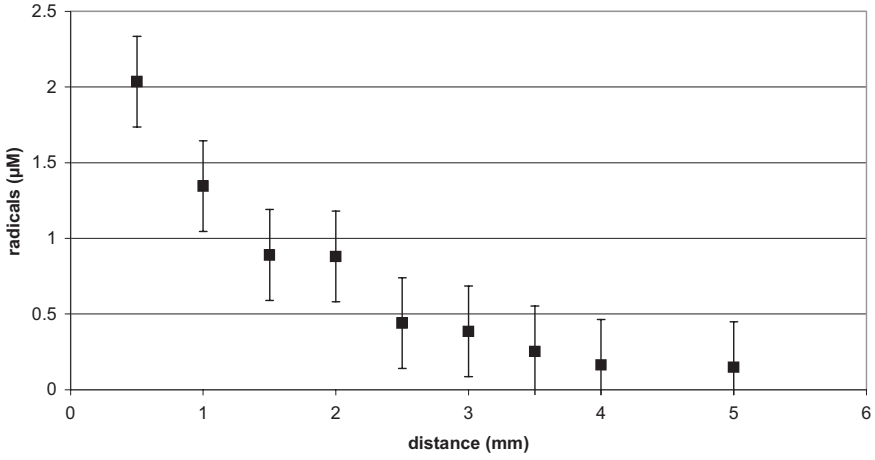

Figure 9 Radical concentration as a function of distance from the tip of the needle to the surface of the liquid. The treatment time was 2 min, the *x*-position was 0 mm.

expanded and a thin dark sheath at the object's surface was visible. As the needle was moved away, the glow remained confined in the closes vicinity of the pin. This occurred at distances larger than 2 mm.

In another experiment we changed the plasma composition, to check its influence on the amount of produced radicals. First, we determined the radical densities for different positions of the tip of the needle with respect to the end of the Perspex tube (*x* distance in Fig. 2). As observed during Raman scattering experiments, the longer the exposed part of the pin (outside the tube), the higher the air influx into the plasma. However, the number of radicals decreased as the needle was pushed further out of the tube (Fig. 10), even though at the same time the influx of molecular species into helium increased. This can be explained by the unfavorable effect of oxygen and nitrogen on the plasma. Both of them cause dissipation of the electron energy due to vibrational and rotational excitation. Moreover, oxygen is electronegative, and its presence creates a sink for plasma electrons due to negative ion formation. This means that at the same power level, less energy is available for the production of active radicals when the air content in the plasma is high. This decrease of plasma activity is also evident from visual observation: the glow shrinks and the emission intensity decreases. This situation can be to some extent compensated by increasing the voltage (power), but then the glow-to-arc transition may take place and the plasma becomes difficult to control [4].

In another experiment we measured the radical densities as a function of oxygen admixture in the plasma. From the Raman spectrum we deduced that the amount of oxygen at the position of the needle was normally well below 0.1%. By adding pure O_2 into the helium flow we observed that even an addition as small as 0.2% caused the plasma to shrink significantly; the color of plasma emission changed

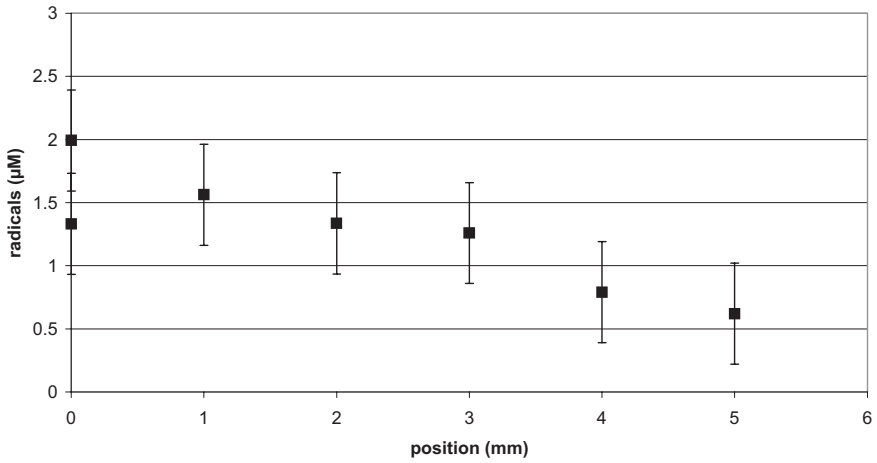

Figure 10 Radical concentration as a function of the position of the tip of the needle with respect to the end of the Perspex tube (*x*-position in Fig. 2). The treatment time was 2 min, the needle-to-surface distance was 1 mm.

from pink to white. The radical density (Fig. 11) also decreased as a function of oxygen admixture. As in the previous experiment (Fig. 10), this can be explained by the influence of O_2 on the plasma: electron attachment causes depletion of plasma electrons and a decrease of plasma activity.

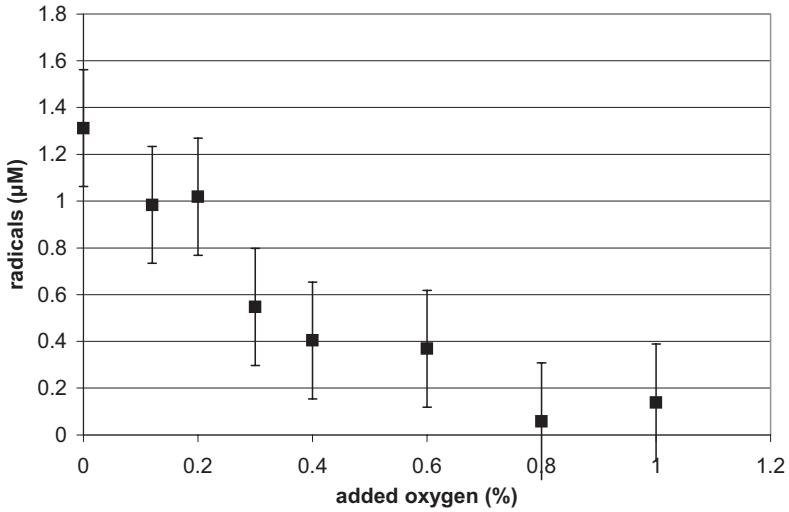

Figure 11 Radical concentration as a function of oxygen admixture into helium flow. The treatment time was 2 min, the *x*-position was 0 mm, the needle-to-surface distance was 1 mm.

At the present stage we cannot decide whether the concentration of radicals in the liquid is appropriate for the treatment of living tissues. This has to be defined in advanced in vivo experiments, and is also dependent on the desired effect of the therapy. In the biological studies on oxidative stress the exact concentrations are seldom mentioned. However, we can state that plasma does not produce dangerously high reactive oxygen species concentrations in the liquid phase. In fact, the amount of reactive oxygen species is comparable to that produced by the body itself, e.g. to fight bacterial infection or during increased metabolism. Radical concentrations found in vivo are in micromolar range. In high concentrations (0.5 mM) radicals may induce both necrotic and apoptotic cell death [28]. This is at least a factor 10 higher than the concentration that was found for plasma radicals. The inaccuracy in the calibration measurements for the radical concentrations is within the right proportions to draw the conclusion that the mild oxidative properties of the plasma may have a beneficial effect on the tissue (e.g. sterilizing or increasing the cell activity). This is in agreement with previous experiments on living cells, in which we established that plasma treatment usually did not kill the cells.

22.4 Conclusions

The use of a fluorescent probe for radical detection has proven to be a valuable method in plasma diagnostics. It can be used in any atmospheric and nonthermal plasma, and it gives information about the radical fluxes towards the surface. These data are useful in monitoring the plasma performance in surface processing (etching, cleaning, chemical and biological decontamination). In this work we tested this method using the plasma needle and a probe for detection of reactive oxygen species. The radicals from the plasma had sufficiently long lifetimes to reach the solution and bind with the probe. The radical flux into the liquid was 10^{12} s^{-1}; the radical density in the plasma was estimated to be 10^{19} m^{-3}. The radical density decreased with increasing distance from the needle. Addition of extra oxygen or air decreased the plasma activity and resulted in lower radical concentrations. For optimal reactivity, the plasma should be kept within 2 mm from the surface that is to be treated, and the air content should not be higher than 0.5%.

The reactive plasma species dissolve in the liquid and reach living cells that are cultured on the bottom of the wells-plate. The radicals generate oxidative stress that in principle is harmful, but at low radical concentrations the interactions with cells can have beneficial effects. The radical concentrations in liquid phase, generated by the plasma needle, are only in the order of μM, and we observe that under normal conditions plasma does not cause cell death.

References

[1] J. Park, I. Henins, H.W. Herrmann, G.S. Selwyn, and R.F. Hicks, *J. Appl. Phys.* **2001**, *89*, 20

[2] M. Laroussi, *IEEE Trans. Plasma Sci.* **2002**, *30*, 1409

[3] M. Moisan, J. Barbeau, S. Moreau, J. Pelletier, M. Tabrizian, L.'H. Yahia, *Int. J. Pharmac.* **2001**, *226*, 1

[4] E. Stoffels, A. J. Flikweert, W. W. Stoffels, and G. M. W. Kroesen, *Plasma Sources Sci. Technol.* **2002**, *4*, 383

[5] E. Stoffels, I.E. Kieft and R.E.J. Sladek, *J. Phys. D.: Appl. Phys.* **2003**, *36*, 2908

[6] I.E. Kieft, J.L.V. Broers, V. Caubet-Hilloutou, D.W. Slaaf, F.C.S. Ramaekers, E. Stoffels, *Bioelectromagnetics*, **2004**, *25*, 362

[7] T.M. Buttke and P.A. Sandstrom, *Immunol. Today* **1994**, *15*, 7

[8] K. M. Anderson, T. Seed, D. Ou, and J. E. Harris, *Medical Hypotheses* **1999**, *52*, 451

[9] B. Halliwell and J. M. C. Gutteridge, *"Free Radicals in Biology and Medicine"*, University Press, Oxford 1999.

[10] T.C. Montie, K. Kelly-Wintenberg, and J.R. Roth, *IEEE Trans. Plasma Sci.* **2000**, **28**, 41

[11] H.-U. Simon, A. Haj-Yehia, and F. Levi-Schaffer, *Apoptosis* **2000**, *5*, 415

[12] S. Hayashi, K. Kawashima, N. Ozawa, H. Tsuboi, T. Tatsumi, M. Sekine, *Sci. Tech. Adv. Mater.* **2001**, 555

[13] J.P. Booth, G. Cunge, L. Biennier, D. Romanini, A. Kachanov, *Chem. Phys. Lett.* **2000**, *317*, 631

[14] J. Benedikt, R.V. Woen, S.L.M. van Mensfoort, V. Perina, J. Hong, M.C.M. van de Sanden, *Diam. Relat. Mater.* **2003**, *12*, 90

[15] J.P.M. Hoefnagels, A.A.E. Stevens, M.G.H. Boogaarts, W.M.M. Kessels, M.C.M. van de Sanden, *Chem. Phys. Lett.* **2002**, *360*, 189

[16] C. P. LeBel, H. Ischiropoulos, and S. C. Bondy, *Chem. Res. Toxicol.* **1992**, *5*, 227
[17] H. Kojima, Y. Urano, K. Kikuchi, T. Higuchi, Y. Hirata, and T. Nagano, *Angew. Chem. Int. Ed.* **1999**, *38*, 3209
[18] R. Cathart, E. Schwiers, B.N. Ames, *Anal. Biochem.* **1983**, *134*, 111
[19] B. Li, P.L. Gutierrez, N.V. Blough, *Anal. Chem.* **1997**, **69**, 4295
[20] M.J. van de Sande, *"Laser scattering on low temperature plasmas"*, Ph.D. thesis, Eindhoven University of Technology, Eindhoven 2002
[21] Y. Ueki, H. Nakamura, K. Matsumoto, T. Tominaga, S. Miyake, Y. Kita, Y. Katayama, S. Fukuyama, Y. Hirasawa, K. Yoshida and K. Eguchi, *Blood Coag. Fibrinolysis* **2002**, *13*, 75
[22] P.C. Ford, D.A. Wink, and D.M. Stanbury, *FEBS Lett.* **1993**, *326*, 1
[23] P. Neta, R.E. Huie, A.B. Ross, *J. Phys. Chem. Ref. Data* **1988**, *17*, 1027
[24] N. C. Baird, *J. Chem. Educ.* **1997**, 74, 817
[25] D.R. Grymonpre, A. K. Sharma, W.C. Finney, B.R. Locke, *Chem. Eng. J.* **2001**, 82, 189
[26] I. Platzer, N. Getoff, *Radiat. Phys. Chem.* **1998**, 51, 73
[27] T.I. Gombosi, *"Gaskinetic Theory"*, Cambridge University Press, Cambridge 1994
[28] T. Andoh, S.Y. Lee, C.C. Chiueh, *FASEB*, **2000**, *14*, 2144

Text for table of contents:

The plasma needle is a nonthermal atmospheric microdischarge. The diffusion of plasma radicals into the liquid was measured using a fluorescent probe dissolved in water. After reaction of the probe with a radical the product emits fluorescence when it is irradiated with a laser. The method allows a quantitative analysis of plasma radicals.

23
RF-Plasma Treatment on the Inside of Small Functional Devices for Biomedical Application

C. Oehr, D. Hegemann, M. Müller, U. Vohrer, M. Storr

Abstract

For biomedical application, an increasing amount of polymers is used. Therefore, the polymeric surface properties have to be controlled to give the appropriate answer in contact with the biological medium. Whilst the surface properties of flat objects are often described to be successfully modified by plasma techniques, the three-dimensionality of some devices is an outstanding challenge. This contribution demonstrates the potential of plasma treatment in pores and other cavities of devices for biomedical use.

23.1
Introduction

Plasma treatments are very effective in the modification of solid surfaces relating to cleaning, etching, activation, functionalization, and coating. All common materials (polymers, metals, ceramics, glasses, etc.) can be treated in the gas discharge, if they are stable under vacuum conditions. The surface–plasma interaction mainly proceeds via ions, radicals, and VUV. Depending on the gas type and the plasma parameters used, degradation or deposition occurs. Using rather mild plasmas, i.e. low power input, functional groups are retained and chemically bonded to the surface [1]. The development of these numerous modifications is generally performed on flat surfaces in order to obtain a homogeneous treatment and to simplify the characterization. Much effort is carried out to upscale these processes, for example, for large-area coatings. However, many functional devices are three-dimensionally formed and possess recesses like cavities (e.g. capillaries), pores (e.g. membranes) or openings (e.g. stencils, textiles or hollow fibers).

Therefore, this work investigates the penetration of active plasma species into small fissures, as well as the inner modification of hollow fibers. For the plasma treatment, RF discharges (13.56 MHz) were used and the reactor geometry and gas flow were adjusted to the sample geometry. To examine the treatment in small fissures with width varying from 6 mm to 15 µm and aspect ratios >1, a plane parallel electrode configuration was chosen. Due to collisions in the gas phase and surface

diffusion, the conformity inside the fissures is better than expected from a pure "sticking" model.

The modification and the film thickness inside the recesses are measured using field emission scanning electron microscope (FESEM) (in cross section), small-spot ESCA and AES (sputtering techniques). The treatment or deposition rate is compared to flat geometries. Plasma activation, functionalization, and coating were investigated. Examples are given for devices with trenches, which may be arranged parallel or perpendicular to the electric field.

23.2 Experimental

For the treatment, functionalization and coating of polymers, a modular, symmetrical plasma reactor with two plane-parallel electrodes (stainless steel) was developed. A polymeric frame (polycarbonate shielded inside with glass) between the electrodes forms the vacuum chamber confining the plasma (Fig. 1).

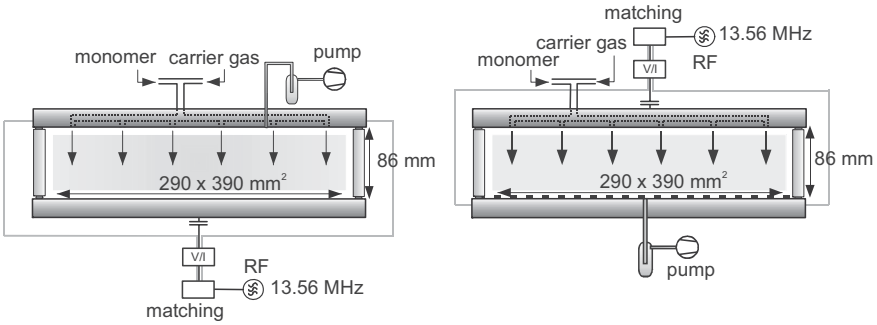

Figure 1 Schematic drawing of the modular, symmetrical reactors for plasma treatment, functionalization and coating. The left version enables gas feeding and pumping on one side, whereas the right version supports homogeneous "flowing through".

Thus no outer vessel is needed that may force plasma instabilities and no additional bias voltage is produced. In one setup, an integrated gas feeding and pumping system inside the top electrode enables homogeneous deposition over large areas (up to 290×390 mm^2). The lower (substrate) electrode is capacitively coupled to a 13.56 MHz RF transmitter (Dressler CESAR 1312 D). In another setup (of the same size), the RF coupling is on the upper electrode. Through the lower, grounded electrode the plasma chamber is evacuated. This electrode is also used for treatment. A V/I probe (ENI Model 1065) measures applied voltage and current.

The reactor is used for the experiments presented in the scheme of Fig. 2, where molded paddings of a polymer (ABS) are used to realize trenches of different widths

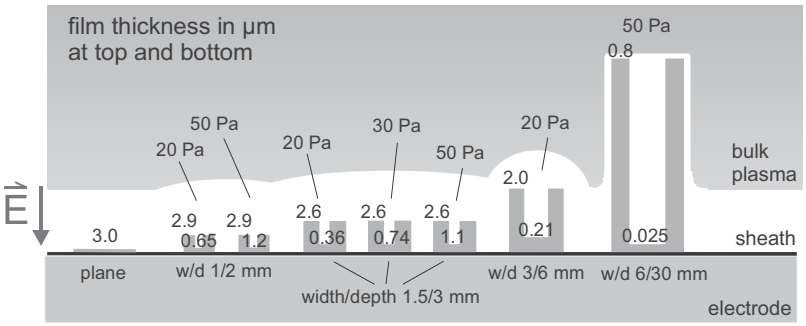

Figure 2 SiO_x film thickness at the top and bottom of polymeric molded paddings with trenches in the millimeter range. To analyze the conformity of the plasma process, the pressure was varied between 20 and 50 Pa. The highest sample is immersed in the plasma, i.e. at floating potential, whereas the smaller samples are surrounded by the plasma sheath.

and heights. The coatings are deposited from hexamethyldisiloxane/oxygen mixtures HMDSO/O_2-mixtures at a pressure of 0.2, 0.3 and 0.5 mbar. The applied power density was 0.25 W/cm^2. The thickness of the deposited coatings on the top or in the depth of trenches are measured by producing steps (measured via AFM) on small silicon pieces positioned in the trenches or in the case of smallest trenches by examining the cross section (via SEM). The deposited SiO_x layers are glass-like with a small amount of carbon (according to ESCA-measurements: 29.1% Si, 66.2% O and 4.7% of C) for the deposition pressure of 0.2 mbar. For higher pressures the carbon content increases up to 5.1%.

23.3 Results and Discussion

23.3.1 Devices with Geometrically Well-described Trenches Oriented Parallel to the Applied Field

Quartz-like coatings derived from RF-excited O_2/HMDSO plasmas are well-known to be scratch resistant and hydrophilic. Recently, we were able to show that their mass deposition rates depend on the generalized reaction parameter power input per gas flow W/F_{mc}, where the total gas flow F_{mc} is an addition of monomer flow (HMDSO) and carrier gas flow (O_2) as $F_{mc} = F_m + a\ F_c$ with a being around 0.6 [2, 3]. This reaction parameter controls the plasma volume processes like fragmentation and radical formation. On the other hand, it is also well known that ion-assisted processes during film growth yield a reduction of the residual carbon content and a crosslinking of the growing films, which enhances the SiO_x film quality [4]. Furthermore, considering the interphase formation when deposited on polymers, their adhesion to different polymer substrates can be improved [2, 5]. Thus, these coat-

ings can be used to improve the surface properties for different applications. However, the film quality is generally optimized for thin, plane substrates lying on the electrode to make use of the ion bombardment in RF plasmas. Potential drops of 100–200 V across the plasma sheaths are typical for good-quality SiO_x films. Therefore, it should be regarded that an increasing part of the electrical field across the plasma sheath is applied to the polymer itself, when the polymer thickness is raised, since it is a dielectric [6].

We have found that this effect leads to a reduction of deposition rate [7]. Hence, the deposition rate is determined by plasma volume, controlled by W/F, and plasma surface processes, controlled by V_{sh} (approximately proportional to $(W/p)^{0.5}$). To maintain the SiO_x film properties in RF plasmas, power input W should be increased (or pressure p decreased) at constant W/F ratio to maintain a comparable ion bombardment when thicker polymer substrates are used. However, when the polymeric substrates are substantially thicker than the plasma sheaths (or are immersed into the plasma bulk), they can be considered to be at floating potential where the potential drop is reduced to about 10 V. These effects should also be regarded besides others when recesses in the millimeter range occur in polymeric parts to be coated. Therefore, we investigated the deposition rate of SiO_x films in small fissures with a width varying from 6 mm to 15 µm and aspect ratios larger than 1 (Fig. 2). We found that the conformity of the growing film inside the fissures is better than expected from an isotropic "sticking" model, i.e. the incoming particle sticks where it hits the surface [8].

Three effects are responsible for this finding: First, due to the potential drop, the incoming particles are not isotropic, so that more particles are able to enter the fissures. Secondly, collisions inside the fissures yield a better distribution of the film-forming particles. And thirdly, ion-assisted effects enhance the surface diffusion. Thus, it can be inferred that increased pressure at maintained ion bombardment, improves the conformity of the plasma-deposited layers inside the small fissures. Note, that with increasing power input, also the flow must be increased to keep the reaction parameter W/F constant. This was proved to be true for width of the fissures down to around 100 µm. At smaller recesses collisions inside the fissures are less important and thus the supporting influence of the pressure diminishes.

Nevertheless, small fissures e.g. 15 µm in width and 75 µm in height can be coated inside with SiO_x layers (Fig. 3). Thus these polymeric parts can be rendered hydrophilic or hydrophobic, when depositing siloxane-like HMDSO layers [9].

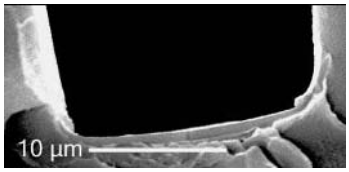

Figure 3 REM picture on a cross section of a 3D structure in polycarbonate. The bottom of the 15-µm wide fissure is coated with ~600 nm SiO_x, while ~1500 nm are deposited on top of the structure.

Thus we can conclude that for a system of geometrically well-defined slits that are vertically oriented with respect to the electrodes the deposition rate inside the small fissures is not only dependent on the reaction parameter W/F as found for flat geometries directly laid on the electrode in the used reactor setup, but also on the electrical field, which accelerates ions towards the electrode, VUV radiation and the working pressure as far as the dimensions are larger than the mean free path of the particles (~200 µm).

These conditions are given for some small medical devices, such as for example in the spring guidance on brackets used in dental applications. Furthermore, these conditions are well examined in microelectronics for anisotropic etching.

23.3.2
Devices with Geometrically Defined Trenches Oriented Nonparallel to the Applied Field

In many other applications such an arrangement as described above is not given. For example, if plasmas are used for sterilization or cleaning of devices, slits and fissures are stochastically arranged with respect to the electrical field and only species of long lifetimes are able to undergo reactions in deep fissures and slits. Here, an example derived from a cleaning process using oxygen plasmas is given [10]. A metallic surface (stainless steel) was accurately defined contaminated with a very thin organic film. This film results in 40 to 45 at% carbon content on the surface according to ESCA measurements. After oxygen-plasma cleaning the carbon content is reduced to 5 at% or less. The contaminated surface was placed on the electrode and covered in a way that only a slit of dimensions of 0.5 mm height, 6 mm width and a length of 100 mm above the contaminated surface is in contact with the plasma gas, which has access from just one side into the slit (Fig. 4). Applying an oxygen glow discharge (20 Pa, 40 W) for 10 min shows that reactive species from the plasma diffuse into the slit and demonstrate their activity after several hundred collisions (mean free path for oxygen under these conditions ~300 µm) at least 65 mm

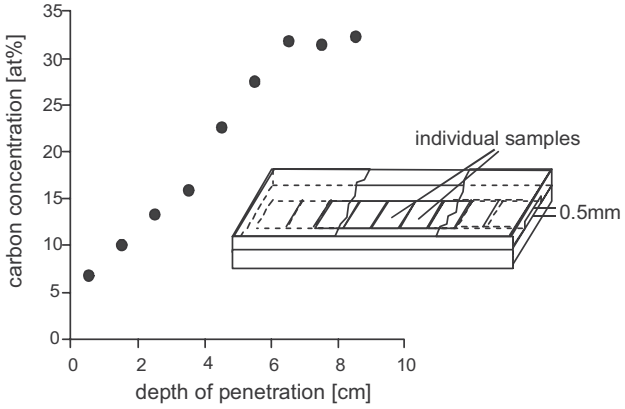

Figure 4 Penetration depth of reactive species from an oxygen plasma into a small slit.

away from the opening without the assistance of the ion bombardment and VUV.

Thus it has to be mentioned that the penetration depth is a complex function of the material treated, the dimensions and the orientation of trenches in a plasma environment. In addition, the lifetimes of the most stable reactive species at given pressure and power conditions have to be considered.

23.3.3 Devices with Pores in Micrometer Dimension

Beside, devices that can be arranged in a proper way for optimized penetration into slits, and those with at least a well defined geometry of the trenches, a third category of polymeric materials used in bioapplications is represented by textiles, nonwovens and separation membranes. In these materials cavities and pores in the range of few micrometers are presented. It is still a challenge to modify the integral surface of such porous materials. For the modification of textiles, some processes exist also to reach the inner surface of the textile as well as of nonwovens [11]. Some of the earliest attempts to evaluate the possibility of the modification of the inner surface of textiles are described by Krenstel et al. [12]. They tried to modify the inner surface of three packages of ten nonwoven PET/PBT sheets; each placed perpendicular to the gas flow in the reactor by CF_4- and C_2F_4-plasmas. This examination results in the conclusion, that surface treatment only for the outer sheets is flow controlled, the inner sheets are more or less treated by diffusion-controlled impact of species. Due to differences in plasma polymerization of these two monomers, the penetration depth varies with both compounds and with duration. We use acrylic acid as monomer resulting in hydrophilic films and hexamethyldisiloxane for hydrophobic coatings. The substrate is a polyester tissue, woven of 20-µm monofilaments (Fig. 5 (a)). With both precursors and without flow support (samples were positioned on a silicon wafer lying on one electrode) the deposition pattern gained by deposition through one layer of textile can be observed with light microscope, AFM and other tools on the underlaying wafer (Fig. 5). The marked hilly structure gained on the wafer and shown by the AFM pictures (Fig. 6) is only observed if one sheet of tissue is positioned on the wafer.

This is due to the enhancement of deposition by the electric field and "free fall" through the squared 10 µm holes of the tissue. The deposition can be compared with those described in the literature in trenches [13] supposing an overall sticking probability of 0.1 to 0.2 for the carboxylic coating as well as for the siloxane coating.

Using more than one sheet of the fabric, the hilly structure is no longer pronounced due to the fact that only diffusion is effective. With stacks of two or more sheets, penetration is also observed but to a much less extent and the pattern on the wafer becomes flat. With four or more sheets on the stack, the thickness of the layer deposited on the wafer below the stack becomes smaller than 5 nm (Fig. 5).

This thickness is still sufficient to change the surface tension to hydrophilic or hydrophobic character by its chemical composition, which is of interest for biomedical application. In addition, the "apparent" contact angle [14] differs from the "real" contact angle due to the geometric structure of the surface. This can be shown by contact-angle

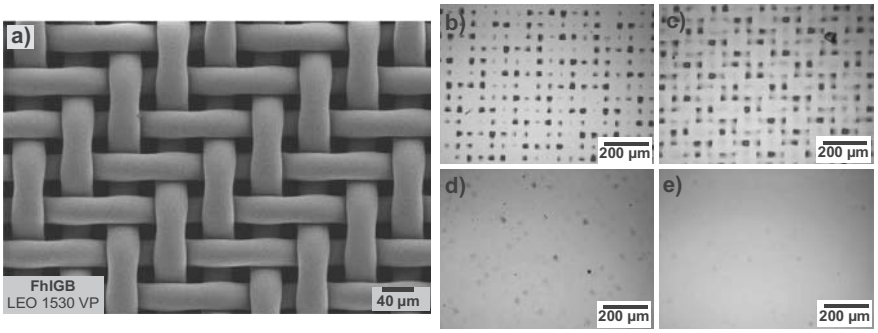

Figure 5 (a) SEM picture of the polyester fabric (b) penetration through two fabric sheets visualized by light optical microscopy on underlaying wafer (sheets parallel oriented), (c) penetration through two fabric sheets (sheets twisted with an angle of 45°), (d+e) penetration through three or four fabric sheets, respectively.

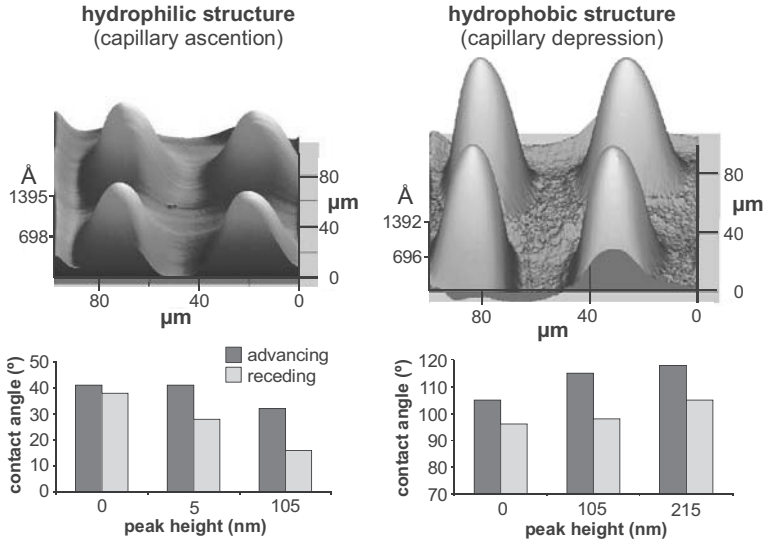

Figure 6 Left side: AFM and contact-angle results of carboxylic pattern on silicon wafers. Right side: AFM and contact-angle results of siloxane pattern on silicon wafers.

measurements on the negative pattern caused by the textile mask. With the hilly structure on the wafer, hydrophilicity seems to be enhanced by capillary rise of the water into the valleys and hydrophobicity is enhanced by capillary depression. As is expected, in the first case the receding contact angle reacts more sensitive to deviation from flat surfaces and in the hydrophobic case the advancing one.

The main medical application of polymeric separation membranes is blood dialysis. This process is realized in several steps [15]. In a first step, today blood cells are

separated from the blood plasma before it is further purified. In this starting step hollow fiber microfiltration membranes are used. The surface of such membranes has to fulfil several requirements. First, it must not release components when it is used in blood contact. Secondly, it has to reveal pores for separation of blood cells by geometric means and thirdly, it has to be blood compatible in the way that no reactions such as the coagulation cascade are actuated. It would be of benefit if at this first separation step endotoxines, sometimes present in the blood, could also be separated. Attempts have been made to immobilize endotoxine scavengers on the membrane surface. This scavenger immobilization has to be restricted to the outer surface and the inner pore surface, while the lumen surface (inner surface of the cylinder-like membrane) of the membrane has to retain its compatibility with respect to blood cells and must not be modified. Thus pores and the outer surface of the hollow fiber membranes are to be modified for immobilization of endotoxine scavengers. These scavengers are fixed to primary amino groups, which are regioselectively deposited on these surfaces. The modification is done by using different amino group bearing precursors in a 13.56-MHz plasma [16].

For analytical purposes, pentafluoro-phenyl-alanine is bonded onto the amino groups by an appropriate derivatisation procedure after the plasma treatment.

The fluorine signal from the derivatived surface is measured with a small-spot ESCA (Kratos Axis Ultra) across the cross section of the hollow fiber membrane in the way that seven analytic areas (cross section 27 µm) are well positioned along the diameter of the membrane (Fig. 7 (a)). From the diagram (Fig. 7 (b)) it can be seen that the fluorine content that means the amino functionalization shows a gradient from the outer to the inner surface of the capillary and it is restricted to the pore structure and the outer surface. The effectiveness of this functionalization after scavenger immobilization is expressed by the broad reduction of the endotoxine concentration in contaminated blood [17]. The effective penetration depth mainly depends on pressure and on active species produced by the plasma as well as on membrane material and pore size. The corrected curve shown in Fig. 7 (b) is due to the considered degradation of the fluoro-derivative under ESCA conditions.

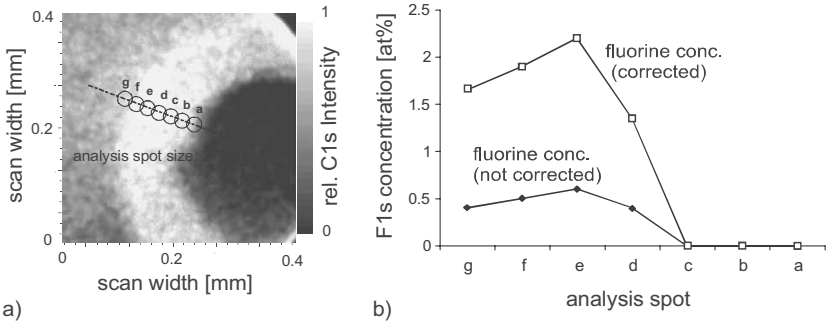

Figure 7 (a) Cross section of a hollow fiber membrane. (b) Fluorine signal due to regioselective plasma functionalization across the membrane wall.

23.4 Conclusions

It is shown that the existence of slits, trenches and pores causes several arrangements for appropriate plasma treatment especially if compatibility in biomedical applications is a goal of the treatment. Three types of devices are differentiated: Devices with geometrically well-defined trenches or slits, which can be arranged along the electric field in the plasma. Devices with well-defined trenches arbitrarily oriented in the electric field of the plasma and devices with pores in the micrometer dimension. In the first case the lifetime, the electric field and VUV radiation together cause the modification effect. In the other cases the modification is mainly depending on diffusion parameters and lifetime of the species. The examination of modification potential of plasmas in cavities and pores is mainly carried out on a very empirical level. Some data of lifetimes of fragments from precursors would be helpful for further investigation.

Acknowledgements

This work was in part supported by the German Ministry of Education and Research (BMBF). We would also like to thank V. Sciarratta for deposition of carboxylic layers, J. Mayer for AFM-Measurements and M. Riedl for small spot-ESCA measurements on hollow fibers.

References

[1] C. Oehr, D. Hegemann, M. Müller, V. Sciarratta, U. Vohrer, Proc. 14th Int. Symp. Plasma Chem. **Vol. IV**, 1747 (1999).
[2] D. Hegemann, H. Brunner, C. Oehr, Proc. 45th SVC Conf., 174 (2002).
[3] D. Hegemann, H. Brunner, C. Oehr, Surf. Coat. Technol. 174–175, 261–265 (2003).
[4] L. Martinu: in Plasma Processing of Polymers, eds. R. d'Agostino, P. Favia, F. Fracassi, NATO ASI Series E: Appl. Sci. **346**, 247 (1997).
[5] D. Hegemann, H. Brunner, C. Oehr, Proc. 16th ISPC (2003), this volume.
[6] Y.P. Raizer, M.N. Shneider, N.A. Yatsenko, Radio-Frequency Capacitive Discharges, CRC Press, Boca Raton, 1995.
[7] D. Hegemann, H. Brunner, C. Oehr, Surf. Coat. Technol. **142–144**, 849 (2001).
[8] M.A. Lieberman, A.J. Lichtenberg, Principles of Plasma Discharges and Materials Processing, J. Wiley, New York, 1994.
[9] D. Hegemann, H. Brunner, C. Oehr, Plasmas Polym. **6**, 221 (2001).
[10] C. Oehr, U. Vohrer, Metalloberfläche (MO) **49/1**, 22 (1995).
[11] C. Oehr, B. Schindler, U. Vohrer, M. Müller, Method and apparatus for plasma modification of flat porous articles, EP 0 695622 B1.
[12] E. Krentsel, H. Yasuda, M. Miyama, T. Yasuda, J. Polym. Sci: Part A. Polym Chem. **33**, 2887 (1995)
[13] J.A. Theil, Mater. Res. Soc. Symp. Proc. **385**, 97 (1995)
[14] A.B.D. Cassie, Discuss. Faraday Soc. **3**, 11(1948)
[15] H. Goehl, R. Deppisch, M. Storr, R. Buck: Blood Purif. **15 (suppl. 2)**, 36 (1997).
[16] M. Mueller, C. Oehr, Surf. Coat. Technol. **116–119**, 802 (1999).
[17] M. Müller, C. Oehr, M. Storr: "Regioselective plasmachemical modification of hollow fiber membranes for applications in medical therapy", Proc. 14ème Colloque International sur les Procédés Plasma, CIP 2003, Antibes 29 juin au 3 juillet 2003, Societe francaise du vide, Paris 2003.

24
Plasma Sterilisation: Mechanisms Overview and Influence of Discharge Parameters

Francois Rossi, Riccardo De Mitri, Sophie Bobin and Rosy Eloy

Abstract

Mechanisms of plasma sterilisation are reviewed and analysed in terms of radiation-induced desorption, UV radiation effects and etching. Different gas mixtures are analysed with optical emission spectroscopy in order to find optimum conditions of UV emission and radicals production. The different gas mixtures are compared as a function of pressure, power and gas composition. These effects are compared and related to effective sterilisation rates obtained from the literature and experimentally on *Bacillus subtilis*. It is shown that UV emission is the major contribution for sterilisation in Phase I. SEM analysis of spores at different times of treatment show the degradation of the outer shell of the spores, as well as size and coverage reduction as the treatment duration increases. The time scales of these observations show that the sterilisation effect of Phase I is not related to etching but solely to UV emission, while Phases II and III are influenced by etching. A strategy for optimised sterilisation treatment is proposed.

24.1
Introduction

Manufacturers of medical devices can draw from a broad spectrum of techniques to sterilise medical components, but new physical and chemical processes are still needed and continue to be developed. A leading reason for this continued search for new methods is to meet the needs of an increasing number of cost-conscious hospital and clinical environments, which are foregoing the use of single-use, disposable devices in favor of devices that can be used more than once. The general trend is to suppress the wet sterilisation because of effluents and to substitute polymers to glass. In this case, a low-temperature sterilisation method is required.

Traditional methods of sterilisation, like steam and ethylene oxide (EtO), successfully treat many devices but present the drawback of compatibility with materials (humidity, high temperature, corrosion, loss of polymer properties in the case of steam sterilisation) or problems linked to environment, safety of personnel and toxicity (in the case of EtO). The newer and most promising sterilisation techniques are

based on the use of low-temperature plasmas, such as the hydrogen peroxide gas plasma (Sterrad system, Johnson & Johnson). The advantage of plasma relies on the production of very active molecules in the discharge that permit, under specific conditions, a high-efficiency sterilisation at low temperature using small concentrations of active product. However, the Sterrad system is more a conventional vapor sterilisation system since it was demonstrated that the use of plasma has *no effect* on the sterilisation kinetics, but was necessary to desorb and decompose the hydrogen peroxide adsorbed on the surfaces.

A large amount of work related to the use a plasma discharge, either in direct or post-discharge has been made [1–3]. The mechanisms of plasma sterilisation were analysed in terms of the action of UV emission and interaction with radicals produced in the plasma [4–6]. A complete review of the mechanisms of plasma sterilisation can be found in [4], where it is proposed that the kinetics of sterilisation obeys 3 superimposed/successive mechanisms i) Phase I: direct damage to the genetic material of micro-organisms by UV interaction, ii) Phase II: erosion by intrinsic photodesorption induced by UV and iii) Phase III: etching of the micro-organism shell by radicals produced in the discharge. However, the model proposed is still qualitative in many aspects, and several experimental results are still difficult to explain, in particular the occurrence of Phase III (direct etching of the spore material), which seems to occur with a latency period difficult to understand from the mechanisms proposed.

In an attempt to analyse and understand the different phenomena operating during plasma sterilisation, we try to correlate the UV emission flux and radicals of several gas mixtures used in a microwave plasma operating in the near post-discharge, to the sterilisation rates obtained with *Bacillus subtilis*.

24.2 Experimental

The experimental plasma source used is represented in Fig. 1. The stainless steel chamber is a cylinder 200 mm in diameter and 380 mm in length with three 25 mm windows for in situ diagnostics, one window for gas input (O_2, CO_2, H_2O, vapor pressures) and a 100-mm flange for pumping, on which is laid out a 25-mm window for optical spectroscopy. Different ports for diagnostics allow determination of the species produced during the discharge and leading to sterilisation. The plasma is excited in the 0.1 to 1 Torr pressure range by microwave power supply working at 2.45 GHz introduced in the chamber through a silica window placed at the extremity of a circular 100-mm waveguide. The microwave circuit includes the microwave supply (2 kW), a circulator, a three-stub impedance matching system, and a rectangular-circular waveguide transition. The chamber is evacuated by a primary pump and a roots blower allowing a base vacuum of 5×10^{-2} Torr. The pressure is regulated by a throttle valve and measured by a baratron. The gas flows are controlled by mass flow controllers and mixtures of Ar, O_2, N_2, H_2 and H_2O have been studied.

Optical emission spectroscopy (OES) is performed with an Avantes AVS-PC2000 plug-in spectrometer, with a 2048-element linear CCD-array detector responsive from 200–1100 nm. A 600-µm diameter fused silica optical fiber is used to transmit the signal to the spectrometer. The optical detection is made through a quartz window. A semiquantitative evaluation of the species present in the different conditions is obtained by using the actinometric approach whenever applicable [7,8]. In this case, argon was used as actinometer with a flux of 5 sccm.

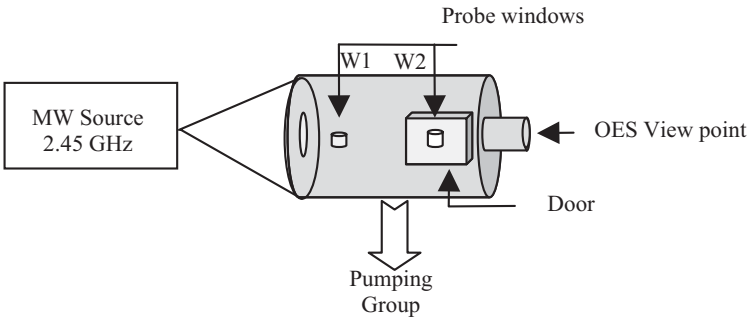

Figure 1 Experimental apparatus.

The samples to be sterilized were glass bottles of 5 cm height and 1 cm diameter, contaminated with approximately 10^6 *Bacillus subtilis* spores. Validation of the bio-burden estimation methodology was performed according to the ISO 11737-1 and NF/EN 1174 standards. After the selection of a technique for removal of micro-organisms adapted to the devices, several factors were studied, for each assay on three samples:

- Evaluation of the efficiency of removal of micro-organisms from samples. A correction factor for recovery efficiency was established. The inoculation method on the product was selected.
- Screening for the release of substances adversely affecting bio-burden estimates.
- Validation of the culture conditions.

The following technique for removal of micro-organisms has been chosen: the samples were filled up with 1 ml peptoned water with 0.05% polysorbate 80. They were then submitted to 1 min vortex agitation. 1 culture media have been validated (Trypcase-soja agar plates under aerobic conditions). The absence of substance released from the device was demonstrated and due to the specificity of the product, a correction factor of 1.95 was determined.

In the experiments described below, the samples are placed at 10 cm from the source and are thus treated in the plasma discharge.

24.3 Results

In the first part of the experiments, the UV emission from different gas mixtures was evaluated. For this, OES spectra were acquired and the integral of the signal between 250 and 300 nm was calculated. Increasing the range of wavelength does not change the results and the contribution below 250 nm does not produce significant changes in the results. These values have been selected following the results of Munakata et al. [9] who showed the efficiency of UV emission in this wavelength range. Figure 2 indicates the value of the UV emission for the different gases used, at different pressures. It can be seen that the highest UV emission is obtained for O_2/N_2 mixtures between around 4 to 10% of oxygen. The lowest is obtained with Ar/O_2.

The different gas mixtures have been used for sterilisation studies of *bacillus subtilis* for duration of 1, 2 and 5 min at 500 W and 500 mTorr. Results of Log reduction vs time are presented in Fig. 3 (a). It can be seen that the Log reduction of spores varies linearly with time. The slope of the lines in Fig. 3 (a) has been reported vs UV

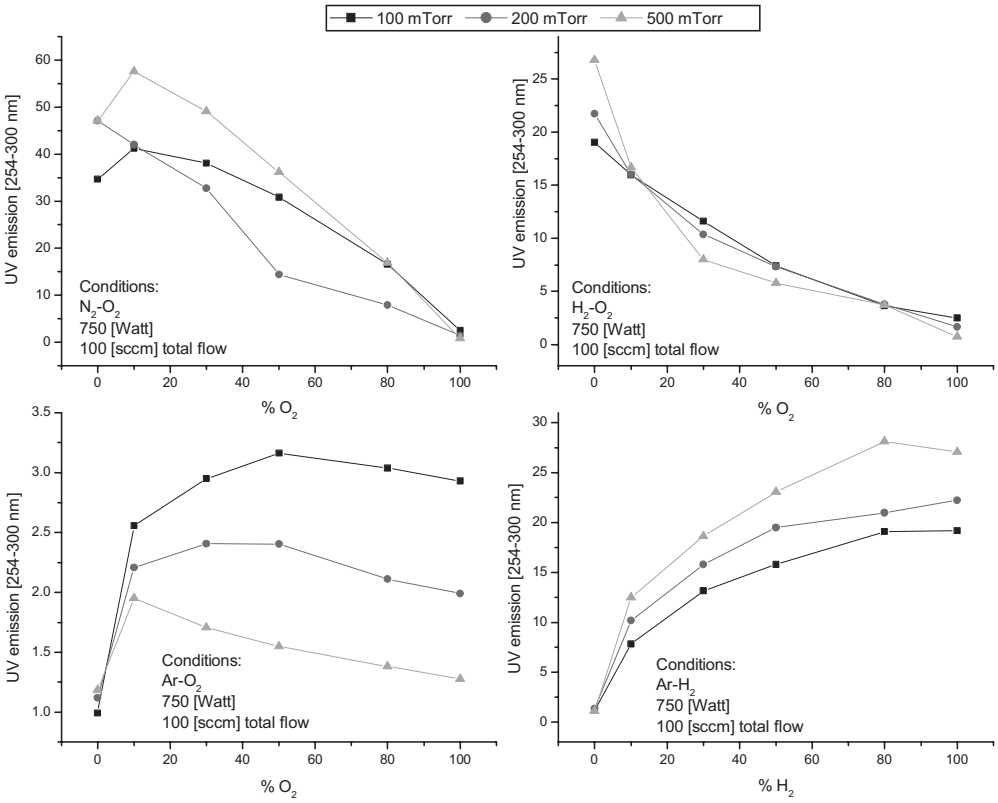

Figure 2 Integral of the UV spectra from 250 to 300 nm for different gas mixtures at 100, 200 and 500 mTorr.

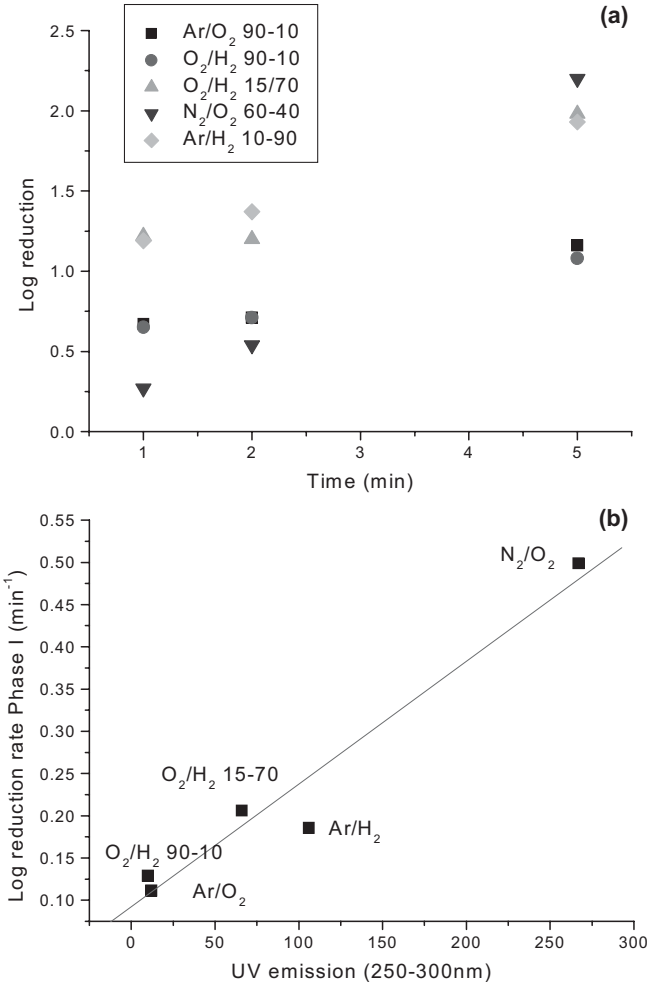

Figure 3 (a) Log reduction of *bac. subtilis* vs time for 5 different gas mixtures (500 W, 500 mTorr). (b) Slope of the lines in (a) (Log reduction rate) as a function of UV emission (250–300 nm).

emission (250–300 nm) as presented in Fig. 3 (b) (sterilisation rates). It can be seen that the sterilisation rate is proportional to the UV emission, the largest effect being obtained with N_2/O_2 mixtures.

The actinometric value of the atomic oxygen density, as measured by O (777.19 nm)/Ar(750.38 nm) intensity ratio as a function of power and pressure for N_2/O_2 mixtures has also been measured. These values are proportional to the concentration of atomic oxygen in the discharge, for the conditions indicated. Figure 4 shows the UV emission and O signal for the 3 gas mixtures tested, as a function of power. It can be seen that the UV emission is maximum around 8% while the partial pressure of atomic oxygen P_o increases linearly with the discharge power.

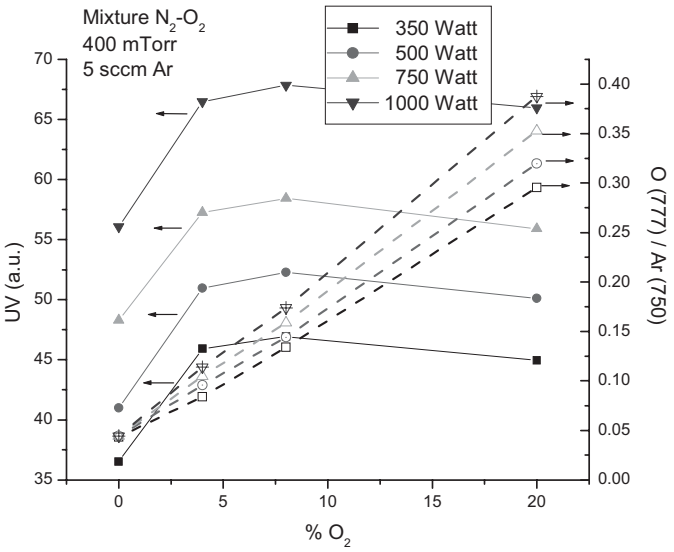

Figure 4 UV emission (250–300 nm) and O(777)/Ar(750) signals as a function of gas composition for 4 different powers (N_2/O_2 mixtures at 400 mTorr).

Table 1 reports the results of sterilisation obtained for different conditions for 5-min treatment time, i.e. corresponding to Phase I of sterilisation [4]. For the same conditions, the relative value of the O line intensity, at 777.19 nm, normalized to the Ar 750.38 nm line are reported, giving a relative value of the partial pressure of atomic oxygen in the discharge. The integral of the UV emission signal between 250–300 nm is also reported. We find that sterilization efficiency is highest for 4% O_2 in the gas mixture. The variation of sterilization efficiency vs O signal and UV emission are presented in Fig. 5. It can be seen that the sterilisation efficiency in Phase I scales with the UV emission and not with O concentration.

Table 1 Sterilisation results obtained for 5-min treatment with different gas mixtures and powers.

Gas mixture	Pressure (mTorr)	Total gas flow (sccm)	Power (W)	UV emission 250–300 nm	O(777)/Ar (750)	Log reduction
N_2–20% O_2	920	1000	350	55.36	0.391	2.18
N_2–20% O_2	920	1000	500	56.11	0.438	2.36
N_2–20% O_2	920	1000	750	61.84	0.478	2.65
N_2–4% O_2	780	1000	350	51.04	0.124	2.15
N_2–4% O_2	780	1000	500	54.18	0.134	2.28
N_2–4% O_2	780	1000	750	60.56	0.150	3.38
N_2–8% O_2	790	1000	350	53.96	0.192	2.58
N_2–8% O_2	790	1000	500	56.11	0.210	2.69
N_2–8% O_2	790	1000	750	62.69	0.231	2.81

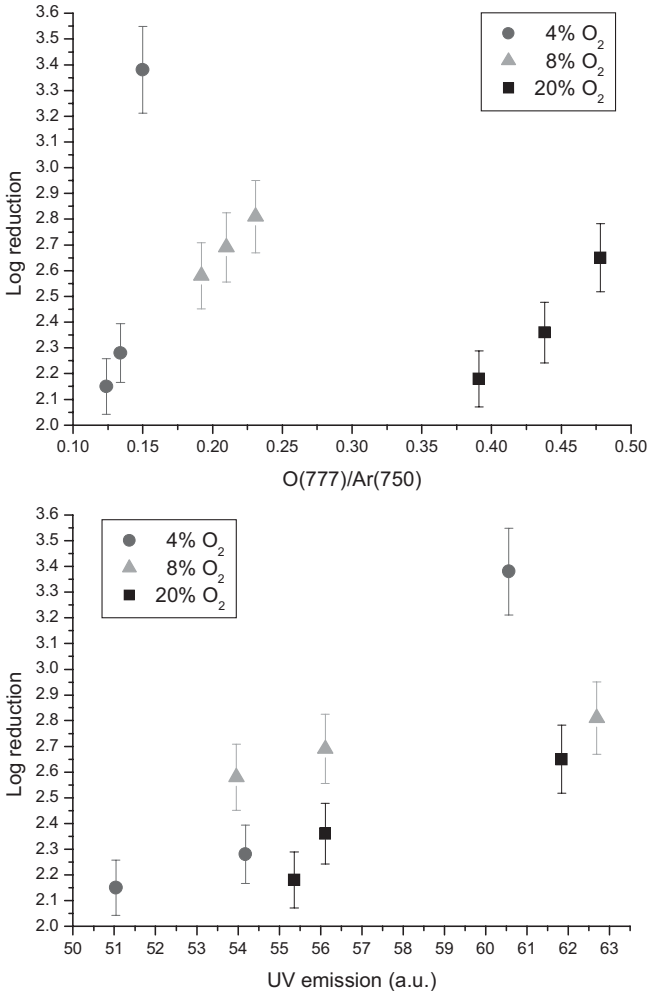

Figure 5 Sterilisation efficiency vs O signal and UV emission for 3 N_2/O_2 compositions (values from Table 1).

Figure 6 (a) shows the Log reduction in spore contamination as a function of time for different plasma treatments, at 4 and 8% of O_2 in a N_2 /O_2 mixture, at 350 mTorr and different powers. It can also be seen that, as in the post-discharge, 3 successive kinetics of spore destruction appear, more or less clearly depending on the power applied. Comparison with the results of ref. [5] show that Phase I is faster in the discharge than in the post-discharge, while the phase II kinetics are of similar magnitude, although the O concentrations are very different.

However, the above observations have to be taken with caution since the UV emission between 250 and 300 nm increases of a few percents with O_2 concentration in the gas feed, while P_o increases by 50 to 60%.

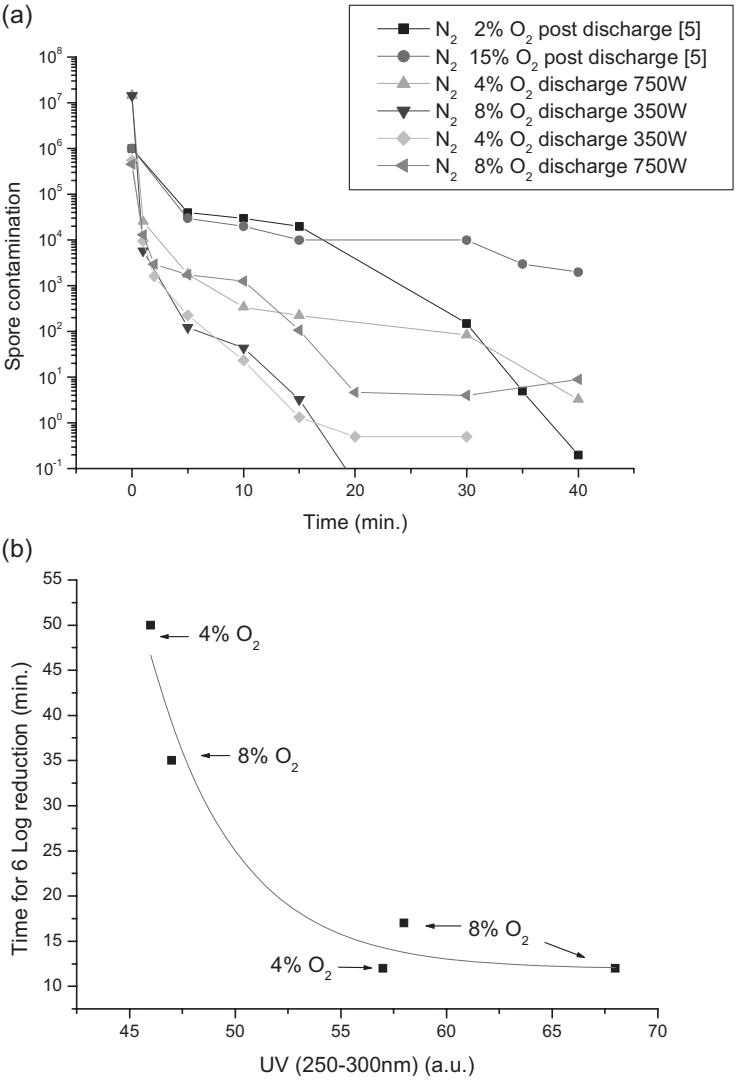

Figure 6 (a) Log reduction as a function of time for 4 and 8% of O_2 in N_2/O_2 mixture Values related to post-discharge are from ref. [5]. (b) Time needed for 6Log reduction as a function of UV emission (our results).

This illustrates that atomic oxygen plays a minor role in the overall sterilisation process. One possible explanation for the efficiency of the 4% mixture is related to the UV emission below 250 nm, as suggested in other work and which we could not measure for experimental reasons. Figure 6 (b) shows the total time needed for a 6Log reduction from the data of Fig. 6 (a). A clear decrease of the overall sterilisation duration is observed with the UV emission as already mentioned. This figure also

seems to indicate that the sterilisation time, based on the mixture N_2/O_2 reaches a saturation level.

The effect of etching of the spores by plasma has been studied by scanning electron microscopy (SEM). Figure 7 shows the spores colonies after different treatment times for a N_2/O_2 mixture. The pictures are shown with a magnification of ×50k. The morphological modification of the spores' membrane is clearly visible with a

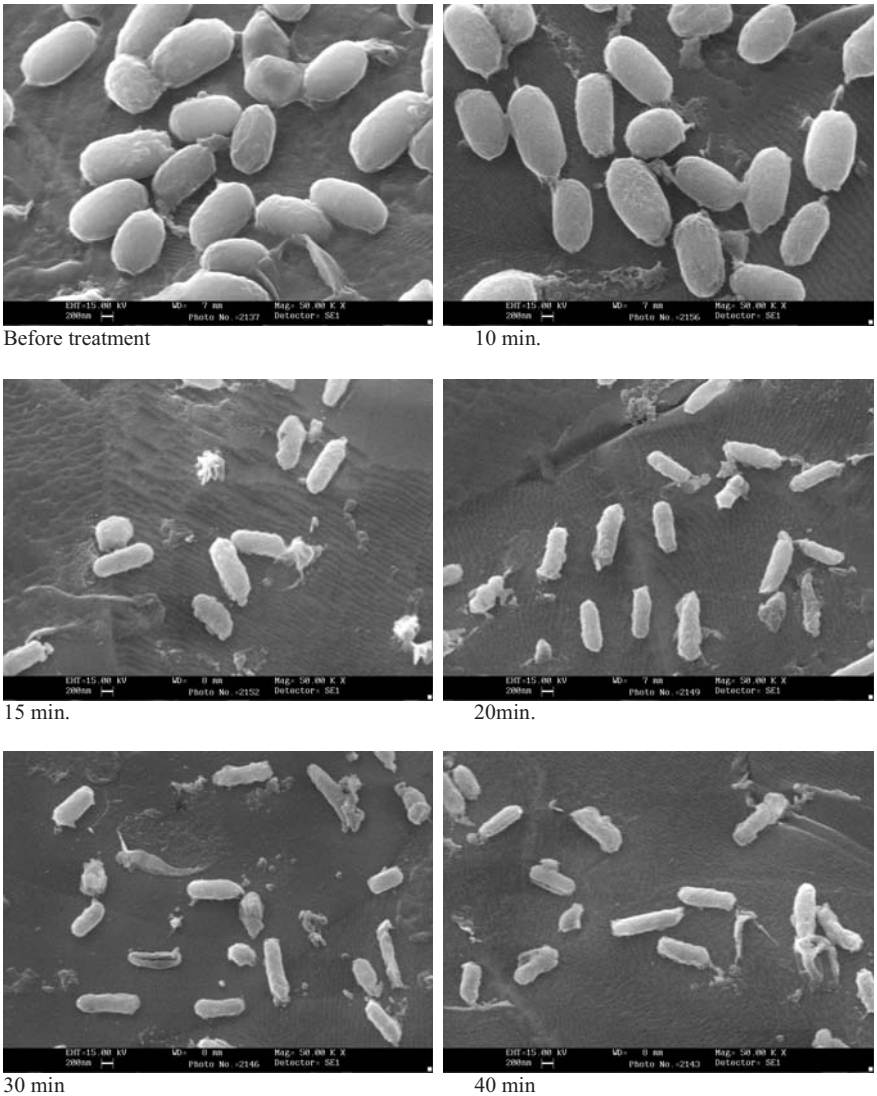

Figure 7 Scanning electron microscopy images of *Bacillus subtilis* at different treatment times. N_2/O_2 50% plasma 1000 W P = 100 mTorr. Magnification ×50k.

reduction of size and area occupied by the spore colonies. Before 10 min, the size of the spore is not changed much as compared to a nontreated sample, while a large change in aspect and dimension is observed after approximately 15 min.

Figure 8 (a) shows the variation of the spore size as a function of time with a mixture at 50% of N_2 and O_2 at 1000 W and 100 mTorr. It can be seen that the dimension of spores decreases with time and reached a plateau after 20 min. The rapid decrease of size is observed on a time scale of 10 to 15 min, and thus is related to

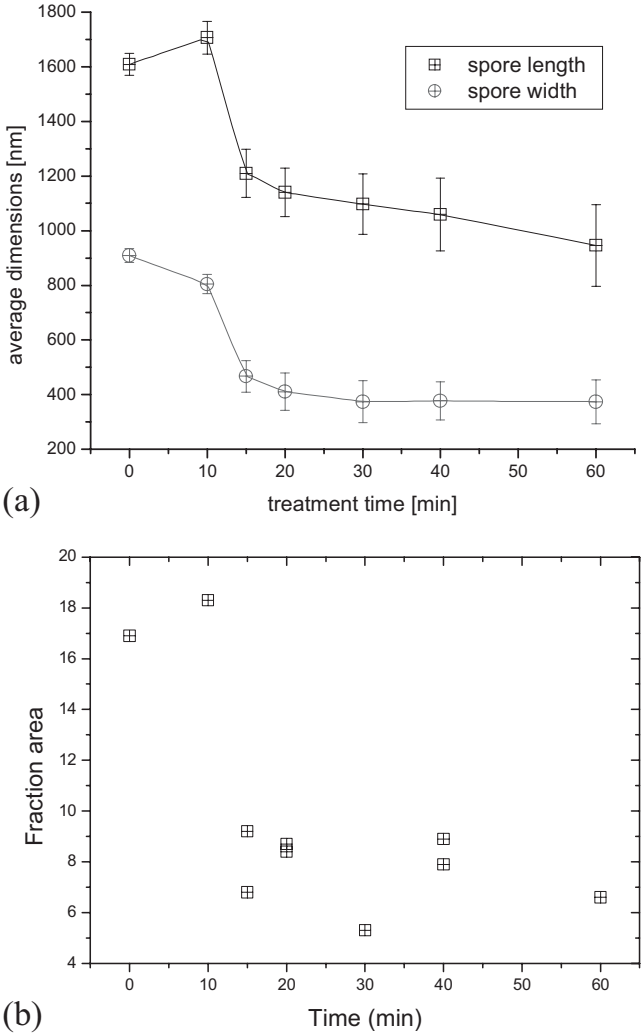

Figure 8 (a) Average spore length and width as a function of treatment duration (N_2/O_2 50% mixture, 1000 W, 100 mTorr). (b) Fractional area of SEM pictures occupied by the spore colonies as a function of time.

Phase II and III of our observations (see Fig. 6 (a)). Figure 8 (b) shows the fraction of the area of the SEM pictures (magnification × 5 k) occupied by the spore colonies after image analysis. It can be seen that here again, the decrease of the surface occupied by the spores decreases strongly after 10 min. and then remains quasiconstant, in relation to Phase II of the sterilisation process. Figure 9 represents the spore after a 30-min treatment at a larger magnification (× 100 k). It can be seen that some of the spores have been emptied and there remains only the external layers that are more resistant to etching.

Figure 9 SEM picture of spores after a 30-min treatment N_2/O_2 50% plasma 1000 W P = 100 mTorr.

24.4 Discussion

The results above illustrate the influence of the O intensity line and UV emission on the sterilisation efficiency (Log reduction) for the different gas compositions. Figure 5 confirms that there is a correlation between the UV emission and the sterilisation efficiency in Phase I, while no correlation exists with the O concentration. This confirms that Phase I is indeed related to UV destruction of genetic material of the spores. Figure 6 (a) gives more contrasted results. It can be seen that for 4 and 8% concentration, the sterilisation kinetics increases strongly with the power applied. However, the fastest sterilisation is obtained for 4%O_2, although Fig. 4 indicates that UV emission and P_o are smaller for 4% than for 8%. This is contrary to what was expected. One of the factors that has been constantly overlooked is temperature, which might increase the surface etching kinetics while Phases I and II develop. Preliminary experiments using fiber optics and a waveguide show that the temperature of the samples varies strongly with the gas mixture (the temperature of the samples increases with O_2 concentration in the discharge) and with time, which may explain the differences in the sterilisation rates as compared to the model. Further work is still needed to support this hypothesis.

The comparison of the evolution of the spore's size with time and sterilization rates shows clearly that etching and sterilization are not directly related as far as

Phases I and II are concerned since a significant sterilization occurs although the spore size remains constant. Phase III begins at time scales where spore size and coverage reduction are significant, which supports the mechanisms proposed in the literature for Phase III [10].

The above observations can be used to optimise the sterilisation process by a microwave plasma discharge: In order to reduce the total sterilisation time, Phases I and II should lead to the maximum reduction of the spore concentration. This can be achieved by maximizing UV emission, for instance with N_2/O_2 mixtures at high power. Ternary mixtures should also be looked at, in order to increase the susceptibility of spores to UV emission, or increase the UV emission itself. Phase III starts when etching of the spores has become significant: this could be increased by using other gas mixtures increasing the etching rate. However, UV emission is also important in this phase since it interacts with the genetic material of buried/masked spores that get exposed when the top layer is removed. An alternative would then be to use sequential treatment where phases of maximum etching and maximum UV emission alternate.

24.5 Conclusions

Sterilisation experiments have been performed with different gas mixtures. We have measured the UV emission between 250 and 300 nm as well as the O (777 nm) signal, representative of the O partial pressure in the discharge. Sterilisation experiments on *Bac. Subtilis* have been performed and compared to the literature. For low kinetics, we find a 3-stage sterilisation as reported elsewhere. Our results suggest that UV emission is the major parameter for all stages of sterilisation, the oxygen partial pressure being necessary but playing a minor role. SEM analysis of spores at different times of treatment clearly shows that the degradation of the spore occurs on time frames that correspond to the onset of Phases II and III. The image analysis of the spores at different times show that the size reduction/area occupied decreases with time and reaches a plateau at times corresponding to Phase II and III. This leads to the conclusion that Phase III corresponds to the destruction of buried contamination, i.e. the spores lying under layers of other spores. Conclusions are drawn on the strategy to optimise a sterilisation treatment based on ternary mixtures and sequential treatments. Future work will also deal with sterilisation-mechanism analysis under controlled temperature in order to determine its effect.

Acknowledgements

This work has been carried out within the EU Growth Project STERIPLAS (G1RD-CT-1999-00137). The authors would like to thank Roland Chery and Sophie Peyrouse from Biomatech, for technical support.

References

[1] S. Moreau, M. Moisan, M. Tabrizian, J. Barbeau, J. Pelletier, A. Ricard and L'H. Yahia, *J. Appl. Phys.* Vol 88 No2 (2000) 1166–1174

[2] S. Lerouge, M. Wertheimer, and L.'H. Yahia, *Plasma Polym.* Vol. 6 No.3 (2001) 175–188

[3] S. Hury, D.R. Vidal, F. Desor, J. Pelletier and T. Lagarde, *Lett. Appl. Microbiol.* 26 (1998) 417–421

[4] S. Lerouge, A.C. Fozza, M.R. Wertheimer, R. Marchand and L'H. Yahia, *Plasma Polym.* 5 No.1 (2000) 31–46

[5] M. Moisan, J. Barbeau, S. Moreau, J. Peletier, M. Tabrizian and L'H. Yahia, *Int. J. Pharmaceut.* 226 (2001) 1–21

[6] N. Philip, B. Saoudi, MA Crevier, M. Moisan, J. Barbeau and J. Pelletier, *IEE Trans. Plasma Sci.* 30, No. 4, (2002) 1429–1435

[7] J. W. Coburn, M. J. Chen, *J. Appl. Phys.* 51 (1980) 3134–3136

[8] R. d'Agostino, F. Cramarossa, S. De Benedictis, G. Ferraro, *J. Appl. Phys.* 52 (1981) 1259–1265

[9] N. Munakata, M. Saito and K. Hieda, *Photochem. Photobiol.* 54 (5) (1991) 761

[10] S. Lerouge, M.R. Wertheimer, R. Marchand, M. Tabrizian and H. L'Haya. *J. Biomed. Mater. Res.* 51 (1) (2000) 128–135

25
Improvement of Low-pressure Microwave Plasma-assisted Amino Functionalization of Polymers

K. Schröder, B. Finke, A. Ohl

Abstract

For the functionalization of polymer surfaces with amino groups, ammonia plasmas are preferred from the technical point of easy processing. Microwave plasma processes run in normal low-vacuum plasma reactors enable surface densities of about 1.5%–NH_2/C on polystyrene (PS). Normal processes performed in a UHV environment create about one per cent more amino groups. A number of investigations were surveyed on both fundamental and application aspects of amino functionalization under very clean process environments and strict processing regimes. These studies rendered possible higher densities of 5% and 2.5%–NH_2/C on PS in the UHV and low-vacuum environment, respectively. XPS investigations on the role of carbon-centered surface radicals utilising NO quenching reactions indicate that further improvements might be possible.

25.1
Introduction

The modification of polymer surfaces with amino groups by plasma processing is still a challenging task. During recent decades, much empirical knowledge on this topic has been accumulated, including functionalization with nondepositing gases like nitrogen and ammonia, plasma-induced grafting of amines, and plasma polymerization of nitrogen-containing molecules. Most of these activities were undertaken regarding the special advantages of a selective reactivity of the nucleophilic amino group, which opens many unique possibilities for tailor-made polymer surfaces in combination with the general advantages of plasma processing. However, none of these methods work sufficiently well up to now.

From the technical point of easy processing, a short-term gas-discharge plasma functionalization utilizing nonpolymerising gases only is preferred. But a rather poor quality of the amino functionalization is obtained. The density of amino groups is low and secondary reactions and post-plasma processes occur, which lead to different additional oxygen functional groups. A density up to about 2%–NH_2/C is typical for plasma functionalization in gas phases like ammonia. In a rough approach, it is

independent of the processing conditions. For example, similar values were obtained on polyethylene using RF plasmas [1] and on polystyrene using microwave plasmas [2].

The alternative method is the deposition of plasma polymers. This results in high densities of amines on surfaces. Values up to 18%–NH_2/C are reported [3]. From a technical point of view, however, these deposition processes are expensive and effects like reactor contamination and nonuniform coatings necessitate considerable additional processing efforts.

In addition, these results give evidence that the density of amino groups on surfaces can be much higher than a few per cent as reported for plasma functionalization. Furthermore, most papers dealing with amino functionalization have a strong application-oriented background, i.e. processing is performed without too much attention to specific plasma-processing regimes. Therefore it is not clear yet whether this limitation of plasma functionalization results is fundamental or not.

Without doubt, a technically simple processing method would be useful to achieve higher densities of amines at polymer surfaces. Table 1 summarizes a number of applications where polymer surfaces were equipped with amino groups by plasma-assisted techniques [4–19] including metallization [8, 10], lamination [6, 7], pervaporation [11], cell and protein adhesion [13–19] and immobilization of enzymes [20]. Several of these applications would benefit from an increase of the amino group density. Certainly, this will be the case if strong interfacial adhesion is necessary, e.g. for adhesion improvement between advanced organic fibers and epoxy resins [4]. Even applications in the field of biomedical technology could be improved. This field is one of the most prospective and innovative fields of plasma-assisted amino functionalization. For example, the signal intensity of diagnostic assays using immobilized molecules will depend on the surface density of bonding sites. It is often argued that a common low-density, low-quality surface functionalization is sufficient for immobilization of very large sized biological molecules, especially for cell-culture applications. However, this is a rather simplified argumentation. It neglects the complexity of the cell–matrix interaction, which is characterized by a large number of components, including molecules of extremely different size. A basic prerequisite for the study and for control of this interaction are defined, controllable surfaces conditions.

In this paper we review some of our investigations of plasma-assisted amino functionalization using low-pressure microwave plasmas with special emphasis on the above-mentioned question of fundamental limitations. Both basic investigations and application-oriented experiments are reported. Basic investigations concentrate on the influence of process parameters and the role of surface radical generation during amino functionalization. An in situ derivatization technique was applied to study different carbon-centered radicals on polystyrene surfaces. These experiments were performed under very well defined, clean plasma conditions. Less clean, but nevertheless very well-defined plasma conditions were used for the application-oriented experiments. High-quality cell-culture surfaces were obtained in this case.

All investigations suggested that elaborate plasma functionalization processes could result in higher than usual amino densities.

Table 1 Exemplified applications of ammonia plasma treated polymer surfaces.

Field of activity	Substrate	Reaction/interaction with	Intention	Literature (example)
adhesion	aramid, PE	epoxy resin	glueing	Brown 1993 [4]
adhesion	carbon fibres	polymer matrix	fibre-matrix composites	Loh 1987 [5]
adhesion	PTFE	phenol-type adhesive	polymer laminate to nitrile rubber	Inagaki 1989 [6]
adhesion	PP	PA 6	polymer laminate to PA 6	Gancarz 2001 [7]
metallization	PP	Al	well-adherent metal layer	Arefi 2000 [8]
metallization	PS	Pd	supported transition metal complex as catalyst	L'Argentiere 2000 [9]
metallization	PTFE	Al	well-adherent metal layer	Baumgärtner 2001 [10]
membranes	cellulose triacetate	solvents	separation of a iso-propanol/water mixture	Bhat 2000 [11]
membranes	PVDF	amino acid	microfiltration	Müller 1999 [12]
cell adhesion	PS, PE	cell-culture medium	artificial cornea, corneal epithelial cells	Sipehia 1990 [13]
cell adhesion	PS	cell-culture medium	human FL cells (derived from omnion)	Nakayama 1988 [14]
cell adhesion	PTFE	cell-culture medium	endothelial cells	Simon 1996 [15]
cell adhesion	poly(D,L-lactide)	cell-culture medium	fibroblasts, tissue engineering	Yang 2002 [16]
protein adhesion	PP (Celgard 2400)	albumin	improved biocompatibility by protein coating	Sipehia 1982 [17]
covalent protein immobilization	PET	cystein	optimized plasma condition for grafting of high amount of nitrogen-containing groups	Giradeaux 96 [18]
covalent protein immobilization	PS	poly-L-lysine	reduce conformational changes of poly-L-lysine	Moy 1994 [19]
covalent enzyme immobilization	PP	glutardialdehyde	immobilization of glucose oxidase and peroxidase	Sipehia 1988 [20]

PE = polyethylene, PTFE = polytetrafluorethylene, PP =. polypropylene,
PVDF = poly (vinylidene fluoride) PET = poly (ethylene terephthalate),
PA = polyamide.

25.2 Experimental

25.2.1 Plasma Processing

Surface functionalization processes are extremely sensitive to process contaminations. For this reason, here extraordinary diligence was taken to clean process environments and to employ strict processing regimes.

The basic experiments on the role of surface radicals were performed in a UHV cluster tool, which combines clean plasma reactors with quasi in situ XPS analysis and gas-phase derivatization [21]. After switching off the plasma, the polystyrene samples (PS, Falcon™ tissue culture dishes, Becton-Dickinson, NJ, USA, used without any chemical cleaning) were transported via the UHV-transfer system to the XPS and the derivatization chamber, respectively. The separately pumped UHV-transfer system ($p = 10^{-8}$ mbar) ensures contamination-free sample exchange between the three subsystems. In order to avoid wall contamination, the UHV-plasma reactor (base pressure: 5×10^{-7} mbar) was kept free of oxygen-containing gases at all times. Oxygen impurities are known to reduce the amino functionalization efficiency [22, 23]. Additional cleaning procedures were as follows: First, an Ar/H_2-plasma was run for 30 min as the initial cleaning of the reaction vessel prior to the experiments each morning. Secondly, only ammonia, hydrogen and inert-gas plasma processes were carried out in the UHV reactor.

The MW plasmas were generated in a surface-wave-sustained (SWS) mode forming a disc-like plasma glow of 22 cm in diameter and 2 cm in width in close contact to the MW-coupling window at the standard pressure of 0.1 mbar. The polymer samples were treated in the afterglow 9 cm below the active plasma zone.

Experiments were carried out in continuous-wave (cw) plasma mode with short treatment times. The gas flow rate of NH_3 was 15 sccm. A more detailed study of the excitation mode is given in [24].

Application-oriented experiments were performed in a customer-specific version of an o-ring sealed V55G low-pressure plasma processor (Plasma-Finish Corp., Schwedt, Germany). The base pressure was not better than 0.1 mbar and oxygen could not be avoided as much as in the UHV reactor. Again, a strict processing scheme was kept to suppress gas impurities and wall contaminations as much as possible [2]. The reactor was operated with plasmas containing ammonia and/or argon gases, nearly exclusively. Prior to the experiments, the reactor was first evacuated to check for leaks. Then, an ammonia plasma was run in the empty reactor for ten minutes. Plasma functionalization experiments were performed using automatic process-control sequences. First, the reactor was evacuated to the base pressure. Then, it was flushed by the reaction gas to carry off residual contaminations. After ammonia plasma treatment, the reactor was pumped out to dissipate waste gas and was purged with dry nitrogen twice for 15 s. The front door was opened under nitrogen overpressure to prevent unwanted air inflow.

Additionally, care was taken not to treat too many different materials at once. PS and polyetheretherketone (PEEK, Reichelt Chemietechnik, Heidelberg, Germany) were modified mainly. On demand, contact angles were measured on a standard PS sample after a standard ammonia plasma treatment to assure a reproducible functionalization.

25.2.2 Surface Diagnostics

XPS measurements were performed using an Axis Ultra (Kratos, Manchester, GB) in a standard configuration including a conventional hemispherical analyzer, a monochromatic AlK_α source (1486.6 eV), and charge neutralization. The X-ray source was operated at 150 W. The pass energy was 80 eV for the measurements of the element content and 10 eV for highly resolved peaks presented in the Figs. 4–7. Charge compensation was applied to adjust the main C–C, C–H component to 285.0 eV. The N 1s signal was fitted with peaks of functional groups according to Wilken et al. [25, 26]. The procedure was carried out using CasaXPS software (Casa Software, Wilmslow, UK). The fitting parameters were a Gauss-Lorentz (30% Lorentz) distribution, Tougaard-baseline, and a restricted FWHM between 1.1 and 1.5 eV. In Figs. 4–7, R denotes hydrocarbon residuals. The peaks in the range of 398.5–399.8 eV ($-\underline{N}H_xR_y$) cover amines ($x = 2–0$, $y = 1–3$), nitriles ($-C\equiv\underline{N}$), and possibly hydrazines ($H_xR_y\underline{N}-\underline{N}H_xR_y$). These functionalities can not be distinguished by XPS. They were fitted with two formal peaks denoted $-C-\underline{N}H_2$ and $-\underline{N}H_xR_y$.

A UHV transport equipment was used to transfer plasma-treated PS samples from the UHV reactor system to the XPS without air contact.

25.2.2.1 Determination of Amino-Group Density

Quantification of the amino groups was performed via fluorine surface density determined ex situ after reaction with trifluoromethylbenzaldehyde (TFBA) at 40 °C for 2 h [1, 2]. The standard XPS system used for quantifying the fluorine content consists of an unmonochromated MgK_α X-ray source operated at 200 W and a multichannel electron analyzer EA125 U5 (Omicrometer, Taunusstein, Germany). No charge neutralization was applied. The elements F, O, N, and C were analyzed five times at a pass energy of 50 eV for 1 min to reduce uncertainties and minimize sample damage.

25.2.2.2 Surface Radical Analysis

The reaction of carbon-centered radicals with NO [25] was used to determine surface radicals by means of XPS (see Fig. 1). For this purpose, plasma experiments with and without subsequent NO derivatization were carried out in parallel. The derivatization reaction was performed quasi in situ in a stainless steel derivatization chamber at 400 mbar and ambient temperature for 1 h starting not later than five minutes after plasma treatment.

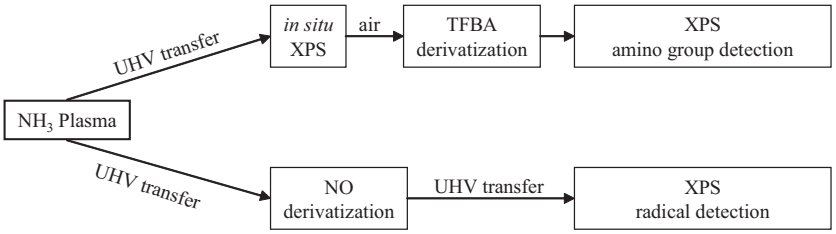

Figure 1 Scheme for detection of amino group density and radical analysis after ammonia-plasma treatment of PS in the UHV reactor system.

25.3 Results and Discussion

25.3.1 Amino Functionalization in the UHV Plasma System

A comparison of the latest results on kinetics of polystyrene functionalization with results of earlier investigations [24] demonstrates that real improvements could be achieved by using more sophisticated processing regimes. Figure 2 compares the results of both experimental series.

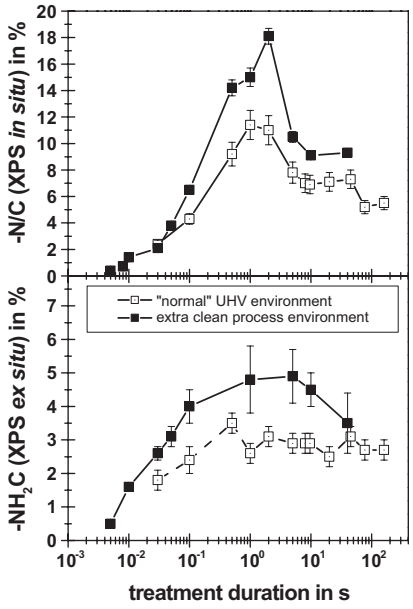

Figure 2 Dependence of PS nitrogen and amino group surface density on the duration of a cw MW NH_3 plasma treatment in extra clean and "normal" UHV process environment [24].

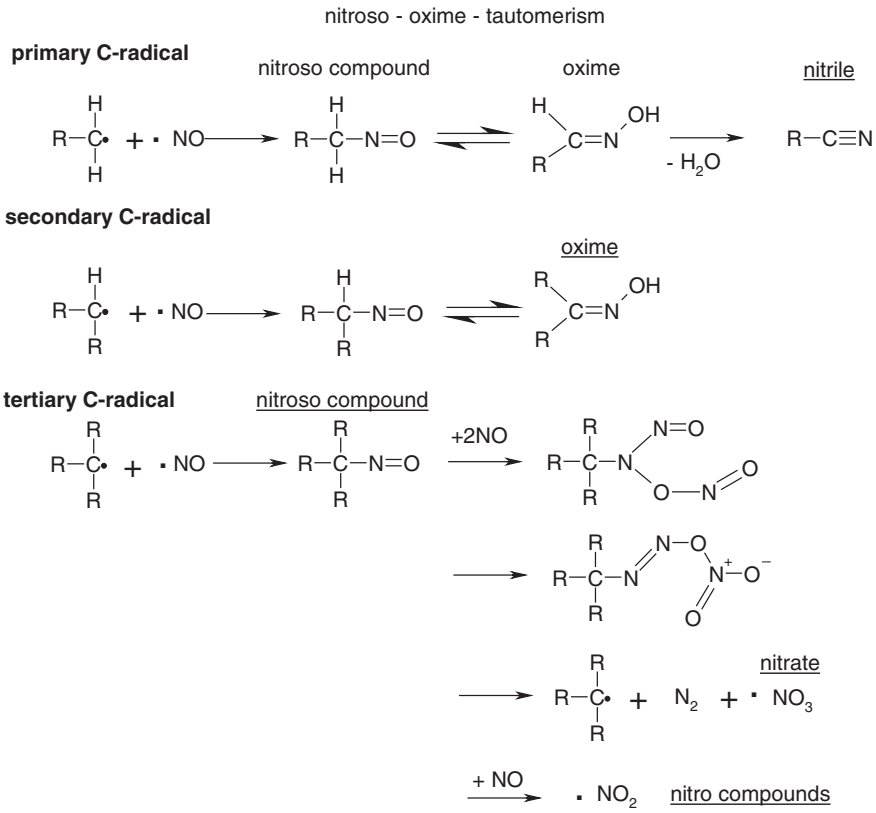

Figure 3 Reaction paths of primary, secondary, and tertiary C-based radicals with the scavenger NO according to [25, 26].

The nitrogen surface density could be increased from about 12% N/C to 18% N/C by ensuring improved processing conditions (Fig. 2). As expected, both curves exhibit a very similar behavior: After an initial increase during the first 2 s, N/C decreases again and then exhibits a tendency to saturate. The decrease at longer processing times can be interpreted as a result of the limited supply of fresh NH_3. The high NH_3 decomposition rate of 5×10^{21} m^{-3} s^{-1} in the MW plasma leads to a considerable production of atomic hydrogen [27]. Atomic hydrogen produced in H_2 plasmas is known to be more efficient in etching nonamino nitrogen functional groups [1, 24] than amino groups. Consequently, the nitrogen surface density decreases with treatment duration after a maximum for short-time processes.

A similar trend was obtained for the amino group densities (Fig. 2). The maximum density ratio $–NH_2/C$ could be enhanced from 2.9% to a value of about 5%. These values are considerably smaller than the total nitrogen density of around 18% N/C. This means that only every fourth nitrogen atom belongs to an amino group.

In contrast, very short NH_3 plasma treatments (about 30 ms) yield 100%–NH_2/N, this means a monofunctionality is possible. The amino group density reaches 2.5%–NH_2/C in this case, at maximum.

Obviously, monofunctionality and maximum amino group density occur on different time scales. Initially, amino groups seem to be grafted faster than nonamino nitrogen groups, suggesting a special role of prompt dissociation products of NH_3 like NH_2 or NH radicals, for amino group creation. Also, an adequate balance of gas-phase radicals and free-radical sites at polymer surfaces may be supposed. On the contrary, nonamino groups are created at longer processing times. In addition, a surplus of surface radicals can be assumed since a general observation is the accompaniment of the amino functionalization by post-plasma oxidation processes [28]. This post-oxidation is ascribed to the stepwise oxidation of surface radicals on contact with air. It can be suppressed by a quenching with radical scavengers [28, 29].

To be precise, a detailed analysis of the formation of different nitrogen-containing surface functional groups and their derivation from primary, secondary and tertiary carbon-centered surface radicals is necessary to understand the limitations of amino group creation. For this purpose, quenching reactions with NO were performed immediately after closing the plasma process. NO should mainly react with carbon-centered radicals. The products of these reactions (for instance nitriles, oximes, nitroso and nitro compounds, nitrites and nitrates, see Fig. 3) appear at significantly different chemical shifts in the XPS N1s region. They can be determined by peak fitting, following a procedure according to the literature [25, 26]. A discussion of these XPS results with respect to the complex reaction scheme of Fig. 3 may result in more detailed information about surface radical formation reactions. Thus, an attempt was made to quantify carbon-centered radicals on PS surfaces after ammonia plasma treatments.

Figures 4 and 5 show the peak fit of the N1s signal of PS treated with cw NH_3 plasma for 40 s without and with subsequent NO-derivatisation.

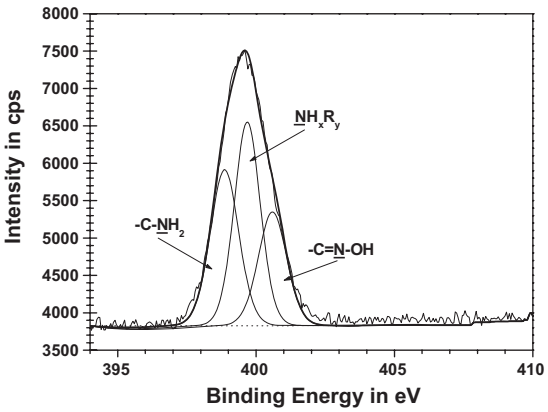

Figure 4 XPS spectrum of an NH_3-plasma-treated PS, using long treatment time (40 s cw MW, comp. Fig. 2).

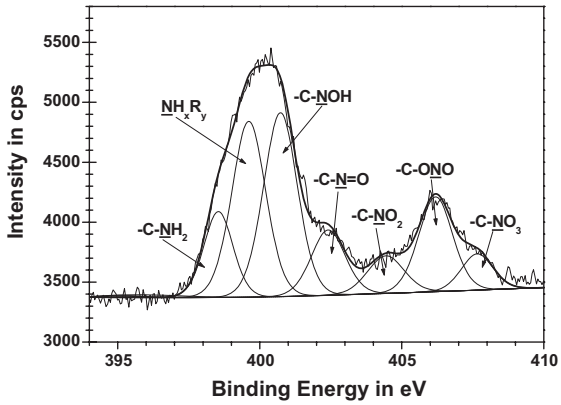

Figure 5 XPS spectrum of a long-time NH_3-plasma-treated PS after NO-derivatisation. The plasma process was identical to that applied in Fig. 4 (40 s cw MW).

A broad N1s signal is visible already without in situ NO-derivatization (Fig. 4). This suggests nitrogen in different binding states. The high intensity around 399.5 eV indicates a successful amino functionalization and mainly oxygen-free groups like amines and nitriles. With respect to an amino functionalization, a density of nitrogen N/C of about 8% was obtained with an amino group density $–NH_2$/C of up to 3.2% and a selectivity $–NH_2$/N of 40% under these plasma-treatment conditions.

According to the reaction paths of carbon-based radicals, the reaction products after NO derivatization can be assigned to different radicals:

nitriles –C–CN (399.1–399.5 eV):	primary radicals
oximes –C=N–OH (400–402 eV):	secondary radicals
nitroso –C–N=O, nitro –C–NO_2, nitrite –C–ONO and nitrate –C–NO_3 compounds (403–408 eV):	tertiary radicals

A second characteristic N1s signal appears at circa 403–408 eV in the XPS spectrum, which can be assigned to nitroso, nitro, nitrite and nitrate compounds, Fig. 5.

Likewise, a considerable surplus of C-radicals after ammonia plasma treatment is indisputable. The radical density was evaluated from the difference of the fitted peak areas ΔN/C. Approximately 3% tertiary radicals/C were roughly estimated.

Unfortunately, an additional reaction of the scavenger NO with amino groups seems to reduce their density. A considerable decrease of the peak areas of the functional amino and nitrile groups (–C–NH_2 and $–NH_xR_y$), a small increase of oximes (400–402 eV), and the appearance of the reaction products of tertiary C-radicals with NO (403–408 eV) can be observed. Thus, it is difficult to quantify surface radicals by this approach.

Nevertheless, the method allows us to check for the formation of tertiary radicals during plasma treatment. This check was applied to functionalization with shorter

processing times. In this case, a more adequate balance of gas-phase radicals and free-radical sites might occur at polymer surfaces.

The XPS-spectra for a processing time of 25 ms are given in Figs. 6 and 7. This duration is below the limit, until monofunctionalization occurs. The XPS spectrum in Fig. 7 demonstrates, that a surplus of tertiary C-radicals (XPS-region: 403–408 eV) must be assumed also for these short times. One might speculate that this is an indication for possible further improvements of amino-functionalization, since the creation of amino groups should proceed via primary or secondary C-radicals as a consequence of initial backbone chain scission and hydrogen abstraction. Tertiary C-centered radicals are likely the result of crosslinking, i.e. subsequent reactions of primary or secondary C-radicals.

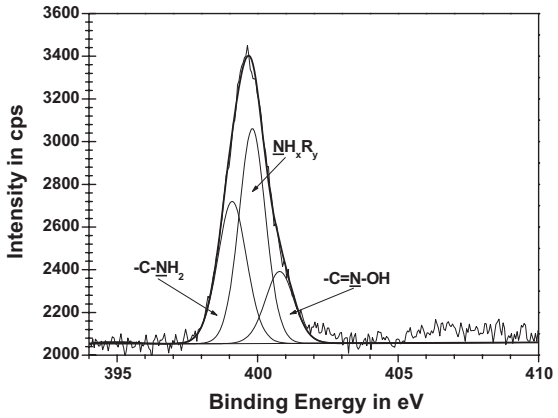

Figure 6 XPS spectrum of 25-ms NH_3-plasma-treated PS. This represents a short treatment duration characterized by a selectivity $-NH_2/N$ of 100%.

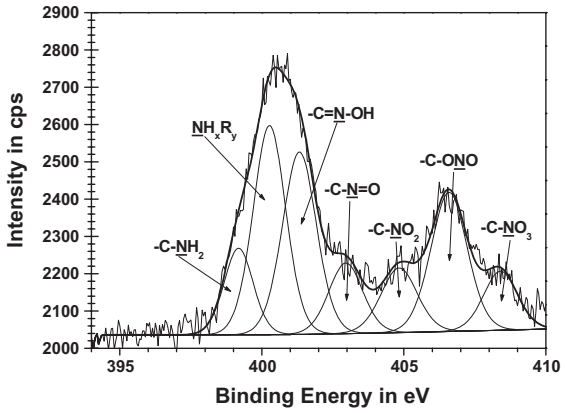

Figure 7 XPS spectrum of 25-ms NH_3-plasma-treated PS after NO-derivatisation.

25.3.2
Amino Functionalization in the Low-Vacuum Plasma Reactor

In general, the options for an improved amino functionalization are reduced in low-vacuum plasma reactors due to the existence of considerable amounts of residual oxygen in the gas phase [2, 22, 23]. Nevertheless, interesting observations could be made using the above-described o-ring sealed plasma processor.

Work over the past few years has enabled the accumulation of a notable number of amino group densities values determined by XPS after derivatization out of some thousands of PS disposables treated in a "normal" ammonia plasma. For analysis, they were simply classified. Measured XPS values were rounded on one position after the decimal point and then assorted in categories of 0.5% with the borders 0.25, 0.75, 1.25 and so on. The results are given in Figs. 8 and 9 for PS and PEEK samples, respectively.

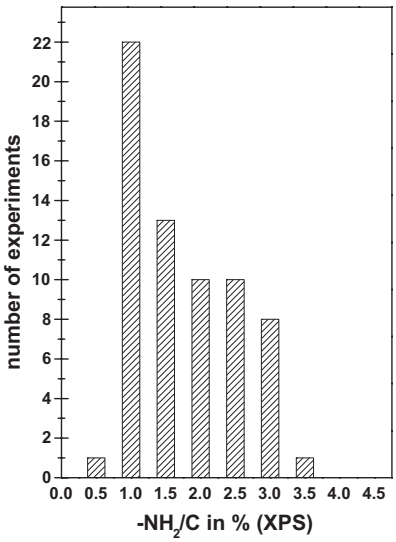

Figure 8 Histogram of the distribution of the amino group density on 65 randomly chosen tests samples out of 900 remote plasma treatments of different disposables made from PS performed in a low-vacuum reactor.

Usually, for a sufficiently large number of repetitions of a single experiment under unchanged conditions one would expect a symmetric distribution of data points around a mean value for this type of classification. Obviously, this is not the case in Fig. 8. We explain this by the inhomogeneity of the data set. As expected, the majority of the results group around a value of 1–1.5%–NH_2/C, which is typical for not very clean low-vacuum condition. But some measurements added up to values of 2.5 and 3%–NH_2/C. This could be related to improved process conditions in compliance with the strict processing regime for some of the investigations for PS.

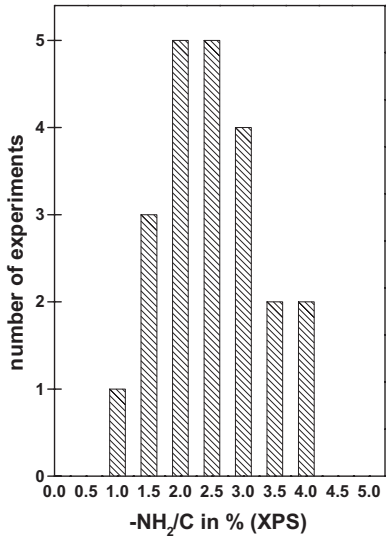

Figure 9 Histogram of the distribution of the amino group density on 22 XPS measurements out of 300 experiments on PEEK foils in the HV reactor under optimal conditions.

A weak argument for this explanation is given by the results presented for PEEK in Fig. 9. There, average amino group densities of more than 2%–NH_2/C were obtained.

A more detailed discussion is possible considering the fact that optimum plasma functionalization is possible for short treatment duration not exceeding a few seconds, only.

This is a very general rule verified already by the data given in Fig. 2 for a UHV-processing environment. It calls for even shorter ammonia plasma treatment durations, if high-quality, nearly mono amino-functional surfaces are to be obtained. The respective results for the low-vacuum plasma processor are given in Figs. 10 and 11. A very interesting detail of all the figures is the steep initial increase of the curves followed by a relatively small peak. In this region, the most interesting results are obtained but they are difficult to stabilize. So it seems reasonable to assume that polymer surfaces can be equipped with densities of 5–8% N/C and with higher levels of $–NH_2$ concentrations than usual also for low-vacuum conditions. Optimized amino-group densities reach more than 3%–NH_2/C, i.e. 50% of the implemented nitrogen (50%–NH_2/N).

Such relatively slight improvements can already be interesting for many applications. For example, it is well known that the behavior of living cells in culture depends on the chemical as well as on the physical surface characteristics including wettability, charge, roughness, and rigidity. More precisely, the control of physico-chemical surface characteristics is important for adhesion of cell signalling molecules from tissue-culture medium. Cell-culture results are influenced in this manner.

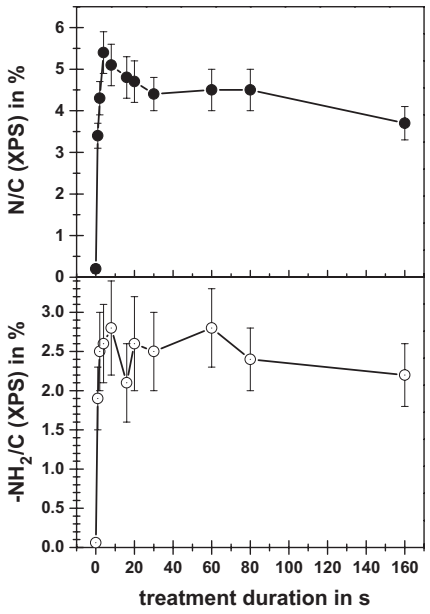

Figure 10 Nitrogen and amino group density in dependence of treatment duration in cw ammonia plasma for PS.

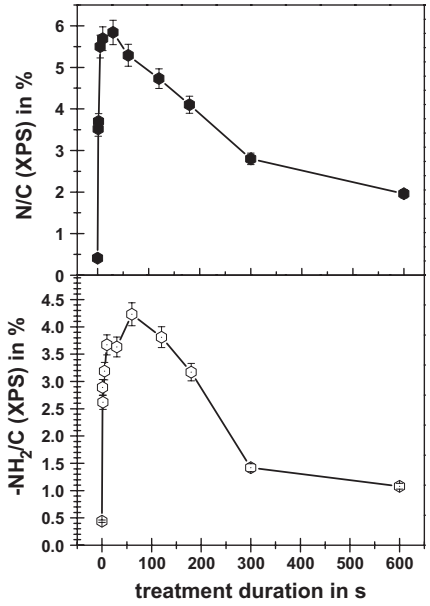

Figure 11 Nitrogen and amino group density in dependence of treatment duration in cw ammonia plasma for PEEK.

To investigate this, selected signal molecules can be covalently bound to the polymers surface by wet grafting procedures ("surface biologization"). It is still unclear as to what densities of surface functional chemical groups are necessary for best functionality of immobilized signal molecules. In this context, different strategies of surface biologization of PEEK were investigated, which were all based on one and the same well-defined plasma functionalization. A 5-s ammonia plasma treatment was used to realize a very high amino group density ($-NH_2/C$) of about 3.5%. Apart from culturing directly on plasma-treated surfaces, Collagen I (COLL I) coated surfaces were investigated. For immobilization of COLL I, the plasma-functionalized samples were transferred from the reactor to an attached biological work space under clean room conditions. Then, liquid-phase chemical reactions were performed, e.g. with a polyethylene glycol (PEG) spacer containing diacid ($HOOC–PEG_{10}–COOH$ in PBS) by the so-called carbodiimide (EDC) method [30]. Finally, COLL I was immobilized.

Compared to untreated PEEK, culturing on purely plasma-treated PEEK resulted in a much better cell adherence. Interestingly, cell adherence on ammonia-plasma-treated surfaces was comparable to results obtained on surfaces with immobilized COLL I via PEG spacer (Fig. 12). Additional parameters for cell behavior were investigated, especially morphology, spreading, and proliferation [31]. Spread and polygonal cells with a distinct cytoskeleton were obtained on the plasma-treated and COLL I immobilized PEEK surfaces in contrast to the untreated sample. The results demonstrate real improvements of cell-culture quality on the amino-functionalized as well as on COLL I-coated PEEK substrates [32].

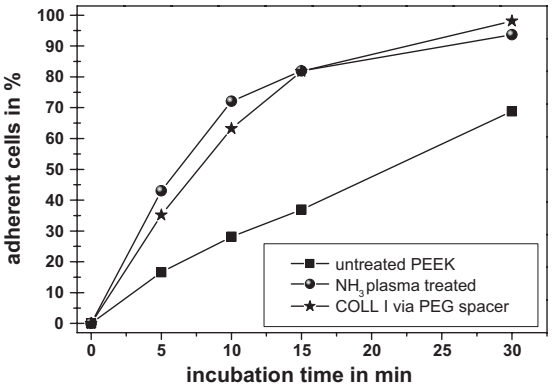

Figure 12 Time-dependent adhesion of MG-63 osteoblastic cells on differently treated PEEK surfaces.

These results are concordant with results of more than 200 cell-culture experiments on the ammonia plasma-modified PS surfaces. Treatments were performed in the UHV as well as a low-vacuum reactor. Cell cultures exhibited cell densities exceeding that on commercial TCPS including high-quality versions like Primaria™ [32–34].

25.4 Summary

For the functionalisation of polymer surfaces with amino groups a multitude of different ammonia-plasma treatments were performed. These treatments attracted attention due to the technical point of easy processing. Normal microwave-plasma processes enable surface densities of about 1.5%–NH_2/C on PS, processes run in an UHV environment create about one per cent more. Very clean process environments and strict processing regimes render possible higher densities of amino groups in the UHV and low-vacuum environment, respectively. This is the result of a survey of a number of investigations on both fundamental and application aspects of amino functionalization, which were run using very clean process environments and strict processing regimes.

An in situ derivatization technique using NO quenching reactions of radicals was applied to study the role of radicals on PS by XPS measurements.

With respect to an amino functionalization, a N/C ratio of maximum 18% was obtained with an amino group density –NH_2/C up to 5% after some seconds of treatment. Using much shorter treatment durations of some ten milliseconds, a selectivity of 100%–NH_2/N was achieved at the expense of amino group density. Nevertheless, this density could be as high as 2.5%–NH_2/C. For both conditions, a surplus of mainly tertiary C-radicals can be assumed after ammonia plasma treatment, although it is difficult to exactly determine the quantity of radicals.

Also, a notable number of amino group densities were determined during numerous application-oriented investigations using low-vacuum conditions. The analysis of these random data points demonstrated improvements possible by strict processing regimes from initially 1–1.5% to values of more than 2.5%–NH_2/C. Already such moderate improvement could be valuable for certain applications. This was demonstrated for the example of cell culturing.

Acknowledgements

The authors thank our technicians Urte Kellner, Uwe Lindemann, and Gerd Friedrichs for excellent assistance. Cell cultures on PEEK are a result of a very fruitful cooperation with Roland Ihrke (INP), Anette Diener, Barbara Nebe, and Joachim Rychly from the University of Rostock, Department of Internal Medicine. Financial support by the Federal Ministry for Education and Research (BMBF, FKZ: 13N8054) and the "Stifterverband für die deutsche Wissenschaft", Grant No. H 150 5503 5010 00386 is gratefully acknowledged.

References

[1] P. Favia, M. V. Stendardo, R. d'Agostino, "Selective grafting of amine groups on polyethylene by means of NH_3-H_2 RF glow discharges", Plasmas Polym. **1** (1996) 2, 91–112.

[2] K. Schröder, A. Meyer-Plath, D. Keller, W. Besch, G. Babucke, A. Ohl, "Plasma-induced surface functionalization of polymeric biomaterials in ammonia plasmas", Contrib. Plasma Phys. **41** (2001) 6, 562–572.

[3] J. Friedrich, G. Kühn, R. Mix, "Polymer surface modification with monofunctional groups of different type and density", International Symposium on Plasma Chemistry, (ISPC-16), Taormina (Italy), 22–27.06.2003, CD and book of abstracts, p.439.

[4] J. R. Brown, P. J. Chappell, G. A. George, "Plasma surface modification of advanced organic fibers, evidence of chemical bonding between epoxy resins and fiber surface amine groups", J. Mater. Sci. Lett. **12** (1993), 754–757.

[5] I. H. Loh, R. E. Cohen, R. F. Baddour, "Modification of carbon surfaces in cold plasmas", J. Mater. Sci. **22** (1987), 2937–2947.

[6] N. Inagaki, S. Tasaka, H. Kawai, "Improved adhesion of poly(tetrafluorethylene) by NH_3 plasma treatment", J. Adhes. Sci. Technol. **3** (1989) 8, 637–649.

[7] I. Gancarz, J. Piglowski, "Studies on adhesion of polyamide 6 to microwave-plasma-modified polypropylene", Polimery **46** (2001) 9, 622–630.

[8] F. Arefi-Khonsari, M. Tatoulian, J. Kurdi, J. Amouroux, "Plasma processing of polymers for enhanced adhesion to metals and other materials", High Temp. Mater. Proc. **4** (2000), 537–551.

[9] P. C. L'Argentiere, H. A. Taher, "$PdCl_2$ anchorage onto the surface of polystyrene films via oxygen and ammonia plasma treatment", J. Chem. Technol. Biotechnol. **75** (2000), 25–28.

[10] K. M. Baumgärtner, J. Schneider, A. Schulz, J. Feichtinger, M. Walker, "Short-time plasma pre-treatment of polytetrafluorethylene for improved adhesion", Surf. Coat. Technol. **142–144** (2001), 501–506.

[11] N. V. Bhat, D. S. Wavhal, "Preparation of cellulose triacetate pervaporation membrane by ammonia plasma treatment", J. Appl. Polym. Sci. **76** (2000), 258–265.

[12] M. Müller, C. Oehr, "Plasma aminofunctionalisation of PVDF microfiltration membranes: comparison of the in plasma modifications with a grafting method using ESCA and an amino-selective fluorescent probe", Surf. Coat. Technol. **116–119** (1999), 802–807.

[13] R. Sipehia, "The enhanced attachment and growth of endothelial cells on anhydrous ammonia gaseous plasma modified surfaces of polystyrene and poly(tetrafluorethylene)", Biomat., Art. Cells, Art. Org. **18** (1990) 3, 437–446.

[14] Y. Nakayama, T. Takahagi, F. Soeda, K. Hatada, S. Nagaoka, J. Suzuki, A. Ishitani, "XPS analysis of NH_3 plasma-treated polystyrene films using gas phase chemical modification", J. Polym. Sci. A: Polym. Chem. **26** (1988), 559–572.

[15] F. Simon, G. Hermel, D. Lunkwitz, C. Werner, K. Eichhorn, H. J. Jacobasch, "Surface modification of expanded poly(tetrafluorethylene) by means of microwave plasma treatment for improvement of adhesion and growth of human endothelial cells", Macromol. Symp. **103** (1996), 243–257.

[16] J. Yang, J. Z. Bei, S.G. Wang, "Improving cell affinity of poly(D,L-lactide) film modified by anhydrous ammonia plasma treatment", Polym. Adv. Technol. **13** (2002) 3–4, 220–226.

[17] R. Sipehia, A.S. Chawla, "Albuminated polymer surfaces for biomedical application", Biomater. Med. Dev. Art. Org. **10** (1982) 4, 229–246.

[18] C. Girardeaux, N. Zammatteo, M. Art, B. Gillon, J.J. Pireaux, R. Caudano, "Amination of poly(ethylene terephthalate) polymer surface for biochemical applications" Plasmas Polym. **1** (1996) 4, 327–346.

[19] E. Moy, F.Y.H. Lin, J. W. Vogtle, Z. Policova, A. W. Neumann, "Contact angle studies of the surface properties of covalently bounded poly-L-lysine to surfaces treated by glow-discharge", Colloid Polym. Sci. **272** (1994), 1245–1251.

[20] R. Sipehia, A.S. Chawla, J. Daka, T. M. S. Chang, "Immobilization of enzymes on polypropylene bead surfaces by anhydrous ammonia gaseous plasma technique", J. Biomed. Mater. Res. **22** (1988), 417–422.

[21] A. Ohl, W. Schleinitz, A. Meyer-Sievers, A. Becker, D. Keller, K. Schröder, J. Conrads,

"Design of a combined UHV reactor system for plasma surface treatment of polymer materials", Surf. Coat. Technol. **116–119**, (1999), 1006–1010.

[22] R. Förch, N. S. McIntyre, R. N. S. Sodhi, D.H. Hunter, "Nitrogen plasma treatment of polyethylene and polystyrene in a remote reactor", J. Appl. Polym. Sci. **40**, (1990) 1903–1915.

[23] J. Behnisch, A. Holländer, H. Zimmermann, "Surface modification of polyethylene by remote dc discharge plasma treatment", J. Appl. Polym. Sci. **49** (1993), 117–124.

[24] A. Meyer-Plath, K. Schröder, A. Ohl, "Current trends in biomaterial surface functionalization – nitrogen-containing plasma assisted processes with enhanced selectivity", Vacuum **71** (2003) 3, 391–406.

[25] R. Wilken, A. Holländer, J. Behnisch, "Nitric oxide radical trapping analysis on vacuum-ultraviolet treated polymers", Macromolecules **31** (1998), 7613–7617.

[26] R. Wilken, A. Holländer, J. Behnisch, "Surface radical analysis on plasma-treated polymers", Surf. Coat. Technol. **116–119** (1999), 991–995.

[27] A. Meyer-Plath, B. Finke. K. Schröder, A. Ohl, "Pulsed and cw microwave plasma excitation for surface functionalization in nitrogen-containing gases", Surf. Coat. Technol. **174–175** (2003), 877–881.

[28] B. Finke, A. Meyer-Plath, K. Schröder, A. Ohl, "Analysis of plasma-generated radicals on polymer surfaces", International Symposium on Plasma Chemistry, (ISPC-16), Taormina (Italy), 22–27.06.2003, CD and book of abstracts, p.28.

[29] J. Friedrich, I. Retzko, G. Kühn, W. Unger, A. Lippitz, "Metal doped plasma polymer films" in "Metallized Plastics 7: Fundamental and Applied Aspects", ed. K.L. Mittal, VSP 2001, 117–142.

[30] D. A. Puleo, R. A. Kissling, M. S. Sheu, "A technique to immobilize bioactive proteins, including bone morphogenetic protein-4 (BMP-4), on titanium alloy", Biomaterials 23 (2002), 2079–2087.

[31] A. Ohl, R. Ihrke, A. Diener, B. Nebe, J. Rychly, K. Schröder, "Defined biologization of artificial polymer surfaces using covalent coupling strategies", Biomaterialien **4** (2003), 136.

[32] K. Schröder, R. Ihrke, A.A. Meyer-Plath, B. Finke, A. Diener, B. Nebe, A. Ohl, "Surface functionalization in ammonia microwave plasmas for biomedical applications", International Symposium on Plasma Chemistry, (ISPC-16), Taormina (Italy), 22–27.06.2003, CD and book of abstracts, p.446.

[33] A. Meyer-Plath, K. Schröder, A. Ohl, "Improved Functionalization for Chemically Patterned Polystyrene Surfaces", proceedings of the 48th American Vacuum Society (AVS) Symposium, 29.10–2.11.2001, San Francisco, p.221.

[34] K. Schröder, A. Ohl "Plasma functionalized plastics for the culture of adherent cells" In vitro News (2001), 1, 3.

26
PE-CVD Modification of Medical-grade PVC to Inhibit Bacterial Adhesion: PEO-like and Nanocomposite Ag/PEO-like Coatings

D.J. Balazs, K. Triandafillu, E. Sardella, G. Iacoviello, P. Favia, R. d'Agostino, H. Harms, and H.J. Mathieu

Abstract

Medical-grade poly(vinyl chloride) was modified by RF-plasma deposition of Ag/PEO-like coatings to study how the combination of the non fouling properties of poly(ethylene-oxide) materials and the well-known bacterial toxic effects of Ag^+ ions influence *Pseudomonas aeruginosa* adhesion. Nanocomposite Ag/PEO-like coatings were plasma deposited in a mixed RF PE-CVD/sputtering process and consist of nanometric silver clusters embedded in a PEO-like matrix. Thin Ag/PEO-like coatings were deposited in an asymmetric RF plasma reactor equipped with a silver RF electrode, and fed with diethyleneglycol-dimethyl-ether vapors and Ar buffer gas. PEO-like films without Ag clusters were also produced and served as controls to identify the origin of the antibacterial effects of the films. A systematic study of the deposition parameters, Ar flow rate and power input, was completed. X-ray photoelectron spectroscopy and water contact-angle measurements were used to characterize the various coatings. Ag-free PEO-like films with the highest possible PEO character were determined to be non fouling, and prevented adsorption of both albumin and fibrinogen. Despite their poor non fouling character, Ag/PEO-like coatings completely prevented the adhesion of the four *P. aeruginosa* strains tested, whereas the Ag-free PEO-like films were not effective in preventing bacterial adhesion.

26.1
Introduction

Recent publications have outlined the necessity to develop a strategy to reduce bacterial adhesion to endotracheal devices [1–3]. Briefly, *Pseudomonas aeruginosa* (*P. aeruginosa*) is one of the most prevalent bacterial pathogens in a clinical environment and is responsible for 30% of hospital-acquired infections [4]. Prolonged endotracheal intubation is one of the greatest risk factors for ventilator-associated pneumonia (VAP) occurring in intubated and mechanically ventilated patients [5]. Colonization of the intubation device and upper respiratory tract by *P. aeruginosa* precedes over 90% of VAP cases, 40% of which are fatal, despite aggressive antibiotic therapies [4]. For these reasons, several approaches based on surface modification of the

polymer used for this application, medical-grade poly(vinyl chloride) (PVC), are under investigation. In previous publications, the oxygen-plasma treatment described was based on the alteration of physicochemical properties of PVC to create surfaces that demonstrated to be 70% less adhesive to four different *P. aeruginosa* strains [1,2]. Another surface modification investigated by Balazs et al. [3], consists of a chemical treatment by sodium hydroxide and silver nitrate in order to incorporate the antimicrobial agent, monovalent silver. The chemically treated surfaces exhibited a 100% reduction in initial bacterial adhesion, underlining the potential of wet treatments that incorporate silver as an antimicrobial agent.

In the present publication, we evaluate an additional strategy that consists of coating the PVC substrate with a plasma-deposited, silver-containing poly(ethylene-oxide) (PEO)-like (Ag/PEO-like) coating, which combines the non fouling properties of conventional PEO materials [6–9] and the well-known bacterial toxic effects of silver ions released in water media [3,10–12].

Over the past decade, PEO has been elected as the material of choice in many biomedical applications [6,7], because of its superior ability to reduce protein adsorption to many substrates, including hydrophobic polymers [8,9]. Once in contact with a biomaterial, proteins from the environment can adsorb onto the surface through specific or nonspecific interactions, in a process referred to as conditioning [13]. The resulting protein layer may provide receptor sites for the firm attachment of bacteria [14] and other cells. Since PVC is hydrophobic, PEO represents an attractive option for creating protein/bacterial antiadhesive surfaces.

Although an extensive amount of research has been performed, the ideal method of creating a PEO-rich surface by chemical methods has not been found. Many of the methods have limitations, such as physical or chemical instability, low surface coverage, changes of bulk properties, or harsh reaction conditions [15]. The literature describes PEO surfaces prepared by direct grafting [16–18], grafting with Ar glow discharges [15], photochemical immobilization [19], and the physisorption of PEO-based block copolymers, Pluronics® [20–23], all of which have been successful in preventing protein adsorption. However, surfaces with greater stability may be prepared by means of plasma-enhanced chemical vapor deposition (PE-CVD), which delivers what are known as PEO-like surfaces.

Non fouling, PEO-like coatings have been created using glow discharges fed with various low weight glycol monomers, including di-ethylene-glycol-dimethyether (DEGDME, $CH_3O(CH_2CH_2O)_2CH_3$ or diglyme) [24-26], tri-ethylene-glycol-dimethyl-ether (TEGDME, $CH_3O(CH_2CH_2O)_3CH_3$ or triglyme) [24], tetra-ethylene-glycol-dimethyl-ether ($CH_3O(CH_2CH_2O)_4CH_3$, tetraglyme) [26–28], as well as tri-ethylene-glycol-monoallyl-ether [29]. Regardless of the monomer employed, there is no dispute in the literature that the level of the non fouling properties achieved is due to the degree of incorporation of ethylene-oxide (EO, $-CH_2CH_2O-$) moieties in the film. In addition, it is also commonly accepted that the films with the highest PEO character, or best monomer retention, are produced under reduced monomer fragmentation regimes in the plasma and reduced positive-ion bombardment at the surface of the substrate (i.e., low power input, modulated power, etc.) [25,27,30].

PE-CVD PEO-like films with high PEO character have been shown to be resistant to adsorption of albumin [27,29], fibrinogen [27,28], platelets [27], macrophages [28] and *P. aeruginosa* [26], where the reduction was shown to be dependent on the degree of monomer retention. PE-CVD of PEO-like films, thus, may represent a simple, one-step solution to the problem of bacterial adhesion to the PVC substrates under scrutiny.

Favia et al. [25] have deposited nanocomposite Ag/PEO-like coatings using a mixed RF PE-CVD/sputtering process, employing a silver RF electrode (cathode) in an asymmetric plasma reactor, DEGDME vapors as a monomer, and argon as buffer gas. Silver quantity and non fouling character of the films can be tailored to specific requirements by altering deposition parameters such as power input, pressure and Ar flow rate. The silver present in the Ag/PEO-like coatings is in the form of nanometric metal (oxidation state zero) clusters embedded in a PEO-like matrix, as found with transmission electron microscopy (TEM) and X-ray photoelectron spectroscopy (XPS) investigations, respectively (please refer to ref. [25] for further details). A thin silver oxide layer is probably present at the cluster-matrix interface. In water media, the Ag/PEO-like coatings swell and monovalent Ag^+ ions are released into the medium, as shown in ref. [31]; the oxidation state +1 has been demonstrated to be key to the germicidal properties of silver [10].

PEO-like and Ag/PEO-like films were deposited on medical-grade PVC substrates, employing the method describe in ref. [25]. XPS and water contact-angle (WCA) measurements were used to investigate the chemical nature and wettability of PVC following the modifications. In order to identify the origin of the antibacterial effects of Ag/PEO-like coatings, two different forms of silver-free PEO-like films, having a low and high PEO character, are used as control surfaces. We present a systematic study of the deposition parameters, Ar flow rate and RF input power, that are known to be important in determining non fouling character and Ag-content of Ag/PEO-like coatings. Ar flow rate and RF input power were varied until a coating with a high Ag-content, while maintaining a significant PEO character, was obtained. Samples were mass produced under these conditions for protein and bacterial adhesion studies. Protein adhesion was studied by incubating the samples in bovine serum albumin and fibrinogen; bacterial adhesion studies were completed using four different strains of *P. aeruginosa*.

26.2 Materials and Methods

26.2.1 Substrate Preparation

PVC issued from Mallinckrodt Hi-Lo™ endotracheal tubes was used as a substrate. The tubes were flattened to allow microscopic counting of bacteria as previously described [1,2]. Briefly, the PVC tube was split and cut into pieces of 2×1 cm^2, and the pieces were then heated, below the melting point of PVC, between two clean,

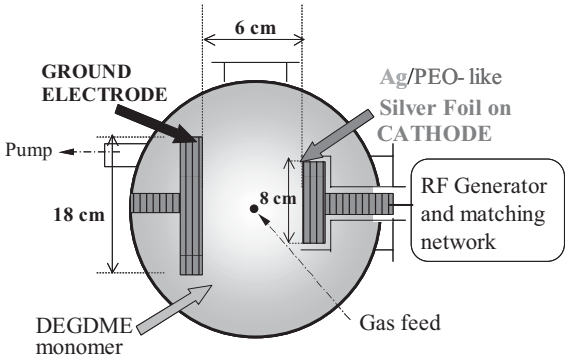

Figure 1 chematic representation of the asymmetric plasma reactor used for the PEO-like and Ag/PEO-like coating deposition [25].

glass microscope slides for 90 s at 180 °C. Although no statistically significant changes were observed in surface chemistry, or contact angle, the flattening procedure leaves native PVC with some surface microroughness (see Fig. 6, as an example), probably due to the softening of the PVC surface layers under heat conditions (for further details pertaining to native PVC flattening procedures, refer to Balazs et al. [1]). All experiments were performed on flattened Mallinckrodt™ PVC substrates, referred to hereafter as native PVC.

2.2 Plasma-Deposition Processes

Thin Ag/PEO-like coatings were deposited on native PVC substrates through a mixed PE-CVD/sputtering process. DEGDME vapors were used as gas feed with Ar as a buffer gas [25]. DEGDME (162 °C boiling point) was fed from a reservoir through a needle valve and a steel line, all heated to 35 °C. The asymmetrical, parallel plate plasma reactor shown in Figure 1 [25] has been utilized. The reactor is equipped with a silver RF electrode; the ground and the RF electrodes are 18 cm and 8 cm in diameter, respectively, and are separated by a gap of 6 cm. Due to the smaller area of the cathode, under proper experimental conditions (high RF power, low pressure, low DEGDME/Ar flow ratio), a bias-induced ion bombardment results at this electrode, which prevents the deposition of any coating, and induces the sputtering of silver atoms, as evidenced by optical emission spectroscopy [24–26]. Substrates positioned at the large, ground electrode, where ion bombardment is very low, experience the deposition of a PEO-like coating with embedded silver clusters. The chemical composition of Ag/PEO-like films (C/O/H composition, PEO character, Ag-content), as well as the dimensions of the Ag clusters can be tuned by adjusting the deposition parameters. In our experimental apparatus, the deposition of a coating at the cathode that quenches the sputtering of Ag atoms occurs under the

following conditions: low RF power (≤ 5 W), high pressure (≫ 50 mTorr) and high DEGDME/Ar flow ratio (Ar ≤ 7.5 sccm). Under such conditions, PEO-like coatings without silver embedded grow at the ground electrode, and their PEO character will depend on the degree of monomer fragmentation [24–26].

In order to investigate the effects of Ar flow rate and RF power on the composition of Ag/PEO-like coatings, native PVC substrates were positioned with a sample holder, on the ground electrode of the reactor illustrated in Fig. 1. The system was then evacuated and 0.25 sccm of DEGDME vapors were introduced, followed by 10–30 sccm of Ar. The chamber pressure was maintained at 100 mTorr. The plasma was then generated at an RF power input of 15–25 W for a period of 15 min. The effects of Ar flow rate and RF power were investigated separately; unless varied, these parameters were fixed to 15 sccm and 20 W, respectively.

PEO-like films without Ag clusters were produced as controls, using a stainless steel cathode and proper experimental conditions, i.e. 0.4 sccm of DEGDME vapor, 5 sccm of Ar, and 400 mTorr of pressure. 5 or 15 W of RF power input were utilized, for a deposition time of 15 min, in order to produce two different forms of PEO-like films with high and low ether/carbon content, respectively [24,25]. The different PEO-like films are hence referred to as '5 W' and '15 W'.

26.2.3 Protein Adsorption

The effects of conditioning layers of two important blood serum proteins, albumin and fibrinogen, which are also minor components of saliva [32,33], were investigated. Protein adsorption to the various surfaces was studied using bovine serum albumin (BSA) and fibrinogen (F) (Sigma, catalog nos. A4161, and F8630, respectively). The samples were incubated for 3 h at 37 °C in solutions of albumin (1 mg/mL) and fibrinogen (0.2 mg/mL) in phosphate buffered saline (PBS, 0.01 M phosphate buffer, 0.0027 M KCl, 0.137 M NaCl, pH 7.4) After the incubation, the samples were rinsed 3 times with PBS and analyzed by the various surface characterization techniques.

26.2.4 XPS Analysis

XPS analysis was performed using an imaging Kratos Axis Ultra (UK) XPS spectrometer equipped with a conventional hemispherical analyzer. A monochromatized AlK_α (1486.6 eV) X-ray source was employed, operated at 150 W. Spectral acquisition was performed under ultrahigh vacuum (UHV; 10^{-7} Pa) conditions. Analysis was performed on a 0.21 mm^2 (300 μm × 700 μm) sample area at a take-off angle of 90° relative to the substrate surface. Pass energies were 80 eV and 20 eV for wide-scan and high-resolution scans, respectively, corresponding to energy resolutions of 1.6 and 0.4 eV, respectively. Charge compensation was performed with a self-compensating device using field-emitted low-energy electrons (0.1 eV) to adjust the main hydrocarbon (C–C, C–H) component to 285.0 eV. Data reduction (atomic concentra-

tion, shift, curve fitting, etc.) was performed with CasaXPS Version 2.0.69 software. The operating software, Vision v2, corrects for the transmission function. The sensitivity factors were 0.328, 0.891, 0.278, 5.987, 0.78, for Si 2p, Cl 2p, C 1s, Ag 3d and O 1s, respectively. Spectra were fitted after linear background subtraction assuming a Gaussian–Lorentzian (70/30) peak shape. Prior to XPS analysis, all samples were outgassed overnight, under UHV, to maintain an appropriate pressure in the analysis chamber.

26.2.5 Contact-Angle Measurements

The advancing water contact angles on the various surfaces were measured with a Ramé Hart 100 goniometer, using a deionized water droplet with a volume of 4–6 µl. All values reported are the average of three measurements per sample (standard deviation, ± 3°). The deposition of hydrophilic coatings, such as PEO-like and Ag/PEO-like, onto the microrough native PVC substrates (see Sect. 2.1) results in WCA values that are lower than those expected for flat surfaces that do not exhibit microroughness [34], such as polished silicon wafers.

26.2.6 Bacterial Adhesion

PEO-like and Ag/PEO-like films deposited on native PVC were evaluated for bacterial adhesion, using native PVC samples as controls. The initial adhesion assays were performed using four different *P. aeruginosa* strains, including the wild-type strain PAO1 [35] (obtained from the Laboratory of Microbial Biology, University of Lausanne, Switzerland), the mutant AK44 [36], and two genotypically different, pulmonary clinical isolates 1.1.A1 and 19G12 obtained from colonized intubated patients (obtained from the University Hospital of Geneva).

Batch adhesion experiments were carried out in glass vials (volume, 15 cm^3) containing a PVC patch and filled to the top with degassed PBS according to a method adapted after Rijnaarts et al. [37]. After the concentrated bacterial suspension (4×10^7 cells/mL) was gently injected (injected volume, 250 µL), the vials were placed on a slantwise rotating wheel (7 rpm; amplitude, 10 cm) to avoid sedimentation of bacteria and incubated at room temperature. After 2 h of incubation, the vials were opened and rinsed with cell-free PBS. The samples were carefully removed from the vials to prevent dewetting as much as possible, placed on a microscope slide and covered immediately with a cover slip. The slides were observed under a light microscope (magnification × 1250; BX-60, Olympus Optical Co. Ltd., Tokyo, Japan) equipped with a digital camera (SenSys, Photometrics Ltd., Tucson, USA). The number of adherent cells was counted for six randomly chosen locations per sample. Each experiment was done in triplicate. Levels of adhesion were given as numbers of cells per square centimeter and calculated by averaging the values of the 18 adhesion locations obtained for the 3 samples.

26.3 Results and Discussion

26.3.1 PEO-like Film Deposition

In the following section we present surface analysis data for PEO-like coatings deposited at 5 W and 15 W on native PVC. These data will provide insight into the effects of RF power on the PEO character of the films, and will further serve as a comparison for the investigation of the operating parameters employed for the deposition of the Ag/PEO-like films. For details pertaining to native PVC spectral interpretation, refer to Balazs et al. [1].

26.3.1.1 XPS Analysis

Wide-scan XPS analysis of native PVC detected silicon, chlorine, carbon, and oxygen; while on 5 W and 15 W PEO-like films only carbon and oxygen were detected, as expected for PEO-like materials [27]. We use the O/C elemental ratios in order to interpret the differences in the level of oxygen incorporation in the different PEO-like coatings. The surface composition and O/C elemental ratios for native PVC and PEO-like coatings are represented in Table 1. Here it is shown that Cl and Si signals disappear after PEO-like deposition; thus, it can be concluded that the PEO-like films completely mask the PVC surface, within the limits of the XPS information depth. The fittings of the C 1s scans will later validate this hypothesis.

Table 1 Atomic percentages and elemental ratios for the native PVC and PEO-like films deposited with varying input power, 5 and 15 W, respectively (average over 4 samples per group). Other deposition parameters include: a DEGDME flow rate of 0.4 sccm, an Ar flow rate of 5 sccm and a chamber pressure of 400 mTorr.

	C 1s	O 1s	Cl 2p	Si 2p	O/C
	(%)	(%)	(%)	(%)	
Native PVC	68.1	13.9	10.9	7.1	0.20
5 W	71.3	28.7	–	–	0.40
15 W	75.8	24.3	–	–	0.32

Table 1 also illustrates the evolution of oxygen incorporation for PEO-like films as a function of the RF power input. Coatings deposited at 5 W show an O/C ratio of 0.40, attesting to a good retention of the monomer structure (O/C is 0.5 for DEGDME), while at 15 W the O/C ratio lowers to 0.32. This indicates that oxygen incorporation and monomer structure retention in the film is much higher at a lower power input. In order to better determine the effects of power on PEO character [26], the C1s and O1s high-resolution spectra must be examined.

Figure 2 illustrates the typical C 1s high-resolution spectra that were studied in detail to identify the chemical binding states of the native and PEO-like coatings. Six peaks were used to fit the C 1s high-resolution scans of native PVC [1]; the C 1s scans

of the PEO-like films were fitted 4 peaks, as shown in Table 2, according to Favia et al. [25] and Johnston et al. [26,38]. The hypothesis that the PEO-like films mask the native PVC substrate is confirmed by the C 1s and O 1s high-resolution fittings, as there was no evidence of the characteristic chlorine-containing signatures of standard PVC materials, i.e. the C–C–Cl and C–Cl contributions, identified for the PEO-like coatings.

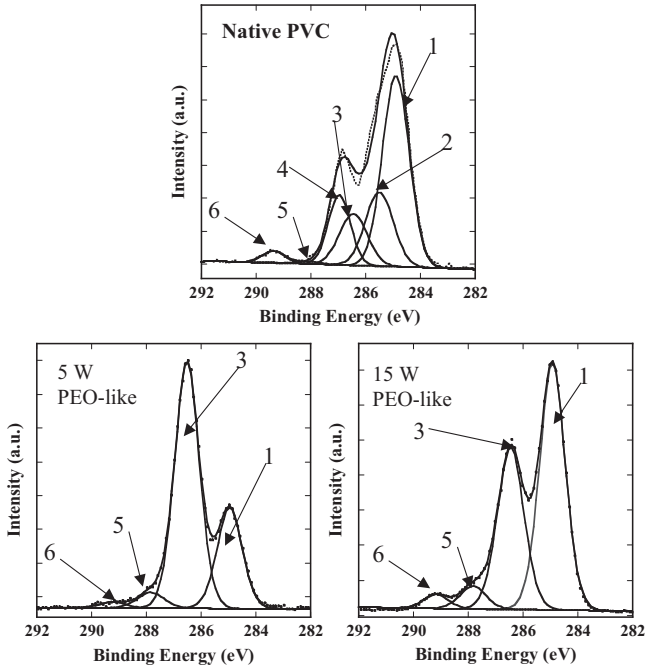

Figure 2 C 1s high-resolution fittings of the native PVC and PEO-like films deposited with varying input powers of 5 and 15 W, respectively. Other deposition parameters include a DEGDME flow rate of 0.4 sccm, an Ar flow rate of 5 sccm, and a chamber pressure of 400 mTorr.

The peak-fitting parameters, as well as the relative abundances of the fitted carbon and oxygen components are summarized in Table 2.

Retention of the monomer structure, often referred to as the 'PEO character', has been demonstrated to be the determining factor of the non fouling nature of plasma-deposited PEO-like coatings [26,27]. The PEO character is commonly defined as the relative percent of ether carbon functionalities (BE = 286.5 eV) of the C 1s high-resolution scans [26]. The data presented in Table 2 show that 5 W PEO-like films have a much higher PEO character than 15-W films (65%, and 40%, respectively). Furthermore, the PEO-like coatings deposited at 15 W exhibit a higher percentage of hydrocarbon groups than the coatings formed at 5 W, with area percentages of 51% and 29%, respectively. Also, this finding confirms that higher power input results in

Table 2 Peak-fitting parameters and percent peak areas for the C 1s and O 1s high-resolution scans of the native PVC and PEO-like films deposited with varying input powers of 5 and 15 W, respectively. Other deposition parameters include a DEGDME flow rate of 0.4 sccm, an Ar flow rate of 5 sccm, and a chamber pressure of 400 mTorr (average over 4 samples per group).

	Binding			Input Power	
Peak	Energy (eV)	FWHM (eV)	Native PVC % area	5 W % area	15 W % area
C 1s					
C_1-C / C_1-H	285.0	1.1	51.4	28.9	51.4
C_2-C-Cl	285.5	(± 0.05)	15.8	–	–
C_3-O-C, C_3-OH	286.4		13.2	**64.8**	**40.0**
C_4-Cl	287.0		16.2	–	–
C_5 = O	288.0		0.8	4.5	5.6
O-C_6=O	289.2		2.6	1.7	3.0
O 1s					
SiO_2 1	531.8	1.3	22.2	–	–
O_2=C	532.1	(± 0.05)	3.9	6.2	11.5
O_3-C	532.6		60.7	91.3	82.7
O_4-C=O	533.7		13.3	2.5	5.8

greater monomer fragmentation in the glow, producing a PEO-like film with a low ether-carbon and high hydrocarbon content.

26.3.1.2 Contact-Angle Measurements

As WCA measurements are extremely surface sensitive [38], a change in surface wettability can be used to qualitatively indicate changes in surface chemistry. Figure 3 illustrates the evolution of surface wettability of native PVC, 5-W and 15-W

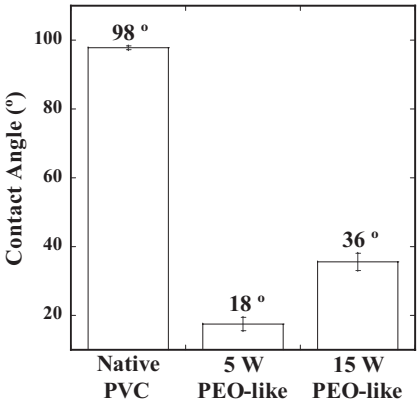

Figure 3 Evolutionof the advancing WCA achieved following the deposition of PEO-like films with varying input power of 5 and 15 W, respectively. Other deposition parameters include a DEGDME flow rate of 0.4 sccm, an Ar flow rate of 5 sccm, and a chamber pressure of 400 mTorr (average over 4 areas per sample) .

PEO-like films. Figure 3 also shows how PEO-like coating deposition on native PVC greatly reduces the advancing WCA, due to the creation of a surface dense with hydrophilic functional groups, such as hydroxyl and ether carbons [39,40]. The 5 W PEO-like films do indeed show a much lower advancing WCA, as compared to the 15-W films, with values of 18° and 36°, respectively. This agrees with the XPS data, attesting that PEO-like films deposited at 5 W have significantly higher oxygen content than 15-W films.

26.3.2 Ag/PEO-like Films

The plasma deposition of Ag/PEO-like films can be described as a mixed process, including the deposition of a PEO-like matrix and the sputtering of silver atoms [25]. In the previous section, we demonstrated that a film with a high PEO character is deposited at low power input, or a low monomer fragmentation regime. On the contrary, the sputtering of silver necessitates that the discharge is operated at conditions that favor ion bombardment of the cathode, which unfortunately, also results in an increase in the fragmentation of DEGDME [25]. Therefore, the deposition of Ag/PEO-like films can be considered as a compromise between having an acceptable quantity of silver to add an antibacterial property, and having a PEO character that is sufficient to maintain part of the non fouling properties of the coatings. Indeed, plasma-deposited PEO-like coatings with full non fouling properties for proteins and cells should exhibit at least a 75% PEO character [41].

In the following section we present a systematic study on the individual effects that the deposition parameters Ar flow rate and RF power input have on PEO character and Ag-content of Ag/PEO-like films. Variations of Ar flow rate were investigated for 10, 20 and 30 sccm, while the other parameters were kept fixed (DEGDME 0.25 sccm; power 20 W; pressure 100 mTorr); variations of power input were investigated for 15, 20 and 25 W, also in this case the other parameters were kept fixed (DEGDME 0.25 sccm; Ar 15 sccm; pressure 100 mTorr).

26.3.2.1 XPS Analysis

XPS analysis of Ag/PEO-like films detected carbon, oxygen and silver, according to the wide-scan spectra. Surface composition and O/C elemental ratios of films deposited while varying Ar flow rate and power input are represented in Table 3. The XPS data show that the O/C ratio of Ag/PEO-like coatings decreases with increasing both Ar flow rate and input power, respectively. On the contrary, the silver content follows a reverse trend and increases with both parameters investigated.

The highest silver content achieved for the Ar flow rate variation, 3.5%, is achieved with 20 sccm Ar; the highest input power tested, 25 W, produced the highest quantity of silver embedded, 3.1%. According to ref. [25], these observations are logical, as Ar flow rate and power input are the main parameters that drive the sputtering of silver from the cathode, as well as the fragmentation of the DEGDME precursor in the plasma.

Table 3 Atomic percent and elemental ratios for the Ag/PEO-like films deposited with varying Ar flow rate, 10, 20 and 30 sccm, and varying input power, 10, 15 and 20 W, respectively (average over 4 samples per group).

	C 1s (%)	O 1s (%)	Ag 3d (%)	O/C
Ar Flow Rate				
10 sccm	77.8	21.1	1.1	0.271
20 sccm	76.3	20.2	3.5	0.265
30 sccm	77.4	19.2	3.4	0.248
Input Power				
15 W	71.9	24.7	2.7	0.344
20 W	76.2	20.8	3.0	0.273
25 W	77.6	19.3	3.1	0.249

In order to verify that the PEO character of the films follows the same trends as the O/C ratio, the fittings of the C 1s high-resolution scans were evaluated. Figure 4 illustrates the typical C 1s high-resolution spectra of the Ag/PEO-like films deposited while varying Ar flow rates and RF power input. The peak-fitting parameters, as well as the relative abundances of the fitted carbon and oxygen components are summarized in Table 4. Like the Ag-free PEO-like films, the C 1s scans of Ag/PEO-like films were fitted with 4 peaks, according to ref. [25]. There was no evidence of any of the characteristic signatures of native PVC in any of the Ag/PEO-like films. Thus, Ag/PEO-like films also mask native PVC substrates within the sampling depth of XPS.

Table 4 Peak-fitting parameters and percent peak areas for the C 1s and O 1s high-resolution scans of the native and Ag/PEO-like films deposited with Ar feeds of 10, 20 and 30 sccm, and input power, 10, 15 and 20 W, respectively (average over 4 samples per group).

Peak	Binding Energy (eV)	FWHM (eV)	Native	Ar Flow Rate			Input Power		
				10 sccm % area	20 sccm % area	30 sccm % area	15 W % area	20 W % area	25 W % area
C 1s									
C_1-C / C_1-H	285.0	1.1	51.4	60.4	54.9	66.6	57.3	60.1	66.1
C_2-C-Cl	285.5	(± 0.05)	15.8	–	–	–	–	–	–
C_3-O-C, C_3-OH	286.4		13.2	**28.1**	**27.5**	**23.7**	**30.7**	**27.0**	**22.6**
C_4-Cl	287.0		16.2	–	–	–	–	–	–
C_5=O	288.0		0.8	8.3	11.3	6.6	8.4	9.1	7.7
O-C_6=O	289.2		2.6	3.2	6.3	3.1	3.6	3.8	3.6
O 1s									
$SiO_{2\ 1}$	531.8	1.3	22.2	–	–	–	–	–	–
O_2=C	532.1	(± 0.05)	3.9	20.9	27.8	19.9	22.8	21.7	19.9
O_3-C	532.6		60.7	70.8	59.7	70.9	69.5	63.7	70.9
O_4-C=O	533.7		13.3	8.3	12.5	9.2	7.7	14.6	9.2

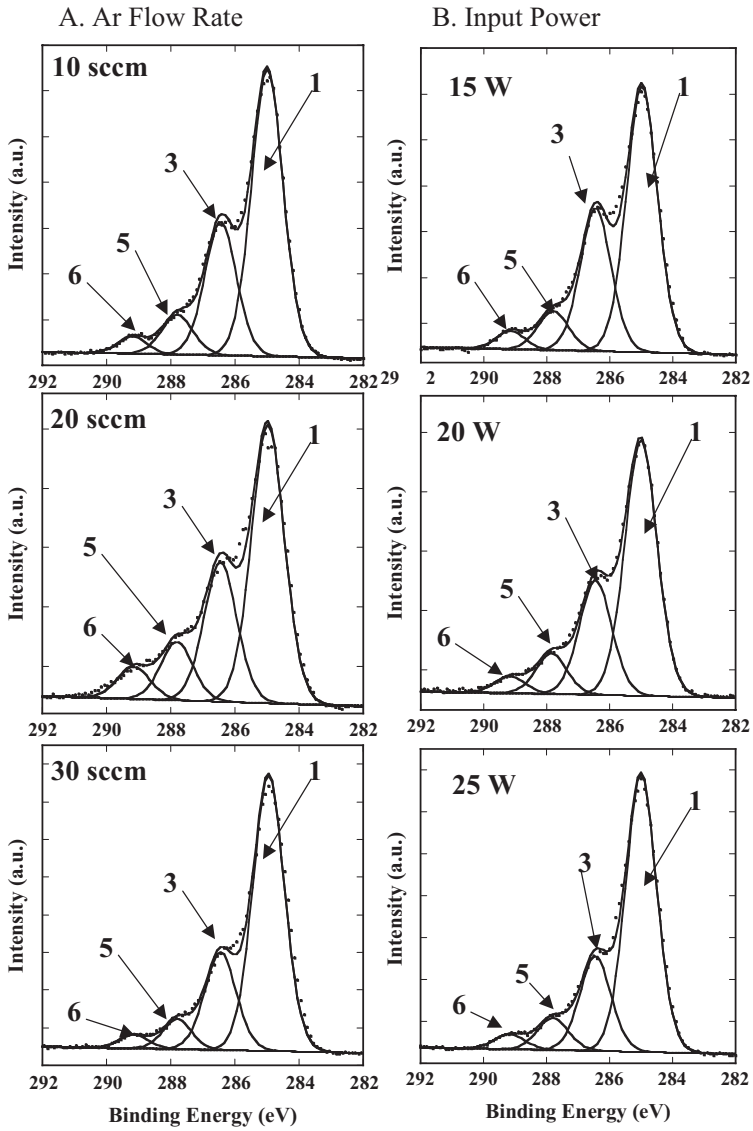

Figure 4 1s high-resolution fittings for the Ag/PEO-like films deposited with Ar feeds (A) of 10, 20 and 30 sccm, and varying input power (B), 10, 15 and 20 W, respectively (average over 4 samples per group).

Both Fig. 4 and Table 4 illustrate that the PEO character (ether carbon, peak component 3) of all Ag/PEO-like films decreases when both Ar flow rate and input power increase, respectively. This was also indicated by the O/C ratio values of Table 3. The loss of PEO character observed for the increase in Ar flow rate can be

explained as the increased fragmentation of DEGDME in the glow. As was seen for PEO-like films lacking silver particles, increasing the power input when depositing Ag/PEO-like coatings enhances the fragmentation of DEGDME, and, slightly enhances the ion bombardment at the ground electrode where the substrates are positioned. Evidence of monomer fragmentation is also seen as the increasing trend of the hydrocarbon groups (peak component 1) with increasing power.

It was found that the PEO characters were 30.7%, 27.0% and 22.6% for power values of 15, 20, and 25 W, respectively. As expected, the best PEO character was achieved for the lowest power investigated (15 W), which would correspond to the lowest monomer fragmentation regime, in the range of power input tested. In addition, as previously stated, the PEO character is directly related to the non fouling nature of these coatings [26,27]. Thus, the Ag/PEO-like films should exhibit stronger protein adsorption properties than the silver-free 5-W and 15-W PEO-like films, as their PEO character is noticeably lower.

So far the interpretation of the XPS data has been centered on the effects of Ar flow rate and RF power input on the PEO character of the Ag/PEO-like coatings. It is equally important to know the dependence of Ag content on the deposition parameters. It has been verified that the increased ion bombardment of the cathode with power input and Ar flow rate also produces an increase of Ag sputtering, hence, Ag/PEO-like coatings with higher Ag-content. Figure 5 displays the trends observed in Ag atomic percent and ether-carbon content as a function of Ar flow rate and input power. Table 3 and Fig. 5 demonstrate that the maximum silver incorporation, 3.5%, is achieved at 20 sccm of Ar flow rate; further increases do not improve the silver content when the other deposition parameters are fixed to the following: DEGDME 0.25 sccm; power 20 W; pressure 100 mTorr. Furthermore, the loss of PEO character at 30 sccm Ar is far more substantial than for 10 and 20 sccm. Although the best PEO character, 28.1%, is achieved at 10 sccm Ar, the Ag-content of this film is quite low, 1.1%. Thus, an Ar flow rate of 20 sccm offers the best compromise between PEO character (27.5%) and silver content (3.5%) for this work. Similarly, from Figure 5 and Table 4 it is seen that an input power of 20 W yields the best compromise in a PEO character (27.0%) and silver content (3.0%).

26.3.2.2 **Contact-Angle Measurements**

Table 5 illustrates the WCA evolution of the Ag/PEO-like films over the range of Ar flow rate and power input studied. Generally, all Ag/PEO-like coatings, having values in the 60–80° range, exhibit much higher WCA values as compared to Ag-free PEO-like coatings.

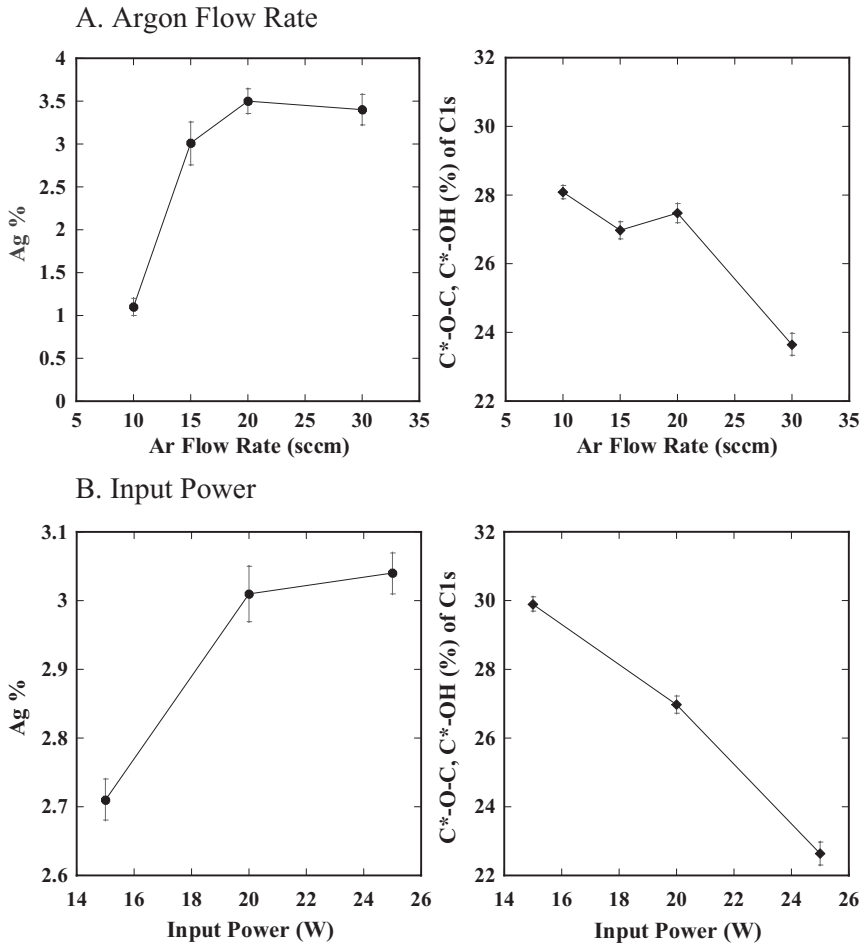

Figure 5 Graphs illustrating the effects of increasing Ar flow rate on the silver content (left) and PEO-like character (right) of the Ag/PEO-like coatings deposited with Ar feeds (A) of 10, 15, 20 and 30 sccm, and varying input power (B) of 10, 15 and 20 W, respectively (average over 4 samples per group).

The silver-free PEO-like films produced in the high DEGDME fragmentation regime, 15 W, had an advancing WCA of 36°. The WCA of Ag/PEO-like films, instead, showed much higher values, even for the lowest fragmentation regimes (Ar 10 sccm, 15 W of power, respectively). This substantial increase for Ag/PEO-like coatings can be attributed to the combined effects of: a relative decrease in ether-carbon content, the incorporation of Ag particles, and a relative increase of the hydrocarbon content [25], as evident from XPS data.

Table 5 Evolution of the advancing contact angles achieved following the deposition of Ag/PEO-like films with varying Ar flow rate and varying input power (average over 4 samples per group).

	WCA (± 3°)
Ar Flow Rate	
10 sccm	70.0
20 sccm	69.3
30 sccm	75.3
Input Power	
15 W	67.6
20 W	70.5
25 W	68.5

26.3.2.3 Condition for Mass Production of Ag/PEO-like Coatings

As seen above, the deposition of Ag/PEO-like films is a compromise between having an acceptable quantity of silver and maintaining a sufficient PEO character, to eventually preserve both antibacterial and non fouling properties. It was demonstrated in the previous sections that films produced at an Ar flow rate of 20 sccm and RF power of 20 W gave the best compromise of PEO character (27.5%) and Ag content (3.5%). Thus, the following deposition parameters have been utilized to deposit Ag/PEO-like films for protein adsorption and bacterial adhesion assays:

Ar flow rate: 20 sccm	DEGDME flow rate: 0.25 sccm
Input power: 20 W	Chamber pressure: 100 mTorr

26.2.3 Evaluation of Protein Adsorption

The literature on protein-conditioning films is very rich and many proteins have been studied for their effects on bacterial adhesion including albumin, fibrinogen, fibronectin, and collagen [14,42,43]. We have investigated the effects of conditioning layers of two important blood serum proteins, albumin and fibrinogen, which are also minor components of saliva.

Evidence of protein adsorption in XPS spectra is commonly identified as an increase in nitrogen content, due to the amino acid structural units of proteins [44], as determined by the intensity ratio of the N 1s and C 1s signals (N/C) [45–47]. The investigation of protein adsorption to the PEO-like surfaces is facilitated due to the chemical nature of the coatings. As the PEO-like and Ag/PEO-like coatings do not contain nitrogen functional groups, evidence of protein adsorption to these materials can be easily identified and qualitatively compared by XPS.

The XPS surface composition and O/C and N/C atomic ratios for the Ag-free 5-W and 15-W PEO-like films, and for Ag/PEO-like films after incubation in protein solution are displayed in Table 6. The data show that 5-W PEO-like coatings (i.e., the material with the highest PEO character) are the most effective at reducing and/or

preventing protein adsorption, and therefore show the best non fouling properties. The 5-W PEO-like coatings completely prevented the adsorption of albumin, within XPS detection limits, as wide-scans did not detect an N 1s signal. Only minimal adsorption of fibrinogen was detected (N 1s% = 0.4; N/C = 0.01). Moreover, the O/C ratio of the film is maintained after albumin exposure.

Table 6 Atomic percent for the 5 W and 15 W PEO-like and Ag/PEO-like films, following incubation in the protein solutions, bovine serum albumin and fibrinogen. In this figure BSA represents bovine serum albumin and F represents fibrinogen.

	C 1s (%)	O 1s (%)	Ag 3d (%)	N 1s (%)	O/C	N/C
5 W PEO-like	71.3	28.7	–	–	0.40	–
5 W PEO-like + BSA	71.7	28.3	–	–	0.39	–
5 W PEO-like + F	70.6	28.9	–	0.4	0.41	0.01
15 W PEO-like	75.8	24.3	–	–	0.32	–
15 W PEO-like + BSA	77.3	19.4	–	3.3	0.25	0.04
5 W PEO-like + F	70.0	20.8	–	9.2	0.30	0.13
Ag/ PEO-like	76.3	20.2	3.5	–	0.27	–
Ag/ PEO-like + BSA	73.8	18.9	1.6	5.7	0.26	0.08
Ag/ PEO-like + F	67.0	21.1	0.9	11.0	0.31	0.16

As expected, 15-W PEO-like films cannot be considered non fouling, due to their low PEO character, as both albumin and fibrinogen were found to adsorb to the coating. Albumin adsorbed to a much lower extent than fibrinogen, as attested by the N/C ratio of 0.04 and 0.13, respectively.

Of the three coatings tested, Ag/PEO-like films exhibited the lowest non fouling character, as they were found to exhibit the highest level of protein adsorption. Fibrinogen adsorbed to a much higher extent than albumin, with corresponding N/C ratios 0.16 and 0.08, respectively.

Lopez et al. [27] and Johnston et al. [26] suggested that a high retention of EO-monomer structure, or PEO character, is the key factor in determining the non fouling, protein- and cell-repulsive nature of plasma-deposited PEO-like coatings. These observations have been confirmed by our results, as 5-W, 15-W PEO-like and Ag/PEO-like coatings having very different PEO characters, 64.8%, 40.0% and 27.5%, respectively, exhibited the following trend of protein adsorption:

5-W PEO-like < 15-W PEO-like < Ag/PEO-like

The protein-adsorption characteristics of PEO-like materials have also been linked to surface wettability. It is known that proteins adsorb to a higher extent onto hydrophobic surfaces than to hydrophilic ones, usually in an irreversible fashion [48]. Besides the PEO character, the protein-adsorption trends of our films also follow the same trend of the advancing WCA values, as is evident by examining the data shown throughout this paper. As surface wettability is to some extent linked to the ether-

carbon content, it can be hypothesized that the non fouling nature of the films studied is related to both their PEO character and surface wettability.

26.3.4 Evaluation of Bacterial Adhesion

In order to identify the effects of combining non fouling and germicidal properties in one surface, 5-W, 15-W PEO-like and Ag/PEO-like coatings deposited on native PVC have been tested in a bacterial adhesion assay, using native PVC as reference. Adhesion was evaluated for four different *P. aeruginosa* strains including, the wild-type PAO1, the mutant AK44, and two different clinical isolates, 1.1.A1 and 19G12.

Figure 6 illustrates the micrographs following the testing of PAO1 adhesion to native PVC and Ag/PEO-like surfaces. Initial adhesion values to native PVC found for *P. aeruginosa* are 1.71×10^6, 2.24×10^6, 3.69×10^6, and 0.17×10^6 cells/cm^2 for the PAO1, AK44, 1.1.A1, and 19G12 strains, respectively. As illustrated, the Ag/PEO-like films deposited for this work, i.e., with Ag% of 3.5 and PEO character of 27.5%, completely prevented the adhesion of the four *P. aeruginosa* strains tested, with a 100% reduction in bacterial adhesion. On the contrary, silver-free 5-W and 15-W PEO-like films were not nearly as effective (data not shown) since their bacterial adhesion data reached the same value as for native PVC.

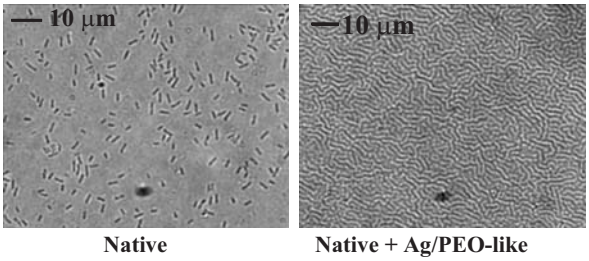

Figure 6 Micrographs illustrating the bacterial adhesion to native PVC (left) and Ag/PEO-like coatings (right) deposited using the following parameters: an Ar flow rate of 20 sccm, a DEGDME flow rate of 0.25 sccm, an input power: of 20 W and a chamber pressure: 100 mTorr. Note: the reader should be aware that the mosaic pattern seen on the Ag/PEO-like micrograph does not correspond to bacterial cells, it is in fact the surface morphology of the Ag/PEO-like coating on native PVC.

If the non fouling properties of the Ag/PEO-like coatings were to have a special effect on the initial adhesion of *P. aeruginosa* due to the creation of a combined non fouling and germicidal surface, then a difference in the initial adhesion values would be observed between native PVC and non fouling 5-W PEO-like surfaces. However, no difference was observed, probably because the PEO character (64.8%) of our 5-W PEO-like coatings is not sufficient to have an effect on bacterial adhesion, in our experimental conditions. Moreover, the Ag/PEO-like surface, which was ob-

served to adsorb albumin and fibrinogen significantly (see Table 6), was the only surface tested that proved to be 100% effective at reducing bacterial adhesion. This comparison allows us to state that the abatement of bacterial adhesion on Ag/PEO-like coatings is only due to the presence of silver. In aqueous environments, Ag/PEO-like coatings swell, very likely with water; this interaction leads to a leaching of Ag^+ ions into the surrounding medium, where they may exert a germicidal action. Evidence of the release of Ag^+ ions in water has been published in ref. [31]; in this logic, Ag/PEO-like coatings may be considered as thin "drug release" thin layers.

The mechanisms of interaction of silver with micro-organisms were understood only recently and are explained in the literature (for further details, please consult Balazs et al. [1] and Davies and Etris [10]). Due to its unique interaction with oxygen, the effects of metallic or monovalent silver (oxidation state 0 or +1) on microbial activity are of primary interest. Both metallic and monovalent silver have an affinity for sulfhydryl (–SH) groups exposed on the cell membranes of bacteria. In the case of metallic silver, the atomic oxygen adsorbed on the surface of the metal reacts with the pairs of the –SH groups on the surface by replacing the hydrogen atoms (as water), polymerizing the proteins through polycondensation reactions rendering them inactive [10]. The resultant R–S–S–R bonds blocks bacterial respiration and electron transfer, resulting in cell disintegration and death. Monovalent silver ions also react readily with –SH groups, producing –S–Ag groups that inhibit hydrogen transfer, which is the main energy-transfer system of bacteria, resulting in cell death.

The toxic effects of metallic and monovalent silver are bacterial-specific and contact will prove fatal to pathogens containing sulfhydryl functional groups [11]. Silver has been proven effective in killing over 650 disease-causing organisms, and is active against gram-negative bacteria, like *P. aeruginosa*, as well as gram-positive bacteria, funghi, protozoa, and certain viruses [11]. The 2500-year history of application in water purification has further established the nontoxicity of silver at low concentrations [10,49], and Davies and Etris [10] further describe that monovalent silver is nontoxic to mammalian cells because sulfhydryl (–SH) groups are not exposed on the membranes. However, the cytotoxicity of Ag is still under scrutiny, for certain medical applications [50]. As mammalian cell nontoxicity is an extremely important attribute for a surface-modification method intended for medical devices that are in contact with mammalian tissues, we are currently evaluating silver release and cytotoxicity to various mammalian cells [41].

Due to the bacterial-toxic effects of released silver ions [10], it is hypothesized that plasma-deposited Ag/PEO-like films may offer long-term resistance to bacterial adhesion and prevent the colonization of biomaterial surfaces.

Hence, Ag/PEO-like coatings created by PE-CVD may thus represent a very attractive option to solve the problem of bacterial adhesion to biomaterial surfaces. Glow-discharge plasma processes have been widely used in the surface modification of polymers, due to the localized surface treatment that is possible, without changing bulk properties, such as mechanical stability [51–53]. Additional advantages include the fact that successful plasma processes can be performed on various sub-

strates, leading to strongly adherent and pinhole free coatings [51–53]. Properly designed reactor configurations allow scientists to homogeneously process the external surfaces of various three-dimensional substrates [52]. Thus, PE-CVD of organic thin films represents a simple, one-step coating process that can be combined with plasma-sterilization methods to yield large-scale production processes [27]. After having identified appropriate deposition parameters, Ag/PEO-like coatings could be deposited on most biomedical materials. This further demonstrates the versatility of PE-CVD methods for applications in biomaterials modifications.

26.4 Conclusion

We have presented a strategy to eliminate bacterial adhesion to medical-grade PVC that attempts to combine the non fouling properties of conventional PEO materials and the bacterial-toxic effects of silver ions. Ag/PEO-like films [25] were adapted to native PVC substrates and deposition parameters were identified that maximize the Ag content while maintaining a certain PEO character. In order to identify the origin of the antibacterial effects of the Ag/PEO-like coatings, two different forms of silver-free PEO-like films, having a low and high PEO character, are used as control surfaces.

The effects of input power on the PEO character of the PEO-like films lacking silver were investigated. It was observed that a film with the best PEO character resulted at low input power, or a low DEGDME monomer fragmentation regime.

In addition, the roles of argon flow rate and input power on the Ag/PEO-like film composition were studied to identify the trends in PEO character and silver content of the films. Increases in both argon flow rate and power input produced a decrease in PEO character and an increase of Ag content of Ag/PEO-like films, respectively. Ar flow rate and input power were determined to be deposition parameters that drive the sputtering of the silver from the cathode, as well as the fragmentation of DEGDME in the glow.

This publication further examined protein adsorption and *P. aeruginosa* adhesion to PVC substrates coated with PEO-like and Ag/PEO-like coatings, in order to identify any link between non fouling and antibacterial properties in the films. The 5-W PEO-like films completely prevented the adsorption of albumin, and only minimal fibrinogen adsorption was detected. The 15-W PEO-like films cannot be considered a completely non fouling surface as both albumin and fibrinogen were found to adsorb to the coatings. Ag/PEO-like coatings were found to exhibit the highest level of protein adsorption. It was concluded that it is PEO character and, consequently, the related surface wettability of the plasma-deposited films that is responsible for the different non fouling characters of the coatings.

Although PEO-like films with the highest PEO character showed protein repulsive, non fouling characteristics, they did not prevent the adhesion of *P. aeruginosa*. On the contrary, Ag/PEO-like films, despite their poor non fouling properties, exhibited a complete reduction in bacterial adhesion as compared to native PVC. It is

indeed the silver content of Ag/PEO-like films that is essential to the antibacterial properties of these coatings.

PE-CVD of Ag/PEO-like coatings represents a possibility to produce an antibacterial surface that can be adapted to almost any biomaterial surface.

Acknowledgements

The authors would like to thank Nicolas Xanthopoulos for his assistance with XPS analysis. We greatly acknowledge the financial support of the Common Program on Biomedical Engineering and Research, Universities of Lausanne and Geneva and EPFL, (1999-2002).

References

[1] Balazs DJ, Triandafillu K, Chevolot Y, Aronsson B-O, Harms H, Descouts P, Mathieu HJ. Surface modification of PVC endotracheal tubes by oxygen glow discharge to reduce bacterial adhesion. Surf Interface Anal 2003; 35: 301–309.

[2] Triandafillu K, Balazs DJ, Aronsson B-O, Descouts P, Tu Quoc P, van Delden C, Mathieu HJ, Harms H. Variability in the adhesion of Pseudomonas aeruginosa strains to PVC of endotracheal tubes and oxygen plasma-treated PVC. Biomaterials 2003; 24: 1507–1518.

[3] Balazs DJ, Triandafillu K, Wood P, Chevolot Y, van Delden C, Harms H, Hollenstein C, Mathieu HJ. Inhibition of Bacterial Adhesion on PVC Endotracheal Tubes by RF- Oxygen Glow Discharge, Sodium Hydroxide and Silver Nitrate Treatments. Biomaterials 2004; 25: 2139–2151.

[4] Vincent JL, Bihari DJ, Suter PM, Bruining HA, White J, Nicolas-Chanoin MH, Wolff M, Spencer RC, Hemmer M. The prevalence of nosocomial infection in intensive care units in Europe. Results of the European Prevalence of Infection in Intensive Care (EPIC) Study. J Am Med Assoc 1995; 274: 639–644.

[5] Sottile FD, Marrie TJ, Prough DS, Hobgood CD, Gower DJ, Webb LX, Costerton JW, Gristina AG. Nosocomial pulmonary infection: Possible etiologic significance of bacterial adhesion to endotracheal tubes. Crit Care Med 1986; 14: 265–270.

[6] Gombotz WR, Guanghui W, Horbett TA, Hoffman AS. Protein adsorption to poly(ethylene oxide) surfaces. J Biomed Mater Res 1991; 25: 1547–1562.

[7] Tirelli N, Lutolf MP, Napoli A, Hubbell JA. Poly(ethylene glycol) block copolymers. Rev Molec Biotechnol 2002; 90: 3–15.

[8] Jeon SI, Lee JH, Andrade JD, De Gennes PG. Protein-surface interactions in the presence of polyethylene oxide I. Simplified theory. J Colloid Interface Sci 1991; 142: 149–158.

[9] Bergström K, Holmberg K, Safranj A, Hoffman AS, Edgell MJ, Kozlowski A, Hovanes BA, Harris JM. Reduction of fibrinogen adsorption on PEG-coated polystyrene surfaces. J Biomed Mater Res 1992; 26: 779–790.

[10] Davies RL, Etris SF. The development and functions of silver in water purification and disease control. Catal Today 1997; 36: 107–114.

[11] Fox CL, Rappole BW, Stanford W. Control of Pseudomonas infection in burns by silver sulfadiazine. Surg Gynecol Obstet 1969; 128: 1021.

[12] Wysor MS. Silver sulfadiazine. In: Antibiotics, VI. Hahn FE, (ed.) Berlin: Springer-Verlag, 1983.

[13] Vacheethasanee K, Marchant RE. Surfactant polymers designed to supress bacterial (*Staphylococcus epidermidis*) adhesion to biomaterials. J Biomed Mater Res 2000; 50: 302–312.

[14] Gristina AG, Naylor PT, Myrvik QN, Wagner WD. Microbial adhesion to biomaterials.

In: High Performance Biomaterials: A Comprehensive Guide to Medical and Pharmaceutical Applications. Lancaster: Technomic Publishing Company, Inc., 1991. p. 143–154.

[15] Sheu M-S, Hoffman AS, Ratner BD, Feijen J, Harris JM. Immobilization of polyethylene oxide surfactants for non fouling biomaterial surfaces using an argon glow discharge treatment. J Adhes Sci Technol 1993; 7: 1065–1076.

[16] Leckband D, Sheth S, Halperin A. Grafted poly(ethylene oxide) brushes as non fouling surface coatings. J Biomater Sci Polym Ed 1999; 10: 1125–1147.

[17] Kidane A, Lantz GC, Jo S, Park K. Surface modification with PEO-containing triblock copolymer for improved biocompatibility: in vitro and *ex vivo* studies. J Biomater Sci Polym Ed 1999; 10: 1089–1105.

[18] Holmberg K, Bergström K, Brink C, Osterberg E, Tiberg F, Harris JM. Effects of protein adsorption, bacterial adhesion and contact angle of grafting PEG chains to polystyrene. J Adhes Sci Technol 1993; 7: 503–517.

[19] Defife KM, Hagen KM, Clapper DL, Anderson JM. Photochemically immobilized polymer coatings: effects on protein adsorption, cell adhesion, and leukocyte activation. J Biomater Sci Polym Ed 1999; 10: 1063–1074.

[20] Dewez J-L, Berger V, Schneider Y-J, Rouxhet PG. Influence of substrate hydrophobicity on the adsorption of collagen in the presence of pluronic F68, albumin, or calf serum. J Colloid Interf Sci 1997; 191: 1–10.

[21] Amiji M, Park K. Prevention of protein adsorption and platelet adhesion on surfaces by PEO/PPO/PEO triblock copolymers. Biomaterials 1992; 13: 682–692.

[22] Lee JH, Kopecek J, Andrade JD. Protein-resistant surfaces prepared by PEO-containing block copolymer surfactants. J Biomed Mater Res 1989; 23: 351–368.

[23] Balazs DJ, "Surface Modification and Characterization of Endotracheal Tube Surfaces to Reduce Pseudomonas aeruginosa adhesion: Plasma Treatments, Plasma Polymerization and Chemical Methods," Swiss Federal Institute of Technology, 2003.

[24] Favia P, Creatore M, Palumbo F, Colaprico V, d'Agostino R. Process control for plasma processing of polymers. Surf Coat Tech 2001; 142–144: 1–6.

[25] Favia P, Vulpio M, Marino R, d'Agostino R, Mota RP, Catalano M. Plasma-deposition of Ag-containing polyethyleneoxide-like coatings. Plasmas and Polymers 2000; 5: 1–14.

[26] Johnston EE, Ratner BD, Bryers JD. RF plasma deposited PEO-like films: surface characterization and inhibition of Pseudomonas aeruginosa accumulation. In: Plasma Processing of Polymers. d'Agostino R, Favia P, Fracassi F, (eds). Dordrecht: Kluwer Academic Publishers, 1997, p. 465–476.

[27] Lopez GP, Ratner BD, Tidwell CD, Haycox CL, Rapoza RJ, Horbett TA. Glow discharge plasma deposition of tetraethylene glycol dimethyl ether for fouling-resistant biomaterial surfaces. J Biomed Mater Res 1992; 26: 415–439.

[28] Shen M, Pan YV, Wagner MS, Hauch KD, Castner DG, Ratner BD, Horbett TA. Inhibition of monocyte adhesion and fibrinogen adsorption on glow discharge plasma deposited tetraethylene glycol dimethyl ether. J Biomater Sci Polym Ed 2001; 12: 961–978.

[29] Beyer D, Knoll W, Ringsdorf H, Wang JH, Timmons RB, Sluka P. Reduced protein adsorption on plastics via direct plasma deposition of triethylene glycol monoallyl ether. J Biomed Mater Res 1997; 36: 181–189.

[30] Favia P, d'Agostino R. Plasma treatments and plasma deposition of polymers for biomedical applications. Surf Coat Technol 1998; 98: 1102–1106.

[31] Favia P, d'Agostino R, Lusvardi G, Menabue L. Ag/PEO-like Plasma Deposited Coatings: Process Control and Ag^+ Release. il Vuoto 2000; 75: 3–4.

[32] Jones DS, McGovern JG, Woolfson AD, Gorman SP. Role of physiological conditions in the oropharynx on the adherence of respiratory bacterial isolates to endotracheal tube poly(vinyl chloride). Biomaterials 1997; 18: 503–510.

[33] Milleding P, Carlen A, Wennerberg A, Karlsson S. Protein characterisation of salivary and plasma biofilms formed in vitro on noncorroded and corroded dental ceramic materials. Biomaterials 2001; 22: 2545–2555.

[34] Good RJ. Contact angle, wetting, and adhesion: a critical review. In: Contact Angle, Wettability and Adhesion. Mittal KL, (ed.) Utrecht, The Netherlands: VSP, 1993. p. 3–36.

[35] Holloway BW. Genetic recombination in Pseudomonas aeruginosa. J Gen Microbiol 1955; 13: 572–581.
[36] Lightfoot J, Lam JS. Molecular cloning of genes involved with expression of A-band lipopolysaccharide, an antigenically conserved form, in Pseudomonas aeruginosa. J Bacteriol 1991; 173: 5624–5630.
[37] Rijnaarts HHM, Norde W, Bouwer EJ, Lyklema J, Zehnder AJB. Bacterial adhesion under static and dynamic conditions. Appl Environ Microbiol 1993; 59: 3255–3265.
[38] Johnston EE, Ratner BD. Surface characterization of plasma deposited organic thin films. J Electron Spectrosc 1996; 81: 303–317.
[39] Inagaki N. Hydrophilic surfaces (plasma treatment and plasma polymerization). In: CRC Press, Inc., 1996.
[40] Asfardjani K, Segui Y, Aurelle Y, Abidine N. Effect of plasma treatments on wettability of polysulfone and polyetherimide. J Appl Polym Sci 1991; 43: 271–281.
[41] Favia P. Unpublished results.
[42] Dankert J, Hogt AH, Feijen J. Biomedical polymers: bacterial adhesion, colonization, and infection. Crit Rev Biocompat 1986; 2: 219–301.
[43] An YH, Friedman RJ. Concise review of mechanisms of bacterial adhesion to biomaterial surfaces. J Biomed Mater Res (Appl Biomater) 1998; 43: 338–348.
[44] Stryer L. Biochemistry, fourth edn, New York: W. H. Freeman and Co., 1995.
[45] Dewez J-L, Schneider Y-J, Rouxhet PG. Coupled influence of substratum hydrophilicity and surfactant on epithelial cell adhesion. J Biomed Mater Res 1996; 30: 373–383.
[46] Dewez J-L, Lhoest J-B, Detrait E, Berger V, Dupont-Gillain CC, Vincent L-M, Schneider Y-J, Bertrand P, Rouxhet PG. Adhesion of mammalian cells to polymer surfaces: from physical chemistry of surfaces to selective adhesion on defined patterns. Biomaterials 1998; 19: 1441–1445.
[47] Tidwell CD, Castner DG, Golledge SL, Ratner BD, Meyer K, Hagenhoff B, Benninghoven A. Static time-of-flight secondary ion mass spectrometry and X-ray photoelectron spectroscopy characterization of adsorbed albumin and fibronectin films. Surf Interface Anal 2001; 31: 724–733.
[48] Paulsson M, Kober M, Freij-Larsson C, Stollenwerk M, Wesslén B, Ljungh A. Adhesion of staphylococci to chemically modified and native polymers, and the influence of preadsorbed fibronectin, vitronectin and fibrinogen. Biomaterials 1993; 14: 845–853.
[49] Guidelines for drinking-water quality. In: Health criteria and other supporting information. Geneva: World Health Organization, 1996. p. 338–343.
[50] Stickler DJ. Biomaterials to prevent nosocomial infections: is silver the gold standard? Curr Opin Biotech 1999; 13: 389–393.
[51] Yasuda H. Plasma Polymerization London: Academic Press, Inc., 1985.
[52] Morosoff N. An introduction to plasma polymerization. In: Plasma Deposition, Treatment, and Etching of Polymers. d'Agostino R, (ed.) San Diego: Academic Press, Inc., 1990. p. 1–93.
[53] Ratner BD, Chilkoti A, Lopez GP. Plasma deposition and treatment for biomaterial applications. In: Plasma Deposition, Treatment, and Etching of Polymers. d'Agostino R, (ed.) San Diego: Academic Press, Inc., 1990. p. 463–516.

27
Plasma-aided Micropatterning of Polystyrene Substrates for Driving Cell Adhesion and Spreading

E. Sardella, R. Gristina, G.S. Senesi, R. d'Agostino, P. Favia

Abstract

Coatings with polyethylene oxide (PEO)-like films deposited by RF (13.56 MHz) glow discharges and featuring a total cell-repulsive effect were deposited on polystyrene (PS) samples. Substrates containing tracks of PS of petri dishes surrounded by PEO-like domains have been prepared with a good spatial resolution by using a masking procedure. The behavior of the substrates after seeding NCTC2544 human keratinocytes and 3T3 Murine fibroblasts has been studied. It has been found that also PS tracks are able to drive cells up to confluence, provided that a longer incubation time is provided. A phenomenological interpretation is suggested.

27.1
Introduction

Several years ago pharmacological therapies and surgery were the only possible approaches to solve injuries and malfunctions of human organs, while transplants were still considered just a hope. Today, instead, cell and tissue engineering open new frontiers in reconstructive medicine. The fundamental principle of this young, fast-growing discipline can be found in the fact that properly surface/bulk-engineered 2D/3D scaffolds of certain materials, seeded in vitro with cells, can support the growth of new biological tissues that could possibly be implanted. To transform this hypothesis into a real goal in medical applications, it is necessary to understand how a material could influence cell adhesion. Many contributions show that cells "feel" the surface of the material where they adhere, in terms of chemistry and morphology, and react to such stimuli in different ways [1–6]. Attachment and/or spreading of eukaryotic cells is observed on 2D-patterned surfaces containing features that have dimensions larger than large molecules (~1–10 nm) and smaller than or equal to cellular dimensions (~1–50 μm) [7]. Another important piece of information in this background, well known for years [8], is that the reaction of cells to external surfaces in biological media is mediated by a thin layer of adsorbed proteins, which is generally driven by surface chemistry.

The fact that cells react to surface topography, down to about 5 nm of roughness, has been recognized only recently; it opens interesting opportunities in tissue engineering. Specific cell/surface interactions are on the way to be fully explained and utilized in reconstructive therapies [9–15]. In general, microarrangement of cells on simple patterns allows to obtain information on environmental factors influencing cell adhesion and spreading [16,17]. Cell cultures on micropatterned materials are nowadays studied for a wide range of applications, including biosensors, and diagnostics [18–22], besides cell and tissue engineering.

PEO polymers show high resistance to the absorption of biomolecules and to adhesion of cells in water media and, for this reason, are designed as non fouling materials [23–26]. In fact, several methods have been proposed to immobilize PEO moieties on biomaterial surfaces [27–30]. On the other hand, low-pressure plasmas, have gained a large popularity in the last thirty years for their suitability to make "customized" surfaces [31–33]. Such discharges have also been utilised for depositing PEO-like thin films featuring fouling resistance that appears to overcome some drawbacks correlated to conventional chemical synthesis, like the risk of leaches from chemically modified surfaces, since plasma-deposited films are covalently bonded to the substrate [34,35].

Plasma-deposited PEO-like thin films (PD-PEO) are mainly composed by ether carbon ($–CH_2CH_2O–$) units, as in conventional PEO polymers; also other moieties, however (i.e. ester, carbonyl, carboxyl, hydrocarbon), including a certain degree of crosslinking, are usually present. Many papers indicate a tight relationship between the per cent of ether carbon of PD-PEO and their ability to resist to biomolecules adsorption and/or cell adhesion. This parameter, the PEO character, expresses how much the structure of the coating resembles that of a conventional PEO, i.e. it gives a quantitative measure of the structure retention. The PEO character can be quantified by X-ray photoelectron spectroscopy (XPS) with the ratio of ether carbon component (C1 component, ~286.5 eV of binding energy [35,36]) to the total C1s signal of the coating. The more intense the C1 component, the higher the PEO character of the coating, the better its non fouling properties [37].

PD-PEO produced under "soft" plasma conditions (i.e., low power input, modulated regime, etc.) are characterized by a very high PEO character (70–80%; [38–40]).

This paper deals with PD-PEO characterised by a high PEO character, deposited on PS substrates to discourage adhesion of keratynocyte and fibroblasts cell-lines.

Plasma techniques can be used either for a conformal modification of flat or textured surfaces, or as a tool for microstructuring surfaces. Simple plasma-patterning procedures use a physical mask (e.g., a metal grid for TEM, or a laser-cut polymer or metal sheet) to expose only certain zones of the substrate to a plasma process. It is important to report that pattern defects on the final surface can often be attributed to a loose mask–substrate contact [41]. In spite of this inconvenience, however, this technique allows patterning of large areas with different geometries, on a scale that is in the range of cellular dimensions, with a relatively cheap procedure. By this technique, PD-PEO microdomains were spatially arranged on PS to drive cell adhesion along predefined directions.

This study is aimed to:

- evaluating the ability of the microstructuring procedure to transfer the pattern on flat PS;
- producing different patterns to promote cell adhesion and orientation along predefined directions;
- studying the effect of topographical and chemical constraints on cell morphology.

Different patterns were investigated by changing the physical mask.

27.2 Materials and Methods

27.2.1 Surface Modifications

shards of Cell-culture PS petri dishes (ccPS) and crystalline optically flat PS discs (∅ 12 mm, thickness 1.2 mm; Goodfellow) were used as substrates for depositing PEO-like coatings. Tissue-culture PS or ccPS is the material commercially available for manufacturing Petri dishes widely used for inducing cell attachment and spreading in cell-culture procedures. In ccPS waves, PS is primarily modified by corona discharges or by plasma treatments with O- or N-containing gases.

In these work an asymmetric stainless steel plasma reactor was used, with two vertical parallel-plate stainless steel electrodes [43] The smaller electrode was connected to an RF (13.56 MHz) power supply trough a matching network unit, whereas the largest electrode, sample holder, was grounded. The pressure, kept at 400 mTorr, was monitored with a MKS baratron. Glow discharges fed by a mixture of di(ethyleneglycole) di(methylether) (DEGDME, Sigma Aldrich) vapors and argon (0.4 sccm DEGDME, 5 sccm Ar) were used to obtain PD-PEO coatings at 5 W RF power value.

Microstructuring was obtained by depositing PD-PEO onto PS substrates through round copper grids (G50p, 80 μm bars, 400 μm gaps, ∅ 3 mm, 500 μm border; G150p, 40 μm bars; 200 μm gaps; ∅ 3 mm, 500 μm border; both <10 μm thick, TAAB Laboratories). The grids were tightly attached to the substrate by making use of Kapton adhesive tape at grid edges; some pressure was applied to assure a better mask/substrate contact and to reduce the undesired plasma processing of mask-covered regions leading to the formation of flaw edges. A deposition time of 60 min has been utilized for all experiments resulting in coatings 60 ± 20 nm thick, as measured by an alpha-step 500 KLA-TENCOR profilometer.

27.2.2 Surface Diagnostic

A PHI 5300 XPS instrument equipped with nonmonochromatic MgK_α and AlK_α X-ray sources has been used to probe homogeneous coatings, at a take-off angle of 45°

(sampling depth ~7 nm). XPS wide-scan (BE = 0–1000 eV) and detailed C1s and O1s spectra were acquired C1s spectra were best-fitted into four peak components; before charging correction, the positions of the peaks were fixed at +1.6 eV (C1; C–OH(C)), +3.6 eV (C2; (C=O, O–C–O) and +4.2 eV (C3; COOH(C)) respectively, from the hydrocarbon C0 (C–H(C)) peak component; the C0 peak was set at 285.0 eV as reference. A Gaussian per cent of 85–100% and FWHM values in the range 1.5–2.1 eV were used in the best fitting. Elemental compositions were averaged from five replicates. An AXIS Ultra (Kratos) spectrometer was used at the Fraunhofer Institute for Interfacial Engineering and Biotechnology (Stuttgart, Germany) to obtain chemical information at high spatial resolution on microstructured samples. A monochromatic AlK_{α} X-ray source and an incorporated electrostatic deflection system allowed multipoint analysis and 2D 800 µm × 800 µm "chemical maps". Choosing the energy of the C0 component of the C1s signal and scanning the focal point of the lenses of the XPS instrument across the sample we get information about the lateral distribution of the corresponding species (chemical state) at the surface. Multipoint spectral analyses were performed by a small X-ray spot, 27 µm wide.

Water contact angles (WCA) were measured with a Ramé-Hart 100-00 goniometer within 10 min after processes. Advancing WCA (θ_a) were measured by increasing the volume of the water drop, 2-µl steps, until the WCA remained constant. Receding WCA (θ_r) were measured by decreasing the volume of the drop until the WCA value remained constant and the solid/liquid interface started to decrease. Values reported result from the average of at least 5 individual measurements per sample.

Morphological analysis of homogeneous and micropatterned substrates was performed by atomic force microscopy (AFM, AutoProbe CP-Research) scans in non-contact mode as needed for "soft" materials, to investigate the topography of the samples at the nanometer scale. The square mean roughness (R_{rms}) is defined as:

$$R_{rms} = \sqrt{\frac{\sum_{n=1}^{N} (a_n - \overline{a})}{N-1}}$$

where a is the height and a is the mean height.

27.2.3 Cell Culture

Infinity Telomerase Immortalised human NCTC2544 keratynocyte and murine 3T3 fibroblast cell lines were used. Each experiment was performed on at least four samples for each kind of substrate; native PS discs, and ccPS plates (Falcon) were used as control. Cells were obtained after trypsinization of confluent or near-confluent cultures, seeded at 2×10^4 cells/well in suspension on all test materials and incubated (37 °C; 5% CO_2 / 95% air) in Dulbecco's modified Eagle's medium (DMEM) supplemented with 10% fetal bovine. The number and morphology of cells attached on flat substrates are determined at various time intervals using digital images acquired from a phase contrast light microscope (Leica DM IL). The number of

adherent cells was counted on at least 10 areas of 0.8 mm^2 per sample and, for morphological studies, cells were divided in round and spread cells according to their shapes. We assume cells to be spread when the ratio between the two main diameters is higher than 1.5. The unpaired Student's t-test was used to evaluate the statistically significant differences in the number of adhered and spread cells between test samples. Data were taken to be significant when a $p < 0.05$ was obtained.

Cells were fixed in 4% paraformaldehyde/PBS. Fixed cells have been stained with Coomassie blue.

Scanning electron microscopy (SEM) analysis were performed on hTERT-BJ1 cells in the Centre of Cell Engineering, University of Glasgow. For SEM, cells were fixed with 1% glutaraldehyde /0.1M sodium cacodylate solution, and dehydrated through a series of alcohol/water solutions. The samples were then sputter-coated with gold before examination with a Hitachi S800 field emission SEM (accelerating voltage 10 keV).

27.3 Results and Discussion

27.3.1 PD-PEO Coatings

Native and PEO-like coated substrates were characterised by means of XPS analyses; no elements other than carbon and oxygen are present on native PS, ccPS and PEO-like coatings (Table 1). After plasma deposition (400 mTorr, 5 sccm Ar, 0.4 sccm DEGDME, 5 W, 1 h) PS substrates were coated by PD-PEO, whose C1s spectrum is shown in Fig. 1. The signal can be best fitted in three peaks,

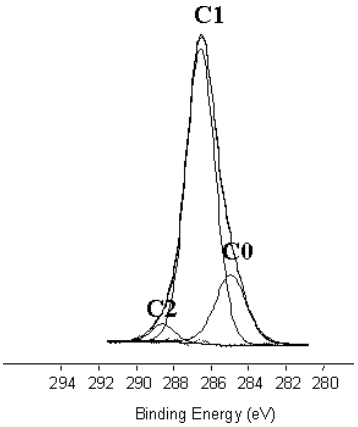

Figure 1 C1s spectrum of a PEO-like coating deposited on PS at 60 min of deposition time (thickness 60 nm). Similar results were acquired on PEO-like coatings deposited at 15 min as deposition time.

C0 (21 ± 2%), C1 (76 ± 3%), C2 (3 ± 1%), attesting to the very high PEO character of the coating. To check whether the functionality originating the C1 contribute were ether or hydroxyl or both, the C1s/O1s XPS intensity ratio (measurements properly corrected for atomic sensitivity factors) was compared to the same ratio calculated from the best-fitting C1s data, assuming that the C1 contribute is exclusively due to the ether (C–O–C) carbons. Negligible differences in two C/O ratios were found, thus showing that, for PEO-like coatings with high PEO character, the C1 component is really due only to ether groups (Table 2).

Table 1 Atomic percent of carbon and oxygen on: tissue culture PS (ccPS); conventional PS (PS); PEO-like coated PS (PS+PEO-like; 5 W, 0.4 sccm DEGDME, 5 sccm Ar, 400 mTorr) deposited at 60 min and 15 min of deposition time. The spectra were acquired at 45° as take-off angle.

Substrate	%C	%O
ccPS	89.2 ± 0.4	10.8 ± 0.4
PS	99.0 ± 0.2	1.0 ± 0.2
PEO-like	70.6 ± 1.0	29.4 ± 1.0

Table 2 XPS C/O ratio of PD-PEO coatings (0.4 sccm DEGDME, 5 sccm Ar, 400 mTorr, 1 h, 5 W) calculated from the corrected C1s/O1s intensity ratio (C/O_{exp}), with the same ratio calculated from the C_n ($n = 0$–3) components of the best fitted C1s signal assuming that: *) the C1 contribute is exclusively due to the ether (C–O–R) carbons; **) the C1 contribute is exclusively to hydroxyl (C-OH) carbons. C2 and C3 contributes were always associated, respectively, to carbonyl and carboxyl groups.

C/O_{exp}	C0 (%)	C1 (%)	C2 (%)	C3 (%)	(*)C–OR/O	(**)C–OH/O
2.38 ± 0.03	17 ± 2	80 ± 2	2.8 ± 1	0.2 ± 0.1	2.3 ± 0.1	1.2 ± 0.1

PEO materials and PD-PEO generally exhibit hydrophilic properties due to the interactions of EO units and other polar groups, eventually present in the coating, with water molecules.

The hydrophilic character of PEO-like coatings was investigated by WCA measurements. PD-PEO coating showed θ_r of 36 ± 2°, and θ_a of 56 ± 2°, much lower than the WCA measured on untreated PS (85 ± 2°). To ascertain the stability of the coatings in water media, coated PS samples were soaked in distilled water for 15 days; it was found that the chemical composition of the coated surfaces remained unmodified, indicating good stability and good adhesion (results not shown). PD-PEO coatings were scanned by means of non contact mode AFM, showing a very low and constant R_{rms} value (0.5 ± 0.1 nm), which is in the dimension range of large macromolecules (1–10 nm). These low Rrms values allowed us to exclude any hypothesis of correlation between cell resistance of PEO-like coatings and their topography [7].

In order to check the non fouling properties of PD-PEO, keratinocyte (NCTC2544) and fibroblast (hTERT BJ1, 3T3 Murine) cell lines were seeded on

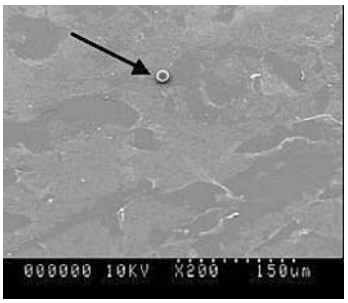

Figure 2 hTERT BJ1 human fibroblast cell line on PEO-like coated PS. As shown only one spheric-like cell adheres on the whole PEO-like coated substrate (arrow).

plasma-modified substrates. No cells were found on the coatings, even after 7 days of culture, thus confirming the excellent cell-repulsive character of PD-PEO. SEM images confirm that only very few hTERTBJ1 cells were found, occasionally, on PD-PEO (e.g., a single cell on the entire area monitored). In these few cases cells appear with a perfectly globular morphology, which minimizes the membrane/material contact area and all possible cell/substrate interactions (Fig. 2). Similar results were obtained on NCTC2544 Human keratinocytes and 3T3 Murine fibroblasts.

The complete absence of eukaryotic cells on PEO-like surfaces might also be ascribed to a cytotoxic effect of the coating, but this was not supported by any observation. For example, the optical micrographs in Fig. 3 allow us to observe that, although only clusters of dead cells float in the cell-culture medium, a good cell adhesion is observed at the bottom of the wells where the PEO-like coated samples were

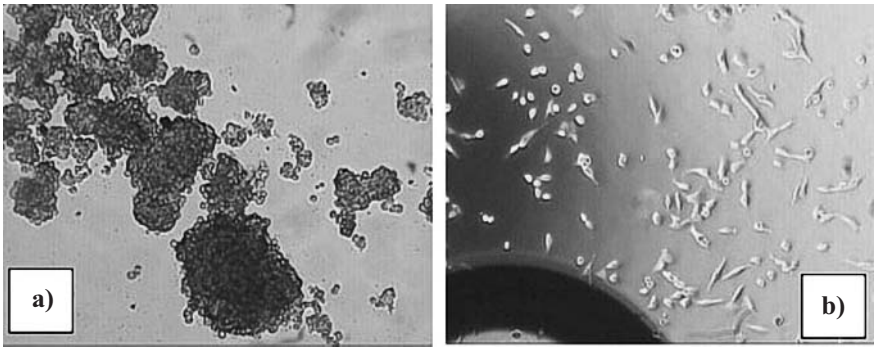

Figure 3 Optical microscopy images of 3T3 fibroblasts seeded on PEO-like coatings (400 mTorr, 0.4 sccm DEGDME, 5 sccm Ar, 5 W) deposited on PS. (a) no cells adhere on the substrate and only clusters of dead cells floating in the culture medium are observed; (b) 3T3 fibroblasts cells adhere on the well where the PEO-coated sample is placed, attesting to the noncytotoxicity of the PEO-like coatings.

cell-seeded; this means that no toxic effects are produced by PD-PEO, i.e., the coating does not release toxic molecules in the cell-culture medium.

For cell-culture experiments uncoated PS substrates were used as reference. The cell morphology of NCTC2544 human keratinocytes on native and ccPS appears to be influenced by the chemical characteristics of the substrate, but also by the incubation time (Fig. 4). After 21 h there are more spread cells on both PS substrates than after 3 h of incubation. The above experiments confirm that ccPS is a material more suitable to support cell-adhesion than native PS, very likely due to the presence of oxygen-containing groups on ccPS surface. Similar results were obtained for 3T3 Murine Fibroblasts.

Although native PS is considered an unsuitable material for cell attachment and spreading, still it is able to support cell growth much more than PD-PEO. Chemical patterns leading to cell-adhesive domains alternated with cell-repulsive ones have been proposed among other methods to create micropatterns and study the effect on cell- adhesion and morphology. In this work, PS has been used as "cell-adhesive" domains in micropatterned surfaces.

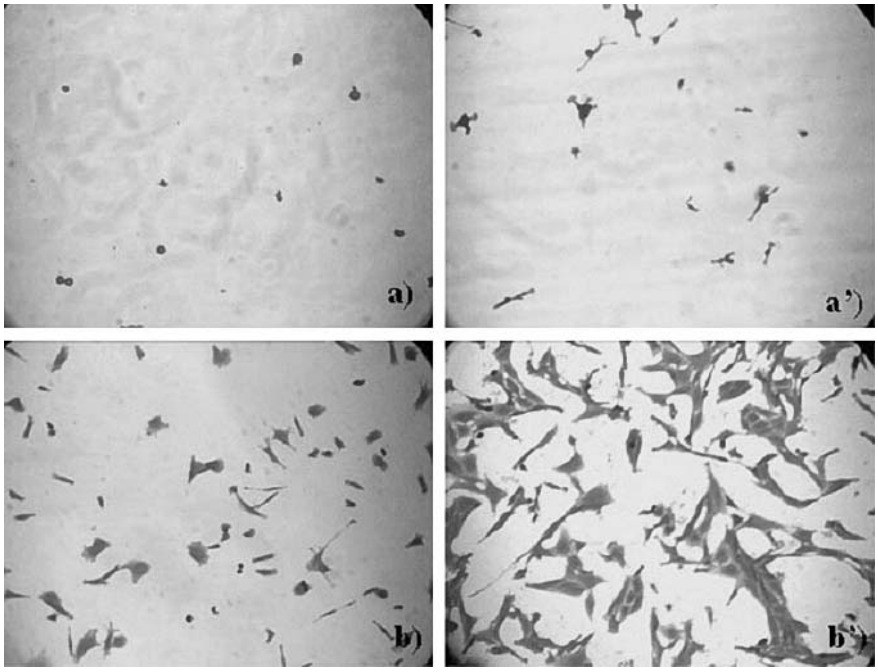

Figure 4 NCTC2544 human cell lines on native PS (a and a′) and on ccPS (b and b′). After PFA fixation cells were stained by Comassie blue. Native PS can be considered a nonsuitable material to support cell-adhesion and spreading because after 3 h (a) and after 21 h (a′) few cells adhere on native PS, mostly with a spherical shape. On ccPS a higher number of adhered cells was observed both after 3 h (b) and after 21 h (b′) incubation time. Most of the adhered cells on ccPS are spread.

27.3.3
Micropatterning of PEO-like Coatings

The "physical mask" procedure described in Sect. 2.1 was used on both native PS and ccPS; round TEM copper grids were used as physical masks: G50p, 80 µm bars spaced by 400 µm gaps; G150p, 50 µm bars spaced by 200 µm gaps. The external border ring of these masks is 500 µm wide.

Microstructured samples consisted of microarrangements of "cell-adhesive" tracks (native PS or ccPS) alternated with wider cell repulsive PEO-like domains.

Due to the imperfect mask/substrate contact, the PEO-like deposition partially entered below the mask, and PS tracks resulted shrunk with respect to the masking elements (bars, border) of the grid (Fig. 5).

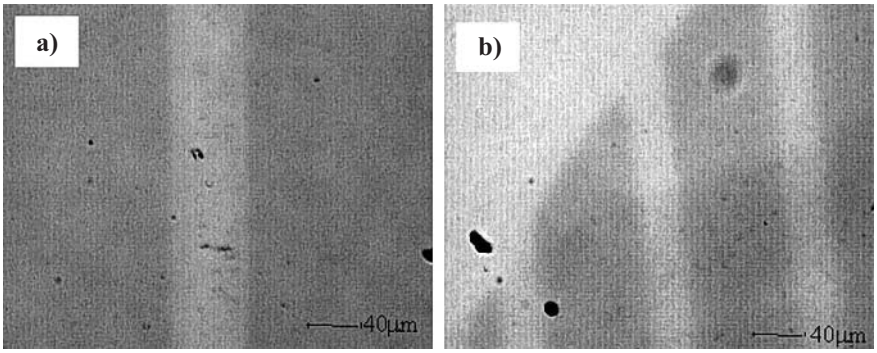

Figure 5 Optical micrographs of PD-PEO patterns on native PS masked with G50p (a) and G150p (b).

AFM Scanned PS tracks of patterns obtained by different physical masks are shown in Fig. 6. From the figure it is evident that the profile of the tracks is not sharp. Rather than the expected sharp steps, slopes with flaw edges are recorded, whose extent depends on the width of the bars of the mask. These may be due to the non perfect adhesion of the mask to the substrate that produces a thin coating near the board of the tracks.

The chemical characterisation of PS tracks has been performed with "small spot" (∅ 27 µm) XPS analysis, as described in Sect. 2.2 while a large X-ray spot (∅ 800 µm) was utilised for sampling a wide area and acquiring a chemical map of some patterned zones. The results show that only carbon and oxygen were detected on the patterned zone of each substrate, attesting to the absence of contaminant due to the patterning procedure.

Large-spot XPS mapping has allowed detection of the chemical differences between tracks and surrounding domains. The chemical contrast was set by using the C0 component of the C1s spectrum. As shown in Fig. 7, PS tracks (C0 more intense) surrounded by PEO-like domains (C0 less intense) were clearly evidenced. The results obtained by the small-spot confirm a stronger C1 component outside the

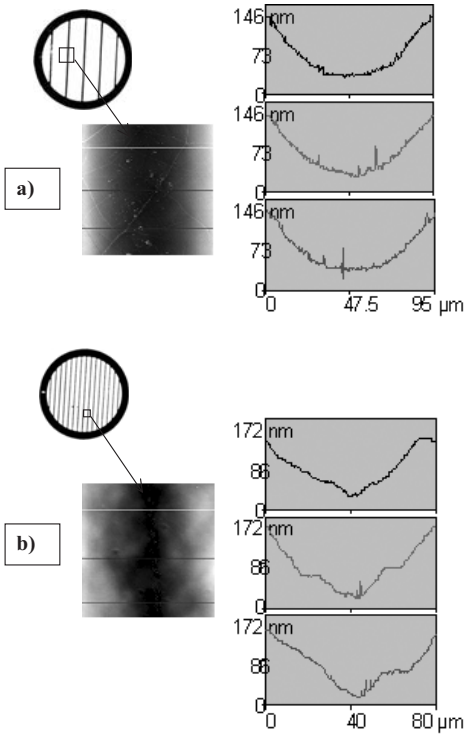

Figure 6 AFM scans of patterned PD-PEO coatings on samples obtained by using G50p (A) and G150p (B) masks. The figure shows the depth profile (on the right) of the investigated tracks as represented in the middle of the figure (topographic image).

track, similar to that measured on homogeneous PEO-like films (Table 3). Inside the track there is some PD-PEO, in agreement with AFM profiles but this is either a very thin (less than the XPS sampling depth) or a non uniform coating.

Table 3 Small-spot results

Investigated stripe zone	C/O	C0 (%)	C1 (%)	C2 (%)
Whole pattern	1.8	14.2	80.5	4.0
Inside	2.7	45.8	50.3	3.9
Outside	2.0	15.1	80.4	4.5

For the aims of this work, however, the most important piece of evidence of the pattern transferring with the masks comes from cell-culture tests. Substrates with PEO-like domains and ccPS tracks allow us to obtain a microarrangement of eukaryotic cells like NCTC 2544 keratinocytes with a very good spatial resolution (Fig. 8).

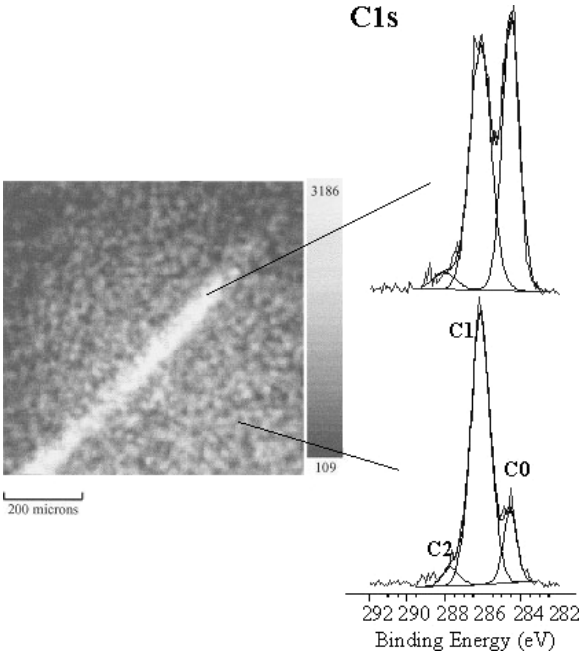

Figure 7 Small spot (27 µm) XPS analysis of native PS substrates patterned with PEO5W coatings deposited through a G50p mask. The chemical map was acquired by setting the XPS detector to the binding energy value of the C0 contribute of the C1s signal acquired. By a 27-µm wide spot a chemical analysis inside and outside of the track reveals that the C1 component (PEO character) of the C1s spectra (right) is more intense outside the track (PEO-like coating) than inside the track (uncovered conventional PS).

After 24 h keratinocyte cells adhere on the adhesive tracks (i.e. the bare ccPS), while absolutely no cells can be found on the PEO-like coated domains surrounding the tracks. It is important to observe in Fig. 8 how well the cellular microarrangement reproduces the geometry of the masks. Similar results have been obtained with 3T3 murine fibroblasts as well.

Cell-culture tests have been made also on patterned substrates containing PS-tracks. The chemical differences between the two kind of PS, i.e. ccPS and PS, are evidenced by XPS showing almost a complete absence of oxygen in PS. The known unsuitability of PS for promoting adhesion, spreading and mobility of cells, has strongly reduced our expectation for PS-tracks. Figure 9 (a) shows cells adhered on PS-tracks after 24 h, apparently confirms our expectation and shows few clusters of circular cells on PS-tracks. Surprisingly, however, Fig. 9 (b), corresponding to the situation after 7 days incubation, shows a picture of cellular confluence on tracks, with spread cells.

This unexpected result induced us to study the evolution from 24 h to 7 days, in fact we have made tests also at intermediate incubation times. The situation at 72 and 96 h (Fig. 10) in the border ring of PS tracks is an example: a few cells very well spread and adhere to PS. Although the border ring is a large track, which

enables random distribution of cells inside the track, at 72 h it seems that cells at the edges, we found spindle-shaped cells, where there is the step. Later (96 h), the cells present a spread morphology also in the track center.

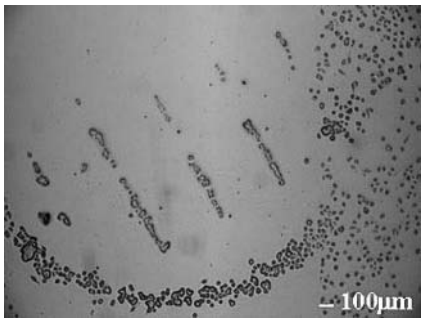

Figure 8 Micrograph of NCTC 2544 keratinocytes seeded on patterned PEO-like/ccPS G50p pattern.

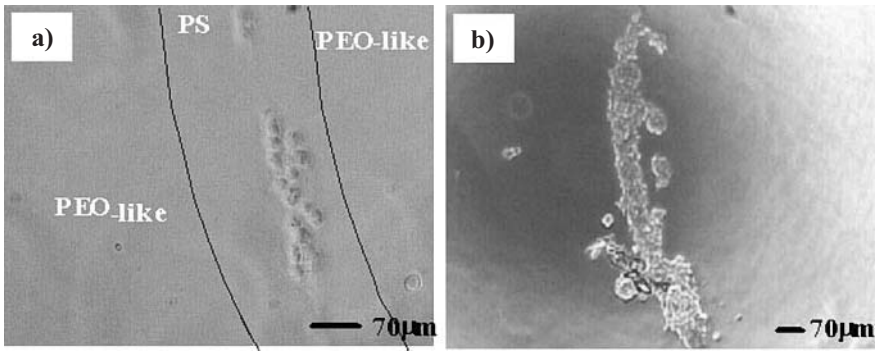

Figure 9 Micrographs of 3T3 Murine fibroblasts seeded on patterned PEO-like/PS G50p pattern after 24 h (a) and 7 days (b) of incubation time.

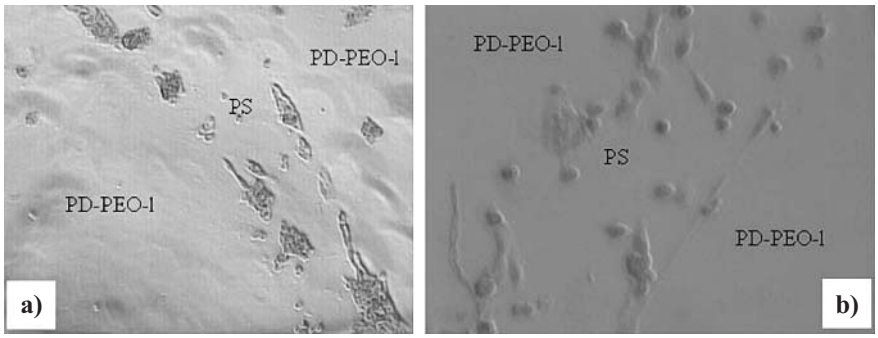

Figure 10 Micrographs of 3T3 Murine fibroblasts on G50p, PEO-like/PS G50p pattern. Fibroblasts on the border of the mask are shown after 72 h (a) and 96 h (b) of incubation time.

When the behavior of cells seeded on different patterned substrates is compared, it confirms a clear influence of the topographical constraints other than the chemical ones on cell morphology (Fig. 11). On G50p patterns two or more cells are present across the width of the PS tracks, while no more than two cells were observed on G150p PS tracks. These results confirm that the tracks containing uncoated PS are thinner than those of the physical mask.

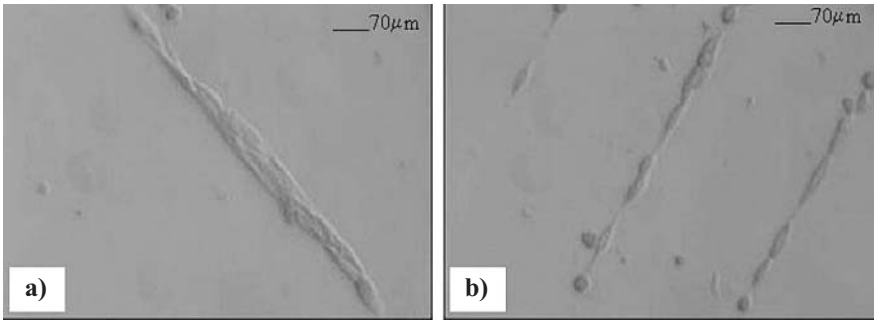

Figure 11 3T3 Murine fibroblasts, after 7 day, aligned along PS-tracks obtained by different masks: G50p (a) and G150p (b).

27.4 Conclusions

Although our investigation is still ongoing and some effects have to be definitely proved, it seems that some partial conclusions can, however, be drawn from this work:

- PEO-like coatings are excellent cell-repulsive surfaces preventing cell adhesion and spreading;
- track structures can easily be made by plasma-masking procedures;
- by alternating non fouling domains with PS or ccPS tracks cell driving along tracks can be easily reached;
- the chemistry of strongly cell-repulsive domains is very important in driving the cells inside the tracks;
- the chemistry of the track appear to be very important only for short times (24 h). This long-term effect on cell adhesion and spreading can be attributed to biological molecules produced by the cells themselves;
- in the long run PS tracks exhibit the same abilities of ccPS, although the chemistry does not act in favor of this;
- even PS tracks can promote the adhesion of cells to reach confluence provided there is a real cell-repulsive coating surrounding the PS.

Acknowledgments

This research has been developed in the framework of the MIUR FIRB RBNE01458S_006, MIUR-COFIN '99 "Biomaterials with micro- and nanostructured surfaces" and EC "NANOMED" QLKE-CT-2000-01500 projects, whose financial contribution is gratefully acknowledged.

Dr. C. Oehr and Dr. M. Müller of the Fraunhofer Institute for Interfacial Engineering and Biotechnology, Stuttgart, Germany, are gratefully acknowledged for their assistance in μ-spot XPS. The COST 527 Action "Plasma polymers and related materials" is acknowledged for funding the stay of one of the authors (E.S.) at the Fraunhofer Institute for Interfacial Engineering and Biotechnology (Stuttgart, Germany). Prof. A. Curtis, Dr. M. Dalby, Dr. C. Berry and Dr. M. Riehle (University of Glasgow, UK) are gratefully acknowledged for their scientific support and for the use of laboratory facilities.

References

[1] A. Harris, *Exp. Cell. Res.* 77 (1973) 285
[2] R. Sipehia, *Biomat., Art. Cells, Art. Org.* 18–3 (1990) 437
[3] J. H. Griesser, C. R. Chatelier, T. R. Gengenbach, G.Johnson, J. G.Steele, *J. Biomater. Sci. Polym. Edn.* 5–6 (1994) 531
[4] R.M. France, R. D. Short, E. Duval, F. R. Jones, *Chem. Mater.* 10–4 (1998) 1176
[5] B. Gupta, C. Plummer, I. Bisson, P. Frey, J. Hilborn, *Biomaterials*, 23 (2002) 863
[6] S. I. Ertel, A. Chilkoti, T. A. Horbett, B. D. Ratner, *J. Biomat. Sci. Polym. Edn.* 3–2 (1991) 163
[7] C.D.W. Wilkinson, M. Riehle, M. Wood, J. Gallagher, A.S.G. Curtis, *Mater. Sci. Eng.* 19 (2002) 263
[8] B.D. Ratner, in: *Biomaterials Science: An Introduction to Materials in Medicine*, (1996) B.D. Ratner (Ed.) Academic Press, San Diego
[9] J.B. Park, *Biomaterials: An Introduction*. (1979) Plenum Press
[10] J. Black, *Biological Performance of Materials: Fundamentals of Biocompatibility*. (1981) Marcel Dekker, Inc.
[11] D.F. Williams, R. Roaf, *Implants in Surgery*. (1973) W.B. Saunders Co. Ltd.
[12] B.D. Ratner, in: *Comprehensive Polymer Science* 7 (1989) 201; S.L. Aggarwal, ed., Pergamon Press
[13] G.U. Lee, *US Patent* 6, 086,821, July11 (2000)
[14] D. L. Taylor, *US Patent* 6, 103,479, August 15 (2000)
[15] S.N. Bathia, M.L. Yarmush, M. Toner, *US Patent* 6,133,030, October 17, (2000)
[16] D.K. Gilding, R.W. Paynter. J.E. Castle, *Biomaterials*, 1 (1980) 163
[17] N. Kawamoto, H. Mori, N. Yui, M. Terano, *J. Biomater. Sci., Polym. Ed.* 9 (1998) 543
[18] Y. Hanein, Y. V. Pan, B.D. Ratner, D. D. Denton, K. F. Böhringer, *Sens. Actuators B*, 81 (2001) 49
[19] A.Y. Fu, C. Spence, A. Scherer, F.H. Arnold, S. R. Quake, *Nature Biotechnol.* 17 (1999) 1109
[20] G. Fuhr, *Analytical Methods and Instrumentation*. Special Issue of '96mTAS (1996) 39
[21] P.C.H. Li, D.J. Harrison, *Anal. Chem.* 69 (1997) 1564
[22] S.R. Quake, A. Scherer, *Science*, 290 (2000) 1536
[23] P. Kingshott, H.J. Griesser, *Current Opin. Solid State Mater. Sci.* 4 (1999) 403
[24] J.H. Lee, P. Kopeckova, J. Zhang, J. Kopecek, J.D. Andrade, *ACS Polym. Mater. Sci. Eng.*, 59 (1988) 234
[25] S. Nagaoka, Y. Mori, H. Takiuchi, K. Yokota, H. Tanzawa, S. Nishiumi, *ACS Polym. Prep.* 24 (1983) 67
[26] S. Nagaoka, A. Nakao, *Biomaterials*, 11 (1990) 119
[27] J.H. Lee, J. Kopecek, J. Andrade, *ACS Polym. Mater. Sci. Eng.*, 57 (1987)
[28] K.L. Prime, G.M. Whitesides, *Science*, 252 (1991) 1164

[29] P. Harder, M. Grunze, R. Dahint, G.M. Whitesides, P.E. Laibinis, *J. Phys. Chem. B*, 102 (1998) 426

[30] M.S. Sheu, A.S. Hoffmann, J. Feijen, *J. Adhes. Sci. Tech.* 6-9 (1992) 995

[31] M. Malmsten (Ed.), *Biopolymers at Interfaces, Surfactant Science Series*, New York (1998)

[32] M. Malmsten, B. Lassen, K. Holmberg, V. Thomas, G. Quash, *J. Colloid. Interface Sci.* 177 (1996) 70

[33] H.M. Patel, *Crit. Rev. Ther. Drug. Carrier Syst.*, 9 (1992) 39

[34] Y.J. Wu, A.J. Griggs, J. S. Jen, S. Monolache, F.S. Denes, R.B. Timmons, *Plasmas Polym.*, 6–3 (2001) 123

[35] F. Palumbo, P. Favia, M. Vulpio, R. d'Agostino, *Plasmas Polym.*, 6–3 (2001) 163

[36] E.E. Johnston, *Ph.D. Thesis*, University of Washington (1997)

[37] M. Morra, in *Water in Biomaterials Surface Science*, M. Morra (Ed.); John Wiley and Sons, Ltd, 12 (2001) 307

[38] G.P. Lopez, B.D. Ratner, C.D. Tidwell, C.L. Haycox, R.J. Rapoza, T.A. Horbett, *J. Biomed. Mater. Res.* 26 (1992) 415

[39] R. d'Agostino, L. Martinu, V. Pische, *Plasma Chem. Plasma Proc.*, 11 (1991) 1

[40] E.E. Johnston, B.D. Ratner, J.D. Bryers in: *Plasma Processing of Polymers*, R. d'Agostino P. Favia, F. Fracassi (Eds), *NATO ASI Series E: Applied Sciences*, 346, Kluwer Acad. Publ. (1997)

[41] A. Ohl, K. Schröder, *Surf. Coat. Technol.* 116 (1999) 820

[42] P. Favia, M. Creatore, F. Palumbo, V. Colaprico, R. d'Agostino, *Process Control for Plasma Process Polym. Surf. Coat. Technol.* 1 (2001) 142

[43] J.E. Meredith Jr, B. Fazeli, M.A. Schwartz, *Mol. Biol. Cell.* 4, (1993) 953

[44] S.M. Frisch, H. Francis *J. Cell Biol.* 124–4, (1994) 619

[45] D. Mooney, L Hansen, J. Vacanti, R. Langer, S. Farmer, D. Ingber *J. Cell Physiol.* 151–3 (1992) 497

28
Plasma-deposited Acrylic Acid Coatings on Flat and Nanostructured Substrates for Cell-Culture Experiments

L. Detomaso, R. Gristina, G.S. Senesi, L.C. Lopez, P. Favia, R. d'Agostino

Abstract

Thin coatings with different chemical properties were plasma-deposited (pd) from acrylic acid (AA) vapors on flat and nanostructured surfaces. These films, when deposited in a low monomer fragmentation regime, were inhomogeneous and non-conformal due to poor adhesion to substrates. Pretreatments of substrates in NH_3 plasma, however, improved the surface/coating interfaces and led to homogeneous, conformal pdAA films, also when they were deposited on nanostructured surfaces. The coatings deposited in the high fragmentation regime, with low COOH content and high crosslinking degree, resulted homogeneous, conformal, extremely stable after prolonged exposure to water and, therefore, they were utilized as substrates for cell-culture experiments with NCTC 2544 human keratinocyte and hTERT-BJ1 human fibroblast cell lines.

28.1
Introduction

Many different kinds of plasma-deposited organic coatings have been proposed to modify the surface of biomedical polymers in order to drive adhesion, spreading and proliferation of cells in different applications, for in vitro cell cultures, for blood compatible surfaces, and for in vivo tissue-engineering experiments [1–7]. In particular, hydrophilic, functional coatings with tunable surface density of –COOH groups, such as pdAA coatings, have been investigated by certain authors as cell-adhesive layers [8–10] and primer functional layers for biomolecule immobilization [11–15]. Plasma-deposited acrylic acid coatings can be obtained from glow discharges performed in different monomer fragmentation regimes to control the surface density of carboxylic groups and their related surface properties. CO molecules, and other emitting species resulting from the fragmentation of the AA monomer in the plasma, can be utilized as "markers" of the process, in that their relative density in the plasma could be correlated to the surface density of –COOH groups in the resulting pdAA films [16]. Low fragmentation (low input power, modulated conditions) and negligible substrate ion bombardment conditions generally result in

highly hydrophilic, highly –COOH surface-dense coatings, while high fragmentation regimes (high input power, continuous discharges) and intense ion bombardment of the growing film lead, on the contrary, to coatings with lower hydrophilic character and –COOH surface density, but higher crosslinking degree.

Micro- and nanopatterning techniques produce surfaces with predetermined morphology able, in principle, to drive and control adhesion, spreading and growth of cells in tissue-engineering experiments [17–27]; in this context plasma techniques capable of tuning the surface chemistry of nanopatterned materials while leaving intact their topography may obviously play a leading role. Micro- and nanopatterning techniques have determined, in the last ten years, an escalation in the biomedical research aimed to deliver affordable fabrication techniques for producing large areas of "smart" micro- and nanopatterned biomedical surfaces with controlled morphology and chemistry.

We have found that pdAA coatings deposited in low fragmentation regimes generally lead to nonconformal, nonhomogeneous layers, with weak resistance to prolonged exposure to cell culture and water media; pretreatments of substrates (polymers, but also glass) in NH_3 RF (13.56 MHz) glow discharges have been found beneficial in improving the compatibility and adhesion of the substrate with these kinds of pdAA coatings. PdAA coatings deposited in high-fragmentation regimes, although with a much lower density of –COOH groups, resulted in much better substrate adhesion and water stability. In this paper we present also how it is possible to deposit conformal and stable cell-adhesive pdAA layers of controlled chemical composition (i.e., COOH surface density) on nanopatterned polymer surfaces obtained, in our case, by means of polymer demixing [28] and by colloidal lithography [29] techniques.

28.2 Experimental

28.2.1 Substrates

Silicon (Si), glass, and polystyrene (PS) flat substrates were coated with pdAA coatings; nanostructured surfaces of biomedical interest were also utilized to check the conformality of pdAA coatings. For these experiments polyethylenterephtalate (PET) and polystyrene/polybromostyrene (PS/PBrS) samples structured with features of nanometric size by means of colloidal lithography (cones, 125 ± 10 nm mean height) and polymer demixing (bumps, 35 ± 5 nm mean height) respectively, were utilized. The reader is addressed to the specific literature for the fabrication details of substrates produced by colloidal lithography [29] and by PS/PBrS polymer demixing [28]. Substrates were cleaned in ethanol and dried at room temperature before being plasma processed.

28.2.2
Plasma Reactors and Processes

A stainless steel parallel-plate plasma reactor was utilized, fed with an AA (3 sccm, degassed with freeze-thaw cycles, Sigma-Aldrich) / Ar (20 sccm, Air Liquid) mixture at 150 mTorr of pressure. A RF (13.56 MHz) generator was utilized at 20 or 100 W of power in continuous (CW) or modulated mode to ignite the discharges between the upper (stainless steel, shielded, RF connected) and the lower (grounded, sample holder) electrode. A pulse generator was used to modulate on/off (time on= t_{on}; time off = t_{off}) the AA/Ar discharge at a duty cycle (DC = 100 t_{on}/ (t_{on} + t_{off})) of 3%. Modulated pdAA depositions were performed with a fixed period t_{on} + t_{off} of 100 ms [30]. PdAA coatings in the lower monomer fragmentation regime were deposited at 20 W and 3% DC for 1 min; 100 W, CW (100% DC) mode discharges performed for 5 min, were utilized to deposit pdAA coatings in the high-fragmentation regime. The discharge duration was always kept low enough to obtain very thin pdAA coatings that would not alter the morphology of the substrate underneath.

NH_3-plasma pretreatments of flat and nanostructured substrates were performed to improve the homogeneity of pdAA coatings on flat substrates and to assess their conformality on the nanostructured ones, also after prolonged immersion in bidistilled water. The pretreatments were performed in a tubular Pyrex parallel plate RF reactor (13.56 MHz, CW mode, 20 W, 10 sccm NH_3, 200 mTorr, 1 min) with the substrates positioned on the ground lower electrode. Mild pretreatment conditions, i.e., low power and short treatment time, were selected on the basis of our previous experience in plasma-grafting processes of polymers [30]. Mild treatment conditions, in fact, result in reduced surface damage and satisfactory selectivity of the grafting toward $–NH_2$ groups, whose basic character could improve the interfacial adhesion with pdAA coatings.

28.2.3
Surface Characterization

X-ray photoelectron spectroscopy (XPS), water contact-angle (WCA) measurements, profilometry and atomic force microscopy (AFM) were utilized to characterize chemistry and morphology of the plasma-processed surfaces.

Wide-scan and high-resolution (C1s, O1s and N1s) unmonochromatized AlK_α XPS spectra were acquired with a PHI 5300 ESCA spectrometer at an electron take-off angle of 45°, within one hour after each process. Sample charging was corrected by setting the hydrocarbon component (C0) of the C1s signal at 285.0 eV. The C1s signal was best-fitted with four peak components (FWHM = 2.00 eV), corresponding to C atoms with zero, one, two and three carbon–oxygen bonds: C0 (C–H(C); BE = 285.0 eV, reference), C1 (C–OH (OC); BE = 286.6 ± 0.2 eV), C2 (O–C–O, C=O; BE = 288.2 ± 0.2 eV) and C3 (COOH, COOR; BE = 289.1 ± 0.2 eV). The relative importance of the C3 component (C3%) can be considered representative of the surface density of –COOH groups in pdAA coatings.

Static WCA measurements were carried out soon after each process with a Ramè-Hart NRL 100 goniometer with bidistilled water. Thickness/deposition rate of pdAA coatings were measured with an Alpha-Step® 500 KLA TENCOR Surface Profiler on properly masked silicon samples. AFM (Autoprobe CP-Research) in contact (c) mode was utilized to control the conformity of pdAA thin films on nanostructured samples; commercial, unmodified silicon nitride tips were used.

To evaluate the effect of water on pdAA films in terms of leaching of soluble components and/or surface restructuring, samples were XPS, WCA and AFM analyzed before and after soaking in 7 ml of bidistilled water for up to 50 h, in nonstirring conditions, followed by overnight drying at room temperature.

28.2.4
Cell-Culture Experiments

Cell-culture experiments were performed on 12-mm diameter flat (PS cover-slips, PET) and nanopatterned (colloidal-lithography PET) pdAA-coated substrates. NCTC 2544 human keratinocyte and hTERT-BJ1 fibroblast cell lines were utilized, obtained from stocks routinely grown in Dulbecco's modified eagle medium (DMEM) supplemented with 10% fetal bovine serum, 50 IU/ml penicillin, 50 IU/ml streptomycin and 200 mM glutamine, under 5% CO_2/95% air at 37 °C. Plasma-processed and control samples were placed, modified side up, in 24-well culture plates (Iwaki 24 wells). Cells, obtained after trypsinization of confluent or near-confluent culture, were seeded at 2×10^4 cells/well (1×10^4 cells/well for hTERT-BJ1) in 1 ml of DMEM medium on the substrates and incubated at 37 °C under 5%CO_2/95% air. Cell attachment, distribution and morphology were determined at various time intervals from digital images acquired with a phase contrast microscope (Leica DM IL). The number of adherent cells was determined in at least 10 areas of 0.8 mm^2 per sample. For morphological studies cells with laminae were distinguished from cells without. The unpaired Student's t-test was used to evaluate statistical significant differences among tests performed on at least four repeated samples per experiment. Data were considered significant when $p<0.05$ was obtained. After 24 h of incubation, fixed and dehydrated cells seeded samples were sputter coated with gold to be examined with an Hitachi S800 field emission scanning electron microscope (SEM, 10 keV).

28.3
Results and Discussion

We have shown in a previous publication [30] how carefully tuning external plasma parameters such as RF power input and duty cycle, results in finely controlled pdAA surface composition. Increasing both plasma parameters, in fact, leads to a more pronounced fragmentation of the AA monomer in the plasma, thus to pdAA coatings with lowered C3 (COOH/R) and increased C0 (hydrocarbon, carbon–carbon) C1s components. C1 and C2 are just slightly altered. Figure 1 shows the surface

compositional trend for the C3 component in pdAA coatings deposited at variable RF power and duty cycle. For low power input, due to the high monomer structure retention it is reasonable to neglect the COOR contribute to C3 XPS component; this was attested to by means of XPS analysis of pdAA samples derivatized with trifluoroethanlol (data not shown) for the "titration" of –COOH groups. It can be noticed that very mild plasma conditions lead to pdAA coatings with COOH density very close to that of the starting AA monomer.

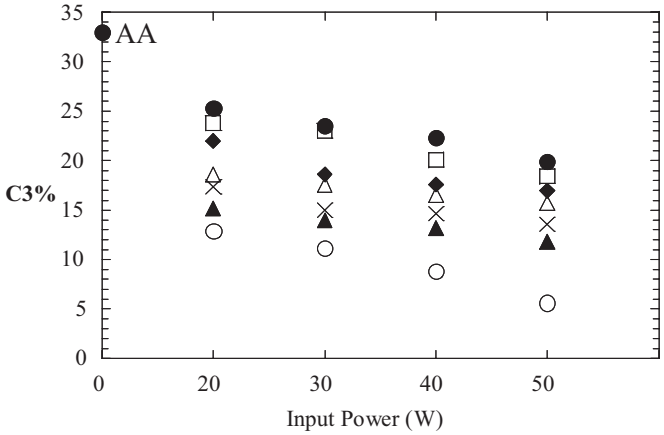

Figure 1 C3 component of pdAA coatings deposited at different values of duty cycle (● 3%; □ 5%; ◆ 10%; △ 20%, × 30%; ▲ 50%; ○ 100%) and RF input power. The value on the ordinate axis refers to the C3 composition of the AA monomer.

Two pdAA deposition regimes were investigated for this paper, low (20 W, 3% DC) and high (100 W, CW) AA monomer fragmentation in the plasma, in order to obtain homogeneous, conformal, water-stable and cell-adhesive pdAA coatings with very different –COOH surface density.

Very thin (< 10 nm) pdAA layers deposited in the low-fragmentation conditions resulted in nonhomogeneous and irregular coverage of flat substrates and in nonconformal coatings on nanostructured (35-nm nanohills) PS/PBrS substrates, as clearly evident in the AFM photos reported in Fig. 2 (B) (for PS) and Fig. 3 (B), respectively. Nonhomogeneity, unevenness and patchiness of pdAA (20 W, 3% DC) coatings were also attested by highly substrate-dependent XPS and WCA data (not shown), recorded for coatings deposited either on hydrophilic (like glass) or on hydrophobic (like PS) flat substrates, as well as on the nanostructured ones. Pretreatments of substrates in NH_3 glow discharges were found to be extremely beneficial in solving this problem, and obtaining homogeneous coatings. Figures 2 and 3 (case C) display two examples of substrates, flat PS and nanostructured PS/PBrS, plasma-coated with pdAA (20 W, 3% DC) films, where it is evident that NH_3-plasma pretreatments offered a much better pdAA/substrate interface and led to complete coverage and homogeneity of the deposited layer on flat surfaces, and to a good con-

formality (i.e., the coating follows the profile of the structures with even thickness) on nanostructured substrates. A very low WCA value, close to 10°, could be measured, as well as a very high –COOH surface density (see graph in Fig. 1) and XPS O/C ratio, on all substrates, highlighting considerable monomer structure retention. NH_3-plasma treatments of polymers are known to graft nitrogen-containing groups at their surface; this increases both their wettability and their surface density of basic groups. Grafted polar functionalities could interact more efficiently with active species formed in the AA discharge, resulting in a more stable modified substrate/coating interface. These surface characteristics (high density of polar groups, hydrophilic character), may result advantageous in driving adhesion and spreading of cells on artificial surfaces [31–33], but lead also to problems of integrity of the coating under cell-culture conditions. In our cell-culture experiments we found, in effect, that pdAA (20 W, 3% DC) coatings sustained the growth of NCTC 2544 human keratinocytes and hTERT-BJ1 human fibroblasts but, well within 24 hours of incubation, marked swelling, compositional changes and partial delamination of the coating occurred, very likely coupled with leaching of soluble compounds in the cell-culture medium (Gristina, unpublished results). To investigate the resistance of the NH_3/pdAA coatings to water, samples were soaked in bidistilled water for different periods of time up to 50 h. It was observed that within 24 h a delamination and/or changes of the surface composition occurred for pdAA (20 W, 3% DC) coatings. This was attested by the increase of WCA values close to the values of untreated substrates, by a relevant decrease of the C3 component (even down to 4%) in the C1s XPS signal, by a drastic change of the O/C XPS ratio and by the appearance of the XPS signal (e.g., Si2p for glass) of the native substrates. Very likely the high surface density of –COOH groups, typical of pdAA coatings deposited in low-fragmentation conditions, leads to a strong water/pdAA interactions (e.g., hydrogen bonds, swelling) that, combined with the low crosslinking degree of the coatings, induce delamination and/or leaching of hydrophilic moieties. Although this lack of stability is a drawback for materials intended as cell-growth substrates for long time, and coatings with different properties have to be optimized for prolonged exposure to cell-culture and physiological media, it may be considered an advantage when biodegradable coatings are sought, or surfaces able to sustain cell proliferation for short time, capable soon after of releasing the cells to a selected environment (e.g., to living wounded tissues). The matter of plasma-deposited biodegradable coatings is worthy of further investigations, and reports on this topic now start to appear in the literature [34].

The stability of pdAA coatings to water media was increased with increased intensity of the AA fragmentation in the plasma (increase of power and of duty cycle of the discharge), thus with the decrease of –COOH surface density. To obtain highly crosslinked, and more water-stable pdAA coatings, deposition discharges were performed in a drastically higher fragmentation regime (100 W, CW). In these deposition conditions a 3–4% of C3 component and WCA values of about 60–65° were recorded, whatever the substrate. The homogeneity and conformality of such coatings were found to be satisfactory, also on PS/PBrS nanostructured substrates, with no need of NH_3 pretreatment of the substrate, very likely also due to the more

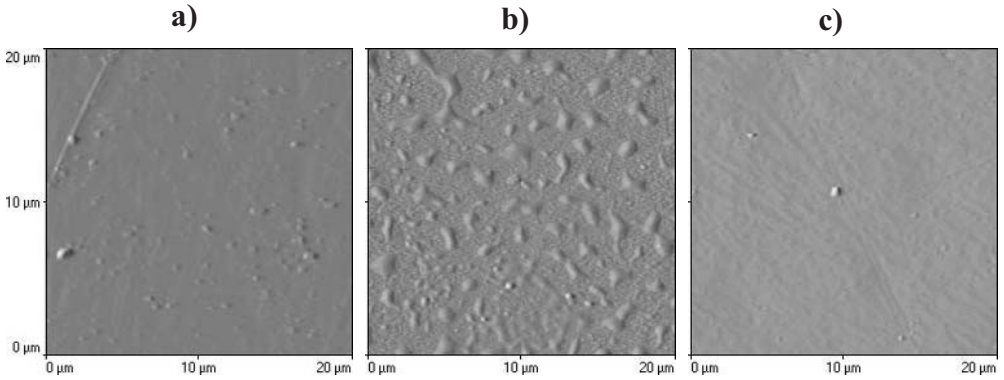

Figure 2 c-AFM images of very thin pdAA coatings deposited on untreated and NH_3-plasma pretreated flat PS: untreated (a); pdAA coated (3% DC, 20 W) without (b) and with (c) NH_3-plasma pretreatment.

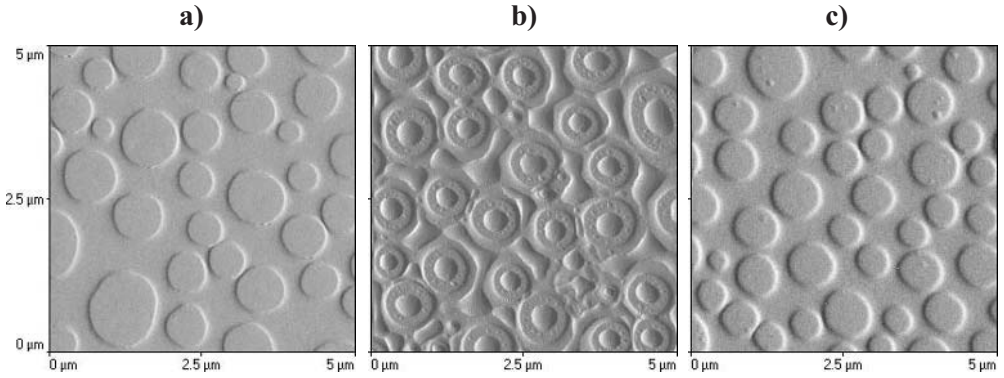

Figure 3 c-AFM images of very thin pdAA coatings deposited on untreated and NH_3-plasma pretreated PS/PBrS substrates nanostructured with 35-nm nanohills: untreated (a); pdAA coated (3% DC, 20 W) without (b) and with (c) NH_3-plasma pretreatment.

intense power-related plasma-surface ion-bombardment during the deposition. Figure 4 shows WCA data and C1s XPS signal of (100 W, CW) pdAA films before and after 50 h soaking in water, that attest to the stability of such particular coatings in water. In contrast to films synthesized in low-fragmentation conditions, the effect of substrate was found to be negligible, no chemical and morphological changes were also recorded after water soaking.

These (100 W, CW) pdAA coatings were tested for their ability to sustain cell adhesion and growth; hTERT-BJ1 human fibroblasts were cultured on coated flat PS substrates, using native PS as control. As attested by the graph of Fig. 5 (left), where the number of adhered fibroblasts is shown at different culture time, few cells were

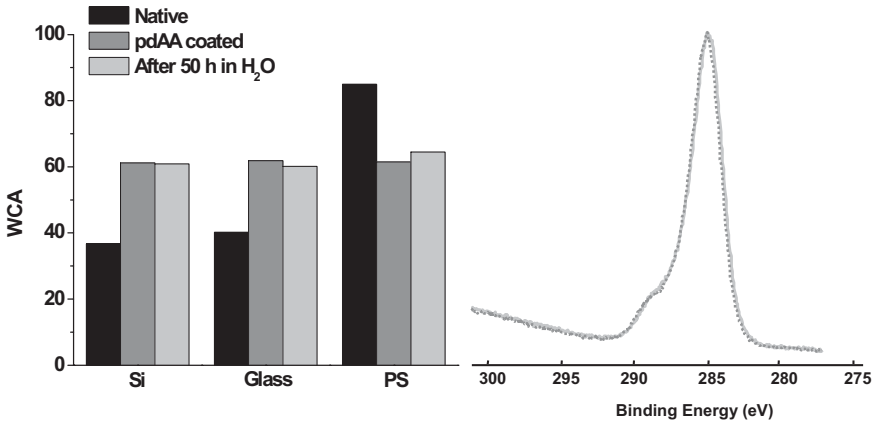

Figure 4 On the left: WCA values of (100 W, CW) pdAA coatings deposited on flat substrates before and after 50 h in H_2O (error ± 3°). On the right: the C1s XPS signals of the same pdAA coatings recorded before (grey curve) and after (dotted curve) 50 h in H_2O.

found adhered onto uncoated PS, while many more cells were observed adhering on the (100 W, CW) pdAA surfaces after 3 and 24 h of culture. A high percent of cells without protruding laminae was observed on native PS, while a very small number was recorded on (100 W, CW) pdAA surfaces as shown in Fig. 5 (right). SEM images of Fig. 6 shows that hTERT-BJ1 cells after 24 h of incubation on (100 W, CW) pdAA coatings, were much more spread than cells on PS substrate. The cell spreading, by protruding laminae, can be considered a further sign of the biocompatibility of the substrate itself.

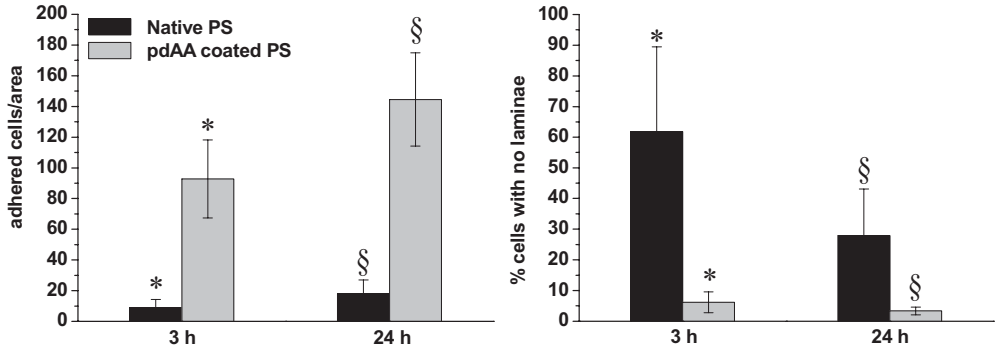

Figure 5 On the left: number of adhered hTERT-BJ1 human fibroblasts on native and on (100 W, CW) pdAA-coated PS after 3 and 24 h of cell culture. On the right: percent of fibroblasts cells without laminae on the same surfaces. *, § = $p < 0.05$.

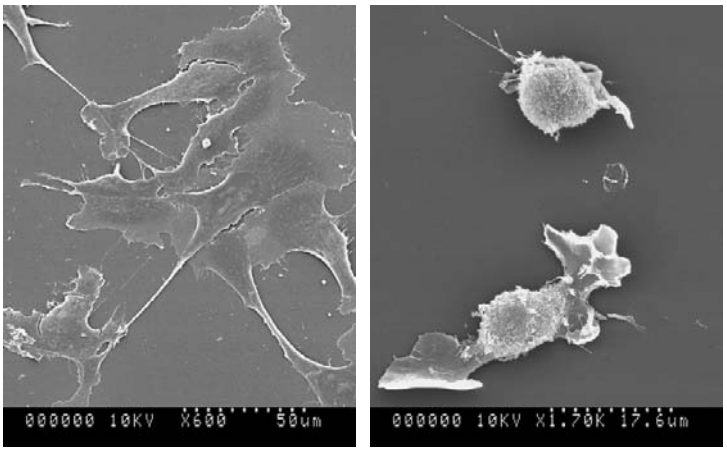

Figure 6 SEM images of hTERT-BJ1 human fibroblasts adhering on (100 W, CW) pdAA-coated (left) and on uncoated PS (right) after 24 h of culture.

To assess their conformity on rough/nanopatterned surfaces, (100 W, CW) pdAA coatings were also deposited on PET samples nanopatterned by colloidal lithography with 125-nm high conical features [29]. The presence of the nanometric surface features has been shown to increase *per* se the adhesion of different cell types (19,21) with respect to flat samples. A comparison of the AFM images displayed in Figs. 7 (a) and (b) show clearly that, due to the high-fragmentation conditions, very thin (100 W, CW) pdAA coatings did not affect significantly their morphology, resulting in a conformal layer of different surface chemistry with respect to the substrate underneath.

This, and other findings, allow us to propose pdAA as coatings capable of modifying surface chemistry and cell-adhesive properties of nanostructured biomedical surfaces, a property that is of obvious interest in tissue engineering. WCA data of Fig. 8 (left) show that the wettability of (100 W, CW) pdAA coatings deposited on flat PET substrates was different from that achieved on cone-patterned ones, and changes only slightly after immersion in water, while the surface chemical composition (Fig. 8, right), as expressed by the C1s spectrum, was always the same. The difference in WCA values can be due to a surface topography effect. As is shown in Fig. 9 the C1s XPS signals for uncoated conical (Fig. 9 (a)) and flat (Fig. 9 (b)) PET were different but, after plasma deposition, the same signal was recorded either on conical or on flat samples (Fig 9 (c)) showing that pdAA-coated flat and nanostructured samples presented the same chemical composition.

For preliminary cell-culture experiments, NCTC 2544 keratinocyte cells were grown on (100 W, CW) pdAA coated and uncoated flat and conical 125 nm high nanofeatured PET samples; the experiments were performed to observe whether the pdAA coating and the presence of nanostructures on the substrate could influence cell adhesion, and to what extent. Figure 10 shows that, in effect, after 90 min of cell

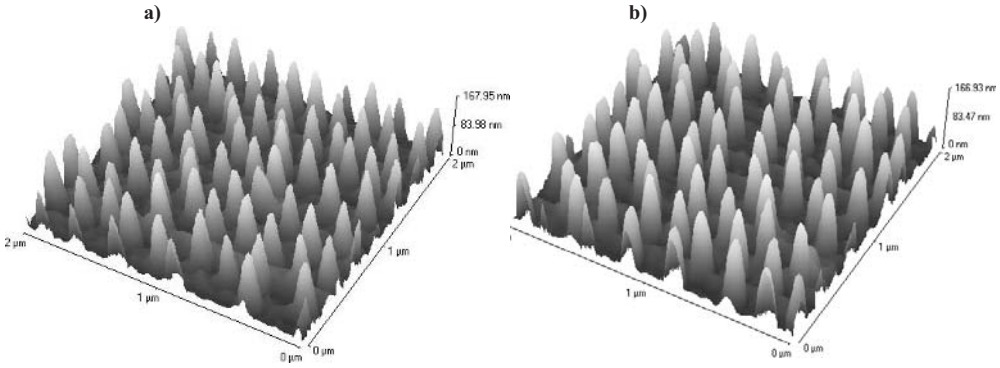

Figure 7 c-AFM images of conical 125 nm nanofeatures on PET as it (a) and (100 W, CW) pdAA coated (b).

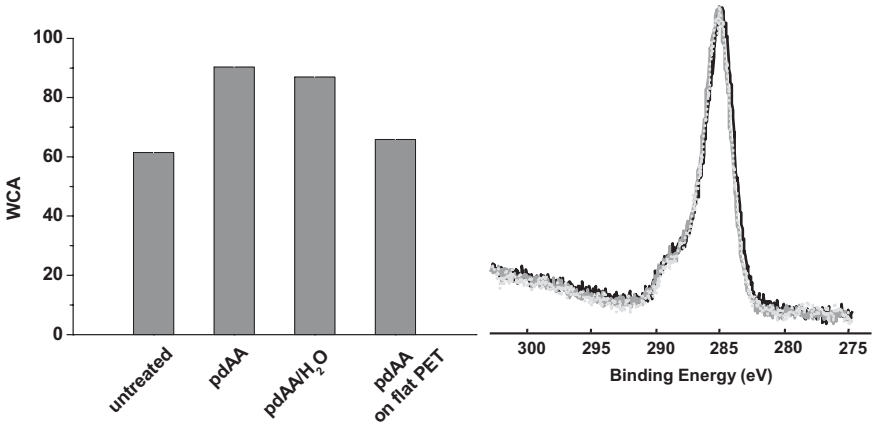

Figure 8 On the left: WCA values on (100 W, CW) pdAA-coated conical 125 nm nanofeatures and flat PET samples; on the right: C1s XPS signal of 100 W pdAA on conical 125 nm nanofeatures PET before (black curve) and after (dark grey curve) 50 h in H_2O, of 100 W pdAA on flat PET (light grey curve).

culture, the presence of the conical nanofeatures induced an increase of cell adhesion with respect to the flat PET substrates, very likely due to the increase of surface area and roughness; when (100 W, CW) pdAA water-stable coatings were deposited on the conical nanofeatured substrates, no significant enhancement of cell adhesion was observed, with respect to the native substrates, very likely due to a certain similarity in surface chemistry between the two substrates, as shown before. In this case, evidently, the effect of the nanofeatures on the substrate was already enough to induce an increase of cell adhesion.

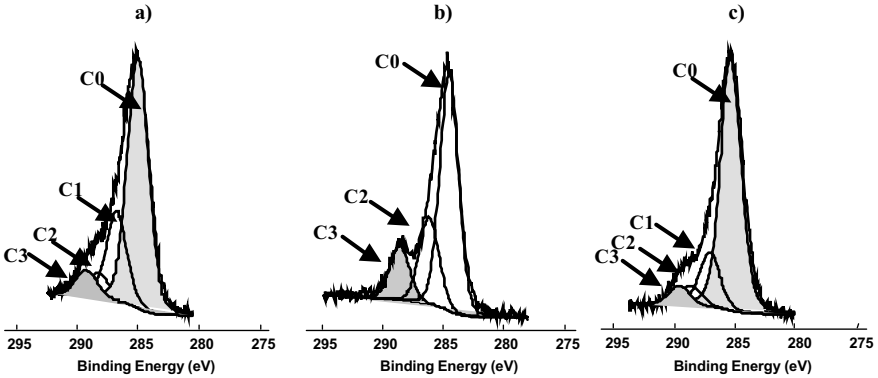

Figure 9 C1s XPS signal of (a) native conical PET (C0 = 65 ± 1; C1 = 23 ± 1; C2 = 5 ± 1 ;C3 = 7 ± 1); (b) native flat PET (C0 = 62 ± 1; C1 = 18 ± 1; C2 = 24 ± 1; C3 = 14 ± 1) and (c) pdAA-coated flat PET (C0 = 72 ± 1; C1 = 18 ± 1; C2 = 5 ± 1; C3 = 5 ± 1) (The same signal was recorded on pdAA-coated conical PET).

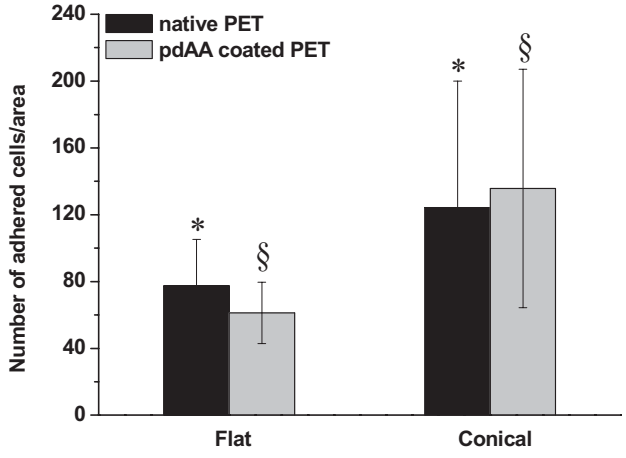

Figure 10 Number of adhered NCTC 2544 human keratynocytes after 90 min of culture on native and pdAA-coated PET samples with and without nanostructures. *, § = $p < 0.05$.

Further experiments are aimed to plasma deposit water-stable conformal coatings of different chemical composition and properties (hydrophobic-hydrophilic; fouling-non fouling, etc.) on surfaces nanostructured in different ways, in order to independently measure the effect of both chemistry and morphology on adhesion and growth of different cell types.

28.4 Conclusions

The deposition of pdAA coatings is a very promising method to enhance cell attachment and proliferation onto a variety of materials not suitable to promote cell adhesion at their surface. Interface optimization may be needed, in certain cases, and it was found to be beneficial for flat and nanostructured surfaces coated with highly hydrophilic films. Conformal pdAA deposition on nanostructured surfaces can be attempted successfully, in order to obtain cell-adhesive surfaces with well-characterized surface morphology. Future works include the plasma deposition of water-stable conformal coatings characterized by a wide range of chemical composition and properties on nanostructured surfaces, in order to independently investigate the effect of both chemistry and morphology on adhesion and growth of cell types of interest in tissue engineering.

Acknowledgements

Prof. S. Affrossman (University of Strathclyde, UK) is acknowledged for having provided polymer demixed samples. Dr. Sutherland (Chalmers University, Gothenburg, SWE) is acknowledged for having provided colloidal lithography samples. Prof. A. Curtis (University of Glasgow, UK) is acknowledged for experiments with hTERT-BJ1 human fibroblasts. Dr. A. Milella (University of Bari, I) is gratefully acknowledged for its helpfulness in performing AFM analyses. The EC project Nanobiotechnology and Medicine "NANOMED" (QLK3-CT-2000-01500, EC 5thFP Quality of Life) is acknowledged for funding this research.

References

[1] Ratner BD, Chilkoti A, Lopez GP. Plasma deposition and treatment for biomaterial applications. In: d'Agostino R. editor. Plasma Deposition, Treatment and Etching of Polymers. San Diego: Academic Press, 1990. p. 463–516.

[2] Favia P, Sardella E, Gristina R, Milella A, d'Agostino R. Functionalization of biomedical polymers by means of plasma processes: plasma treated polymers with limited hydrophobic recovery and PE-CVD of –COOH functional coatings. J Photopolym Sci Tech 2002; 15: 341–350.

[3] Favia P, Sardella E, Gristina R, d'Agostino R. Novel plasma processes for biomaterials: micro-scale patterning of biomedical polymers. Surf Coat Technol 2003; 169:707–711.

[4] Daw R, O'Leary T, Kelly J, Short RD, Cambray-Deakin M, Devlin AJ, Brook IM, Scutt A, Kothari S. Molecular engineering of surface by plasma copolymerization and enhanced cell attachment and spreading. Plasmas Polym 1999; 4: 113–132.

[5] Garrison MD, Luginbühl R, Overney RM, Ratner BD. Glow discharge plasma deposited hexafluoropropylene films: surface chemistry and interfacial material properties. Thin Solid Films 1999; 352: 13–21.

[6] Wu YJ, Timmons RB, Jen JS, Moloch FE. Nonfouling surfaces produced by gas phase pulsed plasma polymerization of an ultra low molecular weight ethylene oxide containing monomer. Colloid Surf B 2000; 18: 235–248.

[7] Gengenbach TR, Chatelier RC, Griesser HJ. Universal correlation of nitrogen 1s and oxygen 1s photoelectron binding energies with chemical composition in nitrogen-containing plasma polymers. Plasmas Polym 1999; 4: 283–307.

[8] Bisson I, Hilborn J, Wurm F, Meyrat B, Frey P. Human urothelial cells grown on collagen adsorbed to surface-modified polymers. Basic Sci 2002; 60: 176–180.

[9] Bisson I, Kosinski M, Ruault S, Gupta B, Hilbor J, Wurm F, Frey P. Acrylic acid grafting and collagen immobilization on poly(ethyleneterphtalate) surfaces for adherence and growth of human bladder smooth muscle cells. Biomaterials 2002; 23: 3149–3158.

[10] Daw R, Candan S, Beck AJ, Devlin AJ, Brook IM, Macneil S, Dawson RA, Short RD. Plasma copolymer surfaces of acrylic acid/1,7 octadiene: surface characterization and the attachment of ROS 17/2.8 osteoblast-like cells. Biomaterials 1998; 19:1717–1725.

[11] Favia P, Palumbo F, d'Agostino R, Lamponi S, Magnani A, Barbucci, R. Immobilization of Heparin and highlysulphated hyaluronic acid onto plasma-treated polyethylene. Plasmas Polym 1998; 3: 77–95.

[12] Kang ET, Neoh KG, Tan KL, Senn BC, Pigram PJ, Liesegang J. Surface modification and functionalization of polytetrafluoroethylene films via graft copolymerization. Polym Adv Tech 1997; 8: 683–692.

[13] Vasilets VN, Hermel G, Knig U, Werner C, Mller M, Simon F, Grunke K, Ikada Y, Jacobasch HJ. Microwave CO_2 plasma-initiated vapor phase graft polymerization of acrylic acid onto polytetrafluoroethylene for immobilization of human thrombomodulin. Biomaterials 1997; 18: 1139–1145.

[14] Wölcker N, Klee D, Höcher H, Langefeld S. Functionalization of silicon rubber for the covalent immobilization of fibronectin. J Mater Sci:Mater Med 2001; 12: 111–119.

[15] Bae JS, Seo EJ, Kang IK. Synthesis and characterization of heparinized polyurethanes using plasma glow discharge. Biomaterials 1999; 20: 529–537.

[16] Favia P, Creatore M, Palumbo F, Colaprico V, d'Agostino R. Process control for plasma processing of polymers. Surf Coat Technol 2001; 142: 1–6.

[17] Dalby MJ, Yarwood SJ, Riehle MO, Johnstone HJH, Affrossman S, Curtis ASG; Exp Cell Res 276 (2002) 1–9.

[18] Curtis ASG, Gadegaard N, Dalby MJ, Riehle MO, Wilkinson CDW, Aitchison G. Cells react to nanoscale order and symmetry in their surroundings. IEE Trans Nanobiosci 2004; 3: 61–65.

[19] Dalby MJ, Gadegaard N, Riehle MO, Wilkinson CDW, Curtis ASG. Investigating filopodia sensing using arrays of defined nano-pits down to 35 nm diameter in size. Int J Biochem Cell Bio 2004; 36: 2015–2025.

[20] Curtis ASG, Casey B, Gallagher JO, Pasqui D, Wood MA, Wilkinson CDW. Substratum nano-topography and the adhesion of biological cells. Are symmetry or regularity of nano-topography important? Phys Chem 2001; 94: 275–283.

[21] Dalby MJ, Yarwood SJ, Riehle MO, Johnstone HH, Affrossman S, Curtis ASG. Increasing fibroblasts response to materials using nanotopography: morphological and genetic measurements of cell response to 13-nm-high polymer demixed islands. Exp Cell Res 2002; 276: 1–9.

[22] Dalby MJ, Yarwood SJ, Johnstone HH, Affrossman S, Fiehle M. Fibroblasts signaling events in response to nanotopography: a gene array study. IEE Trans Nanobiosci 2002; 1: 12–17.

[23] Anderson A-S, Olson P, Lidberg U, Sutherland D. The effects of continuous and discontinuous groove edges on cell shape and alignment. Exp Cell Res 2003; 288: 177–188.

[24] Liao, A.-S. Anderson, D. Sutherland, S. Petronis, B. Kasemo. Response of rat osteoblast-like cells to microstructured model surfaces in vitro. Biomaterials 2003; 24: 649–654.

[25] Dalby MJ, Riehle MO, Johnstone HH, Affrossman S, Curtis ASG. Investigating the limits of filopodial sensing: a brief report using SEM to image the interaction between 10 nm high nano-topography and fibroblasts filopodia. Cell Bio Int 2004; 28: 229–236.

[26] Hanarp P, Sutherland D, Gold J, Kasemo B. Control of nanoparticle film structure for colloidal litography. J Colloid Interf Sci 2001; 241: 26–31.

[27] Dalby MJ, Berry CC, Riehle MO, Sutherland DS, Agheli H, Curtis ASG. Attempt endocytosis of nano-environment

produced by colloidal lithography by human fibroblasts. Exp Cell Res 2004; 295: 387–394.

[28] Dalby MJ, Riehle MO, Johnstone HJH, Affrossman S, Curtis ASG; Biomaterials, 2002; 232: 945–2954.

[29] Denis FA, Hanarp, Sutherland DS, Dufrêne. Fabrication of nanostrucutred polymer surfaces using colloidal lithography and spin coating. Nanolett 2002; 2: 1419–1425.

[30] Favia P, Sardella E, Gristina R, Milella A, d'Agostino R. J Photopolym Sci Technol 2002; 15: 341–350.

[31] Ertel SI, Chilkoti A., Horbett TA, Ratner BD. Endothelium cell growth on oxygen-containing films deposited from radio-frequency plasma-The role of surface carbonyl groups. J. Biomat. Sci. Polym. Ed 1991; 3:163.

[32] Gupta B, Plummer C, Bisson I, Frey P, Hilborn J. Plasma-induced graft polymerisation of acrylic acid onto poly(ethylene terephthalate) films: characterization and human smooth muscle cell growth on grafted films. Biomaterials 2002; 23: 863–871.

[33] Maroudas N.G. Adhesion and spreading of cells on charged surfaces. J. Theor. Biol. 1975; 49: 417.

[34] Jewell-Larsen NE, Pan V, Denton DD, Ratner BD. Controlled substance release through the degradation of biodegradable plasma deposited PLA (poly lactic acid) coatings. J Undergrad Res Bioeng 2001; 1: 77–86.

29
The Model for Origin of Life Precursors Based on Exhaust Utilisation in the Electric Discharge

Marcela Morvová, Imrich Morva, František Hanic

Abstract

The present paper describes the process of CO_2 and combustion exhaust utilisation using a transition electric discharge. The final solid product is a proteinoid composed of various L-amino acids. The time and humidity causes a reconfiguration of the product leading to the formation of microspheres. In the polymerization process during the quench phase, the oxygen is released in a measurable concentration. Such a process could have been involved in the ozonosphere formation on the early Earth without the need of photosynthesis. The technical application of the exhaust utilization leads to CO_2 mitigation.

29.1
Introduction

The early Earth's atmosphere consisted mainly of gases released by the volcanic activity. The composition of the combustion exhaust is similar to the neutral primitive atmosphere, i.e. CO_2, CO, H_2O, N_2, and traces of NH_3, H_2, CH_X. Miller [2] performed the first successful synthesis of individual amino acids in a strongly reducing atmosphere in apparatus with repeated spark discharges between two carbon electrodes (1952). Later (from 1972), in the same type of discharge, an experimental study for medium reducing and (from 1987) for neutral primitive atmospheres was done [1]. As described in [1], it is hardly possible to form various biologically important macromolecules from monomers in polymerization processes without additional energy supply. From the power sources present in the Earth conditions, the most intense is the terrestrial lightning with an available energy of electrons up to ~20 eV, UV radiation ~1–10 eV, and excited particles up to ~15 eV. At present, about 2×10^6 lightning strikes occur daily. With the rising CO_2 concentration the number of lightning increases. In the prebiotic conditions, this number was probably in 3–5 orders of magnitude higher, i.e. to about 10^{10} lightning strikes per day. The heterogeneous process leading to the polymerization on charged rocks was proposed by Orgel in [4]. Ferris [5] proposed submarine vents as another very probable form of energy source. A part of energy available in interstellar conditions (cosmic rays

~MeV, solar wind ~keV, UV radiation ~1–10 eV) can be used also on the Earth in photochemical processes, as described by Bernstein et al. [6]).

29.2 Experimental

The small pilot equipment built for 50–250 N m^3/h of exhaust gas flow operates with spontaneously pulsing electric discharge. The individual discharge channels quickly travel on the surface of the stressed electrode. The discharge channels connect with dielectric spots that are formed during discharge action. This spots have enhanced dielectric constant and catalytic properties. The system was tested in the gas-flow regime using various exhaust types. The residence time of the gas in the discharge zone was about ~ 2 s.

The direct diagnostics of reacting gases before and after the electric discharge reactor was done using IR absorption spectrometry. The final solid product was analyzed by the IR absorption spectrometry, HPLC, X-ray diffraction and thermogravimetric analysis. In situ step by step time development measurements made inside a small discharge reactor placed in the IR gas cell enabled a better insight into conversion processes, reaction kinetics, product development, amino acid formation and establishment of the catalytic surface spots on the electrodes.

Activation of the gas system was performed by electric discharge; involved activating factors were electrons, excited heavy particles, photons and surface catalysis. The process starts in the volume of the discharge zone by formation of electronically excited metastable molecular nitrogen $A^3\Sigma_u^+$with a lifetime of up to 2 s. This excited state could be achieved by a repeated electron impact to achieve the total energy of ~6.8 eV. Due to the reaction of N_2* with CO_2 an intermediate ON–NCO is formed. ON–NCO reacts with water to form amid radicals. Repeated radical polymerization then leads to the formation of the final solid random polycondensate-proteinoid. The analysis of the solid product shows that it contains various amino acids (arginine, lysine, histidine, methionine, glycine, alanine, serine and aspartic acid). This results from the performed experiments that the experimental value of energy consumption necessary for all involved chemical processes is 2.3–4.7 W h/m^3, i.e. 8.3–16.9 kJ/m^3 of exhaust gases. Due to the disproportion in theoretical (sum of energy necessary for individual steps of the chain reaction producing the final proteinoid) and experimental values of energy consumption we have tried to determine the responsible catalytic effects.

A precise analysis of the nonstressed electrode by IR reflection spectrometry gave us more detailed information about the catalytic layer formation. It seems that an important role might be played by oxamidato complexes $(HNCO)_4Cu$. Some other compounds on the electrode surface were found to have catalytic properties as well, namely heterocyclic structures containing pyrrole rings. The presence of metal complexes was supported by thermogravimetric analysis, showing 3–5% residue after heating in nitrogen up to 900 °C. We have tried to analyze some details of these complicated structures. Comparing IR absorption spectrum of the liquid pyrrole with a

single ring and the spectrum of the nonstressed electrode surface (down) in Fig. 1 we conclude that the surface products also contain oligo pyrrole compounds. The final product from prepilot equipment (its IR spectrum is in the upper part of Fig. 1) is a solid powder with fractal structure on microscopic level, with a low specific weight, consisting of chains of flakes as it is seen on SEM microscopic photographs on the right part of Fig. 2. We have produced ~100 g of proteinoid in an abiotic system, i.e. by influencing the combustion exhaust (similar to the primary atmosphere) and the water aerosol with repeated electric discharge. Due to charged water droplets and under the influence of additional humidity and time the produced proteinoid can reconfigure into micelle-like microspore aggregates, i.e. a potential plasma membrane can evolve as we see from the SEM micrographs in Fig. 2.

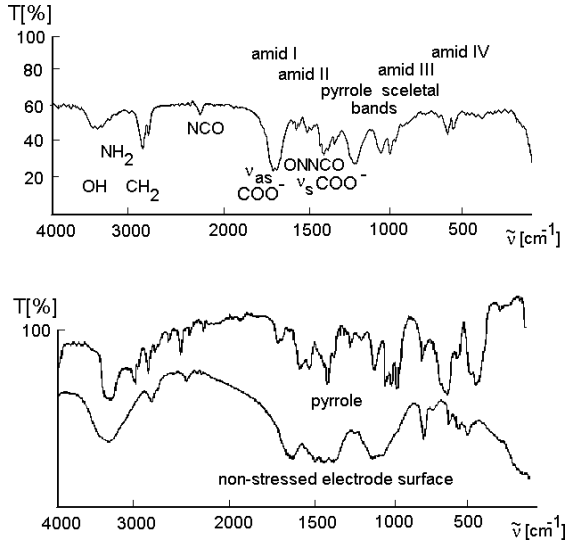

Figure 1 IR absorption spectra of solid condensation product (up), electrode surface and liquid pyrrole (down).

The protocells published by Pappelis and Fox [9] have diameters varying from 0.3–5 μm, our microspheres are in about the same size scale, as we can see from SEM micrographs.

The general overview of the processes taking part in the electric discharge occurring in the combustion exhaust can be seen from Fig. 3. The involved chemistry during the final product formation was extracted from the step-by-step kinetic studies made inside a gas-cell discharge tube. The process can be divided into three important steps:

1. activation
2. formation of energy-rich intermediate species, formation of catalytic spots on electrode surfaces, volume reactions in nonequilibrium plasma condition, surface reactions on electrodes

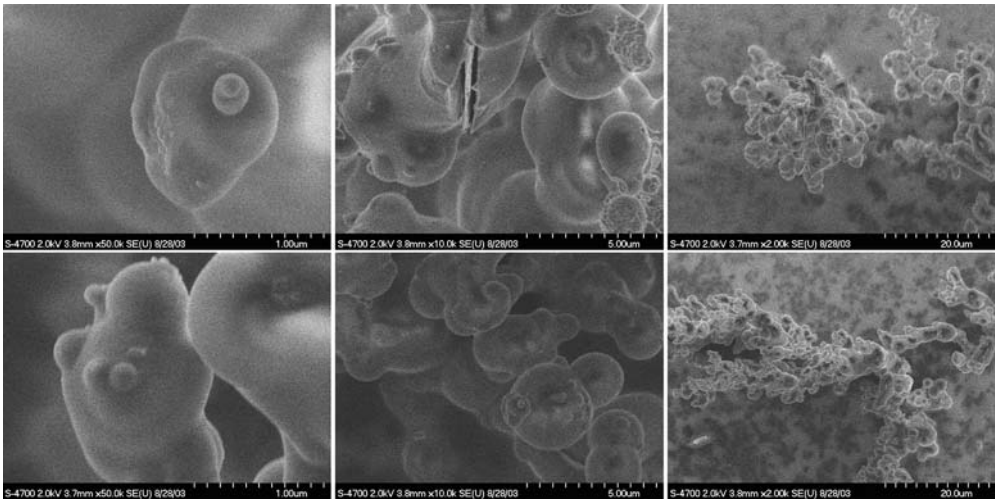

Figure 2 SEM micrographs of the solid product; size bar on left side 1 µm, middle 5 µm and on right side 20 µm.

3. final products

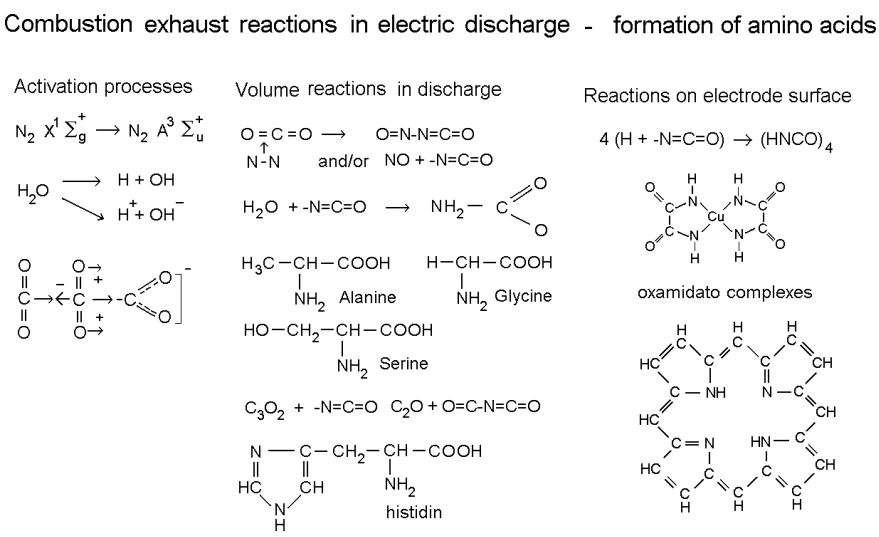

Figure 3 The processes involved in the conversion of combustion exhaust in the spontaneously pulsing electric discharge. Formation of the amino acid condensation product and the catalytic active spots on the electrode surface.

The hypothesis

1. Activation by Terrestrial Lightning

Here we want to show that the return stroke when a lightning beats into the seawater may play a role of an energy source necessary for the important origin of life compounds, as well as polymers up to the micelle-like aggregates in the prebiotic Earth.

A large amount of energy is transferred from the lightning spark channel into water and surrounding air. Due to the adiabatic expansion of the plasma channel (lightning body), the activated species produced by such discharge (electrons, ions, metastable atoms and molecules, light, heat) are transported from the plasma channel to the zones, where the gas temperature is much lower (~200 °C). In such zones, the electric field is no longer disturbed by the lightning and a dc electric field between a cloud and the sea is still present. The lightning streamer body contains mostly positive space charge since the electrons are transported quickly to the seawater due to their large mobility. The above-mentioned factors cause the chain reaction in the gas mixture containing N_2–CO_2–H_2O and water droplets as described in Fig. 3 to develop, leading to L-amino acids. Additionally, ON–NCO and OC–CCO intermediate species form pyrrole-ring-based compounds. These substances and various other fragments form polymeric fractal clusters by a polycondensation process in the zone under ~200 °C. The gas products formed in the discharge are adsorbed inside the cluster. A free positive space charge forms in the discharge channel and attaches to several gaseous, as well as solid species. The fragments expand from the lightning streamer body and are incorporated into the formed fractal cluster.

When the lightning stroke beats into the water, the process is usually associated with huge water evaporation. The extreme heat release also causes the sublimation of volatile aerosols impregnated by minerals from the see bottom. The conductivity of the Earth surface (see bottom) is relatively small. This is why the electrons produced by the discharge cannot be conducted to the Earth quickly enough and due to this a large amount of negative charge is dissolved in the water. From primary atmosphere components, only CO_2 is highly soluble in water. This fact implicated the composition of gas slope inside the stroke part of water to CO_2–H_2O–mineral part (–PO_4, K, Ca, Na)-negative space charge. As inside this slope in water the pressure is very high, nitrogen from the atmosphere cannot diffuse into the slope. Due to the composition of present species and negative space charge, the D form of sugars together with minerals may be formed. This can explain incorporation of –PO_4 into polymer aggregates that can possibly be converted into further RNA, DNA, ADP and ATP. The high pressure in the stroke slope transports the formed compound out from the water surface in the trajectory crossing the trajectory of the amino acid part of the product formed in the discharge channel outside the water. In this way, the fractal cluster containing L-amino acids, D-sugars, unsaturated organic acids, phosphate groups, as well as various minerals, plus attached free positive space charge and bonded positive and negative charge, in the common solid fractal aggregate product may be formed. Due to the electric wind from the cloud to the Earth in the zone with nondisturbed electric field and low temperature, formed fractal clusters are transported to the water surface. Details of the process can be seen in Fig. 4.

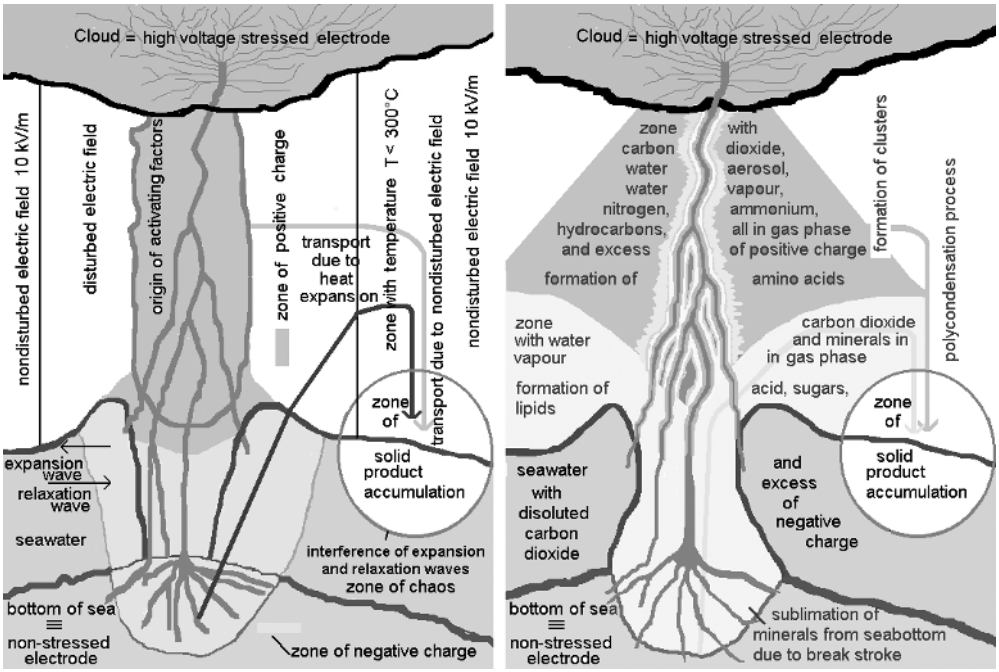

Figure 4 Overview of the gas-dynamic and chemical processes connected with the activation by terrestrial lightning.

2. Origin of the Ozonosphere

The formation of heterocyclic compounds from radicals and activated species generates several molecules of oxygen in each reaction step, as we can see for adenine, cytosine and ribose formation in Fig. 5. We achieved this process also in the pilot discharge system where the residence time of the exhaust was 0.5 s. We have generated in our experimental flowing system from oxygen-free combustion exhaust containing up to 8% of CO_2 oxygen after action of discharge (up to 5% by volume). Such oxygen could form the ozonosphere even earlier then photosynthesis began to work. In the primary atmosphere, the diffusion of formed oxygen to the upper parts of the atmosphere was much more probable due to the high specific weight of the remaining atmospheric gases (CO_2 molecular weight 44, nH_2O for $n \geq 2$ molecular weight ≥ 36, O_2 molecular weight 32). The solubility of oxygen in water is small and varies in between 4.9 and 1.7% (0–100 °C). This implies that oxygen will diffuse up. To estimate the necessary time for ozonosphere origin we have evaluated the amount of ozone produced in one day from the number of lightning strikes ($\cong 10^{10}$ per day), the transported charge in one lightning strike (50 C = 31.2×10^{19} electrons), the probability of oxygen formation 0.1 to the value of 1.04×10^{29} molecules. Then we have estimated the number of ozone molecules in today's ozonosphere (in the case of a 3-mm thickness at atmospheric pressure, the height 25 km, i.e. ozone volume 4.637×10^{12} m^3) to the value 1.12×10^{38} molecules. To generate such amount of

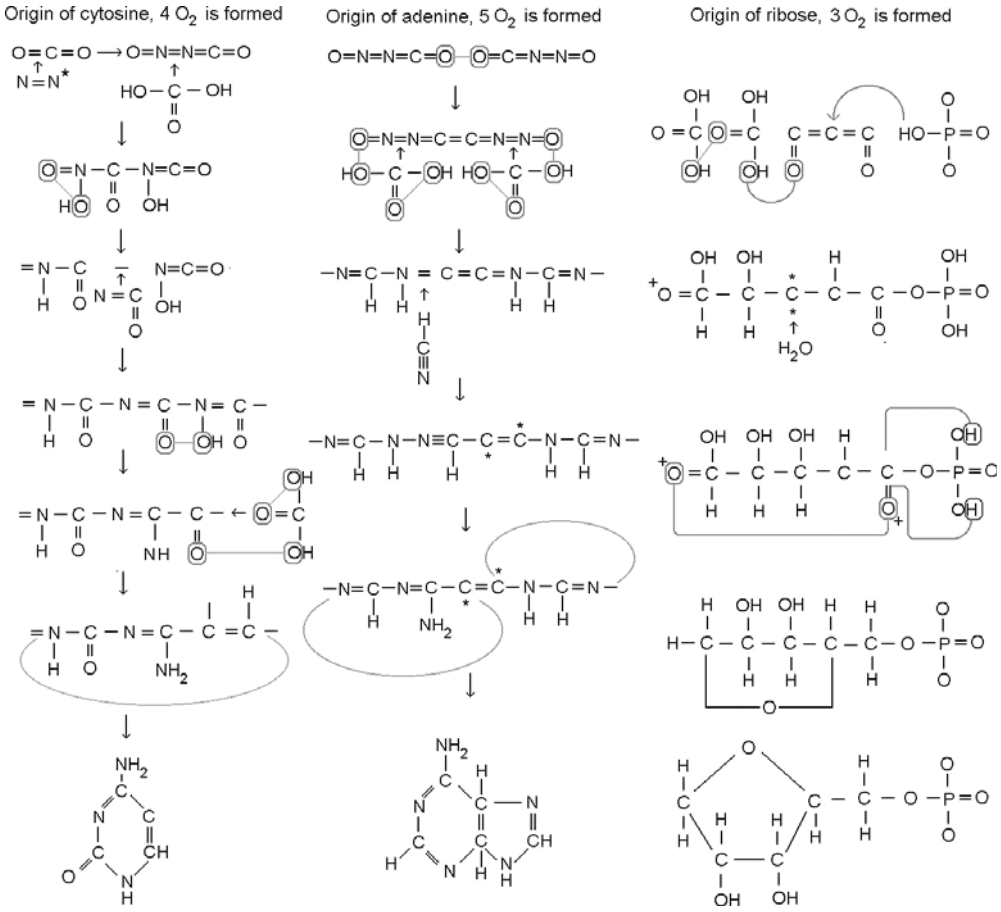

Figure 5 The formation of bases adenine, cytosine and sugar ribose from radicals and activated species leading to the formation of oxygen.

ozone, when we additionally suppose that only 50% of oxygen will diffuse up and probability of ozone generation from oxygen due to UV radiation is 1%, we need 2.154×10^{11} days i.e. about 6×10^{8} years. The gained value 600 million years seems to be a realistic estimate for the time of ozone-layer origin.

3. Protocell Origin (See Fig. 6)

When a fractal cluster with adsorbed gases and attached free positive space charge reaches the water surface 1, water tries to get into the cluster and gases try to go out. The attached positive space charge is set free and due to repulsive forces, forms a positive ball around the fractal cluster. As the water is charged negatively, due to the electrostatic induction the electric bilayer is formed. Inside this bilayer the desorbed volatile compounds are oriented and create micelle-like forms. Such micelle rear-

rangement leads to the formation of a plasma membrane, which covers fractal clusters in the shape of microspheres 2. This was possible to see on samples scanned by the SEM method. The bilayer was established in a relatively short time, i.e. several minutes.

Splitting of the proteinoid inside a microsphere due to the UV radiation leads to the decrease of crosslinking degree and fragmentation of cluster structure 3. Some fragments diffuse into the plasma membrane bilayer to create precursors of future membrane components. Smaller fragments solute in water to produce cytoplasm. Middle-size fragments can lead to the origin of enzymes. Large fragments separate to produce histone-type compounds (RNA, DNA and pigments), proteins and various mixed-type compounds. The conformation of fragments is still random 4. The individual polar parts of the proteinoid chain are surrounded by the opposite charge creating a Debye shielding layer 5. Reconfiguration of the random conformation to thermodynamically more stable (helical) structures 6 causes the destruction of the shielding layer around charged groups. The dipoles are formed due to the hydrogen bonding between amino acid zwitterions 7. Bonded positive as well as negative charge from the shielding layer around the charged groups is set free in the reconfiguration process, but it cannot get out from the micelle. Created free charge is redistributed and used to form intracellular membranes of organelles and in this way to create future protocells 8. We have tried to evaluate the most important parts of charge redistribution inside a cell. The charge of one sector of the structures present in the nucleus (histone components) is in total positive, so the nucleus is located in the center of the cell due to repulsive forces from the cell/plasma membrane. The charge of tetrapyrolle structures present in thylacoids is in total negative, so thylacoids are due to attractive forces from the cell/plasma membrane situated close to the inner part of the membrane. The time necessary for this part of the process was not possible to evaluate, but we have estimated it to several years. The schema of the protocell origin is shown in Fig. 6.

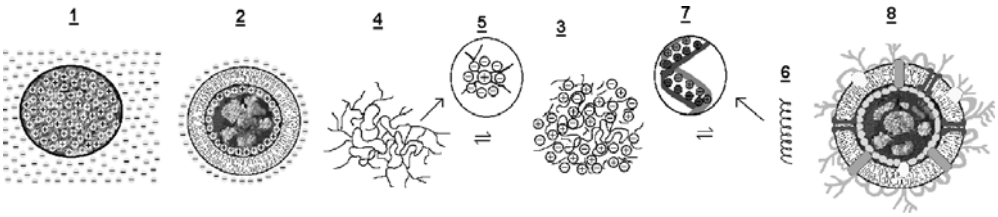

Figure 6 Development of a plasma membrane around the fractal cluster after reaching water, formation of a microsphere, redistribution of the bonded charge and origin of a protocell.

29.3 Conclusions

We investigated a method of CO_2 and combustion exhaust treatment using the electric discharge. This method is interesting from the point of view of greenhouse-effect limitation. Its main advantage is that in a single system, the full utilisation of combustion exhaust inclusive CO_2 takes place. The observed utilisation efficiency is high (40–99% of CO_2 is utilised) and the method works also for NO_X and CH_4 removal with efficiency of up to 95% [7]. The process is closely connected with mechanisms that took part in the prebiotic chemistry, as seen from the article reported in [8].

We have collected in one model most of the points necessary for the origin of life on the Earth. Some valuable experimental results leading to our hypothesis are:

1. We have shown how amino acids and other important life substances and polymers can be formed.
2. We have produced a proteinoid (~100 g) in an abiotic system by treating the combustion exhaust (similar to the composition of the primary atmosphere) and charged water aerosol with the spontaneously pulsing transient electric discharge.
3. We have produced oxygen from oxygen-free combustion exhaust in the electric discharge. We have shown the possibility of oxygen formation before the onset of photosynthesis on the early Earth and estimated the probable time period necessary for the formation of the ozonosphere to about 600 millions of years.
4. Due to charged water/water droplets the produced proteinoid can be converted into micelle-like formations (protocells), i.e. the plasma membrane can be formed as observed by SEM photographs in Fig. 3.

Acknowledgement

The authors wish to thank the Agency for the Support of Science and Technology (APVT) for the financial support given to the bilateral Slovak-US project No.027/2001 and the Slovak Scientific Grant Agency (VEGA) for the financial support given in projects 2/4091/04.

References

[1] S.L. Miller in "Major Events in the History of Life", Ed. J.W. Schopf (Jones&Bartlett, Boston, Mass., 1992) Chap.1, pp. 1–28

[2] S.L. Miller, A Production of Amino Acids Under Possible Primitive Earth Conditions: Science 117 (1953) p. 528–529

[3] H. Dolezalek, Discussion of the fundamental problem of atmospheric electricity, Pure Appl. Geophys., 100 (1972) 8–43

[4] L.E. Orgel, Orig. Life Evol. Biosphere 28 (1998), Polymerization on the Rocks: Theoretical Introduction, pp. 227–234

[5] J.P. Ferris, Marine hydrothermal systems and the origin of life: Chemical markers of prebiotic chemistry in hydrothermal systems. Origins Life Evol Biosphere 22 (1992) 109–134

[6] M.P. Bernstein, S.A. Sandford, L.J. Allamandola, S. Chang: Astrophys. J. 454 (1995) 327–344

[7] M. Morvová, F. Hanic, I. Morva: Plasma Technologies for Reducing CO_2 Emissions from Combustion Exhaust with Toxic Admixtures to Utilisable Products, J Therm Anal Calorim, 61 (2000) 273–287

[8] F. Hanic, M. Morvová and I. Morva: Thermochemical Aspects of the Conversion of Gaseous System CO_2-N_2-H_2O into Solid Mixture of Amino Acids, J Therm Anal Calorim, 60 (2000) 1111–1121

[9] A. Pappelis and S. Fox at http://www.siu.edu/~protocell/photos.htm

Part IV
Chemical Synthesis, Powders and Non-Equilibrium Effects

30
Gliding-Discharge CF_2Cl_2 and CHF_2Cl Decomposition in Reducing Conditions

Teresa Opalińska, Anna Opalska, Krzysztof Schmidt-Szałowski

Abstract

The decomposition yield of freons CF_2Cl_2 and CHF_2Cl in the presence of hydrogen was studied using a gliding-discharge reactor supplied with AC at the frequency of 50 Hz, at atmospheric pressure. The effect of hydrogen content in the starting mixtures of freon+H_2+Ar on the chemical and energetic efficiency of the process was examined. Both the total conversion of freons (U) and effective conversion (U_{ef}) increased with increasing hydrogen content. Acetylene, methane and carbon black were the main products of the freon conversion. The conversion of both CF_2Cl_2 and CHF_2Cl into acetylene decreased with increasing hydrogen molar fraction above 0.2, whereas the conversion into methane and carbon black increased at the same time, being higher for CHF_2Cl than for CF_2Cl_2.

The postreaction gases also contained a number of unwanted halocarbon compounds, mainly $C_2F_4Cl_2$ and CF_3Cl, being formed in the discharge. However, the conversion of the starting freons into the halogen derivatives was greatly reduced when increasing the concentration of hydrogen. The highest total conversion of starting freons (0.963 for CHF_2Cl and 0.921 for CF_2Cl_2) as well as the lowest conversion into halogen compounds (0.022 for CHF_2Cl and 0.005 for CF_2Cl_2) were obtained using mixtures of freon+H_2 with no argon addition. The composition of the reaction products was similar irrespective of the starting freon used, however, the energetic efficiency of CF_2Cl_2 decomposition was higher than that of CHF_2Cl. It may be concluded that in the reactions of halocarbon compounds hydrogenation CH^* radicals are involved.

30.1
Introduction

Simple halocarbon compounds, containing both fluorine and chlorine, usually referred to as freons (CFC) have been widely applied. The compounds of methane and ethane are two essential groups of these compounds. They are characterised by a high thermal stability and a very low toxicity. Being not explosive and practically not combustible, freons are used in cooling installations, for production of insula-

tion foams and aerosols, and as solvents, especially in the electronics industry. However, these compounds, so useful and convenient in practical applications, proved to be harmful in destroying the ozone in the stratosphere and increasing the greenhouse effect. Owing to the high stability freons can penetrate to the upper regions of the atmosphere, being very active in the destruction of the ozone layer. Under the action of ultraviolet radiation CFC molecules liberate chlorine atoms that react with ozone in a chain reaction. Thus, a single Cl atom can destroy from 10 up to 100 000 molecules of ozone [1]. The lifetime of CFC in the atmosphere varies from 60 to 400 years, depending on the kind of freon. Their ability to increase the greenhouse effect is also high compared with CO_2 [2].

Legislative initiatives have been undertaken aiming first at limiting, then at complete prohibition of the production of CFC (the Vienna Convention in 1985, the Montreal Protocol in 1987, the London Conference in 1990, etc.). Any remaining stocks of freons should be destroyed as soon as possible. The classical methods for the freons decomposition consist in thermal [3,4] or catalytic [5–7] processing or in a biodegradation [8]. The Uhole GmbH, a branch of the HOECHST AG, has developed and implemented in 1981 a technology for high-temperature decomposition of CFC in a hydrogen-oxygen flame in the presence of water vapor or/and hydrogen fluoride. The high temperature is necessary to prevent the emission of harmful side products such as the chlorinated dioxins and furans. The limits of admissible concentrations of these compounds in postreaction gases are very low. There are two trends in the catalytic methods for decomposition of CFC. In some methods selective catalysts are used, which enable a substitution of chlorine in the freon molecule by hydrogen atoms [5,6], whereas the other group is based on the catalytic oxidation of CFC [7].

The plasma methods consist in decomposition of freons in a stream of equilibrium plasma [9,10] or under the direct action of electric discharges [11–18]. Most of the plasma processes are carried out in the presence of additional reagents such as oxygen [14,15], air or/and water vapor [11,12,16], as well as hydrogen and oxygen [13]. Other reagents such as nitrogen [17,18] and hydrogen [14] are also applied. An Australian company, SRL Plasma Ltd., is in possession of a verified technology PLASCON [9,10] based on decomposition of halocarbon compounds, with an efficiency of 99.99%, in a stream of argon plasma in the presence of oxygen and water vapor, or of water vapor alone. Under such conditions, CO_2, HCl and HF are the decomposition products. The presence of water vapor reduces significantly the contents of other, unwanted products, such as other freons, dioxins and furans, being formed in the process, [9,10]. A shortcoming of the CFC decomposition in the plasma stream is high losses of Energy in the cooling systems of electrodes and gaseous products. These losses can be minimised if the starting reagents are introduced directly into the electric-discharge zone. In such a way the unit-energy consumption for the freons decomposition may be reduced.

The decomposition of freons in electric discharges was carried out both under atmospheric [11,15–18] and under reduced pressures [12–14]. The concentration of freons in the reaction mixture was varied from several dozens ppm to several dozen per cent. In most references, the main topic was to find the relationships between

total conversion of freon and such parameters as the quantitative and qualitative composition of the starting mixture, pressure, and electric parameters of the discharge. The qualitative and the quantitative composition of the postreaction gases were rarely the object of analyses. Various models for the mechanism of the freons decomposition were proposed. In the most widespread view the decisive steps in this process consist in the dissociation of a freon molecule in a collision with electron and a dissociative attachment of electron to the molecule.

In the course of the present study the decomposition of the selected freons (CF_2Cl_2 and CHF_2Cl) was carried out in a high-voltage gliding discharge at atmospheric pressure (usually referred to as the "Glid Arc" – the name proposed by Czernichowski [19]). The decomposition of CFC was effected in a continuous, although non-stationary plasma process [20–22]. As is generally known, the gliding discharge comprises both the regions of equilibrium and of nonequilibrium plasma, with 80–90% of the energy being released in the latter [21,22]. The temperature of the gas mixture is roughly 2000 K whereas the mean electron temperature may reach up to 10 000 K. Formerly, the gliding discharge was applied for the decomposition of $CFCl_3$, CF_2Cl_2 and CHF_2Cl in the presence of water vapor [23] and oxygen [24,25]. Another method tested was the decomposition of freons in the presence of a reducing agent (hydrogen). The advantage of this method is that simple aliphatic hydrocarbons are the main reaction products [23] and no harmful side products like chlorinated dioxins and furans or phosgene, normally formed in oxidative or redox media, are produced.

In this study the conversions of difluorodichloromethane (CF_2Cl_2) and difluorochloromethane (CHF_2Cl) were investigated in mixtures with hydrogen and argon (H_2+Ar) using a gliding-discharge rector.

30.2 Experimental

30.2.1 Experimental Setup

The experimental setup (Fig. 1) contained a plasma reactor, electric three-phase supply system, gas dosage system, vessels for gaseous-products absorption, and analytical instruments. The reactor was operated by the principle of gliding discharges and was supplied with alternating current at the frequency of 50 Hz. The discharge was generated between three knife-shaped main electrodes with the auxiliary (starting) high-voltage electrode under atmospheric pressure. In order to estimate the electric energy consumption, a three-phase meter was installed in the electric circuit. The mixtures of argon, hydrogen and freons were fed through the mixer into the interelectrode space of the reactor. The flow rates of individual gas streams were controlled by means of mass flow meters (Brooks Instrument B.V.) calibrated for individual gases. The postreaction gases were cooled and passed to a sorption system, where inorganic components (HF and HCl) were absorbed in an aqueous alkali

solution. After that, samples for chromatographic analyses were taken. The flow rate of the postreaction gases was measured with a suitable gas meter.

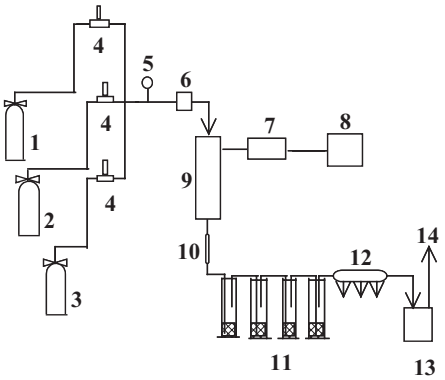

1, 2, 3 - gases, 4 - mass flow controller, 5 - manometer,
6 - mixer, 7 - power supply unit, 8 - power measurement system,
9 - plasma reactor, 10 - cooler, 11 - absorption unit,
12 - gas sampler, 13 - gas measurment system, 14 - vent

Figure 1 Scheme of experimental setup.

30.2.2
Chemical Analysis

The postreaction gas mixture was analysed using gas chromatography by means of the HP 6890 instrument with a flame-ionisation detector. Helium (25 ml/min) was used as the carrier gas. The analyses were carried out using an internal standard method and a column 4 m long and 3 mm internal diameter filled with Carbopack™ B/ 5% Fluorocol™ of granulation 60/80 mesh. The components determined were methane, ethane, ethylene, acetylene, propane and the freons. The standard mixtures used were: Scotty® IV produced by Supelco and Mix 0050B produced by Praxair Poland, as well as pure freons (98 vol%) C_2F_5Cl and CF_3Cl produced by Fluorochem Ltd.

30.2.3
Conditions of Experiments

Two series of experiments were performed under the conditions given in Table 1. In the 1st series the reactant was a mixture of 91 vol% difluorodichloromethane (CF_2Cl_2, freon R12) and 9 vol% difluorochloromethane (CHF_2Cl), whereas in the 2nd series it was almost pure difluorochloromethane. Fluorochlorohydrocarbons were diluted with hydrogen, argon, or with a mixture of H_2+Ar. In all the experiments both the total molar flow rate of the inlet gas mixture and the molar flow rate of the reactants were kept constant. Constant electrode voltage was kept automati-

cally by the applied supplying system, whereas the discharge energy, being generated in the reactor (estimated from the power measurement), depended strongly on the composition of the gas-inlet mixture and increased with increasing concentration of hydrogen. In the 2nd series with CHF_2Cl the discharge power varied from 0.75 kW to 2.21 kW generally being higher than that observed in the 1st series with CF_2Cl_2/CHF_2Cl (0.64–2.07 kW) (Fig. 3). In order to make it simpler, in the next sections only two starting reagents are mentioned: CF_2Cl_2 (1st series) and CHF_2Cl (2nd series). However, it should be noticed that in the 1st series a mixture of CF_2Cl_2 and CHF_2Cl was used (containing mostly the former of these components).

Table 1 Conditions of experiments

Serie	Reactant	Composition of reactant [vol. %]	Total flow of inlet gas mixture [mol/h]	Reactant flow rate in inlet mixture [mol/h]	Hydrogen flow rate in inlet gas mixture [mol/h]	Power generated in reactor [kW]
I	CF_2Cl_2	CF_2Cl_2– 91.0 CHF_2Cl– 9.0	73.9 ± 1.4	1.18 ± 0.01	0 – 71.5	0.64 – 2.21
II	CHF_2Cl	98.0	73.1 ± 0.2	1.04 ± 0.04	0 – 72.0	0.75 – 2.07

30.2.4 Definition of the Process Parameters

The chemical effectiveness of the process is characterised here by the total conversion of a reactant (U) and the effective conversion (U_{ef}).

The total conversion of reactants is given by the formula:

$$U = (n_r - n_r')/\, n_r \quad [\text{mol/mol}], \tag{1}$$

where: n_r – number of reactant moles per hour introduced into the reactor, [mol/h]; n_r' – number of reactant moles per hour that are not converted, [mol/h].

The effective conversion (U_{ef}) characterises the process of reactant conversion into components that do not contain chlorine and fluorine and it is defined as follows:

$$U_{ef} = (n_r - n_r' - \mathrm{S}\ a^* n_{CFC})/\, n_r\ [\text{mol/mol}], \tag{2}$$

where: n_{CFC} – number of moles per hour of unwanted freon being produced in the reaction [mol/h], a – number of carbon atoms in a freon molecule.

The molar ratio of hydrogen (X_{H2}) in the inlet mixture is calculated using the formula:

$$X_{H2} = n_{H2}/(n_{H2} + n_r + n_{Ar}) \quad [\text{mol/mol}], \tag{3}$$

where: n_{H2}, n_{Ar} – number of moles of hydrogen and argon, respectively, in inlet gases [mol/h].

The conversion of reactants into individual freons being formed in the process (U_{CFC}) is defined as:

$$U_{CFC} = a^* n_{CFC} / n_r \quad [\text{mol/mol}]. \tag{4}$$

The conversion of a reactant to an individual hydrocarbon (U_{CxHy}) is defined as:

$$U_{CxHy} = (x^* n_{CxHy}) / n_r \quad [\text{mol/mol}], \tag{5}$$

where: x – number of carbon atoms in the hydrocarbon molecule; n_{CxHy} – number of moles per hour of the product being formed [mol/h].

The conversion of freons, being the starting reagents, into carbon black (U_c) could be calculated based on the overall balance of carbon in the inlet and outlet gases from the formula:

$$U_c = (n_r - n_r' - \text{S}\ a^* n_{CFC} - \text{S}\ x^* n_{CxHy}) / n_r \quad [\text{mol/mol}]. \tag{6}$$

The energetic efficiency of the process is characterised by means of the unit-energy consumption (Z) and the effective energy consumption (Z_{ef}):

$$Z = P/(n_r - n_r') = (P/U)^*(1/n_r) \ [\text{kWh/mol}] \tag{7}$$

$$Z_{ef} = P/(n_r - n_r' - \text{S}\ a^* n_{CFC}) = (P/U_{ef})^*(1/n_r) \ [\text{kWh/mol}], \tag{8}$$

where: P – is the discharge power.

The individual parameters of CF_2Cl_2 and CHF_2Cl mixture conversion (1st series) are calculated taking into account the composition of the inlet mixture in a balance of the carbon.

30.3 Results and Discussion

30.3.1 Essential Parameters of the Process Characteristics

The total conversion (U) and effective conversion (U_{ef}) of freons in both series of experiments depended on the inlet-gas composition and on the discharge power (P). As already mentioned the discharge power increases with increasing molar fraction of hydrogen (X_{H2}) and attains a maximum in pure hydrogen (Figs. 2 and 3). The discharge power depends also on the kind of starting reagent to be decomposed.

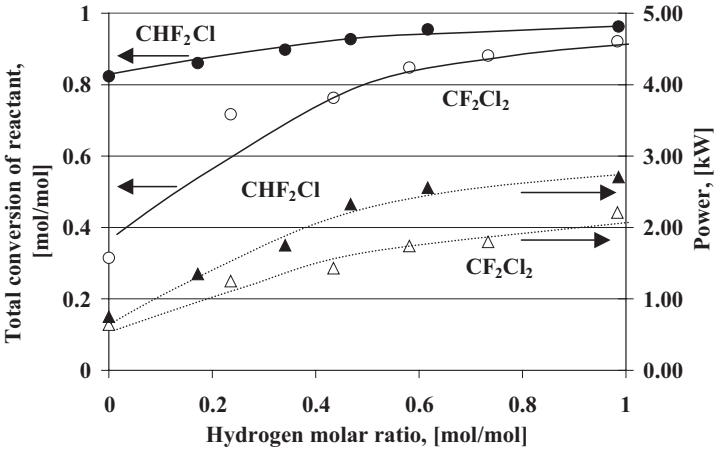

Figure 2 Effect of hydrogen molar ratio (X_{H2}) on total conversion of reactants (U) and power generated in the reactor (P).

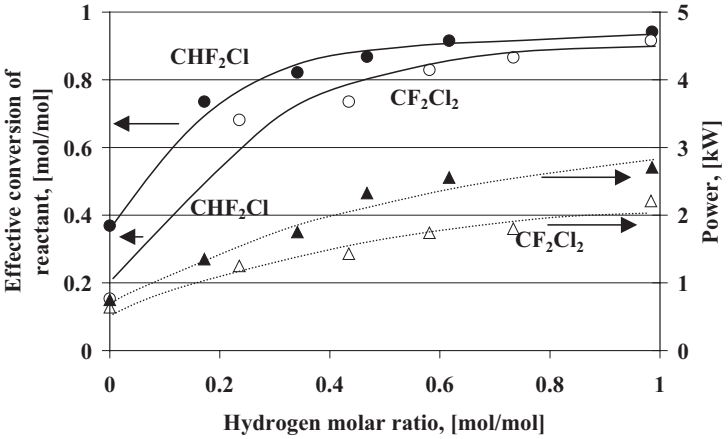

Figure 3 Effect of hydrogen molar ratio (X_{H2}) on effective conversion of reactants (U_{ef}) and power generated in the reactor (P).

Both the total conversion (U) and effective conversion (U_{ef}) increase with increasing content of hydrogen in the mixture of H_2+Ar (Figs. 2 and 3). The maximum conversion of CF_2Cl_2 (0.921) obtained in a mixture with pure hydrogen ($X_{H2} = 0.98$), was lower than that of CHF_2Cl (0.963) obtained at an identical value of X_{H2}. A similar relationship was found for (U_{ef}) under the same conditions: 0.916 for CF_2Cl_2 and 0.941 for CHF_2Cl. The difference between total and effective values of conversion (U–U_{ef}) for each of the reactants decreases with the increasing molar ratio of hydrogen (and the discharge power at the same time). It is to be noted out that the difference (U–U_{ef}) determines the fraction of the reactant that had been transformed into

other fluorine-containing organic compounds, i.e. into other freons. These are, of course, unwanted products of the reaction. It has been found that the differences (U–U_{ef}) in the process of CF_2Cl_2 decomposition are much smaller than those observed in the decomposition of CHF_2Cl in the cases where the molar ratio of hydrogen in the H_2+Ar mixture is smaller than 0.6. The difference (U–U_{ef}) was the smallest when the reaction was carried out in mixtures of freons with hydrogen. These results enable us to conclude that it is the most advantageous to carry out the process in a hydrogen medium with no addition of argon (Figs. 2 and 3).

30.3.2
Main Reaction Products – Hydrocarbons and Carbon Black

Acetylene, methane and carbon black were the main products of conversion of each of the primary reagents: CF_2Cl_2 and CHF_2Cl. It has been found that the conversion of both reagents into acetylene decreases if the molar ratio of hydrogen in the initial H_2+Ar mixture increases above 0.2 (Figs. 4 and 5). The conversion into acetylene was higher for CF_2Cl_2 than for CHF_2Cl, except in cases where the initial mixture was composed only of freon and hydrogen (X_{H2} = 0.98). In such a case, the conversion into acetylene was identical for either of the starting reagents.

The conversion of the reactants into methane increased with increasing molar ratio of hydrogen (Figs. 4 and 5) being higher for CHF_2Cl than for CF_2Cl_2. However, when either of the starting reagents was decomposed in a mixture with pure hydrogen, the conversion into methane was similar (0.317 for CF_2Cl_2 and 0.290 for CHF_2Cl).

The conversion of the freons into carbon black increased with increasing molar ratio of hydrogen in the H_2+Ar mixtures (Figs. 4 and 5). The CHF_2Cl conversion into carbon black was higher than that of CF_2Cl_2. Perhaps it was due to the difference in the discharge power, which was higher in the series with CHF_2Cl than that with CF_2Cl_2 (Figs. 2–5). These results enable us to state that the formation of the main reaction products: methane, acetylene and carbon black depends considerably on the composition of the gas mixture, mainly on the content of hydrogen. The more hydrogen is present in the mixture of H_2+Ar, the smaller is the conversion of the freons into acetylene and the higher into methane and carbon black. It is also possible to conclude that higher discharge powers promote the conversion of the starting reagents into methane and carbon black and suppress their conversion into acetylene, because the discharge power increased with increasing the hydrogen concentration.

The conversion of the freons into ethane increases with increasing molar ratio of hydrogen in the starting mixture up to 0.145 for CF_2Cl_2 and 0.108 for CHF_2Cl in mixtures with hydrogen alone. Similarly, the conversion of both freons into ethylene depends on the molar ratio of hydrogen in the mixtures of H_2+Ar and increases up to 0.163 for CF_2Cl_2 and 0.178 for CHF_2Cl when pure hydrogen is applied (Fig. 6).

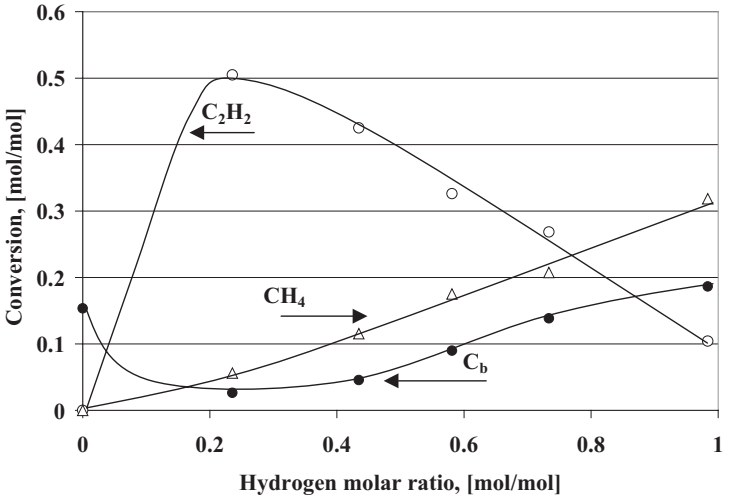

Figure 4 Effect of hydrogen molar ratio (X_{H2}) on the conversion of CF_2Cl_2 into acetylene (U_{C2H2}), methane (U_{CH4}) and carbon black (U_C); C_b – carbon black

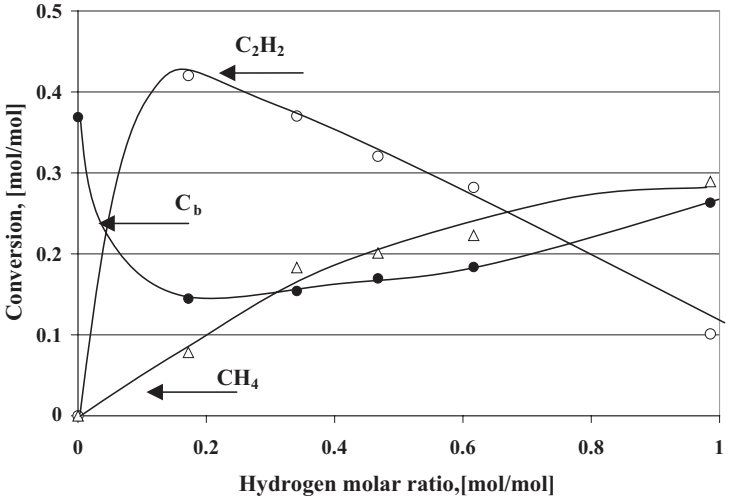

Figure 5 Effect of hydrogen molar ratio (X_{H2}) on the conversion of CHF_2Cl into acetylene (U_{C2H2}), methane (U_{CH4}) and carbon black (U_C); C_b – carbon black.

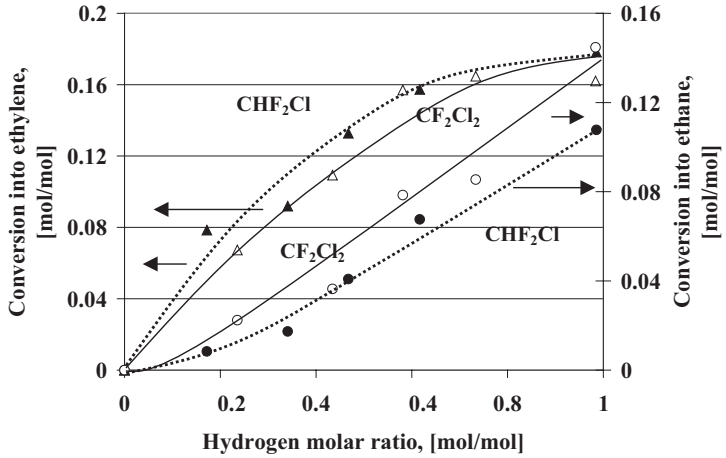

Figure 6 Effect of hydrogen molar ratio (X_{H2}) on the conversion of reactants into ethane (U_{C2H6}) and ethylene (U_{C2H4}).

30.3.3

Formation of Fluorine-containing Organic Compounds

The postreaction gases in the experiment, when a mixture of CF_2Cl_2 with pure argon was applied contained a number of unwanted fluorine compounds. Mostly $C_2F_4Cl_2$ was formed (0.118 of the conversion), however, CF_3Cl and carbon black were also produced. Other freons were present only in vestigial quantities. An addi-

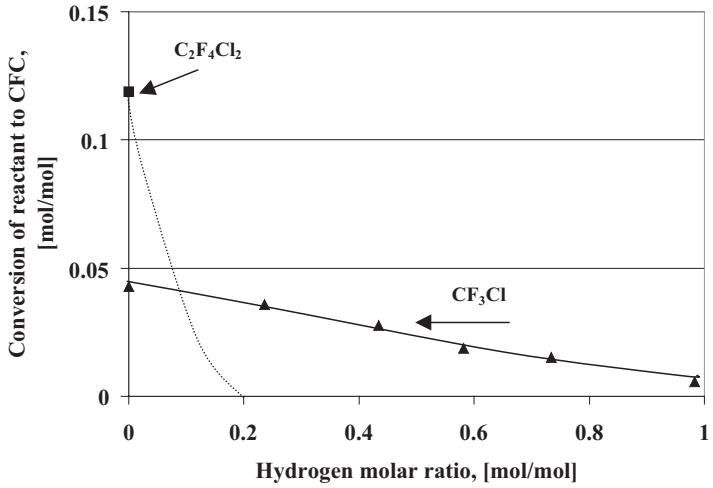

Figure 7 Effect of hydrogen molar ratio (X_{H2}) on the conversion of CF_2Cl_2 into unwanted freons (U_{CFC}).

tion of hydrogen, applied in further experiments, resulted in a drastic change in composition of the reaction products. No $C_2F_4Cl_2$ was formed, and CF_3Cl was the main unwanted products. Moreover, the CF_2Cl_2 conversion into CF_3Cl decreased from 0.036 to 0.006 when the molar ratio of hydrogen in the H_2+Ar mixture increased from 0.23 to 0.98 (Fig. 7). The 0.98 molar ratio of hydrogen was the case with the mixtures containing merely hydrogen and the freon to be decomposed.

In the experiment with a mixture of CHF_2Cl with argon alone, CF_3Cl was obtained as the main product with the conversion as high as 0.187. Also, several other products were obtained: CF_2Cl_2 (0.150 of conversion), CF_4Cl_2 (0.060), $CHFCl_2$ (0.055), C_2F_5Cl (0.003) and carbon black. When hydrogen was added, neither $C_2F_4Cl_2$ nor $CHFCl_2$ were produced and CF_3Cl was the main product of the reaction. The change of the hydrogen molar fraction from 0.17 to 0.98 resulted in a change of CHF_2Cl conversion to CF_3Cl from 0.092 to 0.007 (Fig. 8).

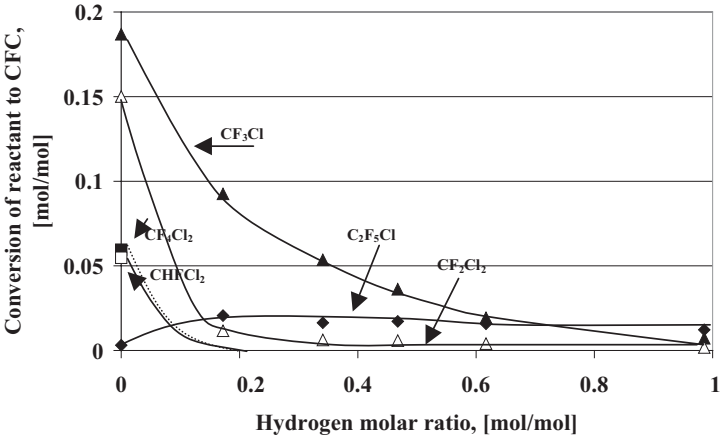

Figure 8 Effect of hydrogen molar ratio (X_{H2}) on the conversion of CHF_2Cl into unwanted freons (U_{CFC}).

It may be concluded that the rise of hydrogen content in the H_2+Ar mixture influenced both the qualitative and quantitative composition of the reaction products resulting in the decrease of the amount of unwanted fluorine compounds. The main F-containing product, CF_3Cl, is formed in the decomposition of either of the reactants, but the conversion of CHF_2Cl yields more fluorine compounds than the conversion of CF_2Cl_2. It is worth mentioning that those products contain, in molar ratios, more fluorine than do the starting reagents. However, the conversion of the starting freons into the unwanted fluorine compounds may be greatly reduced by increasing the concentration of hydrogen in the initial H_2+Ar mixture (with an increase of the discharge power at the same time). As already mentioned, the most advantageous solution was to use pure hydrogen in the initial mixture.

30.3.4
Energetic Efficiency of the Process

The energetic efficiency of the process of freon decomposition was determined in terms of two magnitudes defined above: unit-energy consumption (Z) and effective energy consumption (Z_{ef}). It is worthy of note that the unit-energy consumption (Z) in the process of CF_2Cl_2 decomposition is not much changed within the whole range of molar ratio of hydrogen (Fig. 9). It is the result of compensation of the increase of discharge power by increase of the conversion value. On the other hand, the unit-energy consumption (Z) in the process of CHF_2Cl decomposition increases with increasing molar ratio of hydrogen. In this case the increase of discharge power with increasing molar ratio of hydrogen is more rapid than that of total conversion, as shown in Fig. 2. The effective energy consumption (Z_{ef}) increases, both in decomposition of CF_2Cl_2 and CHF_2Cl, with increasing molar ratio of hydrogen (Fig. 10). This is evidently due to the fact that the rate of increase of discharge power is higher than that of the effective conversion value.

To compare the processes of decomposition of CF_2Cl_2 and CHF_2Cl it is possible to state that both the unit-energy consumption (Z) and the effective energy consumption (Z_{ef}) are smaller in the former than in the latter case. Then the energetic efficiency of CF_2Cl_2 decomposition is higher than that of CHF_2Cl. It should be taken into account, however, that both the total and the effective conversion values were higher for CHF_2Cl than for CF_2Cl_2.

These results have shown that the presence of hydrogen in the reaction medium has a stronger effect on the efficiency of CF_2Cl_2 decomposition than on the decomposition of CHF_2Cl. The differences between the conversion of each of the two freons are small in cases where the process is carried out in pure hydrogen medium. The significant differences between them were observed only in the case of carbon-black formation (Figs. 4 and 5). One can state, with some degree of approximation, that the composition of the reaction products is similar irrespective of the starting reagent used, however, the energetic efficiency of CF_2Cl_2 decomposition is higher than that of CHF_2Cl.

30.4
Conclusions

First, account should be taken of the effect of hydrogen on the freon reactions in gliding discharges. The composition of the products formed in the reaction of either of the freons CHF_2Cl and CF_2Cl_2 in mixtures of H_2+Ar is different from that obtained in the presence of argon alone. Both quantitative and qualitative differences are observed. The addition of hydrogen promotes the formation of hydrocarbons such as methane, ethane, ethylene, acetylene, and small amounts of propane, hence hydrocarbons are, along with carbon black, the main products containing carbon, whereas HCl and HF are the inorganic products. On the other hand, halogen compounds or new freons are the main products in the reactions carried out in the

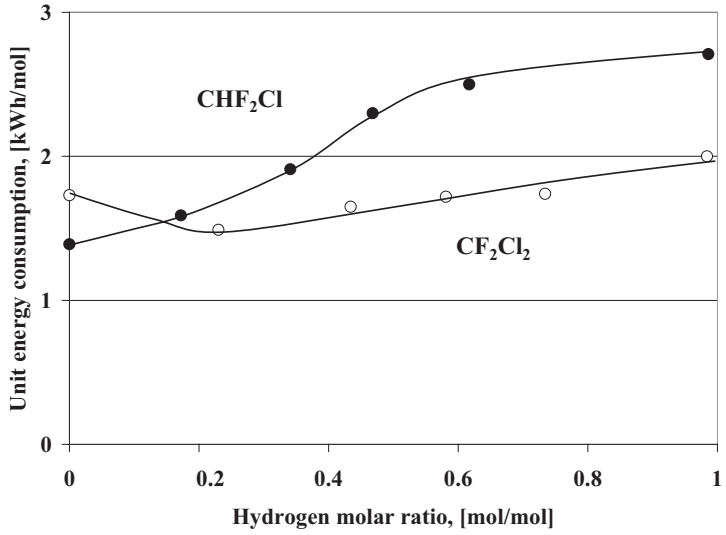

Figure 9 Effect of hydrogen molar ratio (X_{H2}) on the unit-energy consumption (Z).

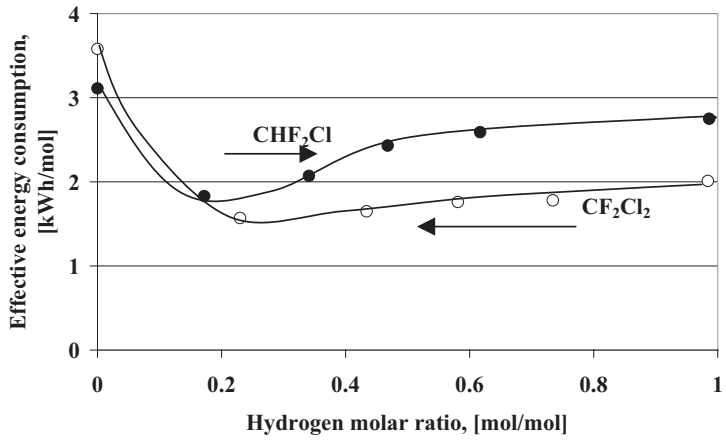

Figure 10 Effect of hydrogen molar ratio (X_{H2}) on the effective energy consumption (Z_{ef}).

medium or argon alone. The conversion of the freons to other halogen compounds decreases with increasing content of hydrogen in the reaction mixture, down to below 0.02 for the reaction carried out in hydrogen alone. In such cases the effective conversion (U_{ef}) is only slightly lower than the total conversion (U).

These results show that hydrogen is an active reagent in the system. One may admit that the increase of hydrogen concentration promotes the reactions of hydrogenation, however, this process is accompanied by accelerated decomposition of the

organic compounds and the carbon-black formation. At low concentrations of hydrogen acetylene was found to be the main product of the hydrogenation. The conversion of the primary freons into acetylene decreases with increasing hydrogen concentration. At the same time the conversion into methane and carbon black increases. Apart of methane and acetylene, ethane and ethylene are also the essential products of hydrogenation. Methane and carbon black are the main products of the reactions carried out in the medium of hydrogen alone. According to the generally accepted view carbon black is the main product of decomposition of the hydrocarbons formed in the hydrogenation of the primary freons. As is generally known acetylene is a compound easy to decompose with formation of carbon black. Free radicals such as CH* are considered to play an important role in the mechanism of this process. To sum up it may be concluded that a number of reactions participate in the decomposition of freons in the gliding discharge. Some of them lead to the formation of new freons (with increased contents of fluorine), whereas hydrogenation is responsible for the formation of hydrocarbons, with carbon black being the final product of hydrocarbons decomposition.

Comparing the decomposition of the two freons used (CF_2Cl_2 and CHF_2Cl) it is possible to state that the conversion into acetylene and ethane are higher for CF_2Cl_2 than for CHF_2Cl. Conversely, the conversion of CF_2Cl_2 into methane, ethylene and carbon black is lower than that of CHF_2Cl. The energetic efficiency of the process characterised in terms of (Z) and (Z_{ef}) values is higher for CF_2Cl_2 than for CHF_2Cl. Both the total and the effective energy consumption increase with increasing content of hydrogen in the starting mixture.

A practical conclusion of these experiments is that under conditions of gliding discharge the decomposition of freons should be carried out in mixtures rich in hydrogen. It is then possible to obtain high total conversion and small amounts of unwanted new freons formed, whereas fluorine and chlorine are transformed into HF and HCl. The concentration of the freons to be decomposed is certainly an important process parameter. This problem will be dealt with in a separate study. Other topics to envisage are the problem of reducing the contents of unwanted products and increasing the overall conversion of the starting materials to values above 0.95.

Acknowledgement

The work was supported by the statutory found of the Industrial Chemistry Research Institute and State Committee for Scientific Researches; grant No3 T09B 095 16.

References

[1] S. Wójcik, Ochrona środowiska, Instytut Ekonomiki Przemyslu Chemicznego, Warszawa1995, pp. 112–113, in Polish

[2] Z. Bonca, Chemik **nr 6**, 1993, in Polish

[3] E.M. Fisher, C.P. Koshland, Combus. Flame **90** 186 (2000)

[4] E. Ranzi, M. Dente, M. Rovaglio, Chem. Eng. Commun. **117** 17 (1992)

[5] A. Wiersma, M. Makkee, J.A. Moulijn, E.J.A. Van de Sandt, H. Van Bekkum, E.J.A.X. Van de Sandt, Appl. Cat. A: General **155** 59 (1997)

[6] Z. Karpiński, W. Juszczyk, A .Malinowski, Appl. Cat. A: General **166** 311 (1998)

[7] J.A. Rosin, M.M. Farris, Ind. Eng. Chem. Res. **32** 1042 (1993)

[8] S.B. Braus-Stromeyer, A.M. Cook, T. Loisinger, Environ. Sci. Technol. **27** 1577 (1993)

[9] A.B. Murphy, J. Proc. Royal Society of NSW **130** 93 (1997)

[10] A.B. Murphy, T. McAllister, A.J.D. Farmer, E.C. Horrigan, 15th Int. Symp. on Plasma Chemistry, Orleans, France 2001, oral contributions, vol II p.619

[11] J.D. Skalny, V. Sobek, P. Lukac, NATO ASI Series, vol G34, Part A, p.151

[12] A. Kohchi, S. Adachi, Y. Nakagawa, Jpn. J. Appl. Phys. **35** 2326 (1996)

[13] Y. Nakagawa, S. Adachi, A. Kohchi, Jpn. J. Appl. Phys. **35** 2808 (1996)

[14] Ya-Fen Wang, Wen-Jhy Lee, Chuh-Yung Chen, Lien-Te Hsieh, Ind. Eng. Chem. Res. **38** 3199 (1999)

[15] F-J. Spiess, X. Chen, S.L. Brock, S.L. Suib, Y. Hayashi, H. Matsumoto, J. Phys. Chem. **104** 11111 (2000)

[16] M. Jasiński, P. Szczucki, M. Dors, J. Mizeraczyk, M. Lubański, Z. Zakrzewski, Int. Symp. on High Pres. Low Temp. Plasma Chemistry, HAKONE VII, Greifswald, Germany 2000, Cont. Pap. p. 496

[17] M. Jasiński, J. Mizeraczyk, Z. Zakrzewski, T. Ohkubo, J-S. Chang, J. Phys. D: Appl.Phys. **35** 1 (2002)

[18] M. Jasiński, J. Mizeraczyk, Z. Zakrzewski, J-S. Chang, Czech. J. Phys. **52** D743 (2002)

[19] H. Lesueur, A. Czernichowski, J. Chapelle, Patent no 88.14932, France

[20] V.D. Rusanov, A.S. Petrousov, B.V. Potapkin, A.A. Frdman, A. Czernichowski, J. Chapelle, Dokl. Akad. Nauk **332** 306 (1993) in Russian

[21] A. Fridman, J. Chapelle, A. Czernichowski, L. Lesueur, A. Petrusev, B. Potapkin, J. Stevefelt, 11th Int. Symp. on Plasma. Chemistry, Loughborough, England 1993, Symp. Proc., p.275

[22] A. Fridman, A. Petrusev, J. Chapelle, J-M. Cormier, A. Czernichowski, L. Lesueur, J. Stevefelt, Phys. III France **4** 1449 (1994)

[23] A. Czernichowski, T. Opalińska, P. Czernichowski, H. Lesueur, Patent no 94.10738 France

[24] A. Opalska, T. Opalińska, J. Polaczek, P. Ochman, Int. Symp. on High Pres. Low Temp. Plasma Chemistry, HAKONE VIII, Puhajarve, Estonia 2002, Cont. Pap., p.191

[25] A. Opalska, T. Opalińska, P.Ochman, Acta Agrophysica **80** 367 (2002)

31
The Oxidation of Streams for Diesel Fuels Formulations by Means of High-voltage Oxygen Plasmas

Pedro Patiño, Eugenio Farrera, and Aurora Mejía

Abstract

The oxidation of three streams, employed for diesel fuels formulations, and a diesel fuel by means of low-pressure high-voltage oxygen plasmas was studied. Additionally, five alkanes, two olefins and two aromatic compounds, all in the liquid phase, were studied at similar conditions of minimum volatility. Both individually and forming part of mixtures, olefins were the most reactive with ground-state atomic oxygen, $O(^3P)$, followed by paraffins, aromatics and cycloalkanes. Products were: epoxides and aldehydes for olefins; alcohols and ketones for alkanes; phenols for aromatics. Addition of 3.1 to 8.9% wt of oxygen was achieved for the streams and the diesel, depending on the particular composition, those with higher content of olefins being favored, followed by those with higher content of alkanes. Polyaromatic compounds were less reactive than monoaromatics, all in agreement with the results for the streams.

31.1
Introduction

Due to environmental policies put into force in developed countries, fossil fuels formulations have been subject to deep changes during the last decade. This has given rise to great efforts by fuel producers to bring refineries to the required standards. In this respect, it has been shown that the use of oxygenate compounds as additives in diesel fuels formulations improves the combustion process in engines because they diminish particulate emissions, non burnt hydrocarbons and carbon monoxide [1].

Diesel fuels are mixtures of streams from diverse crude-oil-refining processes such us catalytic disintegration and hydro-cracking. Recently, various types of oxygen-containing compounds including ethers, alcohols, carbonates, acetals and esters have been tested in engines to determine the effects of oxygenates on exhaust emissions [2–6]. Particulate emission reductions have been proportional to the oxygen content, averaging 26.1% below that of the base fuel for 7% wt. of oxygen.

On the other hand, with the aim of improving their cetane number, the oxidation of fuel oils has been performed classically by means of methodologies based on $KMnO_4$ and $K_2Cr_2O_7$ with appropriate catalysts and pH adjustment [7–9]. More recently, low-pressure oxygen plasmas have been employed to increase the cetane number of a light diesel fuel by 66% [10], and three diesel fuels have added 4.7 to 7.8% wt of oxygen, depending on their particular composition [11].

The interaction of plasmas with gases and solids has been studied extensively, leading to numerous synthesis techniques [12] and methods for surface modifications [13]. Greater selectivity is achieved in heterogeneous reactions of plasmas with liquid surfaces, compared to the gas-phase systems where the hot primary products normally may undergo consecutive reactions before they are thermalized. This is due to the fact that the plasma–liquid systems provide rapid quenching of the primary species. The consecutive reactions of the plasma–solid interactions are avoided here by stirring the liquid; in this way, products are continuously eliminated from the surface layer. $O(^3P)$ atoms produced in oxygen plasmas readily react with liquid organic compounds [14–20].

In this investigation, a comparative study of the oxidation of moderate and long-chain alkanes and olefins as well as monoaromatic and polyaromatic hydrocarbons, all in the liquid phase, has been performed. The impact of the behavior of the different hydrocarbons, depending on the structure and size of the molecules, is analysed when examining the oxidation of three streams and a diesel fuel under similar conditions. These are composed of mixtures of diverse hydrocarbons bases in the range C_{12}–C_{25}.

31.2 Experimental

31.2.1 Equipment

The reactions were carried out by producing an oxygen cold plasma and allowing it to reach the low vapor pressure liquid substrate. The plasma was an alternate glow discharge. A diagram of the experimental assembly is shown in Fig.1. The reactor was a double-walled glass vessel of approximately 300 ml. It was supplied with two electrodes made of aluminum and Teflon. Oxygen was introduced into the reactor through one of the electrodes, which was hollow. The inner part of each of them was cylindrical, with 3 mm external diameter. The plasma was produced by means of a home-made high-voltage continuous wave ac source that supplied up to 1 kV and 200 mA, at 60 Hz. The applied power was measured with a Landis & Gyr model CL2 power meter. The liquid substrate (2 ml) was placed at the bottom of the reactor and this was cooled by means of a methanol-liquid nitrogen bath, the temperature being controlled within ±1 °C. The liquid was magnetically stirred and the system was connected to a vacuum line, equipped with one trap used to collect any possible volatile product and to protect the mechanical vacuum pump. The oxygen flow was

measured with a 247 B-MKS flow meter and the pressure was monitored with a Leybold-Heraeus TM111 thermotron. The products of the reactions were identified and quantified by means of gas chromatography-mass spectrometry, infrared and nuclear magnetic resonance spectroscopies. A Varian 3800 GC/Saturn 2000 MS system was used. The gas chromatograph employed a 25-m fused silica capillary column. The mid-IR spectra were recorded on a Perkin Elmer FTIR model 1700X spectrometer. The NMR spectra were taken on a JEOL ECLIPSE 270 MHz spectrometer. Aldrich analytical grade products were used as standards.

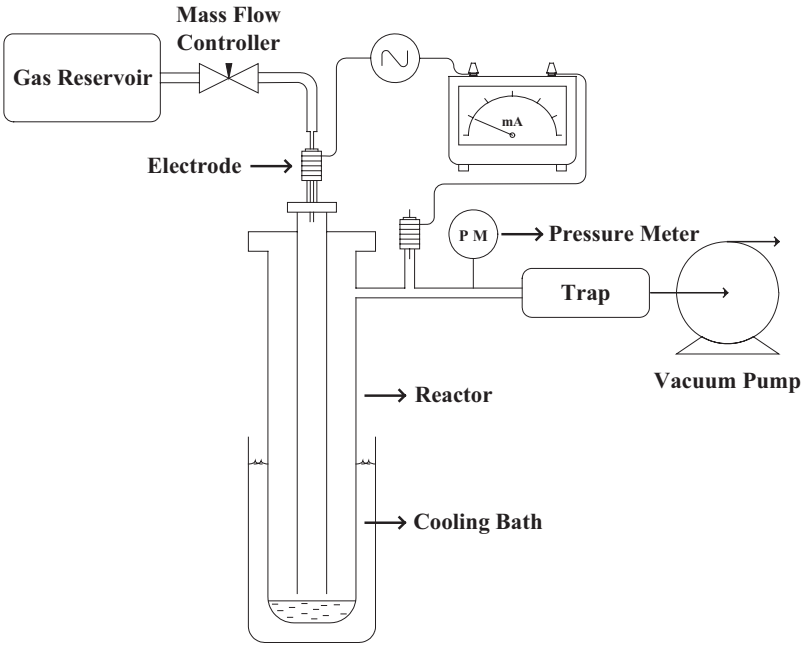

Figure 1 Diagram of the experimental assembly.

31.3 Results

31.3.1 Model Compounds

Results for the hydrocarbons studied are presented in Table 1. Working temperature and vapor pressure of each compound are included. The effects of oxygen pressure, temperature of the liquid, applied power and treatment time were studied for most of the hydrocarbons. The optimum pressure was about 0.2 mbar for all of them and the discussion is later presented for 1-tetradecene. As expected, maximum conversions were observed at temperatures close to the respective freezing points. The

reactivity drastically fell off when the samples became frozen, thus indicating that the interaction was that of a plasma with a solid. From the point of maximum conversion to higher temperatures, the vapor pressure of the substrate increases. Therefore the hydrocarbon molecules, much bigger than O_2, compete advantageously with it for the electrons and hence the amount of $O(^3P)$ in the plasma decreases. This explains why the conversion of the hydrocarbon decreases too. If the temperature of the liquid is set much higher, its vapor pressure increases, then collisions between electrons and molecules in the gas phase dominate the plasma and fragmentation plus condensation products, arising from oxygen-free organic radicals, are the main products.

Table 1 Reactions of different hydrocarbons with the oxygen plasma for 60 min

Compound, *T* (°C), *vp* (mbar)	**Total conversion (%)**	**Product distribution (%)**
n-Heptane, –85, 0.009	26.0	3-Heptanol (21.6); 2-heptanol (19.1); 4-heptanol (16.3); 3-heptanone (14.1); 2-heptanone (10.9); 4-heptanone (9.7)
n-Tetradecane, 8.5, < 0.001	41.0	Alcohols (87.0); ketones (13.0)
Isooctane, –87, 0.009	35.6	Alcohols (100)
Squalane, 2.5, < 0.001	29.4	Alcohols (100)
Cis-decaline, –40, 0.01	10.1	Alcohols (63.8); ketones (36.2)
1-Octene, –89, 0.001	67.3	1,2-Epoxioctane (65.0); ocatanal (35.0)
1-Tetradecene, –10, 0.002	77.4	1,2-Epoxitetradecane (51.8); tetradecanal (36.3); byproducts (11.9)
Toluene, –85, 0.004	15.8	*o*-Cresol (78.7); *p*-Cresol (14.4); *m*-Cresol (6.9)
Naphthalene, –85*, < 0.001	12.9	α-Naphthol (67.7), ß- Naphthol(32.3)

* Dissolved in toluene, 25% wt.

Total conversion of all compounds increased with the time of reaction. This situation is shown in Fig. 2 for n-heptane. The slope of the curve decreases at ~ 2 h. This is due to the amount of ketones that is continuously being produced. At short times alcohols are the only products. Part of them are, in turn, oxidized by $O(^3P)$ to produce ketones that, conversely, do not suffer further reactions. At a certain moment, the amount of original hydrocarbon and alcohols will decrease and so will the reaction rate.

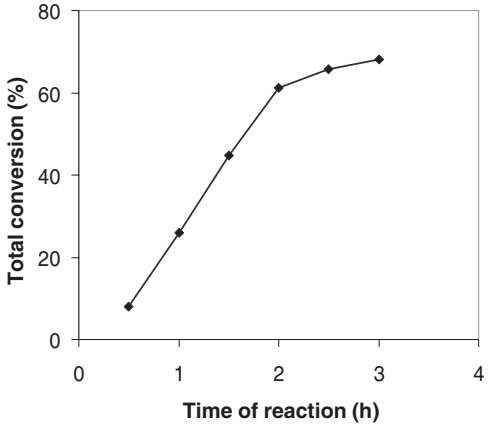

Figure 2 Total conversion rate of n-heptane as a function of time of reaction.

At short to moderate constant time of reaction, conversion increases linearly with applied power. At long times, i.e. 2 h or longer, a plot of conversion versus power is similar to Fig. 2. This means that increasing power at fixed time produces the same effect as explained in the previous paragraph.

With the aim of performing a comparative study of the diverse compounds, the experimental conditions were: oxygen pressure, 0.2 mbar; applied power, 35 W; time of reaction, 60 min. The temperature of each liquid was set as previously explained. Before introducing oxygen, the pressure of the system was 1×10^{-4} mbar.

The most important features observed in the IR spectra of the treated samples were the –OH, –C=O, and –C–O stretchings at about 3400, 1700 and 1100 cm^{-1}, respectively. Integrated areas of NMR spectra, together with the GC-MS information, have been employed to evaluate the conversion of both, the model compounds, the streams and the fuel oil. ^{1}H chemical shifts were (ppm): 0–3 for alkanes; 2.5–5 for epoxides and alcohols; 3.5–6 for olefins; 5.5–8 for aromatics; 8–10 for ketones and aldehydes. ^{13}C regions were (ppm): 7–50 (aliphatic); 50–120 (epoxides and alcohols); 110–116 and 137–140 (olefins); 120–150 (aromatics); 160–220 (carbonyl compounds).

31.3.1.1 n-Heptane and n-Tetradecane

The most important observations with these two alkanes were: 1) Oxidation of n-heptane by $O(^3P)$ resulted in a total ratio of reactivities C3:C2:C4 equals 1.37:1.15:1. Taking into account that the molecule has two C2, two C3 and one C4, the ratio of reactvities per carbon C4:C3:C2 equals 1.73:1.19:1. This could be related to the electronic density distribution on the different C–H bonds that makes C4–H more attractive for the electrophilic character of $O(^3P)$. 2) Total conversion of n-tetradecane was higher than that of n-heptane, probably due to the higher number of $–CH_2–$ in the former that are candidates to be oxidized.

31.3.1.2 Isooctane and Squalane

These two compounds have in common methyl groups bonded to the chain. Excluding the two terminal quasi-inert groups for each molecule, isooctane (2,3,4-trimethylpentane) has 3 CH_3 on 3 reactive carbon atoms; squalane (2,6,10,15,19,23-hexamethyltetracosane) has 6 CH_3 on 22 reactive carbon atoms, i.e. 3 on 11. Considering that tertiary carbons are ~ 26% more reactive than $-CH_2-$ with $O(^3P)$, it was expected that the conversion of isooctane would be higher than that of squalane. This was the result of this work and agrees with the fact that isooctane has 3 tertiary carbons out of 8 per molecule, while squalane has 6 out of 30.

31.3.1.3 *cis*-Decahydronaphthalene

cis-Decaline was the least reactive of the studied compounds. Products were naphthols and decalones, conversion on carbon number 10, i.e., that one close to the tertiary carbon (number 1) was 44%, thus reflecting the inductive effect on that position. Naphthols and decalones amounted to 63.8% and 36.2%, respectively, confirming that the latter are produced by reactions of the former with $O(^3P)$.

31.3.1.4 1-Octene and 1-Tetradecene

The oxidation of 1-tetradecene was studied as a function of the oxygen pressure in the reactor, at a constant temperature of –10 °C, in order to determine the optimum working pressure of the system. The results are shown in Fig. 3. The shape of the curve is very similar to that obtained for the optical emission signal of the $3p\ ^3P \rightarrow 3s\ ^3S$ (λ = 844.6 and 844.7 nm) transition [10], that can be correlated to the population of O I ($2p\ ^3P$), the ground state of atomic oxygen, as shown in the respective Grotrian diagram [21]. This confirms that this species is responsible for the oxidation of the hydrocarbons. No evidence of singlet O_2 ($a^1\Delta_g$) was detected in the optical emission spectrum under the conditions of the discharge. Moreover, the corresponding hydroperoxide, product of the reaction of singlet oxygen with olefins, was not observed in the reaction mixtures of 1-tetradecene and 1-octene.

The olefinic NMR signals virtually disappeared after treatment with the plasma. The conversion of 1-tetradecene was higher than that of 1-octene. That can be associated to the longer number of $-CH_2-$ in the molecule of the former than can be attacked by the oxidizing agent, $O(^3P)$.

31.3.1.5 Toluene and Naphthalene

A solution of naphthalene 25% wt in toluene was treated with the plasma at –95 °C. For toluene, *o*-cresol was the most abundant product, followed by *p*-cresol and *m*-cresol, as expected from the inductive effect of the methyl group, thus confirming the electrophilic character of $O(^3P)$. The conversion of naphthalene was lower than that of toluene, confirming that the inductive effect of the aromatic ring is lower than that of the methyl group.

31.3.2
Streams and Fuel Oil

Table 2 is a résumé of results for the streams and the diesel fuel. Experimental conditions were the same as for the model compounds, except for the temperatures of the liquids. In agreement with the results of the model hydrocarbons, stream 1 was the most reactive, due to its 3.1% of olefins. It has been shown that these compounds react more readily with $O(^3P)$. Second was the diesel, due to its highest content of alkanes and lowest content of aromatics, compared to streams 2 and 3. Stream 3 has the highest percentage of aromatic hydrocarbons, particularly diaromatics (36.1%) and polyaromatics (23.5%). It has the lowest content of paraffins and cycloalkanes too. This is clearly the reason why this sample showed the lowest conversion with the plasma. Stream 2 added more oxygen than stream 3 due to its better ratio alkanes/arenes than that of the latter.

Table 2 Properties of streams and the fuel oil, and % of oxygen added by the plasma

Property	Stream 1 –40 °C	Stream 2 –4.5 °C	Stream 3 –7.5 °C	Fuel –21 °C
Distillation (°C)	181–274	188–363	186–367	162–376
Cetane number	37.7 (50.1)[§]	–	–	41.0
Alkanes (% vol.)	62.1	56.7	27.4	64.5
Naphthenes (% vol.)	38.8	28.0	14.0	35.5
Olefins (% vol.)	3.1	–	–	–
Mono-, di-, tri-aromatics (% vol.)	28.1, 4.6, 2.2	26.7, 14.0, 2.2	13.0, 36.1, 23.5	31.5, 3.5, 0.6
Oxygen content (% wt.)	8.9	4.6	3.1	5.0

[§] After treatment.

31.4
Discussion

All samples were treated under conditions of very low volatility. The vapor pressure (*vp*) for each compound, calculated at the particular working temperature, is given in Table 1. *Cis*-decaline showed the maximum value of 0.01 mbar, thus given a pO_2/vp ratio of 20. The other compounds gave ratios higher than that, in agreement with previous results [10,20]. This was necessary to guarantee that the amount of hydrocarbon molecules in the gas phase was low enough to preclude homogeneous gas-phase reactions from taking place. For this reason, treatment with the plasma was similar to the treatment of polymers, with the advantage that, in the case of this study, stirring of the liquid avoided excessive consecutive reactions on the same fraction of molecules of the samples, i.e., those on their surfaces. All oxidation products were less volatile than the starting compounds thus guaranteeing the condition of no reaction in the gas phase. This was confirmed by monitoring the optical emission spectra of the gas phase. The only signal detected was that of $O(^3P)$, its intensity

drastically diminishing in the vicinity of the liquid surface because the reactions had taken place.

Olefins have been shown to be the most reactive with $O(^3P)$. This is related to the electrophilic character of $O(^3P)$, the most accepted mechanism for the reaction with olefins involving the formation of a diradical triplet transition state [22–24]. The epoxide is formed through the closing of the triplet diradical, and aldehydes and ketones are product of a hydrogen atom migration. Figure 4 shows schematics of the reactions. R_i ($i = 1,4$) are either hydrogen atoms or alkyl groups.

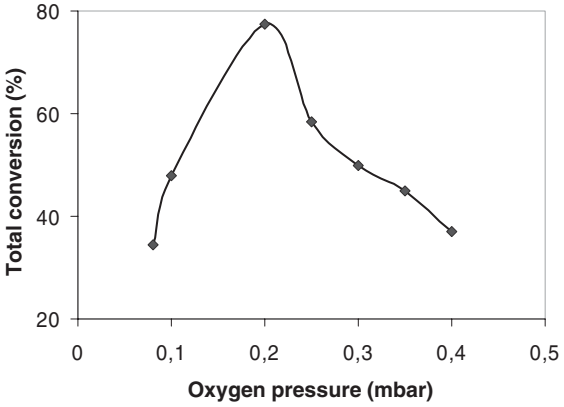

Figure 3 Total conversion rate of 1-tetradecene as a function of the oxygen pressure.

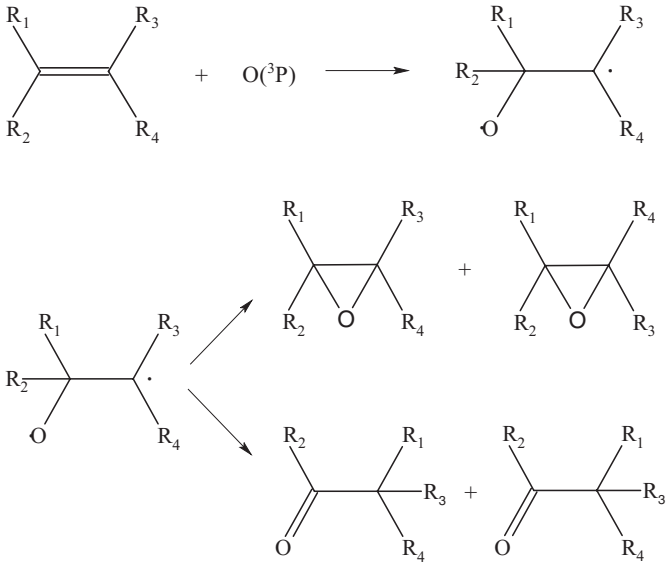

Figure 4 Reaction mechanism of $O(^3P)$ with olefins.

Results differ considerably from those in the homogeneous gas phase. There is hardly any fragmentation, and product formation is far more selective. When $O(^3P)$ reacts with 1-octene in the gas phase, attack at the double bond is only 10 times faster than at the individual C–H bonds [11]. Under such conditions, only 38% of the products come from the reaction at the double bond. In the plasma oxidation of liquid 1-octene, however, all identified products result from such attack.

The accepted mechanism for the reaction of $O(^3P)$ with alkanes is the abstraction of a hydrogen atom to produce an alkyl and an OH radicals, followed by their recombination to produce the corresponding alcohol [25]. A carbonyl compound is produced through the reaction of a secondary alcohol with a second $O(^3P)$.

$$R\text{–}H + O(^3P) \rightarrow R\cdot + \cdot OH \rightarrow ROH, \quad (1)$$

$$ROH + O(^3P) \rightarrow R_1\text{–}CO\text{–}R2. \quad (2)$$

The results for toluene are similar to those for other aromatic compounds [18], and they all agree with the proposed mechanism for reaction of $O(^3P)$ with olefins. Selectivity here has been higher than that of reactions in the gas phase. In fact, oxidation of toluene has been studied in a radio-frequency homogeneous plasma, i.e., by introducing mixtures of oxygen and gaseous toluene in the reactor [26]. In this case, the products are benzaldehyde, benzyl alcohol, phenol, *o*-, *m*-, and *p*-cresol, and bibenzyl, indicating that fragmentation has taken place.

The most important result of this study has been the successful addition of oxygen to the streams and the diesel fuel. They are difficult to oxidize by classical means with inorganic agents [7–9]. According to expectations, stream 1 showed the highest reactivity, due to its highest percentage of olefins. The lowest oxygen percentage of the treated stream 3 can be associated with the higher percentage of aromatics and the lowest of paraffins in its composition.

The cetane number of stream 1 was measured and an increase of 32.9% was observed after the treatment. This is a parameter that represents the autoignition capability of a fuel when it is subjected to compression. It is measured according to the ASTM D-613 motor test [27]. From the chemical point of view it is more appropriate to consider the cetane number as a variable dependent on the composition of the fuel rather than a property of it [28]. Preliminary calculations on energy costs of treatment with the plasma have been given in a previous work [10]. They are lower than those for treatment with inorganic oxidizers [7–9].

31.5 Conclusions

Several model hydrocarbons and fuels were readily oxidized in a one-step process by means of low pressure oxygen plasmas. The cetane number of one of them increased from 37.7 to 50.1. This fulfils the requirements of diesel fuels in devel-

oped countries and should result in improving automotive engine performance and reducing exhaust emissions.

Oxidation with the oxygen plasma is competitive if compared with classical wet methodologies.

Olefins are more reactive with $O(^3P)$ than the other kinds of hydrocarbons. As a result, those fuels with higher percentage of olefins are more easily oxidized. Second in order of reactivity are n-alkanes, followed by aromatics, and cycloalkanes are the least. A factor that favors the upgrading of fuels with oxygen plasmas is the presence of tertiary C–H bonds in their paraffinic fractions.

Acknowledgments

Funding for this research has been provided by CDCH, Universidad Central de Venezuela, through Grant C-03-12-4083-01.

References

[1] I. J. Karas, H. S. Jr. Kesling, F. J. Liotta and M. K. Nandi, *ACS Division of Fuel Chemistry Preprints* **39**(2), 316 (1994).

[2] R. L. McCormick, J. D. Ross and M. S. Graboski, *Environ. Sci. Technol.* **31**, 1144 (1997).

[3] T. Litzinger and M. Stoner, *Int. J. Engine Res.* **1**, 57 (2000).

[4] F. Takahashi and I. Glassman, *Combust. Sci. Technol.* **37**, 1 (1984).

[5] M. Natarajan, E. A. Frame, D. W. Naegeli, T. Asmus, W. Clark, J. Garbak, M. A. González-D., E. Liney, W. Piel and J. P. III Wallace, Society of Automotive Engineers, Inc. Paper N° 01FL-576 (2000).

[6] M. A. González-D., W. Piel, T. Asmus, W. Clark, J. Garbak, E. Liney, M. Natarajan, D. W. Naegeli, D. Yost, E. A. Frame and J. P. III Wallace, Society of Automotive Engineers, Inc. Paper N° 01FL-577 (2000).

[7] Ch. Venkat, N. J. Bellemead, D. E. Walsh and P. Richboro, United States Patent N° 4494961 (1985).

[8] W. F. Taylor and N. J. Mountainside, United States Patent N° 4723963 (1988).

[9] A. Chertkov, E. A. Kunina and T. I. Kirsanova, *J. Appl. Chem. URSS* **53**(7), 1245 (1980).

[10] G. Gambús, P. Patiño, B. Méndez, A. Sifontes, J. Navea, P. Martín and P. Taylor, *Energy Fuels* **15**, 881 (2001).

[11] P. Patiño, A. Mejía, P. Rodríguez and B. Méndez, *Fuels* **82**, 1613 (2003).

[12] H. Suhr, *Plasma Chem. Plasma Process.* **3**, 1 (1981).

[13] R. D'Agostino (Ed.), *Plasma Deposition, Treating, and Etching of Polymers*, Academic Press, Inc., New York, (1990).

[14] S. Hirokami and R. J. Cvetanovic, *J. Am. Chem. Soc.* **96**, 3738 (1974).

[15] E. Zadok, D. Amar, Y. Mazur, *J. Am. Chem. Soc.* **102**, 6369 (1980).

[16] R. Klein and M. D. Scheer, *J. Phys. Chem.* **73**, 1598 (1969), R. Klein and M. D. Scheer, *ibid.* **74**, 613 (1970), M. D. Scheer and R. Klein, R. *ibid.* **74**, 2732 (1970).

[17] H. Suhr, H. Schmid, H. Pfeundschuh and D. Iacocca, *Plasma Chem. Plasma Process.* **4**, 285 (1984).[FettU]

[18] P. Patiño, F. E. Hernández and S. Rondón, *Plasma Chem. Plasma Process.* **15**, 159 (1995).

[19] P. Patiño, M. Ropero and D. Iacocca, *Plasma Chem. Plasma Process.* **16**, 563 (1996).

[20] P. Patiño, N. Sánchez, H. Suhr and N. Hernández, *Plasma Chem. Plasma Process.* **19**, 241 (1999).

[21] W. Grotrian, *Graphische Darstellung der Spektren von Atom und Ionen mit ein, zwei und drei Valenzelektronen*, Springer, Berlin (1928).

[22] S. Sato and R. J. Cvetanovic, *J. Am. Chem. Soc.* **81**, 3223 (1959).

[23] R. J. Cvetanovic, *Can. J. Chem.* **38**, 1678 (1960).
[24] R. J. Cvetanovic, *Adv. Photochem.* **1**, 115 (1963).
[25] P. Andresen and A. C. Luntz, *J. Chem. Phys.* **72**, 5842 (1980).
[26] M. Tezuka and T. Yajima, *Plasma Chem. Plasma Process.* **16**, 329 (1996).
[27] *ASTM Annual Book*, New York, (1950), p. 19103.
[28] D. Indritz, *Symposium of the Division of Petroleum Chemistry, Am. Chem. Soc.*, (1985), pp. 282–285.

32
Acetylene and Ethylene Carbon Blacks Production in Plasma Process

Tomasz Zieliński, Teresa Opalińska, Jacek Kijeński

Abstract

Carbon black is an important raw material for plastics and rubber industries all over the world. The efficient, economical, and environmental friendly process for acetylene and ethylene carbon blacks manufacturing and comparison of their structures and physical-chemical properties were the goals of our investigations. The new method and the apparatus for preparation of high-quality carbon black from acetylene and plasma media, argon and helium, using gliding discharge was proposed.

32.1
Introduction

The increase of use of plastics and rubber products in various branches of industry all over the world, creates the need to find new and safe methods of making carbon black. The competition on the rubber market forces the carbon-black industry to improve, modernize and develop. This is why there is ceaseless necessity of the elaboration of a highly efficient, economical and environmentally friendly process and finding new technologies of carbon-black production of the best quality and purity. Besides the rubber industry, carbon black is used in plastics industry (as a filler) and in the production of paints, lacquers and inks.

Carbon black is a generic name that describes a wide group of industrial carbon products with systematic nanostructures of elementary carbon [1,2]. The conventional processes for carbon-black making under industrial conditions are based on an incomplete combustion of high-boiling aromatic oils or natural gas (furnace and channel processes). These processes are hardly operable and fail to meet the environmental requirements, because of the emission to the atmosphere of carbon monoxide, carbon dioxide, nitric oxides aliphatic hydrocarbons, carbon-black dusts and aromatic hydrocarbons seated on carbon-black particles [3]. There is also known a number of methods of carbon-black making from acetylene mostly under equilibrium plasmas. Up till now, some investigations have been performed where a new process and apparatus were developed for hydrocarbon processing into carbon black by gliding discharge under nonequilibrium plasma conditions.

The present paper shows the results of our investigations relating to some physical and chemical properties and surface development of carbon black received in nonequilibrium plasma from acetylene or ethylene, as feedstocks, and argon and helium, as plasma media.

32.2
Experimental

32.2.1
Apparatus

The gliding discharge was fed by a special three-phase 50 Hz high-voltage power system. The plasma reactor consisted of three stainless steel main bar electrodes of special shape and one ignition electrode. The main bar electrodes were situated symmetrically around the ignition electrode at an angle of 120°. The reactor was connected to the water cooler and cyclone where all the postreaction dust was precipitated from gas. Carbon black was accumulated in a tank situated under the cyclone. Next to the cyclone, the filtering system was located for final removal of the dust from the gas. The cleaned gas was taken to the gas burettes for analysis using a gas chromatography method. The chromatograph was supplied by the flame ioniza-

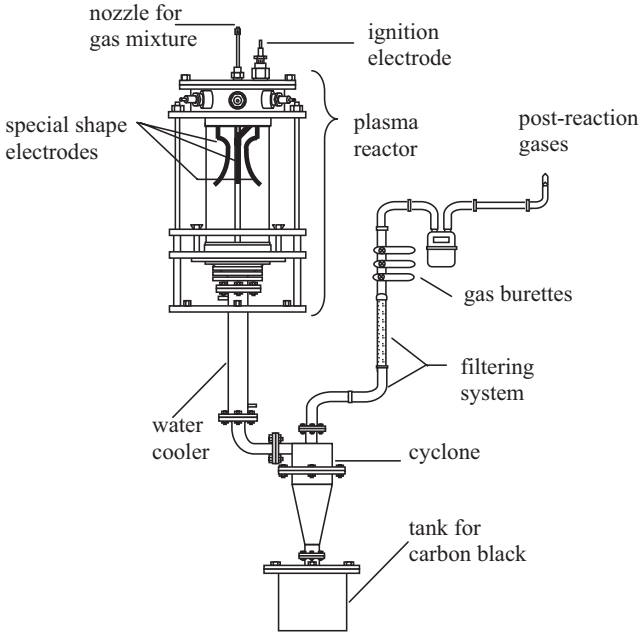

Figure 1 The schema of acetylene and ethylene carbon blacks production apparatus in gliding discharge.

tion detector (FID). B/5% Fluorocol™ Packed Column was put into use with length of 4 m and diameter of 3 mm. Helium was used, as a carrier gas, in the chromatograph, with a flow rate of 25 ml/min. The temperature of the detector was between 30 °C and 50 °C with a heatup rate of 4 °C/min. The equipment allowed the process to be realized continuously. The schema of the apparatus is shown in Fig. 1.

32.2.2 Procedure

A gas stream of suitable composition and flow rate was injected into the reactor by a nozzle, which was situated above the electrodes. The plasma reactor and installation parameters were set up by position of the main electrodes, the ignition electrode and the nozzle of the gas mixture to each other to form the most effective field of reactions in gliding discharge. This field of reactions was situated in the whole plasma flame area, which included the maximum volume of gas mixture during the discharge in the reactor. The optimal setting of the main electrodes, besides the maximum field of reactions, allowed the conversion of gas reactants to reach 77%. The use of scanning electron microscopy (SEM) was possible to characterize the shape and the size of carbon-black particles and all agglomerates [4] formed in the plasma process from various reactants. The tests were carried out using a LEO 1530 scanning electron microscope produced by the Oxford Company, which is a type of a electron microscopy where the electron beam is focused onto the sample's surface to an area with a diameter of 0.1 nm, sweeps the chosen rectangular field by a scanning motion, line by line. The electron beam is accelerated in the electromagnetic field with potential 0.1–30 kV and focused by the electromagnetic lens and the deflection coil gives to it the scanning motion. The electrons penetrate into and come back from the sample, which is called backscattering. The SEM image is the simple ratio of the figurative monitor screen size to the scanning field size.

The most important physical-chemical property of plasma carbon black is adsorption in respect to nitrogen (BET). It is an equation of isotherm of multilayer adsorption of unary steam of Bruauer, Emmett and Teller. The equation of BET adsorption relates to steam adsorption, where under high pressure the condensation is present, can be used for experimental determination of the absorbent surface. The diffraction properties were investigated using Siemens D-500 powder X-ray diffractometer in the Industrial Institute of Electronics, Poland.

The diffraction of carbon black consists in that every point of space, where the plane wave hits, becomes the source of an elementary spherical wave. These waves interfere with themselves and create a new wave front. The diffraction effects proceed for all kinds of wave motion. The carbon-black structural properties, like interplanar distance (d_i), diameter of areas of the aromatic layers (λ_a), the average thickness of layer packets (λ_c), were established using the X-ray diffraction (XRD) method [5,6]. The flow rate of gas mixture was changeable form 0.5 to 1.25 m^3/h and the source gas content was also changeable from 2 to 10 vol% in the gas mixture.

32.3
Results and Discussion

The efficiency of the process and energy consumption depend on the kind of carrier gas in the mixture content of the hydrocarbon in the gas mixture. The term used for total conversion of reactant means the conversion of feedstock to all products in the process. The term used for conversion of reactant to carbon black means the conversion of feedstock only to one main product in the process that is carbon black. For example, total conversion of C_2H_2 to products and conversion of C_2H_2 only to carbon black in an Ar plasma are similar and they increase with increased content of the source gas in the mixture, as occurs in a He plasma (Fig. 2, Fig. 3). This means that there is almost total conversion to the product. Beside the obtained carbon black there is a trace of ethylene in the products in off-gases. The runs of conversions are similar to the case of conversion of ethylene in Ar and He plasmas (Fig. 4, Fig. 5). Figure 2 shows the process conditions of Ar–C_2H_2 gas mixture composition with changeable source gas content from 2 vol% to 5 vol% of C_2H_2 in the mixture with 1.0 m^3/h total flow rate of the gas mixture. Figure 3 shows the process conditions of He–C_2H_2 gas-mixture composition with changeable source gas content from 2 vol% to 10 vol% of C_2H_2 in the mixture with 1.0 m^3/h total flow rate. Figure 4 shows the process conditions of Ar–C_2H_4 gas-mixture composition with changeable source gas content from 2 vol% to 15 vol% of C_2H_4 in the mixture with 1.0 m^3/h flow rate of the gas mixture. The conversion of ethylene to acetylene in off-gases was also observed. There is a possibility to return the off-gases to the process and use the content of acetylene as a plasma medium. Figure 5 shows the process conditions of He–C_2H_4 gas-mixture composition with changeable source gas content from 2.5 vol% to 15 vol% of C_2H_4 in the mixture with 1.0 m^3/h flow rate of the gas mixture. The conversion of ethylene to acetylene in off-gases was observed, as under Ar-plasma conditions. The compositions of the feedstock and products are listed in Table 1.

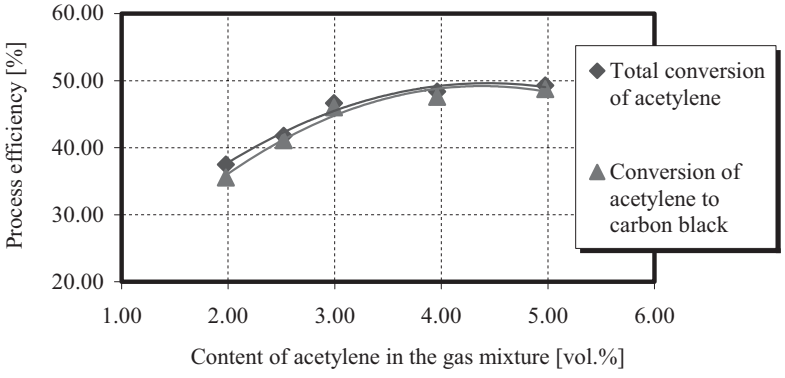

Figure 2 Process efficiency of carbon-black-making process depending on content of acetylene in Ar-plasma.

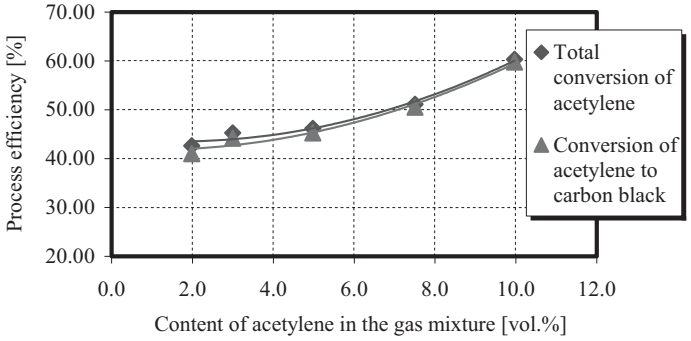

Figure 3 Process efficiency of carbon-black-making process depending on content of acetylene in He-plasma.

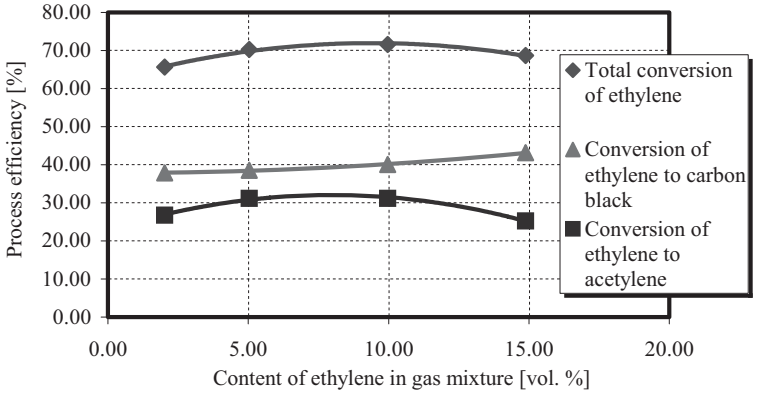

Figure 4 Process efficiency of carbon-black-making process depending on content of ethylene in Ar-plasma.

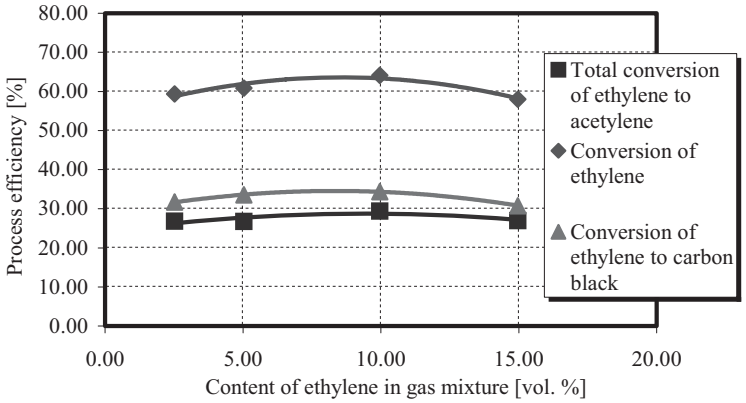

Figure 5 Process efficiency of carbon-black-making process depending on content of ethylene in He-plasma.

Table 1 Compositions of gas streams

Experiment	Feedstock [% by vol.]				Total conversion of feedstock [%]		Conversion of feedstock to products [%]			
	Ar	He	C_2H_2	C_2H_4	C_2H_2	C_2H_4	C	H_2	C_2H_2	C_2H_4
1	95	–	5	–	49.27	–	48.75	47.98	–	0.39
2	–	90	10	–	60.34	–	59.76	58.88	–	0.42
3	90	–	–	10	–	71.57	40.07	55.37	31.21	–
4	–	95	–	5	–	60.84	33.53	51.57	26.77	–

The first group of carbon blacks was obtained from acetylene or ethylene in argon as plasma medium. The results of the investigations indicated that changes of the amount of acetylene or ethylene in the reacting gas and its flow rate do not remarkably influence the properties of the carbon-black surface and its physical-chemical properties. At the different contents of gas reactants in the gas mixture carbon black was obtained with the same structure of the surface. The morphology of the carbon black obtained from acetylene in argon or helium plasma media is shown in Fig. 6. The optimal content of the reactant in the gas mixture was 5 vol% of C_2H_2 and 10 vol% of C_2H_4 in argon plasma and with 1.0 m^3/h of gas mixture flow rate. SEM pictures indicated that the shapes of particles of the obtained carbon black were similar independent of the reaction conditions. They look like fuzzy flakes packed together very tightly.

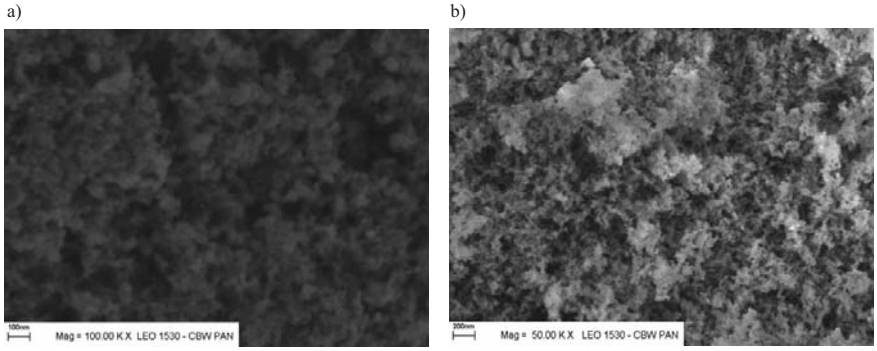

Figure 6 Surface morphology of carbon black made from (a) acetylene – argon and (b) acetylene – helium mixtures.

Neither the concentration of acetylene in the inlet gas nor its flow rate remarkably affected the carbon-black surface and its physical-chemical properties. The replacement of argon by helium resulted in formation of carbon black with better properties. The optimal content of C_2H_2 in the gas stream was 5 vol% in the argon plasma and 10 vol% in the helium plasma and gas flow rate was 1.0 m^3/h. According to the SEM pictures, the shapes of particles were similar independent of the reaction conditions. They look like fuzzy flakes packed very tightly together, which is completely

different in comparison to traditional furnance carbon-black structure, which shows the traditional round and globular particles. The morphology of the traditional furnance carbon black produced by Chemical Company CARBOCHEM in Gliwice in Poland is shown in Fig. 7.

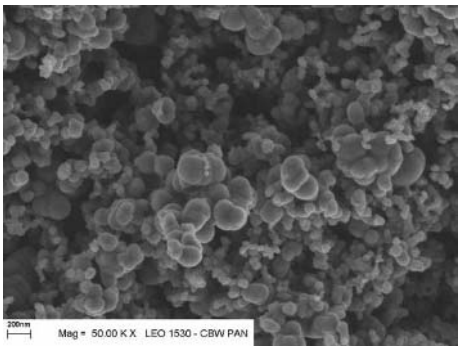

Figure 7 Surface morphology of traditional furnance carbon black.

According to the SEM pictures, the carbon-black particles possessed large specific areas. Fuzzy flakes indicated a very good surface development, which was strictly connected with the high adsorption capacities. The interplanar distance (d_i) between layers measured for carbon black obtained from a gas mixture with 5 vol% of C_2H_2 in Ar plasma was a little larger (Fig. 8) than the interplanar distance in carbon black prepared from gas mixture with 10 vol% of C_2H_2 in He-plasma (Fig. 9). The large distance between layers can be considered as large as graphite layers interplanar distance (~ 3.4 Å) that could be a perfect parameter [7,8]. The diameter of agglomerates of the aromatic layers (λ_a), (Table 2) was also large and the layers did not have a bearing point. The aromatic layers could easily deflect and were mobile. The average thickness of layers packets (λ_c) (Table 2) resulted in good properties and behavior of large agglomerates. The physicochemical properties, mostly the interplanar distance close to graphite (~ 3.4 Å of d_i). The high adsorption capacity of the prepared carbon black with respect to nitrogen (BET), iodine (IA) and dibutyl phthalate (DBF) indicated a good absorbability, allowing molecules of various substances, for example stabilizers, to easily drive into and settle on the carbon-black surface. The results of BET adsorption – the specific surface area was over 80 m^2/g, the iodine adsorption capacity (IA) – over 80 mg/g and dibutyl phthalate adsorption capacity (DBP) – over 100 $cm^3/100$ g, in comparison with the commercial furnance carbon black, confirmed the significant development of the surface. The produced carbon blacks exhibited high absorbability, which could facilitate the drive of molecules of various substances into their internal structure and the subsequent deposition. This was reflected by the results of adsorption like BET, adsorption of iodine (IA) and adsorption of DBP (Table 2).

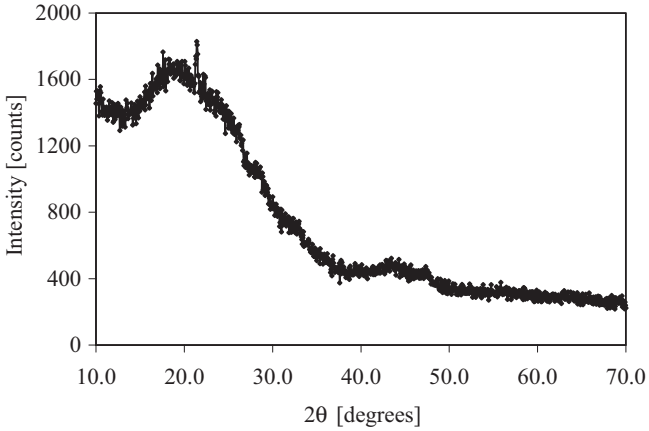

Figure 8 XRD pattern of carbon-black surface (5 vol% of C_2H_2 in Ar).

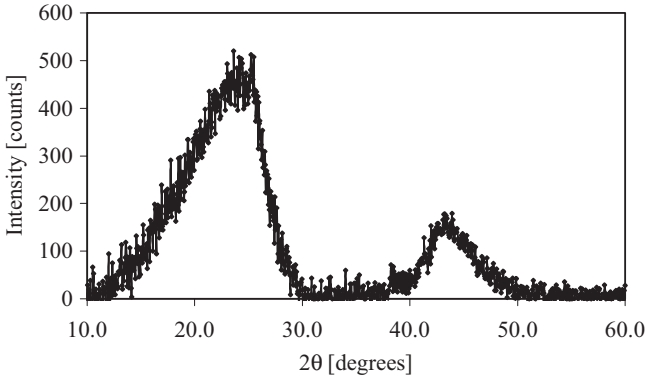

Figure 9 XRD pattern of carbon-black surface (10 vol% of C_2H_2 in He).

Table 2 Results of XRD and adsorption measurements of carbon black made in gliding discharge

Experiment (Table 1)	d_i [Å]	λ_a [Å]	λ_c [Å]	BET [m^2/g]	IA [mg/g]	DBP [$cm^3/100$ g]
1	3.8	7.8	32	156	95	125
2	3.7	10	38	164	127	128
3	3.5	40	59	205	93	125
4	3.5	14	77	254	127	127

The carbon black prepared from ethylene in argon or helium as plasma medium exhibited similar properties to the carbon black obtained from acetylene. The content of C_2H_4 was 5 vol% in Ar-plasma and 10 vol% in He-plasma (Table 1). SEM pictures of C_2H_4 carbon black have shown a similar surface structure as in the case of C_2H_2-derived carbon black. The shape and size of particles had a similar look. Nevertheless, the structure of C_2H_4 carbon black generated in an argon plasma was more agglomerated and less fluffy than C_2H_2 carbon black. The particles were a little smaller than those of C_2H_2 carbon black. The morphology of the carbon-black surface from ethylene is shown on Fig. 10.

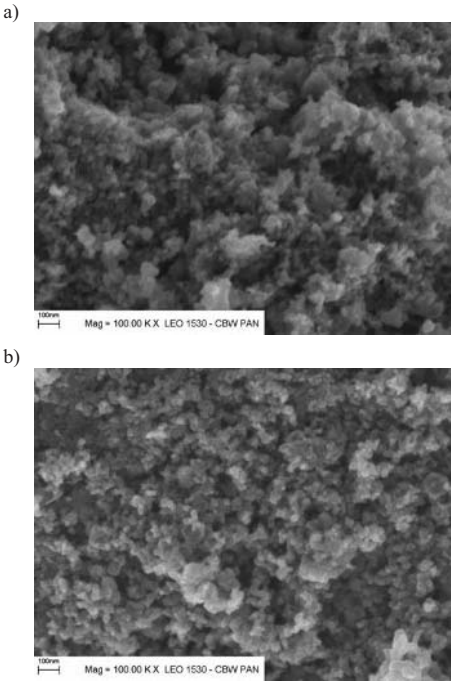

Figure 10 Surface morphology of carbon black made from (a) ethylene – argon and (b) ethylene – helium mixtures.

The structure of C_2H_4 carbon black formed in helium plasma was also similar to that of C_2H_4 carbon black in anargon plasma, however, it was more densely packed and a little less fluffy. The particles had smaller diameter and were a little smaller, but they were more compact.

The interplanar distance (d_i= 3.5 Å) established for carbon black obtained from 10 vol% of C_2H_4 in Ar-plasma was the same (Fig. 10) as the interplanar distance measured for carbon black produced from gas mixture with 5 vol% of C_2H_4 in He-plasma (Fig. 12) and was of a much lower value than the interplanar distance measured for C_2H_2 carbon black (Table 2). The diameter of agglomerates of the aromatic layers (Table 2) of C_2H_4 carbon black prepared from a gas mixture in Ar plasma

equalled 40 Å and was significantly higher than the diameter of agglomerates of C_2H_4 carbon black obtained from a gas mixture in He plasma, which equalled 14 Å. The average thickness of layers packets was higher for C_2H_4-He carbon black (77 Å) than for C_2H_4-Ar carbon black (59 Å). The high values of XRD parameters (λ_a and λ_c), calculated for Ar-C_2H_4 carbon black (Fig. 10) and for C_2H_4-He carbon black (Fig. 11), showed their influence on upgrading the carbon-black physicochemical properties. The large dimension of the agglomerates of the aromatic layers and the large average thickness of layer packets together with small interplanar distance (more densely packed particles, more stable and regular structure) resulted in good commercial properties of the carbon-black surface.

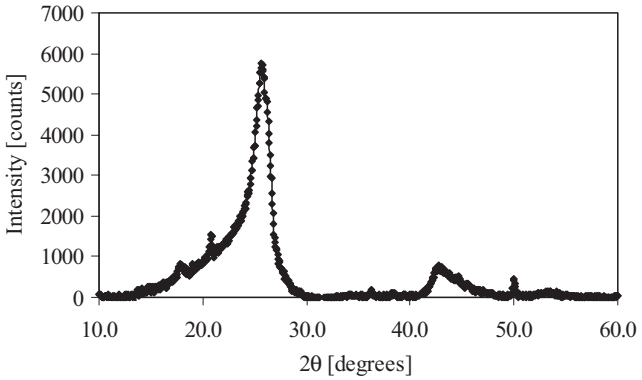

Figure 11 XRD pattern of carbon-black surface (10 vol% of C_2H_4 in He).

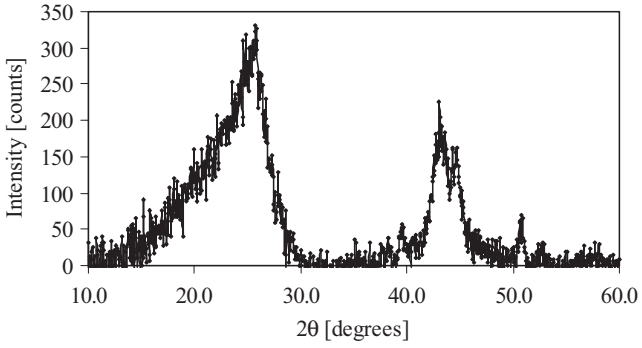

Figure 12 XRD pattern of carbon-black surface (5 vol% of C_2H_4 in He).

The carbon black obtained in helium as plasma medium possessed the largest specific surface area and adsorption capacity (Table 2), independent of the gas reactant used for synthesis. From XRD results one could ascertain that C_2H_4-He carbon black had the best surface properties (facility of drive into and deposition of introduced alien molecules) of all the studied carbon blacks.

32.4 Conclusions

The aim of the study was to investigate the surface development of carbon black made by gliding-discharge plasma treatment of acetylene and ethylene in argon or helium. The results of the studies indicated the high increase of the carbon-black surface area, especially measured by BET adsorption of nitrogen. The application of gliding discharge for the preparation of carbon black from acetylene or ethylene allowed production of material of stable and regular structures. The high adsorption capacity of the prepared carbon black in respect to nitrogen (BET), iodine and dibutyl phthalate indicated a good absorbability, allowing molecules of various substances to easily drive into and settle on the carbon-black surface. This makes it possible to use these kinds of carbon black as fillers in rubbers or plastics. There existed a relationship between the values of XRD parameters, like average interplanar distance, diameter of agglomerates of the aromatic layers, the average thickness of layer packets and studied physicochemical properties. For example, the increase of interplanar distance was reflected in a rise in adsorption capacity. The process efficiency depends on and grows with the increase of source gas content in the mixture, but it has no influence on the properties of the produced carbon black. Therefore the C_2H_2 in Ar-plasma-derived carbon black seemed to be more useful than the one produced from C_2H_2 in He plasma, because of the economy of the process and the much lower commercial price of argon, than helium, as plasma medium.

Acknowledgement

This work has been supported by the State Committee for Science Researches (KBN, Grant No. 7 T09B 107 21).

References

[1] L. Fulcheri, Y. Schwob, B. Variot, G. Flamant, J.M. Badie, G. Vallbona, F. Kassabji, J. Saint Just, A 3-Phase A.C., VDI Berichte, 1166, 525–532 (2003)

[2] L. Fulcheri, Y. Schwob, Int. Workshop on Nanostructured Materials, NANOS 94, Odeilo, France, (1994)

[3] Ullmann's Encycl. of Ind. Chem., vol. A5. Weinheim: VCH Verlags Gesellschaft, 140 (1986)

[4] T. Shirasaki, F. Moguet, L. Lozano, A. Tressaud, G. Nause, E. Papirer, Carbon, 1999, 37, 1981–1990

[5] H. E. Blayden, J. Gibson, H. L. Riley, Proc. Conf. Ultra-fine Structure of Coals and Cokes, BCURA, 1943, 176

[6] G. N. Churilov, L. A. Solovyov, Y. N. Churilova, O. V. Chupina, S. S. Malcieva, Carbon, 1999, 37, 427–431

[7] F. Stoeckli, A. Guillot, A. M. Slasli, D. Hugi-Cleary, Microporosity in carbon blacks, Carbon, 2002, 40, 211–215

33
DCM Production in a Dusty-Plasma Trap

A. Ivanov, V. Mitin, A. Pal, A. Ryabinkin, A. Serov, E. Skryleva, A Starostin, V. Fortov, Yu. Shulga

Abstract

The dusty-plasma technique was used for production of the diamond-nickel disperse composite material (DCM) representing powder that consists of diamond particles having the mean size of 5 μm and covered by nickel. The amount of DCM obtained is quite enough for physical and technologic studies. The coating is shown to be a solid nickel layer of 10 nm thickness with characteristic roughness of 3 nm.

33.1
Introduction

Disperse composite materials (DCM) are composed of small particles having the size of 10^2–10^4 nm covered with a coating. These materials can be used both in the processes of fabricating structural and special materials with unusual properties and in the production of highly efficient catalysts. This report presents some results of studying DCM produced in a dusty-plasma trap by means of the technology that is similar to [1, 2].

The requirements of coatings of DCM include the following: high adhesion of coating with disperse carrier, high accuracy of chemical content of coating, narrow temperature range for crystal formation, precision coating structure and coating thickness. According to these requirements, besides high efficiency, the technology for producing DCM with coatings should possess high controllability of the coating process to provide the necessary accuracy of the given characteristic parameters such as chemical content and energy spectrum of atoms of coating components, power of atom source and exposition time interval, temperature and pressure of plasma-forming gas, temperature and size of particles, and plasma density.

There are a few plasma methods for deposition of coatings upon small particles. One of them uses the technology for dusty plasma based on levitation of particles in a plasma trap either without coagulation or with a precisely controlled one during the coating process, the coating components being injected into the plasma trap as vapor.

The limitations of this method are as follows:

- complexity for maintaining particle temperature within a rather narrow range, which is necessary for formation of coating;
- complexity for producing many-component coatings with precise stoichiometric chemical content.

Closest to the proposed method is that [1, 2] also based on levitation of particles in plasma trap and using magnetron target sputtering as the source for coating components and input of atoms into the plasma trap in the form of a directed flow. This method makes it possible to essentially enhance the efficiency of the process.

Limitations for this method are as follows: i) for coating formation there is too high a heating of particles in the plasma trap (this problem has been investigated for some cases in refs. [3, 4]) and ii) the use of comparatively high pressure during the coating process. This leads to thermalization of the sputtered atom flow, formation of strongly supersaturated vapor, condensation of this vapor and formation of clusters consisting of different coating components in plasma trap. In depositing clusters upon disperse particles the produced coating is loose, has a dendritic structure and inhomogeneous chemical content in thickness. Besides this, thermalised atoms cannot activate the particle surface due to atom energy within the considered temperature range essentially lower than the sorption one, the coating adhesion considerably decreased.

Very good technical results can be achieved by the employment of the reaction chamber with the special plasma trap. When in plasma, disperse particles are negatively charged mainly due to the fact that the electron mobility is considerably greater than the ion one. A typical charging interval for particles is within ~10^{-4}–10^{-5} s [5]. The value of the stationary charge of particles and their floating potential can be estimated due to the condition that electron flow per particle is the same as the ion one. For the value of the diamond particle charge in our conditions the limited orbit motion approach [6] results in (1–2) × 10^4 elementary charges. Charging of dusty particles in the plasma can lead to coagulation suppression [7, 8] and formation of long-lived ordered dusty structures that are known as Coulomb crystals [9]. Application of such stationary dusty structures for DCM production does not provide the conditions for continuity of the process that includes the coating deposition and removal of finished DCM. This restriction can be partially overcome by using coagulation suppression in a dusty plasma [7, 8, 10]. We used this effect in our installation.

33.2 The Setup for DCM Production

The experimental setup for dusty-plasma trap creation includes the vacuum chamber with electrode system inside where the RF discharge plasma is available. The electrode system is powered by the RF generator at the fundamental frequency of 5.28 MHz. The discharge power was up to 30 W. The argon gas was used at pressure

of 0.1–0.3 Pa and 1–5 sccm flow rate. The disperser of the accelerative type, similarly described in [11], was used to inject a cloud of powder particles into the discharge chamber. The cloud levitated in the plasma trap and was exposed to the atom beam from magnetron sputtering system (see Fig. 1). The laser light scattering method [12, 13] was used for observing dusty-plasma traps.

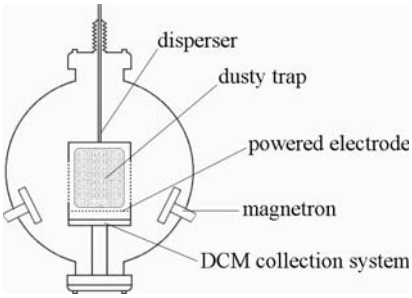

Figure 1 Scheme of the experimental setup.

In this report we present the result of diamond-Ni DCM production. We used synthetic diamond powder with the size distribution presented in Fig. 2.

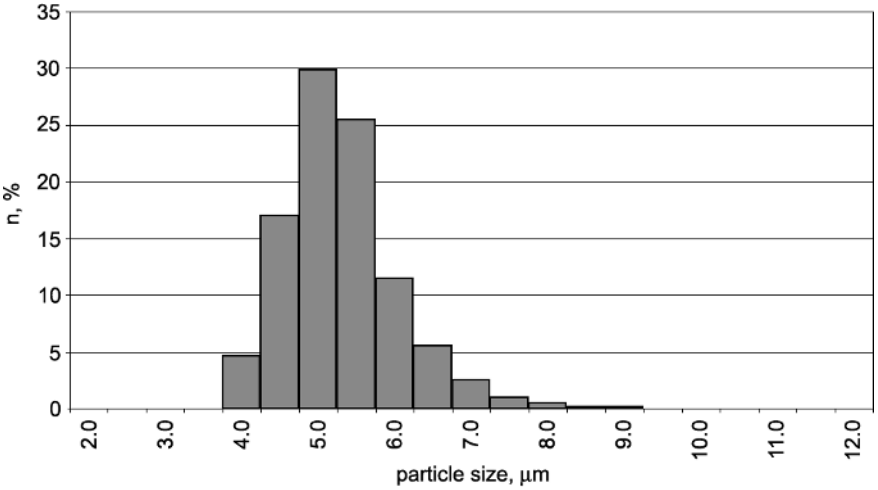

Figure 2 Size distribution of diamond powder.

Two ion-plasma sputtering magnetron devices with cylindrical cathodes were used. In such a device the ring magnetic balanced system is placed inside the water-cooled cathode frame. The magnetic system is pieced together from permanent Nd-Fe-B magnets with a residual induction of 0.45–0.55 T. The sputtering target is placed over the magnetic system. Nickel is a magnetic material, so the target is of special construction providing the effective sputtering of magnetic materials at the magnetron mode of operation where the strong arc magnetic field (0.03–0.04 T) is

present above the target surface. The latter is necessary for trapping of the electrons above the intensive sputtering zone. The target is composed of three elements: central, sputtered and peripheral assembled coaxially with gaps on a copper plate. The gaps were filled with nonmagnetic material. The construction provides the nickel and other magnetic materials sputtering in a high-speed mode at the power density of 45–50 W/cm^2 (intensive sputtering zone takes the ring-shape with an external diameter of 52 mm and area of 19 cm^2).

The magnetron sputtering systems are located close to the RF-electrode and its magnetic fields significantly influence the discharge properties and the dusty-trap location. The pictures of the RF discharge glow over the planar electrode are changed essentially in the presence of a magnetic field. In the absence of a magnetic field at a pressure of 1 Pa or higher, the plasma entirely and uniformly covers the electrode, its layer thickness is practically constant. Stable dusty-plasma traps were not observed under these conditions. In the presence of the magnetic field the glow area covers only the part of the electrode and takes the form of a dish. Disperse particles levitate near the glow contour, and the dusty-plasma trap is stable. In view of the various kinds of electron drift in a magnetic field, measuring the magnetic field space distribution resulted in explaining the features of the formation mechanism of the glow and dusty-plasma trap. For low pressures (<1 Pa) at which the coating process was carried out, random particle fluctuations not damped by viscous friction forces, the trap occupies much greater volume. For this reason the influence of the magnetic field is less marked than for higher-pressure conditions.

33.3 Results and Discussion

Analyzing the fabricated product was accomplished with the use of a number of methods including electron microscopy research, X-ray analysis, cathodoluminescent analysis, X-ray photoelectron spectroscopy, precision chemical analysis, and others.

Electron microscopy of diamond particles coated with Ni was performed using a high-resolution (~30 nm) scanning electron microscope. Electron micrographs show that the coated particles, unlike the particles of the initial diamond powder, are quite sharply defined (Fig. 3). This indicates high electroconductivity of the coating. Within the mentioned resolution the formed coating is quite smooth, follows the substrate relief, and does not contain fractured structures of "cauliflower" type.

Besides this, we obtain the micrographs of the specimens by means of the transmission electron microscope at an accelerating voltage of 50 kV. The specimens were spotted on the copper mesh coated first by collodion and reinforced by carbon. The micrographs of the coated powder particle edge are given in Fig. 4. The edges of the main part of the investigated particles seem to be quite uniform, similar to the edges of the initial diamond. The coating characteristic roughness size is about 3 nm. There are no signs that would be evidence of the nickel coating peeling from the diamond substrate.

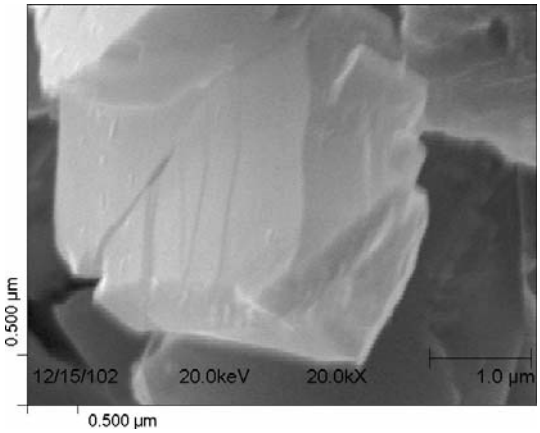

Figure 3 SEM image of the diamond particle covered by nickel.

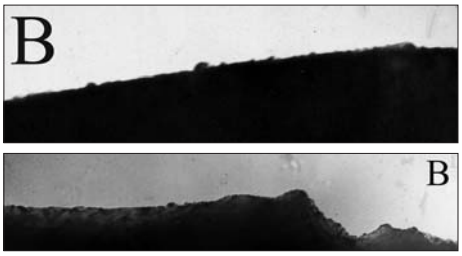

Figure 4 TEM images of the edges of the diamond particles covered by nickel. The height of letter "B" is 57 nm.

33.3.1 Measurement of the Mean Nickel Content

To analyze the nickel content C_{Ni} in the powder we used the method of specimen combustion in oxygen at the temperature of 1673 K. The initial powder completely burns down in this process. The rest of the DCM combustion seems to consist of the nickel oxide NiO. The mass of nickel in the rest to the initial mass of processed specimen is the quota of the metal in the composite material. Three samples from each specimen were burnt to ashes, the obtained data were averaged. Calculated from the averaged data, the concentration of the metal in one of the investigated specimens is given in Table 1.

Table 1 Results of analysis

Specimen	C_{Ni}, mass.%	S, m^2/g	H_c, Oe	C_1, emu/g ($H = 10^4$ Oe)	$C_{f\,Ni}$, mass%
Original diamond powder	0	0.76	0	0	0
Diamond covered by nickel	7.5	1.14	131	0.85	1.55

33.3.2
Measurement of the Specific Surface

The method of argon adsorption at liquid-nitrogen temperature was used for measuring the powder specific surface. The characterization of specific surface S from the adsorption measuring is reduced to the measurment of the quantity of matter that is necessary to cover the surface by the monomolecular layer. This quantity was measured according to the method using the linear form of the adsorption isotherm equation. The specimen was degassed at the temperature of 150 °C. The special argon (5%) – helium mixture was used as the working gas. The relative error in the specific surface measured is 5%. The results are given in Table 1. The mean coating thickness, according to the measured nickel concentration and specific surface values, was not less 10 nm.

33.3.3
X-ray Diffraction Investigations

The X-ray diffractograms were obtained using monochromatic CrK_α radiation. The original diamond diffractograms exhibit the lone peak due to the diamond (111) lattice reflection (Fig. 5).

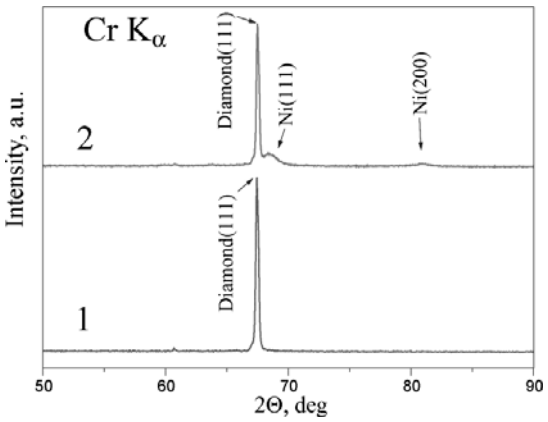

Figure 5 X-ray diffractograms of the original diamond powder (1) and the processed specimen (2).

Nickel is seen in the diffractogram of the processed specimen as two peaks corresponding to the reflections of (111) and (200) face-centered cubic lattice. The lattice-parameter value calculated using these peaks data is 0.3529 nm and exceeds that of bulk nickel (0.3524 nm [14]). The size estimation of the nickel coherent scattering domain corresponding to the coating thickness in the direction that is perpendicular to the plane (200) was carried out. The estimation formula was $D_{200} = \lambda/\beta\cos\Theta$, where λ is the X-ray length, β is the half-width of the Ni (200) diffraction peak. The lower peak was chosen because it is noticeably easier to estimate its half-width compared to the Ni (111) peak, which is overlapped by the diamond (111) peak. The $D200$ value seems to be 12 nm according to the mean thickness value, obtained as the result of the specific surface and the mean nickel content measurements.

33.3.4
Magnetic Properties of the Processed Powder

We studied the magnetic properties of the specimens by means of a vibration magnetometer EG&G PARC M4500. The specimens under investigation were placed in a thin diamagnetic ampoule whose own signal may be allowed in the course of analysis of observations. The magnetization curves of the processed specimens are the hysteresis loops with $H_c = 130$ Oe, where H_c is the coercive force (Fig. 6).

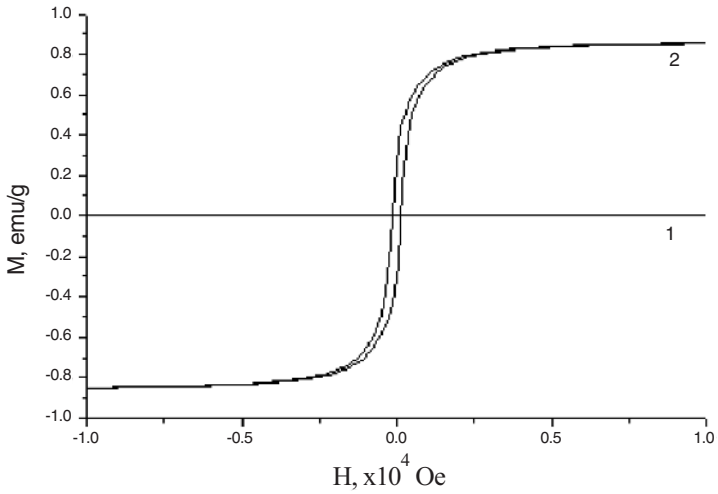

Figure 6 Magnetization curves of the initial diamond (1) and of the processed specimen (2). M is the specific magnetic moment, H is the magnetic strength.

One can see that the saturation state is not achieved even at $H = 10^4$ Oe. Therefore there are superparamagnetic nickel particles in the specimen. One can estimate the relative content of ferromagnetic nickel $C_{f\ Ni}$ in the specimen by the formula $C_{f\ Ni} = M_1/M_s^0$ where M_1 is the experimental value of M at $H = 10^4$ Oe, M_s^0 is the

saturation specific magnetic moment for a bulk nickel (M_s^0 = 55 emu/g [15]). The $C_{f\ Ni}$ value is appreciably smaller than the C_{Ni} value that was estimated using the method of specimen combustion (Table 1). So nickel is thought to be present in the specimen in the form of nickel oxide besides the superparamagnetic nickel particles. Nickel oxide is known to be antiferromagnet [16].

33.3.5
X-ray Photoelectron Spectroscopy

The X-ray photoelectron spectra were taken with a PHI-5500 (Physical Electronics Industries) spectrometer equipped with a precision analyzer of the spherical type. The spot diameter where analysis is carried out was 0.8 mm. The specimens were embedded in indium substrates as a solid layer. The base gas pressure in the spectrometer chamber did not exceed 7×10^{-8} Pa. The ion gun built in the spectrometer chamber makes it possible to clean the specimen surface from the adsorbed admixtures and to carry out the ion etching of the specimen to hundreds of nanometers depth.

The general X-ray photoelectron spectra of the diamond powder before and after the sputtering process are given in Figs. 7 and 8, respectively.

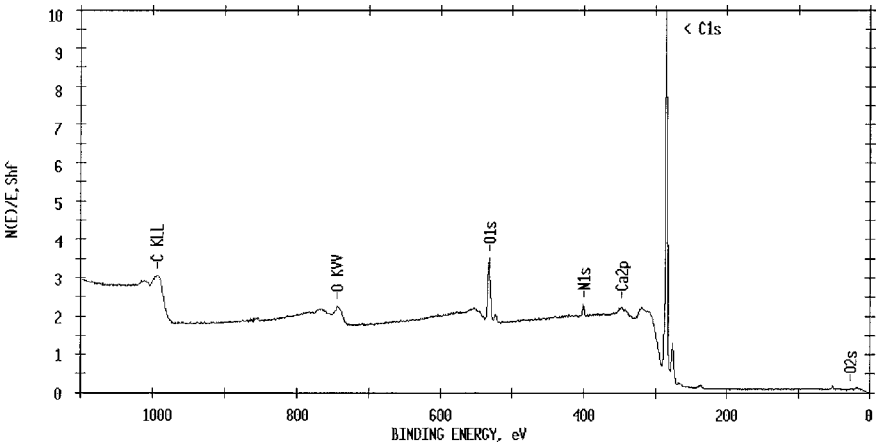

Figure 7 General X-ray photoelectron spectra of the initial diamond powder.

Carbon is seen to be the main element of the initial specimen surface. After the sputtering process, nickel becomes the main one. Nickel is in the specimen surface layer in two forms: as the metal and as the nickel oxide over the metal surface. The Ni 2p (Fig. 8) line is the complicated curve consisting of three peaks, two of which appear to be due to nickel oxide (861.2 and 855.6 eV), and the rest (852.8 eV) due to metal nickel. The correspondence of the peaks was taken from [17]. Cleaning of the smooth surface region of the specimen by $A\Gamma^+$ ions leads to the vanishing of nickel

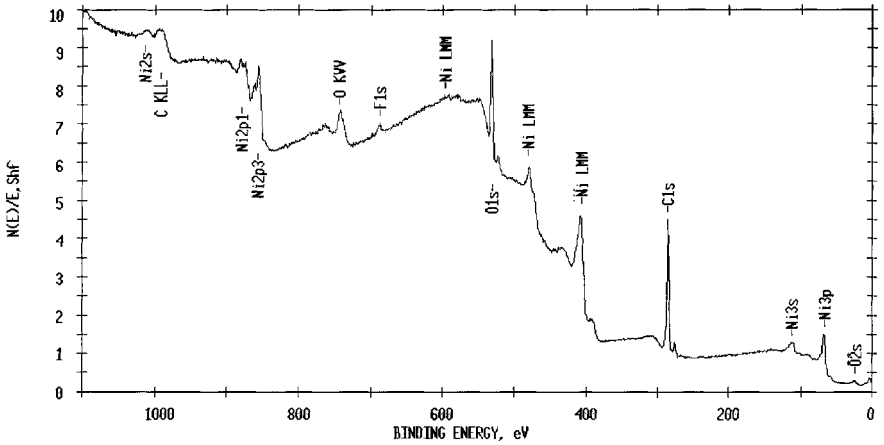

Figure 8 General X-ray photoelectron spectra of the processed powder.

oxide peaks and only to metallic nickel essentially remaining in the surface layer. This means that the coating is quite uniform and even if there are large aggregations on the particle surfaces, their relative part is not great. The short-time etching of the specimen by an ion beam in the chamber of the X-ray photoelectron spectrometer made it possible to practically completely remove the NiO film from the specimen surface. This indicates abnormally low oxidation of the produced composite material in spite of the fact that this material had been kept for quite a long period (about 10 days) in air before it was placed in the chamber of the X-ray photoelectron spectrometer. The Ni coating thickness according to the X-ray photoelectron spectra, obtained in the ion-etching process, was not less than 10 nm and is in good agreement with the above data.

33.4 Conclusion

Disperse composite materials can be used in the processes of fabricating structural and special materials with unusual properties. This technology is aimed at further industrial application. DCM are used as disperse catalysts; for production of abrasive, wear-proof, corrosion-proof, high-strength, magnetically nonpervious and other coatings; constructive composite materials; composite resistors; and in the processes of braze welding of ceramic solids (high-temperature superconductors, solid electrolytes, etc.) with metals. For many applications the 10–20 nm thickness of coatings is quite sufficient.

The performed investigation showed that the dusty-plasma technology made it possible to obtain the diamond-nickel composition material in such amounts that were enough for physical and technologic studies. The coating is a solid nickel layer of 10 nm thickness with characteristic roughness of 3 nm. Dendrite fragments and

coatings with fractal structure are practically absent in the metal layer and the nickel film is strongly bound to the diamond surface.

Such DCM has much potential for compacting of superhard volume composite materials on the basis of synthetic diamond and Ni or Co as catalyst [18, 19].

Acknowledgment

This study was supported by the Russian Foundation for Basic Research (project No. 01-02-17726).

References

[1] V.E. Fortov, H. Hora, A.S. Ivanov et al. Method and equipment for manufacturing disperse composite materials. German Patent Application, No 19832908.3 (July 1998).
[2] H. Kersten, P. Schmetz, G.M.W. Kroesen, Surf. Coat. Technol., **108–109**, 507 (1998).
[3] G. H. P. M. Swinkles, H. Kersten, H. Deutsch, G. M. W. Kroesen, J. Appl. Phys, **88**, 1747 (2000).
[4] H. Kersten, H. Deutsch, H. Steffen, G. M. W. Kroesen, R. Hippler, Vacuum, **63**, 385 (2001).
[5] B.M. Smirnov. Aerosols in gas and plasma (in Russian). M., IVTAN, (1990).
[6] M.S. Barnes, J.H. Keller, J.C. Forster, J.A. O'Neill, D.K. Coultas, Phys. Rev. Lett. **68(3)** 313–316 (1992).
[7] I.A. Belov, A.S. Ivanov, D.A. Ivanov et al., Zh. Exp. Teor. Fiz., **117**, 105–114, (2000).
[8] I.A. Belov, A.S. Ivanov, D.A. Ivanov et al., Pis'ma v ZhTF, **25**, 89–95. (1999).
[9] H. Thomas, G.E. Morfill, V. Demmel, J. Goree, B. Feuerlacher, D. Mohlmann, Phys. Rev. Lett., **73**, 652 (1994).
[10] I.A. Belov, A.S. Ivanov, A.F. Pal, A.N. Ryabinkin, A.O. Serov, Phys. Lett. A, **306**, 52 (2002)
[11] D.P. Sheehah, M. Carillo, W. Heidbrink, Rev. Sci. Instrum., **61**, 12, (1990)
[12] Hiroharu Kawasaki, et al., J. Appl. Phys., **83**, 11 (1998).
[13] H.M. Anderson, S.B. Radovanov, J. Res. Natl. Stand. Technol., **100**, 449–462 (1995).
[14] Card-File of JCPDS – International Center for Diffraction Data, 04-0850 (1995).
[15] C. Kittel, Introduction to Solid-State Physics, Moscow, Nauka, (1978).
[16] N. Ashkroft. N. Mermin, Solid-State Physics, Moscow, Mir, (1979).
[17] Handbook of X-Ray Photoelectron Spectroscopy (Eds C.D. Wagner, W.M. Rigg)
[18] Gigle P.D., Proceedings of the Sixth AIRAPT International High Pressure Conference "High-Pressure Science and Technology" (July, 1977. Boulder). N.Y.: Plenum, 914–922, (1979).
[19] Roberts D.C., SYNDITE - its mechanical and physical properties, Industrial Diamond Review, 237–241, (1979).

34
Dust Particles in the dc Glow-Discharge Plasma: Self-organization and Peculiarities of Behavior

V.E. Fortov, A.G. Khrapak, V.I. Molotkov, O.F. Petrov, M.Y. Poustylnik, V.M. Torchinsky

Abstract

The review of the investigations of strongly coupled dusty plasma in the dc glow-discharge striations is presented. The formation of plasma crystals, liquids and plasma liquid crystals is considered. Observations of different phenomena, e.g. dust vortices and spontaneous excitation of the dust density waves, are presented. Results of the experiments on different external influences on dusty-plasma structures are discussed. Gas-dynamic impact was used to excite nonlinear dust density waves. It is demonstrated that other external influences can be used to measure the grain charge (with the help of a focused laser light) and field of forces acting on a dust grain levitating in the plasma (by means of external thermophoresis).

34.1
Introduction

This work is devoted to investigations of dusty-plasma formations in the dc glow-discharge striations [1, 2]. Striations in the neon gas discharge have been studied in [3, 4].

Striations are ionisation-wave instabilities of the glow-discharge column. The ionisation wave may be running or standing. A running striation has a frequency of the order of 1–10 kHz, so when observed with the naked eye the discharge seems uniform.

In our work we use standing striations. To create a standing striation one needs to introduce some nonuniformity into the discharge. Constrictions of the tubes, nibs and other constructional elements may lead to the appearance of the standing striations.

Figure 1 presents relative distributions of the electric field, plasma density and mean electron energy in a single period (one striation) of the ionisation wave in the glow discharge in neon. The same structure is reproduced several times in the column length, slightly damping from the cathode to anode. It is seen that there is a region where the electric field increases in the direction of the cathode. If the discharge is vertically oriented and the lower electrode is a cathode, stable levita-

tion of dust grains in the striation is possible. Plasma parameters in striations may reach the following values: electric field up to 10–15 V/cm, plasma density 10^7–10^9 cm^{-3}, average electron energy 3–10 eV. Ions are assumed to remain at room temperature. These values just correspond to conditions of the strongly coupled dusty plasma [5].

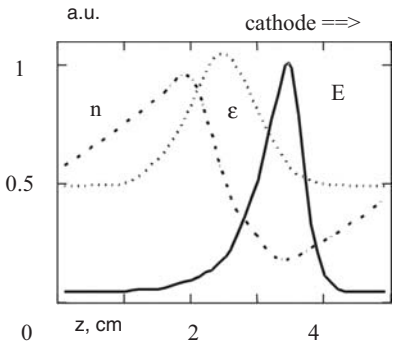

Figure 1 Relative distributions of plasma density *n*, mean electron energy ε and electric field *E* in the neon glow discharge.

The plasma nonuniformity in striations, a presence of the longitudinal electric field gradients lead to the appearance of some peculiarities in the dusty-plasma structures, e.g. convective motions of dust grains, dust-acoustic instability and others.

In Sect. 2 we present the experimental setup for the dc glow-discharge dusty-plasma studies. In Sect. 3 different kinds of dusty-plasma structures formed in the neon glow-discharge striations are given.

Section 4 is devoted to wave phenomena in the dusty component including self-excited waves and waves excited by the gas-dynamic impact. In Sect. 5 we present experimental methods of measuring the charge on the dust grains and the field of forces acting on the dust particle levitating in the plasma.

34.2 Experimental Setup

The experimental setup for studies of the dusty plasma in the dc glow discharge is shown in Fig. 2. It is a vertically positioned glass tube in which the glow discharge with cold electrodes is created.

The upper electrode is the anode and the lower one is the cathode. The tube is filled with neon or with a mixture of neon with hydrogen up to the pressure of 0.1–2 Torr.

The discharge current varies from 0.1 to 4 mA. The standing striations exist in these regimes. The plasma parameters are as given in Sect. 1.

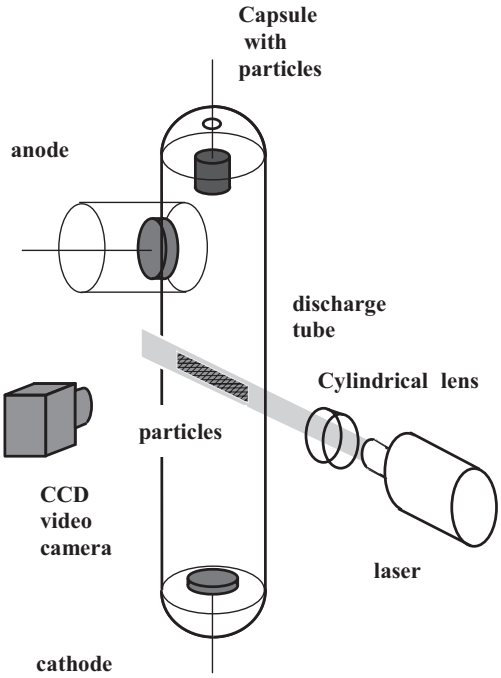

Figure 2 Experimental setup.

The dust particles were held above the discharge area in a container with the grid bottom. When shaking the container the dust grains fell down through the grid and levitated in striations forming the ordered structures.

The dust grains are visualized with a diode laser sheet. The sheet thickness is 150 μm and the width is 1.5 cm. The laser sheet may be positioned both vertically and horizontally. This allowed us to observe the vertical section of the structure as well as the horizontal one. The light scattered by dust grains was imaged by a video camera.

To register fast processes the video camera Phantom 5 with a frame frequency up to 1000 frames per second was used. The video frames were later digitized for computer processing.

The glow discharge with cold electrodes is characterized by discharge oscillations connected with the cathode spot movements. This leads to fluctuations in dusty-plasma structures. To stabilize the column an additional insert with a constriction was placed in the lower part of the discharge tube above the cathode [6]. All our observations are carried out in the first striation that appears over this constriction.

34.3
Plasma Crystals and Liquids

34.3.1
Structures of Spherical Grains

The formation of structures in the dc glow-discharge striations proceeds in the following way: after shaking the container the dust particles fall down and are captured in a trap created by the longitudinal and radial electric forces of a striation and gravity. The charged dust grains form the ordered structure preserved for as long as the discharge exists at constant parameters.

We used spherical particles of different materials: borosilicate glass ($\rho = 2.3$ g/cm^3) in the form of thin-walled, hollow spheres of diameter 50–60 μm with wall thickness 1–5 μm, Al_2O_3 particles ($\rho = 4$ g/cm^3) with diameter 3–5 μm, melaminformaldehyde spheres ($\rho = 1.5$ g/cm^3) with diameters 1.87, 4.82, 10.24, 13.57 μm. The mass of the particles lies in the range from 10^{-12} to 10^{-7} g.

The particles formed in striations ordered structures with a different degree of ordering.

Figure 3 shows a video image of the plasma crystal. The structure was obtained in the discharge in a mixture of neon with hydrogen when the ratio of the length of the visible part of the striation to its total length decreases and the electric field acting on grains increases. The interparticle distance of the plasma crystal presented is about 700 μm. When the discharge current increases the plasma crystal is first melted in the peripheral region and then in the center. This is connected with an increase of the plasma density, decrease of the screening length of the dust grains, weakening of an interaction between dust particles and consequent increase of the dust particle's kinetic temperature.

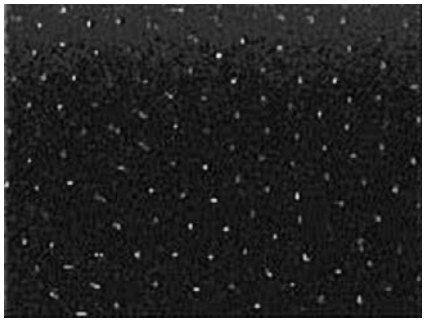

Figure 3 Horizontal section of plasma crystal. Frame size 8.8 × 9.6 mm

In our experiments we observed levitation of separate particles as well as chains of several particles arranged along the axis of the discharge [7]. The formation of structures with a coexistence of different regions has been revealed. It is possible to study complicated formations with the regions of strong ordering (plasma crystal)

and the regions with convective and oscillatory motion of grains (dusty-plasma liquid) [7]. The complicated structures are associated with the peculiar distribution of forces acting on the dust particles: the ion-drag force, the electrical force and distribution of plasma parameters along the striation.

34.3.2 Plasma Liquid Crystal

Besides spherical grains we used elongated cylindrical grains.

To provide the levitation of nylon ($\rho = 1.1$ g/cm^3) microcylinders of diameter 10 µm and length 600 µm a neon-hydrogen mixture was used. These dust grains formed the structures consisting of 3–4 horizontal layers. Lighter particles (diameter 7.5 and 10 µm, length 300 µm) levitated in neon striations and formed much more axially prolonged structures. The structures formed of microcylinders indicated a pronounced short-range order (Fig. 4) [8]. All the particles lay in the horizontal plane and were all aligned in a certain direction.

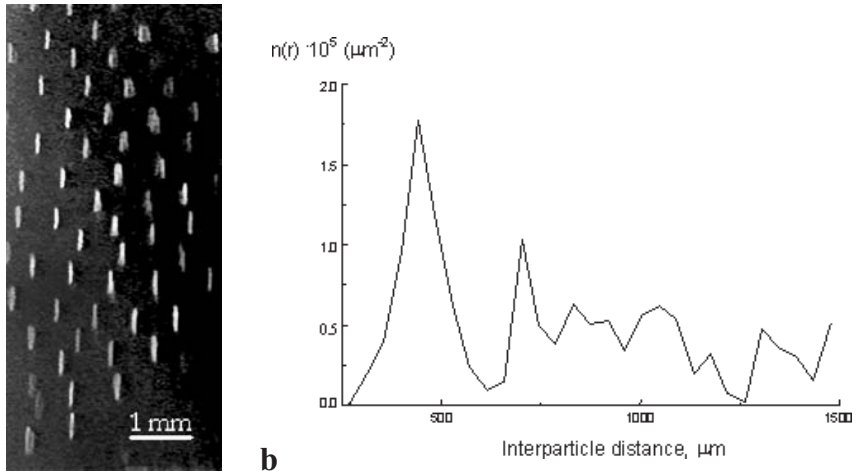

Figure 4 Videoimage (a) and distribution function (b) of a structure of long cylindrical prticles (300 µm length, 15 µm diameter). Discharge in a neon-hydrogen (1:1) mixture. Pressure 0.9 torr, current 3.8 mA.

The preferential direction of the particle orientation seems to originate from the slight constructional asymmetry of the discharge tube. To verify this supposition an asymmetrical distortion was introduced into the discharge. A dielectric plate with a hole placed several centimeters above the cathode induced it.

The plate overlapped the discharge section so that the formation of the column started through the hole with the diameter of 1 cm. The visually observed distortion of the standing striation indicated the presence of the axially asymmetric part of the electric field. The turning of the plate resulted in the change of the orientation of

particles. The charge on the dust particles estimated from the levitation conditions (equilibrium of gravitational and electrostatic forces) is assumed to be about 8×10^5 electrons. The structures formed of the strongly charged elongated cylindrical grains exhibit properties similar to those of nematic liquid-crystal structures, namely, that the positions of the mass centers of gravity of the grains show short-range ordering; the grains are oriented strictly parallel to a common axis. The experiments with microcylinders of diameter 10 μm and length 300 and 600 μm with a thin layer of a conducting polymer revealed that these particles behaved in the same way and formed structures of the same shape as dielectric microrods of the same size.

34.4 Wave Phenomena

Wave phenomena in the dust component are at present of great interest for researchers. The presence of the dust component in a plasma leads to the appearance of new specific modes in the wave spectrum, e.g. dust acoustic waves [9]. It has been demonstrated [10] that the dc glow-discharge dusty plasma is a very useful instrument to study self-excited waves of the dust-component density. It has been revealed that under certain conditions the self-excited dust-acoustic waves could appear in the dc glow-discharge striations.

It was shown [10] that the instability is caused by the joint effect of the ion drift and fluctuations of the dust-grain charge.

To excite instabilities of the dust component we proposed a gas-dynamic impact [11]. The experimental setup was similar to that shown in Fig. 2. But the lower electrode was made as the hollow cylindrical cathode.

The electrodes were separated by 26 cm. In some experiments a grid was inserted into the tube 7 cm above the upper cut of the cathode. The grid was kept under the floating potential.

For the excitation of the waves a plunger was set below the cathode. The plunger was a hollow thin-walled nickel cylinder of 26 mm diameter and height with the bottom made of a polymeric pellicle.

It was freely installed at the bottom of the tube and moved with the help of a permanent magnet manually approached to the plunger from outside the tube. The plunger could be moved upward and downward with a speed of 30–40 cm/s and 4–5 cm space, creating a gas flow with a duration of 0.1 s that displaced the dust grains with respect to the striation. A current of 0.1–1 mA could be driven through this system at a neon pressure of 0.3 Torr. Melamineformaldehyde dust grains 1.03 μm diameter were used to form dusty-plasma structures in striations.

In the case of experiments without the grid it was possible to generate waves of dust-density component. The properties of these waves are similar to the properties of the self-exited waves obtained in [10].

In the case of experiments with the grid quite a new type of instability was obtained.

This occurred at the current value of 0.1 mA. The dusty-plasma structure was very close to the grid (at a distance of 4 mm). After moving the plunger downward the structure was again for some time streaming downward, then it stopped and began moving towards its initial equilibrium position and when it returned to the stable position a disturbance propagating through it appeared (Fig. 5).

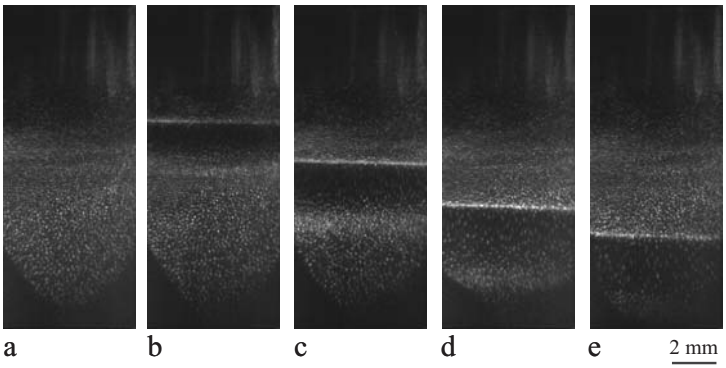

Figure 5 Sequence of video images representing the disturbance.

Figure 6 presents the shape of the compression factor ξ, which is the ratio of the distribution of brightness in the initial structure, at different moments of time. The disturbance consists of two humps (A,C) separated by a dip (B). It is seen that the amplitudes for zones A and C reach to the values of 2.1 and 1.2 and 0.65 for the rarefaction.

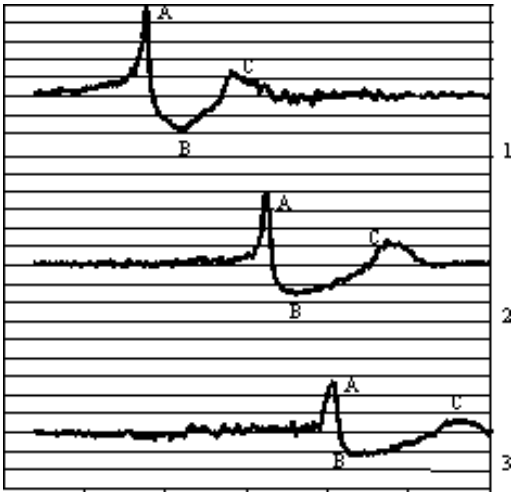

Figure 6 Compression factor in the wave at different moments of time. Time interval between curves 1 and 2–120 ms, between 2 and 3–60 ms.

All three structures move approximately with the same speed of 2–2.5 cm/s. These velocities of the wave lie in the range of the dust acoustic velocity C_{da} estimated from the plasma parameters, dust density and the grain charge. According to this $C_{da} = 1.8–5.2$ cm/s.

The gas pressure in our experiments is rather high and the damping time due to neutral drag force is about 15 ms. But the observed time of the wave propagation is 500 ms. This means that the wave must have an energy source other than the initial impulse. The dust acoustic instability could serve as a mechanism by means of which the energy is supplied to the wave.

34.5
Diagnostics of the dc Glow-Discharge Plasma

34.5.1
Measurement of the Grain Charge

Measurements of the charge were conducted in the following way [12]. The light beam from an Ar^+ laser was focused onto a single particle in the structure. The beam power was up to 200 mW, the waist thickness was about 60 μm and the corresponding power density of the order of 10^3 W/cm^2. Under the effect of the light pressure the particle moves 1.5–3 mm out of the structure, then comes out of the beam and returns back to the structure. When returning back to the structure a dust particle is subject mainly to the radial electric force and the neutral drag force. The radial electric field is found from the ambipolar diffusion condition. Since the deflection of the particle is small compared to the tube radius $R = 18$ mm the linear approximation of the radial electric field can be used (see ref. [1]):

$$E_r = \left(\frac{2.4}{R}\right)^2 \frac{\varepsilon r}{2e}, \tag{1}$$

where ε is the average electron energy, r is the current radius. As follows from the observation, the particle performs aperiodical motion. Starting its way back with the zero radial velocity the particle is first accelerated by the electric force and then, while its velocity increases and the electric field decreases towards the tube center, neutral drag starts to prevail and the particle is slowed down. Thus there must be a maximum of velocity on the return trajectory of the particle. At the point of this maximum the radial electric force must be balanced by the neutral drag:

$$E_r q = \frac{16\pi}{3} p a^2 \frac{v}{v_{th}} \tag{2}$$

where E_r is the radial electric field, q is the charge, a is the grain radius, v is the particle velocity, v_{th} is the thermal velocity of gas atoms. This equation gives the possibility to determine the charge. The estimated accuracy of the εq product measurements is 40%. The results of the measurements are presented in Fig. 7.

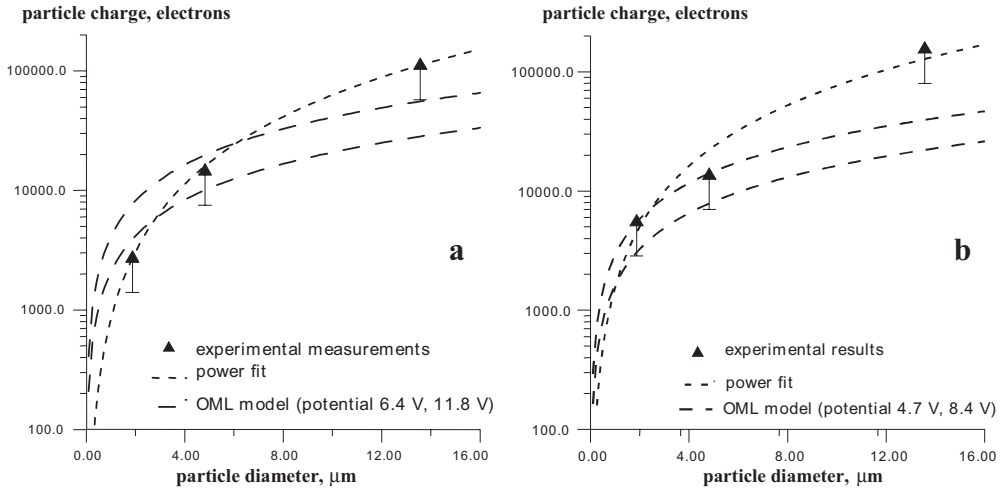

Figure 7 Results of the charge measurements: (a) neon pressure 0.5 torr, $T_e = 3$ eV; (b) neon pressure 1.5 torr, $T_e = 2$ eV.

34.5.2

Application of Thermophoresis for Diagnostics of Dust-Particle Confinement

The thermophoretic force is the force acting on a body in a rarefied medium, in which a temperature gradient exists.

To create the temperature gradient a heater was maintained on a discharge tube [11]. The heater was made as a double-wound wire in order to exclude the influence of the magnetic field. The distance between single wires was 7 mm. The heater was (Fig. 8) installed parallel to the discharge axis. Its length was 16 cm, whereas the tube diameter was 3 cm. So, the temperature distribution produced by the heater could be treated as two-dimensional.

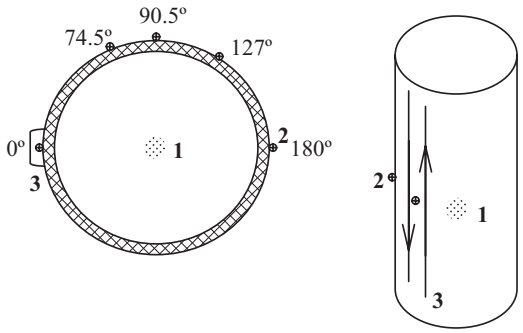

Figure 8 Scheme of the experiment on the thermophoretic influence on the dusty-plasma structures. 1 – dust particles, 2 – thermocouples, 3 – heater.

Temperatures were measured in a certain section of the tube close to the area of levitation of the dust grains. Chromel-alumel thermocouples were employed for temperature measurements. Their sensitivity is of the order of 65 μV/K. Thermocouples were placed in 5 points of the tube semicircle as shown in Fig. 8. The other semicircle is left free to allow the observation of the dust grains. The measured temperature profile is symmetrically depicted onto the free semicircle and in this way the temperature profile on the whole circumference is determined.

To reconstruct the temperature distribution inside the tube we have to solve the following equation:

$$\Delta t = 0$$
$$\frac{T_w(\phi) - T(R,\phi)}{d}\lambda_{glass} = \lambda_{gas}\frac{dT}{d\rho}\Big|_{R,\phi} \tag{3}$$

where ρ, ϕ are polar coordinates, $T(R, \phi)$ is the temperature distribution inside the tube, $T_w(\phi)$ is the interpolation of the measured temperatures over the tube circumference, R is the tube radius, d is the tube wall thickness, λ_{glass} and λ_{gas} are heat conductivities of the glass and gas in the tube respectively. Equation (3) is considered linear since the dependence of the gas heat conductivity on the temperature is negligible due to small temperature variations. The boundary condition accounts for the continuity of the heat flux on the internal surface of the tube.

The experiment proceeds as follows. First a chain of dust particles is formed on the axis of the discharge tube and initial positions of the dust grains are recorded. Then the heater is turned on. It takes about 15 min for the temperature to reach the steady-state distribution. Dust particles acquire new equilibrium positions. Their positions are again recorded and indications of the thermocouples are taken. Then the heater power is increased and the procedure is repeated.

Measured temperatures are interpolated along the circumference and Eq. (1) is solved. In this way the distribution of temperatures for each equilibrium position of dust grains is obtained. In an equilibrium position the thermophoretic force acting on a dust particle is balanced with a confining force of the discharge. The thermophoretic force is expressed as follows:

$$F_{th} = \frac{8}{45}\sqrt{\pi}pa^2 l\frac{\nabla T}{T}, \tag{4}$$

where p is the neutral gas pressure, λ is the mean free path of neon atoms, a is the dust-grain radius. F_{th} can be easily calculated if the temperature distribution and the particle position is known. By calculating thermophoresis for a set of equilibrium positions of the dust grains we acquire the distribution of the confining force.

In Fig. 9 we present an example of the measurements of the confinement force for the melamineformaldehyde dust particles 4.82 µm diameter, neon pressure 0.8 Torr, current 1.66 mA.

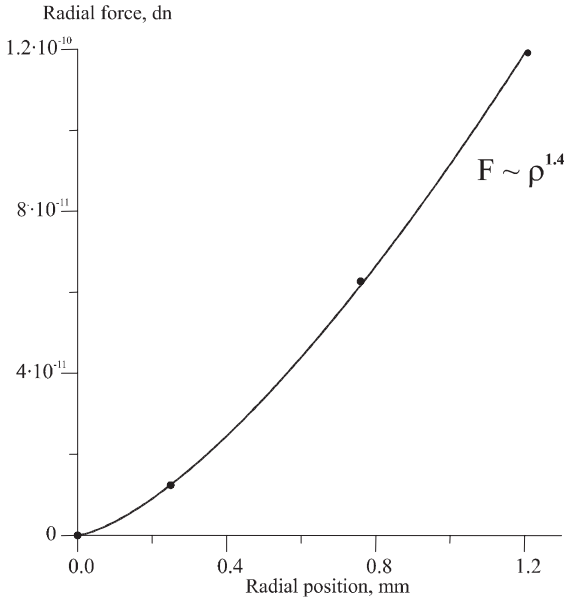

Figure 9 Results of the measurements of the confining-force distribution for plastic dust particles 4.82 μm diameter at neon pressure 0.8 torr, and discharge current 0.66 mA.

34.6 Conclusion

In this work we have presented the results of the investigations of the behavior of the dust grains in the dc glow-discharge striations. It has been shown that dust particles can form structures with short-range as well as long-range order. The experiments were performed with spherical and elongated cylindrical grains. In the structures formed by microcylinders strong orientational order was obtained. These structures were called plasma liquid crystals. It has been demonstrated that the gas-dynamic impact is a useful tool for excitation of high-amplitude waves of dust density. A method for measuring the charge on the dust grains levitating in plasma was suggested. The charges on spherical particles 1–13 μm in diameter were measured and were found to lie in the range of 10^3–10^5 electrons. Influence of thermophoresis on the dust grains was used to measure the field of confining forces of the order of 10^{-10} dn.

Acknowledgements

This work was partially supported by the Russian Foundation for Basic Research, project 03-02-16316.

References

[1] Y. P. Raizer, *Gas Discharge Physics* (Springer, New York, 1991).

[2] P. S. Landa, N. A. Miskinova, Y.V. Ponomarev, Usp. Phys. **132**, 61 (1980).

[3] Y. Golubovsky, S. Nisimov, J. Tech. Phys. (in Russian) **64**, 54 (1994).

[4] Y. Golubovsky, S. Nisimov, J. Tech. Phys. (in Russian) **65**, 46 (1995).

[5] H. Ikezi, Phys. Fluids **29**, 1764 (1986)

[6] A.M. Lipaev, V.I. Molotkov, A.P. Nefedov et al., JETP **85**, 1110 (1997)

[7] V.E. Fortov, A.P. Nefedov, V.I. Molotkov et al., in *Dusty Plasmas in the New Millenium*, eds R. Bharuthram, M. Hellberg, P.K. Shukla, F. Verheest, AIP Conf. Proc. **649**, 394 (2002)

[8] V.I. Molotkov, A.P. Nefedov, M.Y. Poustylnik et al., JETP Lett. **71**, 102 (2000)

[9] N.N. Rao, P.K. Shukla, M.Y. Yu, Planet Space Sci. 38, 543 (1990)

[10] V.E. Fortov, A.G. Khrapak, S.A. Khrapak et al., Phys. Plasmas **7**, 1374 (2000)

[11] V.E. Fortov, A.P. Nefedov, V.I. Molotkov et al., in *Dusty Plasmas in the New Millenium*, eds R. Bharuthram, M. Hellberg, P.K. Shukla, F. Verheest, AIP Conf. Proc. **649**, 390 (2002)

[12] V.E. Fortov, A.P. Nefedov, V.I. Molotkov et al., Phys. Rev. Lett. **87**, 205002 (2001)

35
Controlled Growth of Carbon Nanotubes Using Pulsed Glow-Barrier Discharge

Tomohiro Nozaki, Yoshihito Kimura, Ken Okazaki, Shigeru Kado

Abstract

This paper describes aligned growth of carbon nanotubes using pulsed glow barrier discharge at atmospheric pressure. In the first section we present general aspect of nanotubes deposited with He-based atmospheric pressure glow discharge (APG) generated by a 130-kHz sine voltage. The effect of substrate preparation (Ni/quartz or Ni/Si) and feed gas (CH_4 or C_2H_2) on nanotube morphology is discussed. Then pulsed APG, which would create directional electric field near substrate, is discussed for the improvement of aligned growth. Marginally aligned nanotubes were observed with positive pulsed voltage, while nanotubes became thicker and shorter in the case of negative pulsed voltage. We also found that high temperature (>750 °C) and high pulse duty (>25%) is essential for better alignment in pulsed APG. Finally, we present concluding remarks along with future work for further improvement of APG-assisted chemical vapor deposition.

35.1
Introduction

Atmospheric-pressure glow discharge (APG) has been attracting substantial attention in industry because highly reactive nonequilibrium uniform plasma is readily available via a much simpler means. Several benefits are (1) atmospheric-pressure operation is desired for large-scale industrial applications, (2) APG minimizes the dependence on the vacuum system and batch processes, and (3) APG would be able to shorten process time. The easiest way to produce APG is to dilute the process gas with a large amount of helium. Production of metastable helium by electron impact and associated Penning ionization significantly decreases operating voltage [1], avoiding formation of filamentary discharges at atmospheric pressure. The presence of impurity promotes Penning ionization, and up to 10% of admixture (e.g. a mixture of H_2 and CH_4) was acceptable in our experiment. Computer simulation performed in He/N_2 mixture shows that the electron density increases up to 10^{11} cm^{-3} in the cathode region when current pulse reaches a maximum [2]. A strong electric field is simultaneously produced in this region. N_2-based APG is also used for CVD

[3]; however, the amount of process gas is limited below 0.1%, and electron density (10^8 cm^{-3}) does not reach high enough to produce cathode region [2]. From these aspects, authors focused on carbon-nanotube deposition with He-based atmospheric pressure glow discharge [4,5]. Although the presence of an intense cathode region near substrate is essential for nanotube deposition, aligned nanotubes were hardly seen probably due to the lack of directional electric field near substrate. Because dielectric barrier forces apply to alternating voltage in order to maintain a series of stable glow discharges. In this paper we first describe the effect of catalyst–substrate combination and precursors, and then discuss application of pulsed APG, which the enhances directional electric field near substrate, for aligned growth of carbon nanotubes. Finally some of the important aspects are summarized along with future work.

35.2 Experimental

Glow barrier discharge reactor including power circuit and fundamental growth parameters are shown in Fig. 1 and Table 1, respectively. The electrode system, which generates glow discharge in the gap between two parallel-plate electrodes, was situated in a vacuum chamber, while an alumina plate of 0.5 mm thickness covered upper electrode. The chamber was evacuated after a sample was loaded on the metallic bottom electrode, and then a He/H_2 mixture ($He:H_2 = 900:100$ sccm) was introduced up to 760 Torr. Two types of samples were tested: Ni/SiO_2 (quartz: 25 mm diameter and 1 mm thickness) and Ni/Si (p-type: 15 mm square and 0.5 mm thickness) substrates. A 20-nm nickel layer was coated by metal plating simply because the authors aimed to eliminate as many vacuum processes as possible. Magnetron sputtering, for example, can also be applied as a promising technique for this purpose. The electric heater embedded in the bottom electrode maintained the appropriate growth temperature, which was monitored with a thermocouple embedded 1 mm below the surface of bottom electrode. When the appropriate temperature was reached the $He/H_2/CH_4$ mixture was introduced. Either a sine-wave or pulsed voltage was applied through the upper electrode. In order to measure the voltage drop across the gap and the dielectric barrier, a test capacitor (0.036 μF) and a current probe were installed after the bottom electrode. When deposition was completed, the chamber was evacuated and filled with pure He, while the heater was switched off. The bottom electrode was cooled down below 200 °C before unloading the sample. Otherwise nanotubes will be destroyed by air exposure at high temperature. Deposited materials were characterized by Raman spectroscopy (JASCO NRS-1000, green laser 532 nm), high-resolution transmission electron microscopy (JEOL JEM-3010, 300 kV – 0.17 nm), and scanning electron microscopy (HITACHI S-4700, 30 kV – 3nm). EDX (EDAX, UTW-CDU-ME) was also used to characterize nickel thin film prepared by metal plating.

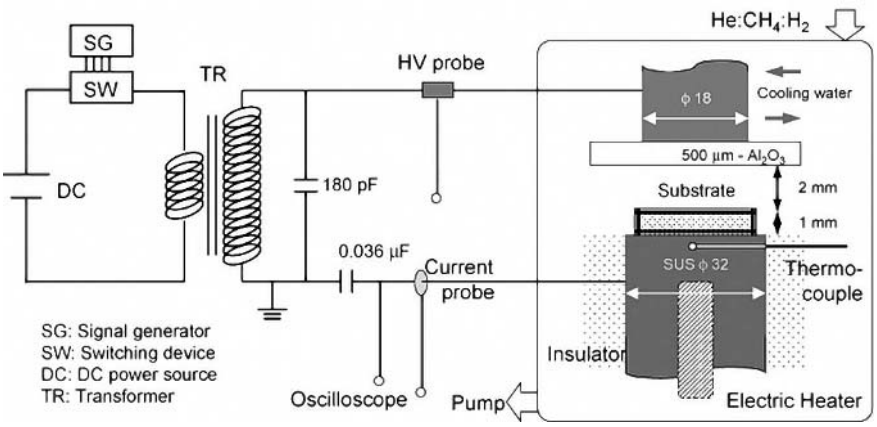

Figure 1 Experimental setup.

Table 1 Basic conditions

Si substrate (100): 15 mm square × 0.5 mm with 20 nm Ni
Quartz substrate: ϕ 25 mm × 1.0 mm with 20 nm Ni

He	H_2	CH_4	Gap	Pressure	Temp.	Time
900 sccm	100 sccm	10 sccm	2 mm	760 Torr	600 °C	5–30 min

35.3
General Aspects of Carbon-Nanotube Deposition with He-based APG

In the previous work, the minimum requirements for nanotube growth in He-based APG have been summarized. Some of the important aspects are (1) H_2/CH_4 ratio must be higher than five, (2) growth temperature must be higher than 600 °C, (3) filamentary discharge severely deteriorates catalyst nanoparticles and was not able to produce carbon nanotubes. Based on these facts, the first experiment focused on the effect of catalyst/substrate combination and process gas on nanotube morphology. A high-voltage sine wave was applied with a frequency between 125 kHz and 135 kHz so that the best matching was established between the external circuit and APG. Otherwise, filamentary discharges tended to superimpose on the glow discharge, and nanotubes were hardly deposited.

Figure 2 show SEM and TEM pictures of multiwall carbon nanotubes deposited on nickel-coated quartz substrate. Ni/SiO_2 (quartz) substrate is the ideal catalyst/-substrate combination for nanostructured carbon deposits [6]. Results were successful, but nickel nanoparticles were easily coagulated in this case. In addition, the diameter of nanotubes became larger and widely distributed. TEM pictures clearly show that number of nickel grains heavily coagulates. Figure 3 shows nanotubes deposited on Ni/Si substrate. Although we could not confirm specific improvement of the growth rate (~0.2 µm/min) and wall structure from the Raman spectra, the

diameter of nanotubes became much thinner than those deposited on Ni/SiO_2 as shown in SEM pictures. However, this type of nanotube was not always deposited on Ni/Si substrate. There is no doubt that nickel is one of the effective transition metal catalysts to grow nanotubes, but the catalytic activity depends strongly on a combination of alloying materials including the substrate itself. According to the literature [7], Ni/Si seems to be an ineffective combination unless appropriate pretreatment such as ion bombardment or chemical etching is performed, whereas Ni/SiO_2 (quartz) is one of the effective catalyst/substrate combinations for the growth of carbon-fiber structures. Deposition of analuminum or chromium underlayer remarkably enhances nanoparticle formation almost independently of substrate material and then increases the number of reactive sites on catalyst surface [8]. Figure 4 shows the result of elemental analysis of nickel coating. The data reflects a 150-μm square region of the surface of the nickel layer included approximately 10 mol% of phosphorus (P) as an impurity that is required during metal plating. Although the precise role of phosphorus in nanoparticle formation is not known, nanotubes were occasionally deposited on Ni/Si substrate in our experiment. Although Ni/Si substrate provided thinner nanotubes, the rest of the experiments were carried out with nickel-coated SiO_2 (quartz) substrate.

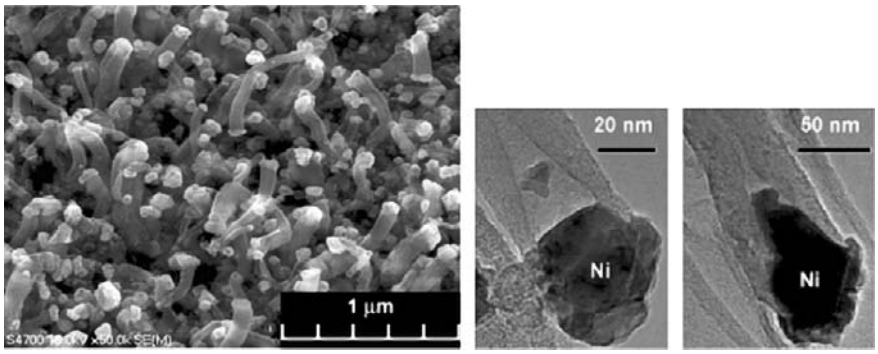

Figure 2 SEM: Ni-coated (20 nm) quartz substrate (600 °C, $H_2/CH_4 = 10$).

The effect of precursor was also examined using acetylene and methane. Acetylene is a reactive precursor and commonly used in nanotube growth. However, if the electrode temperature exceeded 500 °C, a large amount of graphite was deposited not only on substrate, but also on the bottom electrode, creating a number of graphite spots that induced filamentary discharges (e.g., $He:H_2:C_2H_2 = 900:100:0.5$). Once filamentary discharge was formed, it accelerated graphite deposition at the corresponding location, and stable glow discharge was no longer maintained. In addition, when the substrate surface was covered with excess graphite, nickel particles quickly lost catalytic activity. Although a small amount of nanostructured carbon was recognized, the substrate was mostly covered with amorphous carbon. Acetylene is favorably used in low-pressure PECVD; excess graphite was deposited at atmospheric pressure. Saturated hydrocarbons such as methane are able to minimize excess graphite formation.

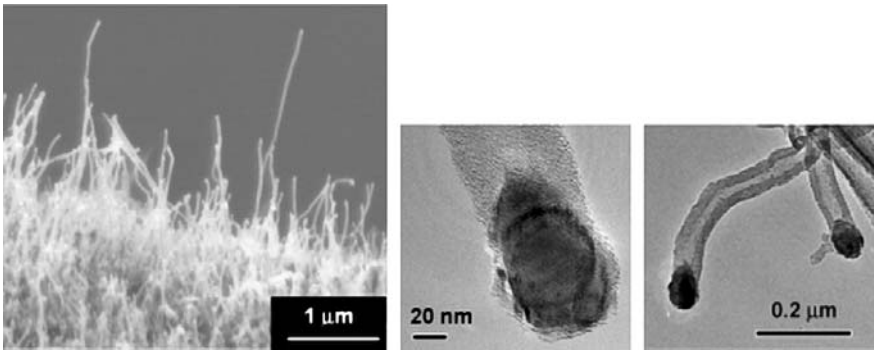

Figure 3 SEM: Ni-coated (20 nm) Si substrate (620 °C, $H_2/CH_4 = 10$).

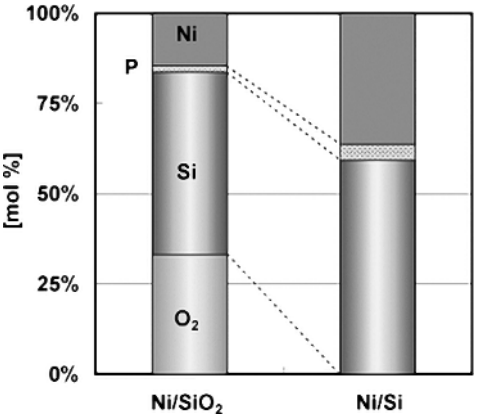

Figure 4 Elemental analysis of Ni film prepared by metal plating. EDX (EDAX, UTW-CDU-ME) was used for this analysis. P stands for phosphorus that was contaminated during metal plating processing.

35.4 Aligned Nanotube Growth with Pulsed APG

There are many different ways to produce carbon nanotubes. These methods are divided into two categories: noncatalytic processes operated at extremely high temperature (>3000 °C) and catalytic processes at relatively low temperature (550–900 °C). Plasma-enhanced chemical vapor deposition (PECVD) is classified into the latter one. The plasma is not always necessary, but the existence of nonequilibrium plasma enhances the well-aligned growth of nanotube on the patterned catalyst for the desired purpose. Although the precise role of the plasma is not quite clear, empirical evidences assume that the directional electric field formed by the

ion sheath play a remarkable role in the alignment of growing nanotubes. On the other hand, marginal alignment due to a crowding effect has been observed in thermal CVD samples [7]. Up to now, individual free-standing and vertically oriented nanotubes are possible with PECVD. In the previous study, the authors pointed out that the existence of intense cathode region is important to grow nanotubes [5,9]. On the other hand, nanotubes were randomly grown due to the lack of directional field near the substrate because dielectric material forces us to use alternating voltage in order to maintain a series of glow discharges. From this fact, the authors generated APG by a pulsed high voltage that enforces single-polarity voltage throughout the deposition process, thus it would provide a directional field on the substrate.

Figure 5 shows a positive pulsed voltage and corresponding current waveform. Frequency could vary from 10 kHz to 125 kHz without particular matching device, but the pulse width was fixed by the secondary circuit of the transformer (~2 μs). Charges accumulated on the dielectric barrier were automatically released through the external circuit since both electrodes are connected to the ground between pulsed voltages. This particular circuit allows us to keep applying either positive or negative pulses to produce stable APG. A single current pulse was formed at the rising and falling part of the pulsed voltage, but the first current pulse was much more intense. Although current was flowing in either direction, a positive potential was applied across the gap, which creates the DC components of the field. Neither current waveform nor breakdown voltage was affected by the presence of substrate. High-temperature operation decreases the breakdown voltage because the gas density between electrodes decreases with increasing electrode temperature; however, we did not observe specific changes in the current waveform at elevated temperature. In this experiment, pulse frequency (duty cycle), growth temperature, and pulse polarity were investigated.

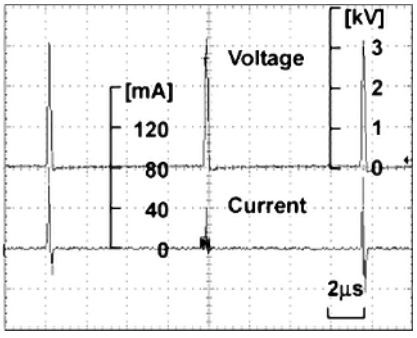

Figure 5 Voltage and current waveforms for positive-pulsed APG. Frequency: 125 kHz, Temperature: 600 °C, Gap: 2 mm, He:H_2:CH_4 = 900:100:10 sccm.

35.4.1
Effect of Pulsed Voltage on Alignment

Figure 6 shows nanotubes deposited with positive-pulsed APG and negative-pulsed APG. The white scale in each picture corresponds to 1 μm. The results clearly show that positive-pulsed APG deposited more aligned and narrow nanotubes, while nanotubes became thicker and shorter with negative-pulsed APG. One possible explanation is that a more intense cathode region is created near the substrate when a positive pulse is applied, which provides sufficient radicals and a strong electric field during breakdown. Although directional movement of ion is lost due to multiple collisions at atmospheric pressure, directional ion etching does not enhance the alignment process [10]. In fact, Figs. 6 (a) and (b) show marginally aligned nanotubes even though directionality of ions is lost. On the other hand, ion energy and flux to the substrate affect the formation of catalyst nanoparticles, which eventually leads to either tip growth or bottom growth [11]. However, ion energy and flux seem to be much lower and less controllable at atmospheric pressure than those in the low-pressure regime. The formation of catalyst nanoparticles would have to be controlled mainly by a combination of catalyst metal and alloying materials in atmospheric-pressure PECVD. Another important issue is tensile/compressive stress that is created across the particle and tube interface [10]. For example, nickel parti-

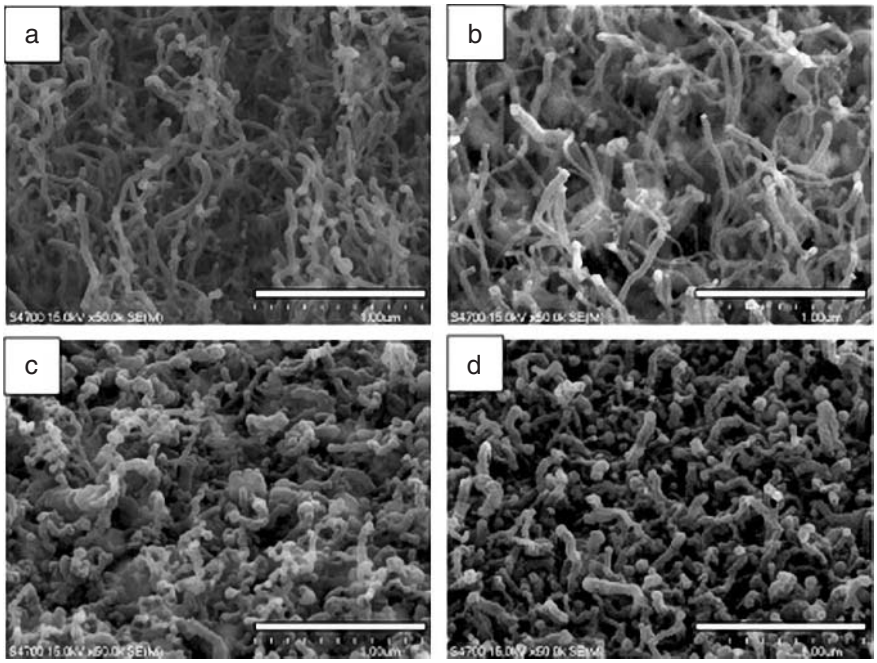

Figure 6 SEM pictures: (a) and (b) positive-pulsed APG and (c) and (d) negative-pulsed APG. Frequency: 125 kHz, growth temperature: 700 °C, $He:H_2:CH_4 = 900:100:10$ sccm.

cles in Fig. 2 show severe coagulation. Those nanoparticles might produce nonuniform tensile/compressed stress at the interface, and then lead to random orientation if the directional field strength is not high enough. On the other hand, nickel nanoparticles seem to heavily coagulate in negative-pulsed APG. Two to five nanotubes stick together during the growing process. Figure 6 (c) shows that each nanotube consists of a number of segments. This fact means that these types of nanotubes would coexist when a sine voltage is applied. It is interesting to note that the Raman spectra shown in Fig. 7 does not show specific differences although morphology of the nanotubes is quite unique. The existence of the G-band peak, which indicates a well-graphitized structure, is essential; however, a higher G-band peak does not necessary mean that the quality of nanotubes is better. Reference [5] compares the intensity ratio of the Dand G bands to characterize the general quality of nanotubes. An extremely high temperature, such as 1000 °C, is likely to result in a small D/G ratio, but the general tendency between D/G ratio and deposition parameters is not clear because D-band attributes to the defect of nanotube structure and amorphous carbon junk as well. The same is true for Fig. 7. Four spectra clearly show the G-band, but the D/G ratio is almost constant. The presence of the G-band does not promise high-quality nanotubes.

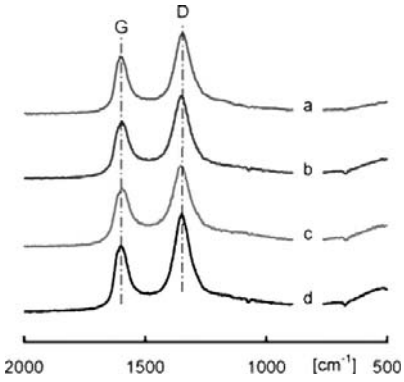

Figure 7 Raman spectra. Each curve corresponds to results presented in Figs. 6 (a)–(d).

35.4.2
Growth Temperature and Pulse Duty

Figure s 8 (a)–(d) show the effect of growth temperature and pulse duty. Figure 8 (c) shows that aligned nanotubes were obtained at higher growth temperature (750 °C) with positive-pulsed APG. Although nickel particles were recognized at lower temperatures (600 °C), nanotubes were not able to grow with this condition. The Raman spectrum did not show a clear G-band in this case. Figure 8 (d) was obtained at 750 °C and 2% pulse duty (10 kHz). Even though the growth temperature was high enough, nanotubes were mostly missing. Growth temperature affects reaction rate,

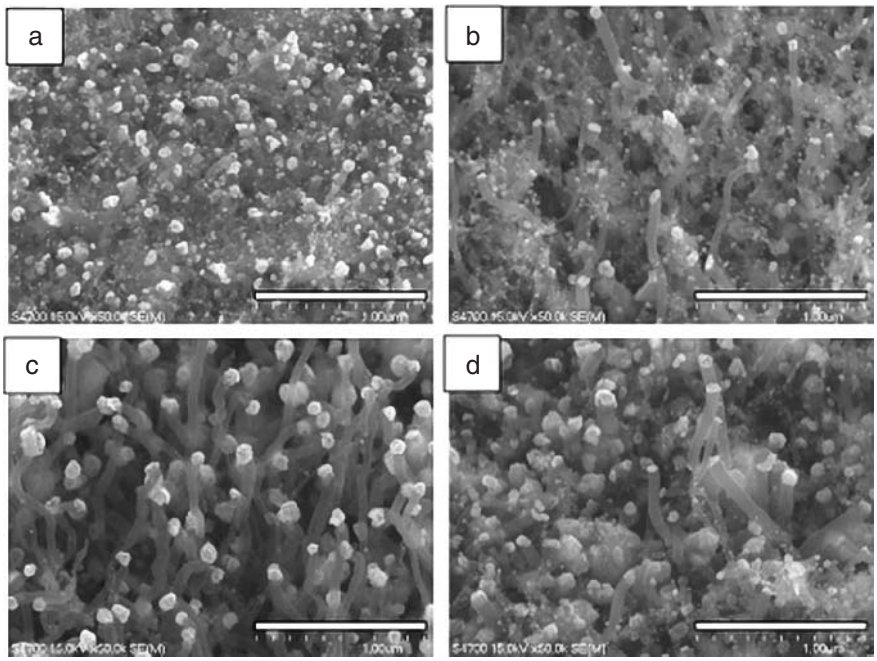

Figure 8 SEM pictures: (a) 600 °C–125 kHz, (b) 680 °C–125 kHz, (c) 750 °C–125 kHz, (d) 750 °C–10 kHz. Positive-pulsed APG, He:H_2:CH_4 = 900:100:10 sccm.

while pulse duty affects input power, respectively. However, even longer deposition time could not grow nanotubes. The existence of APG clearly promotes nanotube growth, and higher pulse duty (>25%) and higher growth temperature (>750 °C) is essential for better alignment.

35.5 Concluding Remarks and Future Work

The presence of APG obviously promotes nanotube growth. However, the quality of nanotubes such as diameter, number density, and orientation was hard to control with current APG that is operated in the 10–130-kHz frequency range. Although marginally aligned nanotubes were obtained with positive-pulsed APG, results were still unsatisfactory. One major problem is that APG is periodically generated with much lower duty cycle. In our experiment effective deposition occurred when the bottom electrode was the temporal cathode, however, the discharge current pulse was limited for 500 ns: effective deposition time was 1/16–1/200 of the process time. In addition, the polarity of voltage changes every half cycle when a sine voltage was applied. This situation minimized the alignment of nanotubes, and even resulted in a bead-shaped structure as shown in Fig. 6 (c). If APG is operated with

high frequency such as 13.56 MHz (> 1 MHz= $(2\times500\ \text{ns})^{-1}$), APG is continuously produced and nanotubes are able to grow in a quasistationary cathode region where a high electric field and high plasma (ions, electrons, and radicals) density is simultaneously maintained. Yuan and Raji [12] have performed computer simulations of radio-frequency atmospheric-pressure glow discharge in He. A high electric field is produced in the cathode region (4 kV/cm) while maintaining an electron density of 10^{10} to 10^{11} cm^{-3}. It is noteworthy that the maximum electron density would temporarily reach 10^{11} cm^{-3} in medium-frequency operated He-based APG [2], which is comparable to a low-pressure plasma source. This means that the plasma density in APG, on time average, is clearly lower than that of low-pressure plasmas. Nevertheless, deposition rates are almost of the same order: growth rate in low-pressure PECVD (mostly 13.56 MHz or DC) is 0.5–6 μm/min [7], whereas 0.2 μm/min was obtained in our experiment. One possible explanation for this is that mass transfer to the substrate is dominated by convection at atmospheric pressure. From the viewpoint of alignment and growth rate, combination of APG and high-frequency operation (> 1 MHz) is strongly desired for further improvement of APG-assisted chemical vapor deposition. Finally, some of the important aspects obtained in this experiment are listed below.

1. Nanotubes were deposited on both Ni/Si and Ni/quartz (SiO_2) substrate. However, nanotubes were mostly missing on Ni/Si substrate. Pretreatment of substrate such as ion bombardment or chemical etching seems to be necessary in Ni/Si substrate case.
2. Nanotubes were easily deposited on Ni/SiO_2 substrate. However nickel grains tended to coagulate, and nanotube diameter was widely distributed.
3. Acetylene was not suitable for atmospheric-pressure glow-plasma processing. Excess carbon deposited graphite spots that eventually induced filamentary discharges. The gas-phase reaction in atmospheric-pressure plasma is substantially different from those in a low-pressure plasma environment. Production of higher-order hydrocarbons including radical species in gas phase tends to deposit excess graphite.
4. Marginally aligned nanotubes were obtained with positive-pulsed voltage where an intense cathode region is produced near substrate. On the other hand, nanotubes became thicker and shorter with negative-pulsed voltage. In the case of a sine voltage, both types of nanotubes would be deposited. In addition to the lack of DC component of electric field, this is another possibility why nanotubes are randomly oriented with a sine voltage in medium-frequency-operated APG.
5. In addition to growth temperature, high-frequency (or high duty cycle) operation is essential for better alignment.
6. Coagulation of nickel particles might produce nonuniform tensile/compressive stress across the catalyst particle and nanotube interface, leading to randomly oriented nanotubes under the lack of directional electric field near substrate. Alignment could be improved if coagulation of catalyst particles is minimized.

7. The presence of a directional electric field is primarily important in order to align nanotubes, while directional etching of ions is less important. Although ion energy and flux seem to affect growth mechanism, it is difficult to control at atmospheric pressure due to high collision frequency between ions and molecules. The formation of nanoparticles, which eventually determines the growth mechanism, would have to be controlled mainly by the combination of catalyst metal and alloying materials in atmospheric-pressure PECVD.

Acknowledgements

This work was partly granted by the Venture Business Laboratory (VBL) of Tokyo Institute of Technology. The authors would like to thank Prof. Naoto Ohtake and Mr. Tomoya Goto (Tokyo Institute of Technology) for supporting this project. The authors also would like to thank Prof. Joachim Heberlein, Prof. Uwe Kortshagen, and Mr. Lorenzo Mangolini (University of Minnesota) for intensive discussion.

References

[1] A Schutze, J Y Jeong, S E Babayan, J Park, G S Selwyn, and R F Hicks, The atmospheric-pressure plasma jet: A review and comparison to other plasma sources, IEEE Trans. Plasma Sci, **26**(6) (1998) 1685–1694.

[2] F Massines, P Segur, N Gherardi, C Khamphan, A Ricard, Physics and chemistry in a glow dielectric barrier discharge at atmospheric pressure: diagnostics and modeling, Surf. Coat. Technol. **174–175** (2003) 8–14.

[3] N Gherardi, S martin, F Massines, A new approach to SiO_2 deposit using a N_2-SiH_4-N_2O glow dielectric barrier-controlled discharge at atmospheric pressure glow discharge, J. Phys. D: Appl. Phys., **33** (2000) L104–L108.

[4] T Nozaki, Y Kimura, K Okazaki, 16th ESCAMPIG and 5th ICRP Joint Conference, Grenoble France, July 14–18, **1** (2002) 37–38.

[5] T Nozaki, Y Kimura, K Okazaki, J. Phys. D; Appl. Phys., **35** (2002) 2279–2784.

[6] K Otsuka, S Kobayashi, S Takenaka, Catalytic decomposition of light alkanes, alkenes and acetylene over Ni/SiO_2, Appl. Catal. A: General **201** (2001) 371–379.

[7] M Meyyappan, L Delzeit, A Cassell, D Hash, Carbon nanotube growth by PECVD: a review, Plasma Sources Sci. Technol., **12** (2003) 205–216.

[8] A M Cassell, S Verma, L Delzeit, M. Meyyappan, J Han, Combinatorial Optimization of Heterogeneous Catalysts Used in the Growth of Carbon Nanotubes, Langmuir **17** (2001) 260–264.

[9] T Nozaki, Y Unno, K Okazaki, Plasma Sources Sci. Technol., **11** (2002) 431–438.

[10] V I Merkulov, A V Melechko, M A Guillorn, D H Lowndes, and M L Simpson, Alignment mechanism of carbon nanofibers produced by plasma-enhanced chemical-vapor deposition, Appl. Phys. Lett. **79**(18) (2001) 2970–2972

[11] L Delzeit, I McAninch, B A Cruden, D Hash, B Chen, J Han, M Meyyappan, Growth of multi wall carbon nanotubes in an inductively coupled plasma reactor, J. Appl. Phys. **91** (2002) 6027–6033

[12] X Yuan and L L Raja, Computational study of capacitively coupled high-pressure glow discharges in helium, IEEE Trans. Plasma Science, **31**(4) (2003) 495–503.

36
Investigation of Excited Species in a Carbon Ablation Plume in Nitrogen Gas Environment

M.A. Bratescu, Y. Sakai, N. Sakura, D. Yamaoka, Y. Suda and H. Sugawara

Abstract

In this work, we investigated a carbon-plasma plume produced by laser ablation of a graphite target in a nitrogen gas environment. The number densities of excited carbon and excited nitrogen atoms were measured using laser absorption spectroscopy. The composition of the carbon ablation plume was determined using optical-emission spectroscopy. The presence of a Si substrate perturbed the evolution and the density of various fractional species of C, N, C_2 and CN in the carbon ablation plume. XPS analysis explained the film properties in connection with the spatial distribution and the mean velocities of the excited particles (C, N, C_2 and CN) in the expanding plasma.

36.1
Introduction

A laser-ablation method for thin-film deposition offers many advantages compared with traditional deposition techniques, due to the possibility of controlling the impurities and of deposition of highly refractory elements as well as different compounds with superior properties than those produced by chemical reaction.

In the last decade, interest in carbon nitrides was increased because this crystalline phase exhibits an interesting property like hardness combined with high elasticity [1]. Understanding of the mechanism of CN_x film formation could improve the film quality. The film property depends on the laser-induced plasma parameters, i.e. velocity, temperature, number density of the ablated species in the plume and chemical composition, and could be controlled if we measure these data. The quality of the CN_x film is determined by the type of bonding between nitrogen and carbon atoms, which depends on the composed species and their dynamics in the plume [2, 3].

In this paper, the number densities of excited carbon and excited nitrogen atoms were measured by laser-absorption spectroscopy. The composition of the carbon ablation plume was observed by optical-emission spectroscopy. In the presence of a Si substrate introduced in the carbon ablation plume, an increase of the nitrogen number density was observed.

From XPS analysis of the film deposited on the Si substrate, the film properties could be understood in connection with the spatial distribution and the mean velocities of the excited particles (C, N, C_2 and CN) in the expanding plasma.

36.2 Experimental Setup

Figure 1 (a) shows the experimental setup along with the arrangement of the laser beams from an excimer laser and a diode laser (DL) and Fig. 1 (b) shows the beam arrangement on a target. A pulsed-laser deposition (PLD) chamber is almost the same as the one given in Ref. [4]. An ArF excimer laser beam (Lambda Physik COMPex205) was focused onto a crystal graphite target at an incidence angle of 53°. The pulse duration of the laser was 20 ns and the fluence was adjustable in the range of $E = 2–4.7\ \mathrm{J/cm^2}$. In order to compare results the laser fluence was fixed to be about $E = 3.2\ \mathrm{J\ cm^{-2}}$.

A setup for the laser absorption diagnostics of the number densities of the excited atoms, $C(3^1P_1°)$ and $N(3^4P_{5/2})$ in a plume was realized with two distinct diode lasers (DL; Hitachi 8325G; 40 mW maximum output with the 830-nm central wavelength at 25 °C). The wavelengths were tuned to the resonance absorption of $C(3^1P_1^0 \rightarrow 3^1S_0)$ at $\lambda_0^C = 833.7$ nm and $N(3^4P_{5/2} \rightarrow 3^4P_{5/2}^0)$ at $\lambda_0^N = 821.859$ nm. To acquire the absorption signal of the excited atoms in the ablation plume we used a digital oscilloscope. The signal to noise ratio (S/N) of the absorption signals was about 10^2. This means that the minimum detectable change of the number density was $\sim 10^9\ \mathrm{cm^{-3}}$. The temporal absorption signal waveform detected by PD1 was simultaneously recorded together with the temporal light emission signal waveform of the excimer laser acquired by PD2. These waveforms offer information about the decay and the delay time (τ) of the absorption signal. The mean expansion velocity of the excited atom in the plume was calculated. The errors in the delay reading were ~ 1 ns.

The DL beam was set at different positions z from the target surface (see Fig. 1 (b)). The spatial resolution of the DL beam was about 0.1 mm. A boxcar integrator (Standford SRS250) that was connected with an oscilloscope in acquisition mode to record the data, accomplished integration of the temporal absorption signal of the excited carbon and the excited nitrogen atoms [4].

When the DL was scanned with a frequency of ~ 5 mHz over the resonance wavelength of the atomic transition, the time-integrated absorption signal was simultaneously recorded with the Fabry–Perot fringes with a 1.5-GHz free spectral range, in order to measure the linewidth of the absorption line ($\Delta\nu$).

The emission spectrum of the ablation plume was analyzed in a range between 300 and 800 nm using a Hamamatsu PMA-11 (Photodiode Multichannel Analyzer). The PMA-11 detector head was set in a (y, z) plane parallel with the (y, z) plane of the plume (Fig. 1 (b)). In PMA-11 the wavelength axis and the spectral-response characteristics have been calibrated in the measurement wavelength region. The measurement wavelength accuracy is ± 1 nm and the wavelength resolution is < 3 nm. The second order of the diffraction grating is already removed. The CCD image

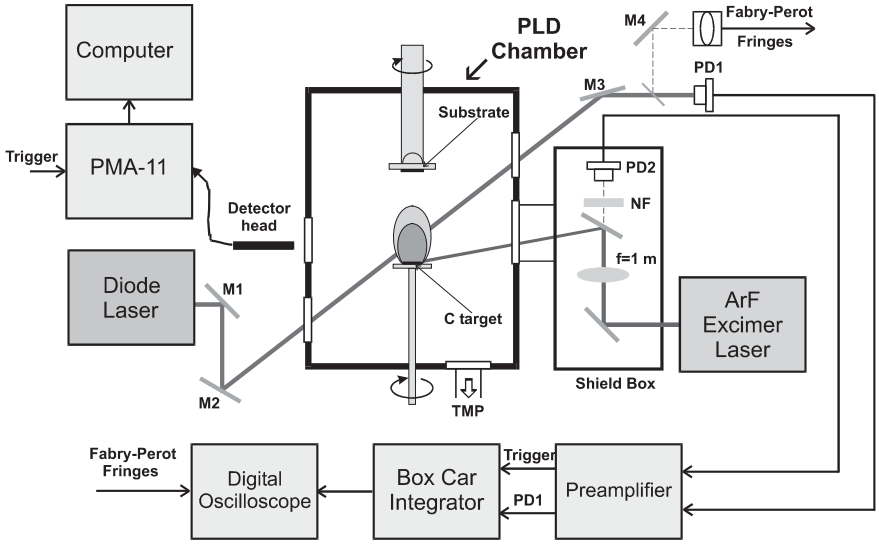

(a)

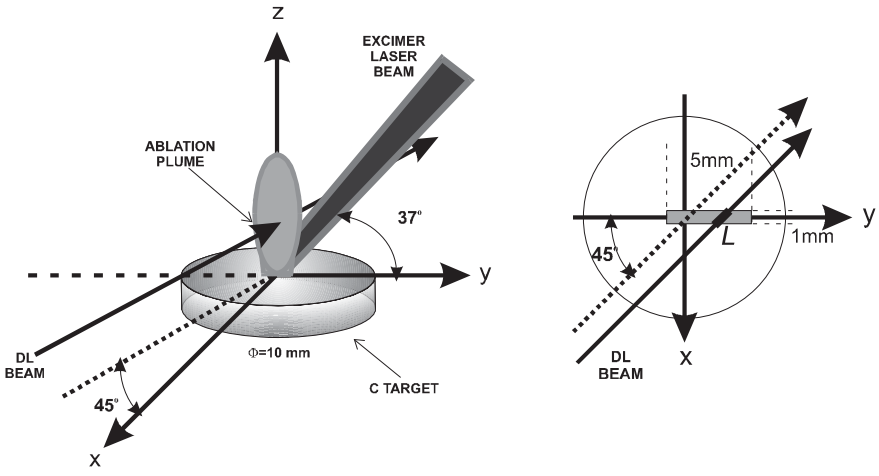

(b)

Figure 1 (a) Experimental setup for the carbon ablation plume diagnostics by laser-absorption spectroscopy and by emission spectroscopy. (b) the arrangement of the laser beams from the excimer laser and the diode laser on the carbon target.

sensor is a high-sensitivity sensor, which is cooled at 0 °C to assure a high signal to noise ratio.

An XPS study characterized the N and C bonds on the film surface.

The nitrogen pressure (p) was varied from 0.1 to 13 Torr, the absorption signals and the emission spectra were measured at the vertical distance (z) from the carbon

target surface from 0 to 25 mm. A Si(100) substrate was set in the plume at different z. Measurements were done with and without substrate.

36.3 Results and Discussion

From the amplitude of the absorption signals, the number density N_N of excited nitrogen on $3^4P_{5/2}$ level at 10.3 eV and the number density N_C of excited carbon on $3^1P_1^\circ$ level at 7.5 eV were calculated by the following relation [4]:

$$N = \frac{8\pi^2 g_1}{g_2} \frac{\Delta n \cdot \ln\left(\frac{I_0(0)}{I_0(L)}\right)}{\lambda_0^2 \cdot A_{21} \cdot L}, \tag{1}$$

where $I_0(L)$ and $I_0(0)$ are the DL intensity after passing through the plume and the incident DL intensity, respectively, at the wavelength of the resonance absorption, λ_0 (λ_0^C or λ_0^N). $g_{1,2}$ is the corresponding statistical weight of the excited level. A_{21} is the Einstein spontaneous emission coefficient. λ is the mean absorption length of the plasma plume (see Fig. 1(b)). $\Delta\nu$ is the absorption linewidth.

We measured the N_C and N_N in the carbon ablation plume as shown in Fig. 2. In the case of a Si(100) substrate being introduced at z= 6 or 8.2 mm, the N_N at z ~4 mm increases slightly and decreases considerably compared with the case of no substrate. This tendency does not depend on the substrate position in the ablation plume. The change of the number density of N_N in the ablation plume could be explained as the backscattering of the nitrogen atoms and as a possible secondary

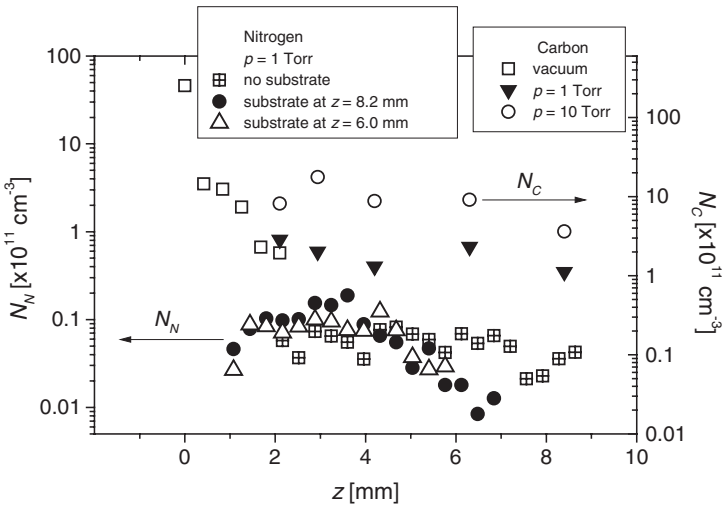

Figure 2 N_C and N_N dependence on z, $E = 3.2$ J cm^{-2} (in the case of carbon without substrate, in the case of nitrogen with and without substrate).

plume excitation at the substrate surface, which may indicate film sputtering, and consequently an increase of the excited nitrogen in this region [3]. A kinetic energy $\varepsilon \sim 12$ eV of C atoms in the ablation plume (as will be shown in the following) higher than the bond energy of the carbon atoms (~4 eV) may produce the displacement of the film surface deposited on the substrate with possible sputtering [3, 5].

Figure 3 shows the N_N as a function of the N_2 pressure p. The N_N increases with increasing p in the present measurement range. The maximum number density was $N_N = 7 \times 10^{10}$ cm^{-3} at $p = 13$ Torr and $z = 1.8$ mm. Figure 2 shows that N_C is $\sim 10^{12}$ cm^{-3} at $z = 1$ mm in vacuum, and decreases to $\sim 5 \times 10^{10}$ cm^{-3} at $p = 1$ Torr. In a $p = 10$ Torr nitrogen gas, N_C is $\sim 10^{11}$ cm^{-3} at $z = 2$ mm, which is higher than that at $p = 1$ Torr. The increase of N_C in nitrogen gas environment was observed as the C($3^1P_1°$) atom number density increased, and the C_2 molecule density increased, as measured by emission-spectroscopy measurements. This result may indicate that nitrogen promotes the production of carbon species [6]. The increase of N_C with p could be explained by the increase of the dissociation of C_2 molecules as a result of the enhancement of the collision with N_2 molecules [7]. Concerning the chemical interaction between a carbon target surface and N_2 molecules at the laser irradiation, it needs further study.

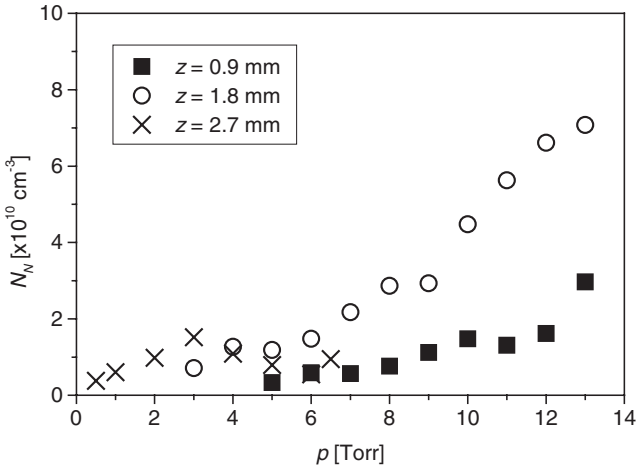

Figure 3 N_N dependence on p for different z and $E = 3.2$ J cm^{-2} (without substrate).

From the delay time of the absorption signal of the excited atom, relative to the temporal light emission signal of the excimer laser, the mean expansion velocity of C($3^1P_1°$) atom, v_C, and the mean expansion velocity of N($3^4P_{5/2}$) atom, v_N, were calculated as $v = z/\tau$. Figure 4 shows the delay time of the C($3^1P_1°$) atoms and the N($3^4P_{5/2}$) atoms in the plume at $p = 1$, 5 and 10 Torr with and without substrate.

Space and pressure dependences of the C($3^1P_1°$) and N($3^4P_{5/2}$) mean velocities could explain the expansion, collisions and chemical reactions between N and C atoms. In vacuum, the C($3^1P_1°$) mean expansion velocity was $\sim 4 \times 10^6$ cm s^{-1}, in the

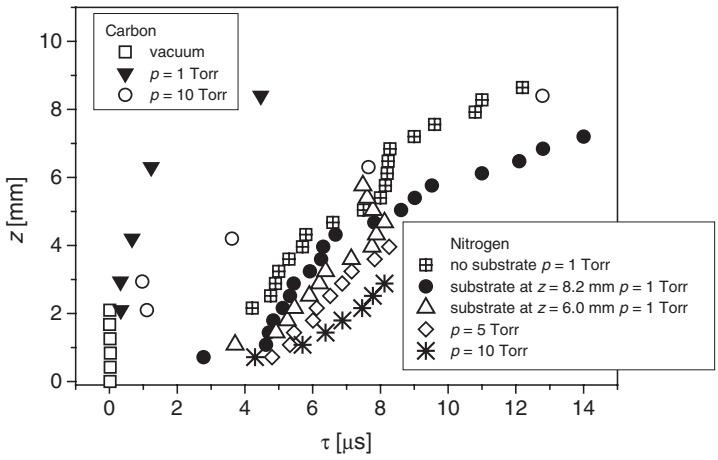

Figure 4 Evolution of $C(3^1P_1°)$ and $N(3^4P_{5/2})$ atoms in the ablation plume, for different pressures p and $E = 3.2\ J\ cm^{-2}$ (in the case of carbon without substrate, in the case of nitrogen with and without substrate).

region near the target surface, for $z < 2$ mm. This high value of v_C may be obtained because the carbon atoms with high initial energy were ablated from the target surface by energetic photons of 6.3 eV (ArF excimer laser) [3, 8]. The mean kinetic energy of the $C(3^1P_1°)$ atoms could be calculated as $\varepsilon = m_C v_C^2$, where m_C is the mass of the carbon atom. In the case of $v_C \sim 4 \times 10^6$ cm s^{-1}, the mean kinetic energy of the $C(3^1P_1°)$ atoms is $\varepsilon \sim 100$ eV. In a nitrogen atmosphere at $p = 1$ Torr, with plume expansion and collisions with N_2 molecules, v_C changed with z. In the region at $z < 2$ mm, v_C was $\sim 1.5 \times 10^6$ cm s^{-1} ($\varepsilon \sim 14$ eV) and at $z > 2$ mm v_C decreased to $\sim 5 \times 10^5$ cm s^{-1} ($\varepsilon \sim 2$ eV). v_C near the target surface decreases from $\sim 10^6$ cm s^{-1} at $p = 1$ Torr to $\sim 6 \times 10^4$ cm s^{-1} at $p = 10$ Torr.

The $N(3^4P_{5/2})$ mean expansion velocity near the target surface ($z < 6$ mm) was $\sim 10^5$ cm s^{-1} in $p = 1$ Torr nitrogen which is higher than $v_N \sim 4.6 \times 10^4$ cm s^{-1} at $z > 6$ mm. v_N depended on the pressure: at $z \sim 3$ mm, v_N decreased from 5×10^4 cm s^{-1} in $p = 1$ Torr to 3×10^4 cm s^{-1} in $p = 6$ Torr. Near the target surface, the ablated particles have high kinetic energies and collide with the buffer-gas molecules and atoms. Therefore $N(3^4P_{5/2})$ atoms have higher mean expansion velocity in this region than that in more distant regions.

v_N and v_C decreased with z due to plume expansion. Expansion of the laser-ablation plume could be described by a drag model. In the present case, this model could be valid for $N(3^4P_{5/2})$ at $p = 1$ Torr, after ablation ($\tau \sim 6\ \mu s$), for $z < 6$ mm. For $z \sim 4$–7 mm, the chemical reaction between N and C atoms occurs and this model may be no longer valid [2, 9].

When the substrate was set at $z = 6$ mm, the delay of the absorption signal of the $N(3^4P_{5/2})$ atom, relative to the excimer laser light was changed as can be seen in Fig. 4. In the vicinity of the substrate surface at $z \sim 5$–6 mm, τ decreased as z

increased. The backscattered and the released nitrogen atoms from the substrate surface may explain this behavior of τ and the slightly increased number density of the nitrogen atoms (see Fig. 2). If we examine the delay of the absorption signal of the $N(3^4P_{5/2})$ atom without substrate in p= 1 Torr we see that τ is almost constant at $z \sim 5$–7 mm. Here the chemical reaction between nitrogen and carbon species is possible to take place in the carbon ablation plume.

Figure 5 shows a typical emission spectrum from the plume. The CN radical molecular bands dominated the emission spectrum from the carbon ablation plume in nitrogen atmosphere. C_2 and N_2 molecules emission-band intensities were about five times lower than the CN emission bands intensities. The identification of the C_2 molecule emission bands has been done using the carbon ablation in vacuum [10]. The C_2 molecule emissions belonging to the Swan System at 473.71 nm and 516.52 nm are reported in a carbon ablation plume [2, 3]. As the C_2 molecule emission band intensities in vacuum were about eight times smaller than in nitrogen atmosphere, the present result confirms that nitrogen could promote generation of the carbon species. The identification of the N_2 first positive system at 750.39 nm have been done by comparing the emission spectrum of carbon ablation plume in N_2 gas environment and the emission spectrum of a RF discharge plasma in N_2 gas, as is described in detail in Ref. [6]. C_2 molecule emission bands in the red region have been identified by comparing the emission spectrum of the carbon ablation plume in vacuum and the emission spectrum of the carbon-ablation plume in a N_2 gas environment.

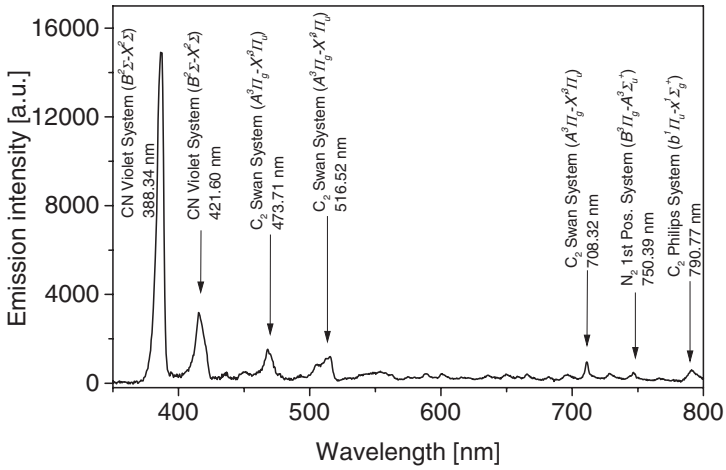

Figure 5 Typical emission spectrum from the ablation plume in p = 5 Torr nitrogen, E = 3.2 J cm^{-2}.

The highest density of the C_2 excited molecule on $d^3\Pi$ level at 3 eV was at $z \sim 5$ mm at pressures of p= 1–5 Torr. At $z \sim 5$ mm high density of the N_2 excited molecule on $B^3\Pi_g$ level at 8 eV and the CN radical on $B^2\Sigma$ at 3.2 eV were detected as shown in Fig. 6. The appearance of CN radical excited on $B^2\Sigma$ level may be explained

taking into account the dissociation channels of C_2 and N_2 molecules and CN radical [11]:

$$C_2(d^3\Pi_g) \rightarrow C(^3P) + C(^3P)$$
$$N_2(B^3\Pi_g) \rightarrow N(^4S^0) + N(^2D^0)$$
$$C(^3P) + N(^4S^0) \rightarrow CN(B^2\Sigma)$$
$$C(^3P) + N(^2D^0) \rightarrow CN(B^2\Sigma)$$

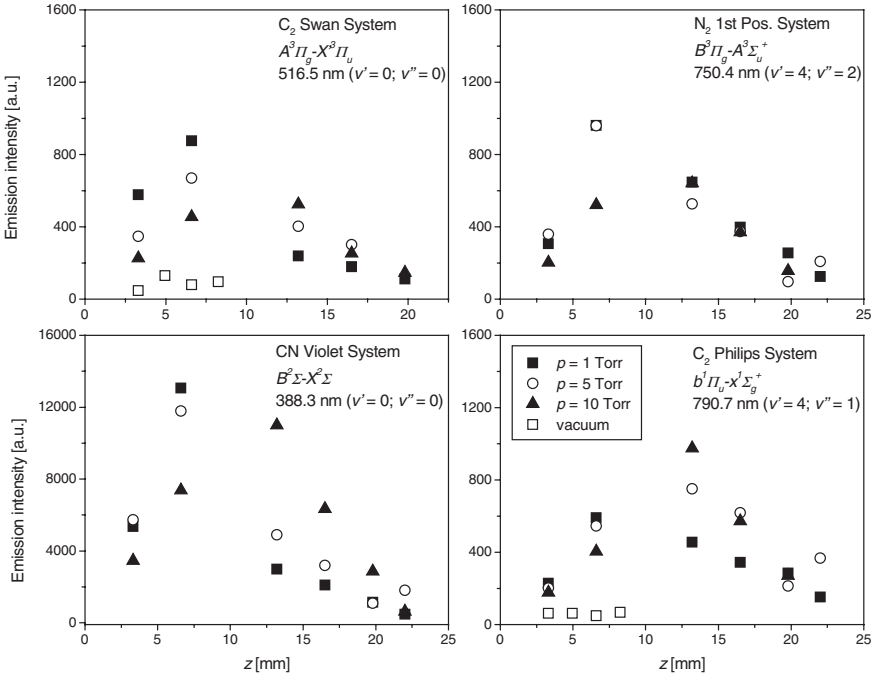

Figure 6 Emission intensities of C_2 molecule at 516.52 nm (Swan System) and at 790.77 nm (Phillips System), N_2 molecule at 750.39 nm (First Positive System) and CN radical at 388.34 nm (Violet System), for different pressures in the carbon ablation plume ($E = 3.2$ J cm^{-2}).

The C_2 molecular band at 790.77 nm (Phillips system) shown in Fig. 6, which corresponds to the electronic level $b^1\Pi_u$ at 1.04 eV, has the maximum emission intensity at z= 13 mm as explained by recombination of carbon atoms on excited electronic levels followed by de-excitation [12]. In the laser-absorption-spectroscopy measurements the maximum number density of the C($3^1P_1°$) and N($3^4P_{5/2}$) atoms was obtained at $z \sim 2$ mm where the electron density and the electron temperature were high. In the same PLD experiment the maximum measured electron density was $\sim 10^{17}$ cm^{-3} for $z < 2$ mm [4]. The intensities in the emission spectrum increased

as the excimer laser fluence increased because the electron energy increased with increasing E [4, 6].

The results of the XPS analysis of the film deposited on the Si(100) substrate in the present carbon ablation plume are presented in Table 1. The deconvolution of the XPS spectra of the films deposited in nitrogen atmosphere showed two main components: the first component at 284.1 eV (linewidth ~ 1.0 eV) corresponding to sp^2 hybridization of the carbon atoms (graphite) and the second component at 285.5 eV (linewidth ~ 1.1 eV) corresponding to sp^3 hybridization of the carbon atoms (diamond). A small intensity peak was also obtained by deconvolution of the XPS spectra, at 286.5 eV and corresponds to CO, which could be present on the film surface [13]. In Table 1 the content of sp^3C hybridization relative to the content of sp^2C hybridization is noted as A_{sp3}/A_{sp2}.

Table 1 XPS analysis of the CN film

p [Torr]	z [mm]	A_{sp3}/A_{sp2}
1	6	0.046
1	10	1.439
1	15	0.512
10^{-8}	6	0.715
10	6	1.814

For p= 10 Torr and the substrate position at z ~ 6 mm, a high density of C_2 molecules and CN radicals were detected in the carbon ablation plume (see Fig. 6). In these experimental conditions the highest content of sp^3C hybridization relative to sp^2C hybridization content was detected in the deposited film. In vacuum, the sp^3C content relative to sp^2C content can be compared with the composition in the film obtained in p= 1 Torr nitrogen and z= 15 mm, but the substrate should be placed close to the target surface at z= 6 mm.

36.4 Conclusions

Optical methods, i.e. emission and laser absorption spectroscopy, are powerful tools for diagnostics of physical and chemical processes of radicals in process plasmas for deposition. As far as we know, there are no reports of measuring carbon or nitrogen number densities in carbon ablation plumes.

The nitrogen as an environment gas promoted generation of $C(3^1P_1°)$ atoms and C_2 molecules in the ArF laser-ablation plume.

The high content of sp^3C on a Si substrate set in the ablation plume at 6 mm from the target surface in a 10-Torr nitrogen pressure was obtained, since high molecular (C_2, N_2, CN) densities were present in this region. Close to the target surface, at z ~ 2 mm, the electron density was high, and the maximum values of the nitrogen

and carbon atoms number density were obtained. The main processes in the ablation plume were considered to be dissociation of N_2 molecule and the excitation of carbon and nitrogen atoms and molecules. In the region of z between 4 and 7 mm, it was presumed that the chemical reaction between N and C atoms occurred.

Acknowledgement

This work was supported in part by a Grant-in-Aid for Scientific Research (C) of JSPS No. 70312379.

References

[1] H. Sjostrom, S. Stafstrom, M. Boman, and J.-E. Sundgren, Phys. Rev. Lett., **75** (1995) 1336–1339

[2] S. Acquaviva, and M. L. De Giorgi, J. Phys.B: At. Mol. Opt. Phys., **35** (2002) 795–806

[3] A. A. Voevodin, J.G. Jones, J. S. Zabinski, and L. Hultman, J. Appl. Phys., **92** (2002) 724–735

[4] M.-A. Bratescu, Y. Sakai, D. Yamaoka, Y. Suda, and H. Sugawara, Appl. Surf. Sci., **197** (2002) 257–262

[5] P. Sigmund, Phys. Rev., **184** (1969) 383–416

[6] M.A. Bratescu, N. Sakura, D. Yamaoka, Y. Sakai, H. Sugawara, and Y. Suda, Appl. Phys. A (to be published)

[7] C. Vivien, J. Hermann, A. Perrone, C. Boulmer-Leborgne, and A. Luches, J. Phys. D: Appl. Phys., **31** (1998) 1263–1272

[8] A.A. Voevodin, J.G. Jones, J.S. Zabinski, Zs. Czigany and L. Hultman, J. Appl. Phys., **92** (2002) 4980–4988

[9] D.B. Geohegan, *"Pulsed Laser Deposition of Thin Films"*, eds D.B. Chrisey, G.K. Hubler, John Wiley & Sons, Inc., (1994) p.148

[10] R.W.B. Pearse, and A.G. Gaydon, *"The Identification of Molecular Spectra"*, Chapman and Hall, Fourth Edition (1975)

[11] A.A. Radzig, B.M. Smirnov, *Reference Data on Atoms, Molecules, and Ions*, Springer Verlag (1985)

[12] S.S. Harilal, R.C. Issac, C.V. Bindhu, V.P.N. Nampori, C.P.G. Vallabhan, J. Appl. Phys., **81** (1997) 3637–3643

[13] P. Merel, M. Tabbal, M. Chaker, S. Moisa, J. Margot, Appl. Surf. Sci., **136** (1998) 105–110

37
Optimization of a DC-RF Hybrid Plasma Flow System Using Statistical Analysis

Kohtaro Kawajiri, Kandasamy Ramachandran and Hideya Nishiyama

Abstract

A DC-RF hybrid plasma flow system has a complex flow structure because of the strong interaction between an RF-ICP flow and a DC plasma jet. Operating conditions of a DC-RF hybrid plasma flow system are effectively optimized by using a statistical analysis. When the central-gas ratio is low and the swirl-gas ratio is high, a DC-RF hybrid plasma flow is produced easily and becomes stable. Nitrogen should be injected with the central gas, and its limit of injection flow rate can be increased by decreasing the central-gas ratio and increasing the swirl-gas ratio. Plasma flame becomes long with decreasing the central-gas ratio and the swirl-gas ratio. The radial distribution of the downstream-gas temperature becomes uniform by increasing the swirl-gas ratio. Regression relations are obtained for different output parameters from the experimental results. Analyzed results confirm the controllability of a DC-RF hybrid plasma flow system and the necessity of flow control.

37.1
Introduction

A radio-frequency inductively coupled plasma (RF-ICP) flow has many advantages such as large plasma volume, low gas velocity and its purity. Then, an RF-ICP flow has been investigated intensively [1–3], and used for material processing such as spraying and fine-particle synthesis [4–6]. However, an RF-ICP flow is very sensitive to the flow conditions or a mixed reactive gas and becomes unstable easily. Then, a DC-RF hybrid plasma flow has been expected to overcome these disadvantages of an RF-ICP flow. It is composed of an RF-ICP flow and a direct current (DC) plasma jet as a supplement to an RF-ICP flow. In a DC-RF hybrid plasma flow system, a DC plasma jet is used to easily produce and keep a stable RF-ICP flow. Its applications have been investigated by Yoshida et al. [7–10] intensively so far. In our previous paper [11], we clarified the thermofluid characteristics of a DC-RF hybrid plasma flow experimentally. A low electric power and high-efficiency DC-RF hybrid plasma process like a chemical process, for example, has been required by industrious fields recently. Therefore, more precise flow control is needed to produce a DC-RF hybrid

plasma flow under an optimized operating condition according to the industrial applications.

The statistical method [12–16] is newly introduced to clarify the plasma characteristics, because this method is very useful to analyze such complex relations between many input and output parameters. The following two parameters, central-gas-flow ratio and swirl-gas ratio, are adopted as inputs, because these are important parameters to clarify the effects of the flow conditions on plasma characteristics in this system. We also adopt the following six parameters, particle residence time in the plasma-core region, appearance and disappearance voltages of an RF-ICP flow, upper limits of the injected nitrogen gas flow rate when nitrogen is mixed with the central gas or with the swirl gas and downstream-gas temperature at the central region, as outputs to evaluate the plasma characteristics, respectively.

Particle residence time is one of the most important parameters for material processing to evaluate heat transfer from a DC-RF hybrid plasma flow to particles. Appearance and disappearance voltages of an RF-ICP flow show how easy it is to produce an RF-ICP flow and how much an RF-ICP flow is stabilized in the DC-RF hybrid plasma flow system, respectively. The upper limit of injected nitrogen gas flow rate shows how much reactive gas can be injected without disturbing a DC-RF hybrid plasma flow. Downstream-gas temperature is also one of the most important parameters for material processing to show how much plasma is elongated to the downstream region.

In the present study, the effects of the inputs and their mutual interactions on the outputs are clarified statistically for the each output parameter. Furthermore, statistical equations, which show the relationship between the input parameters and the output parameters, are obtained by regression analysis. Finally, the operating condition is optimized comprehensively from all obtained results to produce the high qualitative DC-RF hybrid plasma flow.

37.2
Experimental Apparatus and Procedures

Figure 1 shows the schematic illustration of a DC-RF hybrid plasma flow system. It mainly consists of a power supply, a DC-RF hybrid plasma torch, a measuring section with window, an exhaust system and a measuring system with a Nd:YAG laser and a ICCD camera.

Figure 2 shows the schematic illustration of a DC-RF hybrid plasma torch and a gas-injection system. The DC-RF hybrid plasma torch consists of a 3-turn RF induction coil, a water-cooled quartz tube of 44 mm inside diameter, and DC electrodes mounted on the torch head. There are three modes of gas injections to control the plasma-flow characteristics. The sheath gas is the most fundamental gas to produce an RF plasma flow. The central gas, which is discharged to produce a DC plasma jet, is injected through the nozzle of the DC plasma torch of diameter 2mm. The swirl gas is injected to make the sheath gas swirl. Nitrogen gas is used to evaluate a plasma tolerance to a reactive gas. Nitrogen is mixed with the central gas or the

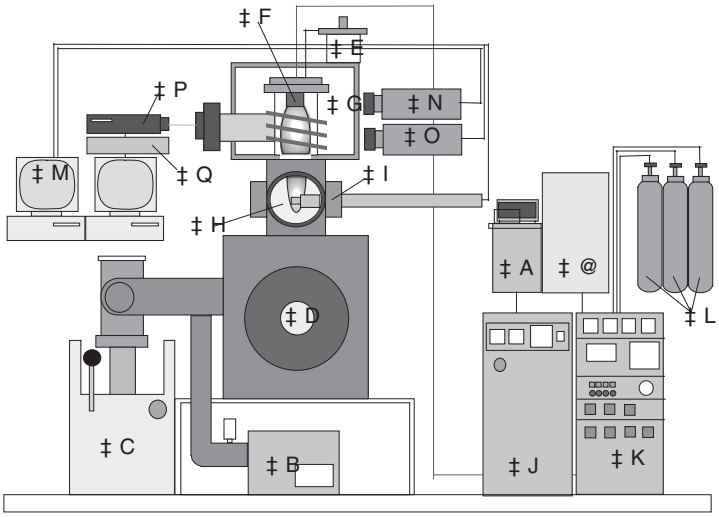

‡ @ Power supply for RF plasma torch
‡ A Power supply for DC plasma torch
‡ B Rotary pump 1
‡ C Rotary pump 2
‡ D Reaction chamber
‡ E Powder feeder
‡ F DC plasma torch
‡ G RF plasma torch
‡ H Window
‡ I Measuring port
‡ J Control panel for DC plasma torch
‡ K Control panel for RF plasma torch
‡ L Compressed gas cyclider
‡ M Monitoring system
‡ N ICCD camera
‡ O Spectroscope
‡ P Nd : YAG Laser
‡ Q Laser pulse synchronizer

Figure 1 Schematic illustration of a DC-RF hybrid plasma system.

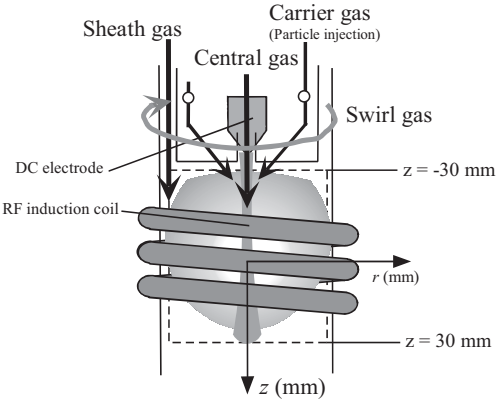

Figure 2 Schematic illustration of a DC-RF hybrid plasma torch and a gas-injection system.

sheath gas selectively, and is injected into the plasma torch. Alumina particles of 10■ ■ ■ diameter, which are injected diagonally into the centerline region with argon carrier gas of 0.5 l/min, are used as a tracer for a particle image velocimetry (PIV) system [11].

Figure 3 shows the particle trajectory in the core region measured by the PIV system. Particle residence time t_R in the centerline (r= 0 mm, z= 0 to 80 mm) is obtained from the particle velocity as shown in Fig. 4. Appearance and disappearance voltages are measured from the plate voltage of the RF induction coil at a moment when an RF-ICP flow is produced and extinguished in a DC-RF hybrid plasma flow. The upper limits of an injected nitrogen flow rate are measured when an RF-ICP flow is extinguished in a DC-RF hybrid plasma flow with nitrogen injection. The downstream-gas temperature (z= 163 mm) is measured by W-Re thermocouples.

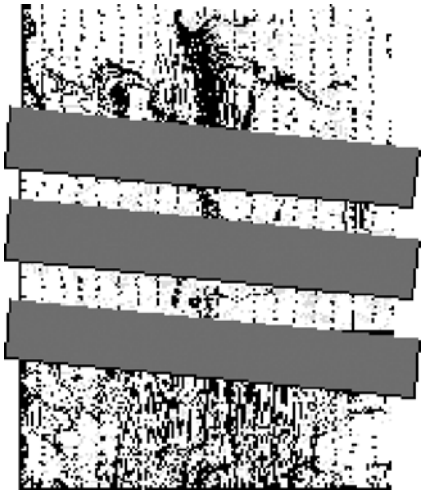

Figure 3 Particle trajectory in the core region.

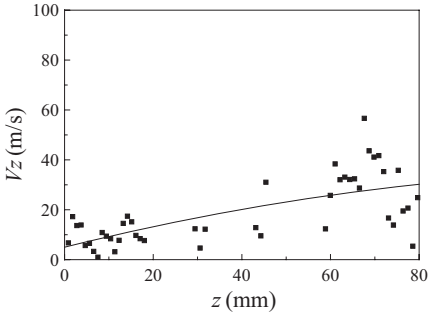

Figure 4 Particle velocity in the centerline.

Operating conditions are as follows. RF power is 5.5 kW at 4 MHz oscillator frequency. DC power is 1 kW and gas is argon or mixture of Ar/N_2. Total gas flow rate is fixed at 20 l/min to keep the constant operating pressure at 9000 Pa. R_C and R_{Sw}, whose values are adopted at four levels (20%, 30%, 40%, 50%), mean the ratio of the central gas flow rate and that of the swirl-gas-flow rate to the total gas flow rate, respectively.

37.3 Results and Discussion

37.3.1 Particle Residence Time

Tables 1 (a) and (b) show the particle residence time t_R (s) in the coil region for each operating condition and the analysis of variance (ANOVA) for t_R, respectively; where subscripts λ, q and c indicate linear, quadratic and cubic in Chebyshev's orthogonal polynomial respectively. The asterisk indicates the interaction and f means the degrees of freedom. S and V mean sum of squares of a effect of R and a variance obtained by dividing a mean sum of squares of source R by its f, respectively. $F0$ is the variance ratio of the source to that of error e. F means F-possibility that is signifi-

Table 1 (a) Particle residence time in the coil region for each operating condition, (b) ANOVA for particle residence time

t_R (s)		R_{Sw}(%)			
		20	**30**	**40**	**50**
R_C	20	0.0051262 (s)	0.005539	0.008196	0.009051
(%)	30	0.00544209	0.003375	0.006948	0.006168
	40	0.00323313	0.003716	0.003257	0.003865
	50	0.00282027	0.002489	0.003365	0.002982

	f	*S*	*V*	*F0*	*F*	*F0′*	*F′*	*ρ*(%)
R_{Cl}	1	0.00004009	0.00004009	65.71285	0.00003970	52.43442	0.00001027	66.15307
R_{Cq}	1	0.00000079	0.00000079	1.301033	0.28701838			
R_{Cc}	1	0.00000067	0.00000067	1.099675	0.32498226			
R_{Swl}	1	0.00000660	0.00000660	10.81962	0.01103325	8.633326	0.01241222	10.8921
R_{Swq}	1	0.00000020	0.00000020	0.332745	0.57991208			
R_{Swc}	1	0.00000263	0.00000263	4.305411	0.07167576			
$R_{Cl} * R_{Swl}$	1	0.00000474	0.00000474	7.763208	0.02369485	6.194517	0.02849062	7.815215
e	8	0.00000488	0.00000061					
T	15	0.00006060	0.00005633					100
(e)	12	0.00000917	0.00000076		0.00000076			15.13961

cant and underlined when this value is less than 0.05 and this value shows a possibility of which case happens accidentally. Furthermore, $F0'$ and F' mean modified $F0$ and F, respectively by adding insignificant f and V values to e's one, which is shown in (e) column. ρ shows a strength of a source influence on obtained results. Particle residence time is increased by decreasing the central-gas ratio but increasing the swirl-gas ratio. The effect of the central gas on the particle residence time is much larger than that of the swirl gas. This is physically reasonable because particles in the centerline region can be mainly accelerated by the central-gas momen-

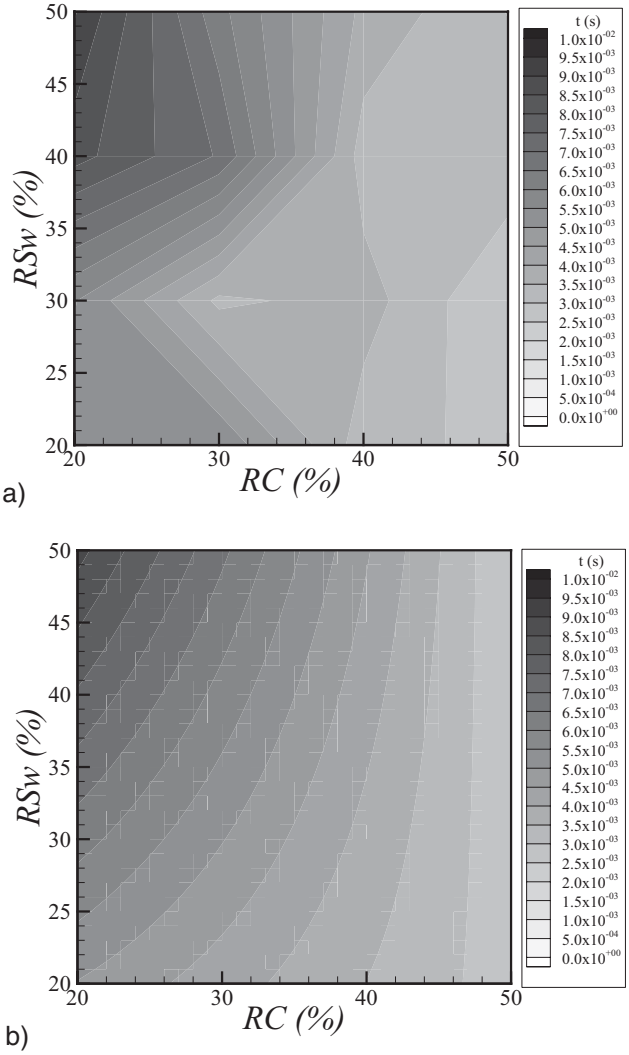

Figure 5 (a) Contour map of t_R obtained by the experiment. (b) Contour map of t_R obtained by Eq. (1).

tum. The error's effect is somewhat large owing to the large effect of R_{Swc} on t_R, which is neglected and added to the effect of error because the F value of R_{Swc} is more than 0.05. Then, the following equation is obtained by regression analysis.

$$t_R = 4.72 \times 10^{-3} - 1.42 \times 10^{-4}(R_C - 35) + 5.74 \times 10^{-5}\,(R_{Sw} - 35) - 4.35 \times 10^{-6}\,(R_C - 35)(R_{Sw} - 35) \quad (1)$$

Figure s 5 (a) and (b) show the contour map of t_R obtained by the experiment and that obtained by Eq. (1), respectively. As compared with Fig. 5 (a), Fig. 5 (b) shows the different tendency when R_{Sw} is 30%. This is because t_R is not calculated accurately by Eq. (1) owing to the large effect of the neglected sources, particularly R_{Swc}. From these results, the central-gas ratio should be controlled at first and be kept lower, but the swirl-gas ratio should be kept higher to increase the particle residence time in the plasma-core region.

37.3.2 Appearance and Disappearance Voltages

Tables 2 (a) and (b) show the appearance voltage V_A (kV) for each operating condition and its ANOVA, respectively. The appearance voltage is decreased by decreasing the central-gas-flow ratio but increasing the swirl-gas ratio. The effect of the central-gas ratio on appearance voltage is rather larger than that of the swirl-gas ratio. This arises from the following reasons: Electron density in the skin region near the side wall in the RF coil, which plays an important role to produce an RF-ICP flow, is effectively increased by decreasing the central-gas ratio. Because the net effect of the specific enthalpy of a DC plasma jet is mainly increased to produce many electrons by decreasing the central-gas ratio. In addition, an increase in the swirl-gas ratio enhances the active electron diffusion from the centerline region of a DC plasma jet to the skin region near the side wall in the RF coil by the centrifugal force of the swirl gas [11, 14]. The following equation is obtained by regression analysis.

$$V_A = 4.34 + 3.83 \times 10^{-2}\,(R_C - 35) - 3.13 \times 10^{-2}\,(R_{Sw} - 35) + 8.50 \times 10^{-4}\,(R_C - 35)(R_{Sw} - 35) \quad (2)$$

Table 2 (a) Appearance voltage for each operating condition, (b) ANOVA for appearance voltage

t_R (s)		R_{Sw}(%)			
		20	**30**	**40**	**50**
R_C	20	4.5 (kV)	3.8	3.5	3.1
(%)	30	4.8	4.2	4.1	3.8
	40	5.1	4.6	4.3	4.1
	50	5.1	5.1	4.7	4.7

Table 2 Continued

	f	*S*	*V*	*F0*	*F*	*F0′*	*F′*	ρ(%)
R_{Cl}	1	2.926125	2.926125	203.5565	0.00000057	176.0075	0.00000002	55.63636
R_{Cq}	1	0.015625	0.015625	1.086957	0.32762515			
R_{Cc}	1	0.015125	0.015125	1.052174	0.33501999			
R_{Swl}	1	1.953125	1.953125	135.8696	0.00000267	117.4812	0.00000015	37.13607
R_{Swq}	1	0.050625	0.050625	3.521739	0.09740910			
R_{Swc}	1	0.003125	0.003125	0.217391	0.65346725			
$R_{Cl} * R_{Swl}$	1	0.180625	0.180625	12.56522	0.00756725	10.86466	0.00638603	3.434343
e	8	0.115	0.014375					
T	15	5.259375	5.15875					100
(e)	12	0.1995	0.016625		0.01662500			3.793226

Figure s 6 (a) and (b) show the contour map of V_A obtained by the experiment and that obtained by Eq. (2), respectively. The output parameter V_A is approximated accurately by Eq. (2), because the error's effect on the results in Table 2 (b) is small.

Tables 3 (a) and (b) show the disappearance voltage V_D (kV) for each operating condition and its ANOVA, respectively. These two tables show the same tendency as that in Tables 2 (a) and (b). However, compared with the values in Table 2 (a), the values in Table 3 (a) are rather small overall. Then, it needs much power to produce an RF-ICP flow in a DC-RF hybrid plasma flow system than to maintain a stable RF-ICP flow in it. The disappearance voltage of an RF-ICP flow is decreased by decreasing the central gas, and the effect of the central-gas ratio on disappearance voltage is rather larger than that of the swirl-gas ratio. This comes from the following two reasons: The first is that the axial gas velocity is increased by the central gas effectively. Therefore, the electrical density in the skin region near the side wall in the RF coil, which plays an important role to enhance an RF-ICP flow, is decreased by increasing the central-gas ratio owing to the strong thermal convection to the downstream region. The second reason is that the net effect of the specific enthalpy of a DC plasma jet increases with decreasing central-gas ratio, and then the electron density in the skin region near the side wall in the RF coil increases. Disappearance voltage of an RF-ICP flow is also decreased by increasing the swirl-gas ratio. An RF-ICP flow is stabilized by an increase in the swirl-gas ratio. Because the interaction between a DC plasma jet in the centerline region and an RF-ICP flow in the skin region near the side wall in the RF coil is suppressed by centrifugal force of the swirl gas [11]. From the results in Tables 3 (a) and (b), the following equation is obtained by regression analysis.

$$V_D = 3.81 + 1.88 \times 10^{-2} (R_C - 35) - 1.43 \times 10^{-2} (R_{Sw} - 35) \quad (3)$$

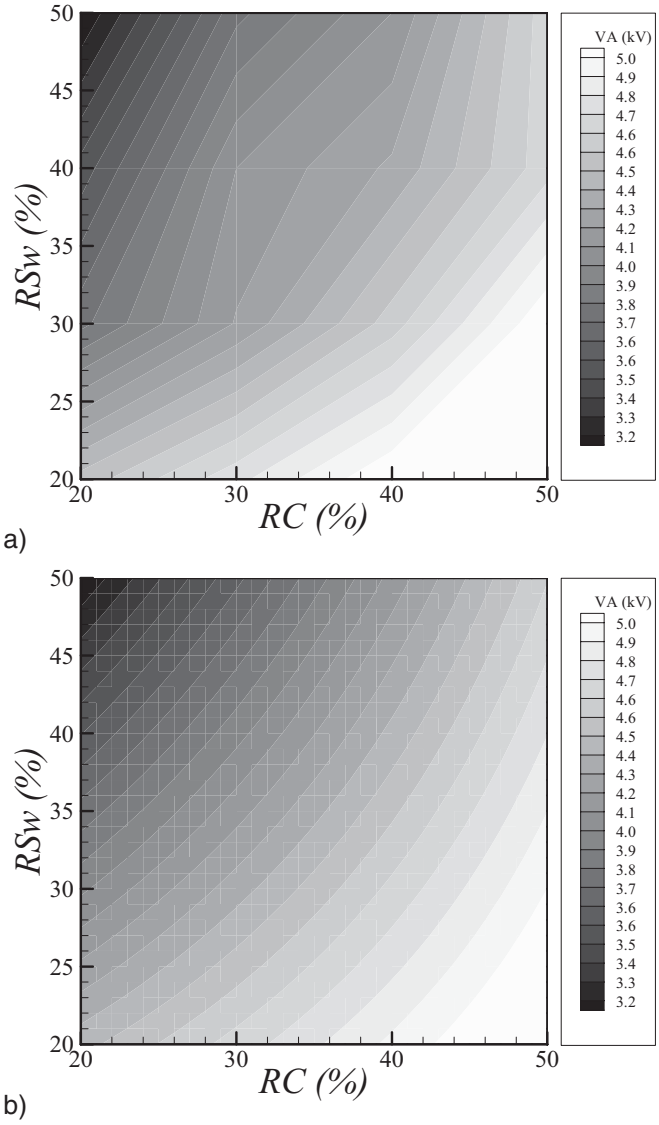

Figure 6 (a) Contour map of V_A obtained by the experiment. (b) Contour map of V_A obtained by Eq. (2).

Table 3 (a) Disappearance voltage for each operating condition, (b) ANOVA for disappearance voltage

t_R (s)		R_{Sw}(%)			
		20	**30**	**40**	**50**
R_C	20	3.8 (kV)	3.5	3.5	3.1
(%)	30	3.9	3.8	3.8	3.6
	40	4.2	3.9	3.8	3.8
	50	4.2	4.2	4	3.8

	f	***S***	***V***	***F0***	***F***	***F0′***	***F′***	ρ**(%)**
R_{Cl}	1	0.703125	0.703125	63.63122	0.00004459	65.23194	0.000000201	56.27814
R_{Cq}	1	0.030625	0.030625	2.771493	0.13452271			
R_{Cc}	1	0.003125	0.003125	0.282805	0.60931424			
R_{Swl}	1	0.406125	0.406125	36.75339	0.00030172	37.67797	0.00003554	32.50625
R_{Swq}	1	0.000625	0.000625	0.056561	0.81799418			
R_{Swc}	1	0.010125	0.010125	0.91629	0.36648053			
R_{Cl} * R_{Swl}	1	0.007225	0.007225	0.653846	0.44212181			
e	8	0.0884	0.01105					
T	15	1.249375	1.172025					100
(e)	13	0.140125	0.010779		0.01077885			11.21561

Figure s 7 (a) and (b) show the contour map of V_D obtained by the experiment and that obtained by Eq. (3), respectively. The experimentally obtained V_D is nearly approximated by Eq. (3). From the obtained results, the following conclusions are obtained. An RF-ICP flow is produced easily and kept stable in a DC-RF hybrid plasma flow by keeping the central-gas ratio lower and the swirl-gas ratio higher. The central-gas ratio should be controlled at first. Much power is required rather to produce an RF-ICP flow in a DC-RF hybrid plasma flow system than to maintain a stable RF-ICP flow in it.

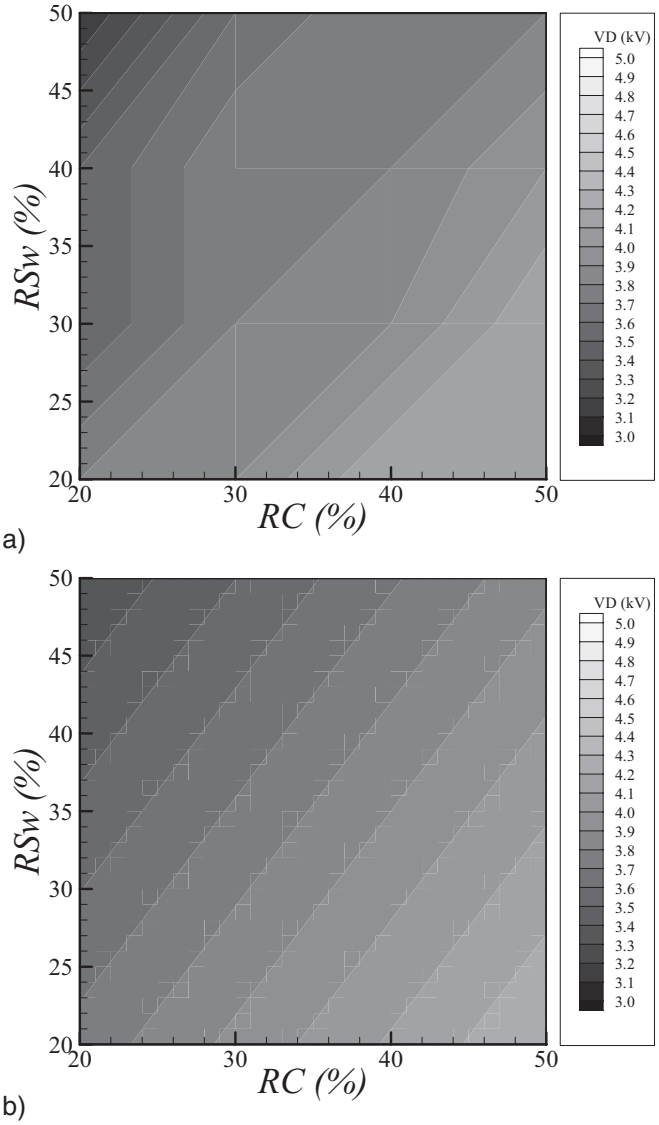

Figure 7 (a) Contour map of V_D obtained by the experiment. (b) Contour map of V_D obtained by Eq. (3).

37.3.3 Upper Limit of Injected Nitrogen Flow Rate

Tables 4 (a) and (b) show the upper limit of injected nitrogen flow rate λ_C (l/min) for each operating condition and the ANOVA for λ_C, respectively, when nitrogen is injected with the central gas. The upper limit of injected nitrogen flow rate is

increased by decreasing the central-gas ratio but increasing the swirl-gas ratio, particularly when the central-gas ratio is 20% and the swirl-gas ratio is 50%. This arises from the fact that the net effect of the specific enthalpy of a DC plasma jet is increased by decreasing the central-gas ratio. Consequently, a large nitrogen flow rate can be injected without suppressing a DC-RF hybrid plasma flow. In addition, the upper limit of injected nitrogen flow rate is increased by increasing the swirl-gas ratio owing to the stabilizing effect of the swirl gas. The effects of the central-gas ratio and the swirl-gas ratio on the upper limit of injected nitrogen flow rate are nearly equal, as shown in Table 4 (b). The error's effect in Table 4 (b) is rather large because the large effect of R_{Cq} is neglected in Table 4 (b). The following equation is obtained by the regression analysis for Tables 4 (a) and (b).

$$L_C = 1.82 - 5.18 \times 10^{-2} (R_C - 35) + 5.23 \times 10^{-2} (R_{Sw} - 35) - 3.97 \times 10^{-3} (R_C - 35)(R_{Sw} - 35) \quad (4)$$

Table 4 (a) Upper limit of injected nitrogen flow rate for each operating condition when nitrogen is injected with the central gas, (b) ANOVA upper limit of injected nitrogen flow rate when nitrogen is injected with the central gas

t_R (s)		R_{Sw}(%)			
		20	**30**	**40**	**50**
R_C	20	1.3 (l/min)	2	2.6	6
(%)	30	1.2	1.4	1.8	2
	40	1.2	1.2	1.5	1.6
	50	1.1	1.1	1.5	1.6

	f	***S***	***V***	***F0***	***F***	***F0′***	***F′***	ρ(%)
R_{Cl}	1	5.356125	5.356125	11.17198	0.01019397	10.15716	0.00781850	25.40329
R_{Cq}	1	1.755625	1.755625	3.661939	0.09201641			
R_{Cc}	1	0.190125	0.190125	0.396569	0.54642685			
R_{Swl}	1	5.460125	5.460125	11.3889	0.00971701	10.35438	0.00738425	25.89655
R_{Swq}	1	0.525625	0.525625	1.096365	0.32566684			
R_{Swc}	1	0.021125	0.021125	0.044063	0.83898338			
R_{Cl} * R_{Swl}	1	3.940225	3.940225	8.218647	0.02093098	7.4721	0.01814802	18.68789
e	8	3.8354	0.479425					
T	15	21.08438	17.7284					100
(e)	12	6.3279	0.527325		0.52732500			30.01227

Figure s 8 (a) and (b) show the contour map of λ_C obtained by the experimental results and that obtained by Eq. (4) respectively. Compared with Fig. 8 (a), Fig. 8 (b) seems to have the same tendency as that in Fig. 8 (a). However, when R_C and R_{Sw} are 20 and 50%, respectively, in Fig. 8 (a), the value of λ_C is much larger than the value in Fig. 8 (b) because of the large error's effect in Table 4 (b) due to the neglect of R_{Cq}.

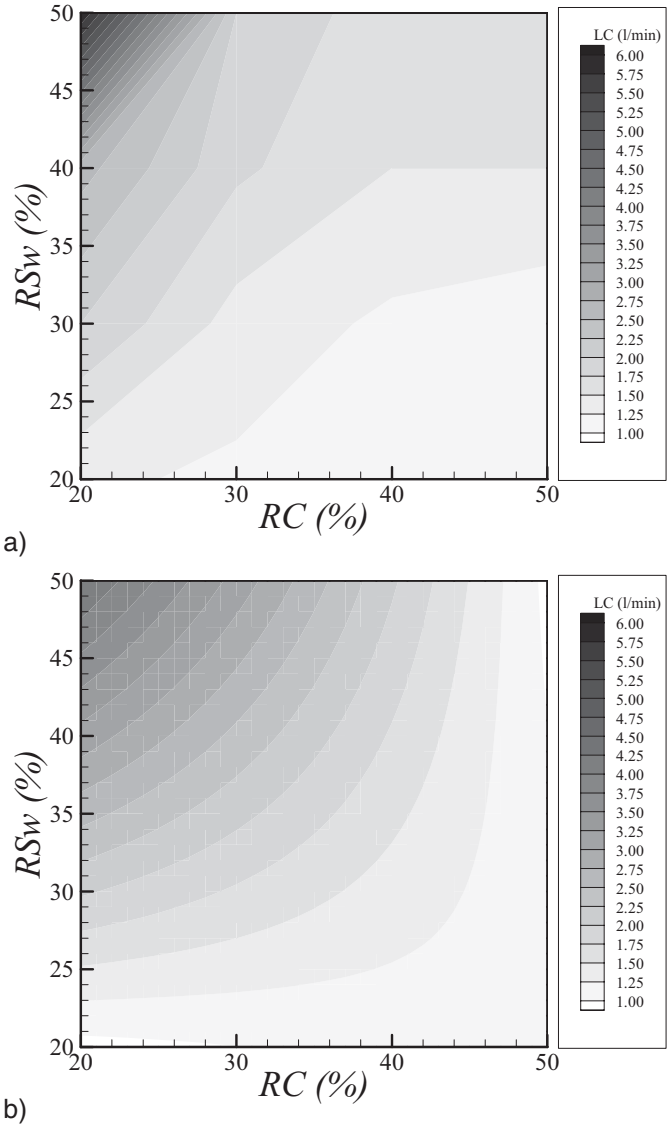

Figure 8 (a) Contour map of λ_C obtained by the experiment. (b) Contour map of λ_C obtained by Eq. (4).

Tables 5 (a) and (b) show the upper limit of injected nitrogen flow rate λ_{Sw} (l/min) for each operating condition and the ANOVA for λ_{Sw} respectively, when nitrogen is injected with the sheath gas. Compared Table 5 (a) with Table 4 (a), λ_{Sw} is much smaller than λ_C. The main reason for this depends on the location where nitrogen gas is dissociated in a DC-RF hybrid plasma flow. An RF-ICP flow is kept stably by high electrical density in the skin region near the side wall in the RF coil. If nitrogen

is mixed with the sheath gas and injected into the skin region directly, it takes much energy to dissociate nitrogen from an RF-ICP flow in that region. As a result, an RF-ICP flow becomes unstable. When nitrogen is injected with the central gas, the dissociation occurred is much smaller than that when nitrogen is injected with the sheath gas. Therefore, nitrogen should be injected with the central gas to inject a large amount of nitrogen. The effects of the central gas and the swirl gas in Tables 4 (b) are drastically different from those in Table 5 (b). This is physically reasonable because the effect of the central gas becomes stronger when nitrogen is injected with the central gas, and the effect of the swirl gas becomes stronger when nitrogen is injected with the sheath gas. The error's effect in Table 5 (b) is very large because the neglected effect of R_{Swq} on λ_{Sw} is large. The following equation is obtained by regression analysis for Tables 5 (a) and (b).

$$L_{Sw} = 0.29 - 2.15 \times 10^{-3} (R_C - 35) + 4.05 \times 10^{-3} (R_{Sw} - 35) \quad (5)$$

Table 5 (a) Upper limit of injected nitrogen flow rate for each operating condition when nitrogen is injected with the sheath gas, (b) ANOVA upper limit of injected nitrogen flow rate when nitrogen is injected with the sheath gas

t_R (s)		R_{Sw}(%)			
		20	**30**	**40**	**50**
R_C	20	0.22 (l/min)	0.28	0.46	0.36
(%)	30	0.22	0.33	0.3	0.3
	40	0.21	0.29	0.3	0.33
	50	0.19	0.24	0.29	0.32

	f	*S*	*V*	*F0*	*F*	*F0′*	*F′*	ρ(%)
R_{Cl}	1	0.009245	0.009245	4.581269	0.06473709	4.817034	0.04694580	13.79851
R_{Cq}	1	0.0004	0.0004	0.198216	0.66796520			
R_{Cc}	1	0.000605	0.000605	0.299802	0.59894574			
R_{Swl}	1	0.032805	0.032805	16.25619	0.00377807	17.09279	0.00117512	48.96269
R_{Swq}	1	0.007225	0.007225	3.580278	0.09510885			
R_{Swc}	1	0.00032	0.00032	0.158573	0.70088990			
R_{Cl} * R_{Swl}	1	0.000256	0.000256	0.126858	0.73092232			
e	8	0.016144	0.002018					
T	15	0.067	0.052874					100
(e)	13	0.02495	0.001919		0.00191923			37.23881

Figure s 9 (a) and (b) show the contour map of λ_{Sw} obtained by the experiment and from Eq. (5), respectively. As compared with Fig. 9 (a), Fig. 9 (b) shows the different tendency when the central-gas ratio is low and the swirl-gas ratio is high, because of the large error's effect in Table 5 (b). From these obtained results, the reactive gas should be injected with the central gas and the central-gas ratio should be kept low. The swirl-gas ratio should be kept high so as to inject as much reactive gas as possible.

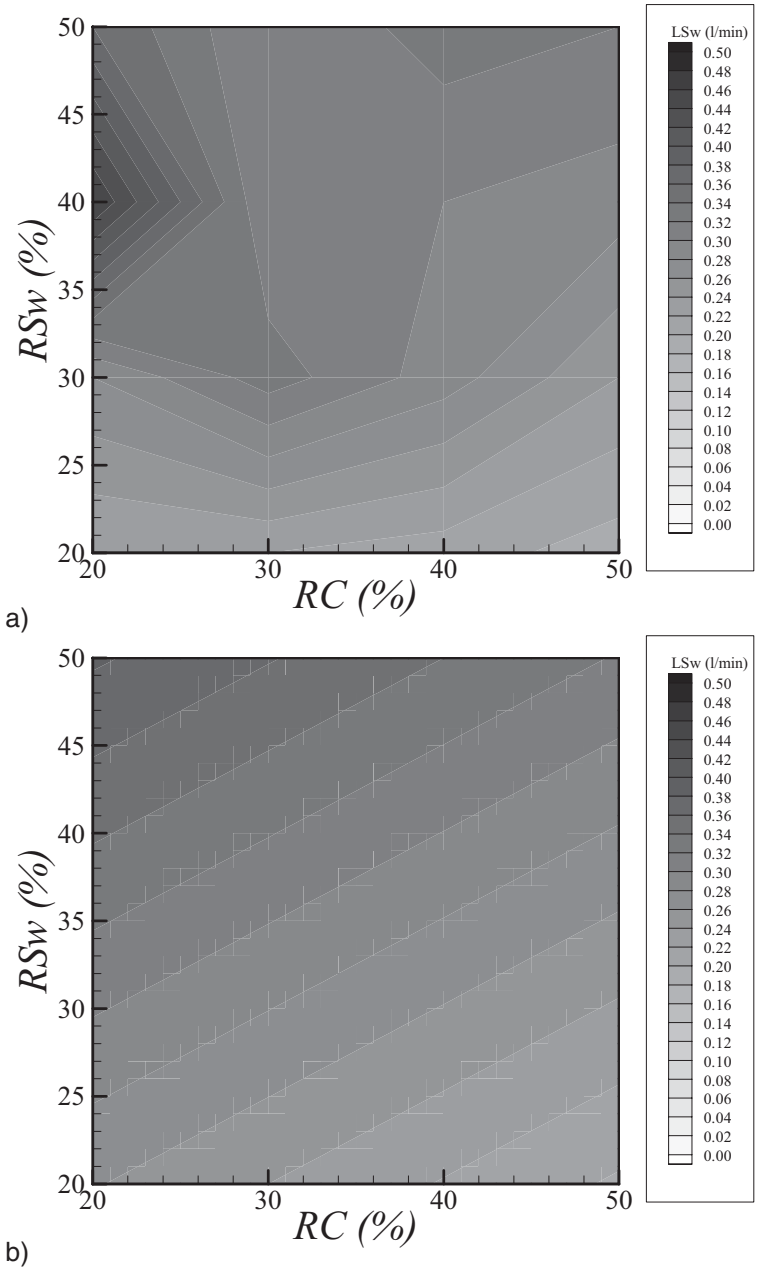

Figure 9 (a) Contour map of λ_{Sw} obtained by the experiment. (b) Contour map of λ_{Sw} obtained by Eq. (5).

37.3.4
Downstream-Gas Temperature

Tables 6 (a) and (b) show the downstream-gas temperature T_g (K) in the central region for each operating condition and the ANOVA for T_g, respectively. The downstream-gas temperature is increased by decreasing the central-gas-flow ratio and decreasing the swirl-gas ratio. The central gas gives the stronger effect on downstream-gas temperature in the central region than that of the swirl gas. This comes from the fact that a net effective of the specific enthalpy of a DC plasma jet is increased with decreasing the central-gas-flow ratio, and then a DC-RF hybrid plasma flame is elongated effectively in the axial direction. Equation (6) is obtained by regression analysis from the results in Tables 6 (a) and (b).

$$T_g = 1.31 \times 10^3 - 3.61(R_C - 35) + 1.32 \times 10^{-1}\,(R_C - 35)^2 - 2.31(R_{Sw} - 35) - 1.94 \times 10^{-1}(R_C - 35)(R_{Sw} - 35) \quad (6)$$

Table 6 (a) Downstream-gas temperature in the central region for each operating condition, (b) ANOVA for downstream-gas temperature

t_R (s)		R_{Sw}(%)			
		20	**30**	**40**	**50**
R_C	20	1474.808 (K)	1406.748	1307.66	1307.66
(%)	30	1345.80746	1345.807	1307.66	1280.681
	40	1280.68088	1280.681	1269.948	1253.907
	50	1269.94761	1269.948	1269.948	1269.948

	f	*S*	*V*	*F0*	*F*	*F0′*	*F′*	ρ(%)
R_{Cl}	1	26136.31	26136.31	71.25601	0.00002961	76.66909	0.0000274	49.47403
R_{Cq}	1	2795.627	2795.627	7.621781	0.02464593	8.200782	0.01541425	5.291908
R_{Cc}	1	349.1681	349.1681	0.951945	0.35780075			
R_{Swl}	1	10698	10698	29.1662	0.00064557	31.38186	0.00015985	20.25049
R_{Swq}	1	39.18681	39.18681	0.106836	0.75216351			
R_{Swc}	1	427.1634	427.1634	1.164585	0.31197544			
R_{Cl} * R_{Swl}	1	9448.529	9448.529	25.75974	0.00095857	27.71662	0.00026650	17.88534
e	8	2934.356	366.7945					
T	15	52828.34	50260.78					100
(e)	11	3749.874	340.8976		340.89763208			7.098224

Figure s 10 (a) and (b) show the contour map of T_g obtained by the experiment and that obtained by Eq. (6), respectively. The downstream-gas temperature in the central region is approximated accurately by Eq. (6) because the error's effect in Table 6 (b) is small.

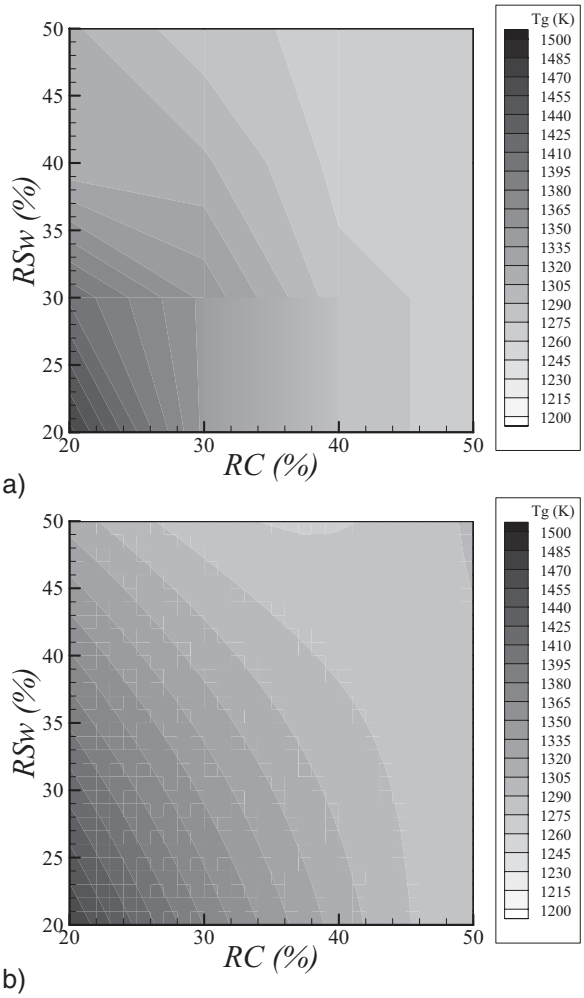

Figure 10 (a) Contour map of T_g obtained by the experiment. (b) Contour map of T_g obtained by Eq. (6).

Figure 11 shows the radial distribution of the downstream-gas temperature when the central-gas-flow ratio is kept at 20% and the swirl gas flow ratio is increased from 20 to 50% by 10%. The radial distribution in the downstream-gas temperature becomes uniform with increasing swirl-gas ratio, because convective heat transfer in the radial direction is enhanced by strong centrifugal force of the swirl gas flow. Then, the maximum temperature in each distribution is decreased by increasing the swirl-gas ratio and downstream-gas temperature becomes uniform in the radial direction. Based on the previous results and discussions, the central-gas-flow ratio should be controlled at first to increase the downstream-gas temperature effectively. The downstream-gas temperature is increased by decreasing the central-gas-flow

ratio and the swirl-gas ratio. However, the swirl-gas ratio should be increased in some cases despite the decrease in maximum temperature in the downstream region, because temperature uniformity in the downstream region is also one of the important parameters for particle processing.

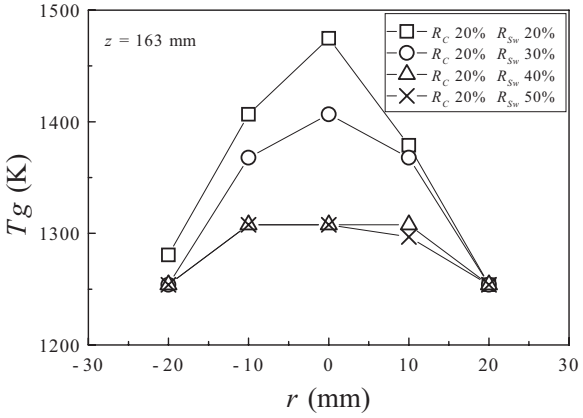

Figure 11 Radial distribution of the downstream-gas temperature.

37.3.5 Optimization

Table 7 shows how to control the central-gas-flow ratio and the swirl-gas ratio to optimize the operating conditions for each output parameter; where the central-gas-flow ratio and the swirl-gas ratio are controlled to increase particle residence time, decrease the appearance voltage of an RF plasma flow, decrease the disappearance voltage of an RF plasma flow, increase the upper limit of injected nitrogen and increase the downstream-gas temperature. For the downstream-gas temperature, the asterisk indicates that the swirl-gas ratio should be decreased when an increase in maximum temperature in the downstream region is required. On the contrary, the swirl-gas ratio should be increased when temperature uniformity in the downstream region is required according to an object. Then, an operating condition can be adjusted according to Table 7. Controllability of a DC-RF hybrid plasma flow system is confirmed as shown in Table 7, because every output, except for the downstream-gas temperature, is improved by decreasing the central-gas ratio and increasing the swirl-gas ratio.

Figure s 12 (a) and (b) show the plasma flow under the normal operating condition and that under the optimized operating condition in which the maximum temperature in the downstream central region is achieved. Compared with Fig. 12 (a), a remarkable plasma elongation is observed in Fig. 12 (b). Figure 12 (c) shows the plasma flow under the optimized operating condition in which temperature uniformity of the downstream-gas temperature is achieved. Though this figure looks

almost the same as Fig. 12 (a), there is the uniform high-temperature region in the downstream region.

Table 7 How to control the central-gas-flow ratio and the swirl-gas ratio to optimize the operating condition for each output parameter

	t_R (s)	V_A (kV)	V_D (kV)	L_C (l/min)	L_{Sw} (l/min)	T_g (K)
R_C	–	–	–	–	–	–
R_{Sw}	+	+	+	+	+	*

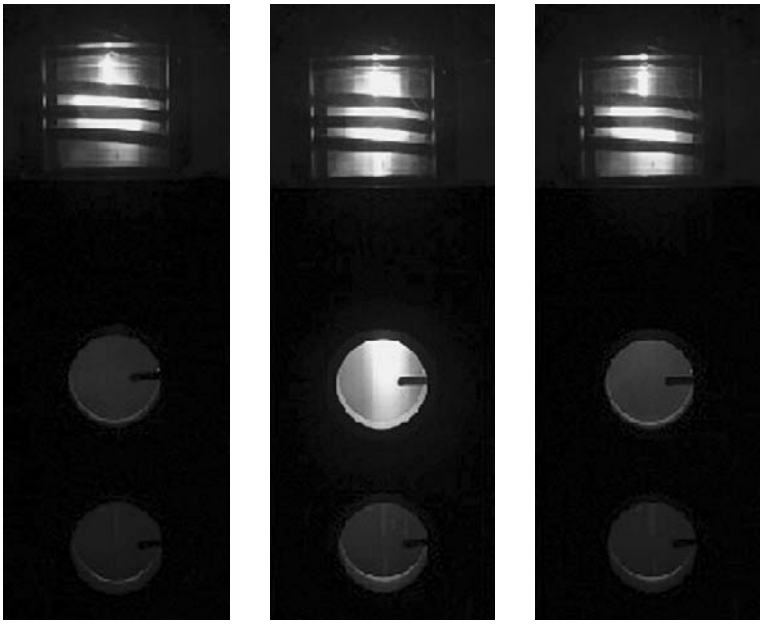

(a) (b) (c)

Figure 12 Plasma flow in each condition. (a) $R_C = 50\%$, $R_{Sw} = 50\%$, (b) $R_C = 20\%$, $R_{Sw} = 20\%$, (c) $R_C = 20\%$, $R_{Sw} = 50\%$.

37.4 Conclusion

Statistical analysis is carried out effectively to optimize the operating conditions of a DC-RF hybrid plasma flow system for particle processing. The effects of the input parameters on each output parameter are clarified by actual values. The important input parameters are identified by statistical analysis. The relationship between the input parameters and each output parameter are shown in the equation by regression analysis. The obtained results are as follows:

1. The particle residence time increases an decrease in the central-gas ratio but increasing the swirl-gas ratio. In particularly, the control of the central-gas ratio is important for the particle residence time.
2. By keeping the central-gas ratio lower and the swirl-gas ratio higher, an RF-ICP flow can be produced easily and can be kept stable in a DC-RF hybrid plasma flow system.
3. Nitrogen gas should be injected with the central gas rather than the swirl gas as a reactant. The injection limit of nitrogen gas flow rate increases with decreasing central-gas ratio but increasing swirl-gas ratio.
4. Downstream-gas temperature is increased with decreasing central-gas ratio and the swirl-gas ratio. However, the swirl-gas ratio should be increased when temperature uniformity in the downstream region is required.
5. Controllability of a DC-RF hybrid plasma flow system is achieved using the statistical analysis because almost all output parameters are improved by the same operation.

Acknowledgements

This work was partly supported by a grant-in-aid for Scientific Research (B) from the Japan Society for Promotion of Science (2001, 2002) and Institute of Fluid Science, Tohoku University, Japan. We would like to give our sincere thanks to senior technician Mr. K. Katagiri for his kind assistance in the experiment.

References

[1] M. I. Boulos, *IEEE Trans. Plasma Science*, **4** (1) (1976) 28–39.
[2] J. Lesinski and M. I. Boulos, *Plasma Chem. Plasma Process.*, **8** (2) (1988) 133–144.
[3] J. Kim, J. Mostaghimi and R. Iravani, *IEEE Trans. Plasma Sci.*, **25** (5) (1997) 1023–1028.
[4] M. Sugasawa, N. Kikukawa, N. Kayano and T. Kimura, *Proc. 15th Int. Symp. Plasma Chem.*, **2** (2001) 691–696.
[5] P. Bushner, H. Ferfers, H. Schubert and J. Uhlenbusch, *Plasma Sources Sci. Technol.*, **6** (1997) 450–459.
[6] J. H. Park and S. H. Hong, *IEEE Trans. Plasma Sci.e*, **23** (4) (1995) 532–537.
[7] T. Yoshida, T. Tani, H. Nishimura and K. Akashi, *J. Appl. Phys.* , **54** (2) (1983) 640–646.
[8] T. Yoshida, T. Okada, H. Hamatani and H. Kumaoka, *Plasma Sources Sci. Technol.*, **1** (1992) 195–201.
[9] N. Yamaguchi, T. Hattori, K. Terashima and T. Yoshida, *Thin Solid Films*, **316** (1998) 185–188.
[10] T. Sakuta, N. Sakashita, T. Yoshida, T. Takashima and M. Miyamoto, *IEEE Trans. Plasma Sci.*, **25** (5) (1997) 1029–1033.
[11] K. Kawajiri, T. Sato and H. Nishiyama, *Surf. Coat. Technol.*, **171** (2003) 134–139.
[12] G. Taguchi, *Systems of Experimental Design*, Japanese Standards Association, vol. **1**, **2** (1976, 1977).
[13] N. Logothetis and H. P. Wynn: *Quality Through Design* (Clarendon Press, Oxford, 1994).
[14] K. Kawajiri, K. Ramachandran and H. Nishiyama, *Proc. 16th Int. Symp. on Plasma Chem.*, no. ISPC-536 (CD-ROM).
[15] P. Saravanan, V. Selvarajan, S. V. Joshi and G. Sundararajan, *J. Appl. Phys.*, **34** (2001) 131–140.
[16] J. R. Mawdsley, Y. J. Su, K. T. Faber and T. F. Bernecki, *Mater. Sci. Eng.*, **308** (2001) 189–199.